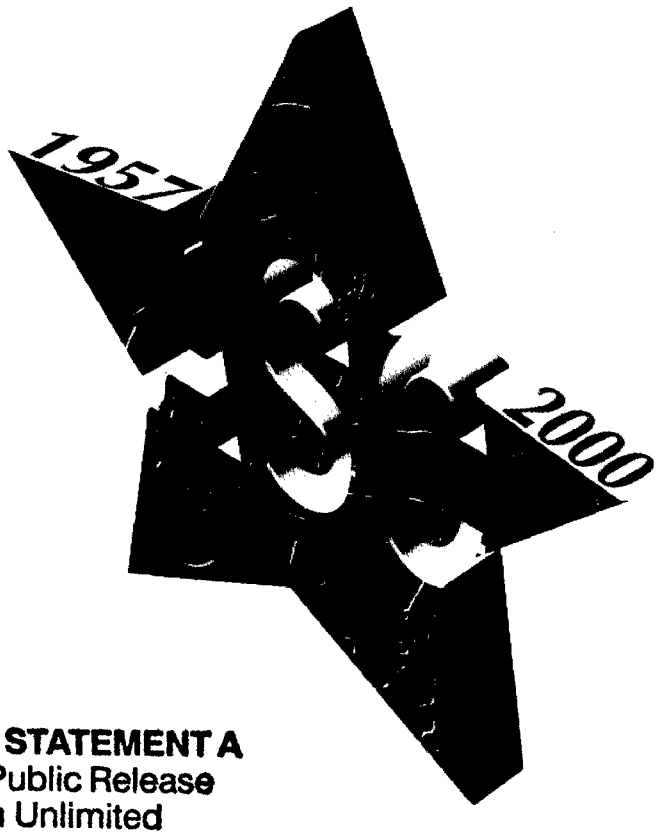
22nd Army Science Conference

"Accelerating the Pace of the Transformation to the Objective Force"



DISTRIBUTION STATEMENT A
Approved for Public Release
Distribution Unlimited

20010510 008

11-13 December 2000
Baltimore, Maryland

SUMMARY DIGEST

This document has been approved release to the public domain; its distribution is unlimited.

SUMMARY DIGEST

22ND ARMY SCIENCE CONFERENCE
BALTIMORE, MARYLAND

11-13 DECEMBER 2000



Sponsored by the
Assistant Secretary of the Army
(Acquisition, Logistics and Technology)

CONTENTS OF THE SUMMARY DIGEST

Session A - Advanced Materials and Manufacturing

AO1 **Metal Matrix Composites for Ordnance Applications** 3
C. P. R. Hoppel, *J. H. Beatty, J. S. Montgomery, J. M. Bender, and T. A. Bogetti, U.S. Army Research Laboratory*

AO2 **Rate Dependent Properties of Silane-Based Sizing Interphase in Glass-Fiber Composites for Armor Applications** 5
R. E. Jensen and ***S. H. McKnight***, *U.S. Army Research Laboratory; G. R. Palmese, Drexel University*

AO3 **Novel Elastomeric Membrane for Soldier Protective Clothing** 7
D. M. Crawford, *J. M. Sloan, N. C. Beck Tan, and E. Napadensky, U.S. Army Research Laboratory; Q. Truong, U.S. Army Soldier and Biological Chemical Command*

AO4 **Electrospun Nanofibrous Membranes of Photovoltaic Dyes and Nanocrystalline TiO_2 Materials** 9
Kris J. Senecal, *David Ziegler, Margaret Auerbach, and Lynne Samuelson, U.S. Army Soldier and Biological Chemical Command*

AO5 **The Elimination of Hazardous Chemicals in the Preparation of High Performance Transparent Armor for Soldier Protection** 11
Douglas J. Kiserow, *U.S. Army Research Laboratory; George W. Roberts, North Carolina State University; Stephen M. Gross and Joseph M. DeSimone, University of North Carolina*

AP1 **Advanced Magnetic Materials for Curie-Temperature Controlled Bonding** 13
E. D. Wetzel *and B. K. Fink, U.S. Army Research Laboratory; Y. F. Li and J. Q. Xiao, University of Delaware*

AP2 **Improving the Rod-Penetration Algorithm for Tomorrow's Armors** 15
Steven B. Segletes, *Rick Grote, and John Polesne, U.S. Army Research Laboratory*

AP3 **Development of Techniques for Strengthening Deteriorated Concrete Using Bacterially-precipitated and Enzymatically-precipitated Mineral Phases** 17
D. B. Ringelberg, *C. A. Weiss, Jr., and P. G. Malone, U.S. Army Environmental Research and Development Center*

AP4 **Toughened Interpenetrating Polymer Networks (IPNs) for Electron-Beam Cure of Composites and Adhesives** 19
James M. Sands, *Steven H. McKnight, and Bruce K. Fink, U.S. Army Research Laboratory; Giuseppe R. Palmese, Drexel University*

AP5 **Temperature-Dependent Energy Loss in ALON** 21
Bruce J. West, *U.S. Army Research Laboratory*

AP6 **Thermo-Mechanical Analyses of Dynamically Loaded Viscoelastic Rubber Cylinders** 23
Arthur R. Johnson *and Tzi-Kang Chen, U.S. Army Research Laboratory*

AP7 **Effects of Processing on Connectivity of Ferroelectric $Ba_{0.55}Sr_{0.45}TiO_3$/MgO Composite Structures** 25
Jennifer Synowczynski *and Bonnie Gersten, U.S. Army Research Laboratory*

AP8 **Laser Pulse Heating Simulation of Firing Damage on Coated Gun Bore Surfaces** 27
P. J. Cote, *G. Kendall, and M. Todaro, U.S. Army Tank-automotive and Armaments Command-Armament RD&E Center, Benét Laboratories*

AP9 **Nafion® Membranes: A Structural Evaluation for Advancement of the Materials Used in Chem/Bio Protective Clothing and Direct Methanol Fuel Cells** 29
S. F. Trevino, *Sandra K. Young, and Nora C. Beck Tan, U.S. Army Research Laboratory*

AP10 **The Development of an Affordable Manufacturing Process for Multifunctional Structural Armor** 31
***Shawn M. Walsh**, Elias J. Rigas, William A. Spurgeon, and Walter N. Roy, U.S. Army Research Laboratory; Dirk Heider and Jack Gillespie, University of Delaware*

Session B - Microelectronics and Photonics

B01 **Development of Advanced Interband Cascade Lasers for IRCM Applications** 35
***John L. Bradshaw**, John D. Bruno, and John T. Pham, U.S. Army Research Laboratory; Donald E. Wortman and Rui Q. Yang, Maxion Technologies Inc.*

BO2 **Single Step Microlens-Antireflective Structures for Infrared Focal Plane Arrays** 37
*M. R. Banish and D. B. Chenault, SY Technology, Inc.; D. R. Brown, MEMS Optical LLC; A. J. Stoltz, E-OIR Measurements, Inc.; M. Martinka, J. H. Dinan, and **J. D. Benson**, U.S. Army Night Vision Electronic Sensors Directorate; P. R. Boyd, U.S. Army Research Laboratory*

BO3 **Force Detected Magnetic Resonance of CaF_2 and GaAs** 39
***Kent Thurber**, John A. Marohn, and Doran D. Smith, U.S. Army Research Laboratory; Lee Harrell, U.S. Military Academy; Raul Fainchtein, Johns Hopkins University*

BO4 **Evaluation of the High Field Transport Properties of Wide Bandgap Semiconductor Materials and Devices for Future Combat Systems** 41
***M. Wraback** and H. Shen, U.S. Army Research Laboratory; J. C. Carrano, U.S. Military Academy; T. Li, C. Collins, J. C. Campbell, D. J. H. Lambert, U. Chowdhury, M. M. Wong, and R. D. Dupuis, The University of Texas at Austin; M. J. Schurman and I. T. Ferguson, EMCORE Corporation*

BO5 **Measurement of Fundamental Parameters and Control of Coherent Phenomena in Bulk and Multiple Quantum Well III-Nitride Materials** 43
***Henry O. Everitt**, U.S. Army Research Laboratory; Umit Ozgur, Chang Won Lee, and H. Craig Casey, Jr., Duke University; Michael J. Bergmann and Amber Abare, CREE Research; Stacia Keller and Stephen P. DenBaars, University of California; John F. Muth, North Carolina State University*

BP1 **Fundamental Loss Rates in Solid-State Lasers** 45
***Michael E. Crenshaw** and Charles M. Bowden, U.S. Army Aviation and Missile Command*

BP2 **High-Bandwidth Multi-Channel Optoelectronic Interconnects for Smart Sensors and Sensor Fusion** 47
***G. J. Simonis**, J. J. Liu, W. Lawler, B. Riely, W. Chang, P. H. Shen, M. Taysing-Lara, P. Newman, and Z. Kalayjian, U.S. Army Research Laboratory; B. Koley and M. Dagenais, University of Maryland; A. Andreou, Johns Hopkins University*

BP3 **Asymmetry in Semiconductor MSM Detectors and Its Implication in FM/cw Ladar Systems** 49
***Paul H. Shen**, Michael Stead, Monica Taysing-Lara, William Ruff, and Barry Stann, U.S. Army Research Laboratory; Parvez Uppal, Sanders, A Lockheed Martin Company*

BP4 **Integrated, Optically-Pumped, Lossless Splitters: Progress and Challenges** 51
***David M. Mackie**, U.S. Army Research Laboratory; Hong Koo Kim, University of Pittsburgh; Colleen M. Fitzpatrick, Rice Systems*

BP5 **Dielectrics for High-Temperature Silicon Carbide Power Devices** 53
***C. J. Scozzie**, A. J. Lelis, F. B. McLean, and B. R. Geil, U.S. Army Research Laboratory*

BP6 **Smart Electronic Muzzle Reference Light Source** 55
***Mark Johnson** and Paul Cote, U.S. Army Tank-automotive and Armaments Command-Armament RD&E Center, Benét Laboratories*

BP7 **Tunneling of Semiconductor Laser Pulses Through Single Barriers** 57
***Mark Bloemer**, Charles Bowden, and Shawn Pethel, U.S. Army Aviation and Missile Command; Krishna Myneni, SAIC; Michael Scalora, Time Domain Corporation; Marco Centini, Giuseppe D'Aguanno, Concita Sibilia, and Mario Bertolotti, University of Rome*

Session C - Advanced Propulsion Technologies

CO1 **Formulation of a Free Jet Shear Layer Ignition Model for Application to Direct Injection Diesel Engines** 61
***Peter Schihl**, Walter Bryzik, and John Tasdemiroglu, U.S. Army Tank-automotive and Armaments Command RD&E Center*

CO2 **Rarefaction Wave Gun Propulsion** 63
***E. Kathe**, R. Dillon, S. Sopok, and M. Witherell, U.S. Army Tank-automotive and Armaments Command-Armament RD&E Center, Benét Laboratories; S. Dunn and D. Coats, Software Engineering Associates, Inc.*

CO3 **Computational Modeling of an Advanced Propulsion Technology: Numerical Simulation of Hypergolic Combustion in the AMCOM Vortex Engine** 65
***Michael J. Nusca**, U.S. Army Research Laboratory; R. Scott Michaels, U.S. Army Aviation and Missile RD&E Center*

CO4 **Smart Design of Insensitive High-Energy Materials Using Quantum Mechanical Calculations** 67
***Betsy M. Rice** and Jennifer J. Hare, U.S. Army Research Laboratory*

CO5 **Experiments to Define Plasma-Propellant Interactions** 69
***Richard A. Beyer** and Rose A. Pesce-Rodriguez, U.S. Army Research Laboratory*

CP1 **Atomistic Modeling of Nitrate Ester Based Gun Propellants** 71
***S. W. Bunte** and M. S. Miller, U.S. Army Research Laboratory; H. Sun, Molecular Simulations, Inc.*

CP2 **Density Functional Theory Characterization of DMAZ – A Potential Replacement for Hydrazine-Based Hypergolic Fuels** 73
***Michael J. McQuaid**, Betsy M. Rice, Cary Chabalowski, and Kevin McNesby, U.S. Army Research Laboratory; Darren Thompson, U.S. Army Aviation and Missile Command*

CP3 **A New Approach to Propellant Formulation: Minimizing Life-Cycle Costs Through Science-Based Design** 75
***Ronald D. Anderson**, Martin S. Miller, Anthony J. Kotlar, and Betsy M. Rice, U.S. Army Research Laboratory; Randall J. Cramer, Naval Surface Warfare Center*

CP4 **Effects of Pressure and Oxygen on Laser Ignition of XM39 Propellant** 77
*A. Cohen and **R. A. Beyer**, U.S. Army Research Laboratory*

CP5 **Wave-Rotor Research and Technology for Fuel-Efficient Gas Turbine Engines** 79
***Gerard E. Welch**, U.S. Army Research Laboratory*

CP6 **Simulations of Dynamic Behavior of Solid Explosives** 81
***Betsy M. Rice**, U.S. Army Research Laboratory; Dan C. Sorescu and Donald L. Thompson, Oklahoma State University*

CP7 **Improved Self-Recirculating Casing Treatment Concept for Enhanced Compressor Performance** 83
***Michael D. Hathaway**, U.S. Army Research Laboratory*

Session D - Biomedical and Behavioral Sciences

DO1 **Conceptual Skills and Adaptable Leaders** 87
***Jon J. Fallesen**, U.S. Army Research Institute for the Behavioral and Social Sciences*

DO2 **Training for Digital Proficiency** 89
Brooke Schaab *and J. Douglas Dressel, U.S. Army Research Institute for the Behavioral and Social Sciences*

DO3 **Development of Medical Countermeasures to Sulfur Mustard Vesication** 91
W. J. Smith *and M. C. Babin, U.S. Army Medical Research Institute of Chemical Defense; R. C. Kiser and R. P. Casillas, Battelle Memorial Institute*

DO4 **Control of Nerve Agent-Induced Seizures Is Critical for Neuroprotection and Survival** 93
T.-M. Shih, S. M. Duniho, and ***J. H. McDonough****, U.S. Army Medical Research Institute of Chemical Defense*

DO5 **Experimental Duplication of an Uncontrolled Hemorrhage in Swine By a Computer-Driven Feedback Control System** 95
Michael A. Dubick*, Jill L. Sondeen, Guy A. Drew, and Victor A. Convertino, U.S. Army Institute of Surgical Research*

DP1 **Cognitive Workload and Task Performance for Indirect Vision Driving with Fixed Flat Panel Displays** 97
Christopher C. Smyth*, U.S. Army Research Laboratory*

DP2 **Misson Rehearsal in Virtual Places** 99
Bob G. Witmer*, U.S. Army Research Institute for the Behavioral and Social Sciences; Wallace J. Sadowski, University of Central Florida; Neal M. Finkelstein, U.S. Army Simulation, Training, and Instrumentation Command*

DP3 **Rifle Shooting Accuracy During Recovery from Fatiguing Exercise** 101
Max A. Ito*, Marilyn A. Sharp, Richard F. Johnson, Donna J. Merullo, and Robert P. Mello, U.S. Army Research Institute of Environmental Medicine*

DP4 **Organizational Commitment and Military Readiness** 103
Paul A. Gade *and Ronald Tiggle, U.S. Army Research Institute; Walter Schumm, Kansas State University*

DP5 **Model for Predicting the Growth and Death of Pathogenic Bacteria in Food** 105
I. A. Taub*, E. W. Ross, and F. E. Feeherry, U.S. Army Soldier and Biological Chemical Command*

DP6 **Progress in Developing an Active Topical Skin Protectant** 107
E. H. Braue, Jr.*, S. T. Hobson, E. K. Lehnert, N. Lewis, C. R. Nalls-Braue, B. F. Doxzon, R. T. Simons, P. A. DiLeonardi, T. L. Nohe, and J. S. Graham, U.S. Army Medical Research Institute of Chemical Defense*

DP7 **Protection Against Chemical Agent-Induced, Seizure-Related Neuronal Cell Death** 109
Gerald P. H. Ballough, La Salle University; ***Margaret G. Filbert****, U.S. Army Medical Research Institute of Chemical Defense*

DP8 **Maximizing the Performance of U.S. Army Aviators in Sustained Operations: Dexedrine Is an Effective Fatigue Countermeasure** 111
J. A. Caldwell*, U.S. Army Aeromedical Research Laboratory*

DP9 **USAISR: Exploring Military Medical Applications of Laser Technology** 113
Ronald S. Walton*, Kathy L. Ryan, David G. Baer, and Albert T. McManus, U.S. Army Institute of Surgical Research*

DP10 **Internet-Based Training: Learner Performance and Instructional Feedback** 115
Robert A. Wisher*, U.S. Army Research Institute for the Behavioral and Social Sciences; Michael W. Freeman, U.S. Army Forces Command; Kenneth L. Morris, Battle Command Battle Laboratory*

Session E - Environmental and Geosciences

EO1 **Biodegradation of Decontaminating Solution 2 (DS2)** 119
Michael H. Kim, Geo-Centers, Inc; ***Joseph J. DeFrank****, U.S. Army Soldier and Biological Chemical Command*

EO2 **Science and Modernization in Hydroenvironmental Modeling Systems** 121
J. P. Holland*, J. F. Peters, and S. E. Howington, U.S. Army Engineer Research and Development Center; R. S. Maier, U.S. Army High Performance Computing Research Center*

EO3 **Isolation of an RDX-Degrading Acetogenic Bacterium from a Mixed Culture that Degrades TNT, RDX, and HMX Under Anaerobic Conditions** 123
Neal R. Adrian *and Clint M. Arnett, U.S. Army Engineer Research and Development Center*

EO4 **Bacterial Pathogens of Animals and Plants: Homologous Genetic Targets Within the Type III Secretion Systems** 125
Sheila J. Wood*, U.S. Army Soldier and Biological Chemical Command*

EO5 **Support for Rapid Environmental Assessment Using Airborne Lidar Technology** 127
J. L. Irish *and W. J. Lillycrop, U.S. Army Engineer Research and Development Center; R. W. Pope, U.S. Naval Meteorology and Oceanography Command*

EP1 **Non-Thermal Plasmas: A New Remediation Technology for Cleanup and Decontamination** 129
Michael J. Nusca*, Andrzej W. Miziolek, and Robert G. Daniel, U.S. Army Research Laboratory; Louis A. Rosocha, Los Alamos National Laboratory; John T. Herron and Robert E. Huie, National Institute of Standards and Technology; K. Urashima and J. S. Chang, McMaster University*

EP2 **Enhanced Coastal Trafficability Using Sand-Fiber Stabilization** 131
R. L. Santoni*, J. L. Tingle, and S. L. Webster, U.S. Army Engineer Research and Development Center*

EP3 **Broad Bandwidth Lidar for Standoff Bioaersol Size Distribution Determination** 133
James B. Gillespie*, David L. Ligon, Paul M. Pellegrino, and Nicholas F. Fell, Jr., U.S. Army Research Laboratory*

EP4 **Passive Acoustic Localization in Atmospheric Turbulence: Experiment and Theory** 135
D. Keith Wilson *and Sandra L. Collier, U.S. Army Research Laboratory*

EP5 **Remote Sensing of Atmospheric Plumes with a Millimeter-Wave Radiometer** 137
Robert W. McMillan *and Osborne Milton, Jr., U.S. Army Space and Missile Defense Command*

EP6 **Evaluation of a High Resolution Wind Model Over a Complex Terrain Surface** 139
S. S. Chang, R. M. Cionco, ***J. J. Mercurio****, D. M. Garvey, C. C. Williamson, and G. Huynh, U.S. Army Research Laboratory*

EP7 **Meteorological Model Improvements on Simulated Artillery Round Targeting Accuracy** 141
Terry C. Jameson *and David Knapp, U.S. Army Research Laboratory*

Session F - Engineering Sciences

FO1 **Degradation of Components of Mustard Agent Filled Assembled Chemical Weapons in Laboratory and Pilot Scale Immobilized Cell Bioreactors** 145
M. A. Guelta*, N. A. Chester, and J. J. DeFrank, U.S. Army Edgewood Chemical Biological Center; S. Lupton and M. Koch, Honeywell International*

FO2 **A Physically Based Cone Penetration Interpretation Theory to Accurately Characterize Soils and Emplaced Granular Materials** 147
J. B. Johnson*, U.S. Army Engineer Research and Development Center*

FO3 **Exact Networks for Resonant Piezomagnetic Structures** 149
***Arthur Ballato**, U.S. Army Communications-Electronics Command*

FO4 **Development of a Rapidly Installed Breakwater for Army Force Projection** 151
***D. T. Resio**, J. E. Fowler, and J. A. Melby, U.S. Army Engineer Research and Development Center*

FO5 **Road Characterization for Vehicle Contract Specification** 153
***David J. Gorsich** and Milton Chaika, U.S. Army Tank-automotive and Armaments Command; Tzechien Sun, Wayne State University; Marc Genton, North Carolina State University*

FP1 **Computational Fluid Dynamic Modeling of Flow Over Fabric Covered Cylinders: Application to Protective Clothing** 155
***Phillip Gibson**, U.S. Army Soldier Systems Center*

FP2 **Nondestructive 2-D and 3-D Visualization of Interface Defeat Based Ballistic Impact Damage in TiC Ceramic Target Disk** 157
***J. M. Wells**, W. H. Green and N. L. Rupert, U.S. Army Research Laboratory*

FP3 **The Web Mapping Technology Initiative: A Public-Private Partnership** 159
***Dan Specht**, Bill Ryder, and Randy Swanson, U.S. Army Engineer Research and Development Center*

FP4 **Metal-Like Mechanical Properties of Confined Energetic Materials** 161
***Donald A. Wiegand**, Energetics and Warheads Division, Warheads, Energetics and Combat Support Armaments Center, Armament RD&E Center*

FP5 **Flexural Behavior of Reinforced Concrete Members Strengthened Using Mechanically Fastened Fiber Reinforced Polymer Plates** 163
***James C. Ray** and David W. Scott, U.S. Army Engineer Research and Development Center; Anthony J. Lamanna and Lawrence C. Bank, University of Wisconsin-Madison*

FP6 **The Cordless Kitchen: Logistical Reductions While Sustaining the Objective Force** 165
***D. W. Pickard**, U.S. Army Soldier and Biological Chemical Command; D. L. Brownell, E. C. Guyer, and K. G. Coumou, Yankee Scientific, Inc.*

FP7 **Alternative Energy Conversion Technologies** 167
***H. S. Coombe**, S. N. Matthews, and P. D. Shively, U.S. Army Communications-Electronics Command Research, Development and Engineering Center*

FP8 **Halon Replacements: Laboratory Studies and Field Testing of Advanced Fire Suppression Agents** 169
***K. L. McNesby**, R. T. Wainner, R. G. Daniel, A. W. Miziolek, R. R. Skaggs, P. J. Peregino, and A. E. Finnerty, U.S. Army Research Laboratory; W. R. Bolt and B. A. Sokolis, U.S. Army Aberdeen Test Center; S. J. McCormick, U.S. Army Tank-automotive and Armaments Command*

FP9 **Mooring Analyses of Rapidly Installed Breakwater (RIB) System for JLOTS** 171
***Z. Demirbilek** and C. E. Pollock, U.S. Army Engineer Research and Development Center; X. Chen and J. Zhang, Texas A&M University*

Session G - Force Protection

GO1 **Long-Range Propagation of Intense Ultra-Short Laser Pulses in Air** 175
***C. M. Bowden** and N. Aközbek, U.S. Army Aviation and Missile Research, Development, and Engineering Center*

GO2 **Development and Evaluation of Selectively Permeable Membranes for Lightweight Chemical Biological Protective Clothing** 177
***Eugene Wilusz** and Quoc T. Truong, U.S. Army Soldier and Biological Chemical Command*

GO3 **Recombinant Antibodies for the Detection of Bacteriophage MS2 and Ovalbumin** 179
Kevin P. O'Connell, *Peter A. Emanuel, Akbar S. Khan, and James J. Valdes, U.S. Army Soldier and Biological Chemical Command; Timothy J. Stinchcombe and Robert Shopes, Tera Biotechnology Corporation; Maha Khalil and Mohyee E. Eldefrawi, University of Maryland*

GO4 **Putative Role of Proteases and Other Inflammatory-Neuronal Molecules in the Toxicity of Nerve and Blister Chemical Warfare Agents: Implications for Universal Medical Countermeasures** 181
F. M. Cowan, *C. A. Broomfield, D. E. Lenz, and W. J. Smith, U.S. Army Medical Research Institute of Chemical Defense*

GO5 **Demonstration of a Crashworthy Composite Fuselage Concept** 183
Karen E. Jackson *and Edwin L. Fasanella, U.S. Army Research Laboratory; Norman F. Knight, Jr., Veridian MRJ Technology Solutions*

GP1 **A Consistent Approach to EM Protection of Digital C4I in Future Joint Operations** 185
Robert Pfeffer, *U.S. Army Nuclear and Chemical Agency*

GP2 **Phosphotriesterase Mutants with Enhanced VX and G-Agent Activity** 187
Steven P. Harvey, *Jan E. Kolakowski, and Joseph J. DeFrank, U.S. Army Edgewood Chemical Biological Center; Misty Chen-Goodspeed, Miguel Soborb, and Frank M. Raushel, Texas A&M University*

GP3 **Detection and Identification of Chemical Agents in Water Using Surface Enhanced Raman Spectroscopy (SERS) on Gold and Silver Doped Sol-Gels** 189
Steven Christesen *and Kate Ong, U.S. Army Edgewood Chemical Biological Center; M. Edward Womble, Raman Systems, Inc.; Richard Clarke and Ranjith Premasiri, Boston University*

GP4 **Changes in Gene Expression After Exposure to Organophosphorus (OP) Agents** 191
Jennifer W. Sekowski, *Kevin P. O'Connell, Akbar S. Khan, and James J. Valdes, U.S. Army Soldier and Biological Chemical Command; Maryanne Vahey and Martin Nau, Walter Reed Army Institute of Research; Maha Khalil and Mohyee E. Eldefrawi, University of Maryland*

GP5 **Impact of Winter Environment on Radar and Infrared Detection of Buried Landmines** 193
Gary Koh, *U.S. Army Engineer Research and Development Center*

GP6 **Peptide Epitopes and Mimetics** 195
Roy G. Thompson, *Akbar S. Khan, Ameneh Aresteh, and James J. Valdes, U.S. Army Soldier and Biological Chemical Command*

GP7 **Non-Intrusive Analysis of Chemical Agent Identification Sets (CAIS) Using a Portable Fiber-Optic Raman Spectrometer** 197
Steven Christesen, *Brian MacIver, Larry Procell, and Dave Sorrick, U.S. Army Edgewood Chemical Biological Center; Michael Carrabba and Job Bello, EIC Laboratories, Inc.*

GP8 **A Novel Compact High-Power-Microwave (HPM) *L*-Band Antenna** 199
Joseph R. Miletta, *William O'Keefe Coburn, Steve Kaplan, and Louis J. Jasper, U.S. Army Research Laboratory*

GP9 **The Potential Use of Submillimeter-Wave Spectroscopy as a Technique for Biological Warfare Agent Detection** 201
D. L. Woolard, *U.S. Army Research Laboratory; T. R. Globus, B. L. Gelmont, M. Bykhovskaia, J. L. Hester, T. W. Crowe, University of Virginia; A. C. Samuels, J. O. Jensen, J. L. Jensen, and W. R. Loerop, U.S. Army Soldier and Biological Chemical Command*

Session H - High-Performance Computing and Simulation

HO1 **Analysis and Optimization of Explicitly Parallel Scientific Codes with Combined Memory Consistency Modeling** 205
***Dixie M. Hisley**, U.S. Army Research Laboratory; Lori Pollock, University of Delaware*

HO2 **Rigorous Electromagnetic Modeling of Targets and Discrete Clutter in a Lossy Half-Space** 207
***Anders Sullivan**, U.S. Army Research Laboratory*

HO3 **Navier-Stokes Computations of Finned Missiles at Supersonic Speeds** 209
*David J. Haroldsen, U.S. Military Academy; **Walter B. Sturek, Sr.**, U.S. Army Research Laboratory*

HO4 **Coupled Macro-Micro Nonlinear Transient Asymptotic Expansion Homogenization Method on Scalable Computers for Heterogeneous Structures** 211
***Raju R. Namburu**, Peter W. Chung, and Rama R. Valisetty, U.S. Army Research Laboratory*

HO5 **Validation of the MUVES-S2 Computer Model Using Bradley Fighting Vehicle Live-Fire Test Data** 213
***Russell E. Dibelka**, William E. Baker, Richard Saucier, Theodore M. Muehl, Ricky L. Grote, U.S. Army Research Laboratory*

HP1 **Radar Signature Prediction for Army Ground Combat Vehicles** 215
***Ronald J. Chase**, U.S. Army Research Laboratory*

HP2 **Objective Force Command and Control: Course of Action Analysis** 217
***Barry Bodt**, Joan Forester, Charles Hansen, Eric Heilman, Richard Kaste, and Janet O'May, U.S. Army Research Laboratory*

HP3 **Methodology for Nonlinear Analysis of Thick-Section Composites** 219
***Travis A. Bogetti,** Christopher P. R. Hoppel, and Bryan A. Cheeseman, U.S. Army Research Laboratory*

HP4 **Virtual Modeling and Simulation of Military Ground Vehicles** 221
*Michael D. Letherwood and **David D. Gunter**, U.S. Army Tank-automotive and Armaments Command-Tank-automotive Research, Development and Engineering Center*

HP5 **Simulation with Learning Agents** 223
***Michelle Kalphat** and Robert Sottilare, U.S. Army Simulation and Training Command; Erol Gelenbe, Esin Seref, and Zhiguang Xu, University of Central Florida*

HP6 **ZNSFLOW Computational Fluid Dynamics Software for High Performance Computers** 225
***H. L. Edge**, J. Sahu, W. Sturek, J. Clarke, D. Pressel, M. Behr, K. Heavey, P. Weinacht, C. Zoltani, and C. Nietubicz, U.S. Army Research Laboratory*

HP7 **Use of Commodity Based Cluster for Solving CFD Aeropropulsion Applications** 227
***Issac Lopez**, U.S. Army Research Laboratory; Thaddeus J. Kollar, Integral System, Inc.; Richard A. Mulac, AP Solutions, Inc.*

HP8 **Multiresolution Representation of Urban Terrain by L_1 Splines, L_2 Splines and Piecewise Planar Surfaces** 229
***John E. Lavery**, U.S. Army Research Laboratory; David E. Gilsinn, National Institute of Standards and Technology*

HP9 **Computer Modeling to Defeat Chemical Erosion in Gun Tubes: Theoretical Chemistry Models of Gun Tube Erosion** 231
***C. F. Chabalowski**, G. Krasko, and M. M. Hurley, U.S. Army Research Laboratory; D. Sorescu, University of Pittsburgh; G. H. Lushington, PET-CCM*

Session I - Soldier Systems

IO1 **Backpack Packing Optimization for Reducing the Soldier's Energy Expenditure During Load Carriage** 235
L. Piscitelle and S. Yuhaski, U.S. Army Soldier and Biological Chemical Command

IO2 **From Theoretical Equations to Practical Army Applications: The High Performance of Polymer Electrolyte Membrane Fuel Cells for Individual Soldier and Future Combat System Applications** 237
Deryn Chu, Rongzhong Jiang, and Charles Walker, U.S. Army Research Laboratory; Kris Garnder, Richard Jacobs, and James Stephens, U.S. Army Communications-Electronics Command Research, Development and Engineering Center

IO3 **Human Performance Issues in Battlefield Visualization** 239
Michael J. Barnes and Linda G. Pierce, U.S. Army Research Laboratory; Christopher D. Wickens, University of Illinois; Mary T. Dzindolet, Cameron University; Jerzy W. Rozenblit, University of Arizona

IO4 **The Integration of Automatic Speech Recognition and Spatial Auditory Displays in High Noise, Stressful Tank Environments** 241
Ellen Haas, U.S. Army Research Laboratory; Robert Shankle, Applied Research Associates; Deborah Travers and Ted Wheeler, U.S. Army Test Center

IO5 **Solubility and Molecular Transport in a Permselective Fabric** 243
D. Rivin, N. S. Schneider, C. E. Kendrick, and P. Gibson, U.S. Army Soldier and Biological Chemical Command

IP1 **Biotechnology Techniques to Characterize and Enhance the Antibacterial Properties of a Novel Food Preservative** 245
Wayne S. Muller, Anthony Sikes, Alfred L. Allen, and Andy Senecal, U.S. Army Soldier and Biological Chemical Command

IP2 **Applications of Spatial Audio Displays for Use Within Attack Rotary Wing Aircraft** 247
Russell D. Shilling, Naval Postgraduate School; Russell L. Storms and Tomasz Letowski, U.S. Army Research Laboratory

IP3 **Dynamic Nutrition Model** 249
P. M. Short and I. A. Taub, U.S. Army Soldier and Biological Chemical Command; T. J. Doherty and V. E. Middleton, Simulation Technologies, Inc.; R. W. Hoyt, U.S. Army Research Institute of Environmental Medicine

IP4 **Spatial-Audio (3-D) Displays Improve Speech Communication in the Command and Control (C^2V) Vehicle** 251
Nancy Vause, Kim Abouchacra, Tomasz Letowski, and Eileen Resta, U.S. Army Research Laboratory

IP5 **Microencapsulated Phase Change Materials: Thermal Insulation Applications for Military Footwear** 253
Thomas L. Endrusick, William R. Santee and Richard R. Gonzalez, U.S. Army Research Institute of Environmental Medicine; James R. Brennick, U.S. Army Soldier Systems Center

IP6 **Exploring Novel Dehydration Technologies for Military Ration Development** 255
T. C. S. Yang, U.S. Army Soldier and Biological Chemical Command

IP7 **Methodologies for Determining the Impact of Situation Awareness on Individual and Small Unit Effectiveness of Dismounted Infantrymen** 257
Cynthia L. Blackwell, U.S. Army Soldier and Biological Chemical Command; Elizabeth Redden, U.S. Army Research Laboratory

Session J - Sensors and Information Processing

JO1 **Dual-Band FLIR ATR – Status and Value to FCS** 261
*Lipchen Alex Chan, **Nasser M. Nasrabadi**, and Sandor Z. Der, U.S. Army Research Laboratory*

JO2 **Using Magnetic Sensors in the Battlefield as Unattended Ground Sensors** 263
***A. S. Edelstein**, J. Fine, D. M. Hull, L. D. Flippen, Jr., N. Gokemeijer, and G. A. Fischer, U.S. Army Research Laboratory*

JO3 **Support Vector Machines and Target Classification** 265
***Robert E. Karlsen**, David J. Gorsich, and Grant R. Gerhart, U.S. Army Tank-automotive and Armaments Command*

JO4 **An Electronic Scanning Antenna Concept for Future Combat Systems** 267
*Eric Adler, Edward Burke, Robert Dahlstrom, **Steve Weiss**, and Wolfgang Wiebach, U.S. Army Research Laboratory*

JO5 **Polarization Imaging for Future Combat Systems** 269
***James D. Howe** and David M. Teale, U.S. Army Communications-Electronics Command; Miranda A. Miller, Robert V. Blumer, and Thomas E. Petty, TRW Systems & Information Technology; Mark A. Stevens, Lockheed Martin Missiles & Fire Control; Matthew H. Smith, University of Alabama*

JP1 **Paper Withdrawn** 271

JP2 **Microwave-Based Army Airdrop Ground Sensor** 273
*Nicholas Rosato, U.S. Army Soldier and Biological Chemical Command; **Joseph McGrath**, U.S. Army Research Institute of Environmental Medicine*

JP3 **Simple and Robust Radio Modulation Classification** 275
***Ananthram Swami** and Brian M. Sadler, U.S. Army Research Laboratory*

JP4 **Selective and Specific Personal Biosensors for Organophosphate Chemical Toxins Composed of Polyurethane Immobilized Enzymes** 277
***Richard K. Gordon**, Alper T. Gunduz, Shawn R. Feaster, and Bhupendra P. Doctor, Walter Reed Army Institute of Research*

JP5 **Linear Shift Invariance of the Atmospheric Turbulence Modulation Transfer Function for Infrared Target Acquisition Models** 279
***Keith Krapels**, Ronald Driggers, and Richard Vollmerhausen, U.S. Army Night Vision and Electronic Sensors Directorate; Norman S. Kopeika, Ben-Gurion University of the Negev; Carl Halford, University of Memphis*

JP6 **LIBS: An Emerging Chemical Sensor Technology for Field Use in Warfare and Peacetime Applications** 281
*Richard T. Wainner, Kevin L. McNesby, **Andrzej W. Miziolek**, and Russell S. Harmon, U.S. Army Research Laboratory; Patrick D. French, ADA Technologies, Inc.*

JP7 **Sensing Targets in Foliage Using Multiple Ladar Images Taken at Different Locations** 283
***John F. Dammann, Jr.**, U.S. Army Research Laboratory*

JP8 **Laser-Scanning Electronic Holography** 285
***Bradley W. Schilling** and Glen C. Templeton, U.S. Army Communications-Electronics Command Research, Development and Engineering Center*

JP9 **Development of a Clutter Complexity Measure** 287
*K. R. Namuduri and L. M. Kaplan, Clark Atlanta University; **N. N. Nasrabadi** and L. A. Chan, U.S. Army Research Laboratory*

Session A
Advanced Materials and Manufacturing

Chair
Dr. James W. McCauley
U.S. Army Research Laboratory

Co-Chair
Dr. Irwin A. Taub
U.S. Army Soldier and Biological Chemical Command

Keynote Address
Dr. Peter Bridenbaugh
Alcoa, Inc. (Retired)

THIS PAGE INTENTIONALLY LEFT BLANK

METAL MATRIX COMPOSITES FOR ORDNANCE APPLICATIONS

C. P. R. Hoppel*, J. H. Beatty, J. S. Montgomery, J. M. Bender, and T. A. Bogetti
U.S. Army Research Laboratory
Weapons and Materials Research Directorate
Aberdeen Proving Ground, MD 21005

Extended Abstract

Metal matrix composite (MMC) materials offer tremendous potential for the U.S. Army in applications such as lightweight projectiles and gun systems. For advanced artillery projectiles, MMCs can be used to manufacture shell bodies over 50% lighter than steel shells with 67% less parasitic volume than polymer matrix composite (PMC) shells, allowing more payload to be carried for a given weight and volume. Another potentially high payoff application for MMC technology is in the development of lightweight jackets for steel-lined gun barrels. MMC technology can allow the manufacture of gun barrels 50% lighter than steel barrels; or, where reduced barrel weight is not a priority (due to recoil concerns), MMCs can be used to make longer, stiffer, or higher pressure barrels at equivalent weights compared to current designs.

Figure 1 is an Ashby diagram that shows why continuous fiber-reinforced metal matrix composite materials are of immediate interest to the Army. The specific stiffness and the specific strength of the continuous alumina fiber-reinforced aluminum (labeled MMC) in the fiber-reinforced direction (labeled L) is superior to all conventional metals. While polymer matrix composites offer superior properties in the fiber direction, their poor properties in the transverse directions (labeled T) often requires designers to dilute these properties by altering the fiber architecture. For certain applications, the poor thermal conductivity and thermal stability at elevated temperature of polymer matrix composites also limits their utility in sustained high temperature applications (such as gun barrels). Therefore, MMCs provide unbeatable material properties when weight, temperature resistance, transverse properties, and space efficiency are critical concerns.

Despite the tremendous promise of continuous fiber-reinforced MMC materials, these materials have not been widely implemented by the Army for two main reasons: 1) relative cost, and 2) the lack of a reasonable production base. In general, the total production of these materials has been low—this has led to high costs (>$2,000/lb) and inconsistent material properties. However, the 3M Corporation recently socialized the establishment of a large-scale production base of continuous alumina fiber-reinforced aluminum MMCs at prices competitive with thermoplastic prepregs. This was done to affect commercial economies such as the electric power transmission line. This 3M program offers the affordable production base necessary for the Army to take advantage of this class of materials.

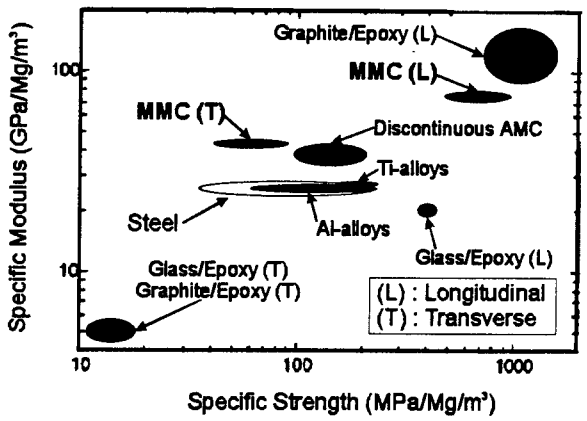


Figure 1. Specific Strength vs. Specific Stiffness of Engineering Materials.

To take full advantage of aluminum matrix composites, the Army is developing the specific modeling and processing technologies necessary to utilize them in ordnance applications. Specific failure assessment tools are being developed for MMCs subjected to ballistic loading conditions. These tools include a failure assessment methodology for multi-axial MMC laminates subjected to triaxial loading conditions. This work will extend the predictive tools developed for PMCs subjected to ballistic loading conditions (the LAMPAT suite of predictive tools).

The non-linear analysis methodology is demonstrated in Figure 2, which shows the tensile stress vs. strain predictions for an MMC with 65% Al_2O_3 fibers in an Al matrix with a [0/+45/0/-45]s architecture using both linear-elastic and nonlinear prediction techniques. For this type of loading in graphite fiber-reinforced PMCs, there would be very little difference between the linear and nonlinear predictions. However, in the MMC system, the +45 and –45 plies undergo shear yielding during the

loading, thus there is substantial difference in the response. This difference is critical for the design of artillery shells where design loads can be as high as 80% of the material strength.

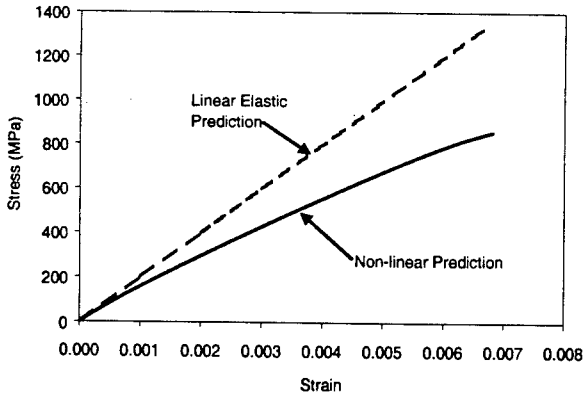


Figure 2. Comparison of stress vs. strain predictions for an MMC with a [0/+45/0/-45]s architecture using both linear-elastic and nonlinear prediction techniques.

If these design advantages are to be realized in actual components, processing of continuously reinforced metal matrix composites is vitally important. We have investigated methods of infiltrating continuous fiber preforms with molten aluminum matrices such as pressure infiltration and squeeze casting as well as consolidation of composite plies or pre-preg (pre-impregnated) materials. Consolidation processes are of interest because 3M manufactures infiltrated MMC wire for the power line industry as well as a fiber-reinforced tape. A low-cost method of consolidating wire or tape into structural components may allow more control of critical structural parameters (such as fiber straightness) than pressure infiltration or squeeze casting.

The three consolidation techniques that were evaluated included diffusion bonding, transient liquid phase bonding (TLPB) and soldering. Of these techniques TLPB offered the best combination of process characteristics that would allow fabrication of large structures from the MMC wire in a production environment.

The MMC technology has been demonstrated with the fabrication of an MMC artillery shell. The shell offered 57% weight reduction as compared to steel and 17% more volume than a PMC shell. In a static crush test (Figure 3), the shell supported an axial load that exceeds the peak launch loads for artillery projectiles.

This paper describes in detail the analysis and processing methodologies developed for continuous fiber reinforced MMCs and demonstrates their utility to the U.S. Army.

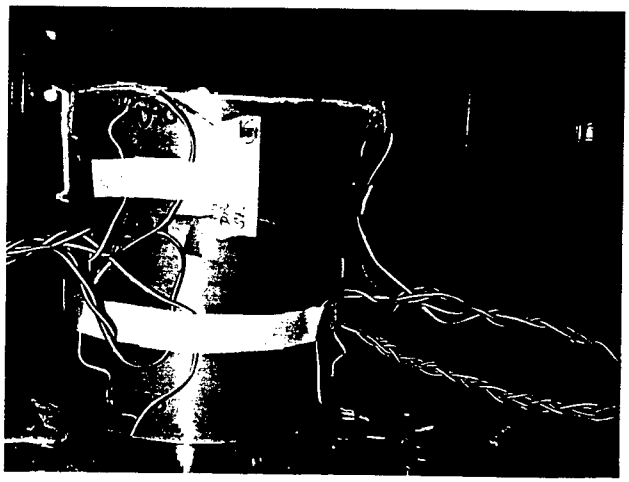


Figure 3. Crushed 155-mm MMC Cylinder.

REFERENCES

Bogetti, T. A., C. P. R. Hoppel, and B. P. Burns. "LAMPAT: A Software Tool for the Analysis and Design of Thick Laminated Composite Structures." ARL TR 890, APG, MD, 1995.

Bogetti, T. A., C. P. R. Hoppel, V. M. Harik, J. F. Newill, B. P. Burns, "Predicting the Nonlinear Response and Progressive Failure of Composite Laminates," *Composites Science and Technology*, accepted for publication, Sept. 2000.

Chou P. C., J. Carleone, and C. M. Hsu. "Elastic Constants of Layered Media." *J. of Compos. Materials*, vol. 6, pp. 80–93, 1972.

Deve, H. E. "Compressive Strength of Continuous Fiber Reinforced Aluminum Matrix Composites," *Acta. Mater.*, vol. 45, No. 12, pp. 5041-5046, 97.

Holloway, S. R. "Designing With Continuous Fiber Aluminum Matrix Composites." *Composite Manufacturing and Tooling 2000*, Society of Manufacturing Engineers, Newport Beach, CA. 25 Feb. 2000.

Pickett, F. "Technology for High Pressure Rocket Motors." *Proceedings of the 49th JANNAF Propulsion Meeting*, Tucson, AZ, Dec. 1999.

Ramamurty, U., F. W. Zok, F. A. Leckie, and H. E. Deve. "Strength Variability in Alumina Fiber-Reinforced Aluminum Matrix Composites," *Acta Mater*, vol. 45, no. 11, pp. 4603-4613, 1997.

Zok, F. W., M. Y. He, A. G. Evans, F. A. Leckie, and H. E. Deve. "Strength-Limited Design of Composite/Monolith Transitions in Metallic Structures." *Composites Part A*, vol. 28A, pp. 399-407, 1997.

RATE DEPENDENT PROPERTIES OF SILANE-BASED SIZING INTERPHASE IN GLASS-FIBER COMPOSITES FOR ARMOR APPLICATIONS

R. E. Jensen, S. H. McKnight*
Army Research Laboratory
Aberdeen Proving Ground, MD 21005

G. R. Palmese
Chemical Engineering Department
Drexel University
Philadelphia, PA 19104

ABSTRACT

Future Combat Systems have been envisioned that are lighter, faster, and more transportable than their existing counterparts. Glass-fiber reinforced composite materials are foreseen as a solution to meet both structural and ballistic requirements for emerging lightweight army ground vehicle applications. Macroscopic energy absorption mechanisms, such as delamination and matrix fracture, are small in comparison to micro-mechanical debonding. The response of the fiber-matrix interphase, which may only compose as little as one percent of the total volume of material, plays the most critical role with respect to the overall durability and mechanical performance and dominates these micro-mechanical debonding mechanisms. (Madhukar and Drzal, 1991; Lesko et al., 1994; Reifsnider, 1994) In addition to the well-known consequences of the fiber-matrix interphase on composite durability and fatigue performance, it is now believed that the interphase may control the ballistic properties of composites used in lightweight armor applications. The challenge in tailoring the interphase of composite armor is in enhancing the ballistic response while maintaining desired fatigue durability, as the materials design criteria for these two aspects of performance do not coincide. Thus the properties of the sized glass fiber-matrix interphase must be quantified to develop new sizings with optimal ballistic and structural performance.

The fiber-matrix interphase possesses physical, chemical, and mechanical properties differing from the glass fiber and matrix material. The fiber sizing, which is used to aid in the handling of the fibers during manufacture and enhance fiber wetting and adhesion with the matrix, is the usually the origin of the interphase. Sizings placed on glass fibers are complex multi-component systems that are applied during manufacture from aqueous solutions. Three important components found in commercial glass fiber sizings, which are applied from aqueous suspension, are a silane coupling agent, film former, and surfactant. Upon drying, the silane undergoes condensation at the fiber surface to form a crosslinked siloxane surface layer. It is widely known that a portion of this siloxane layer is extractable and can dissolve from the surface during composites processing. Additionally, a bound portion remains on the fiber that contributes to the interphase properties in the composite by forming an interpenetrating network structure with the matrix resin. Previous research at our labs has identified the amount and chemical composition of the bound and extractable portions of a commercial sizing using NMR, FTIR, and HPLC techniques. (Tanoglu, 2000) Preliminary mechanical testing of the fiber-matrix interphase at high strain rates, which mimic a ballistic event, revealed that the properties of the bound layer influence the elastic shear deformation of the interphase. These factors are critical to the ultimate strength and energy absorption properties in composite armor applications. (Tanoglu, 1998) Our work seeks to identify the rate dependent micro-mechanical properties of this bound siloxane interphase upon cure of the composite material.

Experimental study and measurement of the properties of the interphase have traditionally been very difficult, due to the small nano to micro volume scales of material present in an actual composite as well as masking by the fiber reinforcement. Here, the thermal and mechanical properties of the interphase were further examined using a novel approach of synthesizing a bulk model system. This synthesis is based on the aqueous sol-gel reaction of 3-glycidoxypropyltrimethoxysilane in the presence of a nonionic surfactant and epoxy film former. The aqueous phase of the sol-gel reaction was evaporated from the condensed sizing and the insoluble fractions of film former and surfactant were removed through Soxhlet extraction with acetone, leaving a large quantity of insoluble siloxane powder. The "bound" insoluble fraction of sizing has been shown to be composed of 73 % silane, 8 % film former, and 19 % surfactant using NMR analysis, which is similar to actual compositions derived from commercially treated fibers. (Tanoglu et al., 1998) This material is incorporated into an epoxy matrix (diglycidyl ether of bisphenol A epoxy resin cured with bis (p-aminocyclohexyl) methane) in large volume fractions (50 %) to form a "composite" absent of glass fibers.

The static "composite" properties are evaluated using a micro-mechanics model to derive the properties of the model interphase material. In addition to quantifying the static properties of the interphase, rate dependent modulus

was also predicted using dynamic mechanical analysis and the time-temperature superposition (ttsp) principle. The goal of this research is to relate the chemical and physical properties of the interphase to the rate dependent mechanical and durability properties of the composite that are required for proposed Army FCS ground vehicles.

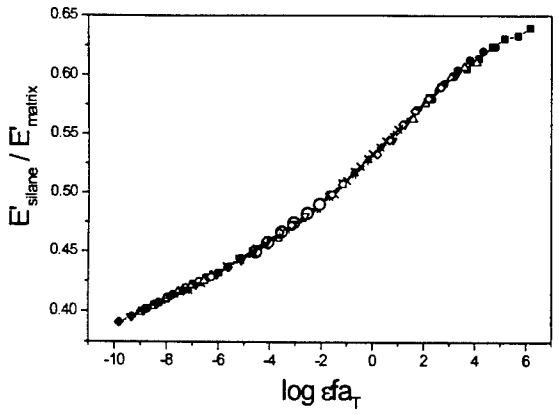


Figure 1. Dynamic storage modulus master curve plotted versus strain rate for epoxy-silane IPN interphase material.

The isotherms of the master curve are shifted horizontally on the log time or frequency axis relative to some reference temperature (T_R). The amount of horizontal shift is called a shift factor ($\log a_T$). The shift factor simply represents the ratio of the apparent relaxation times (τ^*) at the new temperature in comparison to the apparent relaxation times at the reference temperature. The shift factors are often plotted versus $T-T_R$. The empirical Williams-Landel-Ferry (WLF) equation (1) is often fitted to the shift factor plots.

$$\log(a_T) = \log\frac{\tau^*(T)}{\tau^*(T_R)} = \frac{-C_1(T-T_R)}{C_2+T-T_R} \qquad (1)$$

By collecting dynamic mechanical data at multiple frequencies and using time- temperature superpositioning to construct master curves, one can determine the C_1 and C_2 constants of the sample in question for the WLF equation. This is done by plotting $1/\log(a_T)$ versus $1/\log(T-T_R)$ and linearizing. The shift factors will be known for each temperature once the master curve is made. The activation energy of the α-transition (E_α) can then be found through the following equation:

$$E_\alpha = R\frac{d[\ln(a_T)]}{d(1/T)}\bigg|_{T=T_R} = 2.303R\frac{C_1T_R^2}{C_2} \qquad (2)$$

where R is the molar gas constant.

REFERENCES

Madhukar, M. S. and Drzal L. T., "Fiber-Matrix Adhesion and its Effect on Composite Mechanical-Properties .1. In-plane and Interlaminar Shear Behavior of Graphite Epoxy Composites," *J. Comp. Mat.*, Vol 25, No. 8, pp. 932-957, August 1991.

Madhukar, M. S. and Drzal L. T., "Fiber-Matrix Adhesion and its Effect on Composite Mechanical-Properties .2. longitudinal (0-Degrees) and Transverse (90-Degrees) Tensile and Flexure Behavior of Graphite Epoxy Composites," *J. Comp. Mat.*, Vol 25, No. 8, pp. 958-991, August 1991.

Lesko, J. J.; Swain, R. E.; Cartwright, J. M.; Chin, J. W.; Reifsnider, K. L.; Dillard, D. A.; Wightman, J. P., "Interphases developed From Fiber Sizings and Their Chemical-Structural Relationship to Composite Compressive Performance," *J. Adhesion*, Vol 45, No. 1-4, pp. 43-57, 1994.

Reifsnider, K. L., "Modeling of the Interphase in Polymer-Matrix Composite-Material Systems," *Composites*, Vol 25, No. 7, pp. 461-469, August 1994.

Tanoglu, M.; McKnight, S. H.; Palmese, G. R.; Gillespie, "A New Technique to Characterize the Fiber/Matrix Interphase Properties Under High Strain Rates," *Comp. Part A – Appl. Sci. and Manufact.*, Vol 31, No. 10, pp. 1127-1138, 2000.

Tanoglu, M.; McKnight, S. H.; Palmese, G. R.; Gillespie, J. W., "Use of Silane Coupling Agents to Enhance the Performance of Adhesively Bonded Alumina to Resin Hybrid Composites," *Int. J. Adhesion and Adhesives*, Vol 18, No. 6, pp. 431-434, 1998.

NOVEL ELASTOMERIC MEMBRANE FOR SOLDIER PROTECTIVE CLOTHING

D. M. Crawford, J. M. Sloan, N. C. Beck Tan, E. Napadensky
U. S. Army Research Laboratory, Weapons & Materials Research, Polymers Research Branch, APG, MD

Q. Truong
Soldier Biological Chemical Command, Natick Soldier Center, Natick, MA

ABSTRACT

The technical challenge involved in the development of advanced chemical protective materials for soldier applications is multifaceted. The materials must transport air and water vapor while blocking the transport of harmful chemicals, and must be lightweight and flexible over a broad temperature range. In this work, we describe the design and evaluation of an innovative materials technology for chemical protective applications: self-assembled block copolymer ionomers. Structure/property relationships in these copolymers have been evaluated using a variety of analytical techniques. The materials display an impressive combination of mechanical properties, low temperature flexibility, selective transport, ease of processability and cost-effectiveness, making them promising candidates for next generation soldier systems.

1. INTRODUCTION & SIGNIFICANCE

The U. S. Army requires that all fielded systems be survivable in a chemical warfare environment. Materials currently used for chemical protection of the soldier have many shortcomings. Butyl rubber (BR) is often used due to its good barrier properties. However, BR is nearly impermeable to air and moisture (Lee, et al., 1990) and imposes a tremendous heat stress on the soldier when used in clothing. Activated carbons, which are used in protective garments and masks, are non-selective and prone to contamination in storage that reduces their effectiveness. Though numerous approaches have been taken to address these problems, no single technology has emerged that satisfies all technical requirements and presents a cost-effective alternative to current materials.

The technical challenge involved in the development of advanced chemical protective materials for Army applications is multifaceted. Such applications require materials that readily transport air and water vapor while simultaneously blocking the transport of harmful chemicals. The materials must also be lightweight and flexible enabling the soldier to move freely. To meet this challenge, our research has been directed toward the development of a novel, flexible, tri-block copolymer with "perm-selective membrane" characteristics, formed via molecular self-assembly.

2. BACKGROUND

Self-assembled morphologies occur in block copolymers that are composed of thermodynamically immiscible constituent blocks (Lu, et al., 1993). When a portion of the polymer chain contains an ionic group, the block copolymer is classified as an ionomer. Association of ionic groups occurs in ionomers, which may affect morphology and the thermal, mechanical, and transport properties of the polymer (Weiss, et al., 1990, Mani, et al., 1999).

A novel class of self-assembled block copolymers has been designed and investigated. These materials, based on ionomeric forms of polystyrene-polyisobutylene-polystyrene (PS-PIB-PS) block copolymers, exhibit transport and mechanical properties that show potential for soldier clothing applications. The major component (70%) of the copolymer is polyisobutylene (PIB) lending low temperature flexibility to the material and good barrier properties. Polystyrene (PS) forms the glassy component, which aggregates within the PIB matrix lending mechanical integrity to the polymer. The thermodynamic immiscibility of the two components results in spontaneous microphase separation into hexagnally packed cylinders. The PS block is ionically modified such that the cylinders provide a channel for water transport, while the PIB matrix acts as a chemical barrier. This morphology is shown schematically in Figure 1.

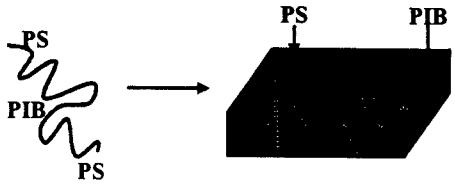


Figure 1. Schematic of tri-block copolymer morphology

Modification of the PS blocks was performed by conversion of different percentages of the styrene monomer to styrene-sulfonic acid (Mountz, et al., 1997). The chemically modified tri-block copolymer exhibits hydrophilic character and its' ability to selectively transport water has been demonstrated. Ionomeric modification of the polymer does not adversely effect the material's flexibility over a broad temperature range, or its solubility in common solvents, which makes processing economically feasible.

1. RESULTS & DISCUSSION

The polymers were characterized using dynamic mechanical analysis (DMA), fourier transform infrared spectroscopy (FTIR), and small angle x-ray scattering

(SAXS). Structure/property relationships in the polymers were studied as a function of degree of sulfonation. SAXS confirmed the cylindrical morphology of the unmodified PS-PIB-PS copolymer. Figure 2 shows the SAXS patterns from hexagonally packed cylindrical phases that are characterized by scattering peaks occurring at positions q*, $\sqrt{3}$q*, $\sqrt{4}$q*, $\sqrt{7}$q*,$\sqrt{9}$q*.

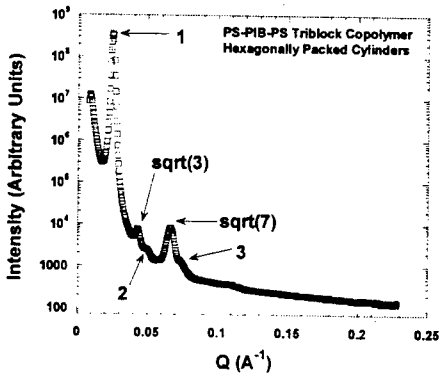


Figure 2. Pattern of unmodified PS-PIB-PS block copolymer

The DMA data from the block copolymers shows that the storage modulus (E') is unaffected by increasing sulfonation up to 8%, however at 17% sulfonation, the E' increases dramatically. These data are shown in Figure 3. The DMA data are in agreement with SAXS results that indicate there is a microphase transition from cylindrical to lamellar morphology in this sulfonation range. Although the block copolymer exhibits increased stiffness at higher levels of sulfonation, the elastomeric properties of the tri-block copolymer are not compromised and the temperature of the PIB glass transition remains at ~ -60°C. This suggests that the block copolymer ionomers will remain flexible over a broad temperature range as required for soldier clothing.

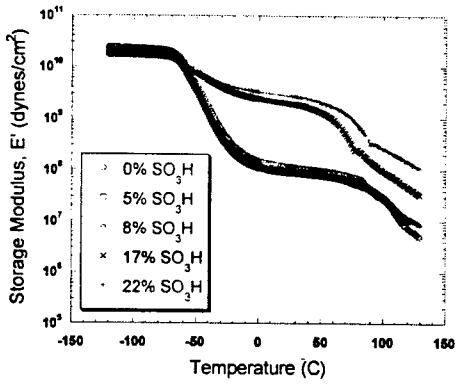


Figure 3. Effect of sulfonation level on E'

Transport of water and alcohols through the copolymers has been studied using attenuated total reflectance (ATR) FTIR. Alcohols were chosen as penetrants as they represent small diffusing molecules that vary in both size and polarity. From these experiments, breakthrough times and diffusion coefficients for penetrants were measured. Figure 4 shows breakthrough time for water and alcohols as a function of sulfonation level, which clearly decrease as sulfonation level increases. Methanol, the smallest alcohol, diffuses fastest through the ionomers, followed by water and higher alcohols. This data demonstrates that water readily diffuses through the tri-block membrane, and the membrane is selective to liquid penetrants depending on their size and polarity.

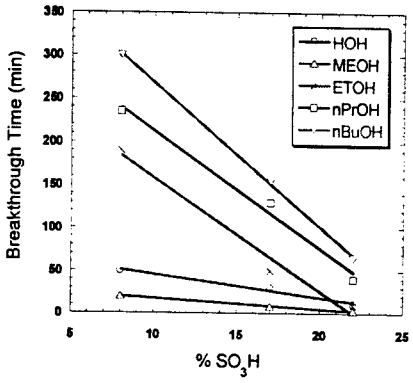


Figure 4. Breakthrough time of water and various alcohols as a function of sulfonation level in the PS-PIB-PS block copoloymer

4. SUMMARY

The properties of novel, self-assembled, PS-PIB-PS tri-block copolymer ionomers designed for soldier protective clothing applications have been evaluated. In the unmodified form, the copolymer behaves as a barrier material, blocking water and polar organics. Ionomeric modification of styrenic components does not disrupt the self-assembly process. However, materials with high sulfonation levels formed lamellar, rather than cylindrical, microphase separated structures. The transition in structure is accompanied by a modulus increase, but flexibility over a broad temperature range is maintained. The block copolymer membranes readily transport water, with transport rates increasing as sulfonation level increases. Experimental results are promising, demonstrating the potential of the novel tri-block copolymer for chemical protective clothing applications.

REFERENCES

Lee, et. al., *Polymer Engineering & Science,* 1990, *36,* 1217.

Lu, et. al., *Macromolecules*, 1993, *26*, 6525.

Mani, et. al., *Macromolecules*, 1999, *32*, 3663.

Mountz, et. al., *ACS Polymer Preprints,* 1997, *39*, 383-384.

Weiss, et. al., *Polymer Communications,* 1990, *31*, 220.

ELECTROSPUN NANOFIBROUS MEMBRANES OF PHOTOVOLTAIC DYES AND NANOCRYSTALLINE TIO_2 MATERIALS

Kris J. Senecal, David Ziegler, Margaret Auerbach, and Lynne Samuelson
US Army SBCCOM, Natick Soldier Systems Center
Natick, MA 01760

Abstract

Electrospinning has been used to prepare nanofibrous composite membranes of semi-conducting particles and photovoltaic dyes. Electrospinning is a relatively simple technique where electrical forces are used on polymeric solutions to produce nanoscale fibers. In this work light harvesting dyes and semiconductor nanoparticles have been electrospun into composite membranes using polyacrylonitrile (PAN) as the carrier polymer. SEM and TEM micrographs show the presence of both the dyes and the semiconductor nanoparticles in fibers ranging from 25-700 nm in diameter, with an interconnected fiber structure and a high degree of porosity. In addition, an interesting correlation between the type of dye used and the degree of dispersion of the semiconductor nanoparticles suggests that electrospinning may be used to control the organization of the nanoparticles along the fibers. This type of interfacial control at the nanometer level offers exciting new possibilities towards the fabrication of photovoltaic nanocomposite materials for solar cell applications.

1. Introduction

Electrospinning performed in the last 50 years, has been described as a process driven by electrical forces on free charges on the surface or inside a polymeric liquid. These charges, generally ions, move in response to the electric field transferring a force to the polymeric liquid. Spinning of fiber occurs when the electrical forces at the surface of a polymer solution overcome the surface tension causing an electrical jet to be ejected. As the jet dries or solidifies charged fibers remain (Reneker and Chun, 1996). In the military there is a need to develop lightweight, flexible wearable materials for power generating devices for next generation military materials. Desirable devices for the Army include wearable or man-portable solar batteries that may provide either modular, supplemental or recharging power units in the soldier system and in canvas materials for shelters and vehicles. It is believed that the technique of electrospinning may be a way of processing these lightweight materials for the future.

Recent studies on solar power generation by Gratzel and others have focused on organic/inorganic hybrid solar cells featuring low cost dye sensitized nanocrystalline semiconductor particles. The concept of the hybrid solar cell differs from current silicon solar cells. Instead of the semiconductor assuming both the task of light absorption and charge carrier transport, the two functions are separated. Light is absorbed by a sensitizer (light harvesting dyes such as: ruthenium, phthalocyanines, cyanines and merocyanines), which is anchored to the surface of sintered nanocrystalline semiconductor particles (examples: TiO2, ZnO and Nb2O5). Charge separation takes place at the interface via photo-induced electron injection from the dye into the conduction band of the nanocrystalline solid. Nanocrystalline particles derivatized with suitable dye(s) yield efficiencies for the conversion of incident photons into electric current exceeding 90% for the specific wavelength absorption range. To date, the best organic solar cells, using titanium dioxide as a semiconductor, yield overall light-to-electric-energy conversion at 12-15% in diffuse daylight and 10% under direct (AM1.5) solar irradiation (Gratzel, 1993, Gratzel, 2000, Rothenberger et al., 1999).

The present work focuses on the use of electrospinning as a new way to integrate the components of these organic based devices into high surface area, nanofibrous composite membrane structures. Phthalocyanines were chosen for the light harvesting dyes because they are known as very promising and stable photovoltaic dyes for organic solar cell research. Many researchers have investigated this class pigments because of their high photoconductivity in the visible region and exceptional thermal stability (Wesphalen et al., 2000, Rudiono and Takeuchi, 1999).

Phthalocyanine, zinc phthalocyanine, copper phthalocyanine and dilithium phthalocyanine dyes were each electrospun with TiO2 semiconductor nanoparticles and the matrix polymer, polyacrylonitrile (PAN). Nanofibrous PAN composite membranes containing the dyes and TiO2 nanoparticles were formed. The morphology and dispersion of these materials in the electrospun membranes was characterized using Transmission Electron Microscopy (TEM) and Scanning Electron Microscopy (SEM) and these results are presented.

2. Experimental

All of the phthalocyanine dyes and the polymer polyacrylonitrile (PAN) were purchased from Aldrich Chemical Co. and used as received.

The polymer spin dope solutions were drawn into a disposable glass pipette and mounted horizontally. The live electrode wire from a DC power source (Gamma High Voltage Research, Inc. model HV ES30P/100) was inserted into the pipette holding the polymeric solution. A grounded target such as metal or conductive Indium Tin Oxide (ITO) was used to collect the nanofibrous materials. Direct spin application on electron microscopy grids was used for the electron microscopy characterization. The nanofibrous membranes were prepared at a 10-15kV potential and 14 cm between the electrode and the target. Microscopy characterization of the electrospun membranes included both TEM and SEM (with the energy dispersive x-ray and backscattering options.)

3. Results and Discussion

The fiber sizes for the electrospun membranes ranged from 25 to 700 nanometers in diameter. Spherical TiO2 particle size was estimated between 25-150 nanometers. General observations on the electrospun nanofibrous membranes indicate TiO2 particles were contained both in and outside the fiber but always associated with the fiber as observed by TEM (figures 1,2,3,4). Isolated titanium particles were not observed in any of the images. Dispersion of the titanium dioxide particles seemed to be dependent on the specific dye used in the spin dope. In figures 1 and 2, dispersion of the titanium is uneven on the fibers, most notably with the copper phthalocyanine dye fibers where some length of fiber does not have any titanium. In contrast, the membranes that have either zinc or dilithium phthalocyanine dye components, show a more dense and uniform dispersion of the titanium along the fibers (figures 3,4).

Energy dispersive x-ray characterization for the titanium element in the zinc phthalocyanine/TiO2 electrospun membrane (not shown) indicates that the titanium is closely associated throughout the fiber, corroborating the TEM observations. The elemental trace for the zinc component of the phthalocyanine dye (not shown) shows that although the dye is associated with the fibers, it is not as widely distributed as the titanium element. This may be explained by zinc being only a minor component of the dyes' total weight. It is important to note however, that the zinc and the titanium are always observed in close proximity to each other in the fibers.

We believe that this is the first demonstration showing the direct association and dependence of photovoltaic dyes with semiconductor nanoparticles in electrospun fibers. Since it is well known that device efficiencies in dye-based solar cells is directly dependent on interfacial interaction of the dyes with the semiconductors, these results suggest that electrospinning may be an exciting new and facile processing approach for solar cell fabrication. Judicious choice of the materials added to the spin dope should allow one to tailor the membranes towards specific properties such as mechanical toughness, thermal stability and color (for camouflage). Future work includes photoelectric conversion studies, optimization and device fabrication with these electrospun membranes towards the development of next generation lightweight and conformal power generating devices.

Gratzel, M.. "Nanocrystalline thin-film PV cells," *MRS Bull.* ol. 18, no. 10, pp. 61-66 1993.

Gratzel, M., "Perspectives for dye-sensitized nanocrystalline solar cells," *Prog. Photovoltaics* vol. 8, no.1, pp. 171-185 2000.

Reneker, D H. and Chun, I., "Nanometer diameter fibers of polymer, produced by electrospinning," *Nanotechnology* vol. 7, no. 3, pp.216-223 1996.

Rothenberger, G., Comte, P., Gratzel, M., "A contribution to the optical design of dye-sensitized nanocrystalline solar cells," *Sol. Energy Mater. Sol. Cells* vol. 58 no.3 pp. 321-336 1999.

Rudiono, F., and Takeuchi, M., "Morphological characteristics of perylene-doped phthalocyanine thin films and their photovoltaic effect, *"Applied Surface Science* vol. 142 no.1-4 pp. 598-602 1999.

Wesphalen, K., Rostalski, U., Luth, H., Meissner, D. "Metal cluster enhanced organic solar cells," *Solar Energy Materials and Solar Cells* vol. 61 pp. 97-105 2000.



Fig. 1 Pc +TiO2



Fig. 2 CuPc + TiO2



Fig. 3 Dilithium Pc + TiO2



Fig. 4 ZnPc + TiO2

THE ELIMINATION OF HAZARDOUS CHEMICALS IN THE PREPARATION OF HIGH PERFORMANCE TRANSPARENT ARMOR FOR SOLDIER PROTECTION

Douglas J. Kiserow*
U.S. Army Research Office
PO Box 12211
RTP, NC 27709-2211

George W. Roberts
Department of Chemical Engineering
North Carolina State University
Raleigh, NC 27695-7905

Stephen M. Gross and Joseph M. DeSimone
Department of Chemistry
University of North Carolina
Chapel Hill, NC 27599

1. MOTIVATION AND RELEVANCE TO DOD

Transparent armor plays a critical role in soldier protection by combining a clear field of vision with ballistic protection. Key DoD uses include rotorcraft bubbles, visors, faceshields, goggles (including those for laser-eye protection), and portholes in armored vehicles. Poly(bisphenol A carbonate) is the polymeric material used by DoD for transparent armor due to its desirable properties, which include exceptional toughness, thermal stability, strength, and transparency. In addition polycarbonate is extensively utilized in the private sector in industries related to law enforcement, music, electronics, and in electrical, automotive and architectural applications. However, there is one critical drawback to polycarbonate use. Polycarbonate is prepared by an interfacial reaction between phosgene dissolved in methylene chloride and an aqueous alkaline solution of bisphenol A. The result of this synthesis, which is used in the production of more than 2.7 billion pounds of polycarbonate per year, is the production and use of phosgene, a chemical so hazardous it was used as a chemical weapon in World War I. In addition the process generates hazardous aqueous and chlorinated organic waste streams that pose a significant threat to the environment resulting in expensive post-production treatment.

Prior to our research, a viable, environmentally benign approach to polycarbonate synthesis has never been proposed. Our research describes a new approach to polycarbonate synthesis that is solvent free and carried out in solid particles. This is accomplished by polymerizing low molecular weight polycarbonate beads without using solvents, and at very low temperatures, creating the possibility of significant energy savings for large-scale production.

2. RESEARCH BACKGROUND

Solid state polymerization is the method of choice by industry for step growth polymerizations. It is used in the manufacture of polyethylene terephthalate, PET, a large-scale step-growth polymer that is used for plastic soda bottles, milk bottles, and viewgraphs (a critical Army application), to name a few. In a solid state polymerization, a semicrystalline oligomer is heated between its glass transition temperature, T_g, and its melting temperature, T_m. At the same time a sweep fluid is passed over the surface of the particles to remove the condensate by-product driving the forward reaction to produce high molecular weight polymer particles. Prior to our research polycarbonate has not been prepared like PET because it does not thermally crystallize. However polycarbonate can be made semicrystalline using supercritical CO_2 (Beckman et al., 1987). This has been used by our group as the basis for exploring a solvent-free, solid state polymerization for polycarbonate.

3. RESEARCH RESULTS

Initially bisphenol A and diphenyl carbonate were reacted in a melt condensation reaction to form low molecular weight prepolymer in the range 2,500 - 5,000 g/mol (Gross et al., 1999). Low molecular weight prepolymer is used because it avoids problems caused by high viscosity and high reaction temperatures during chain extension reactions. The prepolymer was exposed to supercritical CO_2 at temperatures and pressures in the ranges 40 - 70 °C and 204 - 340 bar, depending on prepolymer molecular weight, to generate semicrystalline morphology. This is critical to prevent coalescence and melting during solid state polymerization. The semicrystalline prepolymer was heated between T_g and

T_m while a sweep gas or fluid, N_2 or supercritical CO_2, was flowed over the particles to remove phenol, the reaction by-product.

The percent crystallinity and the molecular weight were determined as a function of time and radial position (defined as core = 0 - 0.4 mm, intermediate = 0.4 - 1.4 mm, and shell = 1.4 - 1.8 mm) for polycarbonate beads that were 3.6 mm in diameter (Gross et al., 2000). Both are strong functions of the particle radius due to the slow diffusion of phenol out of the polycarbonate beads. The result is a molecular weight gradient that ranges from 6000 g/mol in the core where phenol is trapped, to nearly 18,000 g/mol in the shell where phenol can readily escape due to contact with the sweep fluid. Molecular weight and crystallization gradient data are important results that demonstrate the role of prepolymer particle size in the solid state polymerization process. This dependence is not observed for melt phase polymerization, which industry uses to produce polycarbonate.

The use of supercritical CO_2 as a sweep fluid was explored because it plasticizes polycarbonate, potentially enhancing the reaction rate in the amorphous region. This is expected to drive the forward reaction to high molecular weight polymer. In addition phenol is highly soluble in supercritical CO_2 potentially facilitating higher conversion through its efficient removal. Because N_2 is commonly used in industry it was also used in this study for comparison to supercritical CO_2 as shown in **Figure 1**. The polymerization rate was always higher in supercritical CO_2 at otherwise comparable conditions, and more significantly, the temperature of the reaction was 90 - 120 °C when using supercritical CO_2 compared to 180 - 240 °C when using N_2. In order to achieve high molecular weight polycarbonate using N_2, the temperature is ramped from 180 - 240 °C for up to 24 hours to compensate for changes in crystallinity and T_m as the polymerization progresses. We propose that supercritical CO_2 plasticizes the amorphous regions of the polymer, thereby increasing chain mobility and the rate of phenol diffusion out of the polymer. This permits the reaction temperature to be reduced and suppresses side reactions that lead to color body formation, which produces discolored polycarbonate.

4. CONCLUSIONS

The research reported herein describes the first use of supercritical CO_2 with solid state polymerization to produce high molecular weight polycarbonate. It was found that the increase in molecular weight is a strong function of CO_2 pressure and temperature. Further, the solid state polymerization of polycarbonate in the presence of supercritical CO_2 can be accomplished at temperatures as low as 90 °C. This suppresses side reactions that lead to colorbody formation and produces polycarbonate with excellent optical clarity and color. This synthesis can be scaled-up to industrial levels and could completely eliminate the use and production of toxic chemicals, significantly reduces the reaction temperature, and generates high-quality polycarbonate for use as transparent armor and numerous other commercial applications.

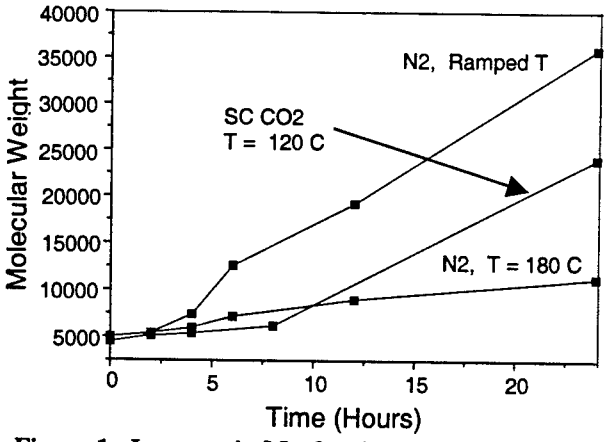


Figure 1. Increase in M_W for three polycarbonate beads for solid state polymerization under different reaction conditions. The N_2 flow rate is 2 mL/min. The time-temperature profile for the reaction was 180 °C for 0 - 2 hours, 205 °C for 2 - 4 hours, 230 °C for 4 - 6 hours, and 240 °C for 6 - 24 hours. The CO_2 flow rate is 1 mL/min and the pressure is 204 bar.

ACKNOWLEDGMENTS

The authors thank the U.S. Army Research Office and the Kenan Center for the Utilization of CO_2 in Manufacturing for funding.

REFERENCES

Beckman, E. and Porter, R., "The Crystallization of Bisphenol A Polycarbonate by Supercritical CO_2" *J. Polym. Sci., Part B:Polym. Phys.*, 25, p. 1511, 1987.

Gross, S., Flowers, D., Roberts, G., Kiserow, D., and DeSimone, J., "Solid State Polymerization of Poly(bisphenol A carbonate) using Supercritical CO_2", *Macromolecules*, 32, p. 3167, 1999.

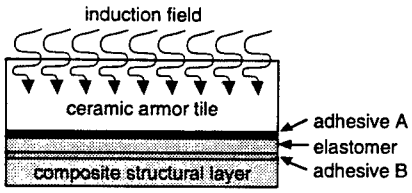
Gross, S., Roberts, G., Kiserow, D., and DeSimone, J., "Crystallization and Solid State Polymerization of Poly(bisphenol A carbonate) Facilitated by Supercritical CO_2", *Macromolecules*, 33, p. 40, 2000.

ADVANCED MAGNETIC MATERIALS FOR CURIE-TEMPERATURE CONTROLLED BONDING

E. D. Wetzel and B. K. Fink
Army Research Laboratory, Weapons and Materials Research Directorate / APG, MD
Y. F. Li and J. Q. Xiao
University of Delaware, Dept of Physics / Newark, DE

Synopsis
We have developed a fundamental science base for predicting the heating behavior of magnetic particles during induction heating processes. This analysis has allowed us to determine criterion for selection and design of materials for bonding applications, which has been demonstrated through the successful creation of a special class of advanced magnetic ceramics.

Background
The need to reduce weight and improve survivability in Army vehicle and weapons systems has led to increasing usage of polymer-matrix composites and ceramic materials for structural and armor applications. These materials, however, pose major challenges for integration into complex assemblies due to limitations in joining technology. Unlike metallic structures, which can be welded or fastened mechanically, composites and ceramics require surface bonding methods such as thermoplastic hot-melt bonding or adhesives.



Both hot-melt bonding and elevated temperature adhesives require a means of heat generation at the interface. One promising approach is the use of induction heating. In this technique, a susceptor material is placed at the bondline. In the presence of a high frequency electromagnetic field, the susceptor heats, melting the thermoplastic or curing the adhesive. The major advantages of this process are that it is non-contact and generates heat directly at the bondline. These properties are critical for successful implementation of multi-material, multi-functional armors (figure), which require rapid, localized heating without direct bondline access.

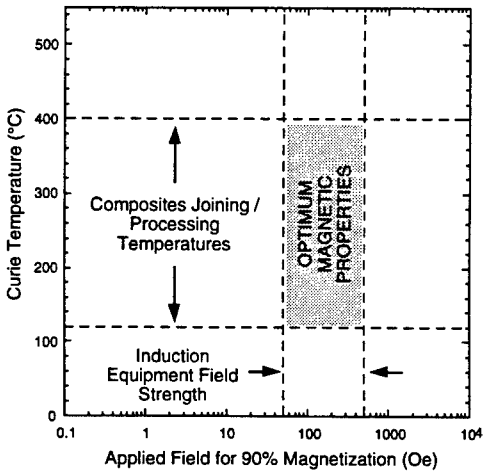
Traditionally, conductive fillers or metal screens are used as the susceptor [1]. These materials heat due to eddy current losses, providing rapid heating. However, there is no upper bound to the heating mechanism, so bondline temperature sensing and power regulation are required to prevent overheating. A more advanced technique utilizes magnetic nickel powder as the susceptor material [2]. This susceptor heats primarily due to magnetic hysteresis losses. The major advantage of this approach is that above the Curie temperature of nickel, ~354°C, nickel becomes nonmagnetic. Therefore, in a high frequency magnetic field, nickel powder will heat no higher than its Curie temperature. This automatic temperature regulation prevents potentially damaging overheating of the bondline, and greatly simplifies the sensing and control hardware necessary for processing.

While nickel powder has demonstrated the potential of Curie-temperature limited hysteresis-based bondline heating, it is only applicable to joining processes at one particular temperature. Nickel powder also presents some difficulty in terms of particle production and environmental stability. In order to enable the development of improved materials for particulate susceptors, an analysis of the magneto-thermal process was undertaken.

Analysis
In order to utilize the Curie-temperature heating limit, the susceptor must heat due to magnetic hysteresis losses but must not be susceptible to eddy current heating. This property is of major concern for magnetic metallic materials such as nickel, whose high conductivity may allow significant eddy current heating past the Curie temperature. The ratio of eddy current heating to hysteresis heating was found to obey the dependence

$$\frac{\text{eddy heating}}{\text{hysteresis heating}} \propto \frac{D_o^2 f}{\rho}$$

where D_o is the particle diameter, f is the applied field frequency, and ρ is the material resitivity. This relation shows that eddy current heating is minimized by using small particles and high resitivity materials.



To ensure maximum heating efficiency, hysteresis losses in the material must be maximized. Materials that are magnetically

"soft", or easy to magnetize, have relatively small hysteresis losses per magnetization cycle. Materials that are magnetically "hard" have large hysteresis losses, but also require prohibitively large applied field strengths to utilize their full energy density. Therefore, "semi-hard" magnetic materials are optimal for hysteresis heating. These materials offer generous hysteresis losses when subject to the moderate magnetic field strengths typical of high frequency electromagnetic field sources. Because such materials are poorly suited for traditional magnetic material applications such as transformer cores (soft materials) and permanent magnets (hard materials), they are a largely unstudied class of materials.

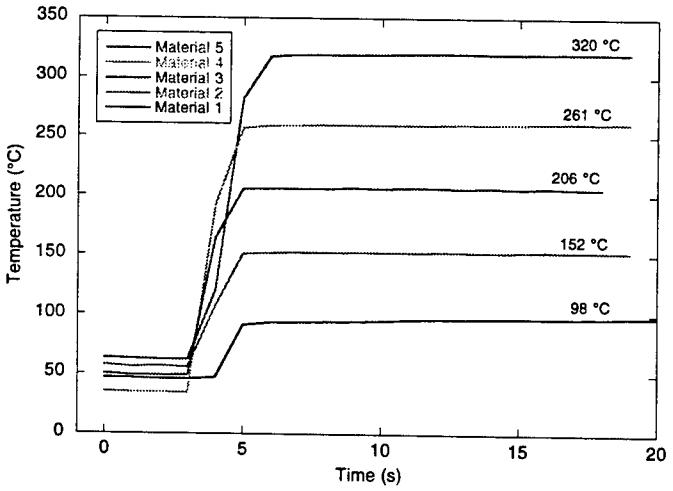
In addition to the above properties, the susceptor material should have a controllable Curie temperature between 120 and 400°C, the typical range of processing temperatures for elevated temperature adhesives and engineering thermoplastics. The material should be environmentally stable to prevent transformation to non-magnetic secondary phases and bondline deterioration during long-term service. Finally, the material must be amenable to particle production methods which reduce the particles down to 1-10 μm size, which ensures proper heat distribution.

Heat transfer modeling has also been performed to complement the material modeling efforts. These analyses have determined the effects of particle volume fraction, particle size, and adherend material and geometry on the bondline heating behavior.

Material Selection

We have formulated ferrite materials which meet all of the above criteria. Ferrites are magnetic ceramics, which provide many properties which are superior to magnetic metallic alloys. Ferrites are non-conductive, eliminating eddy current heating at any sub-millimeter particle size. They are environmentally stable oxides, and due to their brittleness are relatively easy to reduce to fine powders. There are a nearly limitless range of ferrite formulations to choose from. The particular family of ferrites we have selected (patent application in process) are magnetically semi-hard. Their Curie temperature can be customized to within 5°C anywhere between 100 and 390°C through careful alloying of secondary elements.

The plot below shows the heating behavior of five of the specialized ferrites. The experiments were performed using a 2.3 MHz Huettinger induction source with a 3-turn pancake coil. The field amplitude is estimated to be ~50 Oe. The samples were not dispersed in any thermoplastic or adhesive matrix, in order to characterize the heating behavior of the powder without volume fraction effects. Note the rapid heating and dwell behavior. Full temperature rise is achieved within a few seconds, and the particles deviate in temperature by only a few degrees during the dwell period. We should reemphasize that no power regulation or temperature sensing feedback was necessary in order to produce these results.



Heating behavior of magnetic particles in high frequency magnetic field.

References

[1] B. K. Fink et al. "Non-polluting Composites Repair and Remanufacturing for Military Applications: Induction-Based Repair of Integral Armor." ARL Tech. Rep. ARL-TR-2121. November 1999.

[2] B. K. Fink et al. "Ferromagnetic Nano-Particulate and Conductive Mesh Susceptors for Induction-Based Repair of Composites." Proc. of Army Science Conf. Norfolk, VA. June 1998.

IMPROVING THE ROD-PENETRATION ALGORITHM FOR TOMORROW'S ARMORS

Steven B. Segletes*, Rick Grote, John Polesne
U.S. Army Research Laboratory
Aberdeen Proving Ground, Maryland 21005

ABSTRACT

The performance of the respected Frank-Zook penetration algorithm (Zook *et al.*, 1992) is examined in light of an anticipated class of target technologies involving laminated targets whose layers are thin relative to the projectile diameter. This class of target designs encompasses multifunctional integral armors and, in the limiting case, armors incorporating functionally-graded materials. Such armor classes represent potential candidates for the Army's Future Combat System.

1. INTRODUCTION

Traditional penetration methodologies, like those of Tate (1967) and Alekseevskii (1966), were developed for rods penetrating idealized semi-infinite target blocks. As such, target resistance variations along the shotline were not an issue. Later analyses (Wright and Frank, 1988; Tate, 1986; Walker and Anderson, 1995) showed that, in fact, the property of target resistance represents an integral of stresses throughout the plastic zone in the target, ahead of the rod/target interface. In the course of penetration, when this plastic zone crosses the interface between two adjacent target plies, one may infer that the local target properties should be properly composed of material properties from both of the entrained plies. In this manner, the transition of "effective" material properties penetrating from one target ply into the next should be continuous, rather than discrete.

The Frank-Zook (FZ) algorithm (Zook *et al.*, 1992), used widely within ARL for both terminal ballistic evaluation and vulnerability assessment, considers this interply transition process. However, since it was developed when long rods and relatively thick target elements represented the prevalent engagement scenario, the FZ algorithm computes this transition effect a single target element at a time (*i.e.*, it only senses one target element in advance). Unfortunately, for a target that comprises multiple thin element layers or varies continuously in properties, the plasticity zone will entrain not two, but a larger number of target element layers simultaneously (Fig. 1). For such targets, the FZ algorithm will be ill-suited to model the transition of "effective" target resistance and density along the shotline. Though the problem can be quite severe when the target-layer thickness is a fraction of the projectile diameter, the effect is still evident to a much lesser extent, even as the target-element thickness is increased to several projectile diameters.

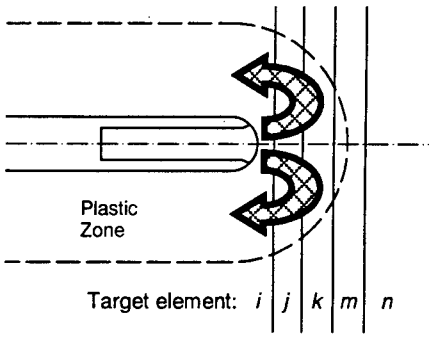


Fig. 1. Plastically entrained elements contribute to "effective" target properties, e.g., resistance $H = H(i, j, k, m)$.

2. DISCUSSION

A remedy to this type of problem is offered and accomplished by a novel adaptation of elements from a model by Walker and Anderson (1995) into the FZ framework. In so doing, the target's material properties and nonsteady-kinematic properties are dynamically composed via an integration through the plastic zone in the target, ahead of the rod/target interface. Though the Walker-Anderson model does not even address the issue of multilayer targets, the assumed flow field kinematics of their model provide enough information to isolate and dynamically calculate an integrated contribution from each layer in a given laminate target towards the aggregated or "effective" target properties.

The resulting extended-Bernoulli relation for rod/target interaction includes aggregated terms summed from all the layers of target material that are entrained in the plastic zone:

$$\left(k_P - \frac{1}{2}\cdot\frac{\dot{s}}{\dot{L}}\right)\rho_P (V-U)^2 + Y - \frac{\rho_P s}{2}(\dot{V}+\dot{U}) = k_T \overline{\rho} U^2 + \overline{H} + X_U \frac{\dot{U}}{U} + X_\alpha \frac{\dot{\alpha}}{\alpha} + X_R \frac{\dot{R}}{R} \quad , \tag{1}$$

where k_P, ρ_P, Y, V, and s are the shape factor, density, strength/resistance, velocity, and plastic-zone extent in the rod of length L, while k_T, $\overline{\rho}$, $\overline{H}$, U and α are the corresponding values for the target interface. In particular, for a plastic zone of thickness $(\alpha - 1)$ times the crater radius R, spanning across target elements m to n [where each target interface is positioned at $z = (\beta - 1)R$ with respect to the rod/target interface], the following generalized expressions for the target parameters are obtained:

$$\overline{\rho} = \sum_{i=m}^{n} \frac{\alpha^4}{(\alpha^2-1)^2}\left[\frac{(2\beta_i^2-1)}{\beta_i^4} - \frac{(2\beta_{i+1}^2-1)}{\beta_{i+1}^4}\right]\rho_{Ti} \quad , \qquad (2)$$

$$\overline{H} = \sum_{i=m}^{n} \frac{\ln(\beta_{i+1}/\beta_i)}{\ln(\alpha)} H_i \quad , \qquad (3)$$

$$X_U = UR \sum_{i=m}^{n} \frac{\rho_{Ti}}{(\alpha^2-1)}\left[\frac{(\beta_i^2+\alpha^2)}{\beta_i} - \frac{(\beta_{i+1}^2+\alpha^2)}{\beta_{i+1}}\right] \quad , \qquad (4)$$

$$X_\alpha = UR \sum_{i=m}^{n} \frac{2\rho_{Ti}\alpha^2}{(\alpha^2-1)^2}\left[\frac{(\beta_{i+1}^2+1)}{\beta_{i+1}} - \frac{(\beta_i^2+1)}{\beta_i}\right] \quad , \text{and} \qquad (5)$$

$$X_R = UR \sum_{i=m}^{n} \frac{\rho_{Ti}\alpha^2}{(\alpha^2-1)}\left[\frac{(2\beta_i-1)}{\beta_i^2} - \frac{(2\beta_{i+1}-1)}{\beta_{i+1}^2}\right] \quad . \qquad (6)$$

These results reduce to those of Walker and Anderson (1995) for the case of monolithic targets.

3. RESULTS

A series of tests were conducted at ARL's Experimental Facility 110, using the 14.5 mm B32 armor-piercing projectile, weighing 63.5 g and consisting of a 53 mm, 41 g hardened-steel (Rc 65) core surrounded by a brass jacket. The gun-breech powder loading was altered to systematically vary the projectile velocity. The projectile was modeled as a 63.5 g homogeneous steel slug, 66.5 mm long x 12.45 mm diameter, equaling the overall length and mass of the B32 projectile. Because the sharpened B32 core penetrates as a rigid body, the shape factor, k_T, of the target flow was set to 0.15 rather than 0.5. This was based on the B32-core nose angle, reflecting the reduced momentum transfer imparted to a sharpened body as compared to the stagnation flow of blunt-body penetration.

The residual-velocity curves in Fig. 2 depict both the kind of inconsistency that can occur when the FZ model is applied to targets comprising thin layers, as well as the correction offered by the revised modeling. The baseline target consists of a 23 mm plate of 5083 aluminum ($\rho = 2.7$ g/cm^3, $H = 1.92$ GPa), followed by 9.6 mm of high-hard armor (HHA) ($\rho = 7.85$ g/cm^3, $H = 6.15$ GPa). The test-case target takes the baseline and inserts a relatively weak 2.8 mm acrylic interply ($\rho = 1.19$ g/cm^3, $H = 0.624$ GPa) between the two primary target plies. In reality, this interply should have little effect on the penetration resistance of the target. However, the FZ model perceives these two target configurations quite differently. For the baseline case without the interply, the FZ algorithm properly senses the influence of the strong HHA plate while penetrating the 5083 aluminum, but fails to detect the weak, free surface of the target prior to actually entering the HHA element. Thus, the original algorithm underpredicts the residual velocity (V_r) exiting the baseline target.

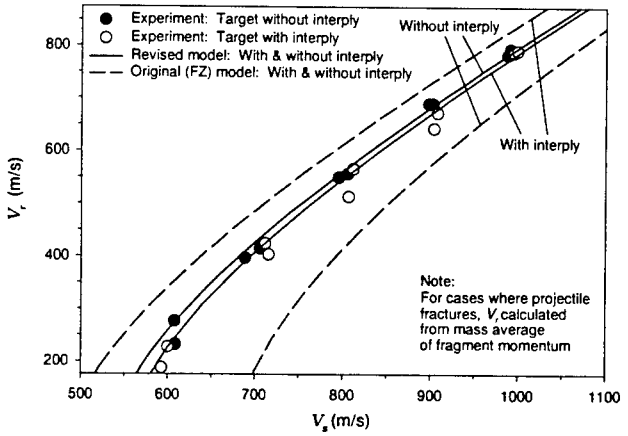


Fig. 2. Effect of thin interply layer on original and revised models.

For the test case containing the acrylic interply, the influence of the hard HHA plate is not sensed by the FZ algorithm while penetrating the 5083 element, until the acrylic is actually reached. Rather, the 5083 plate senses only the weak acrylic interply. As such, the original algorithm overpredicts the residual velocity exiting the test-case target. In contrast, the revised algorithm, by simultaneously accounting for all the relevant target elements and free surfaces in proportion to their actual influence, properly captures both the magnitude and sense of the ballistic trend.

4. CONCLUSIONS

When investigating the ability of the current FZ penetration algorithm to predict the ballistic performance of targets comprising thin (or functionally-graded) elements, a deficiency was noted, arising from the algorithm's inability to examine the influence of more than one leading target element at a time. A remedy has been offered that incorporates elements of a model by Walker and Anderson (1995) into the existing FZ framework. The revised model compares well to data. These modeling remedies and enhancements are being considered for incorporation into the Army Research Laboratory's MUVES code, as part of ARL's vulnerability/lethality calculation methodology.

REFERENCES

Alekseevskii, V. P., *Comb. Expl. and Shock Waves*, Vol 2, pp. 63–66, 1966.

Tate, A., *J. Mech. Phys. Solids*, Vol 15, pp. 387–399, 1967.

Tate, A., *Int. J. Mech. Sci.*, Vol 28, No. 8, pp. 535–547, 1986.

Walker, J. D. and Anderson, C. E. Jr., *Int. J. Impact Engng.*, Vol 16, No.1, pp. 19–48, 1995.

Wright, T. W., and Frank, K., "Approaches to Penetration Problems," U.S. Army Ballistic Research Laboratory, BRL-TR-2957, December 1988.

Zook, J. A., Frank, K., and Silsby, G. F., "Terminal Ballistics Test and Analysis Guidelines for the Penetration Mechanics Branch," U.S. Army Ballistic Research Laboratory, BRL-MR-3960, January 1992.

Development of Techniques for Strengthening Deteriorated Concrete Using Bacterially-precipitated and Enzymatically-precipitated Mineral Phases

D.B. Ringelberg*, C.A. Weiss, Jr. and P.G. Malone
U.S. Army Environmental Research and Development Center, Vicksburg, MS, 39056

1. ABSTRACT

Bacteria were isolated from guano that showed a capacity to facilitate the precipitation of ammonium magnesium phosphate (in the mineral phase, struvite) in artificial media and on concrete surfaces. Direct enzymatic catalysis of the precipitation reaction was demonstrated and shown to result in a two-fold increase in crystal yield. This investigation demonstrates a novel technique for crack repair that can possibly be used to reduce concrete deterioration in a safe, environmentally friendly way with reduced cost and improved performance.

2. INTRODUCTION

Fractures in concrete are often of such small sizes that the introduction of a material that will fill or close the fractures is not practical using normal chemical injection or impregnation techniques. Techniques that use bacteria that will precipitate carbonate mineral phases (calcite, aragonite or vaterite) have been suggested for use in fractured rock (Zhong and Islam, 1995; Ramakrishnan and Bang, 1999). Growth conditions in concrete, however, are more severe than those bacteria normally tolerate. Thus, an ability to be metabolically active in environments with pH ranges of pH 8.0 to 10.5 is required. Furthermore, any system proposed must produce a precipitate that is strong and durable enough to serve as an infilling and bonding component in the concrete.

A survey of biogenic mineral phases indicated that ammonium magnesium phosphate (in the mineral phase, struvite) would be a suitable repair material. Inorganic cements based on ammonium magnesium phosphate have been developed for rapid runway repair and have a proven record for strength and durability (Seehra, et al., 1993). Bacterial precipitation of struvite in the production of *in vivo* mineral deposits (stones) has been widely studied; but the organisms typically involved are considered human pathogens and are unsuitable for widespread use (Clapham, et al., 1990). The production of struvite crystals has also been observed during the decomposition of high-protein wastes and the bacteria associated with this occurrence are typically non-pathogenic and thrive under a wide variety of environmental conditions (i.e. those associated with waste treatment systems and in soil).

3. RESULTS and DISCUSSION

A novel species of *Bacillus* has been isolated from bat guano that is capable of catalyzing the precipitation of struvite. *Bacillus* sp. SB1 is a rod shaped Gram-positive bacterium capable of growth at a pH of at least 9.0 and temperatures as high as 45°C. Nucleic acid analysis of the 16S ribosomal DNA fragment indicated a 97% and 91% similarity with that of B. *sphaericus* in alignments to GeneBank and RDP (Ribosopmal Database Project) entries, respectively. Fatty acid analysis indicated the presence of iso and anteiso terminally branched saturated moieties (C15 and C17), which is also consistent with the genus *Bacillus*. Although both phenotypic and genotypic descriptions were consistent, a species identification was not possible since the genetic difference between the guano isolate and B. *sphaericus* was equal to the genetic difference between B. *sphaericus* and another known Bacillus, B. *fusiformis*.

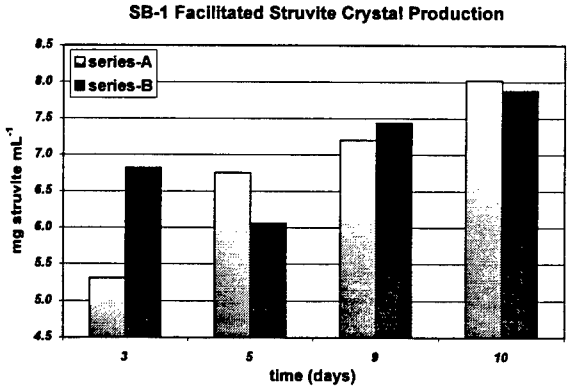


Figure 1. Weight per volume of struvite crystal formed as a result of *Bacillus* sp. SB1 metabolism at room temperature over a 10 day period. Series-A was inoculated at a cell density of 10^6 cells mL^{-1} and series-B at 10^7 cells mL^{-1}.

Bacillus sp. SB1 is believed to be non-pathogenic and produces abundant struvite crystals when grown in a relatively simple culture medium: tryptic soy, urea,

magnesium salts (carbonate>chloride>nitrate>sulfate) and a dibasic phosphate buffer. Struvite yields were in the range of 8 mg mL^{-1} after 10 days of incubation at 28°C (Figure 1). The organisms ability to grow at a pH of at least 9.0 is fortuitous in concrete applications. Concrete contains lime from the hydration of Portland cement, and water in contact with a concrete surface will generally have a pH in range of 9.0 to 10.5. Initial tests with concrete substrates indicated that *Bacillus* sp. SB1 does catalyze struvite crystal production and that the crystals adhere to the concrete surface (Figure 2).

Bacillus sp. SB1 is ureolytic positive, which is believed to be the principal mechanism catalyzing struvite crystal formation in liquid culture. Ureolytic positive organisms produce the enzyme urease, which enables the bacteria to derive ammonia and carbon dioxide from urea. The ammonia resulting from urease activity is well suited for chemical reactions with magnesium and phosphate in the formation of struvite crystals. A simplified concrete treatment system that used a solution of magnesium and phosphate salt along with synthetic urea and urease proved to be very useful in producing struvite crystals, in the absence of the bacteria. Commercial urease concentrates (extracts of jack bean meal) retain their activity at an elevated pH and produce a product similar to that obtained with bacterial incubations, but at greater yields. Typical struvite crystal yields, from the addition of 50 mg mL^{-1} urease, averaged twice that obtained with the bacteria (Table 1). Since crystal formation is not instantaneous, but occurs at a rate corresponding to the activity of the enzyme, a urease based solution can be used to infiltrate pores and microfractures in concrete before the urea is decomposed to ammonia leading to struvite precipitation.

Table 1. Struvite Crystal Yields (mg mL^{-1}) Resulting from the Addition of Varying Concentrations of Jack Bean Urease over a 10 day Period.

Urease[1] concentration (mg mL^{-1})	Struvite (mg mL^{-1})
25	10 ± 0.1[2]
50	19 ± 0.3
100	19 ± 0.4

[1] jack bean urease Type IX: 62,100 units g^{-1}
[2] ± one standard deviation (n=2)

4. CONCLUSION

This enzymatically induced precipitation reaction shows promise of becoming a successful method of treating concrete to produce a denser surface and to "heal" microfractures. Potential applications for this treatment include the reduction of freezing and thawing deterioration of bridge decks and increased durability of concrete precast construction. The bacteria isolated in the program also have a potential role in the conversion of animal wastes to a slow-release fertilizer, similar to naturally occurring guano.

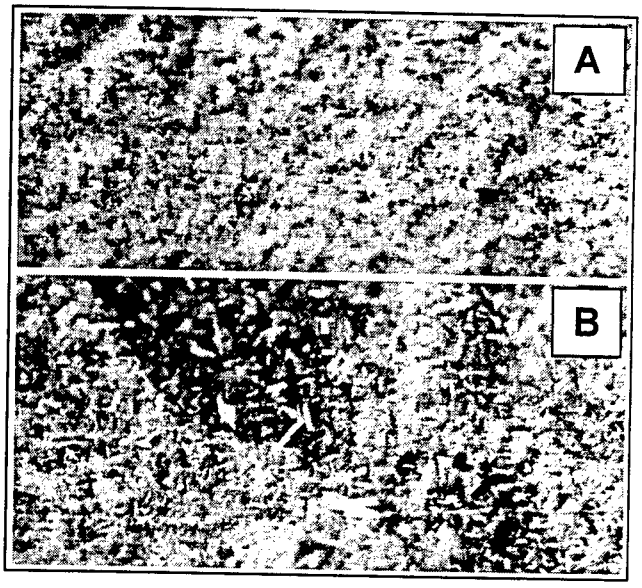


Figure 2. Panel A- Lawn of struvite crystals on concrete formed via catalysis with jack bean urease. Panel B- Lawn of struvite crystals on concrete formed via catalsis with *Bacillus* sp. SB1.

5. REFERENCES

Clapham, L., McLean, R.J.C., Nickel, J.C., Downey, J., and Costerton, J.W. 1990. The influence of bacteria on struvite crystal habit and its importance in urinary stone formation. J. Cry. Gro. **104**:475-484.

Ramakrishnan, V., and Bang, S.S. 1999. A novel technique for repairing cracks in concrete using bacteria. Presented at the American Concrete Institute Fall Convention, Oct. 31 – Nov. 5, 1999, Baltimore, MD.

Seehra, S.S., Gupta, S., and Kumar, S.S. 1993. Rapid setting magnesium phosphate cement for quick repair of concrete pavements – Characterization and durability aspects. Cement and Concrete Res. **23**(2):254-266.

Zhong, L. and Islam, M.R. 1995. A new microbial plugging process and its impact on fracture remediation. Paper No. 30519. Proceedings of the 70th Annual Technical Conference and Exhibition of the Society of Petroleum Engineers, Dallas, TX, 22-25, October, 1995. http://www.geo.mtu.edu/lzhong/microbial.html.

TOUGHENED INTERPENETRATING POLYMER NETWORKS (IPNs) FOR ELECTRON-BEAM CURE OF COMPOSITES AND ADHESIVES

James M. Sands*, Steven H. McKnight, and Bruce K. Fink
Army Research Laboratory
Aberdeen Proving Ground, Maryland 21005

Giuseppe R. Palmese
Drexel University
Philadelphia, PA 19104

Polymer composites and adhesively bonded hybrid composite structures (e.g., composite-ceramic integral armor) are promising candidates for ultra-lightweight structural armor for FCS. Understanding and optimization of ballistic performance of composites is necessary to fully realize the anticipated weight reduction. Resin-dominated failure modes (e.g., compression, fatigue, Mode I and II delamination, adhesive debonding, etc.) have been shown to be critical to the success of integral armor with respect to structural integrity and ballistic protection. The development of composite resins with improved properties will speed insertion of lightweight materials into FCS platforms. The shortfall in suitable resins may be addressed through exploitation of new electron beam (E-beam) curable systems including recently-developed interpenetrating polymer network (IPN) systems. E-beam curing of composites and adhesives offers many advantages including reduced cycle times, low-temperature cures for reduced residual stress, and through-thickness curing of thick-section composites and multi-material assemblies. Due to the complexity and thickness of composite integral armor structures, E-beam curing is an attractive processing method for FCS applications.

Despite the processing advantages derived from E-beam curing, E-beam resins have historically performed poorly when compared to existing resin systems. The poor performance has been attributed to the low toughness of the e-beam-cured materials. In this paper, the development of toughened e-beam curable polymers based on a unique IPN architecture is reported. IPNs are polymers that are formed from the independent polymerization of two or more distinct networks, which results in unique molecular and physical microstructures offering improved properties (Baidak 1997). The final properties of the IPN are critically dependent on the composition of the two networks as well as the polymerization mechanisms and kinetics of each network, but synergistic property improvements are frequently observed.

Specifically, the structure and properties of co-polymerized sequential-interpenetrating networks (SeqIPNs) synthesized from amine-cured epoxies and free-radical polymerized dimethacrylates have been examined. Synthesis proceeds by initially polymerizing the first network (epoxy-amine) thermally to form a template matrix for subsequent radiation-induced polymerization of the second (methacrylate) network. Fourier transform infrared (FTIR) spectroscopy was used to monitor epoxy-amine step-growth polymerization *in situ* and to measure final cure conversion of methacrylates. Two unique approaches to improve toughness have been employed. First, a bifunctional coupling additive was synthesized to promote bonding of the two independent networks in the IPN. The coupling monomer (B-DGEBA) was synthesized by partial methacrylation of a bisphenol-A diepoxide using methacrylic acid (Doyle 1967). Use of the B-DGEBA permits control of connectivity and influences resin properties including modulus, glass transition temperature, and toughness. Also, reactive liquid rubbers (e.g., epoxy-terminated butadiene nitrile - ETBN), which phase separate during cure to yield increased toughness have been introduced into these IPNs via reactive blending. The key challenge is achieving complete rubber phase separation during the initial polymerization of the epoxy-amine network in the presence of the methacrylates that act as diluents to suppress phase separation. Turbidity measurements were used to construct a phase diagram for the elastomer-modified IPN materials. Careful selection of composition, polymerization conditions, and rubber reactivity resulted in phase-separated structures. Materials with maximum toughness and minimum impact on modulus and T_g were obtained. Toughness of the neat IPN nearly doubled that of either independent network and the rubber-modified systems exhibited an order of magnitude increase in toughness.

Structural examination of the IPNs using atomic force microscopy (AFM) and scanning electron microscopy (SEM) revealed microphase separation in the neat-IPN materials and macroscopic phase separation of rubber-rich domains for elastomer-modified networks as illustrated in Figure 1. Dynamic mechanical analysis (DMA) of the IPN determined that the properties of the network are strongly dependent on the cure conditions. Furthermore, the viscoelastic behavior of the E-beam-cured IPN could be adequately described by the Williams-Landel-Ferry (WLF) and Kohrausch-Willams-Watts (KWW) equations, presumably due to a strong coupling

between the epoxy-amine and methacrylate networks via the introduction of the B-DGEBA monomer.

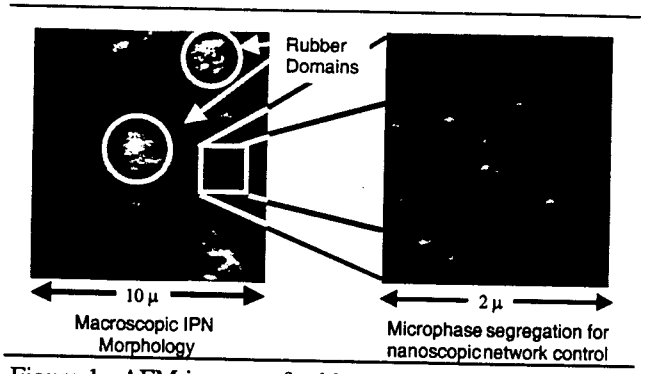


Figure 1. AFM images of rubber-modified IPN material.

Next, IPN-based adhesives and composites were formulated for evaluation using the toughened systems. The adhesive properties exceeded all existing e-beam adhesives, and approached or exceeded the properties of thermally-cured commercially available products as shown in Figure 2. Composite properties were also excellent and approached or exceeded properties reported for commercially-available resins designed for preimpregnated composite laminae (Dalal 1999). The control of properties via network design and morphology development have enabled the production of viable resins for use in composites and adhesives envisioned for composite integral armor.

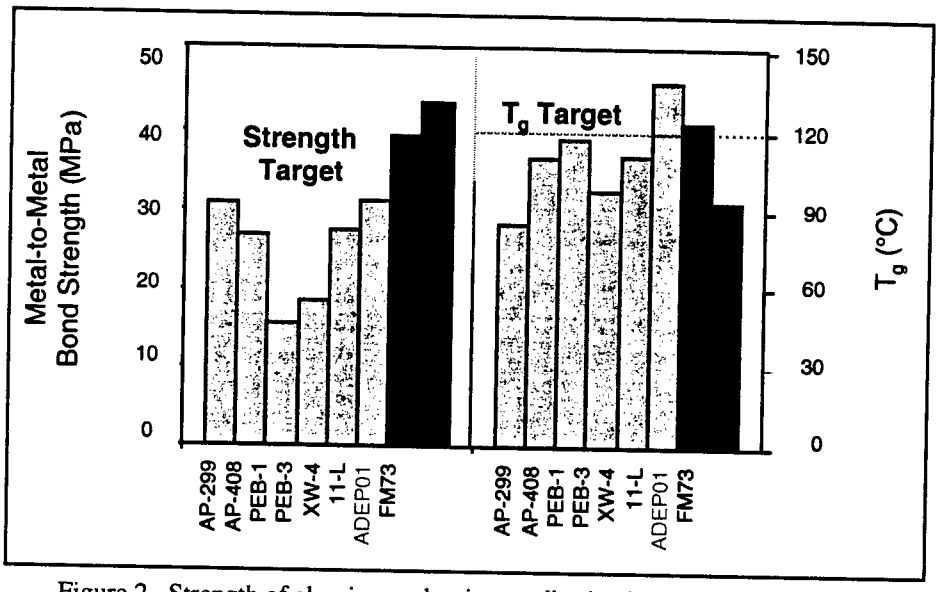


Figure 2. Strength of aluminum-aluminum adhesive joints and adhesive T_g.

REFERENCES

Baidak, A.A., Liegeois, J.M. and Sperling, L.H., "Simultaneous Interpenetrating Networks Based on Epoxy-Acrylate Combinations," *J. Polym. Sci. Polym. Phys.*, Vol 35, No 12, pp. 1973-1982, 1997.

Dalal, U.P., Master's Thesis, "Formation of In-Situ Sequential Interpenetrating Networks via Thermal and Radiation Curing," Department of Chemical Engineering, University of Delaware, pp 1-155, August 1999.

Doyle, T.E., Fekete, F, Kennan, P.J., and Plant, W.J. "Combination Catalyst-Inhibitor For Beta-hydroxy Carboxylic Esters," U.S. Patent No. 3,317,465, 1967.

TEMPERATURE-DEPENDENT ENERGY LOSS IN ALON

Bruce J. West
Mathematics and Computer Science Divison
US Army Research Office
Research Triangle Park, NC 27709-2211

SUMMARY

Aluminum oxynitride, also known as ALON, is a polycrystalline ceramic consisting of differing amounts of aluminum oxide and aluminum nitride, with the aluminum-nitride content between 27 and 40 mole-percent. The resulting material. a face-centered cubic with spinel structure, is cubic aluminum oxide that is nitrogen stabilized and is a transparent ceramic. It has been termed a non-stoichiometric spinel because some cation sites are occupied by vacancies, constituting an important class of imperfections in the crystalline structure [1]. ALON has been proposed for use in domes for missiles, transparent armor and sensor protection. It is 33% lighter than corresponding glass/plastic. It is commercially available and is technology adaptable to EM windows.

Recent measurements indicate that the energy loss in ALON, determined by the imaginary part of the complex dielectric coefficient, the so-called loss tangent, has an inverse power-law dependence on frequency. In addition the data also show that the overall level and the power-law index in this experimental loss tangent are temperature-dependent. These experimental results were recently discussed by West and McCauley [1].

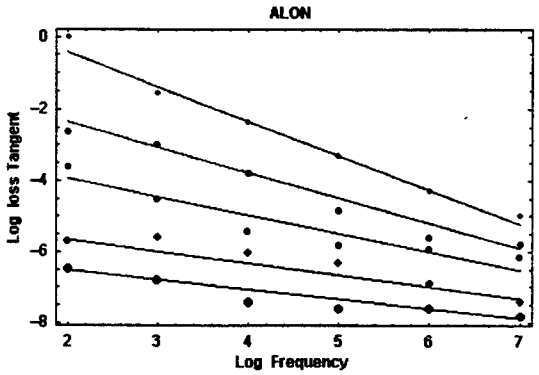


Figure 1: The five data sets are for temperatures of 500, 400, 300, 150, 25 $^{\circ}K$, starting from the top and going down. The straight lines are the best linear regression of the logarithm of the loss tangent to the logarithm of the frequency. The slope of the curve gives the power-law index, which changes with temperature. {Taken from [1]}

It the present study the author has constructed a thermodynamical model of the physical structure of ALON that can describe the dielectric properties observed in Figure 1. The measurements are made by applying a time varying electric field to ALON and measuring the polarization field, that latter being determined from the former in terms of the susceptibility. The dielectric coefficient is proportional to the susceptibility of the material, which using equilibrium statistical mechanical arguments is given by the integral

$$\chi(\omega)=\int_0^{\infty}\phi(t)e^{-i\omega t}dt=\chi'(\omega)-i\chi''(\omega) \tag{1}$$

where $\phi(t)$ is the molecular dipole-dipole correlation function. The dielectric loss tangent is proportional to the imaginary part of the susceptibility, $\chi''(\omega)$, where from Figure 1 [1]

$$\chi''(\omega)=\frac{A}{\omega^{\mu}} \tag{2}$$

where the power-law index is in the interval, $0 \le \mu \le 1$, and both A and μ are temperature dependent. Physically the inverse power-law susceptibility means that as the frequency of the external field increases, the dipole response starts to lag behind the field, and eventually the field oscillates so rapidly that the dipoles do not respond at all. This limiting behavior of the dielectric coefficient indicates that as the molecules begin to lag behind the external field, they absorb energy from the field, as measured by the imaginary part of the susceptibility, and continue to absorb energy until the frequency becomes sufficiently high that it is outside the dynamic range of the dipoles and they can no longer respond.

Using the data from Figure 1, the power-law index is shown to be quadratic in temperature (T) [2]

$$\mu = \mu_0 + \mu_1 T^2 \tag{3}$$

and the overall level of the susceptibility to be polynomial in temperature [2]

$$A = A_0 \exp\left[A_1 T + A_2 T^2\right]. \tag{4}$$

Substituting the two expressions for the parameters (3) and (4) into (2) we obtain a temperature-dependent susceptibility,

$$\chi''(\omega) \propto \frac{\exp\left[.0038T + .000023T^2\right]}{\omega^{.27+.0000027T^2}} \tag{5}$$

with the five numerical coefficients, $A_0, A_1, A_2, \mu_0, \mu_1$, fixed. The resulting dielectric loss tangent for five different temperatures is given in Figure 2:

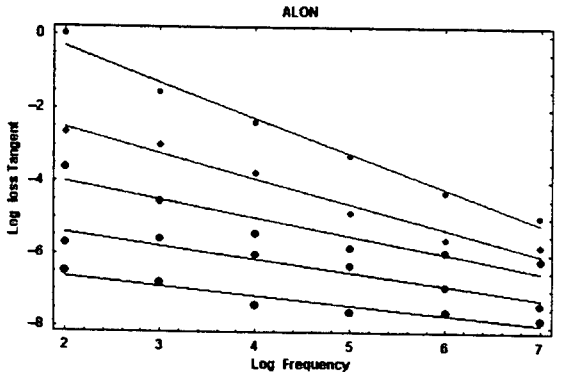


Figure 2 : The same five data sets shown in Figure 1 are indicated. The straight lines are not regression curves, however, they are all given by the single temperature-dependent equation (5). {Taken from [2]}

Comparing the results of the regression fit in Figure 1 with the graphs from the single equation (5) in Figure 2, we find very little difference. Thus, the latter equation captures certain essential properties of ALON.

West [2] constructed a stochastic model of the complex susceptibility of aluminum nitride (ALON) using nonequilibrium statistical mechanics arguments. His proposed model yields an inverse power-law dependence of the susceptibility on frequency, with the observed temperature dependencies of the parameters, given by (3) and (4), being a consequence of the thermodynamical properties of the molecular dipoles in the material. In particular, the molecular dipole-dipole correlation function is an inverse power law in time

$$\phi(t) = \frac{A^\beta}{(A+t)^\beta}. \tag{6}$$

The mean relaxation time, that is, the integral of the correlation function over all times, diverges when the power-law index is in the interval $0 \le \beta \le 1$, and correspondingly, $0 \le \mu = 1 - \beta \le 1$. This divergence of the mean relaxation time indicates that there is no characteristic time scale for the dynamics of the dipoles. This lack of a characteristic time scale suggests that the time series for the net dipole moment of ALON is fractal, which is to say, the dipole dynamics form a fractal random process.

[1] B.J. West and J. McCauley, "Scaling of the Susceptibility in ALON", submitted to J. Appl. Phys.
[2] B.J. West, "Temperature-dependent Susceptibility in ALON", unpublished

THERMO-MECHANICAL ANALYSES OF DYNAMICALLY LOADED VISCOELASTIC RUBBER CYLINDERS

Arthur R. Johnson and Tzi-Kang Chen
Army Research Laboratory, MS 240
Analytical and Computational Methods Branch
NASA Langley Research Center
Hampton, VA 23681-0001

ABSTRACT

A procedure that models coupled thermo-mechanical deformations of viscoelastic rubber cylinders by employing the ABAQUS finite element code is described. Computational simulations of hysteretic heating are presented for several tall and short rubber cylinders both with and without a steel disk at their centers. The cylinders are compressed axially and are then cyclically loaded about the compressed state. The non-uniform hysteretic heating of the rubber cylinders containing a steel disk is presented. The analyses performed suggest that the coupling procedure should be considered for further development as a design tool for rubber degradation studies.

1. SUMMARY

1.1 Background.

Rubber is employed to carry large loads in tires, gaskets, and tank track pads. It is also used to provide damping and system stability in complex mechanical systems such as helicopter rotors. In these applications the rubber is typically stiffened by the addition of carbon black. The filled rubber tends to be a poor conductor of heat yet it also exhibits very large hysteretic energy loss during cyclic loading. Also, the mechanical properties of rubber are strongly dependent on temperature. Designers interested in modeling the detailed response of complex shaped rubber components need to be able to computationally simulate the coupled thermo-mechanical behavior of highly viscous rubber materials.

An example of the importance of understanding the thermo-mechanical response of filled rubber is given in a series of papers presented at the "Thirty Second Sagamore Army Materials Research Conference" held at Lake Luzerne, NY in 1985. In these papers hysteretic heating, thermo-mechanical degradation, and fatigue of rubber coated road wheels and tank track pads are all discussed. Uncoupled thermo-mechanical analyses were conducted. Sensitivity studies were made with the finite element codes which determined that the viscoelastic properties and the geometric design are the most important factors in determining temperature rise (Lesuer, Goldberg, and Patt, 1986.) Degradation studies indicated that the failure of cyclically loaded "rubber-like" polyurethane blocks depended on the segment transition temperature (Mead, Singh, Roylance, and Patt, 1986.) Experiments were conducted which proved that the large strain hysteretic heating rate did not correlate with the heating rates predicted using the popular complex moduli material data (Mead and Pattie, 1986.) It was also determined that failure under cyclic loading can be "significantly different from that obtained in constant rate testing (McKenna, Bullman, Flynn, and Patt, 1986.) These conclusions suggest that detailed computational simulations of the large strain dynamical loading of rubber-like solids requires accurate modeling of the large strain viscoelastic properties and a coupling with the thermal properties.

In the paper we outline the formulations for large strain rubber viscoelasticity and heat transfer employed in ABAQUS. Detailed information on these two algorithms is available in the ABAQUS Theory Manual (Hibbitt, Karlsson, and Sorensen, 1996.) Additional information on formulations for rubber viscoelasticity is available in the literature.

1.2 Rubber Viscoelasticity

The virtual work statement, without inertial effects included, for a solid of volume V and surface area S is:

$$\delta W_I = \int_V \boldsymbol{\sigma} : \delta \mathbf{D}_v \, dV = \int_S \delta \mathbf{v}^T \mathbf{t} \, dS + \int_V \delta \mathbf{v}^T \mathbf{f} \, dV \quad [1]$$

where δW_I is the internal energy due to the virtual displacement $\delta \mathbf{v}$, $\boldsymbol{\sigma}$ is the Cauchy stress, $\delta \mathbf{D}_v$ is the virtual rate of deformation, $\mathbf{t}$ is the traction stress vector acting on S, and $\mathbf{f}$ is the body force vector acting within V. Equation [1] is used to build the finite element equations for mechanical equilibrium.

1.3 Heat Transfer.

The variational statement of the energy balance equation for heat transfer, together with Fourier's law, for a deformed solid of volume V, and surface area S is:

$$\int_V \rho \frac{dU_\theta}{dt} \delta\theta \, dV + \int_V \frac{\partial \delta\theta}{\partial \mathbf{x}} \mathbf{k} \frac{\partial \theta}{\partial \mathbf{x}} dV = \int_V \delta\theta \, r \, dV + \int_S \delta\theta \, q \, dS \qquad [2]$$

where θ is the temperature, U_θ is the internal thermal energy, ρ is the density, q is the heat flux per unit area, r is the heat supplied per unit volume, $\mathbf{k}$ is a conductivity matrix, and $\delta\theta$ is a virtual temperature field satisfying the essential boundary conditions. Equation [2] is used to build the transient heat transfer finite element equations.

1.4 Coupled Thermo-Mechanical Model.

Finite element discretization of the mechanical and thermal variational statements given above results in systems of time dependent mechanical and thermal differential equations. Coupling due to the viscoelastic effects can be approximated by computing the rate of energy dissipation due to the viscoelastic material properties, and inputting that rate into the heat transfer equations. ABAQUS internally computes and stores the total energy dissipated as a function of time. A "USER SUBROUTINE" is written which stores the dissipated energy as a state variable, computes its increment across a time step, converts the increment to a rate, and sends the rate to the heat transfer algorithm for the next time step. With this method, the heating rate, which couples the mechanical and thermal equations, lags by one time step. At small time steps the method approximates coupled thermo-viscoelasticity for large deformations of highly viscous rubber components.

2. RESULTS

An example of the nonuniform heating of a rubber cylinder containing a cylindrical steel inclusion is shown in Figure 1. An axial cyclic load was applied. The heating is most pronounced at the radial end of the rigid steel inclusion.

3. REFERENCES

Hibbitt, Karlsson, and Sorensen, ABAQUS Theory Manual, Version 5.8, 1080 Main St., Pawtucket, RI, 02860, 1996.

Lesuer, D. R., Goldberg, A., and Patt, J., "Computer Modeling of Tank Track Elastomers," in Elastomers and Rubber Technology, Eds. R. E. Singler and C. A. Byrne, Library of Congress 86-600600, pp. 211 - 228.

Mead, J. L., and Pattie, E. R., "Thermal and Dynamic Mechanical Properties of Elastomers," in Elastomers and Rubber Technology, Eds. R. E. Singler and C. A. Byrne, Library of Congress 86-600600, pp. 273 - 280.

Mead, J. L., Singh, S., Roylance, D. K., and Patt, J., "Thermomechanical Degradation of Elastomers," in Elastomers and Rubber Technology, Eds. R. E. Singler and C. A. Byrne, Library of Congress 86-600600, pp. 251 - 268.

McKenna, G. B., Bullman, G. W., Flynn, K. M., and Patt, J., "Fatigue of a Rubber Tank Track Compound Under Tensile Loading," in Elastomers and Rubber Technology, Eds. R. E. Singler and C. A. Byrne, Library of Congress 86-600600, pp. 525 - 534.

Pitts, D. R. and Sissom, L. E., Heat Transfer, McGraw-Hill Book Co. Library of Congress 77-20255, 1977.

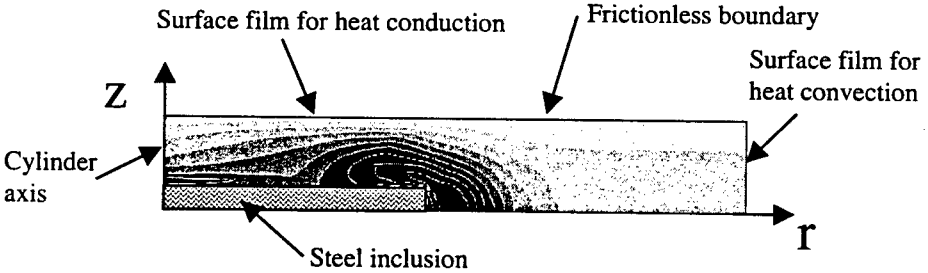


Figure 1. Axisymmetric view of viscoelastically heated rubber block with inclusion.

EFFECTS OF PROCESSING ON CONNECTIVITY OF FERROELECTRIC $Ba_{0.55}Sr_{0.45}TiO_3$ / MgO COMPOSITE STRUCTURES

*Jennifer Synowczynski and Bonnie Gersten
U.S. Army Research Laboratory
Weapons and Materials Research Directorate
Aberdeen Proving Grounds, MD 21005-5069

1. INTRODUCTION

A major hurdle to the digitizing the battlefield command initiative is the requirement to maintain secure rapid communications between on-the-move combat systems and command stations. In order for this vision to be realized, phase shifting antenna technology will need to be integrated into the entire Army arsenal. Currently, the system cost for SATCOM communications between DSCS satellites and HMMVs is approximately $400k/system (Harris RAP Array). Forty percent of the cost for these systems is in the Ferrite T/R modules. Lower cost phase shifting technologies have been developed to replace the T/R modules including MMIC, MEMs and Ferroelectric phase shifters. Of these, ferroelectric phase shifters have the greatest potential for higher (> 30 GHz) frequency communications. They do not require expensive manufacturing processes or hermetic packaging like their MMIC and MEMs counterparts. In addition, the phase shift is created by changing the permittivity of the ferroelectric with an applied electric field. Therefore, there are no mechanically moving parts involved in the phase shifting process. This translates into increased reliability and operational lifetime.

1.1 Ferroelectric Composite Materials

The critical materials parameters for many microwave devices are low dielectric constant (for impedance matching), low dielectric loss tangent (high efficiency), high tunability (i.e., percent change in permittivity with applied voltage) and small temperature coefficient of permittivity (temperature stability). Unfortunately, ferroelectric materials are lossy, meaning that much of the RF radiation is dissipated inside the ferroelectric. To improve the loss tangent of ferroelectrics, investigators at ARL have developed an innovative approach (Synowczynski et al, 1998; Sengupta et al, 1997). This new approach involves compositing the ferroelectric material ($Ba_{0.6}Sr_{0.4}TiO_3$ $\tan\delta = 0.0908$ @ 10GHz) with a low-loss, temperature-stable dielectric such as MgO ($\tan\delta = 0.0003$ @ 1MHz). Conceptually, the prime contributor to the reduction in the dielectric loss tangent is through ferroelectric dilution. However, the compound MgO has several additional positive influences on the crystal structure and microstructure that also reduce the dielectric loss tangent. For example, MgO acts as a grain growth inhibitor in $BaTiO_3$ (Kishi et al, 1999), eliminating exaggerated grain growth and narrowing the grain size distribution. This results in a more uniform microstructure, which improves the temperature stability and dielectric loss characteristics. Using this approach, we have succeeded in producing voltage tunable dielectric materials with permittivities in the range from 800 to 100 and loss tangents as low as 0.008 at 10 GHz (Synowczynski et al, 1998; Sengupta et al, 1997).

1.2 Effect of $(Ba,Sr)TiO_3$ Grain Connectivity

The most important parameter for composite systems is the connectivity between the two phases. This is especially true for ferroelectric/nonferroelectric composite systems such as the $(Ba,Sr)TiO_3$ / MgO system. Compositions with > 40 weight percent MgO begin to suffer from electrical isolation, limiting and ultimately eliminating the tunability of the composite (Sengupta et al, 1997). The connectivity between the ferroelectric grains can be significantly influenced by the processing procedures used to manufacture the phase shifters. The objective of this paper is to compare the effect of ferroelectric powder processing (solid-state reaction vs. hydrothermal synthesis), green body densification (dry press vs. tape cast), and sintering (conventional vs. diffusion enhanced sintering) on the connectivity and tunability of 40wt% $Ba_{0.55}Sr_{0.45}TiO_3$ / 60wt% MgO composite structures.

2. EXPERIMENTAL PROCEDURE

All $Ba_{0.55}Sr_{0.45}TiO_3$ starting powders for the samples in this study except for the hydrothermal samples were made by ball milling the proper ratio of refined $BaTiO_3$ and $SrTiO_3$ powders (Ferro Co., Penn Yan, NY, 99.95% pure) in ethanol for 24 hr. Subsequently, the powders were calcined in air at 1100°C for 2 hr to remove residual organics and form phase pure $Ba_{0.55}Sr_{0.45}TiO_3$. The hydrothermal $Ba_{0.55}Sr_{0.45}TiO_3$ (TPL, Inc., Albuquerque, NM) powders were chemically synthesized in water and then calcined at 450 °C for 4 hr to remove structural hydroxyl groups. After calcination, both starting powders were characterized for their particle size, surface area, phase purity, and morphology.

The calcined $Ba_{0.55}Sr_{0.45}TiO_3$ powders were mixed with MgO (Alfa, MA, 99.95% pure), and ball milled in ethanol for 24 hr. The slurries were dried under infrared heating lamps and sieved through a 425-mesh sieve. To study the effects of green body densification on the final microstructure, the composite powders were consolidated using both colloidal processing techniques (tape casting) and uniaxial dry pressing. Tape cast samples were prepared from $Ba_{0.55}Sr_{0.45}TiO_3$ and MgO powders dispersed with fish oil in an ethanol/xylenes solution and milled for 34 hr. During the last 10 hr, butyl benzyl phthalate and poly (vinyl butyral) were added to the slurry. The viscosity was measured using a Brookfield Viscometer RV-4 spindle at 20 rpm. The slurry was then de-aired, cast at 20 in/min onto silicized mylar and air-dried for an additional 10 hr. Dry-pressed samples were consolidated in a 1" stainless steel die at 9,000 psi. No additional binders were required to increase the green strength. Several dry pressed samples were doped with an additional 0.5 mole percent Mn_2O_3 (Alfa, 98% pure) to enhance diffusion during sintering.

The sintering profiles were developed using Archimedes density measurements and Simultaneous Thermal Analysis to determine optimum temperatures for removing residual organics. All green bodies for this study were sintered in a flowing air atmosphere. To expose the grain boundaries, samples for microstructural analysis were thermally etched at 10 °C below their sintering temperatures for 15 min. Finally, the sintered microstructures were characterized for phase purity, elemental identification, and microstructural homogeneity. The sintered composites were then ranked according to a figure of merit which ratios the interfacial area between connective and unconnective $Ba_{0.55}Sr_{0.45}TiO_3$ grains.

Dielectric property measurements were conducted as a function of temperature at low frequency (250kHz) using LCR capacitance measurements under 2V/μm biasing field with a guarded electrode configuration. Permittivity and dielectric loss were also measured at high frequency (10 GHz) using a cavity resonator method (Geyer et al, 1997). Detailed descriptions of both dielectric measurement techniques are available in the references.

3. RESULTS

3.1 Microstructural analysis

XRD confirmed the existence of only MgO and $Ba_{0.55}Sr_{0.45}TiO_3$ phases in the sintered microstructure. EDS identified the dark phase as MgO and the lighter phase as $Ba_{0.55}Sr_{0.45}TiO_3$. $Ba_{0.55}Sr_{0.45}TiO_3$ segregation occurred in the dry-pressed samples processed from solid-state-reacted powders due to the differences in particle size and density between the MgO and $Ba_{0.55}Sr_{0.45}TiO_3$ powders. Results showed that the connectivity between the $Ba_{0.55}Sr_{0.45}TiO_3$ grains was greatest for the hydrothermal composite structures. The figure of merit rankings were as follows:
1) Hydrothermal Powder Synthesis (FOM = 0.44)
2) Diffusion Enhanced Sintered (FOM = 0.29)
3) Tape Cast (FOM = 0.23)
4) Dry-Pressed Solid-State Reacted (FOM = 0.15)

3.2 Dielectric Properties

The tunability rankings at -20°C and 2V/μm DC bias directly correlated to the microstructural rankings:
1) Hydrothermal Powder Synthesis (26%)
2) Diffusion Enhanced Sintered (20%)
3, 4) Tape Cast, Dry-Pressed Solid-State-Reacted (16%).
The enhancements were most significant below the Curie temperature. This is explained by the cooperative nature of ferroelectricity. Ferroelectric behavior is strongly dependent on the boundary conditions and interfaces. As the $(Ba,Sr)TiO_3$ grains transition through the Curie temperature, a volume expansion occurs. This expansion is resisted by the MgO grains, creating a compressive stress state at the interface. This stress results in a depolarization force that reduces the tunability of the material. The interface effect is especially significant in the ferroelectric temperature regime. The dielectric properties measured at 10 GHz are: Diffusion Enhanced Sintered (ε_R = 96, tanδ = 0.0068); Tape Cast (ε_R = 79, tanδ = 0.0071); Dry Pressed Solid-State-Reacted (ε_R = 100, tanδ = 0.008).

4. CONCLUSIONS

Three processing stages were evaluated in this study: powder synthesis, green body densification, and sintering. The powder synthesis method had the most profound effect on the connectivity of the ferroelectric grains and, hence, tunability of the ferroelectric composite (Baseline: 16% ⇒ Hydrothermal 26% @ 2V/μm, -20°C). Tape casting improved the mixing between the $Ba_{0.55}Sr_{0.45}TiO_3$ and MgO powders directly prior to producing the green body. However, it was not as effective in increasing the tunability as the diffusion enhanced densification. This illustrates how critical the sintering conditions are for the tunability of the composite. A sound strategy for manufacturing these structures is to use processing techniques that directly produce the green body from the particles dispersed in a liquid medium (i.e., tape casting, slip casting, screenprinting, sol-gel, etc) and sintering aids to enhance the diffusion during densification.

LASER PULSE HEATING SIMULATION OF FIRING DAMAGE ON COATED GUN BORE SURFACES

P. J. Cote*, G. Kendall and M. Todaro
US Army Armament Research, Development and Engineering Center, Benet Laboratories
Watervliet, NY, 12189

ABSTRACT

Laser pulse heating was used to simulate the effects of thermal shock loading on plated gun bore surfaces during firing. The aim is to provide new insights into the erosion process and develop the method as an evaluation tool for developmental coatings. This report discusses results of cyclic thermal pulsing experiments on high contractile and low contractile chromium plated gun steel, sputtered tantalum coated gun steel, and uncoated steel.

1. INTRODUCTION

Laser pulse heating was used to simulate the effects of thermal shock loading on gun bore surfaces during firing. in an attempt to gain new insights into the erosion process. Gun bore surfaces are typically subjected to short (5-10 milliseconds) pulses of high thermal energy during firing of a round. Included among the deleterious thermal effects are melting, metallurgical transformations, thermal and transformational stresses, and surface cracking.

Bore surfaces are often electroplated with high contractile (HC) chromium to enhance resistance to erosion. (The terms high contractile and low contractile (LC) refer to the differences in shrinkage and cracking during deposition and annealing of HC and LC chromium electrodeposits.) Low contractile chromium electroplated coatings for large caliber gun bores were recently developed in order to exploit benefits of coatings with lower crack densities. Current efforts are also underway in developing alternatives to chromium (e.g., magnetron sputtered tantalum).

There is extensive experience with gun bore protective coatings including HC and LC chromium [Ahmad, 1988, Burlow, 1946, Dowding and Montgomery, 1996]. The most extensive compilation of this experience remains the 1946 National Defense Research Committee Report "Hypervelocity Guns and the Control of Gun Erosion"[Burlow, 1946].

A recent survey study of chemical attack initiation in HC and LC chromium plated gun bore surfaces [Cote and Rickard , 2000] showed that damage to the steel substrate begins at the tips of chromium cracks by propellant gas-metal reactions. The reaction products appear as gray layers or gray zones in the steel. These layers are iron oxide, iron sulfide, or mixtures of these two compounds, depending on the constitution of the propellant additives.

HC chromium is significantly more cracked than LC chromium after firing [Burlow, 1946, Cote and Rickard, 2000]. The as-plated LC chromium is uncracked while the as-plated HC already possesses a high density of embedded and surface cracks. Laser pulse heating was applied to gain insights into chromium cracking processes.

Sputtered tantalum coatings are under consideration for gun bores. Sputtered tantalum frequently deposits as a mix of alpha phase and a hard, brittle, metastable beta phase. Laser pulse heating was applied to alpha and beta phases to provide comparisons of the relative thermal shock resistance of the two phases.

Laser pulse heating was also applied to uncoated steel specimens to determine the effects of cyclic thermal pulsing on steel and to simulate the effects of repeated firing in gun bore areas where the chromium coating is removed by spallation.

2. EXPERIMENTAL

Radiation from a neodymium-doped yttrium aluminum garnet (Nd:YAG) laser is delivered to the test specimen surface through a coiled length of optical fiber and a lens assembly to provide approximately uniform energy over a circular spot. The pulse duration is 5 milliseconds (FWHM), and the spot diameter at the specimen surface is typically 2.6 millimeters. Given typical coating thicknesses of 0.1 mm, the spot diameter to coating thickness ratio is 26 so that most of the central spot area replicates the essentially one dimensional heat flow through the coating at the bore surface. In the present study, the absorbed energy was measured calorimetrically. This method was used to maintain the absorbed energy per pulse at approximately 1 J/mm^2, which is expected to be representative for bore heat flux from conventional high temperature propellants.

3. RESULTS AND DISCUSSION

A sample of the results of this study is given in the present summary. Figure 1 is an optical micrograph of a cross section of an HC chromium electrodeposit on a steel substrate. This specimen area was subjected to 20 pulses at incident energy 2-3 J/mm^2. The figure exhibits all the features of a fired chromium plated gun bore section as shown in Figure 2. This includes recrystallization and

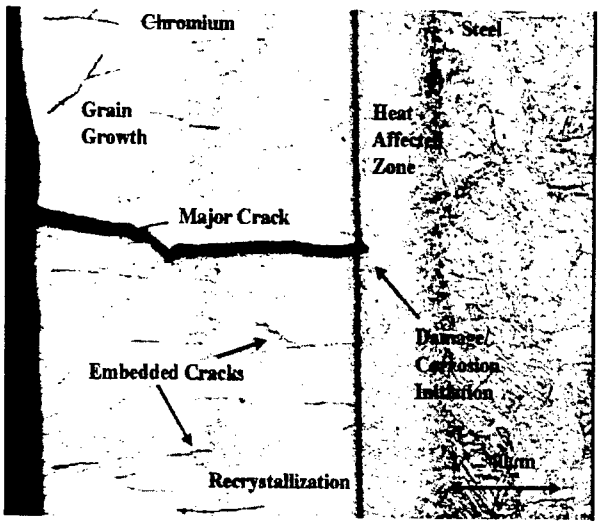


Figure 1: Laser pulse heated specimen showing metallurgical changes, chromium cracking and damage initiation in steel after 20 pulses.

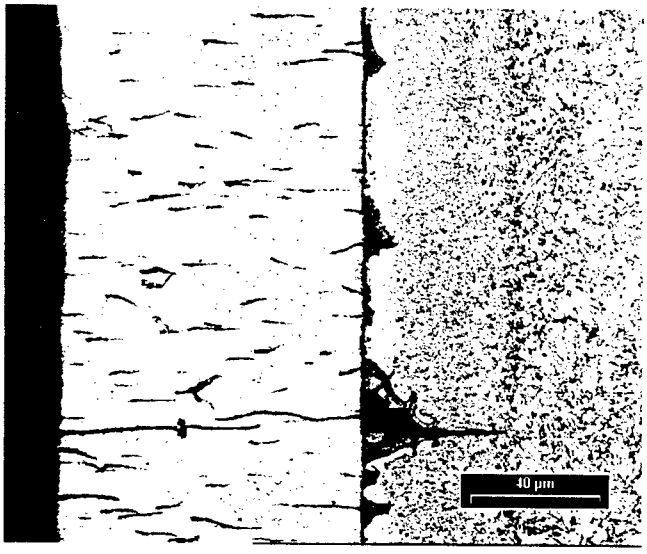


Figure 2: Damage initiation and propagation in steel in a 120 mm gun bore (approximately 80 experimental high temperature rounds and 225 conventional rounds).

grain growth in the chromium, development of major cracks in the chromium, a heat affected zone in the steel, and corrosion attack (iron oxide) at the tip of the cracks in the chromium.

The major cracks (cracks that extend through the coating) in Fig 1 are the result of the thermal pulsing alone. The absence of sharp cracks and the dramatic blunting of the chromium cracks in the brittle heat affected zone of Figure 1 are notable features that are also observed at damage initiation sites on fired gun bore surfaces.

The complete report on results of laser pulsing on HC and LC chromium, sputtered tantalum, and uncoated steel is given in the Conference proceedings.

4. SUMMARY

Laser pulse heating is shown to accurately reproduce the main features of the damage process experienced at the bore surface of fired guns, including rapid oxidation which may be the central gas-metal reaction in the erosion of gun bores. The present results offer new insights into a variety of issues relating to bore coating degradation as a result of severe thermal cycling. They also illustrate the broad range of problem areas relating to bore protective coatings that can be explored with laser pulse heating.

REFERENCES

Ahmad, I., "The Problem of Gun Barrel Erosion – An Overview," *Gun Propulsion Technology*, (L. Steifel, ed.), Progress in Astronautics and Aeronautics Series, AIAA, Washington, DC, , pp. 311-355, 1988.

Burlew, J.S., ed. "Hypervelocity Guns and the Control of Gun Erosion," *Summary Technical Report of the National Defense Research Committee*, Division 1, Office of Scientific Research and Development, Washington, DC, 1946.

Cote, P. and Rickard, C., a. "Gas-Metal Reaction Products in the Erosion of Chromium Plated Gun Bores", *Wear*, 241, (2000), pp17-25;

b. "Gray Layers and the Erosion of Chromium Plated Gun Bore Surfaces", *Technical Report ARCCB-TR-99016*, Benet Laboratories, Watervliet, NY, September, 1999.

Dowding, J.S., and Montgomery, J.S.,eds, *Proceedings of the Sagamore Workshop on Gun Barrel Wear and Erosion*, U.S. Army Reserarch Laboratory. Wilmington, DE, 29-31, July 1996,

NAFION® MEMBRANES: A STRUCTURAL EVALUATION FOR ADVANCEMENT OF THE MATERIALS USED IN CHEM/BIO PROTECTIVE CLOTHING AND DIRECT METHANOL FUEL CELLS

S. F. Trevino, Sandra K. Young, Nora C. Beck Tan
US Army Research Laboratory
Weapons and Materials Research Directorate
Attn: WMSRL-WM-MA / Bldg. 4600
Aberdeen Proving Grounds, MD 21005-516

Summary

Fuel cells are being considered as direct replacements for batteries to power soldier-portable devices used on extended missions, as power supplies for battery chargers, as power for silent watch and remotely placed sensors, and for use in robotics and electric vehicles in support of the Future Combat System.

Polymer electrolyte membrane fuel cell (PEMFC) technology is favored as a man-portable system because of its low operating temperature, fast start-up, lightweight, and high power. Direct methanol fuel cells (DMFC) oxidize methanol fuel to produce hydrogen ions, which are reduced at the air (oxygen) cathode. Current technology uses Nafion 117 as the polymer electrolyte membrane, which conducts protons from the anode to the cathode, as well as serving as the barrier between these two electrodes. However, membrane performance requires two primary areas of improvement. First, methanol permeates the membrane to cause a "chemical short" at the cathode, where it directly reacts with oxygen, thereby decreasing fuel utilization and oxygen cathode performance. Secondly, by improving the proton conductivity of the membrane higher current densities could be realized which could further reduce the size and weight of the fuel cell.

A common goal among many scientists is to determine the structure of Nafion®. Structural determination may provide a better understanding of ionomer properties (mechanical, thermal, ion and solvent transport), along with the possibility of controlling the properties. In addition, structural determination may provide routes for polymer modification, which would address the current problems involved in fuel cell technology.

Nafion® is a perfluorosulfonate ionomer membrane that has been under investigation for 20+ years for a variety of applications including solvent separations and fuel cells. Nafion® contains a tetrafluoroethylene backbone with a perfluorosulfonic acid side chain, which possesses the one hydrogen on the monomer and the site accessible for ion exchange. The structure of the polymer, which is still uncertain, is usually examined by small angle neutron scattering (SANS), small angle x-ray scattering (SAXS) and wide-angle x-ray scattering (WAXS) experiments. Experiments usually include specific pre-treatment to the membrane and, in some cases, exchange to a different counterion besides acid (H+) form.

Published exchange procedures have apparently assumed complete exchange, since no evidence of less than 100% neutralization has been reported. However, repetitive SANS experiments in our research using samples of supposedly the same H^+-form counterion have indicated different polymer structures. We were lead to the use of prompt gamma activation analysis for characterization of Nafion® films. The results indicated that the as received samples contained differing levels of counterions (less than 100% H+-form) with K^+ and Ca^{2+} counterion contamination. Scrutiny of the initialization procedure was indicated, since analysis of the maximum ion-exchanged sample is desired. Through this effort, an initialization procedure was determined for making the H^+-form films that lead to reproducible results, ion-exchange procedures were established for making samples of maximum ion-exchange, and a sample preparation procedure was ascertained for reducing the amount of atmospheric water contamination.

SANS techniques have been utilized to gain information on the polymer morphology. Dry samples of N117 were swollen to equilibrium in a variety of polar and non-polar solvents. Other N117 samples were swollen with water or ethanol to different volume fractions of solvent Three distinct features representing different aspects of the structure of Nafion® are observable in the SANS data. This, in itself, is a significant discovery since previous reports in the literature only were able to identify two features. Measurements as a function of volume fraction were obtained with water, etanol and propanol as swelling agent. The high angle peak is observed to shift with volume fraction whereas the other two features remain unchanged. The length characterized by this peak is observed to increase linearly with increasing volume fraction of solvent. This is true for all three solvents although the slope is different for each solvent.

Previously, most models regarding the structure of Nafion® postulated that the sulfonic acid groups aggregate into spherical cluster-type structures. If this structure of Nafion® is considered, we might assume swelling expands the spheres uniformly, then $d \sim V^{1/3}$. But our experimental data shows that $d \sim V$ linearly. This suggests to us rather that a layered structure exists whose linear dimension increases with increasing solvent.

WAXS was also utilized to determine changes in the crystal structure of the polymer. In these experiments, Nafion® membranes were examined in a variety of states: as-received dry, initialized H^+ form dry, and swollen in water, methanol, ethanol, propanol, butanol, and DMMP (a chem agent simulant). The differences between the as received dry, initialized H^+ form dry, and swollen in water samples were minimal. The diffraction data contained the same crystal features and the features did not appear to shift or change in intensity to any significant degree. However, examination of the methanol, ethanol, propanol, butanol, and DMMP solvent swollen membranes reveals significant changes in the crystal structure of the polymer. Significant shifts of the crystalline peaks are evident and, in some cases, these peaks disappear. This changing of the crystal structure has not been previously reported. It may prove significant for the mechanism of several macroscopic properties of this material.

Relevance to the Military

The relevance to the military is two-fold. The research started through cooperative efforts between the Polymers Branch at ARL and the Materials Science Team at Natick Soldier System Center. The research is directly related to the Force Protection and Soldier Systems efforts in chemical/biological protective clothing.

This research is also directly related to ARL's technology thrust involving Power Generation and Management Technology. It addresses the vision to support communications, transportation and all Mounted/Dismounted Army electric/electronic systems with dramatically more compact and efficient power sources. PEMFC technology is a high priority since fuel cells are expected to fulfill current and future increases in energy and power demands. The work is being correlated with on-going efforts in the Electrochemistry Branch at SEDD.

THE DEVELOPMENT OF AN AFFORDABLE MANUFACTURING PROCESS FOR MULTIFUNCTIONAL STRUCTURAL ARMOR

Shawn M. Walsh, Elias J. Rigas, William A. Spurgeon, and Walter N. Roy
U.S. Army Research Laboratory
Aberdeen, MD. 21005-5069
and
Dirk Heider and Jack Gillespie
University of Delaware, Center for Composite Materials
Newark, DE. 19716

A new process has been developed that will enable the cost-effective manufacture of structures and systems using polymer matrix composite-based multifunctional materials. The process, known as "FASTRAC" (Fast Remotely Actuated Channeling), has quantitatively demonstrated a labor savings of 40% and waste reduction of 30-40% as compared to conventional vacuum assisted resin transfer molding (VARTM) technology. The FASTRAC process was conceived to address unique Army requirements. This includes the need for a flexible, low to intermediate volume, production capability as well as a unified means by which to integrate the dissimilar materials (characteristic of a multifunctional armor) into a single, structurally resilient system. The FASTRAC process provides a means for cost-effective prototyping and manufacturing of current systems such as Crusader and Comanche, while providing an enabling technology to meet the needs of the Future Combat System (FCS).

Multifunctional armor consisting of polymer matrix composites, ceramics, rubber, and a variety of EMI shielding materials are unique to the Army. The composite serves as the primary load bearing structural material and spall liner, while the ceramic provides an effective barrier to ballistic impact. The combination of these materials has been shown to defeat a variety of known ballistic threats. The challenge to ensure affordability is two-fold. First, the total number of multifunctional armored platforms will remain relatively small compared to more conventional vehicle manufacturing (e.g., automobiles). Thus, it is not possible to achieve economies of scale associated with high volume production. It is therefore absolutely essential that waste and rejection rates be minimized by an efficient low to medium volume processing method. A second challenge is presented by the nature of the multifunctional structures themselves; the constituent materials such as polymer matrix composites, ceramics, and rubber are all dissimilar, significantly increasing manufacturing complexity.

The development of FASTRAC was accelerated by the use of computer simulations of the physics that describe the impregnation of a composite system. Specifically, a Darcy's law based model was used to describe the free-surface flow of resin as it permeates the fibrous reinforcement. A series of channel boundary conditions were imposed on the surface of the preform, simulating the behavior of the FASTRAC medium. It was conclusively demonstrated that a significantly enhanced flow pattern could be achieved using multiple channels, the dimensions of which are coupled to the parameters of the part being impregnated. Although the pressure differential is relatively modest (e.g., atmospheric pressure under pure vacuum) the model allows optimization of channel design by explicitly identifying the correlation between flow rate and the number and size of the FASTRAC channels. The result is a process simulation model, which can be used *a prior*, to design and evaluate a FASTRAC medium for a range of applications.

Figure 1 is a schematic of the FASTRAC process. Depending on the resin viscosity, fiber reinforcement, part thickness, and geometry, the computer model is used to design an optimum resin flow path for impregnating the component. This design is subsequently transferred to a computer controlled machining operation, which rapidly fabricates a reusable secondary vacuum bag, containing the three-dimensional imprint of the desired flow pattern. This secondary vacuum bag is subsequently installed over a reusable, Teflon-coated primary vacuum bag. Resin flow is initiated by first pulling a full vacuum between the secondary and primary vacuum bags; this creates channels between the primary vacuum bag and the surface of the fibrous preform to be impregnated. A second vacuum is subsequently applied to the fiber preform, providing the pressure differential that promotes resin flow through the channels and impregnation of the preform. By selectively adjusting the vacuum between the primary and secondary vacuum bags, it is possible to directly control the resin flow rate. FASTRAC thus offers an entirely new means of controlling the rate of resin flow and impregnation. FASTRAC also incorporates an improved method for steering the resin flow front. Based on distributed sensor information, including resin detection at the vacuum lines, an integrated real time control algorithm redirects the primary vacuum. This not only significantly reduces total resin impregnation time, but also minimizes resin waste by preventing excessive and unnecessary resin venting at all vacuum locations.

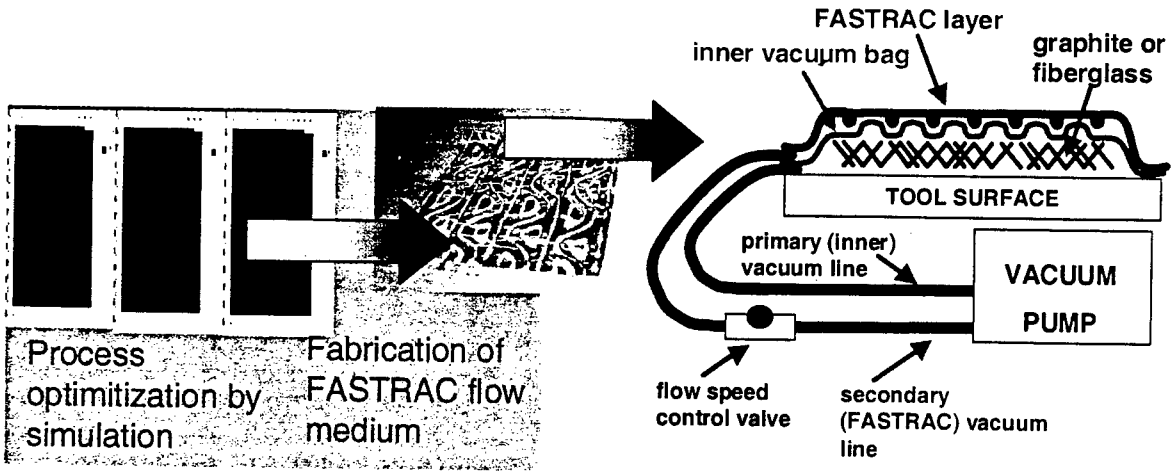


Figure 1. Schematic of FASTRAC Technology

The FASTRAC process has already been successfully demonstrated on several applications. For example, a 4' long, S2 glass armor panel was thoroughly impregnated with a room temperature SC-15 epoxy (viscosity ~250 cp) in 34 minutes with a single resin feed source. This is not possible with current commercial versions of VARTM. Another example is the fabrication of a tank skirt using woven glass fabric and a polyurethane (Adiprene) resin system. The viscosity of the Adiprene at an elevated processing temperature (~140 deg. F) is 2200 cp, far above the 100-250 cp viscosity limitations of conventional VARTM. However, a thorough fill of the woven fabric was achieved with the FASTRAC process using specially designed channels to maximize flow. Further savings are achieved from FASTRAC by avoiding unnecessary installation, removal, and waste associated with commercial VARTM, as shown in Figure 2.

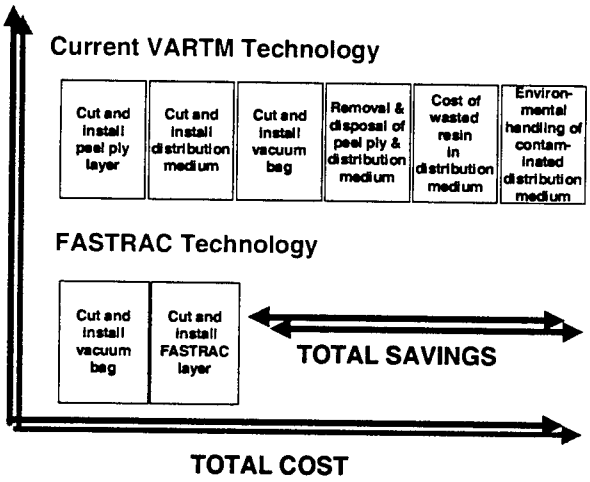


Figure 2. Cost Savings Associated with FASTRAC Process

The FASTRAC process was developed out of a need to affordably and reliably produce composite based materials and structures for a range of current and anticipated Army programs, including FCS. FASTRAC not only minimizes labor and waste, but also broadens the window of opportunity for advanced resin systems, which cannot be processed using currently available methods. Accelerated impregnation cycles, fewer resin feed lines, improved surface finish, and the ability to process resins with higher viscosities and relatively short pot lives are all features of the FASTRAC process which have been conclusively demonstrated.

Session B
Microelectronics and Photonics

Chair
Dr. Michael A. Stroscio
U.S. Army Research Laboratory

Co-Chair
Dr. James Ratches
U.S. Army Communications-Electronics Command

Keynote Address
Dr. Charles M. Bowden
U.S. Army Aviation and Missile Command

THIS PAGE INTENTIONALLY LEFT BLANK

DEVELOPMENT OF ADVANCED INTERBAND CASCADE LASERS FOR IRCM APPLICATIONS

John L. Bradshaw,* John D. Bruno, John T. Pham, Donald E. Wortman,[+] and Rui Q. Yang[+]
U.S. Army Research Laboratory, 2800 Powder Mill Road, Adelphi, MD 20783-1197

ABSTRACT

Recent advances in the development of type-II interband cascade (IC) lasers at ARL are reviewed. We report on the growth, fabrication, and characterization of our most recent lasers with emphasis on recent improvements in continuous wave operation.

1. INTRODUCTION

Army future combat systems will require a new generation of infrared countermeasure (IRCM) technology that must be lighter, compact, and more power efficient than currently deployed systems. We are presently developing interband cascade (IC) lasers that promise to meet or surpass future requirements for IRCM systems. In realizing the stringent performance specifications required for IRCM, IC lasers will also demonstrate applicability to other critical military technologies such as chemical sensing, and trace gas and bio-agent detection.

2. BACKGROUND

IC lasers are a new class of mid-IR light sources that use optical transitions between the conduction and valence bands in a staircase of Sb-based type-II quantum well (QW) structures (Yang, 1994; 1995). These unique lasers take advantage of the broken band-gap alignment in Sb-based type-II QWs to form cascade stages that reuse electrons for sequential photon emissions from serially connected active regions. The cascade nature of the device leads to a quantum efficiency greater than the conventional limit of unity, similar to the intersubband quantum cascade (QC) laser (Faist, 1994). Also, IC laser designs can circumvent the fast phonon scattering loss in intersubband QC lasers and suppress Auger recombination through band-structure engineering, resulting in a low-threshold current density.

The concept of IC lasers was first proposed in 1994 (Yang, 1994; 1995). Recently, we have made significant advances at ARL in developing type-II IC lasers in terms of record-high differential external quantum efficiency (> 600%), peak output power (>6 W at 80 K), pulsed operating temperature (~252 K), continuous wave (cw) operation (~128 K), cw power conversion efficiency (>14% at 80 K), and reproducibility (Bradshaw *et al.*, 1999; Bruno *et al.*, 2000). For a discussion of earlier work, see the review by Yang (Yang, 1999). Below, we report on the growth, fabrication, and performance characteristics of our most recent IC laser structure.

3. EXPERIMENT

The IC laser material was grown by molecular beam epitaxy (MBE) at ARL on a (001)-oriented *p*-type GaSb substrate. The laser structure consists of 18 active regions separated by *n*-type injection regions and is composed of many coupled QWs made from Al(In)Sb, InAs, and Ga(In)Sb layers (Bruno *et al.*, 2000). After the growth, the wafer was processed into gain-guided metal stripe or mesa-stripe devices with several different widths by both wet-chemical and dry-etching techniques. Laser bars were cleaved into cavities from ~0.5 to 2 mm long with both facets left uncoated. The laser bars were mounted epilayer side up onto copper chip carriers with indium and measurements were made with using the temperature-controlled cold finger of an optical cryostat.

4. RESULTS AND DISCUSSION

Under pulsed excitation conditions, several broad-area devices lased at temperatures up to ~252 K and in cw mode to 128 K, depending on their sizes. The lasing wavelength ranged from ~3.64 to 3.83 μm, depending on the current and temperature, red shifting substantially with increasing device temperature.

Figure 1 shows a typical light versus current (*L-I*) characteristic for a gain-guided metal-stripe laser under pulsed excitation conditions. The threshold current density versus temperature (inset) shows a characteristic temperature T_0 of ~80 K at temperatures no higher than 200 K; the threshold current density increases rapidly with a T_0 of ~ 25 K at higher temperatures.

Figure 2 shows the cw characteristics of a 0.11-mm-wide by 1.06-mm-long mesa-etched laser. Note that the voltage-current (*V-I*) characteristic in fig. 2 (lines) shows abrupt kinks in the slope that correspond to the onset of lasing in the *L-I* data. As shown in fig. 2, an output power of 125 mW/facet was observed from this laser at 80 K and a current of 460 mA; at 90 K, the output power was greater than 100 mW/facet at 460 mA current.

Figure 3 shows *I-V-L* characteristics (top figure) and differential resistance and power efficiency (bottom) for a 0.06 × 0.51-mm dry-etched mesa-stripe laser under cw conditions at heat sink temperatures ranging from 70 to 125 K. The maximum cw operating temperature was 128 K. The average differential external quantum efficiency exceeds 300% at 70 and 80 K, with an output power of ~90 mW/facet at a current of 200 mA. An abrupt reduction of differential resistance (solid lines, bottom of

[+] Present affiliation: Maxion Technologies Inc., Hyattsville, MD 20782

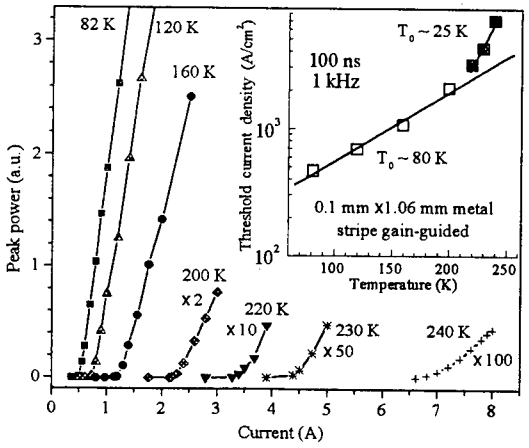


Figure 1. Pulsed current characteristics: peak power vs. current for a gain-guided metal stripe (0.1- × 1.06-mm) laser. The threshold current density vs. temperature is shown in the inset.

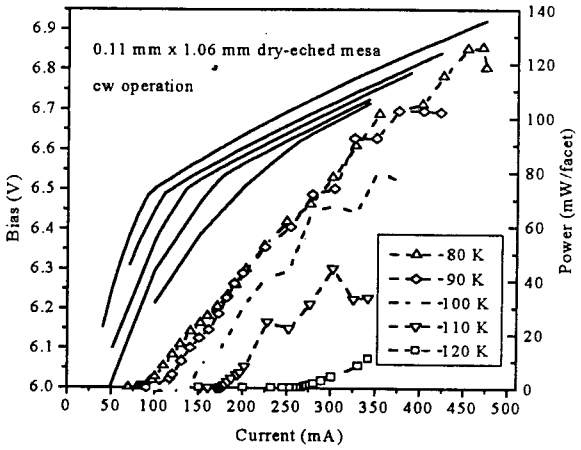


Figure 2. CW current characteristics: current vs. voltage (solid lines) and current vs. power (symbols, dotted lines) for a mesa-etched (0.11- × 1.06-mm) laser.

fig. 3) corresponding to the kink observed in the *V-I* data is observed at the lasing threshold and clearly manifested the startup of lasing action associated with a rapid increase in the pace of carrier transport just above threshold. As shown in the lower dotted curves of fig.3 record-high power efficiencies (>14%) among mid-IR diode lasers were observed at 70 and 80 K.

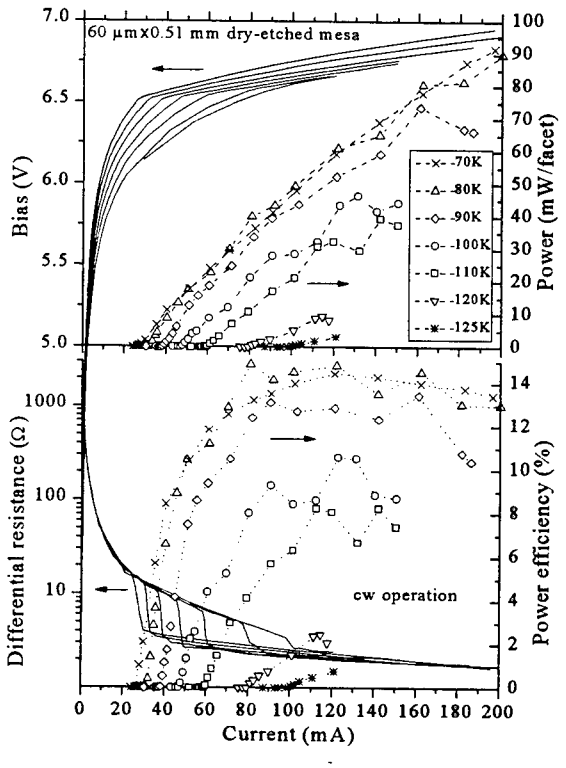


Figure 3. *V-I* and *L-I* characteristics (upper curves) and differential resistance and power efficiency (lower curves) for a 0.06- × 0.51-mm mesa-etched laser.

5. CONCLUSIONS

Although our results are encouraging, our main challenge remains to further improve device performance via increased output power and maximum cw operating temperature. High joule heating within the active region of the device is detrimental to laser performance in this regard. One way to reduce this heating is to make small-area ridge lasers. Another approach is to mount the device epilayer side down to better cool the active region. We will report on our latest progress in these areas.

REFERENCES

Bradshaw, J. L., Bruno, J. D., Pham, J. T., Wortman, D. E., and Yang, R. Q., "High-efficiency interband cascade lasers with peak power exceeding 4W/facet," *Appl. Phys. Lett.*, vol 75, pp. 2362–2364, October 1999.

Bruno, J. D., Bradshaw, J. L., Yang, R. Q., Pham, J. T. , and Wortman, D. E., "Low-threshold interband cascade lasers with power efficiency exceeding 9%," *Appl. Phys. Lett.*, vol 76, pp. 3167–3169, May 2000.

Faist, J., Capasso, F., Sivco, D. L., Sirtoti, C., Hutchinson, A., and Cho, A. Y., "Quantum cascade lasers," *Science*, vol 264, pp. 553–556, April 1994.

Yang, R. Q., "Infrared laser based on intersubband transitions in quantum wells," at *7th Inter. Conf. on Superlattices, Microstructures and Microdevices*, Banff, Canada, August 1994; *Superlattices and Microstructures*, vol 17, pp. 77–83, 1995.

Yang, R. Q., "Mid-infrared interband cascade lasers based on type-II heterostructures," *Microelectronics J.*, vol 30, pp. 1043–1056, 1999.

SINGLE STEP MICROLENS-ANTIREFLECTIVE STRUCTURES FOR INFRARED FOCAL PLANE ARRAYS

M.R. BANISH,[1] D.R. BROWN,[2] A.J. STOLTZ,[3] M. MARTINKA,[4] J.H. DINAN,[4] J.D. BENSON,[4] D.B. CHENAULT,[1] P.R. BOYD[5]

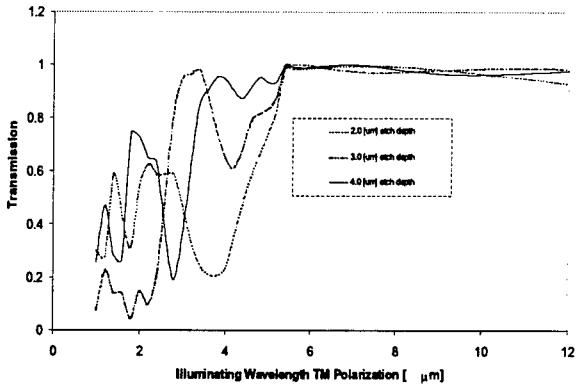
1-SY Technology, Inc., Huntsville, AL 35806
2-MEMS Optical LLC, Huntsville, AL 35806
3-E-OIR Measurements, Inc., Spotsylvania, VA 22060
4-Night Vision and Electronic Sensors Directorate, Ft. Belvoir, VA 22553
5-Army Research Laboratory, Adelphi, MD 28073

To satisfy the needs of Future Combat Systems, the next generation of imaging infrared (IR) sensors will require increased sensitivity. This can be achieved by adding antireflective (AR) structures and microlenses to the focal plane array (FPA) chips used in current generation systems. When formed on the back surface of an FPA, an AR structure can in principle quench the portion of the incoming radiation which is ordinarily reflected away from the chip and allow nearly 100% to propagate into the active region. It has the distinct advantage over conventional deposited AR coatings in that this can be made to occur over quite broad regions of the optical spectrum. The addition of an optically immersed lens - a microlens - to each pixel of an FPA allows the size of the pixel to be decreased, leading to a corresponding increase in signal to noise ratio. We have developed a technique for producing both of these structures in semiconductor wafers using a single inexpensive manufacturing step.

Immersed lens calculations and rigorous coupled-wave analysis (RCWA) modeling tools were used to design microlenses. RCWA modeling was also used to design AR structures with sinusoidal, triangular, and rectangular shapes. A transmission spectrum calculated for a structure designed to minimize reflection in the 8 — 10 micron spectral region is shown in Fig. 1.

The generic technologies which must be applied to transfer patterns into the surface of a semiconductor are photolithography and etching. Conventional binary photolithographic techniques were used to make microlenses of simple shapes. To produce microlenses of arbitrary shape, AR structures useful in the IR, and combinations of these, non-conventional lithography methods were required. Conventional photoresists could, however, be utilized. Patterns were formed in these resists by either a greyscale-mask technique or an interferometric holographic lithographic technique.

Figure 1. Theoretical spectral transmission of sinusoidal structures with various depths.



The required depths of the surface structures and the achievable resist thicknesses were on the order of 2.5 - 4 microns and 0.5 microns respectively. This necessitated etch selectivity values in excess of 5:1, values not achievable with conventional wet chemical etching. Instead, electron cyclotron resonance (ECR) plasma etching, inductively coupled plasma (ICP) etching, and ion milling were used to transfer patterns into the surfaces of interest. For CdTe and CdZnTe surfaces, an ECR plasma was used. For Si, ion milling was used.

Metrology of the surfaces before and after etching was examined with Atomic Force Microscopy and Scanning Electron Microscopy. Total reflection Fourier transform infrared spectroscopy and monostatic reflection and transmission measurements were used to characterize the anti-reflective properties of the surfaces.

Microlenses and antireflective structures have been fabricated in CdTe, CdZnTe, and fused silica. A scanning electron micrograph of a microlens formed on the surface of a CdZnTe wafer using a greyscale mask is shown in Fig. 2.



Figure 2. SEM image of 50 μm microlens array fabricated in (211)A CdZnTe using the gray scale masking technique.

A scanning electron micrograph of the surface of a CdZnTe wafer patterned with a grayscale mask is shown in Fig. 3. Pitch and depth values for this cone-shaped structure were 4 microns.

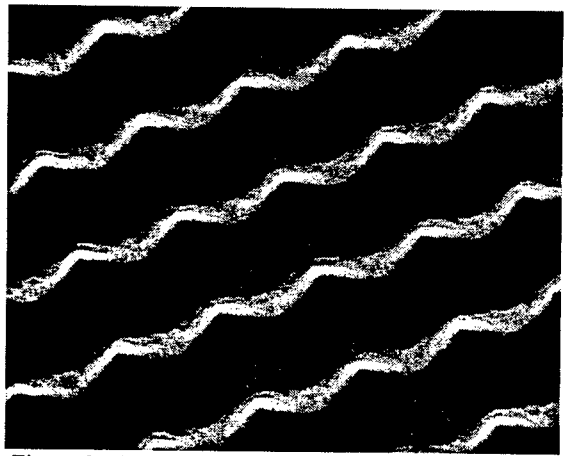
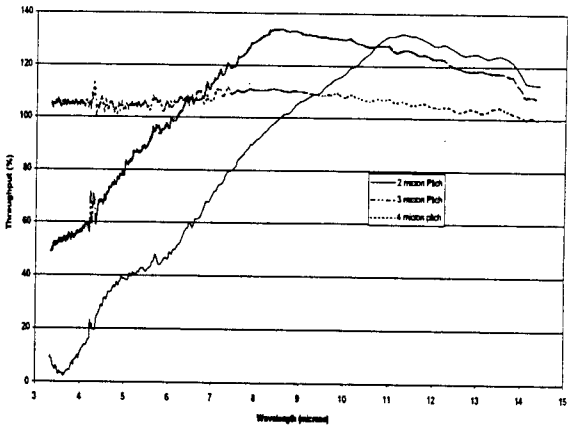


Figure 3: Scanning Electron Micrograph of 4 micron pitch cones with a depth of ~ 4 micron etched into CdZnTe.

The effect of varying the pitch of an AR structure is shown in Fig. 4. It can be seen that near total extinction of reflected intensity over a very broad portion of the spectrum is achieved for



structures with a pitch of 4 microns.

Figure 4. Transmission spectra for sinusoidal CdTe anti-reflective sturctures normalized to the transmission of a planar CdTe surface. Data collected in air.

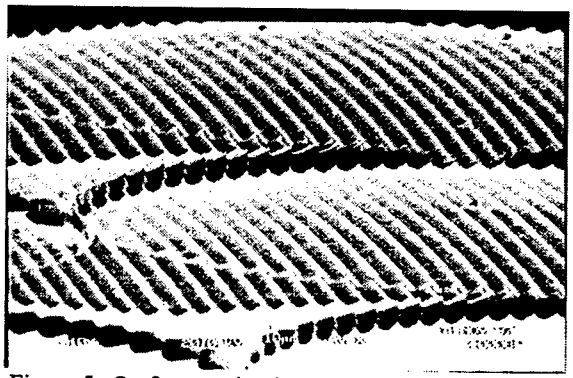


Figure 5. Surface grating integrated into a fused silica microlens.

A feasibility demonstration of the usefulness of non conventional masking and etching technologies is given by the composite microlens/AR structure shown in Fig. 5. Producing such a structure in the CdZnTe backside of a hybrid HgCdTe IRFPA and in a Si wafer for a monolithic IRFPA is a goal of this program. Long term goals are to extend this technology to other IRFPA materials and other optical elements.

FORCE DETECTED MAGNETIC RESONANCE OF CaF_2 AND GaAs

Kent Thurber
SEDD, US Army Research Laboratory, Adelphi, MD 20783 and
Center for Superconductivity Research, Physics Department, University of Maryland, College Park, MD 20742
Lee Harrell
U. S. Military Academy, West Point, New York 10946
John A. Marohn
SEDD, Army Research Laboratory, Adelphi, MD 20783
Raul Fainchtein
Johns Hopkins University Applied Physics Laboratory, Laurel, MD 20723
Doran D. Smith
SEDD, US Army Research Laboratory, Adelphi, MD 20783

We are pursuing a new technical approach to increase magnetic resonance sensitivity: force-detected magnetic resonance or magnetic resonance force microscopy (MRFM). First conceived by John Sidles[1], MRFM entails measuring the force between the magnetic moment of spins in a sample and the magnetic field gradient produced by a nearby magnetic particle. Either the sample or the magnetic particle is attached to a microcantilever, and magnetic resonance is registered as an excitation of the cantilever as sample spins are cyclically flipped by irradiating the sample with the appropriate radio frequency (rf) radiation (see Fig. 1). By flipping the spins at the resonant frequency of the cantilever (several kHz), a periodic force (fN) can be applied to the cantilever at the cantilever's resonant frequency. When driven at its resonant frequency the cantilever's response is enhanced by the mechanical quality factor ($10^3 - 10^6$) of the cantilever. The presence of the magnetic field gradient assures that only spins within a resonant slice contribute to the force signal. Three-dimensional images of the sample can be obtained by scanning the magnetic particle and sample with respect to each other.

Ga(InAlSb)As compounds are extensively used in optoelectronic and electronic components. GaN is the high temperature/high speed material of the future, and HgCdTe is used in many night vision devices. All of these materials are easily observable with MRFM. MRFM can measure isotropic concentration, internal electric fields, internal number density, and strain, all in three dimensions, with nm resolution, nondestructively. MRFM will improve the device designers understanding of the internal structure of devices, thus increasing the speed of device design cycles and ultimately device performance.

The presence of sensors on the battlefield is expected to play a major role in Future Combat Systems (FCS). At the FCS public briefing on Industry Day in Ypsilanti, MI during January 2000 five speakers, Adler, May, Van Fosson, Andrews, and Page all mentioned the extensive role that sensors will play in the battlefield of 2010-2025. Dr. Allen Adler explicitly mentioned sensors on 8 of 27 slides which describe DARPA Technologies for FCS. Dr. Adler outlines FCS operational goals as, 1) using an integrated network of sensors, acquire overall information on both sides' dispositions and battlefield conditions in real time, 2) classify targets with high fidelity, and 3) avoid surprise attack by detecting and classifying enemy movement, mounted or dismounted, within 30 seconds after it begins in the area of operational interest. Themes that he envisions are 1) use sensors aboard ***organic*** unmanned air vehicles, 2) use local sensors; exploit all modes, and 3) integrate sensor data for easy exploitation. A system concept for unattended ground sensors is to provide in scene surveillance and control, using for example, seismic, magnetic, acoustic, and environmental sensors. The sensor network is to provide multisensor

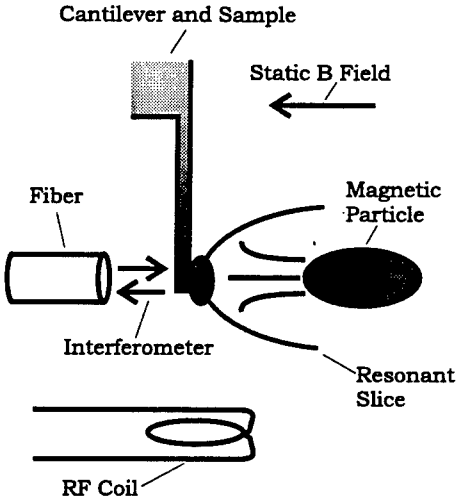


Fig. 1. Diagram of a typical MRFM experiment. A cantilever-mounted sample experiences a uniform static magnetic filed, a magnetic field gradient due to a nearby magnetic particle, and a resonant rf magnetic field from an rf coil which modulates the direction of the sample spins within a resonant slice at the cantilever resonance frequency. The magnetic dipole-gradient force drives oscillations of the cantilever, which are detected by the fiber interferometer.

registration of images and signals. The Senior Advisory Group to FCS has set the C^3 operational goal of the combat team responding to any changes in direction or action by adversary within 5-10 seconds. Additionally they desire that we reduce losses by using robots in high-risk jobs. The operational goals require an unprecedented degree of battlefield awareness that will use as its eyes and ears, *sensors*. Therefore we see MRFM with its ability to improve the speed and quality of a diverse set of sensors as filling an important role for FCS. We especially envision MRFM's direct impact on the Block Upgrades scheduled for 2006-12.

In our paper we will describe our MRFM experiments on CaF2 at record high magnetic fields, and our invention of a new MRFM geometry[2] to overcome systematics we identified that adversely effects all previously proposals for high field MRFM.

The proximate goal of our research is force-detection and imaging of nuclear magnetization in as-fabricated III-V semiconductor devices, with 10 nm resolution. The steps towards the goal that we have completed include 1) construction of a first generation MRFM apparatus suitable for force-detecting NMR at low temperature, 2) demonstration of force-detected NMR using Nd-doped CaF_2 in the first generation apparatus, 3) rebuild of the apparatus to a second generation to allow optical pumping of GaAs, and 4) observation of a force detected signal indicating the presence of optically pumped nuclear polarization of GaAs.

Fig. 2 is a plot of MRFM data obtained on 1% Nd-doped CaF_2. The MRFM signal is recorded as the amplitude of a cantilever excitation vs. magnetic field at a fixed rf frequency of 266 MHz and sample temperature of 20 K. The 10 fN force signal is generated by the dipole/gradient force from a 100 T/m gradient and 4 billion fully polarized ^{19}F nuclei. As the 10 mT width of the resonance is dominated by the magnetic field gradient causing different areas of the sample to experience different local magnetic fields, Fig. 2 represents a one-dimensional MRFM image of ^{19}F concentration. From the observed background, cantilever quality factor, and spring constant, we infer a minimum detectable force of $F_{min}=2.7 \times 10^{-15}$ N/√Hz.

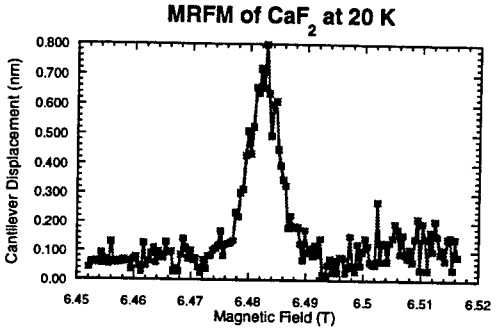


Fig. 2. Magnitude of the MRFM signal on 1% Nd-doped CaF_2 after background subtraction.

Subsequent to demonstrating MRFM at 20 K on CaF_2 we extensively modified the probe to allow illumination of the sample with circularly polarized 780 nm light for optical pumping of the spin polarization of GaAs at 4 K. When circularly polarized light shines on GaAs electrons are excited with a net spin polarization. Through a dynamic spin transfer process involving defects the net spin of the electrons is transferred to the nuclear system. Under ideal conditions the nuclear spin polarization[3] can reach polarization's as high as 50%. We have registered a constant (DC) force from an optically pumped GaAs sample in a magnetic field gradient of 70 T/m by the displacement of a Si_3N_4 cantilever. The GaAs sample has dimensions 3 μm thick x 500 μm x 750 μm and is attached to the end of a 300 μm long cantilever. The 6.8 nm displacement of the cantilever corresponds to a force of $F_{meas} = 3.4 \times 10^{-10}$ N. The force signal varies with laser power and magnetic field values as expected. At an optical pumping power of 1100 W/m^2 and 7 T the time constant for the nuclei to reach steady state is 60 seconds. While at 17,500 W/m^2 and 2 T the time constant is less than 1 second. The force signal is independent of heating.

We are seeing for the first time force detection of optical pumped GaAs. However, the signal is 20 times smaller than expected. We believe this due to the optical pumping wavelength being 780 nm instead of a wavelength near to the band edge of GaAs, about 825 nm. Experiments are currently under way to study the wavelength dependence of the optical pumping efficiency with a wavelength tunable laser. Additionally, the DC force signal provides us with the opportunity to study the rf dependence of the GaAs system. The amplitude and frequency modulation of the rf required to invert Ga and As nuclei, both spin 3/2 nuclei, is considerably more involved than for F (spin ½) especially if the GaAs has any internal electric fields or strain. The DC force signal will be used to optimize the rf needed to invert the nuclear polarization.

[1] Sidles, J., Appl. Phys. Lett. 58 p. 2854 (1991).
[2] Marohn, J. A., Fainchtein, R., Smith, D.D., Appl. Phys. Lett., **73** p. 3778 (1998).
[3] Berkovits, V.L., Ekimov, A.I., Safarov, V.I. Sov. Phys. JETP **38**, pg 169 (1974)

EVALUATION OF THE HIGH FIELD TRANSPORT PROPERTIES OF WIDE BANDGAP SEMICONDUCTOR MATERIALS AND DEVICES FOR FUTURE COMBAT SYSTEMS

M. Wraback and H. Shen
Sensors and Electron Devices Directorate, U.S. Army Research Laboratory,
2800 Powder Mill Rd., Adelphi, MD 20783

J.C. Carrano
Photonics Research Center, U.S. Military Academy,
West Point, NY 10996

T. Li, C. Collins, J.C. Campbell, D.J.H. Lambert, U. Chowdhury, M.M. Wong, and R.D. Dupuis
Microelectronics Research Center, Department of Electrical and Computer Engineering
The University of Texas at Austin, Austin, TX 78712

M.J. Schurman and I.T. Ferguson
EMCORE Corporation
Somerset, NJ 08873

Lightweight, low cost, uncooled optoelectronic sensors and high power, high frequency electronic devices may be essential elements of future combat systems that require a more rapid and more lethal projection of force than that which can be presently achieved. III-nitride semiconductors are emerging materials for these applications because of their wide bandgap, high breakdown voltage, large electron saturation velocity, and potential for operation in harsh, high temperature environments. Ultraviolet photodetectors with bandgaps corresponding to photon energies in the solar blind region of the spectrum offer the possibility of nearly-background-free, all-solid-state detection of low light levels with performance comparable to that of the bulkier and much more expensive existing photomultiplier tube technology. These devices may become important elements in threat warning systems for many Army platforms. Theoretical calculations (Kolnik et al., 1995; Bhapkar and Shur, 1997) of the electron velocity-field characteristic in GaN predict a peak steady-state velocity of $2\text{-}3_{\times}10^{7}$ cm/sec, implying that these materials may also be viable candidates for high frequency devices such as compact, high power density, highly directional millimeter wave radar and communication systems. Although ultrawide-bandwidth AlGaN/GaN heterostructure field effect transistors and very high-speed, transit-time-limited GaN metal-semiconductor-metal (MSM) and *p-i-n* ultraviolet photodetectors have been demonstrated, measurement of electron transit times and carrier velocities in III-N materials cannot be achieved using conventional electronic or optoelectronic techniques. Such studies would help to determine the ultimate speed of electronic devices and provide reliable high field transport data for the design of solar blind detectors based on avalanche photodiodes.

In this paper we discuss an optically-detected time-of-flight technique with femtosecond resolution that monitors the change in the electroabsorption due to charge transport in a *p-i-n* diode, and show how it may be used to determine the electron and hole velocity-field characteristics in III-nitride semiconductors at room temperature. For measurements of the electron velocity in GaN, pump-probe experiments were performed with pulses incident on the *p*-layer of the sample. The spectrum of the pump pulse was centered at 3.41 eV, a photon energy corresponding to the peak photocurrent of the device. This choice of photon energy, at which the absorption length is only $\sim 0.1_{\mu}$m, ensured that almost all of the photogenerated carriers contributing to the photocurrent were generated near the interface of the *p*-type layer and the *i*-region. The diode was biased using 200 ns voltage pulses synchronized with the optical pulses. The change in transmission ΔT of the probe was monitored at a sub-bandgap photon energy chosen to maximize the sensitivity of this quantity to a change in the broadening of the absorption edge under applied electric field (Franz-Keldysh effect). Pump-generated electrons and holes moving under the applied plus built-in electric field E are swept toward the *n*- and *p*-layers, respectively. As the carriers drift apart, a space-charge field of opposite sign creates a potential difference that grows in time until transport is completed. The pump-induced charge density is kept low enough that this screening field ΔE is much smaller than E. The space-charge field causes a reduction in the broadening of the absorption edge and concomitant induced bleaching of the relative probe transmission that tracks the time evolution of the potential difference. The induced bleaching at the measurement photon energy h_{Vm} is given in the thick sample limit by (Schiff et al., 1989; Wraback et al., 2000)

$$\frac{\Delta T(t)}{T} = -\frac{d\alpha_p}{dE}\int_0^d \Delta E(x,t)dx = \frac{d\alpha_p}{dE}\delta V(t), \quad (1)$$

where α_p is the probe absorption coefficient, d is the length of the region over which the field is applied (i.e., the depletion width obtained from CV measurements), $\delta V(t)$ is the change in voltage across the sample due to photocarrier transport, and t is the time delay between the pump and probe pulses. The slope of the normalized bleaching curves at zero time delay may be used to obtain the electron transit time and velocity as a function of electric field (Shank et al., 1981; Wraback et al., 2000):

$$\frac{\partial}{\partial t}\frac{\Delta T(t)}{\Delta T(\infty)} \equiv \frac{1}{\tau} \cong \frac{v_e + v_h}{d}, \quad (2)$$

where the normalization factor $\Delta T(\infty)$ refers to the change in transmission after all the carriers have traversed the sample, v_e and v_h, the electron and hole velocities, respectively, are assumed to be constant, and τ is defined as the transit time. Since the carriers are generated at the interface of the *p*- and *i*-layers, the electrons drift much further than the holes, and the majority of the signal is due to electron transport. It is therefore a reasonable approximation to take τ as the electron transit time.

Figure 1 shows the steady-state electron velocity-field characteristic obtained from our transport data and equation 2. At the lowest fields for which measurements were performed, v_e possesses a weak, quasi-linear dependence on E. Extrapolation of the results to zero field does not provide a realistic estimate of the low-field mobility, however, as ensemble Monte Carlo (EMC) calculations employing multi-valley analytic band structures (Bhapkar and Shur, 1997) predict a steeper linear rise in the velocity-field characteristic only at fields (0-20kV) much less than the smallest field used in our experiments. In the intermediate field regime (50-100kV) corresponding to our low field measurements, calculations show that electrons attain enough excess energy to emit polar optical phonons, causing the velocity-field characteristic to transition to a low slope region (Bhapkar and Shur, 1997) more representative of our data. In the high field regime the electron velocity gradually becomes independent of electric field, reaching a peak of 1.9×10^7cm/sec at ~ 225 kV/cm. The steady-state velocity-field characteristic derived from an EMC calculation including a full Brillouin zone band structure (Kolnik et al., 1995) is shown in figure 1 for comparison with the measurements. The theoretical results are in qualitative agreement with the data. The discrepancies between the experimental and theoretical curves may be associated with poorly known deformation potential scattering parameters, as well as high defect density and polaron effects not accounted for by theory. Also included

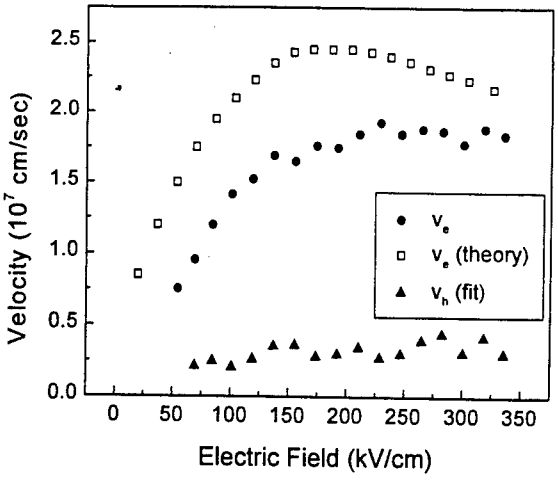


Figure 1 Comparison of experimental and theoretical carrier velocity-field characteristics.

in figure 1 is the hole velocity-field characteristic obtained from fits to the transport data using equation 1. The hole velocity monotonically increases from ~0.25 to ~0.37×10^7cm/s over the range of electric fields shown in the figure. Due to uncertainties in the fitting procedure that may be associated with spreading of the electron distribution, these results represent an upper bound on the hole velocity.

REFERENCES

Bhapkar, U.V. and Shur, M.S., "Monte Carlo calculation of velocity-field characteristics of wurtzite GaN", *J. Appl. Phys.*, Vol. 82, No. 4, pp. 1649-1655, August, 1997.

Kolnik, J., Oğuzman, I.H., Brennan, K.F., Wang, R., Ruden, P.P., and Wang, Y., "Electronic transport studies of bulk zinc-blende and wurtzite phases of GaN based on an ensemble Monte Carlo calculation including a full zone band structure", *J. Appl. Phys.*, Vol. 78, No. 2, pp. 1033-1038, July, 1995.

Schiff, E.A., Devlen, R.I., Grahn, H.T., Tauc, J., and Guha, S., "Picosecond electron drift mobility measurements in hydrogenated amorphous silicon", *Appl. Phys. Lett.*, Vol. 54, No. 19, pp. 1911-1913, May, 1989.

Shank, C.V., Fork, R.L., Greene, B.I., Reinhart, F.K., and Logan, R.A., "Picosecond nonequilibrium carrier transport in GaAs", *Appl. Phys. Lett.*, Vol. 38, No.2, pp. 104-105, January, 1981.

Wraback, M., Shen, H., Carrano, J.C., Li, T., Campbell, J.C., Schurman, M.J., and Ferguson, I.T., "Time-resolved electroabsorption measurement of the electron velocity-field characteristic in GaN", *Appl. Phys. Lett.*, Vol. 76, No. 9, pp. 1155-1157, February, 2000.

MEASUREMENT OF FUNDAMENTAL PARAMETERS AND CONTROL OF COHERENT PHENOMENA IN BULK AND MULTIPLE QUANTUM WELL III-NITRIDE MATERIALS

Henry O. Everitt*
Army Research Office and Duke University, Dept. of Physics
Durham, NC 27708

Umit Ozgur, Chang Won Lee, and H. Craig Casey Jr.
Duke University, Dept. of Physics and Dept. of Electrical Engineering
Durham, NC 27708

Michael J. Bergmann and Amber Abare
CREE Research
Research Triangle Park, NC 27703

Stacia Keller and Stephen P. DenBaars
Univ. of California, Santa Barbara, Dept. of ECE
Santa Barbara, CA 93106

John F. Muth
North Carolina State Univ., Dept. of ECE
Raleigh, NC 27695

ABSTRACT

Using a prism coupling technique, the ordinary and extraordinary refractive indices of $Al_xGa_{1-x}N$ ($0 \le x \le 0.2$) thin films were measured comprehensively for the first time. The indices of refraction were found to vary systematically with wavelength and Al concentration, and a modified Sellmeier relationship was found to reproduce all of the data. Using sub-picosecond optical differential transmission, the rate for electron capture from $In_{0.05}Ga_{0.95}N$ barriers into $In_{0.15}Ga_{0.85}N$ quantum wells in the 10 period multiple quantum well laser structure was measured for the first time. A 100 meV-wide region of efficient capture was observed to correspond to the peak in the photoluminescence excitation spectra and suggests significant material inhomogeneity. Strong coherent acoustic phonon oscillations were observed to be caused by carrier capture and the intense piezoelectric field present in these strained quantum wells. The conditions for creating these acoustic phonon oscillations were elucidated for the first time, and it was found that the oscillations increase with increasing pump intensity and decreasing temperature. Using a two pump-one probe, variable time delay excitation scheme, it was demonstrated that the acoustic phonon oscillations could be cancelled or amplified depending on the relative timing/phase and intensity of the two pulses.

1. INTRODUCTION

Wide band gap semiconductor III-nitride materials have tremendous potential as optoelectronic devices for solar blind detection, green-UV lasing and LEDs, and high power electronics. The importance of the materials system has been so compelling that the rush to develop functioning devices has proceeded without detailed understanding of fundamental phenomena. Simple parameters such as the index of refraction, effective electron and hole mass, sound velocity, and conduction band offset for bulk and heterostructure InGaN, GaN, and AlGaN materials remain uncertain, yet detectors, lasers, LEDs, and transistors based on these materials are now available. Nevertheless, none of these devices can claim optimal performance, and the extent to which these devices improve depends as much on understanding the fundamental physical parameters as it does on improved material quality.

In a series of investigations of the optical properties of III-nitride materials, we have measured or are measuring a number of such fundamental physical parameters, including the ordinary and extraordinary indices of refraction of AlGaN, the electron capture time and sound velocity in an InGaN multiple quantum well (MQW) structure used for blue lasers and LEDs, and the

conduction band offset values for AlGaN/GaN heterostructures. The results of the first three investigations, and the unexpected ability to generate and control coherent acoustic phonons, are described here.

2. INDEX OF REFRACTION OF $Al_xGa_{1-x}N$

The index of refraction can be measured by evanescently coupling laser radiation through a prism into a thin (~1 micron) film of $Al_xGa_{1-x}N$. Coupling to a series thin film waveguide modes, each excited by angle tuning of the prism/thin film system, reveals the effective thickness and index of refraction for a given wavelength. For our measurements of the ordinary and extraordinary indices of refraction of $Al_xGa_{1-x}N$ ($0 \leq x \leq 0.2$), ten different laser wavelengths were used (0.458 – 0.968 microns). The resulting wavelength-dependent index of refraction values were fit with the Sellmeyer relationship in which the fitting parameters were a function of Al content x. The resulting fits demonstrated a smooth, systematic variation of index with wavelength and x and represented the first comprehensive measurement of these indices.[Bergmann, 1999]

3. CARRIER CAPTURE IN InGaN QWs

The capture of carriers from the three dimensional $In_{0.05}Ga_{0.95}N$ barrier states to the two dimensional $In_{0.15}Ga_{0.85}N$ confined quantum well states is a critical step in short wavelength photoemission for lasers and LEDs. Although the electron-hole pair recombination rate has been well characterized for similar structures, the capture time had not been previously measured because it was too fast.[Chibichu, 1999] Using subpicosecond, wavelength-degenerate, pump-probe differential transmission with a frequency doubled, mode-locked, Ti:Sapphire laser, we have measured the capture rate of electrons in a InGaN multiple quantum well structure for the first time.[Ozgur, 2000] A double exponential decay was observed whose faster rate (~0.5 ps) corresponds to electron capture and whose slower rate (20-700 ps) corresponds to cooling of hot electrons in the quantum wells as they relax toward recombination and photoemission. The capture rate was only slightly sensitive to excitation wavelength and intensity, but it was found that efficient capture occurs only within 50 meV of the barrier band minima. As expected, this location concurs with the peak of the photoluminescence excitation spectra, and the 100 meV width of efficient capture suggests materials inhomogenieties and interface roughness still play a major role in optical processes and carrier relaxation.

4. COHERENT ACOUSTIC PHONONS

Unexpectedly, it was observed that following carrier capture, large amplitude coherent longitudinal acoustic (LA) phonons were generated in the InGaN MQW. The mechanism for this generation has been elucidated using the same sub-picosecond differential transmission optical technique described above. Coherent LA phonons were only observed in the same 100 meV region of efficient electron capture, suggesting that the capture of carriers, coupled with the strong, strain-induced piezoelectric field (~1MV/cm) in the quantum wells, leads to the coherent phonon generation. The frequency of the oscillations is simply the ratio of the sound velocity divided by the MQW period, and the decay time constant of the oscillations corresponds to the ballistic transport of the LA phonons away from the excitation region. The peak oscillations occurred near the barrier absorption band edge, further suggesting that the modulation of PZE field screening through the quantum confined Stark effect is the mechanism by which these oscillations are observed. The strength of the oscillations, up to 1% modulation of the probe signal, increased linearly with increasing pump intensity and with increasing absorption as the temperature is decreased, implying that the strength of the oscillations is related to the strength of the captured carrier-induced impulse.

4. CONTROL OF ACOUSTIC PHONONS

Using a two pump-one probe, time-delayed differential transmission technique, we were able to amplify or damp these coherent phonon oscillations. The oscillations induced by the second pump pulse can either constructively or destructively interfere with the oscillations induced by the first, depending on whether the second pulse is delayed by a time corresponding to a whole period or a half period of the LA phonon oscillation. We have demonstrated for the first time complete suppression of induced acoustic phonon oscillations.

REFERENCES

Bergmann, M. J., et al., *Appl. Phys. Lett.* Vol 75, pp. 67-69 (1999).

Chibichu, S. F. et al., *Mater. Sci. Eng.*, Vol B 59, p.298 (1999).

Özgür, Ü. et al., *Appl. Phys. Lett.* Vol 77, pp. 109-111 (2000).

FUNDAMENTAL LOSS RATES IN SOLID-STATE LASERS

Michael E. Crenshaw* and Charles M. Bowden
Weapons Sciences Directorate, AMSAM-RD-WS-ST
U. S. Army Aviation and Missile Command
Redstone Arsenal, AL 35898, U.S.A.

ABSTRACT

For over 50 years, the macroscopic Maxwell equations have been used as the basis for quantizing the electromagnetic field in a dielectric. We show that this quantization is incompatible with fundamental quantum optical principles derived from quantization of the Maxwell equations in a vacuum. This is demonstrated in the context of calculating the fundamental loss rate for lasers.

SUMMARY

Lasers have a wide range of important commercial, industrial, medical, and military uses. As the Army transforms to the Objective Force, lasers, and laser-active optical elements, will become increasingly important as essential components in a wide range of sophisticated sensors and optical communications and information processing systems. Solid-state lasers and devices present a number of distinct fieldability advantages over their vapor-based counterparts for use in future combat systems in regard to miniaturization, weight, power, and durability.

Spontaneous emission is the fundamental loss mechanism in laser physics and therefore impacts the power requirements, heat load, efficiency, and other figures of merit. For atomic vapors, the spontaneous emission rate is given by the well-known Weisskopf–Wigner theory. The spontaneous emission rate relevant to solid-state devices, that is, the spontaneous emission rate of a resonant atom, or ion, placed in a dielectric host medium, has been the subject of a number of studies since the 1950s and has become textbook material. In prior work, it has always been assumed that the dielectric, which consists of a large quantity of matter, is not affected by the presence of a single atom. The dielectric is then lumped with the vacuum, either by a generalized Hopfield transformation of the coupled field-oscillator system or by canonical quantization of the macroscopic Maxwell equations. The result is a macroscopic "bulk" contribution to the renormalization of the spontaneous emission rate associated with the change in the density of radiative states and is limited to an idealized dispersionless and absorptionless dielectric. Incorporating a phenomenological local-field correction yields

$$\Gamma^{diel} = n\ell^2\Gamma_0 \tag{1}$$

for the renormalized spontaneous emission rate in an absorptionless dielectric, where Γ_0 is the vacuum spontaneous emission rate, $\ell = (n^2+2)/3$ is the dielectric local-field enhancement factor, and n is the real, frequency independent, linear index of refraction. More recent work has centered on obtaining results that are consistent with the equal-time commutation relations of quantum electrodynamics for dielectrics with dispersive and absorptive properties.

In this presentation, we describe our recent microscopic many-body quantum electrodynamical derivation of equations of motion for an atom embedded in a dielectric host (M. E. Crenshaw and C. M. Bowden, *Physical Review Letters*, **85**, 1851 (2000); *Physical Review A*, to appear). Our derivation is fully self-consistent, proceeding from the Hamiltonian through the Heisenberg equations of motion to Langevin-Bloch equations using standard quantum optical techniques. We find that the renormalized spontaneous emission rate

$$\Gamma^{diel} = Re(\ell)\Gamma_0 \tag{2}$$

is substantially different from the rate obtained in previous studies of quantization of the electromagnetic field in a dielectric. We are forced to conclude that the quantization procedure that has been applied to the macroscopic Maxwell equations in a dielectric is incompatible with fundamental quantum optical principles derived from quantization of the Maxwell equations in a vacuum. We show that our results are the fully quantized analog of the the Lorentz model of condensed matter in which it is necessary to distinguish the local electrodynamic environment at the site of a dipole from the global macroscopic electrodynamic environment of a dielectric. We describe the role of the local electrodynamic environment of the atom in applying familiar physical principles, such as the electromagnetic energy density, the wave number and wave vector, the density of states, Fermi's golden rule, and canonical quantization.

The foundation of the quantum theory of radiation, due to Dirac, is the quantization of Maxwell's equations in a vacuum wherein each mode of the radiation field is associated with a quantized simple harmonic oscillator. This theory has been extended to linear dielectrics by quantizing the macroscopic Maxwell equa-

tions in which the classical constitutive relations between the macroscopic field vectors has been assumed. We apply the foundational principles of quantum optics, rather than the extended theory, to the calculation of the spontaneous emission rate for a resonant atom in a dielectric, utilizing a model that consists of a single resonant atom of species a and a random distribution of atoms of species b embedded in the vacuum. The atoms are coupled only via the electromagnetic field. The constituents of the total Hamiltonian are the Hamiltonians for the free atoms of species a and b, the free quantized radiation field, and the interaction of the atoms with the quantized electromagnetic field. After obtaining Heisenberg equations of motion for the material and field mode operators, the variables associated with the quantized field modes are adiabatically eliminated yielding coupled equations of motion for the material variables. We take the harmonic oscillator limit for species b by assuming that its resonance frequency is sufficiently detuned from the primary species that the atoms remain in the ground state. Adiabatically eliminating the harmonic oscillators results in a Langevin-Bloch formulation for a two-level atom embedded in a dielectric host that exhibits local-field renormalization of the fluctuations, the radiation field, the dephasing rate, and the population decay rate. The spontaneous emission rate can be identified as the fundamental population decay rate by assuming an initially inverted atom. We find that the spontaneous emission rate in a dielectric is $\Gamma_{diel} = \ell_r \Gamma_0$, where ℓ_r is the real part of the dielectric local-field enhancement factor $\ell = (n^2 + 2)/3$, and n is the complex Drude-Lorentz index of refraction of the dielectric. The fundamental loss rate is much smaller than indicated by previous studies, an enabling result that paves the way for engineering improved efficiency of solid-state lasers and devices.

The quantum optical basis for the Lorentz local-field correction is evident in our development of coupled operator equations of motion for a two-level atom embedded in a dielectric host. Fundamentally, the atom and oscillators are directly coupled only to the electromagnetic field. Then, when the vacuum field mode variables are eliminated, each constituent becomes explicitly coupled to every other constituent. In this manner, the two-level atom experiences a reaction field due to the presence of each of the oscillators that make up the dielectric. Each oscillator experiences a reaction field due to the two-level atom and a reaction field from each of the other oscillators; the latter is associated with the plasma frequency of the classical Drude-Lorentz theory of susceptibility. The interaction that elicits the reaction field, the near-dipole-dipole (NDD) interaction, is short range in nature, on the order of an atomic resonance wavelength, due to the rapidly varying spatial dependence of the exponentials. Then, the evaluation of the integrals and sums that make up the reaction field lead to contact, or delta-function, terms that render the interaction intrinsically local and constitute the local-field correction.

The full many-body microscopic development of equations of motion from the Hamiltonian is cumbersome for discussing many of the physical concepts that are useful in providing context to our understanding of the pertinent electrodynamics. We have developed a simplified lumped-parameter model of a two-level atom in which the local-field effects of the dielectric are embodied in a local-field enhancement factor, rather than by enumeration of the individual oscillators. We define a local electromagnetic energy density in terms of the Bloembergen local field $E_L = \ell_r E$ that acts on an atom in a dielectric host medium, rather than in terms of the macroscopic displacement field. Using the usual quantization procedure, we obtain an effective local Hamiltonian and derive Bloch-Langevin equation of motion for the material operators that reproduce the microscopic results for absorptionless dielectrics. In the process of the derivation, we find, as a consequence of causality, that the wave number that is effective at the location of the atom is greater than its vacuum value by ℓ_r, rather than n. The corresponding local density of radiation states is ℓ_r^3 times larger than the vacuum value and is distinct from the macroscopic density of states of the bulk dielectric because the atom modifies the dielectric in a small region about itself. The spontaneous emission rate in an absorptionless dielectric, $\Gamma_{diel} = \ell_r \Gamma_0$, is obtained as before. Equivalently, Fermi's golden rule, written in terms of effective local quantities, can supply us with the appropriate spontaneous emission rate for an atom in a dielectric using the local electric field operator and the local density of states.

In conclusion, we have derived Bloch–Langevin operator equations of motion for a two-level atom embedded in a host dielectric medium using fundamental quantum optical techniques and demonstrated that the macroscopic formulation of quantum optics in a dielectric is inconsistent with the foundational principles of quantum optics. We developed a lumped-parameter model that allows us to interpret, in a familiar context, the physics of the complete model of an atom embedded in a dielectric and described how it is necessary to distinguish the global macroscopic electrodynamic environment of a dielectric from the local environment at the site of the atom when discussing the electromagnetic energy density, the wave number and wave vector, the density of states, canonical quantization, and Fermi's golden rule for an atom embedded in a dielectric. Furthermore, we demonstrated that the source of the renormalization of the spontaneous emission rate is the effect of the atom on a small surrounding region of dielectric that is fed back to the atom as a self-field, rather than simply a change the density of radiative states.

HIGH-BANDWIDTH MULTI-CHANNEL OPTOELECTRONIC INTERCONNECTS FOR SMART SENSORS AND SENSOR FUSION

G. J. Simonis*, J. J. Liu, W. Lawler, B. Riely, W. Chang, P. H. Shen, M. Taysing-Lara, P. Newman, and Z. Kalayjian
U.S. Army Research Laboratory, AMSRL-SE-EM, Adelphi, MD 20783

B. Koley and M Dagenais
Department of Electrical and Computer Engineering, University of Maryland, College Park, MD 20742

A. Andreou
Department of Electrical Engineering, Johns Hopkins University, Baltimore, MD 21218

Army sensors are rapidly becoming more sophisticated and prolific on the battlefield. Massive amounts of data will be collected by these sensors in Future Combat Systems that must be processed into useful information and distributed in a timely fashion for effective use. Smart sensors rely upon the use of digital electronic processing to distill the useful information from the data at the sensor and to relay that distilled information to the user directly rather than to relay the massive amounts of raw data which usually requires excessive amounts of battlefield communication bandwidth. Adaptive sensors analyze the acquired data and adapt the sensor operating characteristics to optimize data collection and make the sensors more effective and the distilled information even more effective. Very often more information can be collected and extracted by different types of sensors that are fused together than it would be by a group of sensors operating individually. All of these sensor functions rely upon high-performance digital signal processing (DSP) and flow of the data to be effective. Electronic DSP is advancing rapidly, but is encountering technological barriers in the movement of large amounts of data and information within and between sensors and processors. There is now a revolution emerging in the optoelectronic movement of data and information within and between sensors and processors. A similar optoelectronic communications revolution happened first years ago in telecommunications (such as long-haul telephone – up to 100 km) and more recently in data communications (such as Gigabit Ethernet – hundreds to tens of meters) and cable television. It is taking the development of new optoelectronics to extend this optoelectronics communications revolution to the short-distance applications (meters to centimeters) where the cost, performance, and component tradeoffs are quite different. Military applications are leading the way into this next optoelectronics communications revolution which will eventually have an extensive commercial impact as well.

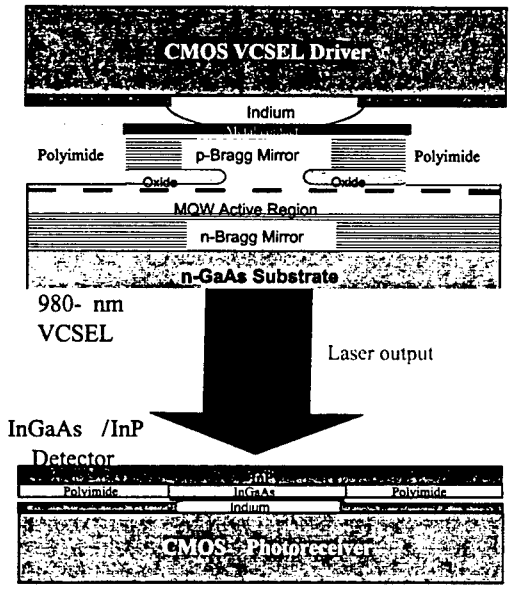


Figure 1. CMOS driven VCSEL-detector optoelectronic interconnect.

The clock speeds of DSPs have advanced relentlessly from 10 MHz to 100 MHz to 1 GHz and beyond. Processing problems are more and more often dealt with by arrays of DSPs working in parallel with the associated need for parallel information flow. Digital hard-drive storage technology also advances rapidly, as does the performance of the sensors being supported. For example, imaging array sensors have advanced in size to tens of megapixels for each image acquired with up to 12 or more bits of intensity resolution in each pixel (up to hundreds of megabits of information for each image acquired). Hyperspectral imaging techniques can involve the acquisition of images of the same scene at hundreds of different wavelengths resulting in tens of gigabits of data for one scene. Imaging sensors sometimes operate at frame rates as high as hundreds of frames per second (such as on fast-moving missiles and other aerial platforms). Army sensors can readily collect terrabits

of image sensor data that needs to be analyzed and reduced in a timely fashion. Synthetic aperture radar sensors can accumulate similar amounts of image-like data. The means of moving information between high-performance DSPs and the associated advancing sensors is encountering technical barriers that can be dealt with by converting the electronic signals to and from an optical format. This optical communications must be highly integrable with the electronics, must be amenable to massive parallelism, and must be VERY cost effective (very competitive with the cost of electronic interconnects having similar performance). The hybridization of optical vertical-cavity surface-emitting laser (VCSEL) emitters and arrays with optical detectors directly onto the electronic chips of the processors is proving to be a very powerful way of achieving this optoelectronic communications. The flip-chip packaging technology that has been so effective in combing several electronic chips into one multi-chip electronic module is now being brought to bear on the problem of combining electronics and optics into one hybrid package.

The ARL VCSEL-interconnect R & D program is dealing with many facets of this technical problem, from the design, fabrication, and characterization of the VCSELs to the development of the interfacing CMOS electronics, to the hybridization flip-chip packaging of the optoelectronic arrays with CMOS, and to the incorporation of these hybrid optoelectronic interconnects into optoelectronic processing of Army sensor data. We grow the needed optoelectronic III-V semiconductor heterostructures one atomic layer at a time by Molecular Beam Epitaxy (MBE). Desirable VCSEL heterostructures incorporate hundreds of semiconductor layers of carefully controlled individual composition and thickness in a stack up to 6 microns in thickness. We employ semiconductor lithographic processing techniques to fabricate lasers and detectors with lateral features and tolerances down to the micrometer range. This results in individual lasers comparable in size to white blood cells that can put out milliwatt optical power levels. We design and model desirable CMOS circuits and then go to the MOSIS CMOS foundry service to have these circuits fabricated. We then flip-chip bond the VCSEL and detector arrays onto the prepared CMOS chips. These optoelectronic multichip modules are then packaged with wire bonding techniques for further experimentation.

We have demonstrated optoelectronic data rates as high as 1 Gb/s and optoelectronic parallelism of up to 8 x 8 arrays with a 125-micrometer spacing between parallel optoelectronic channels. We have developed VCSEL oxidation techniques which have allowed us to reduce lasing current thresholds to as low as 150 μA. Our work will take the bandwidth to several Gb/s and channels to 16 x 16 arrays for the next year. This will constitute a cumulative data rate of hundreds of gigabits per second. We also work with DARPA in the administration of their VLSI Photonics program. This connection has presented us with an opportunity to collaborate with well-funded industrial efforts in this subject area and to facilitate the transition of DARPA-funded developments into Army applications. One such promising area of application is in signal intelligence where massive amounts of data are sometimes collected and processed. We are developing cryogenic VCSEL links that will provide very high data rates out of cryogenic dewars containing high-performance infrared imagers while providing a minimal thermal leakage channel into the dewar and the cooled focal plane array. We are also working with industry and universities to demonstrate the advantages of the use of high-speed silicon-on-sapphire CMOS to achieve higher performance and data rates and more convenient packaging.

Our present work with these optoelectronic interconnect modules involves the demonstration of rapid image transfer and processing through parallel optoelectronic channels from computer to computer. We are also incorporating these interconnects into a missile data bus in a cooperative effort with researchers at U. S. Army AMCOM. We are also collaborating with researchers at the U. S. Military Academy at West Point in the demonstration of a form of image compression called optoelectronic digital half-toning. The use of diffractive optical elements (DOE) in the digital half-toning demonstration provides a means of incorporating optical fan-out and fan-in into the optoelectronic architecture. We have also demonstrated how DOEs can be incorporated into an optoelectronic image processor within which some of the image processing and pattern recognition is achieved through the use of the optical DOE fan-out function.

Many facets of the development of VCSEL-based optoelectronic interconnects are currently being pursued in our lab to enhance the capabilities of Army sensors in Future Combat Systems and the Objective Force.

Asymmetry in Semiconductor MSM Detectors and Its Implication in FM/cw Ladar Systems

Paul H. Shen, Michael Stead, Monica Taysing-Lara, William Ruff, and Barry Stann
U.S. Army Research Laboratory, 2800 Powder Mill Road, Adelphi, MD, 20783

Parvez Uppal
Sanders, A Lockheed Martin company, 65 Spit Brook Road, Nashua, NH 03061

SUMMARY

Future ground combat systems will depend heavily on detailed, accurate situational awareness, which speeds response, and increases survivability and lethality. The Army Research Laboratory (ARL) under its Multi-Domain Smart Sensors (MDSS) program is researching advanced fire-control and target sensors systems. The MDSS will normally detect and identify targets with a two-color FLIR. In situations where a potential target may exhibit poor contrast or is buried in deep clutter, the target will be imaged with a laser radar (Ladar). The ladar provides a high fidelity three-dimensional target image that will support target-clutter separation and insure a high probability of identification. The ARL built a FM/cw ladar breadboard in FY98 using a standard image intensifier tube coupled with a CCD camera as a demodulating receiver. The system was successfully tested in the field to demonstrate general proof-of-principle of the concept. Achieving a compact, light-weight, fieldable version of the ladar requires research and development of new electro-optic devices. This paper reports on research to develop a "self mixing" detector that detects a light signal modulated at microwave frequencies with the application of a local oscillator (LO) and converts it to a low intermediate frequency (IF) signal that is easily amplified and read-out from a focal plane array. Several candidate devices have been investigated with the metal-semiconductor-metal (MSM) detector showing the most promise.

MSM structures have been widely used as high-speed photodetectors. In this application, the important parameters of the device are detectivity and speed. MSM detectors can also be used as optoelectronic (OE) mixers to generate radio-frequency (RF) subcarriers in fiber-optic microwave links. In this application, there is usually ample optical power on the detector so that detectivity is not a major issue. The requirements in a FM/cw ladar application differ from those described above because of the low intensity of the returned signal. With a LO voltage applied, The detector should have a high responsivity with low noise and should also have no average response to background light. More importantly, in the FM/cw ladar application where the LO frequency is chirped, the detector should not develop an output current as a function of the LO frequency when a target is not present. This output current is sometimes referred to as a "self-clutter" signal, which induces false targets. In this paper we demonstrate that the self-clutter signal is related to the voltage asymmetry of the device. We present a theory and define the origin of the asymmetry.

Theoretically, an MSM is two Schottky barriers connected back-to-back. We modeled the two Schottky barriers and found that the asymmetry is related to the asymmetry of the potential barrier heights, variation of doping, and optical intensity distribution. We quantitatively defined two parameters to describe asymmetries, one associated with dark-current asymmetry and the other with the photocurrent asymmetry. The resultant mixed signal is sublinear with LO voltage. The dc component is zero for a perfectly balanced device, and the device will not respond to the background optical power. For an asymmetric device, however, a dc current that is proportional to the total optical power and quadratic to the driving LO voltage is present. We further proved theoretically that this asymmetry is the origin of the self-clutter in a FM/cw ladar system.

We fabricated and characterized three kinds of detector/mixers. Two of them were MSM structures with Schottky contacts; the third one was a structure with transparent, doped semiconductor fingers. We characterized devices as dc detectors, as RF detectors and as OE mixers. The IV characteristic of the devices agreed well with our theory. Devices with MSM opaque contacts usually exhibit high degrees of symmetry while devices with transparent fingers usually exhibit lower symmetric I-V characteristics. From the dc-measurements, we determined responsivity and asymmetry parameters for various devices. As a mixer, all devices demonstrated mixing at frequencies up to 800

MHz. The frequency responses were essentially flat (within 2 dBm) over 100 to 700 MHz. We also found that the mixed signal strength is in good agreement with our theory.

We conducted experiments to compare the performance of a symmetric device to an asymmetric device with similar responsivity. The ideal symmetric self-mixing detector should recover an IF waveform which is a zero mean sine wave whose amplitude is proportional to signal power and whose frequency is proportional to target range. Figures 1(a) and 1(b) show the photocurrent IF waveforms as the LO frequency is chirped from 100 to 700 MHz in 127 ms for an experimental symmetric device and an asymmetric device, respectively. The dashed lines are (in both figures) for returning laser powers (from the target) at 9 nW, while the solid line in Fig. 1(b) is for 0.9 nW. The IF was at 340 Hz, which corresponds to a round-trip path of about 22 m. For the symmetric device, the IF waveform remained flat over LO frequency and was nearly symmetric around zero current thus closely approximating the behavior of the ideal detector. The IF waveform for the asymmetric device (Fig. 1(b)) has the ideal IF waveform riding on a positive slowly changing signal that varied by about 1 nA. This extraneous signal is the self-clutter signal. Note that, this self-clutter signal disappeared (solid line in Fig.1b) at an optical power of 0.9 nW. We also noticed that the self-clutter signal decreased significantly when the LO voltage was dropped to 0.75 V (not shown here). This behavior is consistent with our theory that the self-clutter component is proportional to the optical signal power and quadratic to the LO voltage.

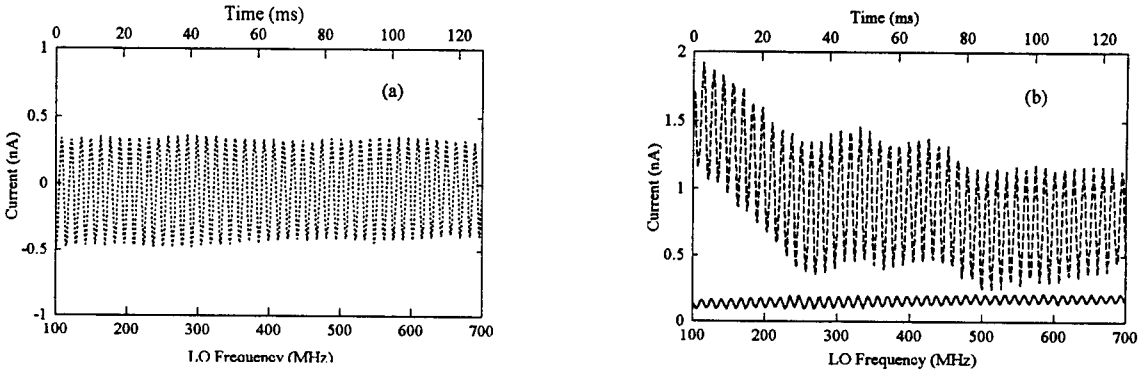


Figure 1: Comparison of mixer performance in a FM/cw ladar system: a) symmetric device, b) asymmetric device. The LO is chirped from 100 MHz to 700 Mhz in about 127 ms. The signal is from a target 11m away with optical power on detector of 9 nW (dotted lines). The solid line in (b) is under a power of 0.9 nW

To further investigate the origin of this self-clutter signal, we turned off the laser and recorded the dark current using the same chirp parameters as before. In Fig. 2, we show the current from the asymmetric detector. The solid and dashed lines are for background light intensity of 9 nW and 4.5 nW, respectively. Note that it followed the same self-clutter waveform as observed in Fig. 1 (b). In fact, our theory tells us that the signal optical power and the background optical dc power should produce a similar self-clutter component. Therefore, we concluded that the origin of the self-clutter signal in the FM/cw ladar is from the voltage asymmetry of the device.

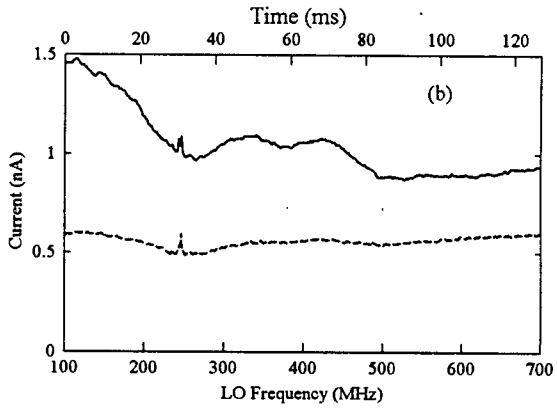


Figure 2: DC current as a function of LO frequency from an asymmetric detector.

MSM structures are geometrically symmetric, while vertical structures usually exhibit different optical generation rates near the top and bottom electrodes resulting in large asymmetry. Therefore MSM devices are advantageous in our applications. From the work presented in this paper, we better understand the relationship between the self-clutter signal and the device's physical parameters (such as doping profile, and surface preparation and metalization). This facilitated the development of the self-mixing detector arrays for FM/cw ladar systems.

INTEGRATED, OPTICALLY-PUMPED, LOSSLESS SPLITTERS: PROGRESS AND CHALLENGES

Dr. David M. Mackie,* Army Research Laboratory, Adelphi, MD 20783
Dr. Hong Koo Kim, University of Pittsburgh, Pittsburgh, PA 15261
Dr. Colleen M. Fitzpatrick, Rice Systems, Irvine, CA 92614

ABSTRACT

In this paper, we first briefly describe potential Army applications of integrated lossless splitters. We then discuss the design, fabrication, and testing of integrated Er-doped glass amplifiers, of Y-branch and multimode interference splitters, of pumping configurations, and of pump refreshing and removal architectures. Lastly, we give preliminary packaging and implementation recommendations.

1. INTRODUCTION

Optical power splitting from a single input into N output channels is a critical function in many photonic architectures. A *lossless* splitter amplifies the signal as well, by a factor of N, so that each output has the same strength as the input. Optical (as opposed to electrical) pumping is necessary for applications requiring a high signal-to-noise ratio (SNR). Er-doped thin-film waveguide amplifiers are promising as loss-compensating devices when degradation of signal level, caused by transmission and distribution losses, is a significant problem.

2. LOSSLESS SPLITTER APPLICATIONS

Phased array antenna systems are key to high data rate/highly mobile communication networks among battlefield commanders. Advantages of photonic control include phase modulation linearity at high RF bandwidth, remoting of the controller from the front end, common module application over a broad RF frequency range, and scalability. Requirements of the lossless splitter include high uniformity, polarization sensitivity, moderate bandwidth, compactness, ruggedness, and moderate power consumption.

An integrated optics rotation sensor (IORS) is a Sagnac interferometer used to measure rotation rates on the basis of two counter-propagating optical beams. By placing a lossless splitter as the output beam splitter, it is possible to compensate for both extraction and attenuation loss, allowing the signal to be regenerated on each pass through the gyro loop.

3. ER-DOPED WAVEGUIDE AMPLIFIERS

Most of the technical challenges associated with the development of Er-doped waveguide amplifiers arise from the fact that Er-doped waveguides typically require two orders of magnitudes higher Er concentration than fiber amplifiers. We have met these challenges by developing Er-doped waveguide amplifiers based on a soda-lime glass matrix. Instead of etching, waveguide fabrication involves a collimated sputtering process in conjunction with either a lift-off process or a silica mesa structure. We have investigated two waveguide structures: a half-ridge structure on a planar quartz substrate and a channel waveguide structure on a deep-mesa-etched quartz substrate. SEM images clearly reveal that the resulting channel regions are well defined with smooth surface and sidewalls.

The gain performance of the Er-doped waveguide amplifiers was characterized with a 110-mW 975-nm fiber-pigtailed laser diode as a pump and a 1-mW 1537-nm fiber-pigtailed laser diode as a signal, combined into a single-mode fiber with a multiplexing fiber coupler, the output of which was butt-coupled to the input facet of an Er-doped waveguide amplifier. The output of the amplifier was collected with a multimode fiber and fed to a monochromator and power meter. Figure 1 shows signal enhancement versus signal input power. As indicated in the figure, we obtained a signal enhancement of up to 12—13 dB with a pump power of 90 mW.

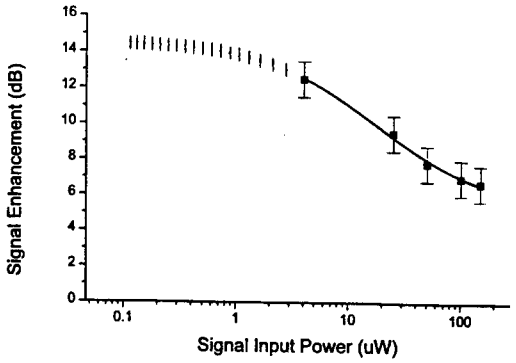


Figure 1: Signal enhancement measured at different signal levels.

4. SPLITTER ARCHITECTURES

To interface with the Er-doped amplifier, we have developed both Y-branch and multimode interference (MMI) 1×2 splitters and demonstrated their beam-splitting performance. We have successfully combined a waveguide amplifier with a Y-branch splitter. The overall length of the fabricated device is 19-mm (a 16-mm-long amplifier followed by a 3-mm-long splitter). Optical characterization measurements with a scanning single mode fiber show two clearly-resolved peaks of identical intensity. Based on these results, 1×*N* splitters (such as 1×4 and 1×8) are being developed by cascading 1×2 splitters.

It is anticipated that production runs would have sufficient process control to allow the use of MMI power splitters and devices for the combination and separation of the pump and signal. Figure 2 shows a schematic of a 1×2 lossless splitter architecture that uses MMI devices first to combine the pump and signal, and, after amplification, to both split the signal and remove the pump.

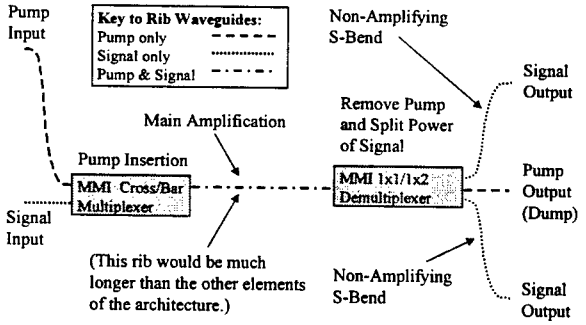


Figure 2: MMI-based lossless splitter architecture.

5. PUMPING ARCHITECTURES

We have demonstrated new Er-doped waveguide pumping schemes that exhibit much higher coupling efficiency and therefore, much higher amplifier gains, than conventional techniques. Using grating-assisted top pumping, pump light is coupled into the amplifier using a grating coupler fabricated directly in the waveguide itself. Using the side-pumping configuration, however, the pump beam is coupled into the amplifier through a flared-end waveguide using special beam-forming micro-optics.

In developing grating-assisted top pumping, we created a grating structure with a period of 330 nm, formed in a 600-nm-thick photoresist layer, coated on a 1-mm-thick silica substrate. The grating was fabricated by exposure of the photoresist layer to the interference pattern of He-Cd laser beams with an angle of incidence of 30° with respect to the surface normal. The gratings were characterized in terms of their beam-coupling efficiency into guided modes, which was measured to be 26%. Computer modeling of this top-pumping configuration predicts a potential coupling efficiency of 30 to 40%. This translates into at least 300 to 400 mW available pump power coupled into an Er-doped waveguide amplifier from a 1-W diode laser bar. This level of pump power is expected to produce 10 to 15 dB optical gain, more than sufficient to compensate for splitter loss

As an alternative, we have fabricated Er-doped waveguides with a flared-end structure and demonstrated the side pumping operation of the waveguide amplifiers. For efficient coupling of a pump beam into the flared-end facet, we have used special beam collimating/focusing optics. Measurements are in progress. Computer analysis predicts 25 to 40% efficiency for this coupling scheme.

6. PACKAGING CONSIDERATIONS

One of the most underestimated challenges is to provide suitable packaging for the lossless splitter. Packaging includes not only designing and fabricating a housing for the device; it also includes such items as proper heat sinking as well as pigtailing the input and output fibers so that they will not break. There are other concerns with securing the device within the packaging and protecting it from its environment. Tradeoffs generally associated with the choice of packaging material involve compromises between weight, thermal stability, and machinability. Figure 3 shows a schematic of a fully packaged 1×4 lossless splitter, complete with thermoelectric (TE) cooler, input and output fiber pigtails, and external housing. The final configuration will depend on the application for which the lossless splitter is to be used.

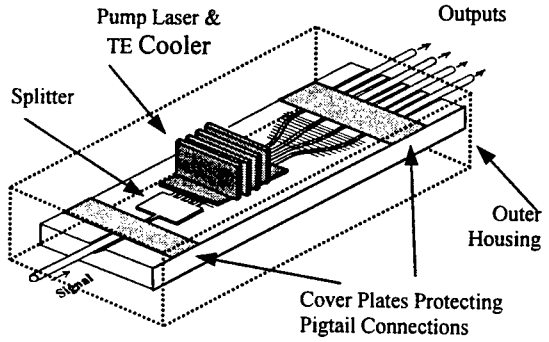


Figure 3: Schematic of packaged Er-doped lossless splitter.

DIELECTRICS FOR HIGH-TEMPERATURE SILICON CARBIDE POWER DEVICES

C. J. Scozzie*, A. J. Lelis, F. B. McLean, and B. R. Geil
U. S. Army Research Laboratory
2800 Powder Mill Road
Adelphi, MD 20783-1197

ABSTRACT

Dielectrics for wide bandgap power devices are critical to the development of high-temperature power electronics required for the Future Combat Systems. Technology issues concerning the use of silicon dioxide as a passivation and gate dielectric layer for high-temperature silicon carbide electronic devices are discussed. The advantages of aluminum nitride as an alternative to silicon dioxide for use as a high-temperature passivation layer are discussed as well.

1. SUMMARY

High-temperature, voltage-controlled silicon carbide (SiC) power devices and digital fault-protection circuitry are required for future military and commercial electric-drive applications. For example, the hybrid electric drive platforms for the Future Combat Systems will require power electronics that are stable and reliable for extended operation (10,000 hours) at junction temperatures up to 350 °C and under operating fields of at least 1 MV/cm. However, the achievement of high-quality, high-reliability SiC metal-oxide-semiconductor (MOS) devices using SiO_2 gate oxides and passivation layers in high-temperature and high-power applications remains elusive. Therefore, other insulators besides SiO_2, especially those with high dielectric constants such as aluminum nitride (AlN), are being investigated for high-temperature SiC device applications. We have initiated a study to understand and characterize the effects of the interface and bulk quality of current state-of-the-art oxides on SiC device performance and reliability. As part of this study, through research contracts with Cree Research Inc. and the University of Maryland, we are investigating the continued development of SiO_2 for use as a gate insulator as well as other alternative insulators for use as gate insulators and passivation layers for SiC.

Because an adherent oxide can be easily grown on SiC just as one can be grown on Si, thermal SiO_2 is typically used as a passivation layer on most SiC devices. Although MOS SiC test structures (capacitors) fabricated on low-doped epi layers have shown SiO_2 to have high dielectric strength (10 MV/cm) and low room-temperature leakage (10^{-8} A/cm^2), devices that are passivated with thermal SiO_2 show leakage currents that are highly thermally activated above ~ 250 °C with activation energies of only about 0.5 eV determined from Arrhenius plot analysis. We have noted this behavior in SiC JFETs [1], MOSFETs, and thyristors, as illustrated in Figure 1. Such a low activation energy suggests that the leakage is extrinsic and probably defect related. This is consistent with the fact that for passivation of such devices thermal SiO_2 must be grown over etched and/or highly doped SiC surfaces which have been shown to degrade the dielectric strength of the oxide significantly [2,3].

Another more significant deficiency of SiO_2 as a passivation layer is its inability at high temperature to support fields in the semiconductor that are a substantial fraction of the critical field, and therefore do not allow device designs to take full advantage of the extremely high (>3MV/cm) critical field in SiC. This is due to the relatively low dielectric constant of SiO_2 as compared to that of SiC coupled with the significant degradation of the dielectric strength of SiO_2 due to the geometry of an active device. The details of this analysis are given in Table 1 where a figure of merit for a passivation layer on a particular semiconductor is derived from Gauss' Law which requires: $\varepsilon_i \cdot E_i = \varepsilon_s \cdot E_s$; where ε_i and ε_s are the relative dielectric constants of the insulator and the semiconductor, respectively, and E_i and E_s are the electric fields in the insulator and the semiconductor. For purposes of our figure of merit, we have taken the electric fields in the insulator and the semiconductor to be the maximum observed operating fields at 300 °C under realistic device stresses and over realistic device designs. at 300 °C for SiO_2 and AlN.

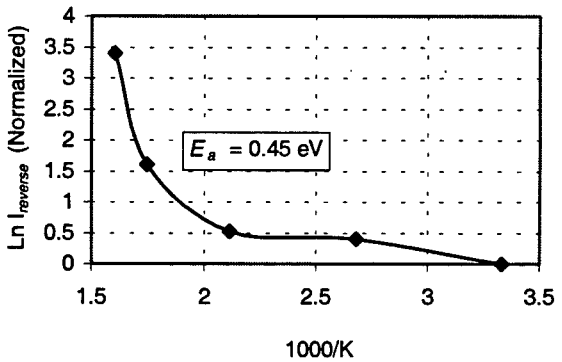


Figure 1. Plot of normalized average reverse bias leakage current as a function of reciprocal temperature for a group of five 4H-SiC thyristors that were passivated using thermal SiO_2.

Table 1. Comparison of relative dielectric constant ε, critical field $E_{Critical}$ at 25 °C, maximum operating field $E_{Operating}$ at 300 °C, and dielectric figure of merit ε $E_{Operating}$ at 300 °C *for* SiO_2 and PLD AlN.

Material	ε	$E_{Critical}$ (MV/cm) @ 25 °C	$E_{Operating}$ (MV/cm) @ 300 °C	ε $E_{Operating}$ (MV/cm) @ 300 °C
SiC	10	3	3	30
SiO_2	3.9	11	<2	7.8
AlN	8.5	>2	>2	17
Si	11.8	0.4	0.4	4.7

The optimum value for the figure of merit for an insulator would be a value at least as large as the product $\varepsilon_s \cdot E_{Operating}$ for the semiconductor. A passivation layer which meets this criterion would then support electric fields in the semiconductor which meets or exceeds its critical field. From the comparison shown in Table 1, it can easily be seen why SiO_2 has proven to be such a good passivation for Si (SiO_2 has a figure of merit of 7.8 compared to that of 4.8 for Si), and why SiO_2 will never be as good a passivation layer for SiC (7.8 versus 30 for SiC). This is why high dielectric-constant insulators are being investigated as alternatives to SiO_2 for the passivation of SiC devices. As mentioned earlier, we are investigating AlN as an alternative passivation layer for SiC due to its high dielectric constant (8.5) and its extremely low leakage current density and reasonably high dielectric strength at high temperatures. The figure of merit for this insulator is at least 17, which is at least twice that of the figure of merit for SiO_2.

Because of the apparent limitations of SiO_2 as a passivant on SiC at temperatures above 200 °C, we have embarked on a collaborative investigation with the University of Maryland on the merits of AlN as an alternative high-temperature dielectric. The university team has developed a successful process for fabricating thin films of AlN via pulsed-laser deposition (PLD) [4]. Figure 2 shows a comparison of current density versus temperature between recent results with the PLD process and that of others reported in the literature. The bottom most curve represents our best data to date [5] for a capacitor on highly doped *n*-type 6H. Just above that lie two almost identical curves — two *n*-type PLD AlN capacitors fabricated at the same time, one on 6H and the other on 4H SiC [6]. The current densities for the PLD AlN devices are orders of magnitude lower than that of any other data reported, even though we have stressed them at higher fields and temperatures than the others. Tin, et al. [7] and Zetterling, et al. [8] both report values only at room temperature for MOCVD AlN. The value of Tin, et al. is much lower than that of Zetterling, et al., probably because the applied field

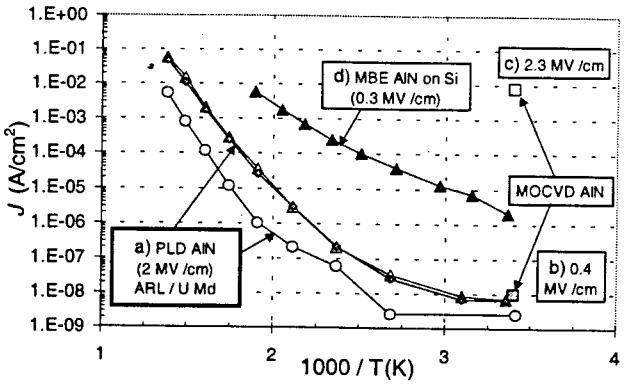


Figure 2. Comparison of dielectric leakage current densities taken from the literature with our recent results. a) PLD AlN on SiC: upper curves from same fab run resulting in identical response for 6H and 4H [6], the lower curve is best to date results (6H) [5]. MOCVD AlN on SiC: b) after Tin et al [7], c) after Zetterling et al [8]. d) MBE AlN on Si, after Ouisse et al [9].

is so much lower: 0.4 versus 2.3 MV/cm. Ouisse et al [9] put AlN down on Si via molecular beam epitaxy (MBE) and although they report current densities up to 300 °C, they only applied 0.3 MV/cm.

We plan to continue the capacitor-level investigation into the high-temperature high-field dielectric properties of PLD AlN and provide a demonstration of the passivation quality of this insulator using a 4H-SiC *pin* diode. In the presentation and paper we will discuss the complete details of this study.

REFERENCES

[1] F. B. McLean, C. W. Tipton, J. M. McGarrity, and C. J. Scozzie, J. Appl. Phys., **79** (1), (1996), p. 545.
[2] L. A. Lipkin and J. W. Palmour, J. Elect. Mat.,**25** (5), 1996, 909.
[3] L. A. Lipkin and J. W. Palmour, IEEE Trans. Elect. Dev., **46**(3), 1999, 525.
[4] R. D. Vispute, S. Choopun, R. Enck, A. Patel, R. P. Sharma, T. Venkatesan, C. J. Scozzie, A. J. Lelis, F. B. McLean, W. L. Sarney, L. Salamanca-Riba, and A. A. Iliadis, to be published in Proc. ICSCRM'99 (March 2000).
[5] C. J. Scozzie, A. J. Lelis, F. B. McLean, R. D. Vispute, S. Choopun, A. Patel, R. P. Sharma, and T. Venkatesan, J. Appl. Phys., 86 (7), (1999), p. 4052.
[6] A. J. Lelis, C. J. Scozzie, F. B. McLean, B. R. Geil, R. D. Vispute, and T. Venkatesan, to be published in Proc. ICSCRM'99 (March 2000).
[7] C. C. Tin, Y. Song, and T. Isaacs-Smith, J. Elect. Mat., 26, No. 3 (1997), p. 212.
[8] C. M. Zetterling, M. Ostling, K. Wongchotigul, M. G. Spencer, X. Tang, C. I. Harris, N. Nordell, and S. S. Wong, J. Appl. Phys., 82 (1997), p. 2990.
[9] T. Ouisse, H. P. D. Schenk, S. Karmann, and U. Kaiser, Materials Science Forum 264-268, Trans Tech Publications LTD, Switzerland, 1998, p. 1389.

SMART ELECTRONIC MUZZLE REFERENCE LIGHT SOURCE

Mark Johnson* and Paul Cote
US Army Armament Research, Development and Engineering Center, Benet Laboratories
Watervliet, NY, 12189

ABSTRACT

A new intelligent muzzle reference light source was designed that is both cost effective and environmentally prudent. It was developed as a candidate to replace the hazardous radioluminescent light source currently being used on the M1 series of tanks. It employs patented sensor technology and advanced concepts in signal processing to attain a component life that exceeds gun service life.

1. INTRODUCTION

A muzzle reference system is used on the M1 series of tanks to measure gun deflection angles as part of an initial alignment procedure. An essential component of the muzzle reference system is a collimator assembly (Figure 1) attached to the muzzle end of the gun which contains a reticle to provide an optical reference for the calibration. A cell housing mounted in the collimator illuminates the reticle when the ambient light is inadequate for accurate measurements. Current systems use tritium, a radioactive isotope of hydrogen, to provide illumination. The tritium source must be replaced every 7 years because of leakage. The costs associated with the acquisition, handling, and disposal of these tritium sources are extremely high. It is estimated that the Army will save approximately 71 million dollars over 10 years if tritium is replaced with an alternative means of illumination.

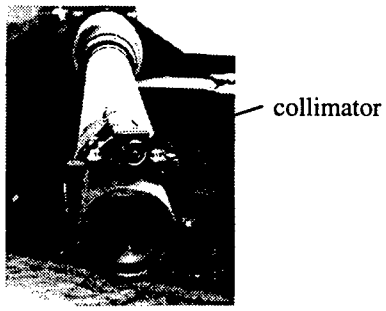


Figure 1. Muzzle reference system Mounted on a 120mm cannon.

2. DESCRIPTION

A new Smart Electronic Muzzle Reference Light Source (SEMRLS) was developed to illuminate the reticle only when the tank is in use and to automatically power down during extended periods of inactivity. The SEMRLS exploits the fact that peacetime tank usage (maneuvers and gunnery practice) seldom exceeds 5 weeks per year. The SEMRLS is comprised of (i) a microcontroller with embedded signal processing algorithms, (ii) a miniaturized version of an in-house patented omnidirectional motion sensor, (iii) the electronics required to interface with the sensor, (iv) an LED for illuminating the reticle, and (v) the circuitry to compensate for temperature effects. The entire package, shown in figure 2, mounts in an existing cell housing and requires no modifications to the collimator assembly.

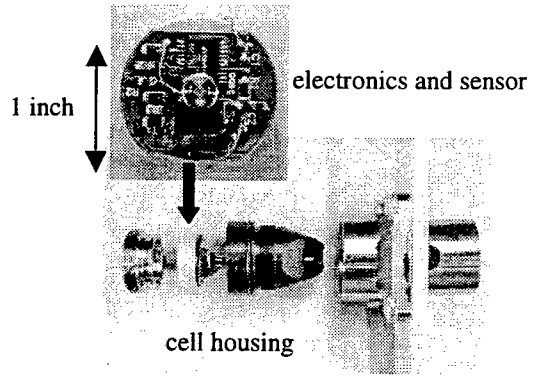


Figure 2. Smart Electronic Muzzle Reference Light Source (SEMRLS)

When the tank is not in use, the SEMRLS shuts off the LED and the electronics operate in a standby mode that requires only nanoamperes of current. When the sensor detects tank activity, the reticle is temporarily illuminated so that gun calibration can be performed.

In an effort to minimize current drain in this active mode of operation, the LED is driven into its most optically efficient mode of operation using pulsing to obtain the proper illumination. Conventional pulsing techniques are unacceptable because of concerns that tanks could be identified by conspicuous power spectral density (PSD) components in the electromagnetic

spectrum generated by a pulsed LED. Therefore, flicker noise concepts have been employed to efficiently drive the LED while generating a virtually undetectable spectral signature. This approach, derived from chaos theory, would generally require that the LED be powered with a set of uncorrelated pulses, with random heights, started at random times. The PSD for such a signal generates $(1/f)^n$ type noise [Jensen, et. al., 1989] given by:

$$S(f) = \frac{\upsilon}{(\pi f)^2} \int_0^\infty d\tau G(\tau) \sin^2(\pi f \tau) \qquad (1)$$

where ν is the pulse rate and G(τ) is the weighted distribution of lifetimes, defined as:

$$G(W) = \int_0^\infty dS\, P(S,W)[S/W]^2 \qquad (2)$$

Where $S(f)$ is the joint probability for a pulse to have area S and width W. However, a significant reduction in conspicuous power spectral density components can be achieved when imposing practical constraints. The SEMRLS electronics significantly reduce the dominant components of the power spectrum using fixed pulse durations and magnitudes (W_{fixed}, S_{fixed}) to drive the LED. In this case, the joint probability density function becomes:

$$P(S,W) = \delta(S - S_{fixed})\, \delta(W - W_{fixed}) \qquad (3)$$

so that (2) and (1) reduce to:

$$G(W) = \left[\frac{S_{fixed}}{W}\right]^2 \delta(W - W_{fixed}) \qquad (4)$$

$$S(f) = \upsilon\left(nW_{fixed}\right)^2 \mathrm{sinc}^2(fW_{fixed}) \qquad (5)$$

The LED requires 30% less power to provide the same effective illumination as continuous operation and generated power spectrum is normally associated with natural phenomena and appears as background noise in spectrum analyzers. Therefore, the electromagnetic spectrum of the SEMRLS cannot be used an electronic signature to identify the tank. Figure 3 shows the resulting power spectrum using conventional periodic pulsing and the SEMRLS flicker pulsing.

The novel techniques utilized by the SEMRLS extend the life of the components beyond the service life of the gun. Therefore, the battery never requires replacement and the entire SEMRLS can be permanently potted into the cell housing to minimize the effect of the severe thermal and mechanical shock experienced by the collimator assembly.

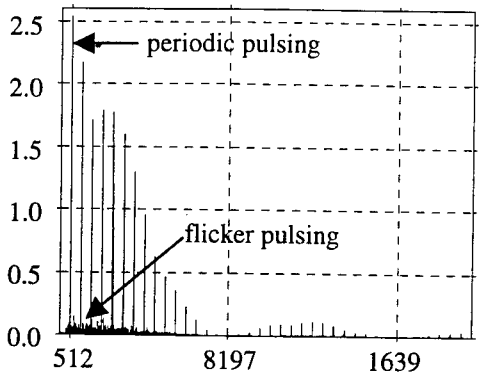


Figure 3. Power spectral density for periodic and flicker pulsing (volts^2-sec vs. sec^{-1})
W=122 ms, S=nW=122 mV-s, and T=1.83 ms

3. PERFORMANCE TESTS

Four prototypes have been fabricated and assembled into 'clean' collimators. The cell assemblies have been successfully tested in alcohol bath from - 60 °C to ambient using an ultra-low temperature refrigeration system and in a laboratory oven from ambient to 160 °C. The units have survived 100 cycles of 460 G shock using Berry Controls gun recoil simulator. There is minimal LED wavelength shift or intensity variation over entire temperature range. Theoretical analysis suggests minimal sensor damage due to M829E2 ballistic shock. The units are currently scheduled for field testing to determine the effects of ballistic shock that cannot be simulated in a laboratory environment.

REFERENCES

H.J. Jensen, K.C. Christensen, and H.C. Fogedby, "1/fnoise, distribution of lifetimes, and a pile of sand", *Phys. Rev. B* **40,** pp. 7425-7427, 1989

TUNNELING OF SEMICONDUCTOR LASER PULSES THROUGH SINGLE BARRIERS

Mark Bloemer, Charles Bowden, Shawn Pethel
U.S. Army Aviation and Missile Command
AMSAM-RD-WS-CM
Redstone Arsenal, AL 35898
Mark.Bloemer@ws.redstone.army.mil

Krishna Myneni
SAIC
6725 Odyssey Dr.
Huntsville, AL 35806

Michael Scalora
Time Domain Corporation
6700 Odyssey Dr.
Huntsville, AL 35806

Marco Centini, Giuseppe D'Aguanno, Concita Sibilia, and Mario Bertolotti
University of Rome, La Sapienza
INFM Department of Energetica
Via Scarpa 16, I-00161 Rome, Italy

Summary

The measurement of tunneling times for optical pulses transmitted through barriers continues to be a topic of considerable interest. In this paper, we present experimental results on tunneling times for the most common type of barrier, and seemingly the most trivial, a single piece of bulk material. Likewise, the optical source used to generate the electromagnetic pulses in the experiment is the most commonly used today, direct current modulation of a semiconductor laser diode. We present tunneling measurements on two different barriers, silica glass and GaAs. In both cases there is weak feedback from the sample/air interface, which causes the optical transmittance to be less than unity at some frequencies. As the laser frequency is tuned, the measurements show unusually large variations in tunneling time compared with the predictions of a stationary phase model for the group velocity. For the 450 μm long GaAs sample, the transit time ranges from +17ps (subluminal) to –8ps (superluminal and negative transit times). A negative transit time means that the peak of the transmitted pulse has exited the sample before the peak of the incident pulse arrives. Superluminal behavior is observed to occur even at transmittance values close to unity, >90%. The results are consistent with causality and are due to a combination of anomalous dispersion associated with the barrier resonances and the chirp profile of pulses generated by semiconductor lasers.

The tunneling of an optical pulse through a barrier is a fascinating subject, which seems to be full of conflicts and misunderstandings. The subject matter tends to force one to reconsider the actual physical meaning of standard quantities like group velocity, tunneling time, and energy velocity. Unusual properties associated with tunneling, such as superluminal transit time, have been observed in low transmittance samples in which the wavefunction decays rapidly with distance into the barrier. Especially noteworthy are the tunneling experiments by Steinberg *et al.*[1] which show superluminal behavior for single photons transmitted through a 1-dimensional photonic band gap material (a quarter-wave dielectric stack). As pointed out by Steinberg, the results are consistent with causality because the tunneling probability was less than unity.

For classical electromagnetic wave packets, those containing many photons, the superluminal tunneling is the result of pulse reshaping. For a quantum mechanical wave packet containing only one photon, the superluminal behavior is explained by the probability distribution of the position of the photon associated with the Heisenberg uncertainty principle. In a tunneling event, it is the leading edge of the probability distribution (quantum mechanically) and the leading edge of the electromagnetic pulse (classically) that passes through the barrier and provides the

superluminal behavior. Thus, the velocity of the peak of the transmitted pulse when referenced to the peak of the incident pulse is superluminal, but the leading edge of the pulse is always causal. Remember that most of the incident pulse has been reflected at the barrier.

In spite of the explanations of pulse reshaping and uncertainty principle, the somewhat surprising result remains: the signal velocity of the packet tunneling through the barrier can approach *c*, the speed of light in vacuum. It behaves as if the medium were not there (aside from the low probability of transmittance). However, we are not aware of any direct measurements of the signal velocity for a tunneling event.

For tunneling phenomena, another level of complexity can be added by considering chirped pulses. The combination of chirped pulses and tunneling opens a broad research area with numerous possibilities for applications ranging from time delay devices to signal propagation through materials at velocities near *c*.

In our previous work[2], we measured the transit time of a pulse propagating through a 1-dimensional PBG sample of GaAs/AlGaAs. The group velocity was found to vary from $0.1c$ to $0.8c$ in the vicinity of the photonic band edge. The motivation of our previous work was to explore the potential for PBG materials as compact, tunable optical delay lines. Based on the positive outcome of the delay measurements we redesigned the measurement apparatus in a configuration more in keeping with the envisioned true time delay device. We replaced the high peak power actively mode locked erbium fiber laser with a simple injection current modulated semiconductor laser diode. Thus, we went from transform limited pulses to chirped pulses. The wavelength chirp in injection current modulated laser diodes is due to fluctuations in the electron density. Consider a laser diode idling just above threshold. As a current pulse is injected, the electron density rises above its' equilibrium value and causes the refractive index to decrease. The lowering of the refractive index is equivalent to a shorter cavity and hence a shortening of the lasing wavelength. Then the electron density falls below its' equilibrium value causing the lasing wavelength to lengthen. The electron density fluctuations result in a chirped optical pulse having higher frequencies at the leading edge of the pulse and lower frequencies on the trailing edge. Typically, the magnitude of the chirp is on the order of the transform limit for the optical pulse.

On calibrating the system with reference samples of bulk GaAs and silica we found that etalon effect were important because the transit time of the peak of the pulse varied with the wavelength. Calculations based on transform limited pulses indicated that the time delay range should vary about the transit time without the etalon effects. For the GaAs sample the calculated delay as a function of wavelength should range from 1 ps to 8 ps. The term time delay or transit time refers to the time it takes the peak of the pulse to propagate the length of the sample relative to an air path of equal length. A time delay or transit time of zero indicates a speed of *c*. The 8 ps transit times occur at a transmittance of unity where the cavity dwell time is the longest and the 1 ps transit time occur at the transmittance minima. We actually measured transit times ranging from −8 ps (superluminal) to 17 ps for the GaAs. This is nearly a fourfold increase in the delay range compared with a transform limited pulse.

Initially we discounted the effects of chirp on the transit time because the magnitude of the chirp, 0.75 GHz, was more than two orders of magnitude smaller than the spacing of the transmittance maxima, 94 GHz for the GaAs sample. Also, the chirp was only a small perturbation on the carrier frequency, the magnitude of the chirp being five orders of magnitude smaller than the carrier frequency. So the power spectrum of the chirped pulse and a transform limited pulse of the same duration is approximately the same, within a factor of two. However, a small chirp can lead to a dramatic increase in the time delay range for an optical pulse transmitted through a simple etalon structure. The experimental results are in good agreement with a theoretical model based on the matrix transfer method.

By implication, we expect similar increases in delay ranges for chirped pulses transmitted through PBG structures. The large increase in the delay range for chirped pulses may prove useful for applications in optical phased arrays and optical control of microwaves.

[1] A.M. Steinberg, P.G. Kwiat, and R.Y. Chiao, Phys. Rev. Lett. 71, 708 (1993).

[2] M. Scalora, R. Flynn, S. Reinhardt, R.L. Fork, M.J. Bloemer, M.D. Tocci, C.M. Bowden, H.S. Ledbetter, J.M. Bendickson, and R.P. Leavitt, Phys. Rev. E **54**, R1078 (1996).

Session C
Advanced Propulsion Technologies

Chair
Dr. Walter Bryzik
U.S. Army Tank-automotive and Armaments Command

Co-Chair
Dr. Arthur Ballato
U.S. Army Communications-Electronics Command

Keynote Address
Prof. Dennis Assanis
University of Michigan

THIS PAGE INTENTIONALLY LEFT BLANK

FORMULATION OF A FREE JET SHEAR LAYER IGNITION MODEL FOR APPLICATION TO DIRECT INJECTION DIESEL ENGINES

Peter Schihl*, Walter Bryzik, and John Tasdemiroglu
U.S. Army TACOM RD&E Center
Warren, MI. 48397-5000

ABSTRACT

A transient, one-dimensional shear layer autoignition model was formulated for direct-injection, quiescent chamber diesel engines and verified against two heavy duty and one light duty power plant. The proposed model incorporates the effect of the spray formation process, the bulk thermodynamic condition, and the initial in-cylinder conditions on the ignition event through solution for both the spray periphery local fuel-air ratio and temperature mixing layer profiles in-conjunction with a defined bulk chemistry model. The proposed model agreed fairly well with eighty data points that covered a broad engine operating range in comparison with a variety of published zero-dimensional models employed within diesel engine cycle simulation codes. On average, the shear layer model yielded an error of 19% in comparison to two representative cycle simulation zero-dimensional models that exhibited mean errors of 23% and 60%. Again, this mean error analysis is based on a broad operating condition regime that thermodynamically is quantifiable to start of injection temperatures, pressures, and densities ranging from 800 to 1100 K, 30 to 100 bar, and 12 kg/m^3 to 40 kg/m^3.

1. INTRODUCTION

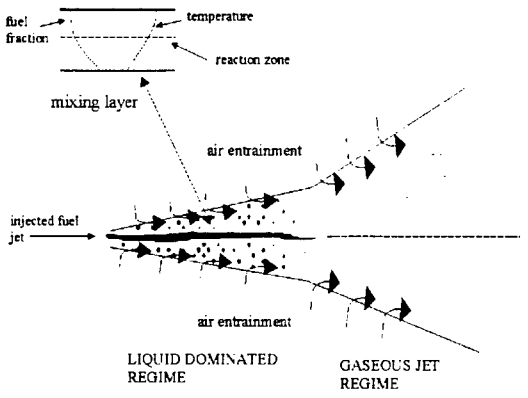
Recent spray visualization experiments for diesel-like jets in constant volume bombs have provided qualitative evidence that autoignition typically occurs in the mixing layer where both evaporated liquid droplets and entrained hot bulk gases converge. Current state-of-the-art optical techniques are not capable of resolving mixing layer temperature and fuel concentration profiles, but do provide macroscopic measurements such as liquid length, mean spray angle, and location(s) of flame propagation. Based on observations made from such data sets, a transient one-dimensional shear layer ignition model was developed with the goal of incorporating injection system design parameters in a manner absent from past zero-dimensional attempts that are currently an integral piece of diesel engine cycle simulation codes.

In general, the ignition delay period for heavy-duty diesel engines is an indicator of ensuing events responsible for indicated reciprocator work, engine out emissions, and noise-vibration-harshness level. In the traditional sense, the ignition delay correlates to the amount of fuel consumed in the premixed and mixing controlled phases of combustion and thus has ramifications on cylinder pressure rise, peak cylinder pressure and temperature, and nitrous oxide and smoke generation. Thus, accurate modeling of this event is an important ingredient in developing engine simulation models given its impact on predicted engine performance. The Army has predominately relied on diesel engines for its ground vehicle fleet and thus has a vested interest in future high performance diesel engines. Advanced combustion and engine modeling is an integral piece in developing future military relevant power plants especially considering the increasing role of simulation in today's engine development projects. The proposed shear layer ignition model provides a methodology for incorporating additional physics into the ignition sub-model for engine simulation codes and thus contributes toward addressing future military power plant needs.

2. FORMULATION

The shear layer ignition model (SLIM) was formulated for a non-impinging jet where ignition occurs during the injection event. In the practical sense, shear layer formation on diesel jets is a three-dimensional process that is highly dependent on the injection system. SLIM attempts to capture the primary physics responsible for the shear layer development process in a one-dimensional manner with the intent of minimizing required computational time while attempting to maintain some semblance of quality predictive capability. Important jet formation sub-processes such as breakup, evaporation, and small-scale mixing are lumped into macroscopic entities such as liquid length, mean spray angle, and turbulent shear layer thickness. Such an approach allows readily for collapse of the three-dimensional problem to a reduced one-dimensional analog.

The conservation of energy and fuel species are solved in a two-step process in order to determine shape fitting parameters for assumed cubic shear layer temperature and fuel mass fraction profiles. This process includes the superposition of both a non-reacting (nil chemistry) and reacting mode solution through careful isolation of chemistry effects as pertaining to shear layer



mass transfer. The non-reacting mode entails utilization of the Von Karman integral technique while the reacting mode is a straightforward local solution using a central finite difference scheme. A simple, one-step chemistry model was employed in this study and 'tuned' for the current data set.

RESULTS

Two large bore, heavy-duty and military applicable diesel engines and one small automotive diesel engine were used in this study to verify SLIM. A total of eighty data points were acquired for this study that include start-of-injection temperature, pressure, and densities in the range of 800 – 1000 K, 30 –100 bar, and 12 – 40 kg/m^3. These parameter ranges are typical of operating conditions for a turbo-charged, after-cooled truck engine. SLIM exhibited a mean error of 19% in comparison to two representative zero-dimensional models that had mean errors of 23% and 65%. SLIM also was within ±20% of the data 65% of the time while the two zero-dimensional models were within ±20 of the data only 20% and 39% of the time. Such an improvement in overall capability does come at the sacrifice of required computational time, i.e. 1 second versus a couple minutes.

All calculations did include incorporation of residual gas fraction for addressing both the induced charge and the initial bulk in-cylinder temperature at start-of-injection. A cycle simulation model was built for one of the three engines and its results were scaled according to compression ratio changes for the other two engines in a manner that provided a mean operating range residual gas fraction. This approach was chosen due to lack of manifold condition data for two of the engines included in this study.

Additionally, SLIM demonstrated sensitivity to injector design parameters in a macroscopic sense through the effective injection velocity. A parametric study based on data acquired for a military applicable heavy-duty diesel engine showed that injection velocity tends to decrease the ignition delay period given the same injected mass quantity. For example, increasing the injection pressure by 20% at medium speed, high load would result in a 20% decrease in the ignition delay period. Such a change could result in reduced pressure rise and peak cylinder pressure, and ultimately alters indicated work output. A zero-dimensional model is insensitive to such injection velocity perturbations.

4. CONCLUSIONS

- A semi-predictive ignition model was developed for non-impinging diesel sprays. This model exhibited an improved predictive capability in comparison to typically employed zero-dimensional models, but at the cost of required computational time, i.e. 1 second versus a few minutes. The model exhibited a mean error of 19% in comparison to 23% and 65% for two representative zero-dimensional models over a wide range of engine operating conditions that included eighty data points from three different diesel engines. Additionally, the model was within 20% of the data 65% of time in comparison to these two zero-dimensional models that were within 20% of the data 39% and 21% of the time.

- The proposed model incorporates injection system design parameters while typical zero-dimensional cycle simulation models are insensitive to such changes. Such parameters include nozzle hole size, entrance length geometry, and injection pressure.

- The proposed model provides a methodology for predicting ignition delay in diesel engines as a function of injector dynamics. Though the current model employs a simple one-step chemistry source term, this methodology readily allows for incorporation of more sophisticated multi-step kinetics mechanisms.

Rarefaction Wave Gun Propulsion

E. Kathe*, R. Dillon, S. Sopok, and M. Witherell
US Army, TACOM-ARDEC Benét Laboratories
Watervliet Arsenal, NY 12189-4050

S. Dunn and D. Coats
Software Engineering Associates, Inc.
Carson City, NV 89701

CONCEPT

RArefaction waVE guN (RAVEN) propulsion constitutes a novel means to dramatically reduce the recoil momentum and heat imparted to future cannons during firing (Kathe, 2000). Reduction of recoil and gun heating would greatly facilitate large caliber gun integration within light future combat system (FCS) vehicles.

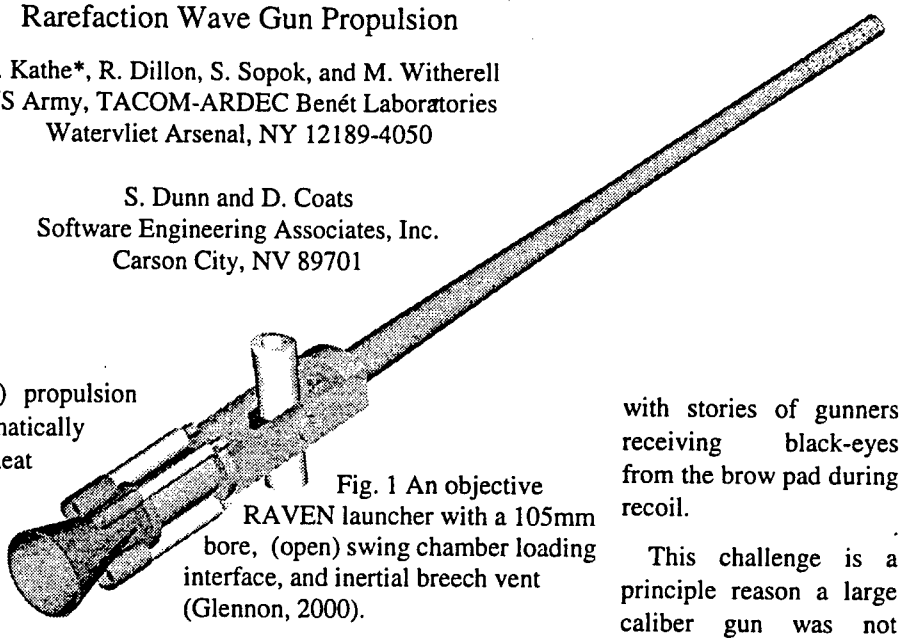


Fig. 1 An objective RAVEN launcher with a 105mm bore, (open) swing chamber loading interface, and inertial breech vent (Glennon, 2000).

The method may be considered a hybrid propulsion technology with features common to both closed-breech cannons and recoilless rifles. For the first stage of propulsion, the gun acts as a closed-breech gun. Later, it behaves as a recoilless rifle. The efficiency of propulsion relative to that of previous recoilless rifles is dramatically improved by the finite sonic velocity at which the rarefaction wave† —released by the delayed chamber venting— may propagate through the propellant gas column to reach the base of the projectile. If delayed sufficiently, shot-exit will occur prior to any compromise in propulsion due to the venting.

Analysis of an M256 120mm cannon firing an ambient M829A2 round has shown that it may be vented when the round has traveled one fourth the way down the bore without compromising the propulsion as shown in Fig. 2. The momentum reduction potential for this system has been estimated to be 60 to 78 percent (depending on throat size, nozzle expansion ratio, and rate of vent opening). A simulation of RAVEN reaction forces during launch using a throat with a 10% area contraction from the chamber and a Mach five nozzle is shown in Fig. 3. Bore heat reduction, caused by the reversal and hastening of blow-down, has been estimated to be as high as 50% for the forward half of the barrel as shown in Fig. 4.

RELEVANCE

Large caliber gun lethality constitutes a time-proven armament technology for fighting vehicles. However, application of large guns to light combat vehicles has often resulted in unacceptable recoil response of the vehicle. Examples include the 152mm gun on the M551 Sheridan with stories of gunners receiving black-eyes from the brow pad during recoil.

This challenge is a principle reason a large caliber gun was not considered feasible for a FCS (Milton, 1998) in the absence of novel gun technology. A solution to either increase the recoil tolerance of FCS gun-vehicle integration (e.g., fire-out-of-battery recoil or an active suspension) or to reduce the momentum imparted by FCS guns (e.g., muzzle brakes) is required to engineer a formidable weapon system. RAVEN will dramatically reduce recoil momentum.

Thermal management of the FCS gun will also prove critical. Since the FCS is severely restricted in weight, focus will be placed upon minimizing gun mass. In addition to recoil challenges that result from reduced cannon mass, current tank guns use thermal mass to enable burst fire.

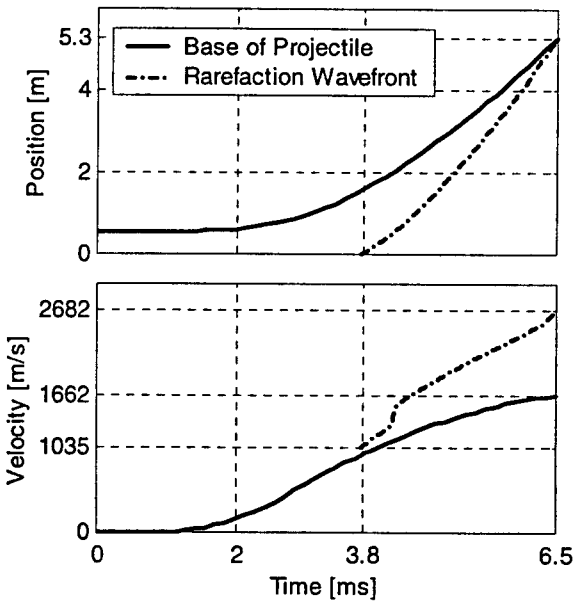


Fig. 2 Plots of the position and velocity of both the base of the projectile and rarefaction wave front versus time.

Convection to the atmosphere constitutes the rate-limiting factor for steady state operation –even for active cooling systems– because the thermal capacity of air is low. Light cannons will simply have a lower thermal mass, regardless of their internal thermal conductivity. RAVEN propulsion will reduce the down-bore heat transfer to the gun by as much as 50 percent as shown in Fig. 4. This will enable the application of composites to the forward end of the gun (which will reduce stabilization demands) without adverse impact on bore temperature during burst fire.

120MM RAVEN CASE STUDY

The favorable effects of RAVEN propulsion have been analyzed for a 120mm gun firing an ambient M829A2 kinetic energy round. The results shown in Fig. 2 indicate that venting the gun 2.7ms prior to shot exit will release a rarefaction wave that does not reach the base of the projectile (and thus compromise propulsion) until the round has exited the muzzle at 6.5ms.

One may validate this knowing the accepted sonic velocity for propellant gas is about 1,000 m/s (Germershausen, 1982). When added to the local gas velocity, which increases from zero at the breech to the muzzle velocity, the delay may be approximated as gun length divided by the sum of sonic velocity and half the muzzle velocity.

In Fig. 3, the dramatic reduction in pressure at the breech upon venting is shown. This dramatic reduction in pressure is critical to mitigate the nozzle erosion that may be anticipated from such a high-pressure vent. In the second plot of Fig. 3, the forward thrust developed by a Mach 5 expansion nozzle is included. The net momentum reduction relative to the closed breech gun for this case was 75%. Since the kinetic energy of recoil relates to the square of momentum, this would be reduced by a factor of 16.

Figure 4 depicts the anticipated reduction in heat transfer to the bore as a result of the venting. Heat transfer to the bore of a gun is essentially proportional to gas velocity, gas density, temperature difference between wall and gas, and duration (Jones, 1965). RAVEN dramatically reduces the gas velocity, gas density, and duration of blow-down. The effect is less pronounced just forward of the chamber. Heat transfer is higher in the chamber where the lack of gas velocity in the closed-breech gun would normally result in very low heating. This may be addressed through the use of a cartridge case.

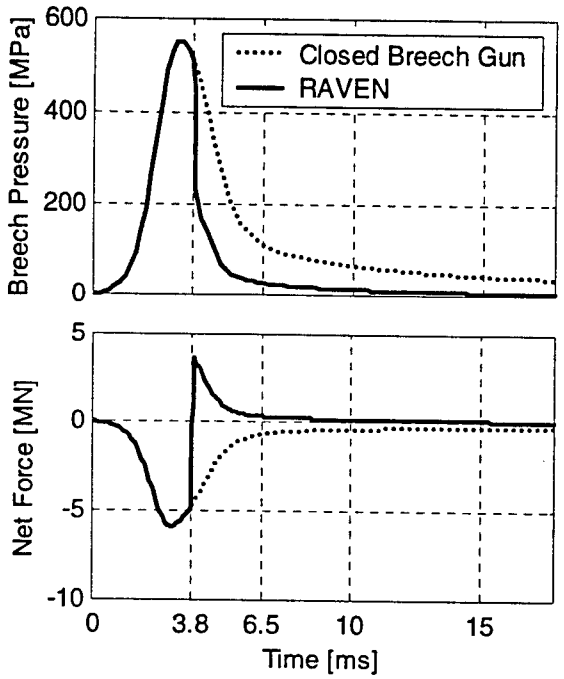


Fig. 3 Plots of breech pressure and net force applied to a RAVEN launcher that includes developed thrust.

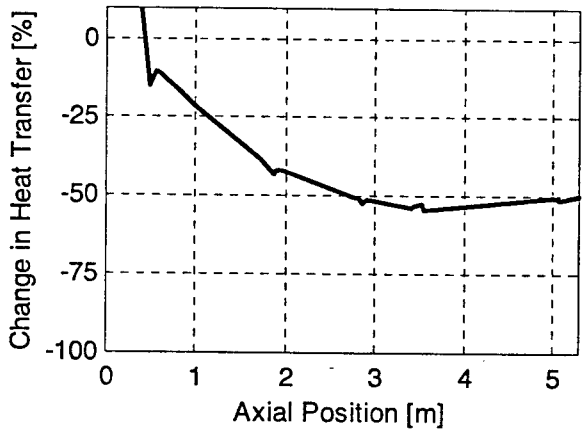


Fig. 4 Plot of reduced bore heating of RAVEN relative to closed-breech gun.

REFERENCES

Germershausen, R. and Melchior, E., "Internal Ballistics," in *Handbook on Weaponry*, First English Edition, Rheinmetall GmbH, Düsseldorf, Germany, 1982.

Glennon, M., Tortorici, R, Hyland, E., and Kathe, E., "RAVEN 105mm Preliminary Design," US Army Benét Laboratories, Watervliet Arsenal, NY, October 2000.

Jones, R. N., Hitchcock, H. P., and Villegas, D. R., *Interior Ballistics of Guns*, AMCP 706-150, US Army Material Command, Alexandria, VA, February, 1965.

Kathe, E., "Sonic Rarefaction Wave Recoilless Gun System," US Patent Application Serial Number 09/631142, 2 August 2000.

Milton, F., Army After Next Presentation Advocating A Hybrid Missile And Medium-Caliber-Gun Future Combat System, 21st Army Science Conference, Norfolk, VA, 15-17 June 1998.

COMPUTATIONAL MODELING OF AN ADVANCED PROPULSION TECHNOLOGY: NUMERICAL SIMULATION OF HYPERGOLIC COMBUSTION IN THE AMCOM VORTEX ENGINE

Michael J. Nusca*
Weapons and Materials Research Directorate
U.S. Army Research Laboratory, Aberdeen Proving Ground, MD 21005

R. Scott Michaels
Propulsion and Structures Directorate
U.S. Army Aviation and Missile Research, Development, and Engineering Center
Redstone Arsenal, AL 35898

SUMMARY

The use of gel propellants for missile propulsion introduces new challenges in flow and combustion. Along with increases in chamber pressure and injector pressure drops, the gels pose a major challenge in mixing the oxidizer and fuel to obtain maximum performance from the combustor. The challenge is increased with the introduction of carbon and other solid particulate used to enhance the density impulse of the propellant system. With conventional engines, the mixing difficulties are typically overcome by increasing the volume available for combustion in the chamber. The impinging stream vortex engine (ISVE) that it is in development at the U.S. Army Aviation and Missile Command (AMCOM) offers an alternative to increasing the length and volume of conventional combustion chambers. The ISVE is radically different from the conventional impinging stream liquid/gel engine in that the propellants are injected tangentially to the chamber wall, imping, and then swirl via the vortex flow that is established with the tangential injection. The initial mixing occurs during stream impingement and the final mixing occurs in the highly turbulent vortex region between the injector orifices and the nozzle throat. There has been some evidence from post-test examination of the engine hardware that the heavier solid particles separate from the gas particles and move toward the chamber wall. It has been postulated that centrifugal movement of the solid particles increases the path length and thus increases the time in the combustion zone. An additional attribute of this injection concept is that the propellants provide transpiration cooling at the injector area and protect the cylindrical chamber wall from the combustion flame. Limited testing of the vortex engine has yielded delivered specific impulse efficiencies in excess of 95 percent of theoretical using inhibited red fuming nitric acid (IRFNA) as the oxidizer and 50 percent carbon loaded monomethylhydrazine (MMH) as the fuel.

Since the ISVE is a relatively new concept, the databases and analytical models relating performance to the engine design parameters are essentially nonexistent. To address these design issues, a cooperative effort was initiated at AMCOM and the U.S. Army Research Laboratory (ARL). Computational modeling of the ISVE is being conducted at the ARL using the ARL-NSRG code -- a time-accurate CFD code that was written by the first author and has been used to simulate unsteady, multi-component, chemically reacting (nonequilibrium) flows in various gasdynamic applications. The NSRG code was written for the solution of the unsteady, 3D Navier-Stokes equations including species diffusion, thermal conduction, viscosity, non-Newtonian fluid effects, and nonequilibrium chemical kinetics. Several kinetics mechanisms have been installed in the code using an Arrhenius formulation. For the present simulations hypergolic combustion model was added. The conservation-law form of the equations is used and a finite-volume discretization methodology is employed. The convective and transport fluxes are resolved using upwind and central-differencing along with flux-limiting methods. Numerical stiffness due to chemical source terms is mitigated by pre-conditioning techniques, thus permitting explicit time integration to use reasonable time steps. Flow turbulence is modeled using an energy/damping approach. Code validation has been performed for a wide variety of DoD applications.

Figure 1a shows a schematic of the vortex engine with an expanded view of the combustion chamber. The combined combustion chamber and nozzle, as shown in Figure 1a, is 7.5 cm long and 2.8 cm in diameter (note that the figure has not been plotted to scale). The injector pairs are shown along the chamber wall. Figures 1b,c,d show the computed water (a predominant combustion product) mass fraction contours for .02s to .20s from the initiation of the fuel and oxidizer injection process. Note that Figures 1a-1d are two-dimensional slices through the engine and thus display a single azimuthal plane from a three-dimensional configuration. In the numerical simulation, while the chemical and thermodynamic properties of MMH and IRFNA have been included in the model, these reactants are assumed to have already

vaporized at the moment of injection. Figure 1b shows that the initial mixing and combustion process occurs along the top of the combustion chamber (note that Figures 1b-1d are oriented 90-degrees with respect to Figure 1a). Arrows indicate the locations of two of the injector pairs. A combustion wave, containing mixing vortices, is seen to form from the chamber top and advance toward the engine nozzle (1b). A second combustion wave forms subsequently (1c). By 0.2s the expanding nozzle flowfield is well established as is a series of combustion waves generated in the chamber (note that fuel/oxidizer injection from the wall continues throughout the simulation). It has been noted that even these initial numerical simulations agree with the observations made at AMCOM when testing the vortex engine. Pressure probes placed at the top of the combustion chamber (see Figure 1a) record a rapid pressure rise followed by some level of pressure oscillation (corresponding to the transient combustion waves). In addition, it has been noted experimentally that combustion may be initiating from the top surface of the chamber and proceeding to the nozzle – a theory supported by the present simulations.

These first such CFD simulations of the vortex engine are being furthered by additional numerical simulations and analysis. The full paper shows good agreement between measured chamber pressure histories and those predicted using the CFD code. The goal is to use experiment and numerical simulations to understand the unique combustion physics of the vortex engine. This understanding will aid in the optimization and scaling of the engine for use in a variety of Army missile systems.

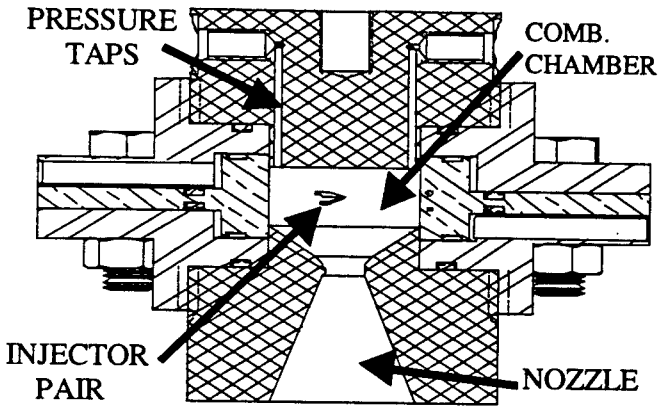


Figure 1a. Schematic of the vortex ISVE in a test block.

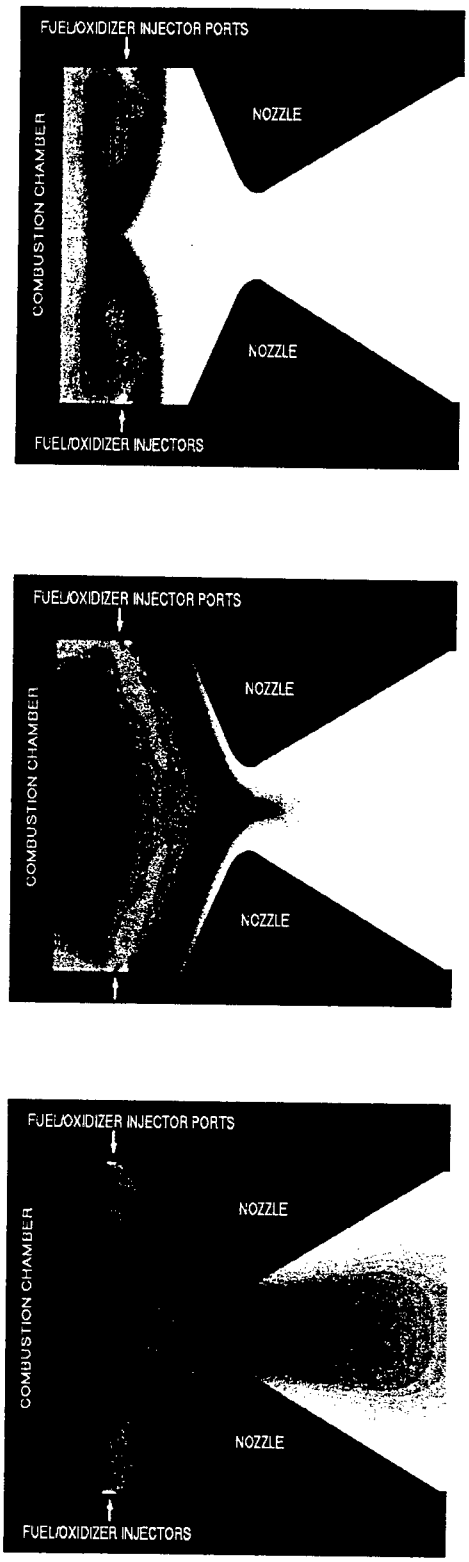


Figure 1b, 1c, 1d (top to bottom). Gray-scale contour plots of computed water mass fraction (0 to .035: white to black) for times = .02, .1, and .2 seconds.

SMART DESIGN OF INSENSITIVE HIGH-ENERGY MATERIALS USING QUANTUM MECHANICAL CALCULATIONS

Betsy M. Rice* and Jennifer J. Hare
U. S. Army Research Laboratory
AMSRL-WM-BD
AMSRL-CI-HC
Aberdeen Proving Ground, MD 21005

The goal of lightening the heavy forces while making them more survivable and lethal will be achieved upon the development and deployment of new weapons systems such as the Future Combat Systems (FCS). Likewise, the success of the FCS will depend on the development and manufacture of advanced energetic materials tailored for optimal performance in the new systems. The current fiscal climate and need for rapid deployment of the new weapons systems dictate a streamlining of the development process in order that these advanced materials might be expeditiously designed and manufactured. In previous times, the development process for new energetic materials was lengthy, and often relied heavily on experimentation and measurement of a variety of candidate materials. Such a procedure has the potential for inordinate waste, particularly when developing and testing a material that turns out to be a poor candidate. This waste can be reduced through rapid and inexpensive screening of candidates through the use of modeling and simulation in the early stages of the development procedure. Predictive models will allow for the evaluation of a notional material for potential performance or vulnerability characteristics. If the candidate shows promise, further and more costly investigation can be justified. Likewise, poor performers are readily eliminated from further consideration.

In this work, we describe our recent efforts in developing a set of computational tools that can be used to rapidly predict properties associated with performance and with vulnerability of energetic materials. The tools are based on quantum mechanical calculations, and describe relationships between the quantum mechanical properties of an isolated molecule with its behavior on the macroscale. The predictive methods all use quantum mechanical predictions of the electrostatic potential that surrounds an isolated molecule.

The first computational tool developed is used to predict Heats of Formation of energetic materials in the gas, liquid and solid state (Rice et al., 1999). This quantity is used to assess detonation properties or potential performance of the material under idealized gun firing conditions. Predicted gas-phase heats of formation for 35 molecules using this computational tool have a root mean square (rms) deviation from experiment of 3.1 kcal/mol. Predicted liquid and solid phase heats of formation for 24 and 44 energetic materials, respectively, have rms deviations from experiment of 3.3 and 9.0 kcal/mol, respectively. Figure 1 shows predictions of heat of formation for these and additional molecules, compared with experimental values and values compiled in the Cheetah 2.0 reactant library (Fried et al., 1998).

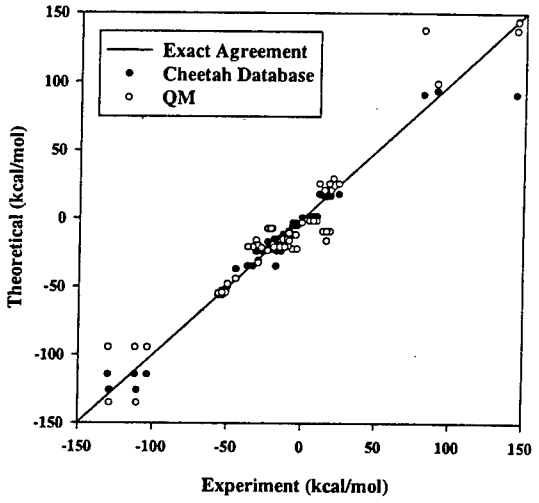


Figure 1. Solid phase heats of formation for explosives contained in the Cheetah 2.0 reactant library (filled circles) and predicted using the QM methods described herein (hollow circles) versus experimental values. Solid line denotes exact agreement.

The Heats of Formation predicted using these methods can be used to predict Heats of Detonation of pure and explosive formulations (Rice and Hare, 2000). The methodology is based on a simple scheme to calculate detonation properties as proposed by Kamlet and Jacobs (1968) and can be implemented from knowledge of heats of formation. We combined our method of predicting heats of formation of explosives with the Kamlet-Jacobs method for calculating Heats of Detonation, and applied this tool to pure explosive and explosive formulations for which experimental data were available. We also compared our results against predictions made using the thermochemical code Cheetah 2.0. For pure explosives, the quantum mechanically based results have a rms deviation from experiment of 0.138 kcal/g, whereas the Cheetah predictions have a rms deviation from experiment of 0.133 kcal/g. For explosive

formulations, the QM predictions are in reasonable agreement with experimental values, with a rms deviation of 0.058 kcal/g. Although the Cheetah calculations have a stronger theoretical basis for prediction of detonation properties, this methodology has the advantage that neither heats of formation nor densities need to be measured or estimated to calculate the heat of detonation of an explosive. A comparison of predicted Heats of Detonation with measured values is given in Fig. 2

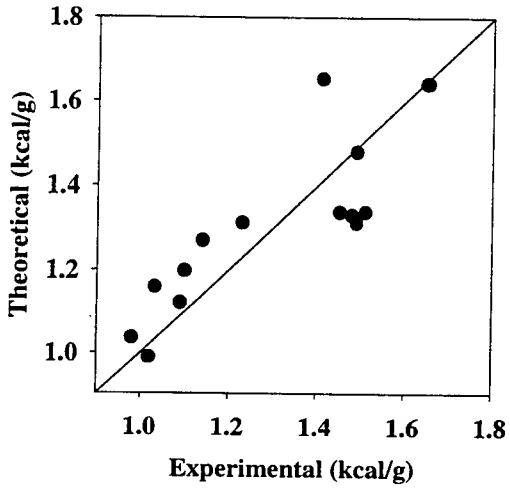


Figure 2. Predicted versus experimental Heats of Detonation. Solid line denotes exact agreement.

Finally, we describe our efforts to establish functional relationships between statistical properties of the electrostatic potentials for a set of energetic molecules and their impact sensitivities. Impact sensitivities are often described as the results of drop weight impact tests, with the results quoted as $h_{50\%}$. We have performed quantum mechanical calculations on 34 polynitroaromatic and benzofuroxan molecules for which such measurements have been performed (Wilson et al., 1990), and established a functional relationship between their $h_{50\%}$ values and properties of the electrostatic potentials and the Heats of Detonation of the molecules.

The predicted values (shown in Fig. 3) are in good agreement with experimental values for materials ranging from the highly sensitive hexanitrobenzene to the highly insensitive explosive TATB. Rms deviation of the predictions from the experimental values is 19 cm.

Impact sensitivities for 11 additional energetic molecules were calculated and compared to experiment in order to determine the predictive capability of the computational tool. These molecules were not used in establishing the correlation, and include PETN, RDX, HMX, β–and ε–CL-20, HNS, methyl picrate, styphnic acid, NTO, NQ and FOX-7. For these materials, there is excellent agreement between the predicted and measured values, with a rms deviation of 22 cm from experiment.

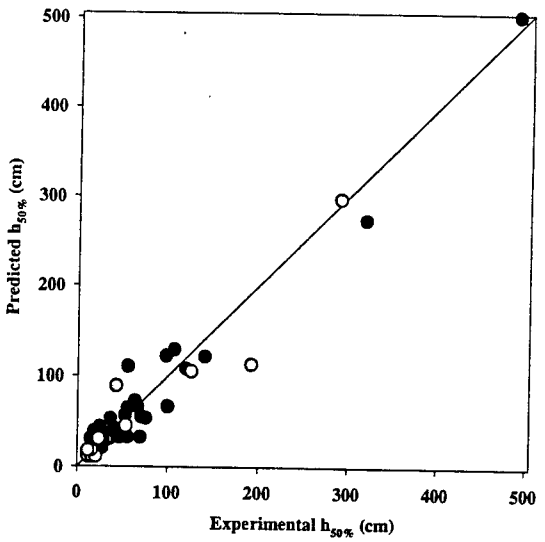


Figure 3. Predicted versus experimental $h_{50\%}$ values for explosives. Solid circles denote 34 explosives whose values were measured by Wilson et al. (1990), and hollow circles denote 11 molecules used to assess the predictive quality of the model. Solid line denotes exact agreement

The quantum mechanical calculations characterizing properties of energetic molecules related to performance and impact sensitivities of explosives have resulted in accurate computational tools that will predict these properties without the need for synthesis and measurement of the actual material. It is hoped that this methodology can be extended to predict other properties of interest to the materials designer, to provide him with a powerful suite of predictive screening tools.

REFERENCES

Fried, L. E., W. M. Howard, and P. Clark Souers, Cheetah 2.0 User's Manual, 1998. UCRL-MA-117541 Rev. 5

Kamlet, M. J. and S. J. Jacobs, J. Chem. Phys. 48 (1968) 23.

Rice, B. M., S. V. Pai and J. Hare, "Predicting Heats of Formation of Energetic Materials using Quantum Mechanical Calculations", Combustion and Flame, Vol. 118, 445 (1999).

Rice, B. M. and J. Hare, "Predicting Heats of Detonation Using Quantum Mechanical Calculations", Thermochimica Acta, submitted (2000).

Wilson, W. S., D. E. Bliss, S. L. Christian and D. J. Knight, "Explosive Properties of Polynitroaromatics", Naval Weapons Center Technical Publication 7073, April, 1990.

EXPERIMENTS TO DEFINE PLASMA-PROPELLANT INTERACTIONS

Richard A. Beyer and Rose A. Pesce-Rodriguez
Army Research Laboratory
Aberdeen Proving Ground, MD 21005

1. INTRODUCTION

The Army research community has been moving swiftly to re-orient itself to provide the technology required to provide the target levels of mobility, lethality, and survivability for the objective force. One element of this force is the Future Combat System (FCS). If the FCS is to be armed with a high-performance cannon within the expected weight and volume restrictions, advances will be necessary in gun performance. One of the promising cannon candidates is a design with a high density charge of a next-generation propellant ignited by an electrothermal plasma, referred to as electrothermal chemical (ETC). The charge will be designed physically and chemically to have optimized ignition characteristics for plasma ignition while maintaining relative insensitivity to threat stimuli.

The key to designing a propellant charge that is "plasma specific" is a detailed understanding of the mechanism of propellant ignition by a plasma. The plasma has several properties that may be important. The temperature of the plasma as it exits the capillary has been measured to be above 10,000K. In shock waves the gases may exceed 50,000K (Beyer & Bunte, 1992). Thus there is a abundance of emitted radiation which goes far into the ultraviolet which may produce effects from photochemical changes within the propellant to in-depth heating. The composition of the plasma is a mix of highly reactive ions and neutrals that can attack propellant surfaces and ignite or predispose them for ignition. The flow has a high velocity which enhances convective heat transfer. The goal of the present research is to separate these properties.

2. EXPERIMENTAL DESCRIPTION

Our approach in this project has been to develop a relatively small scale apparatus for the study of plasma-propellant interactions which will allow a large number of experiments. The heart of these experiments is a polyethylene capillary with a 3 mm diameter bore and 35 mm length. It is mounted in a steel case for structural support and insulated electrically. A schematic diagram is shown in Fig. 1. A fine aluminum wire is initially present between the two electrodes. The device is powered by a capacitor bank with about 675 joules of stored energy and pulse forming network that delivers the energy to the circuit in about 300 μs. At the beginning of the current flow the wire explodes and forms an ionized (conducting) region in the capillary. As the current flows through the capillary, ohmic heating deposits energy onto the wall, which then ablates, decomposes rapidly, and feeds the plasma to maintain the conductivity.

As a first approach to looking for evidence for subsurface reactions, residual samples were analyzed for chemical change. A sensitive and unambiguous indicator for reaction of nitrate esters is the presence of NO. Analysis of NO levels was performed by means of desorption - gas chromatography - mass spectroscopy. Following the ignition experiments, propellant samples were sliced and sectioned to yield rectangular samples.

Three standard gun propellants were used in most of these experiments. They are M9, a hot double base propellant (nitrocellulose with a NG plasticizer), JA2, a modified double-base propellant (nitrocellulose with NG and DEGDN plasticizers), and M30, a high performance triple-base propellant (nitrocellulose, NG, and nitroguanidine).

3. OBSERVATIONS

Three types of interactions were used in attempts to characterize the plasma effect on these propellants. The first method was to mount a flat sample of JA2 at the exit of the capillary in open air. The second setup was to mount a single grain at the exhaust of the capillary so that the plasma discharges from the capillary through the center perforation. The third method used was to insert the single grain into the chamber. The sample mounted at the capillary exhaust provides a highly dynamic flow with strong contact between

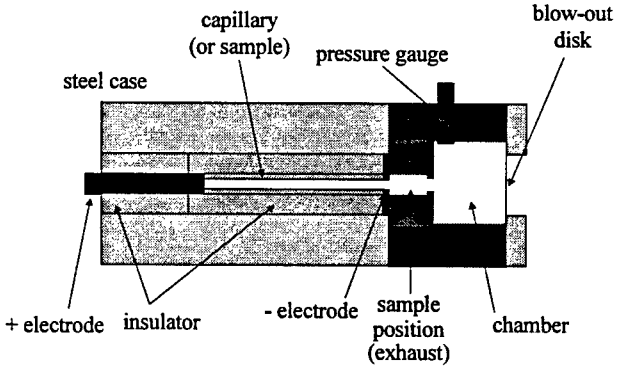


Fig. 1. Schematic diagram of capillary discharge plasma generator and attached chamber.

the plasma and the sample. The location of the sample in the chamber is still a very aggressive environment for ignition, but the plasma has mixed with the ambient air which both cools and dilutes it. In these methods, pressure was the principle real-time diagnostic.

The behavior of the propellants is clearly divided into that during the plasma event and that which follows. Fig. 2 shows the pressure-time behavior of experiments with the four types of propellants. During the plasma pulse, all traces show a pressure increase. That for M30 is always highest while the M9 sample actually affects the flow to the pressure gauge so much that measured pressure falls,as shown in Fig. 3. This effect is thought to derive from subsurface radiation effects, since the M9 is quite transparent optically.

Fig. 4 gives the NO ratio data for JA2 sheet exposed "head-on" to plasma. Plots C and D are for 2 different areas of the section that received direct exposure to the plasma and was obviously blistered and somewhat pitted. The data for these areas suggest NO-level enhancement from the exposed surface to a depth of 0.75 mm.

The significance of enhanced NO-levels is believed to be related to the ability of the radiative and/or conductive components of the plasma to affect the propellant in-depth and somehow "prime" it for decomposition. The M30 samples (not shown) appear to be affected at a depth on the order of 0.5 mm, whereas the JA2 appears to be affected to a depth of 0.75 mm. It is proposed that in-depth reaction results in the generation of decomposition gases that can cause an upwelling of propellant. In the case of M9, it is proposed that in-depth reaction is so extensive that it is quickly blown to bits, and burns very rapidly. This is consistent with observed pressure traces in Fig. 3. Chemical analysis of M9 was not performed because no sample survived a plasma-ignition experiment.

REFERENCE

Beyer, R. A. and Bunte, S. W., "Spatial and Temporal Temperature Studies of Electrothermal Chemical (ETC) Plasmas," Ballistic Research Laboratory Technical report, BRL-TR-3324, AD-a248541, March 1992.

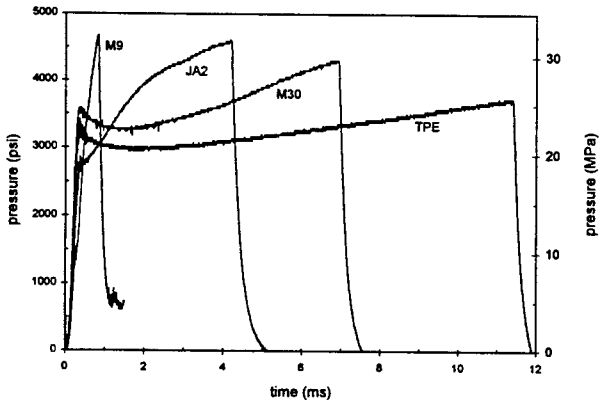


Fig. 2. Pressure records for times after plasma discharge for propellants in plasma exhaust.

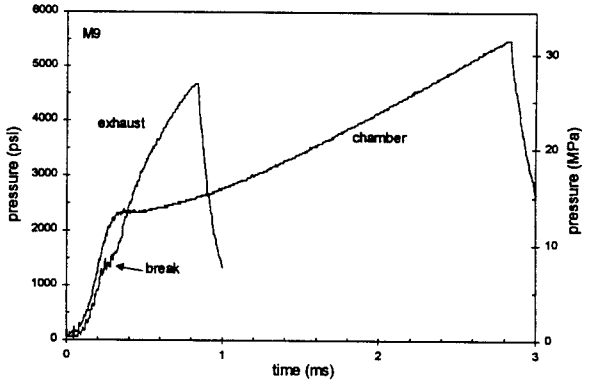
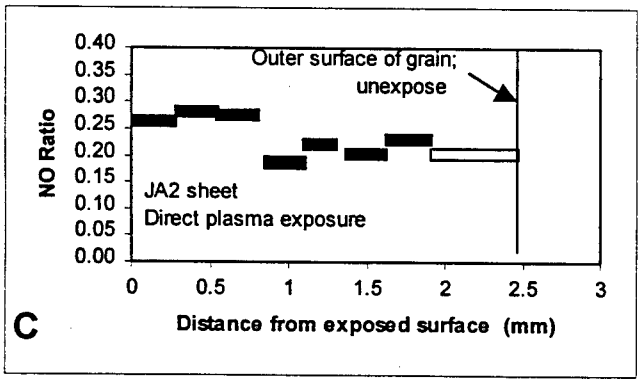


Fig. 3. Comparison of M9 propellant pressure records for plasma interaction by direct exhaust through the perforation and with sample mounted in chamber.



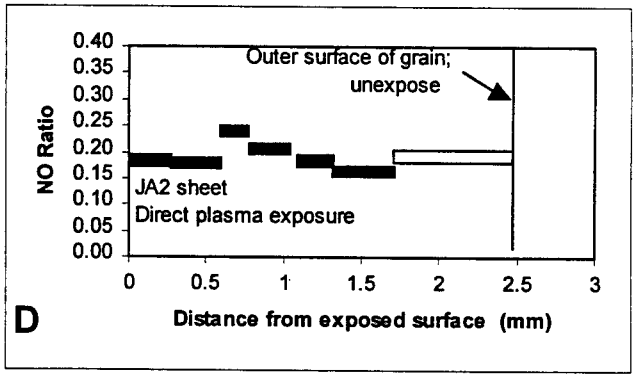


Fig. 4. NO ratios for JA2 propellant sheet. Nominal sample thickness 2.50 mm. Filled boxes represent NO –level in slice whose thickness is the length of the box. Unfilled boxes represent slices for which data was not measured.

ATOMISTIC MODELING OF NITRATE ESTER BASED GUN PROPELLANTS

S.W. Bunte* and M.S. Miller
US Army Research Laboratory
AMSRL-WM-BD
Aberdeen Proving Ground, MD 21005-5066

H. Sun
Molecular Simulations, Inc
San Diego, CA 92121

ABSTRACT

Atomistic simulations have advanced to the degree that the material properties of actual Army gun propellants can be predicted *a priori*. For example, we have used the COMPASS force field to predict the density of the gun propellant JA2 and its energetic ingredients. The predicted density of the propellant is within 1.6% of its measured value. These results are the first *a priori* prediction of the density of a gun propellant and clearly suggest that this methodology can be a valuable tool in the design of new high energy propellant formulations for use in the Future Combat System.

1. INTRODUCTION

Research in Army gun propulsion is currently being driven by the requirements of The Army's Transformation Strategy. This transformation, which is targeted to be complete in the 2010 timeframe, will result in an Objective Force that is more deployable, lethal, survivable, and sustainable than the present force. In terms of gun propulsion, attainment of this vision will require new propellant formulations that contain more energy and are less sensitive than the propellants currently fielded. This paper reports the first application of atomistic modeling to compute the macroscopic properties of real, multi-ingredient gun propellants. This new technology, which represents the fruition of decades of research, may well prove vital to meeting the ambitious performance and timeline goals set for the Future Combat System.

In the past, the determination of gun propellant properties has necessitated direct measurement. This would require the formulation of a large number of candidate mixes. The property of interest would be measured; those that exhibited promise would be kept for further testing, those that were less than promising were discarded. This process is both inefficient and costly. The availability of atomistic and molecular modeling strategies capable of predicting material properties such as density, stability, mechanical properties, and ingredient compatibility would revolutionize the design and formulation of new gun propellants. This report demonstrates that such a valuable tool is now becoming available for practical use. Although computer speed has increased dramatically in recent years, the modeling of large molecular systems and condensed phases has been prohibitive from a first-principles approach. A more empirical approach based on atomic force fields, however, has proved most promising. In less complex cases where both may be employed, the force field method is several order of magnitude faster than any *ab initio* method. In addition, the most important interaction terms in simulating the condensed phase are the nonbonding forces (in particular, the dispersion forces) which are extremely difficult to accurately describe using *ab initio* methods. The COMPASS (Condensed-phase Optimized Molecular Potentials for Atomistic Simulation Studies, Molecular Simulations, Inc.) force field has been specifically designed for material science applications and can be used to accurately predict several molecular properties, including molecular structures, conformations, and vibrations. In addition, the nonbonding terms in COMPASS have been optimized using condensed-phase (liquid and crystal) data so that several thermophysical properties of molecular liquids and crystals can also be well reproduced.

The gun propellant JA2 is composed of three principal energetic ingredients: nitrocellulose (NC, $C_6H_{7.55}N_{2.45}O_{9.90}$), nitroglycerin (NG, O_2NOCH_2-$CHONO_2$-CH_2ONO_2), and diethyleneglycol dinitrate (DEGDN, O_2NO-$(CH_2)_2$-O-$(CH_2)_2$-ONO_2). In the propellant blend, the NC is present as an energetic binder and both NG and DEGDN serve as an energetic plasticizing agent. The common chemical feature in each of these compounds is the nitrate ester (-ONO_2) moiety. We have recently completed the parameterization and validation of the atom types needed to model nitrate ester containing compounds using the COMPASS force field (Bunte and Sun, 2000). We report here the use of molecular dynamics simulations to predict *a priori* the densities of NG, DEGDN, NC, and JA2 using the COMPASS force field.

2. RESULTS

Constant pressure and temperature (NPT) molecular dynamics (MD) simulations were performed to calculate the densities of NG and DEGDN. Both of these materials

are liquids at room temperature hence, of the materials studied, these simulations are the least complicated of the four. The measured density of NG is 1.5910 g/cm^3; the simulation predicted a value of 1.6232 g/cm^3, a difference of 2%. For DEGDN, the experimental density is 1.3770 g/cm^3 and the predicted density is 1.3785 g/cm^3, a difference of 0.1%.

Nitrocellulose (NC) represents a considerably more difficult case than NG and DEGDN. Present in all conventional gun propellants, NC is a long-chain polymer which has three possible sites of nitration, located at C2, C3, and C6 on each monomer unit as shown in Fig 1.

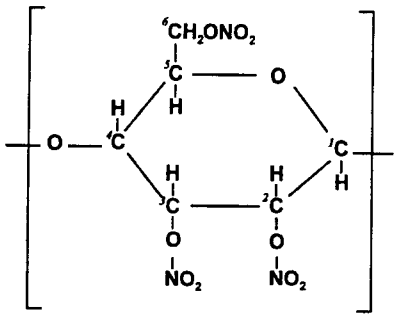


Figure 1. Nitrocellulose monomer unit showing the three possible sites of nitration.

The degree of nitration of a given specimen of NC is characterized by the percent nitration (%N) or average mass of nitrogen per mass of the specimen. Military grades of NC typically have a %N in the range of 12-13%, and it was found by Leider and Seaton (Leider and Seaton, 1979) that they are a mixture of all three nitrate states.

We chose to treat NC as a homogeneous mixture of the three nitration states with their distribution computed from a Monte-Carlo code we developed based on the findings of Leider and Seaton (Leader and Seaton, 1979). They found that the C6 site is always nitrated first and then either the C2 and C3 sites next with equal probability. These results have been confirmed by both experiment and electronic structure calculations.

The NC in JA2 has a %N of 13.1. Using the aforementioned Monte-Carlo code, the distribution of nitrate states for 13.1% N NC polymer was determined to be 11 tri-, 3 di-, and 1 mononitrate for a polymer chain consisting of 15 monomer units. A heteropolymer with this distribution was constructed and a MD NPT simulation was run. This simulation resulted in a computed density of 1.6151 g/cm^3. To our knowledge, the density of 13.1%N NC has not been measured, however, 12.2%N NC has a density of 1.653 g/cm^3 and 13.45%N NC has a density of 1.665 g/cm^3. Interpolating between these two known densities results in an estimated density of 1.661 g/cm^3. Our computed density is within 3% of this value.

The propellant JA2 consists of roughly 60% (by weight) NC (13.1%N), 25% DEGDN, and 15% NG. Having successfully predicted the density of the individual ingredients, we constructed a cell to simulate JA2. The simulation cell consisted of 10 configurations, each containing 2 strands of NC (13.1%N), 18 molecules of DEGDN, and 9 molecules of NG. Figure 2 shows one such configuration. NPT dynamics were run; the average density of the 10 configurations was 1.595 ± 0.018 g/cm^3. The measured density of JA2 is 1.57 ± 0.01 g/cm^3. Our simulated density differs from the measured density by 1.6%. Figure 2 is a most remarkable image, being the first molecular view of a real propellant formulation ever produced.

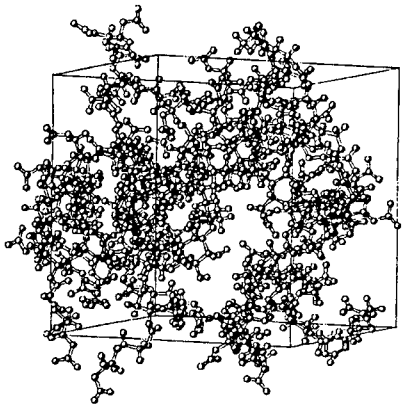


Figure 2. Molecular model of the gun propellant JA2.

3. CONCLUSIONS

We have used atomistic simulation techniques to predict *a priori* the densities of the gun propellant JA2 and its energetic ingredients. The results of these simulations are in excellent agreement with experimental data. This methodology will likely be a valuable tool for propellant chemists and formulators to aid in the development of new high energy propellant formulations for applications in the Future Combat System.

4. REFERENCES

Bunte, S.W. and Sun, H., "Molecular Modeling of Energetic Materials: The Parameterization and Validation of Nitrate Esters in the COMPASS Force Field," *J. Phys. Chem.*, Vol. 104, No. 11, pp. 2477-2489, 2000.

Leider, H.R. and Seaton, D.L., "Nitrate Ester Decomposition and Degradation of Molecular Weight in Nitrocellulose from Thermal Decomposition of PBX-9404 Below 100°C," Lawrence Livermore Laboratory Report UCRL-52776, 1979.

DENSITY FUNCTIONAL THEORY CHARACTERIZATION OF DMAZ – A POTENTIAL REPLACEMENT FOR HYDRAZINE-BASED HYPERGOLIC FUELS

Michael J. McQuaid*, Betsy M. Rice, Cary Chabalowski, and Kevin McNesby
US Army Research Laboratory
Aberdeen Proving Ground, MD

Darren Thompson
US Army Aviation and Missile Command
Redstone Arsenal, Huntsville, AL

ABSTRACT

Computational quantum chemistry was employed to characterize the geometric parameters and vibrational modes of stable and transition states of 2 azido–N,N dimethylethanamine (DMAZ). The theoretical results are corroborated by comparison to mid-IR spectra acquired experimentally. Mappings of DMAZ conformer electrostatic potentials are compared to that of hydrazine and suggest that the conformational dependence of lone pair electrons in DMAZ may play an important role in its rate of reaction with nitric acid.

1.0 INTRODUCTION

Hypergolic liquid (or gel) propulsion systems—i.e., those in which a fuel and an oxidizer react spontaneously upon mixing—are employed throughout the DoD for aviation and missile applications. Having several performance characteristics that make them preferable to competing solid propellant or non-hypergolic fuel-oxidizer-based technologies, the Army, through the Future Missile Technology Integration program, is exploring the development of hypergolic propulsion technology for the modernization of tactical missiles employed with the Bradley Fighting Vehicle. Weapons propelled by such designs will also undoubtedly be considered for employment in the Future Combat System.

One of the drawbacks to hypergolic propulsion systems, however, is that they typically rely on fuels derived from hydrazine, monomethylhydrazine (MMH) and/or unsymmetrical dimethylhydrazine (UDMH). All of these materials are acutely toxic and suspected carcinogens, and thus their use necessitates costly design and handling procedures. These costs are borne because of the superior performance characteristics of these fuels, one of them being their spontaneous, fast (hypergolic) reaction with various oxidizers. Fast reaction times correlate with ignition delay, an important factor in determining the amount of fuel that will accumulate in a rocket motor prior to ignition. Shorter ignition delays reduce accumulation, allowing motors with smaller and lighter combustion chambers to be designed.

To avoid the costs associated with hydrazine-based fuels, alternatives to them have long been sought, but long ignition delays have been a consistent shortcoming of proposed candidates. A breakthrough was achieved, however, in 1994 when AMCOM identified a class of compounds—tertiary amine azides—which demonstrated relatively short ignition delays when reacted with inhibited red fuming nitric acid (IRFNA). Named CINCH (for Competitive Impulse Non-carcinogenic Hypergol), a compound within this class of materials receiving considerable attention is 2 azido–N,N dimethylethanamine [$(CH_3)_2NCH_2CH_2N_3$]. Also referred to as DMAZ, its ignition delay is competitive with Aerozine 50 and is only slightly longer than that for MMH—6 ms vs. 3 ms. In comparison with MMH, DMAZ is less acutely toxic, has a wider temperature range as a liquid, and has a lower vapor pressure, making it a highly desirable candidate. Unfortunately, even though the 6-ms ignition delay for the DMAZ system is far shorter than that observed with other alternative systems, even the slight increase in delay compared to the MMH system prevents DMAZ from being a "drop-in" replacement. This is a concern to the Army because it will create difficulty in gaining acceptance for DMAZ within the wider DoD community; and without its acceptance by the Air Force, from whom the Army purchases all of its missile fuels, the Army will not be able to field it.

As such, there is the desire to establish means for reducing the ignition delays of systems which might utilize DMAZ; or to design new compounds based on what has been or can be learned about the DMAZ–IRFNA system. To develop an understanding of the mechanisms that control ignition delay, ARL is employing computational quantum chemistry to study fuel—nitric acid reactions, the objective being to determine if fuel structure – ignition delay correlations can be established. This paper summarizes the completion of the first phase of the study, namely the structural characterization of DMAZ conformers.

2.0 METHODS

All computations were performed with the generalized gradient approximation non-local density functional routine (B3LYP) and 6-311+G(2d,2p) atomic basis set available in the Gaussian 98 suite of quantum chemistry codes. Most calculations were performed on the high performance computers at the DoD Major Shared Resource Center at ARL. To corroborate the results of the computational study, mid-IR spectra for gas-phase DMAZ were acquired experimentally. The spectra were obtained via an FTIR spectrometer from a 2.5 Torr, room-temperature sample in a long pass cell.

3.0 RESULTS

Nine stable conformers and four transition states were identified in this study. The global minimum energy DMAZ conformer found in the computational study and another low-energy conformer that proves to be important are shown in Figure 1. Like the difference between A and B, the 7 other stable structures are distinguished primarily by the configuration of the CH_2-CH_2-N_3 group. The difference in energy between the highest energy conformer identified and the global minimum was only 2.0 kcal/mole, a value less than the uncertainty in the calculation (1-3 kcal/mol). Thus, any of the conformers could be the true minimum, but the distinction is effectively a moot point because such differences are insignificant at temperatures 298 K and above. Similarly, transition states between conformers A and B, A and C, and C and D were found to be 1.8, 3.3, and 2.2 kcal/mol, respectively, above the lowest energy conformer connected to the state. These values are consistent with expectations for the internal conformational transitions involved, and considered with the relative energies of the equilibrium states, suggest a "floppy" molecule that will populate each of the stable configurations in a room temperature sample.

The mid-IR spectrum for gas-phase DMAZ at room temperature is shown in Figure 2. Included for comparison are synthetic spectra for the two conformers which yielded the best agreement with the experimental result - A and B. It is observed that individually their spectra reasonably reproduce the experiment. However, a

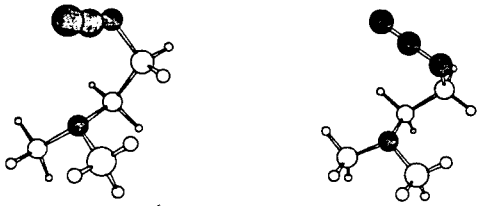


Figure 1. DMAZ conformers A and B.

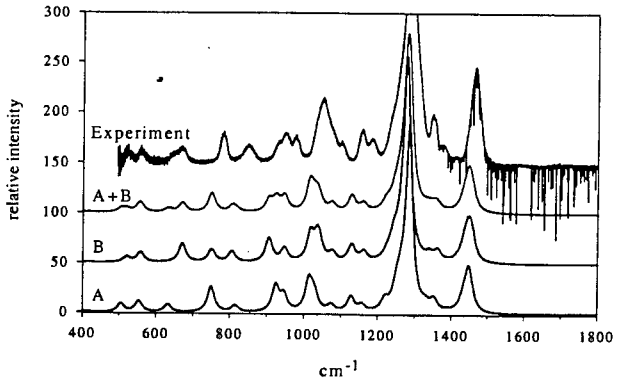


Figure 2. Experimentally acquired mid-IR DMAZ spectrum and synthetic spectra for conformers A and B.

spectrum that combines their contributions reproduces all of the major features, and without producing features that do not exist.

Hypothesizing that proton transfer from nitric acid to the amine nitrogen on DMAZ is the rate-controlling step in the sequence of reactions leading to ignition, the electrostatic potentials of the conformers at van der Waals distances were characterized. Figure 3 compares the electrostatic potentials of DMAZ conformers A and B and hydrazine on an electron isodensity surface of 0.001. The dark regions of the contour plots correspond to lone pair electron sets, and are sites where proton transfer is likely to occur. In hydrazine, the two lone pair sets are nominally oriented in a "semi-cis" configuration. DMAZ has three sets of lone pairs – one on the amine nitrogen, one on the carbon-bonded nitrogen of the azido group, and one on the terminal nitrogen of the azido group. It is observed that conformer B has the (apparently desirable) configuration found in hydrazine while conformer A not only does not have this configuration, the azido group shields the amine nitrogen from the approach of a proton. (All other conformers were found to have essentially isolated lone pair sets.) Thus, the ignition delays obtained with DMAZ might be competitive with (but not quite as fast as) MMH, because conformer B reacts quickly, but its influence is mediated by the population of more slowly reacting conformers. We plan to investigate this matter further through a computational study of the reactions of nitric acid with hydrazine, MMH, UDMH, and DMAZ.

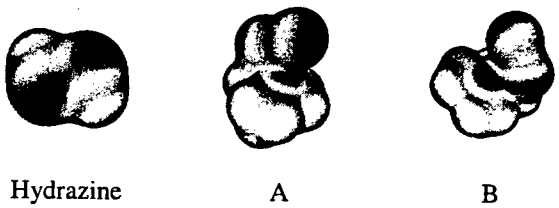


Figure 3. Comparison of the electrostatic potentials of hydrazine and DMAZ conformers A and B.

A NEW APPROACH TO PROPELLANT FORMULATION: MINIMIZING LIFE-CYCLE COSTS THROUGH SCIENCE-BASED DESIGN

Ronald D. Anderson*, Martin S. Miller, Anthony J. Kotlar and Betsy M. Rice
Weapons and Materials Research Directorate
Army Research Laboratory
Aberdeen Proving Ground, MD 21005-5066

Randall J. Cramer
Naval Surface Warfare Center, Indian Head Division

The traditional approach to developing propellants for specific gun applications relies heavily on trial and error. Candidate formulations must be made in small quantities and subjected to burning-rate measurements and small-scale vulnerability assessments. If the properties of these candidates fail to meet expectations, the process must be repeated. This approach, while historically unavoidable, is obviously inefficient in time and expense, but it also can generate considerable waste streams associated with unsuccessful formulations. With added considerations of life-cycle costs including environmental impact at all stages of development, use, and disposal, this traditional approach becomes increasingly unworkable. We propose a new approach that makes maximal use of scientific understanding embodied in models during the early phases of the propellant-development cycle (Miller et al., 2000). This new approach allows for screening of candidate formulations, resulting in the elimination of probable poor performers and the identification of the most promising candidates for further study and testing. Through simple simulations, it is shown that this strategy can have a significant impact on the overall costs of the development process (Miller et al., 2000). In analogy to the DOE program to convert the nuclear-weapon stewardship from testing-based to science-based, we term the new approach "science-based design." It is argued that the modeling contribution to the propellant-development process is most efficiently implemented by subjecting candidate formulations to a hierarchy of models of different sophistication and input-data requirements, reserving the most rigorous models (usually the most data-intensive and least robust) for the most promising candidates. This new approach will require concentration and leveraging of resources toward the most critical early-phase development steps, but it may be the only credible strategy to reconcile the need for higher-performance weapons with the reality of declining resources.

In this presentation, we demonstrate the first phases of the newly-proposed gun propellant formulation process that will minimize life-cycle costs through science-based design (Miller et al., 2000 and Anderson and Rice, 2000). The screening and identification of promising candidate formulations is demonstrated in the study presented here under the assumption of a specific weapon platform and user requirements. The process of selecting a propellant for the assumed gun system application has been distilled into a series of measurable steps leading from a set of candidate materials, through logical and numerical filters, to a shorter list of energetic materials demonstrated as viable choices for the weapon platform. Environmental filtering and performance modeling are used to screen propellants through a well-defined sequence of tests designed to weed out materials not meeting standards in terms of safety, energy, or manufacturability. Because much of the testing is performed by computer modeling, the gun systems and energetic materials need not be present (nor even exist) in order to be described and matched against performance requirements for future applications. The calculations presented here demonstrate that utilizing computer models in the early developmental stages of the formulation process rather than physical testing produces enormous savings in labor, material, and environmental costs, along with a tremendous reduction in the time required to select a "best candidate" propellant.

REFERENCES

Anderson, R. D. and B. M. Rice, "Minimizing Life-Cycle Costs of Gun Propellant Selection through Model-Based Decision Making: A Case Study in Environmental Screening and Performance Testing", Clean Products and Processing, Vol. 2, p. 47 (2000).

Miller, M. S., B. M. Rice, A. J. Kotlar and R. J. Cramer, "A New Approach to Propellant Formulation: Minimizing Life-Cycle Costs through Science-Based Design", Clean Products and Processing, Vol. 2, p. 37 (2000).

THIS PAGE INTENTIONALLY LEFT BLANK

EFFECTS OF PRESSURE AND OXYGEN ON LASER IGNITION OF XM39 PROPELLANT

A. Cohen and R.A. Beyer
U. S. Army Research Laboratory
Aberdeen Proving Ground, MD 21005

INTRODUCTION

The effect of initial pressure on CO_2 laser ignition delays of XM39, an RDX composite propellant, has recently been investigated [Ritchie, et al.] in air. A radiant ignition model which considers global chemical kinetics for the constituents of both condensed and gas phases but neglects possible gas phase oxygen reactions was used to predict ignition delays. In earlier experiments [Cohen, et al.] at 1 atm, the substitution of air for nitrogen did not greatly affect emission delays but did lead to a large increase in initial pressurization rates. Questions exist concerning the pressures at which the kinetics of oxygen reactions need to be considered in modeling XM39 (and RDX) ignition.

An earlier (1980) Russian investigation [Strakovskiy, et al.] of (neat) RDX ignition was done in air at 1 and 5 atm. At low flux densities (less than 100 W/cm^2) ignition (emission) delays decreased monotonically with flux density and were in good agreement with predictions of a condensed phase, radiant ignition model [Vilyunov and Zarko]. The ignition criterion for this model is based on equality between the flux densities due to chemical energy production and irradiation. They concluded that gas phase effects on ignition of RDX (and RDX composites) are not expected to be great, especially at elevated pressure.

This paper presents the results of an investigation of the effect of total pressure and partial oxygen pressure on XM39 emission and pressurization delays and initial pressurization rates during CO_2 laser ignition. Comparison of the measured delays with the phenomenological radiant ignition model is also shown.

EXPERIMENTAL

The experimental techniques have been described previously [Cohen et al.] A 1 liter windowed bomb was used. Pressure was measured with a piezoelectric transducer located at the bottom of the bomb. Emission through one of the glass windows was measured by a photomultiplier (300-800 nm response). The other glass window was used to obtain a video record using a high-speed camera. The videos help interpret the photomultiplier and piezoelectric signals. The cw CO_2 laser beam was focussed by a ZnSe lens on the propellant (flat) surface after passing through the ZnSe window. Average laser power at the sample location was obtained from laser energy measurements and the pulse duration. An "average" flux density (F) was obtained from the power and spot diameter values. The emission (t_e) and pressure (t_p) delays are the times with respect to the start of the laser pulse for signals to rise above noise levels. Pressures were limited to 100 psig. Cylindrical propellant samples (1/8" wide x 1/4" diameter) were cut from solid XM39 strands. The nominal XM39 composition by weight percent is 76 RDX, 4 NC, 12 CAB, 7 ATEC , 0.4 EC.

OBSERVATIONS

Irradiation in the presence of O_2 led to complete consumption of the XM39 samples except for experiments in air, at initial pressures (P)of 15 psi and at the lowest flux density (F=18 cal/cm^2-s). Irradiation in N_2 always led to partial gasification resulting in formation of a crater at the sample surface.

Fig. 1 contains signals from the photomultiplier for experiments in N_2, air (P=115 psi) and a 3:1 O_2:N_2 mixture (P=76 psi) from the experiments in N_2 and the 3:1 O_2:N_2 mixture. The photomultiplier signals in this figure show the effect of (partial) O_2 pressure P_o on initial emission.

The photomultiplier signals in Fig. 2a show the effect of initial pressure with air in the bomb on the emission. The piezoelectric transducer signals in Fig. 2b show the corresponding effect on the pressure increment.

The data in have been plotted in Figures 3 to help show the effects of flux intensity, (partial) O_2 pressure and (total) pressure on initial pressure increments.

Figure 3shows a plot the pressure delay vs. F, for several values of P. In the legend, data labeled (a)-(h) have been recently acquired. Data (k)and (l) are from Ritchie, et al. Data (m) [Cohen and Beyer], (j) and (i) are older data taken with samples obtained from graphite coated, 19 perf XM39 strands. The curve is the phenomenological-model-predicted ignition delay (using the global energy production rate for XM39 determined from DSC measurements [Miller and Kotlar] at atmospheric pressure) for a cw, uniform beam with sample absorption and reflection coefficients of 765 cm^{-1} and 0.08, respectively.

CONCLUSIONS

The sensitivity of emission delays to O_2 decreases with increase in O_2 pressure (P_o) and flux density (F). At flux >87 cal/cm^2-s and P_o >50 psi the sensitivity is minimal. Pressurization rates are sensitive to P_o at $F \leq 130$ cal/cm^2-s. Except for experiments in air at P (psi)=15, R varies inversely with P_o. At present, reasons for this exception are not known. Including chemical kinetic rates of O_2 reactions in radiant ignition models may not be necessary for predicting emission and pressurization delays in high pressure air but may be necessary for predicting pressurization rates. The chemical kinetic mechanism of RDX is better known than that for XM39. Comparison of the effects of pressure and O_2 on pressurization during radiant ignition of RDX in a closed bomb with models which include detailed kinetics mechanisms for both gas and condensed phases may be helpful in evaluating the importance of including O_2 kinetics.

REFERENCES

Cohen A. and Beyer, R.A. *"Laser Ignition of Solid Propellants: I. Ignition Delays,"* ARL-TR-162, July 1993.

Cohen, A., Beyer, R. A., Bilyk S. R. and Newberry J. E., *"Laser Ignition of Solid Propellants: Comparison of Model Predictions with Emission and Pressure Measurements,"* CPIA Publication 593, Vol. 1, p. 123, Oct. 1992.

Miller, M.S., Kotlar, A.J., Cohen, A., Puckett, D.L., and Holmes, H.E., *"Effective Ignition Kinetics for LOVA Propellant,"* BRL Report, MR-3724, 1988.

Ritchie, S.J., Thynell, S. T, and Kuo, K. K., "Modeling and Experiments of Laser-Induced Ignition of Nitramine Propellants," *Journal of Propulsion and Power*, Vol. 13, p.367, May/June 1997.

Strakovskiy , L., Cohen, A., Fifer, R., Beyer, R.A., and Forch B., *"Laser Ignition of Propellants and Explosives,"* ARL-TR-1699, June 1998.

Vilyunov, V. H., and Zarko, V. E., Ignition of Solids, Elsevier, Amsterdam, The Netherlands. 1989.

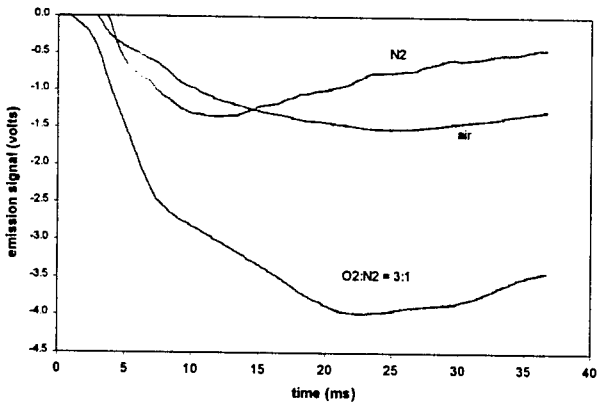


Fig. 1: Experiments at flux = 130 cal/cm^2-sec showing photomultiplier signal.

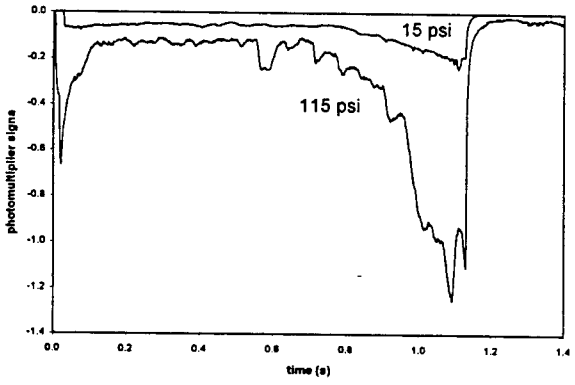


Fig. 2a. Experiments in showing the effect of initial pressure on emission.

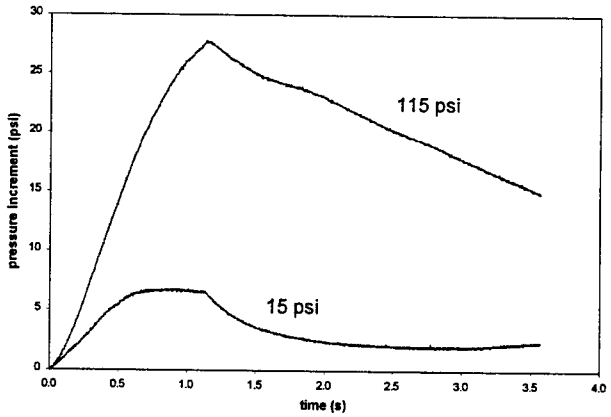


Fig. 2b. Experiments in showing the effect of initial pressure on pressure increment.

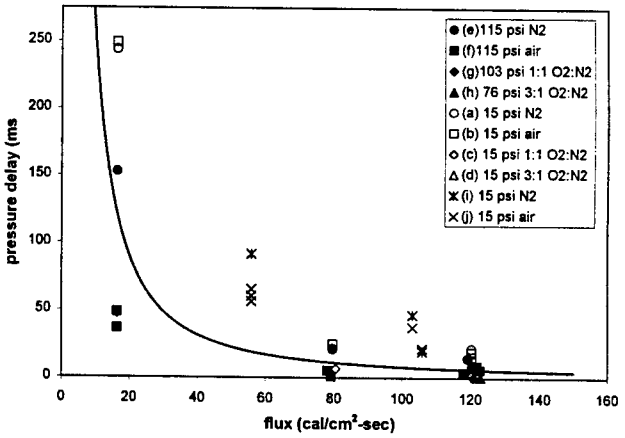


Fig 3. Pressurization delay vs. flux density.

Wave-Rotor Research and Technology for Fuel-Efficient Gas Turbine Engines

Gerard E. Welch
Army Research Laboratory (VTD)
21000 Brookpark Road, M/S 5-10
Cleveland, OH 44135

Introduction

Wave-rotor technology offers the potential to increase the performance levels of gas turbine engines (GTEs) significantly, within the constraints of current material temperature limitations and cooling technology. The wave rotor is self-cooled and aerodynamically compatible with the low corrected flow rates supplied by the core compressors of modern aeropropulsion engines. It can be embedded concentrically within the GTE as a high pressure spool (as shown in Fig. 1) to increase engine overall pressure ratio by 200% and peak temperature by 25 to 30%. Wave-rotor-topped engines are predicted to operate with substantially higher fuel efficiency (*i.e.*, lower specific fuel consumption, SFC) and power to weight-flow ratio (SP, cf. Welch *et al.*, 1997). For example, the impact of adding a wave-rotor-topping unit to an auxiliary power unit (APU) and to a popular helicopter engine is indicated in Table 1. It is evident that the benefits derived by wave rotor topping are significant in these two engine classes.

Table 1. Predicted benefits of wave-rotor-topping cycles in APU and small turboshaft engines (Jones and Welch, 1996 and Snyder and Fish, 1996).

Engine Class	Baseline OPR	SFC* benefit	SP** benefit
APU	4:1	--	+210%
Small turboshaft	8:1	-15 to -22%	+18 to +20%

*Specific fuel consumption (or thrust-SFC) enhancement.
**Ratio of power (or thrust) to mass-flow-rate.

If realized, the potential performance level improvements enabled by the wave-rotor-topping cycle would translate into benefits for both military and civilian sectors. The reduced fuel burn has far reaching implications in terms of fuel economy and the logistics trail of Army missions and, hence, is of strategic importance to the future U.S. Army (Elber *et al.*, 1997). The wave rotor is considered an enabling technology for an alternative path to meet IHPTET III turboshaft engine goals. The lower fuel consumption also translates into reduced emissions which is a driving factor in the evolution of aeropropulsion engines for civilian applications.

The potential performance improvements to be attained by wave-rotor topping have motivated a collaborative research and technology advancement effort by the U.S. Army Research Laboratory (VTD), NASA John H. Glenn Research Center at Lewis Field, and Rolls-Royce Allison. This brief summary introduces wave rotor technology for fuel-efficient GTEs and highlights the elements of the current research effort.

Description of Wave-Rotor-Topping Cycle for Gas Turbine Engines

Component Description

The wave rotor is a machine designed to exchange energy efficiently between gas streams of differing energy density. A tip-shrouded rotor is surrounded by a stationary casing as shown in Fig. 2. The casing endwalls are penetrated by inlet and outlet ducts that port gases of different pressure and temperature to and from the rotor flow-annuli. The rotor hub, tip-shroud, and blade surfaces define rotor passages. Gasdynamic (shock and expansion) waves are initiated as the rotor passages open and close to the ported flows in a timed sequence set by the rotor speed and azimuthal location and extent of the ports. These waves compress and expand the gas as they propagate through the rotor passages. Various gasdynamic wave cycles can be effected by the purposed tangential placement of the various ported flows.

The four-port wave rotor shown in Fig. 2 accomplishes the compression and expansion processes of a high-pressure spool (gas generator) in a single, self-cooled component. It is integrated concentrically within the GTE, between the high-pressure compressor and the high-pressure turbine (cf. Fig. 1). Fresh air discharged from the compressor enters the wave rotor through the low-pressure inlet port. This air is compressed in the wave rotor and is then discharged to an external burner where it is heated to the peak cycle temperature. The heated gas reenters the wave rotor where it is expanded and then discharged to the downstream high-pressure turbine. The turbine entry temperature (equal to that of the untopped baseline engine) is typically 25 to 30% lower than the burner exhaust temperature. The total pressure of the gas delivered to the turbine (*i.e.*, the low-pressure exhaust-port

discharge) is typically 15 to 20% higher than air delivered by the compressor. This is in contrast to the turbine entry pressure of the untopped engine that is lower than the compressor discharge pressure by the loss incurred in the burner *(e.g.*, 5%). The higher availability at the turbine inlet translates directly into increased engine power and efficiency (*e.g.*, see Table 1).

Enabling Features

The wave rotor component is compatible with the high temperature, high pressure conditions of the GTE topping cycle application, within current material temperature limitations, because of several key features:

- *Self-cooling* enables high temperature operation.
- *Compatibility with low corrected flows* assures efficient operation at high engine pressure ratios.
- *Compactness* allows integration with gas generator.
- *Low rotative speed* allows shrouding of rotor.
- *Free-spinning, load-following, concentric installation* obviates need for transmission to other spools.
- *Gasdynamic pressure exchange* enables rapid transient response.
- *Dynamic characteristic* stabilizes engine.

These important enabling features are discussed in detail in the full-length paper.

Technical Challenges

A formidable set of technical challenges balance these enabling features: leakage flows between the rotor and casing endwalls, noise associated with gasdynamic waves emitted into the ports, high cycle fatigue of both the rotor blades (due to unsteady loading) and the downstream blade rows (due to potential interactions), ducting and associated thermal and mechanical loads, and the need for the wave rotor to supply high-pressure-turbine cooling air in some engine applications. The technical challenges are being identified and addressed in a step-wise manner through the systematic research program at NASA GRC.

ARL/NASA Wave-Rotor Research Effort

The wave rotor has been a subject of research at NASA GRC since 1990. The purpose of the effort—conducted collaboratively by the U.S. Army Research Laboratory, NASA Glenn Research Center, and Rolls-Royce Allison—is to develop the tools and knowledge base necessary to develop and demonstrate a wave-rotor-topped GTE. Elements of the current research effort—computational tools development, experimental studies, system studies, a step-wise effort to a planned demonstration of a wave-rotor-topped turboshaft engine, and advanced component studies—are described in detail in the full-length paper. Particular attention is given to the planned demonstrator engine—a wave-rotor-topped Rolls-Royce Allison Model 250 turboshaft (see Welch *et al*, 1999). The wave-rotor-topping unit increases the engine overall pressure ratio from 8:1 to 23:1 and peak temperature by 30%. These substantial changes to the popular helicopter engine lead to predicted SFC reductions of 15 to 20% with concomitant specific power increases of 18 to 20%.

References

Elber, W., Bill, R., Johnson, L., Mann, D., Scully, M., Peyran, R., Baker, G., Ragsdale, L., Franke, H., Musa, L., McGauley, D., Ziegler, D., 1997, "Fuel-Efficient Army After Next, March.

Jones, S. M. and Welch, G. E., 1996, "Performance Benefits for Wave-Rotor-Topped Gas Turbine Engines," ASME-96-GT-075, June; also NASA/TM-1996-107193 and ARL-TR-1065, March.

Snyder, P. H. and Fish, R. E., 1996, "Assessment of a Wave Rotor Topped Demonstrator Gas Turbine Engine Concept," ASME-86-GT-41, June.

Welch, G. E., Jones, S. M., and Paxson, D. E., 1997, "Wave-Rotor-Enhanced Gas Turbine Engines," *J. Engineering for Gas Turbines and Power*, **119**, No. 2, April, pp. 469-477.

Welch, G. E., Paxson, D. E., Wilson, J., Snyder, P. H., 1999, "Wave-Rotor-Enhanced Gas Turbine Engine Demonstrator," *Proc. Gas turbine operation and technology for land, sea, air propulsion and power systems symposium*, NATO/RTO, Oct.; also NASA/TM-1999-209459 and ARL-TR-2113, Oct.

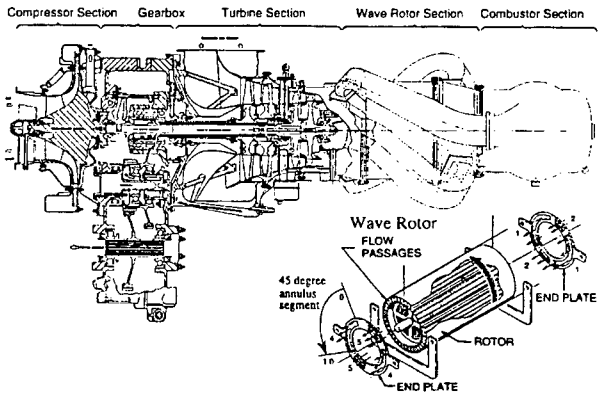


Figure 1. Preliminary layout of wave-rotor-topped Rolls-Royce Allison Model 250 engine (Snyder and Fish, 1996).

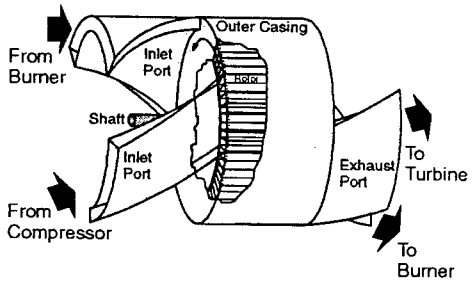


Figure 2. Four-port wave-rotor schematic diagram.

SIMULATIONS OF DYNAMIC BEHAVIOR OF SOLID EXPLOSIVES

Betsy M. Rice*
U. S. Army Research Laboratory
AMSRL-WM-BD
Aberdeen Proving Ground, MD 21005

Dan C. Sorescu and Donald L. Thompson
Department of Chemistry
Oklahoma State University
Stillwater, Oklahoma 74078

The work presented herein describes an extensive assessment of a model used to study dynamic processes in a wide variety of solid explosives. The original intent was to develop a model to study non-reactive processes in the nitramine explosive RDX (1,3,5-hexahydro-1,3,5,-*s*-triazine) (Sorescu et al., 1997). The potential that was developed consisted of atom-atom (6-exp) Buckingham potential terms plus electrostatic interactions. The Coulombic interactions were determined through fitting atom-centered partial charges to a quantum-mechanically determined electrostatic potential for a single RDX molecule whose structure corresponded to that in the crystal at ambient conditions. The remaining Buckingham parameters were adjusted to reproduce the experimental structure of the RDX crystal at ambient conditions. We found that this interaction potential could also describe the geometric parameters and lattice energies of different polymorphic phases of two other nitramine crystals: the polycyclic nitramine 2,4,6,8,10,12-Hexanitrohexaazaisowurtzitane (HNIW, or CL-20) (Sorescu et al., 1998a) and the monocyclic nitramine Octahydro-1,3,5,7-Tetranitro-1,3,5,7-tetraazacyclooctane (HMX) (Sorescu et al. 1998b) Isothermal-isobaric molecular dynamics (NPT-MD) simulations for these crystals predicted cell parameters within a few percent of experimental values, and little translational or rotational disorder of the molecules. Further investigations to explore the limits of transferability of this interaction potential to other energetic molecular crystals were undertaken through performing molecular packing (MP) calculations for 30 nitramine crystals. These included several types of mono- and polycyclic nitramines, particularly crystals of importance in energetic materials (Sorescu et al. 1998c) For most of the crystals, the predicted structural lattice parameters obtained from molecular packing (MP) calculations differ by less than 2% from the experimental structures, with small rotations and practically no translations of the molecules in the asymmetric unit cell. A further assessment on the limits of transferability of the interaction potential was accomplished through molecular packing calculations of 51 crystals containing non-nitramine molecules with functional groups common to energetic materials (Sorescu et al., 1999a) MP calculations using this interaction potential reproduced the crystal structures to within 5% of experiment for these 51 non-nitramine systems, including the explosives pentaerythritol tetranitrate (PETN), nitromethane, 2,4,6-trinitrotoluene (TNT) and several nitrocubane derivatives.

More recently we have analyzed the dynamics of the important energetic crystals RDX, HMX, HNIW and PETN under hydrostatic compression conditions using NPT-MD simulations and this intermolecular potential (Sorescu et al., 199b). In that study we found that the predicted lattice parameters for the RDX, HMX and HNIW crystals are in good agreement with experimental values over the entire range of pressures investigated experimentally. For the PETN crystal, the calculated crystallographic parameters were in acceptable agreement with experimental data for pressures up to 5 GPa. For higher pressures, the disagreements of predictions and experiment were attributed to the inadequacy of the rigid-body approximation (i.e. molecules are not allow to deform) in the simulations of floppy molecules such as PETN.

The validity of the rigid molecule approximation was assumed in our previous studies (Sorescu et al., 1997, 1998a, 1998b, 1998c, 1999a, 1999b). As indicated by our results, this model has been very successful in its ability to describe the equilibrium structures of a variety of organic molecular crystals under ambient conditions and with moderate increases in pressure and temperature. However, the physical and chemical processes of energetic materials that are of most interest occur within the regime of high pressures and temperatures, a regime in which conformational molecular changes become important. Consequently, further developments of the interaction potential are necessary to describe more realistically the intramolecular motion, molecular deformations and the energy flow inside these crystals. For this purpose, we have eliminated the previously used rigid-molecule approximation and extended the current intermolecular potential to include a full intramolecular potential for use in simulations of energetic materials. Particularly, in this work we consider the prototypical explosive, nitromethane.

Nitromethane was selected for our first attempt at developing a fully flexible model of an energetic molecular crystal since numerous experimental investigations of its properties under a wide range of conditions have been performed, thus providing many data for use in assessing the model potential (Sorescu et al., 2000). A particularly sensitive test of this intermolecular interaction is found in its ability to reproduce dynamics associated with the internal rotation of the methyl group in the crystal. The internal rotation of the methyl group in the crystal has received significant attention, since experimental evidence indicates that this motion is almost completely governed by intermolecular interactions. Temperature dependence of the degree of libration of this motion has been measured, as has the activation barrier to this rotation. Also, the influence of pressure on the internal rotational motion of the methyl group has also been examined, and x-ray diffraction measurements indicate a rotational reorientation of the methyl group at 3.5 GPa. The ensemble of the experimental data provides many metrics against which to assess the performance of our interaction potential by molecular dynamics simulations.

Molecular simulations using a fully-flexible model for the description of solid nitromethane were performed for temperatures ranging from 4.2 to 250 K at 1 atm, and at pressures ranging from 0.3 to 7 GPa at room temperature. The analyses performed using constant pressure and temperature molecular dynamics simulations indicate that the proposed potential model is able to accurately reproduce the changes of the structural crystallographic parameters as functions of temperature and pressure for the entire range of values investigated. In addition, the calculated bulk modulus of nitromethane was found in excellent agreement with the corresponding experimental results. Moreover, it was determined that the present potential correctly predicts an experimentally-observed 45° change in methyl group orientation in the high pressure regime relative to the low-temperature configuration. The analysis of the linear expansion coefficients and linear compression data indicate anisotropic behavior for the unit cell edges. Finally, the dynamics of the methyl group motion has been qualitatively reproduced; our calculations predict that the activation barrier to methyl group rotation is 387 cal/mol, in good agreement with reported activation energies (234-576 cal/mol). Additionally, the magnitudes of the methyl group librations are in excellent agreement with the measured values over the temperature range 25-125 K. The successes of this model in describing the explosive nitromethane, coupled with the performances of the model to describe a large number of important energetic materials, provide further incentive to continue developing the model to study more sophisticated dynamical events, such as energy transfer and chemical reactions in the condensed phase.

REFERENCES

Sorescu, D. C., B. M. Rice and D. L. Thompson, "Intermolecular Potential for the Hexahydro-1,3,5-trinitro-1,3,5-s-triazine Crystal (RDX): A Crystal Packing, Monte Carlo and Molecular Dynamics Study", Journal of Physical Chemistry B, Vol. 101, 798 (1997).

Sorescu, D. C., B. M. Rice and D. L. Thompson, "Molecular Packing and NPT-Molecular Dynamics Investigation of the Transferability of the RDX Intermolecular Potential to 2,4,6,8,10,12-Hexanitrohexaazaisowurtzitane", Journal of Physical Chemistry B, Vol. 102, 948 (1998).

Sorescu, D. C., B. M. Rice and D. L. Thompson, "Isothermal-Isobaric Molecular Dynamics Simulations of 1,3,5,7-Tetranitro-1,3,5,7-tetraazacyclooctane (HMX) Crystals", Journal of Physical Chemistry B, Vol. 102, 6692 (1998).

Sorescu , D. C., B. M. Rice and D. L. Thompson, "A Transferable Intermolecular Potential for Nitramine Crystals", Journal of Physical Chemistry A, Vol. 102, 8386 (1998).

Sorescu, D. C., B. M. Rice and D. L. Thompson, "Molecular Packing and Molecular Dynamics Study of the Transferability of a Generalized Nitramine Intermolecular Potential to Non-Nitramine Crystals", Journal of Physical Chemistry A Vol. 103, 989 (1999).

Sorescu, D. C., B. M. Rice and D. L. Thompson, "Theoretical Studies of the Hydrostatic Compression of RDX, HMX, HNIW and PETN Crystals", Journal of Physical Chemistry, Vol 103, 6783 (1999).

Sorescu, D. C., B. M. Rice and D. L. Thompson, "Theoretical Studies of the Solid Nitromethane", Journal of Physical Chemistry, Vol 104, 8406 (2000).

IMPROVED SELF-RECIRCULATING CASING TREATMENT CONCEPT FOR ENHANCED COMPRESSOR PERFORMANCE

Michael D. Hathaway*
Vehicle Technology Directorate
U.S. Army Research Laboratory
Cleveland, OH

SUMMARY

The current state-of-the-art in casing treatment designs utilizes the compressor static pressure rise to provide for a recirculation of end wall fluid from the rear to the front of a compressor rotor (through a path contained within the compressor casing). Due to the rotor work input the recirculated fluid is delivered at high relative total pressure, thus energizing the low momentum fluid in the compressor endwall which contributes to compressor stall range limitations. This advanced self-recirculating casing treatment concept has provided the greatest stall range capability with the least decrement to compressor efficiency of any previous casing treatment concept, however, it still results in an efficiency penalty.

The genesis of the research reported herein was based on: 1) Recognition that there is still room for improvement in casing treatment design, 2) State-of-the-art computational fluid dynamic analysis codes are capable of providing reasonably accurate predictions of compressor rotor end-wall flow fields, and 3) Improved understanding of the compressor end wall flow phenomena which limit compressor stall range will lead to improved casing treatment designs. As such, the goal of this research program was to develop an improved casing treatment concept based on a "first principals" understanding, as derived from state-of-the-art CFD, of end wall flow phenomena which limit stall range.

To achieve this goal a state-of-the-art CFD code (APNASA) was employed in a computationally based parametric investigation of the impact of casing suction and injection on the stability and performance of a low speed fan rotor wherein the stalling massflow was controlled by tip flow field breakdown. The parametric investigation was guided by observed trends in end wall flow characteristics as stall is approached, and based on the hypothesis that application of suction or blowing can mitigate these trends. The best suction and injection configurations were then combined to yield a self-recirculating casing treatment concept which improves on existing recirculating casing treatment designs. The results of this parametric investigation yielded: 1) identification of the fluid mechanisms which precipitate stall of tip critical blade rows, and 2) an approach to recirculated casing treatment design which produces benefits in both compressor stall range and efficiency. Subsequent application of this approach to a high speed transonic rotor successfully yielded similar improvements in stall range with no loss in compressor efficiency. These successful results are of significant interest to military and commercial gas turbine engine users because of the great potential for improved fuel efficiency and gas turbine engine performance, along with greater reliability through enhanced stall range.

THIS PAGE INTENTIONALLY LEFT BLANK

Session D
Biomedical and Behavioral Sciences

Chair
Dr. Albert T. McManus
U.S. Army Institute for Surgical Research

Co-Chair
Dr. Michael D. Drillings
U.S. Army Research Institute

Keynote Address
LTC Robert M. Harris
U.S. Army Medical Research and Materiel Command

THIS PAGE INTENTIONALLY LEFT BLANK

CONCEPTUAL SKILLS AND ADAPTABLE LEADERS

Jon J. Fallesen
U.S. Army Research Institute for the Behavioral and Social Sciences
Fort Leavenworth Research Unit

As the US Army looks ahead to retain its critical position in national security and protection of democratic principles around the world, many speculate that Army Leaders will come under increased demands to apply their ingenuity in the face of novel and complex situations. The research reported here surveys the conceptual skills of Army Leaders to better understand what characteristics adaptable leaders need for the emerging geopolitical environment. A framework of factors is presented that are believed to influence the decision-making abilities of Army officers. The framework is based on work from the ARI research program on developing future commanders.

Officer characteristics surveyed included problem solving approaches and strategies, attitudes associated with critical and creative thinking, beliefs about learning and knowledge, self-insight, and conceptual thinking skills. Situational factors include situation familiarity, problem importance, available time, and a trade-off of effort and accuracy. This research did not directly address technical and direct level leadership, such as troop leading procedures, rather its focus was on the conceptual thinking components required of leaders when there is no immediately known solution to a problem or no clear-cut best option when faced with an opportunity.

Striving for authenticity in task requirements poses a challenge for cognitive research. If an experimenter can observe Army leaders in action and be able to remain inconspicuous during the process, there is much of importance that still will not be capture-able. Some sacrifice in realism allows more insight into how participants think and what factors influence that. The basic paradigm that was used in this research involved having a participant exhibit performance on complex problems. Two tactical vignettes were developed which required the participant to play the role of a Task Force Battalion Commander or an Infantry Company Commander. A short one-page text description was given along with an overhead sketch map of the situation. The participants were asked to look at the situation and tell what they would do as the Commander in the situation. In some research, participants did this in a verbal mode reporting their thoughts to the experimenter and other times in a written mode, writing out their understanding and plans. In the verbal mode, a participant started the session by reporting on a critical problem-solving incident from their own experience. Researchers collected information on characteristics, skills, and performance. Not all measures were collected in all studies. Collection on these factors used a variety of techniques including standard psychological instruments, observation, questionnaires, think-aloud protocols, and self-ratings. Information was collected through a series of experiments.

Experiment 1. Problem solving approaches, strategies, and stituational perceptions. The findings on forty-two company and field grade officers showed that 95 percent of the time they did not follow a concurrent option generation principle recommended by doctrine. Even though they did not follow the doctrine on this point, there was no comparative loss in performance. Under familiar conditions, they used a recognitional approach, and in unfamiliar situations they used a dominant structuring approach most often. This result was surprising because few people realize what dominance structuring is. When people explore an option by determining if it can be made to dominate other options, then they are using dominance structuring. People who followed an adaptable solution rated the importance of 'consideration of the relevancy of information' more highly.

Experiment 2. Assessment of cognitive skill-based training. Armed with the finding that consideration of information relevancy differentiated among solutions, training was created to support this natural-based strategy. There was no difference between two groups on a pre-test measure, but the thirty-one trained personnel used relevancy checking significantly more often and rated it more importantly after only 30 to 40 minutes of training. For situations of low familiarity, trained participants also rated 'looking for flaws' and 'chose the option that was most attractive' as more important. Experiment 2 showed that explicit methods of instruction based on naturally-identified cognitive skills was useful for learning beyond the typical call for more time for study or rote practice. Also the skill that made a difference was focused on the level of quality of thinking more than on specific procedures or techniques.

Experiment 3. Relation of conceptual abilities and leadership characteristics. This research departed from the method used in experiments one and two. This was conducted within the Command and General Staff College's annual Prairie Warrior exercise. Participants served in different command and staff positions (rather

than as an individual role playing a commander in the same situation). Measures of performance centered around behavioral ratings of sixty-five field grade officers' performance on discerning critical information. Characteristics that had no relationship to performance included a measure of conceptual complexity, achievement motivation, dominant leadership, peer leadership, cognitive complexity, need for approval, and treating others as objects. Task motivation had a significant positive relationship with performance, while openness had a significant negative relationship with performance. When the effects of several descriptive and attitudinal variables were removed the negative correlation between openness and discernment became more negative. Conceptual complexity did not relate to anything else when a similar control was used and were concluded to be problematic in its current form.

A series of stepwise multiple regressions showed that half of the variance in discernment performance was predicted by two leadership variables, three style variables, and two situational variables. The variables and/or direction of relationship were unexpected in many cases and reflect that the nature of performance for discerning critical information centered on a convergent, patterned response strategy and not one of divergence and elaboration.

Experiment 4. Critical thinking skills, dispositions, and creativity. Three sets of characteristic data were looked at in terms of their relationship to visualization performance. The performance task was similar to the role playing vignettes from experiments one and two (and five) but used a humanitarian relief setting. Seventy-eight field grade officers reported their visualization of the situation and their course of action. Critical thinking dispositions (truthful, open minded, analytical, systems thinking, self-confidence, inquisitive, maturity) collectively correlated with critical thinking skills (analysis, evaluate, inference). But there were no significant correlations among dispositions and either creativity or visualization performance, nor among skills and either creativity or visualization, nor between creativity and visualization. This experiment demonstrated the importance of attitudes toward critical thinking and the need for a more precise criterion measure.

Experiment 5. Relationship of epistemic beliefs and problem solving approaches and strategies. Epistemic beliefs relate to one's views about knowledge and learning. Beliefs can be ordered from naïve to sophisticated beliefs. For example, believing that knowledge comes from authority figures is a naïve belief. More sophisticated beliefs correlated significantly with higher importance of specific critical thinking strategies such as problem framing, consideration of information quality, and re-examination of options. Ninety-two officers below the rank of Colonel worked on the same vignettes as experiments one and two and filled out questionnaires on beliefs and strategies. Self-assessment of performance correlated significantly with the belief that the ability to learn is not innate. These results showed that one's broad perspective on knowledge and learning influenced the type of process strategies that they use to think. More sophisticated views of knowledge and learning related to higher importance of critical thinking. Also participants who were more confident about their performance held more sophisticated beliefs about learning.

Experiment 6. Conceptual thinking skills. Officers under the rank of Colonel were surveyed and interviewed to derive a set of conceptual thinking skills, their relative importance for future leaders, and examples based on their personal experiences. Three survey protocols were used to reach fifty-five officers. The participants rated six skills as extremely important: situation understanding, mental wargaming and simulation, battlefield visualization, self-understanding, information assimilation, and discriminating relevant cues. Three additional skills were rated as moderately to extremely important: question asking, finding hidden assumptions, and decentering.

Together the findings show the richness and complexity of relationships between performance on different applied leader conceptual tasks and the effects of situational, skill, and attitudinal characteristics. While for some tasks and under some conditions relationships came out one way, for other tasks under other conditions relationships came out another. In one sense these differences suggest that leaders demonstrated different degrees of adaptability to the situation and to the tasks. From another perspective, the unexpected relationships illustrate the careful look that research needs to take at process, product, environmental, and individual variables. The practical implication of these results show (1) importance of conceptual skills, (2) trainability of general cognitive strategies, (3) relationship reversals under different task conditions, (4) importance of attitudes and beliefs on which conceptual skills are used and how, and (5) importance of self-insight and self-regulation to manage adaptation.

TRAINING FOR DIGITAL PROFICIENCY

Brooke Schaab* and J. Douglas Dressel
U.S. Army Research Institute for the Behavioral and Social Sciences
Advanced Training Methods Research Unit

Easy access to large volumes of digital information coupled with smaller units involved in novel situations will result in minute-to-minute decisions being shifted down to the mid- and junior-level digital soldier. In order to improve the 21st century soldier's ability to respond appropriately, the Army needs to train its digital soldiers at all levels in "how to think" in a more flexible and adaptive manner.

This effort describes the results of training research being conducted by the U.S. Army Research Institute for the Behavioral and Social Sciences (ARI) to enhance operations in digital environments. The need for flexible and adaptable task performance will occur more frequently in the future as soldiers encounter novel situations that differ from the conditions under which the trainee learned the tasks. The novel situation could be created by a variety of factors including: a change of hardware, a new software "drop," or a new area of task application.

The U. S. Army Intelligence Center (USAIC) at Fort Huachuca, AZ with assistance from ARI, investigated exploratory learning for junior level soldiers and digital system users. At USAIC, junior enlisted soldiers receive 16 weeks advanced individual training to become intelligence analysts (military occupational specialty [MOS] 96B10). Upon completion of USAIC training, 96Bs are assigned to a variety of staff sections from battalion through corps. As part of this training, they receive seven days of training to learn how to operate a remote workstation (RWS). The RWS is a computer system that receives digital information, allows it to be manipulated and projects it on a computer screen. It is linked to the All Source Analysis System (ASAS), which is an integrated computer system used to help process and disseminate intelligence.

In a traditional training environment, the instructor uses classroom lectures to explain to the 96Bs what they need to accomplish with the RWS and why it's important. After the instructor lectures about the tasks, the 96Bs practice the skills on practical exercises (PEs). This very detailed and time-honored approach tells each 96B the necessary knowledge and information to perform the tasks. The focus is on the instructor delivering a set program of material about how to operate the RWS. Young soldiers are taught the basics of operating the equipment, but this training may or may not have been linked to the other tasks they must perform to take advantage of the system's functionally.

This experiment compared an alternative training approach (exploratory or discovery learning) to the traditional approach. Briefly, in the traditional approach, the instructor gives the students all the information they need in a lecture and will typically demonstrate the task. The students then will individually perform PEs which require hands-on performance of the task's components or complete task. During the PE, the instructor will assist and answer students' questions. Following the PE, the instructor will discuss the answers with the class. In the discovery/exploratory learning approach employed here, the instructor gave only minimal and basic instructions. The students worked in small groups on a series of PEs that stressed problem solving to accomplish all the required tasks, including the most complex and difficult tasks. The PEs built upon one another and prior learning in the course. The soldiers were encouraged to work in small teams and find innovative ways to use and manipulate the data. When one part of the practical exercise was completed, the students debriefed the instructor, then were allowed to move forward at their own pace. No training time was added to the program of instruction. Rather, the training time already blocked out for traditional instruction was dedicated to the same material using exploratory or discovery learning. The responsibility for learning the material was shifted from being centered on the instructor to being centered on the student.

As with traditional learning, the role of the instructor remains a critical link in student-centered learning. After basic information is delivered, the instructor circulates throughout the training facility to coach, suggest, and provide insights about how to address difficulties that arise during the practical exercise. Thus, the role of the instructor is enhanced. The instructor must be a subject matter expert as well as an excellent coach and mentor. By combining subject matter knowledge with positive coaching techniques, the instructor is able to shape and enhance performance dramatically. The instructor has the difficult task of facilitating the learning experience. Traditionally, the instructor would easily answer questions and provide solutions to the soldiers receiving the training. That technique, however, prevents the soldiers from gaining the experience needed to learn and solve problems on their own. Consequently, in the exploratory learning method, the instructor has to be

skilled in the use of behaviors that assist soldiers to learn on their own. For example, when a soldier has difficulty framing a problem regarding the danger posed by the enemy, the instructor coaches the student to think through the problem. The instructor may respond by saying: "It sounds to me as if you're trying to determine what enemy assets pose the greatest threat to your unit. What are some of the things you look for to determine threat?" This type of coaching helps the student clarify the problem and gather information to solve it.

Research by ARI indicates that as 96Bs completed the practical exercises, there was a strengthening of the connection between the training and how it's applied in the unit. Additionally, initial results on a novel PE indicated that the 96Bs who received RWS instruction using exploratory learning achieved up to 20 percent more accurate performance (assessed by tasks correctly performed) than students who were taught using the traditional method. The practical exercises improved motivation because they were structured to place the training in a real world context. Because the 96Bs were encouraged to work with one another, they developed a sense of team collaboration as they defined and solved problems. This encouraged self-learning, teamwork, and an improved memory for the skills that were being developed. The consequence should be 96Bs who can better adapt and transfer their trained skills to the myriad of situations they will face in unit assignments. This then becomes a building block for how to apply technology from basic intelligence staff functions to staff operations in the field.

Student comments indicated very positive reaction to exploratory learning. Responses indicated that exploratory learning challenged them and generated strong motivation to learn. By teaming with other 96Bs, the students thought they learned and retained much more information.

Exploratory or discovery learning may not be the most advantageous learning method in every environment and MOS. However, it almost seems mandatory for any MOS that operates in changing digital environments or requires exchanging ideas, justifications, information, data, and specifications to confirm or refute conclusions. There will be an ever-increasing number of MOSs that require these skills in the Army's transition and the fielding of digital systems. It is true already for 96Bs who must consider different perspectives and who must understand, clarify, elaborate, evaluate, explain, and defend knowledge.

DEVELOPMENT OF MEDICAL COUNTERMEASURES TO SULFUR MUSTARD VESICATION

W. J. Smith*, M. C. Babin
US Army Medical Research Institute of Chemical Defense
Aberdeen Proving Ground, MD 21010-5400

R. C. Kiser, R. P. Casillas
Battelle Memorial Institute
Medical Research and Evaluation Facility
Columbus, OH 43201-2693

ABSTRACT

Sulfur mustard (HD) is an alkylating agent with cytotoxic, mutagenic and vesicating properties. Its use on the battlefield results in debilitating injuries to skin, eyes and the respiratory system (Papirmeister et al., 1991; Smith and Dunn, 1991). To elucidate the toxic sequelae that follow cutaneous exposure to HD, the United States Army Medical Research Institute of Chemical Defense (USAMRICD) has undertaken a broad based research program encompassing both intramural and extramural research. This report summarizes our current understanding of the toxicology of human exposure to HD based on *in vitro* and *in vivo* experimental models.

1. INTRODUCTION

While many of the toxic manifestations that follow HD exposure have been defined, the actual mechanisms of pathology remain elusive. Much of the research in this area has been conducted in the Pharmacology and Drug Assessment Divisions of USAMRICD, the laboratories of our NATO allies and laboratories funded through the Medical Research and Materiel Command extramural contract program. Based on the technological database developed, through this program, we have been able to generate a unifying hypothesis for cellular and tissue events that is critical to explaining the formation of cutaneous blisters following exposure to HD. Studies of individual toxic events, such as alkylation of cellular macromolecules, formation of DNA strand breaks, activation of poly(ADP-ribose) polymerase (PARP), disruption of calcium regulation, proteolytic activation and tissue inflammation, have led to the formulation of six strategies for therapeutic intervention (Smith et al., 1996, 1999). The proposed pharmaceutical strategies are intracellular scavengers, DNA cell cycle modulators, PARP inhibitors, calcium modulators, protease inhibitors and anti-inflammatory compounds.

Compounds in each of these classes are currently being evaluated as medical countermeasures against HD dermatotoxicity. We have validated four *in vitro* testing modules for compound screening: solubility, direct toxicity, protection against HD-induced cytotoxicity and protection against HD-induced depletion of cellular nicotinamide adenine dinucleotide (NAD+) levels. Two additional *in vitro* modules, preservation of cellular adenosine triphosphate (ATP) levels and inhibition of proteolysis, are in the final stages of validation. For *in vivo* screening, we have validated and utilized the mouse ear inflammation assay with associated histopathological evaluation (Casillas et al., 1997) and cutaneous vapor exposure in hairless guinea pigs (Yourick et al. 1991). For systemic drug therapy, we are validating a hairless mouse cutaneous vapor exposure model.

2. EXPERIMENTAL DESIGN

2.1 Decision Tree Network (DTN)

A DTN has been devised to guide the selection process used to evaluate candidate pretreatment or treatment compounds. This DTN consists of pathways through *in vitro* and *in vivo* compound screening modules based on the developed hypothesis and known characteristics of the compounds being evaluated.

2.1a *In Vitro* Screening Modules

As compounds are placed in the Drug Assessment

Compound Tracking System, they are assigned to specific functional categories. Based on their categorization, they are evaluated through a series of validated assays such as aqueous solubility, direct cytotoxicity in human lymphocytes (PBL), protection of PBL against the cytotoxicity of HD, depletion of metabolic factors (NAD+ or ATP), and inhibition of HD-induced proteolysis. Results from these assays are used to prioritize movement of candidate compounds into the *in vivo* screening modules.

2.1b *In Vivo* Screening Modules

Compounds passing the *in vitro* modules or compounds from classes not applicable to *in vitro* screening (i.e., anti-inflammatory compounds) are tested in the Mouse Ear Vesicant Model (MEVM) for edema and histopathologic (i.e., epidermal-dermal separation and epidermal necrosis) evaluation. Other *in vivo* assays available for additional testing as required include cutaneous HD vapor exposure in the hairless guinea pig or the domestic swine and cutaneous HD vapor and liquid exposures in the hairless mouse. These modules usually employ topical treatment with candidate compounds but new modules are being designed to assess systemic treatment regimes.

3. RESULTS

Over 500 candidate prophylactic or therapeutic compounds have been evaluated in either the *in vitro* or *in vivo* antivesicant screening program. Sixty-two compounds have proven capable of providing significant modulation of edema and/or histopathology caused by HD *in vivo*. Of these 62 compounds, nineteen have demonstrated at least 50 % protection against the pathological indicators of mustard injury.

4. CONCLUSIONS

This research is directed at meeting the Medical Chemical Defense Technology Objective (DTO) *Medical Countermeasures Against Vesicant Agents*. Based on results to date, we have met every milestone of the DTO, i.e., "to develop a technological database and define therapeutic strategies that protect against the vesicant injury," and "demonstrate efficacy in an animal model." Having identified at least 19 compounds that are capable of protecting against the *in vivo* pathology of HD, we now have the means to move from the research phase of pharmaceutical investigation into the Concept Exploration phase of drug development. This work, the combined efforts of Army, academic, industrial and contracted research laboratories, has set the stage for development of a fielded medical countermeasure against HD. For the first time, since HD's introduction onto the battlefield more than 80 years ago, we have the true potential of protecting our warfighters against this insidious weapon through pharmacological therapy.

REFERENCES

Casillas, RP, Mitcheltree, LW and Stemler, FW. "The Mouse Ear Model of Cutaneous Sulfur Mustard Injury." *Toxicology Methods*, Vol. 7. pp. 381-397, 1997.

Papirmeister, B, Feister, AJ, Robinson, SI and Ford, RD. *Medical Defense Against Mustard Gas: Toxic Mechanisms and Pharmacological Implications*, CRC Press, Boca Raton, FL 1991.

Smith, WJ and Dunn, MA. "Medical Defense Against Blistering Chemical Warfare Agents," *Arch Dermatol*, Vol 127, pp. 1207-1213, 1991.

Smith, WJ, Martens, ME, Gross, CL, Clark, OE and Cowan, FC. "Therapeutic Approaches to Cutaneous Injury by Sulfur mustard," *Proceedings of the 20th Army Science Conference*. Vol 2, pp. 699-703, 1996.

Smith, WJ, Martens, ME, Gross, CL, Clark, OE, Cowan, FC and Yourick, JJ, "The Use of In Vitro Systems to Define Therapeutic Approaches to Cutaneous Injury by Sulfur Mustard." In *Toxicity Assessment Alternatives: Methods, Issues, Opportunities*, Salem & Katz, eds. Humana Press, Totowa, NJ, pp. 205-212, 1999.

Yourick, JJ, Clark, CR and Mitcheltree, L. "Niacinamide Pretreatment Reduces Microvesicle Formation in Hairless Guinea Pigs Cutaneously Exposed to Sulfur Mustard." *Fundam Appl Toxicol* Vol. 17, pp. 533-542, 1991.

CONTROL OF NERVE AGENT-INDUCED SEIZURES IS CRITICAL FOR NEUROPROTECTION AND SURVIVAL

T.-M. Shih, S.M. Duniho, and J. H. McDonough*

Pharmacology and Comparative Medicine Divisions
U.S. Army Medical Research Institute of Chemical Defense
Aberdeen Proving Ground, MD 21010-5400 USA

The effectiveness of some anticholinergics (atropine, biperiden or trihexyphenidyl) and benzodiazepines (diazepam or midazolam) as an anticonvulsant treatment against seizures induced by six nerve agents (tabun, sarin, soman, GF, VR and VX) were studied in a guinea pig model that closely approximates the use of pretreatment and therapy drugs used as medical countermeasures for nerve agent exposure. All animals were deeply anesthetized and implanted with cortical electrodes for electroencephalographic (EEG) recording. On the day of exposure the animals were pretreated with pyridostigmine (0.026 mg/kg, IM) 30 min prior to challenge with 2 x LD_{50} dose (SC) of a given agent. In separate experiments animals were challenged with 5 x LD_{50} (SC) of soman. One min after agent challenge the animals were treated (IM) with 2 mg/kg atropine SO_4 admixed with 25 mg/kg 2-PAM Cl, and the EEG was observed for seizure onset. Five min after the start of EEG seizures, animals were treated IM with different doses of anticholinergics or benzodiazepines and observed for seizure termination. The time to seizure onset, the time to seizure termination, and 24-hr lethality were recorded. The anticonvulsant ED_{50} of each drug for termination of seizures induced by each agent was calculated and compared. Brain tissue from animals that survived 24 hrs was examined for pathology. With equal toxic doses (2 x LD_{50}) of the agents, continuous EEG seizures (*status epilepticus)* developed in all animals challenged with soman and in more than 90% of the animals challenged with VR, GF, tabun or sarin; only 54% of the animals challenged with VX developed seizures. All drugs were capable of terminating seizure activity: trihexyphenidyl and midazolam were significantly more potent than biperiden against 5 of the 6 agents, and these three drugs were significantly more potent than either atropine or diazepam, which had similar potencies against each agent. The dose of a given drug that was an effective anticonvulsant against a 2 x LD_{50} challenge of soman was equally effective against seizures induced by a 5 x LD_{50} challenge. All nerve agents were capable of producing neuropathology. Regardless of treatment, control of seizure was strongly associated with protection against acute lethality and brain pathology, while failure to stop seizures was associated with increased acute lethality and more frequent and severe brain pathology. These results suggest that all nerve agents produce EEG seizures via a common mechanism and can be controlled by anticholinergic or benzodiazepine anticonvulsant treatment. While control of seizures was known to protect against brain pathology, the relationship between seizure control and the acute lethal effects of these agents appears to have been previously underappreciated. Effective anticonvulsant treatment of a nerve agent casualty is, therefore, critical to immediate and long-term recovery.

THIS PAGE INTENTIONALLY LEFT BLANK

EXPERIMENTAL DUPLICATION OF AN UNCONTROLLED HEMORRHAGE IN SWINE BY A COMPUTER-DRIVEN FEEDBACK CONTROL SYSTEM

Michael A. Dubick*, Jill L. Sondeen, Guy A. Drew, Victor A. Convertino
U.S. Army Institute of Surgical Research, San Antonio, TX 78234-6315.

1. Introduction

Acute hemorrhage accounts for about 50% of the deaths on the battlefield and the forward operating table; a statistic that has remained relatively unchanged since World War I. In addition, hemorrhage is the primary cause of death in about 30% of the injured soldiers who die from wounds. Current dogma dictates that early, adequate fluid resuscitation is crucial to reduce the mortality and morbidity associated with hemorrhagic shock, yet logistic contraints preclude the availability of large volumes of fluid in the far-forward combat arena to successfully stabilize the injured soldier. In addition this practice has recently come under question in the presence of continuing hemorrhage, advocating that resuscitation be tailored to the needs of each casualty. To address these issues, a large body of literature on hemorrhage has accumulated to evaluate various resuscitation regimens that may be applicable to treating casualties in the far-forward combat environment. These studies have employed many different animal models in a variety of animal species, but large variation in reproducibility and hemodynamic responses to bleeding, has raised doubt about the application of results from such hemorrhage models to clinical practice.

Current models of hemorrhage fall into 2 general categories: controlled hemorrhage or uncontrolled hemorrhage. Controlled hemorrhage models have generally been of two types where the animal is either bled to a fixed blood pressure, or a fixed volume of blood is removed. The greatest advantage of this model is its reproducibility across a number of species. However, none of these models rely on the animal's physiologic mechanisms to stop the bleeding and therefore, may fail to truly simulate hemorrhagic hypotension seen in trauma victims.

Most recently, a number of investigators have developed animal models of uncontrolled hemorrhage by inducing an arterial or solid organ injury or simply cutting a rat's tail. Models of uncontrolled hemorrhage have been claimed to be more clinically relevant in that only the animal's physiologic responses (hemostatic mechanisms) can interfere with the progression of the hemorrhage. In addition, the uncontrolled hemorrhage model incorporates some degree of tissue trauma, but in many cases there can be much variability in the degree of bleeding.

Preliminary results from our laboratory and others suggest that there may be more fundamental physiologic differences between controlled and uncontrolled hemorrhage. For example, we have observed that in a fixed pressure model of hemorrhage in swine, a mean arterial pressure (MAP) of 30-35 mmHg can be attained with a blood loss of about 30 ml/kg. In contrast, utilizing an uncontrolled hemorrhage model, we have observed a blood pressure fall to below 30 mmHg with a blood loss of only about 20 ml/kg, and with higher mortality compared to our controlled hemorrhage studies. Similar levels of blood loss were also observed after a grade V liver injury in untreated rats and pigs. However, these studies were not matched for the rate of hemorrhage nor blood volume loss to be more directly comparable. Nevertheless, taken together these studies suggest that the additional afferent or nociceptor inputs associated with tissue injury may contribute to the increased susceptibility of animals to an uncontrolled compared to a controlled hemorrhage. Since experimental investigations into fluid resuscitation protocols employ animal models of controlled or uncontrolled hemorrhage, and fluid resuscitation is generally tied to the volume of blood loss, the need arises to appreciate more completely the hemodynamic and metabolic differences between these models when they are matched for blood volume loss or change in blood pressure profiles in response to blood loss. In addition, data from these animal studies are often applied to artificial intelligence systems designed to treat future warfighters. Thus, it is important to determine systematically whether these types of hemorrhage models differ in response to the same volume or blood pressure stimulus in the absence or presence of a vascular (tissue) injury. Such studies will lead to more rational therapeutic approaches to restore tissue perfusion and limit volume requirements of the injured soldier.

2. Materials and Methods

To understand more fully the relationship between blood loss and blood pressure in uncontrolled vs controlled hemorrhage, we have designed unique methodologies and are currently conducting the following experiments. Immature, female Yorkshire pigs (40 kg) were anesthetized, splenectomized and chronically instrumented with arterial and venous catheters. An ultrasonic flow probe was placed around the ascending aorta to monitor cardiac output. Animals were assigned to one of four groups:: 1) Uncontrolled

hemorrhage, 2) Controlled hemorrhage matched to the blood pressure profile curve over time of the uncontrolled hemorrhage animal, 3) Controlled hemorrhage matched to the blood volume loss profile over time of the uncontrolled hemorrhage animal, and 4) controlled hemorrhage where the same total blood volume in groups 1 and 3 is removed, but over a 45 min period in accordance to our standard control hemorrhage model. An uncontrolled hemorrhage was induced by making a hole in the infrarenal aorta with a 1.5 or 2 mm skin biopsy punch. The total blood loss was captured via a suctioning system placed in the abdominal cavity and recorded over time. Animals were monitored for 3 hr after the start of hemorrhage or until death. Each uncontrolled hemorrhage experiment was followed by 3 controlled hemorrhage studies, where blood was removed from the infrarenal aorta via a catheter inserted through the iliac artery. In the comparison between groups 1 and 2, total blood volume loss was the primary endpoint, while in the comparison between groups 1 and 3, the mean arterial pressure was the primary endpoint. The primary endpoints in the comparison between groups 1 and 4 and groups 3 and 4 were the rate of bleeding and mean arterial pressure. In addition, secondary hemodynamic endpoints such as heart rate, cardiac index, ECG and total peripheral resistance and metabolic endpoints such as lactate, base excess, end tidal PCO_2, arterial and venous blood gases, pH and urine output, and hemoglobin and hematocrit, as part of the complete blood cell count, were also measured. In addition, survival through the 3 hr experimental period was recorded.

The key to the success of this study is the ability to develop the computer program to regulate the rate of hemorrhage by the mechanical pump to mimic the rate of hemorrhage profiles. Experimental duplication of an uncontrolled hemorrhage was accomplished with a computer-interfaced Masterflex peristaltic rotary infusion pump and custom LabVIEW software. At ten-second intervals, the mass (grams) of total blood loss induced by uncontrolled hemorrhage for group 1 was weighed on a balance with simultaneous measurements of MAP. These data were introduced into the computer data file so that profiles of accumulated blood volume (ml) and flow rates (ml/min) could be calculated and plotted. The resulting software program was designed to duplicate and standardize uncontrolled hemorrhage according to the size (weight) of each animal, i.e., mmHg (group 2) and ml/kg (group 3). The program activates the pump at the adjusted bleeding rate and accurately changes the bleeding rate every ten seconds to match the hemorrhage profile (group 3). The length of time for the simulated uncontrolled hemorrhage (groups 2 and 3) was determined by the profile of the actual uncontrolled hemorrhage recording (group 1). Mass and volume of blood loss, and bleeding rates are digitally displayed on the computer monitor, providing real-time status and hemorrhage profile confirmation. Upon reaching the predetermined endpoint for total blood loss volume, the program automatically inactivates the pump.

To accomplish the group 2 hemorrhage profile, the pump control software was integrated with our data acquisition system to provide servo feedback control of MAP. The software program was developed in an identical manner to that used for the group 3 hemorrhage profile except that the feedback signal tracks MAP rather than blood volume loss.

In the hemorrhage profile for group 4, the software program activates the pump at four predetermined constant rates of hemorrhage. This procedure provides a smooth, linear 45-minute hemorrhage profile with an endpoint total blood volume equal to the group 1 total hemorrhage volume.

3. Results and Discussion

In our initial experiments we compared sets of animals in groups 1,3 and 4 bled either 8.5 or 16.2 ml/kg. These results indicate that we have developed a computer program that can duplicate the blood loss response of an uncontrolled hemorrhage in swine, yet retain the reproducibility of controlled hemorrhage models. The system is flexible to adjust for confounding factors and offers us a new technique in our efforts to evaluate novel resuscitation fluids and treatment strategies for the stabilization of combat casualties.

COGNITIVE WORKLOAD AND TASK PERFORMANCE FOR INDIRECT VISION DRIVING WITH FIXED FLAT PANEL DISPLAYS

Christopher C. Smyth
U.S. Army Research Laboratory
Human Research & Engineering Directorate
Aberdeen Proving Ground, MD

ABSTRACT

Cognitive workload and task performances are modeled for indirect vision driving with fixed flat panel displays. The model is derived from the results of a field study in which eight participants negotiated a driving course in a military vehicle with natural and indirect vision. The model considers the effects of scene compression upon the information needs of the driver in a self-paced task. Concurrently, a task analysis mental workload model is derived for indirect vision driving.

1. INTRODUCTION

The Army needs combat vehicles that are smaller, lighter, more lethal, survivable, and more mobile to support a rapidly deployable force. Combined with the need to assimilate and distribute more information to, from, and within the vehicle as the Army moves toward a digital battlefield, there is the need for an increase in vehicle and C4I systems integration and performance. Consequently, the Army will need sophisticated, highly integrated crew stations for these future combat vehicles.

To satisfy the Army requirements, designers of future armored combat vehicles will place the crew stations deep within the hull of the vehicle. The conventional optics, consisting of periscopic vision blocks and optical sights, will be replaced by electronic displays at the crew stations and external vehicle-mounted sensors. These vision systems will most likely show computerized digital images that are captured from camera arrays on the vehicle. The crew member will see a selected portion of the computerized display buffer that depends upon his or her role and viewing direction. The display design may use a set of panel-mounted displays, either cathode ray tube (CRT) or flat panel liquid crystal displays (LCD), which are fixed in a panoramic arrangement about the crew member's station.

One area of interest is the effect of the choice of camera field of view (FOV) upon crew performance for panoramic panel displays. The choice of camera FOV may depend upon the task being performed. This would be the case for a driver operating a tank with a visual display and camera array in place of direct vision from an open hatch or through vision blocks. The driver may prefer a unity view for driving along a known route to increase his perception of potential road hazards. On the other hand, the driver may prefer a compressed image at road turns for route selection because of the wider scene. Of course, the increase in camera FOV without a commensurate increase in display FOV will cause a compression of the camera scene as seen in the displays and a loss of detail. Because of the need to determine design parameters for future vehicles, the U.S. Army Automotive Research Development and Engineering Center (TARDEC) asked the Human Research and Engineering Directorate of the U.S. Army Research Laboratory (ARL) to conduct an experiment on the effects of camera FOV upon driving performance.

In support of this request, ARL conducted a field study of the ability of soldiers to drive a military vehicle with an external vehicle-mounted camera array and panel-mounted video displays as a function of the camera's FOV. Further, ARL investigated the effects of indirect vision driving upon the mental workload measures of attention allocation and perceived workload, situational awareness, induced motion sickness, subjective stress, and the cognitive abilities. The results were compared to direct vision driving as representative of a perfect "see-through armor" vision system. This paper reports the status of the task performance and mental workload models that were derived from the results of the experiment. To provide background information for the modeling effort, the experimental methodology and results are briefly reviewed.

2. EXPERIMENTAL METHODOLOGY

For the indirect vision driving, three fixed flat panel, liquid crystal displays (LCD) were mounted side by side in the front of the cab of a high mobility multipurpose, wheeled vehicle (HMMWV). The displays received video returns from a forward viewing camera array that was mounted on the front roof of the vehicle and tilted slightly downward. The displays provided a panoramic 110° view of the camera returns. Three different sets of camera lenses were used to provide a near unity (150°), wide (205°), and extended (257°) camera FOV. Unity

FOV matches direct viewing in scene resolution. Eight military male volunteers served as participants in this study. They drove the experimental vehicle over a 590-meter driving course which consists of S-curves, berms, and straight-aways, marked by 48 pairs of barrels.

Questionnaires used in this study were (1) attention allocation loading factors, (2) the NASA Task Loading Index (TLX) workload battery, (3) Kennedy's subjective estimation of motion sickness, (4) Selcon nd Taylor's Situation Awareness Rating Technique (SART), and (5) the Subjective Stress Scale. Also applied was a cognitive performance battery test involving addition, logic, spatial rotation, word recall, and map planning.

3. RESULTS

The participants drove the course 25% faster and made a nominal 0.5% fewer lane marker strikes with natural vision than they did with the indirect vision systems. Further, the course speed significantly decreased with increased camera's FOV, while the number of lane marker strikes increased slightly. Workload ratings show a significant increase in perceived workload with indirect vision, while a test of situational awareness shows an increase in the demand component. Most participants reported discomfort associated with motion sickness while in the moving vehicle with the displays. The estimated subjective stress rating of the drivers was least for natural vision and increased with indirect FOV. While the course speed decreased with increasing FOV, the speed of travel was perceived as increased because of the scene compression. In a comparison of the camera's FOV, the driving performance is fastest with the near unity FOV. However, cognitive processing tests show a trend for improved spatial rotation and map planning following the wide FOV trial. The wide FOV was intentionally selected by the researchers to provide a balance of the resolution needed for obstacle avoidance and scene perspective for course following. Finally, the participants rated the near unity as more useful for steering; however, the wider FOVs were preferred for navigation since they allow the driver to see farther for path selection.

4. DISCUSSION

Considering that the driving task is self paced, with the driver adjusting his speed to acquire the scene-related information needed for control decisions, an equation was derived relating the average vehicle speed to the display compression ratio. The equation predicts that the average driving speed is greatest for the direct viewing and decreases with increasing compression. A statistical analysis shows that the equation constants are within the 90% joint confidence intervals for the parameters of an experimental equation derived from the data for the course times. The display compression ratio is the ratio of the camera FOV to that of the display.

A mental workload simulation model is developed using task analysis and an information processing flow network. The simulation is used to model the increase in perceived workload and the demand on situational awareness that occur with indirect vision driving. These workload increases are caused by an increase in mental and temporal demands on the cognitive facilities of the human driver. In turn, these are caused by the physical differences between the natural viewing and indirect vision with the decreased resolution of the displays, lack of stereooptics, and the change in apparent viewpoint with the camera array mounted over the center of the vehicle.

As well as considering the load on the cognitive facilities, the simulation incorporates the effects of motion sickness. Here, at the screen resolution and update rate used in this study, LCDs induced symptoms of motion sickness and increased subjective stress. As well as vestibular system conflicts attributable to differences between the visual scene and head movements, another source of motion sickness may be a loss of convergence accommodation. This loss may be induced by temporal motion blurring of the video display during rapid changes in the scene such as occur during road turns and passages over berms.

The mental workload model was programmed for indirect vision driving with the IMPRINT task analysis simulation program using an SRK (skills-rules-knowledge) human information processing network and the workload data. The total psychological workload predicted by the model is in agreement with the test results. The model is based on a correlation analysis for the workload measures, which produces three significant clusters. One cluster is formed by the correlation of the visual attention loading with those of the cognition and motor. Another cluster is formed from the mental, physical, and temporal workload demands, the workload performance, and the complexity and variability of the situational awareness demand. Finally, the third is formed from the stress, motion sickness symptoms, and frustration.

5. CONCLUSION

The course speeds for indirect vision driving are successfully predicted as a function of the camera's FOV by a mathematical model.

The total mental workload for indirect vision driving was predicted with the IMPRINT task analysis workload (TAWL) simulation program. The simulation uses an SRK model of information processing to describe the driving task.

MISSON REHEARSAL IN VIRTUAL PLACES

Bob G. Witmer*
U. S. Army Research Institute for the Behavioral and Social Sciences
12350 Research Parkway Orlando, FL. 32826-3276

Wallace J. Sadowski
University of Central Florida
12350 Research Parkway Orlando, FL. 32826-3276

Neal M. Finkelstein
U. S. Army Simulation, Training, & Instrumentation Command
12350 Research Parkway Orlando, FL. 32826-3276

In rehearsing specific missions, soldiers frequently must learn about spaces to which they have no direct access. Virtual Environments (VE) representing those spaces can be constructed and used to rehearse the missions, but how do we ensure their effectiveness? Previous research (Witmer, Bailey, Knerr, & Parsons, 1996) showed that route knowledge acquired in a virtual model of a building transferred to the real world, but real world training produced more accurate route learning than VE training. And while route knowledge was readily acquired in a VE, configuration knowledge (distance and direction to locations not in the line-of-sight) was not. Spatial learning in the VE was hampered not only by disorientation resulting from a narrow field-of-view (FOV) and multiple collisions with walls, but also by participants' inability to accurately estimate distances in VEs. Armed with knowledge that some VE characteristics not consistent with real environments hamper configuration learning, we conducted research to determine if certain unique capabilities of VEs could compensate for its deficiencies. Our research goal was to increase the training effectiveness of VEs by further decreasing their resemblance (or similarity) to real world environments. This approach is contrary to the common sense approach that requires the VE to be as similar as possible to the real world. We developed three VE navigation training aids: local and global orientation cues, aerial views, and division of the VE into distinctive themed quadrants. The aids were not provided when testing configuration knowledge.

A computer model of one floor of a large office building used previously was adapted for this experiment. All passageways in the virtual building were widened to reduce collisions, an improved collision detection algorithm was introduced that further decreased the number of collisions, and additional rooms were modeled. Separate VE models were constructed to represent the standard and enhanced environments. The standard environment model portrayed one floor of a typical office building. The enhanced environment model was created by adding theme objects and sounds to the standard environment model. Participants viewed the VE models using a Helmet-Mounted Display. Locomotion through the VE was achieved by tracking body movements while walking in place. Head and body movements were independently tracked.

The participants were 64 young adults who had no previous exposure to the building. The participants were randomly assigned to one of eight training groups. Depending on group assignment, a participant trained using either the standard or enhanced VE, received orientation cues or did not, and could chose to view the VE from an aerial perspective, or was restricted to the normal perspective view. Orientation cues included an arrow projecting from the chest of the participant's avatar and a flagpole centered in the building layout and visible throughout the environment.

Aerial perspective groups could select viewing heights of 49, 98, and 394 feet for periods up to one minute. After one minute, participants automatically returned to the normal perspective view. At 394 feet, but not at 49 or 98 feet, participants could see the entire VE layout simultaneously. While flying, participants could further explore the environment by moving horizontally to other aerial viewing positions. Pressing a button on their hand controller allowed participants to gradually descend to ground level and reenter their virtual body at the exact location where they left it when they started to fly.

The orientation cue groups were asked to relate their current position to their starting position marked by a virtual flagpole. This was accomplished by facing the flagpole upon reaching each destination. The flagpole served as a global orientation cue that allowed participants to continually update their current position based on a known starting position. Participants were told

to use the arrow projecting from the chest of their avatar as an indication of their current heading and as a way of aligning their virtual body so as to avoid collisions with walls and doorways.

The enhanced environment model was divided into four themed quadrants or districts. Groups exposed to the themed environment encountered a theme object at each destination and an associated sound that became louder as the destination was approached. It was expected that the inclusion of theme objects would increase recall of particular destinations and their locations within the building. Upon encountering a theme object in one of the destination rooms, participants were asked to identify the theme represented by that object. This encouraged participants to associate destination rooms with their location in a particular quadrant.

Individual training and testing phases comprised the research. During the first training phase, participants followed a virtual tour guide through the VE, pausing at each destination room and identifying it by name. The tour guide and the participant were both represented by avatars. The tour guide verbally described the 'non-theme related' distinguishing features of each destination. In the second training phase, participants explored the VE, while trying to locate and identify each previously visited destination. In the final training phase, participants tried to find the shortest route from the lobby to each named destination. If the participants did not find the destination within three minutes, they were verbally guided to it. Knowledge of the building configuration was tested by having participants complete the following tasks: (1) take the shortest route between designated rooms, (2) estimate the distance and direction to locations not in the line-of-sight, and (3) place room cutouts of destinations in their correct locations on a map. Participants estimated direction by rotating their bodies to face the perceived target location, and distance by blindly walking the straight-line distance between their current location and the perceived target location. Navigation aids were not provided during these tests. A follow-up room placement test was given one week after the initial test to examine retention of building configuration knowledge.

The purpose of the navigation aids was to offset the effects of VE deficiencies that interfere with the acquisition of configuration knowledge. The orientation cues had no significant effects on configuration knowledge acquisition. Participants receiving the enhanced environment performed better during training than those who received the standard environment, but not on configuration knowledge tests. Only the participants with an aerial view during training performed better both during training and on the configuration knowledge tests. Participants with an aerial view during training also performed better on the 1-week retention test.

The effectiveness of the navigation aids, including an aerial perspective, depended on how the participants used the aids. When the aids were used as a crutch to quickly find a room, they were not effective. Similarly in those cases where the use of multiple navigation aids increased the workload beyond what the participants could handle, no performance gains were realized. The navigation aids seemed to work best when participants were able to use them to mentally structure the environment.

The type of VE enhancements employed in this research would be impractical or impossible to implement in an existing real-world building. A bird's-eye view of interior spaces requires removing the ceiling, as does the inclusion of a virtual flagpole. The local orientation device, while possible in the real world, is not needed there because real world collisions are rare. The themed quadrants that were superimposed on the basic VE would be extremely difficult to implement in the real world, even if practical considerations did not completely rule out such disruptive alterations of the real environment. While these enhancements decrease training realism by reducing the fidelity of the VE, they also provide information that participants can use to structure the VE for increased memorability and recall of the layout.

This research has shown that configuration knowledge can be acquired in a relatively complex VE in an efficient manner without relying on external training aids (e.g., paper maps, written directions). Furthermore, this knowledge can be retained over a one-week period with negligible retention loss. This is especially important for mission rehearsal, where knowledge of enemy areas or facilities needs to be retained for the period of time between mission rehearsal and mission execution. Navigation aids can improve spatial knowledge acquisition, but the manner in which they are used determines their effectiveness. Trainers must ensure that soldiers use the navigation aids to structure and organize the VE to improve acquisition and retention. Trainers may also need to limit the number of aids available at any given time to preclude information overload and allow the soldiers to derive maximum benefit from the aids.

REFERENCES

Witmer, B. G., Bailey, J. H., Knerr, B. W., & Parsons, K. C, "Virtual spaces and real world places: Transfer of route knowledge," *International Journal of Human Computer Studies*, Vol. 45, pp. 413-428, 1996.

RIFLE SHOOTING ACCURACY DURING RECOVERY FROM FATIGUING EXERCISE

Max A. Ito, Marilyn A. Sharp, Richard F. Johnson, Donna J. Merullo, Robert P. Mello
U.S. Army Research Institute of Environmental Medicine
Natick, MA 01760-5007

1. INTRODUCTION

The effects of treadmill exercise on shooting accuracy during exercise recovery were evaluated in a 2-phase repeated measures design study. The purpose was to determine the level of shooting accuracy immediately following exercise, and to examine the relationship between exercise intensity and shooting accuracy during recovery following exercise.

Past studies have shown that there are significant increases in energy cost from prolonged load carriage efforts (Patton et al. 1991), and that decrements in shooting accuracy occur following a maximal effort load carry march (Knapik et al. 1991) and after strenuous aerobic exercise in biathlon skiing (Hoffman et al. 1992). However, the shooting test start time was not always carefully controlled for or was delayed beyond the immediate recovery period. The shooting start times in some of those studies varied from less than 5 minutes to more than 12 minutes post exercise. This study focused on the immediate recovery period, or the first 13 minutes after exercise termination.

2. MILITARY RELEVANCE

Soldiers on a tactical march must immediately and effectively engage the enemy upon contact. This study evaluated the laboratory simulation of exhausted soldiers engaging the enemy with rifle fire immediately after a tactical march. It also assessed how exercise type (load carriage and running) and intensity level affect shooting accuracy under such conditions.

3. TEST PROCEDURES

Twelve active duty soldier volunteers, nine men (22.5 $\pm$ 5.7 yrs) and three women (21.0 $\pm$ 4.4 yrs.), were randomly subjected to two types of treadmill exercise until voluntary exhaustion: (1) marching at 3.0 mph in their BDU's with full combat gear and loaded ALICE backpack, and (2) running on a treadmill while dressed in T-shirts, shorts, and running shoes. Each exercise type had 3 randomly assigned exercise intensities for a total of 6 exercise conditions: running at 70%, 80%, and 90% of VO2max, and marching while carrying a 23.3kg, 35.2kg, and 48.8kg load.

Pre- and post-exercise shooting accuracy were assessed by means of the Rapid Firing Test (RFT) conducted on a Weaponeer M16 Marksmanship Simulator assuming a standing foxhole, sandbag-supported firing position. The RFT consists of shooting at a series of 6 sets of 12 pop-up targets randomly introduced for 2 seconds each at simulated distances of 175m and 300m. The first RFT series started immediately after exercise and the sixth series ended within 13 minutes post exercise.

4. RESULTS

Running and load carriage exercises each had a significant effect on shooting accuracy immediately following exercise. When broken down by exercise type, the number of hits dropped from a mean of 7.3 $\pm$1.4 to 5.4 $\pm$1.3 for running [$F(5,55)=4.7$, $p<0.05$], and from 8.5 $\pm$1.7 to 6.8 $\pm$2.1 for load carriage [$F(5,55)=4.6$, $p<0.05$] conditions. Most volunteers terminated the backpack exercise before the maximum time limit with the medium and heavy loads due to shoulder, neck, and/or back discomfort. Shooting accuracy generally returned to pre-exercise levels by the second RFT (at 1.5 minutes post exercise). The percent of shots within a shot group grid was another measure of shooting performance. The percent of shots within a shot group grid for the 175m target dropped from 75.5 $\pm$12.0% to 69.9 $\pm$10.0% for both running and load carriage combined [$F(5,55)=3.73$ $p<.05$] and for the 300m target dropped from 49 $\pm$14.7%

to 43.1 $\pm$12.8%, [$F(5,55)=4.6$, $p=<.05$] for all running intensities.

Physiological recovery was measured by heart rate (HR). As expected, HR change was most rapid for all exercises during the first and second RFT's, corresponding with the significant improvement in the number of hits by the second RFT. As an example, the 90% VO2max trial had a mean change from 164 to 126 bpm between the first and second RFT or a 24% decrease, while the rate of change was less than 10% for the third set, less than 3% for the forth set and less than 2% for the fifth.

5. DISCUSSION

The results clearly indicate that fit soldiers can recover from physical exhaustion and return to optimal shooting performance very quickly. However, fatigue from load carriage and other strenuous tasks in the operational environment will continue to be a problem that confronts the soldier. Proper military task training and physical conditioning remain as answers to this venerable and age old problem of warriors.

The data may also add to the Soldier Biological Chemical Command's Integrated Unit Simulation System (IUSS) Model database. The IUSS is a computer simulation model that simulates a soldier's performance on the virtual battlefield. It was developed to assist equipment and materiel developers in developing the most effective equipment for the soldier by analyzing proposed equipment's effects on soldier performance. Controllable factors include environment (weather, night), physical state (fatigue, load, terrain effects), battlefield threats, and the materiel or equipment being tested on the virtual soldier. IUSS has already provided combat effectiveness analyses of selected Land Warrior capabilities and body armor design optimization. The database will provide future soldier performance simulation models that will directly impact the development of soldier systems for the Interim and Objective Force, Military Operations in Urban Terrain (MOUT), and beyond.

6. CONCLUSION

The study results show that fit soldiers can rapidly recover shooting accuracy following exhaustion from intense exercise. Human performance researchers should consider the quick post-exercise recovery response when assessing exercise-induced changes in psychomotor performance, such as rifle shooting. Any measurement of shooting accuracy should commence immediately or within 30 seconds post exercise. Commanders may be assured by the findings that soldiers can provide accurate and lethal fire in an engagement with the enemy soon after completing an exhausting tactical road march.

REFERENCES

Hoffman M.D., Street GM. Biathlon shooting performance after exercise of different intensities, *International Journal of Sports Medicine*, 13, 270-273, 1992.

Knapik J.J., Staab M.S., Bahrke M., Reynolds K. Vogel J., O'Conner J. Soldier performance and mood states following a strenuous road march, *Military Medicine*, 156, 197-200, 1991.

Patton J.F., Kazuba J., Mello R.P., Reynolds K.L. Physiological and perceptual responses to prolonged treadmill load carriage, *European Journal of Applied Physiology*, 63, 89-93, 1991.

Sutherland D.M., Short P., Frey M. Designing the soldier system on the virtual battlefield, *The Warrior*, August 1996.

ORGANIZATIONAL COMMITMENT AND MILITARY READINESS

Paul A. Gade* and Ronald Tiggle
U.S. Army Research Institute
Alexandria, VA 22333-5600

Walter Schumm
Kansas State University
Manhattan, KS 66506-1403

As we transform to the objective force soldiers must be more committed than ever to the Army and its full spectrum of missions. But what does it mean to be a committed soldier? Generally when we say we want a committed soldier, we mean a soldier who is strongly attached to the Army as an organization and to his or her unit as part of that organization. We want committed soldiers and families because we expect committed soldiers to perform their work better, be more likely to stay in the Army, and be good citizens of their organizations.

Past research shows that organizational commitment can be measured reliably using scaled items in a questionnaire, and such measures can be related to important outcomes, such as performance and retention, in civilian organizations. Meyer and Allen (1997) have developed three sub-scales to assess different types of organizational commitment; those scales have demonstrated fairly consistent factor structure in a variety of civilian settings. Meyer and Allen define organizational commitment as a combination of three component processes: *affective commitment*, *continuance commitment*, and *normative commitment*. Affective commitment is the *want to* of commitment. It represents a soldier's or a spouse's emotional attachment to, or identification with, the Army or the unit. Continuance commitment is the *need to* aspect of commitment. For example, a soldier or spouse feels the need to continue in the Army because it would be hard to find another job or because he or she has too many years invested in the Army to leave it behind. Normative commitment is the *ought to* of commitment. This represents a soldier's or a spouse's felt obligation to remain with the organization; the soldier or spouse may see the Army as a moral obligation or "calling," not merely a job. In summary, organizational commitment can be viewed as a composite measure of various types of motives to remain with and perform for an organization.

Military researchers have largely ignored the work of Meyer and Allen and others, preferring instead to use ad hoc, atheoretical measures of commitment. The purpose of the research reported here was to assess the factor structure and reliability of organizational commitment scales, adapted from Meyer and Allen, in a variety of military settings and to demonstrate the utility of these measures for predicting outcomes important to the Army. Our research focused on affective and continuance commitment, excluding normative commitment. We did this because current measures differentiate affective from continuance commitment very well, but normative commitment overlaps considerably with affective commitment, making it difficult to distinguish from affective commitment even with sophisticated statistical techniques.

Two samples of reserve and active component soldiers, one sample of military spouses, and a large sample of active component soldiers were used to explore the factor structure and internal consistency of measures of affective and continuance commitment adapted for administration to military personnel. In the fall of 1994, the Meyer and Allen scales of affective (8 items) and continuance (7 items) commitment were modified to measure military organizational commitment and administered to a battalion of 510 reserve and active duty soldiers at Fort Bragg, NC. The scales were imbedded in a written questionnaire dealing with various issues as the battalion prepared for Multinational Force and Observers (MFO) duty in the Sinai. An exploratory factor analysis of these data yielded the two expected factors of affective and continuance commitment. Each scale was reliable yielding a Cronbach's alpha of .75 and .88, respectively, for the affective and continuance commitment scales. In order to develop shorter scales that could be more easily incorporated in to a variety of questionnaires, we selected four items from each scale based on the size of their factor scores. These abbreviated scales yielded alphas of .86 and .84, respectively, for affective and continuous commitment.

In January 1997, we again administered the abbreviated commitment scales as part of a larger, telephone questionnaire to a sample of 289 soldiers from the battalion that had been given the survey in the fall of 1994. In addition, 90 spouses of these soldiers were administered a modified form of the abbreviated

commitment scales as part of a larger, telephone questionnaire about their experiences during their spouses' deployment to the Sinai. A confirmatory factor analysis of the soldier data yielded an adjusted goodness of fit index of .94, indicating that the two-factor structure of affective and continuance commitment was quite strong. The spouse data yielded similar results, but the adjusted goodness of fit index of .83 was below the .90 level usually required to confirm a particular factor structure. The failure of a solid confirmation of the spouse factor analysis probably is due to the small sample size, since the unadjusted index of fit was .91. It seems likely that spouses exhibit affective and continuance commitment to the military that is very similar to that of their husbands.

Since both the exploratory and confirmatory factor analyses were performed on essentially the same soldiers in our first two analyses, we tested the generalizability of these results by administering the abbreviated affective and continuance commitment scale items to 7,955 soldiers as part of the fall 1997 administration of the Sample Survey of Military Personnel (SSMP). The SSMP is an attitude and opinion survey administered to a random sample of Army personnel twice each year, spring and fall. A confirmatory factor analysis of these data again yielded two strong factors of affective and continuance commitment with an adjusted goodness of fit index of .95. Cronbach's alpha for affective and continuance commitment were .89 and .86, respectively, indicating strong internal consistency within each scale. Taken together, these results show that affective and continuance commitment can be reliably measured with our abbreviated scales across a variety of Army samples and delivery media.

If commitment measures are to be useful to the Army they must be reliable indicators of outcomes important to the Army. Meyer and Allen and others hypothesize that affective and continuance commitment should affect retention, performance, citizenship behavior, and perhaps well being. In order to test the utility of our abbreviated commitment measures we examined the relationship between the commitment measures taken on soldiers in the MFO battalion in the fall of 1994 with performance measures made when they were on duty in the Sinai in the spring of 1995. Meyer and Allen's theory of commitment predicted that the best performance should come from those who had a strong emotional attachment to the Army and who did not feel they were trapped into staying in the Army; in other words, those who had high affective commitment and low continuance commitment. Conversely, the worst performance should be found in those who had low affective commitment and high continuance commitment. This is exactly what we found when we divided soldiers into groups according to whether they scored high or low on each commitment scale in the fall of 1994. Soldiers who had high affective commitment and low continuance commitment had the best MFO specific job skills as well as general soldiering skills test scores when we measured them in May 1995. Also as predicted, those who had high continuance commitment and low affective commitment had the worst test scores. We need to measure organizational commitment in a variety of performance settings and with a variety of soldiers to see how general these results are. Never the less, our findings are important because they show that we must measure both affective and continuance commitment to more fully understand and more accurately predict the performance influences of organizational commitment.

Retention is another important outcome that is related to organizational commitment. Meyer and Allen's theory predicts that retention intentions should be positively affected by both affective and continuance commitment and that the highest retention intentions would be found among those in the high affective – high continuance commitment group; while those in the low affective – low continuance group should have the lowest retention intentions. As predicted, when we asked soldiers to indicate their retention intentions on the fall, 1997 SSMP, those in the high affective – high continuance group were significantly more likely to say they would stay in the Army longer than were soldiers in any of the other three groups. And, also as predicted, soldiers in the low affective – low continuance commitment group were significantly more likely to say they would leave the Army.

We also asked these soldiers to indicate their readiness to perform their wartime duties on a five-point scale ranging from not at all prepared to very well prepared. We found that the high affective–low continuance commitment group was significantly more likely to say they were prepared to perform their mission than any of the other groups; while those in the low affective–high continuance commitment group were more likely to say they were less prepared. These findings are consistent with the Meyer and Allen theory of the effect of organizational commitment on performance and with our earlier findings from the MFO soldier performance data.

As an index of soldier well being, we examined the soldiers' responses to the SSMP that asked them to report their level of morale on a five-point scale ranging from *very low* to *very high*. We found that the high affective–low continuance commitment group had a significantly higher mean morale score than any of the other groups; however, both low affective commitment groups had about the same mean morale scores. This seems to indicate that affective commitment is a more powerful determiner of well being, at least as measured here, than is continuance commitment.

MODEL FOR PREDICTING THE GROWTH AND DEATH OF PATHOGENIC BACTERIA IN FOOD

I. A. Taub*, E. W. Ross, and F. E. Feeherry
SBCCOM, Natick Soldier Center
Natick, MA 01760-5018

ABSTRACT

A quasi-chemical model for the growth and death of bacteria in food was developed that describes the population-time profile usually encountered and accommodates the influences of A_w and pH. The introduction of an antagonistic metabolite into the model is an important step in making the model conform to experimental data. This conformity was demonstrated by tracking the population of *S. aureus* in ground bread crumb. From derived equations for the relationships between the rate constants in the model and the environmental parameters, a no-growth set of conditions can be predicted.

1. INTRODUCTION

Controlling the growth of pathogenic bacteria in food is crucial to developing ration components that are stabilized against deterioration without being processed to the point of sterility. Such components are considered more familiar and more fresh-like than components conventionally processed by heating to 121°C for 6 minutes, which degrades quality and nutritional value. Shelf-stable sandwiches, with a moist meat, cheese, or jelly filling enrobed by bread, are illustrative. Safety regulations for non-sterile products require that conditions be established inhibiting the growth of pathogens such as *Staphylococcus aureus, Escherichia coli,* and *Listeria monocytogenes.*

Most approaches taken to inhibit bacterial growth rely on lowering the water activity (A_w) and/or the pH. Simplified determinations of "growth" or "no-growth" are made, and empirical relations are often developed to predict if growth would occur. These predictions do not adequately provide for extrapolations or interpolations to conditions that differ from the experimental conditions. Accordingly, there is considerable merit in establishing a phenomenologically-based model that accurately predicts the rates of growth and/or death of a pathogen with respect to conditions within the food.

2. METHODOLOGY

The basic bread was made according to a US military specification. A_w was altered by either adding glycerol or equilibrating over salt solutions, and pH was adjusted by adding 0.05%, 0.1%, 0.2%, or 0.3% glucono-delta-lactone to the water phase of the bread. Bread was packaged in trilaminate pouches, sealed in the presence of an oxygen scavenger (Fresh Pax) without vacuum, and held at 4°C until use.

Bread crumb was inoculated with three types of *S. aureus* so that the final cell concentration was 10^4 CFU/g. Inoculated samples were sealed in trilaminate pouches under 28 inches of vacuum. All samples were incubated at 35°C. Pouches were withdrawn at designated time intervals and examined for microbial growth.

A_w of the ground breadcrumb was measured in an Aqualab CX-2 (Decagon, Inc.); the pH by a combination spear-tip electrode (Orion Research, Inc.). The experiments produced 22 sets of data, reflecting CFU/mL as functions of storage time.

3. RESULTS AND DISCUSSION

3.1 Empirical Relationships

One major "hurdle" used to control *S. aureus* growth is lowered A_w, which imposes an osmotic stress on the bacterium. For this pathogen in ground bread, the growth at 35°C is normally very rapid at $A_w = 0.9$. However, as A_w is decreased down to 0.84, *S. aureus* takes longer to start growing (lag phase), grows more slowly even at its maximum rate, and reaches a lower plateau value. To lower A_w, either glycerol can be added or partial dehydration can be used. Moreover, growth is eventually replaced by death at the low A_w values. The growth portion of this phenomenon can be described empirically by a logistic equation. The death portion follows simple first order kinetics. Both kinetic expressions incorporate the dependence of the key parameters on A_w, pH, and temperature.

3.2 Quasi-Chemical Model

The growth-death phenomenon can be described in an integrated way by treating the bacterial cycle as one would treat a sequential chemical process. This purely mechanistic approach is schematically shown in Fig. 1. The mechanism includes an activation step, representing the conversion from lag phase to growth phase (k_1); a multiplication step with concurrent formation of an antagonistic metabolite (k_2); a step in which the bacterium reacts with the antagonistic metabolite, sensitizing it to destruction (k_3); and a natural death step (k_4).

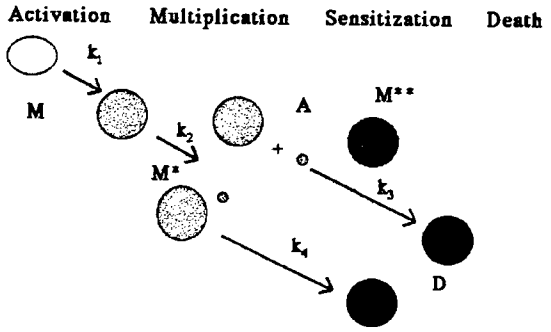


Figure 1. Schematic representation of the mechanism that underlies the mathematical model. M and M* represent metabolizing and multiplying cells, A represents the formed antagonist, M** represents a cell sensitized to destruction by reaction of M* with A, and D represents a dead cell.

The rates of these four reactions can be related to the "concentrations" of the individual entities through a set of differential equations. The rates, denoted by v's, are: $v_1 = k_1x_1$, $v_2 = k_2x_2$, $v_3 = 10^{-9}k_3x_2x_3$, and $v_4 = k_4x_2$, where x_1 through x_4 are the concentrations of M, M*, A, and D, respectively. A separate differential equation for each x can also be described taking into account the reactions responsible for forming or eliminating the entity, as the case for M* (x_2) illustrates:

$$dx_2/dt = k_1x_1 + k_2x_2 - 10^{-9}k_3x_2x_3 - k_4x_2. \qquad (1)$$

The k's can be inferred using optimization techniques that find the best fit to actual data. The resulting solution with best-value k's becomes the predictive equation.

3.3 Model Validation

The model was fitted to each of 22 sets of data with various values of A_w and pH. An example of the curve-fitting results for five of the data sets is shown in Fig. 2.

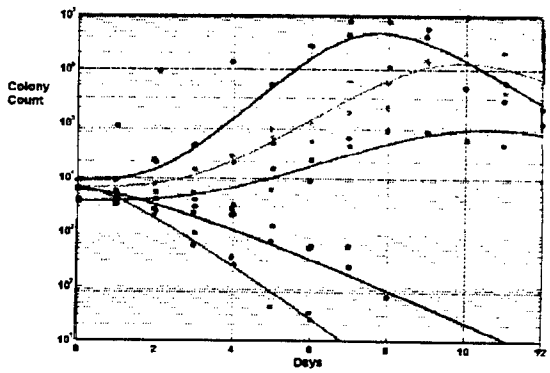


Figure 2. Growth rates and death kinetics of a mixture of three enterotoxin types of *S. aureus* cells for five glucono-delta-lactone concentrations. The curve fittings are based on the predictive mathematical model.

3.4 No Growth Conditions

Viewed strictly in terms of the kinetic mechanism, the model predicts no growth when either $k_1 \sim 0$ or $dM/dt + dM^*/dt = 0$, which is met by:

$$k_2 = 10^{-9}k_3x_3 + k_4. \qquad (2)$$

Since such control implies limited multiplication, antagonist A would be at a low concentration and the value of $10^{-9}k_3x_3$ would likely be less than k_4. Consequently, choosing conditions at which $k_2 = k_4$ should ensure a safe and stable intermediate moisture food.

As an alternative approach, the maximum growth rate, $G = \Delta(\log CFU/mL)/\Delta day$, was determined for each data set. Statistically analyzing the results gives a modestly meaningful relationship ($R^2 = 50.8\%$) among G, A_w, and pH:

$$G = C_o + C_1(A_w) + C_2(pH), \qquad (3)$$

where $C_o \sim -34.57$, $\sigma(C_o) \sim 8.18$; $C_1 \sim 22.19$, $\sigma(C_1) \sim 5.26$; and $C_2 \sim 2.97$, $\sigma(C_2) \sim 0.931$. Based on the estimates given by the above means of C_o, C_1, and C_2, we obtain as the "growth/no-growth" boundary condition:

$$C_o + C_1(A_w) + C_2(pH) = 0. \qquad (4)$$

4. CONCLUSIONS AND IMPLICATIONS

The quasi-chemical model of bacterial growth and death accounts for all of the life cycle phases of *S. aureus* in bread crumb of differing A_w and pH. It includes the influence of an antagonistic metabolite on limiting growth and sensitizing death. It also predicts conditions of A_w and/or pH that either prevent growth or promote death.

PROGRESS IN DEVELOPING AN ACTIVE TOPICAL SKIN PROTECTANT

E.H. Braue, Jr*, S.T. Hobson, E.K. Lehnert, N. Lewis, C.R. Nalls-Braue, B.F. Doxzon, R.T. Simons, P.A. DiLeonardi, T.L. Nohe, and J.S. Graham

U.S. Army Medical Research Institute of Chemical Defense, Aberdeen Proving Ground, Maryland, 21010-5400, USA.

Applying a topical protectant to vulnerable skin surfaces before entry into a chemical combat arena was proposed as a protective measure against percutaneous Chemical Warfare Agent (CWA) toxicity soon after the first use of CWAs in World War I. Topical protectants should augment the protection afforded by the protective overgarments and/or redefine the circumstances requiring mission oriented protective posture (MOPP) levels. The rapid action of vesicating (blistering) agents, such as sulfur mustard (Bis-(2-chloroethyl)sulfide, HD), requires a pre-exposure skin protection system. These approaches also reduce the risk of exposure to nerve agents (organophosphorus CWAs), which in contrast to blister agents are lethal in droplet amounts.

Two non-active Topical Skin Protectant (TSP) formulations were developed at the United States Army Medical Research Institute of Chemical Defense (USAMRICD) and were transferred to advanced development following Milestone Zero (transition to Concept Exploration Phase) in October 1990. The best TSP was selected and its development progressed through Milestone I (transition to Program Definition and Risk Reduction Phase) in 1993, an Investigational New Drug (IND) filed with the FDA in 1994, and Milestone II (transition to Engineering and Manufacturing Development Phase) in 1995, and culminated with New Drug Application (NDA) approval and Milestone III (transition to Production Fielding, Deployment, and Operational Support Phase) in 2000. This new product is now called Skin Exposure Reduction Paste Against Chemical Warfare Agents (SERPACWA) and will be available to warfighters in 2001.

Although the TSP formulation extends the protection afforded by MOPP and allows a longer window for decontamination, it does not completely remove the possibility for contamination because the CWA itself is not neutralized. To avoid contamination of other areas of the battlefield and to preclude the future percutaneous absorption of the CWA, decontamination is still required. Furthermore, although the TSP formulation provides excellent protection against liquid challenges of GD (soman), VX, and HD, its protection against HD vapor is minimal.

To overcome these deficiencies, there is a need for a new TSP that contains an active component. Ideally, this active Topical Skin Protectant (aTSP) will meet the following criteria. First, the active TSP will neutralize CWAs including HD, GD, and VX. Second, the barrier properties of the TSP will be maintained or increased. Third, the protection against HD vapor will increase. And fourth, the cosmetic characteristics (e.g., odor, and texture) of the TSP will be maintained.

The USAMRICD initiated a research effort in 1994 to develop an effective material that acts as both a protective barrier and an active destructive matrix against CWAs. In this paper, we report results on our preparation and evaluation of active Topical Skin Protectants (aTSPs). These active barrier creams are composite materials consisting of a TSP base cream and an active moiety. Using an established base cream of perfluorinated-polyether oil and polytetrafluoroethylene solids, we incorporated over 90 different active components. Classes tested include organic polymers, enzymes, hybrid organic-inorganic materials, polyoxometallates (POMs), inorganic composites, inorganic oxides, metal alloys and small organic molecules. We characterized these materials by light microscopy and Fourier transform infrared (FTIR) spectroscopy. We determined the efficacy of these materials against both HD and GD, using a variety of *in vitro* and *in vivo* models as part of a Decision Tree Network (DTN). Composite materials with optimum active compounds exhibit a 99% reduction of GD vapor break-through after 20 hours (from 6600 ng to 86 ng, Figure 1).

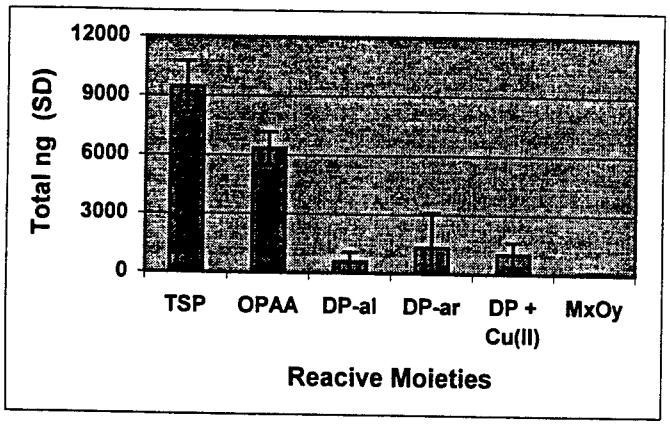


Figure 1. Cumulative amount of GD vapor through aTSP after 20 hours.

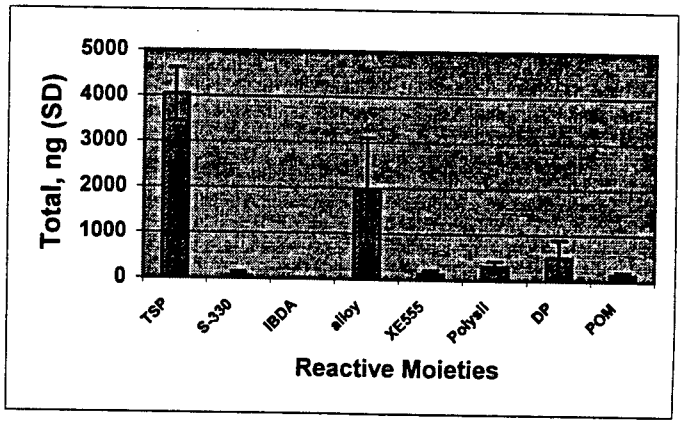


Figure 2. Cumulative amount of HD vapor through aTSP after 20 hours.

Similar composite materials show a 99% reduction in HD vapor break-through after 20 hours (from 4040 ng to 16 ng, Figure 2) and an elimination of erythema versus control in HD vapor challenges to weanling pigs (Figure 3).

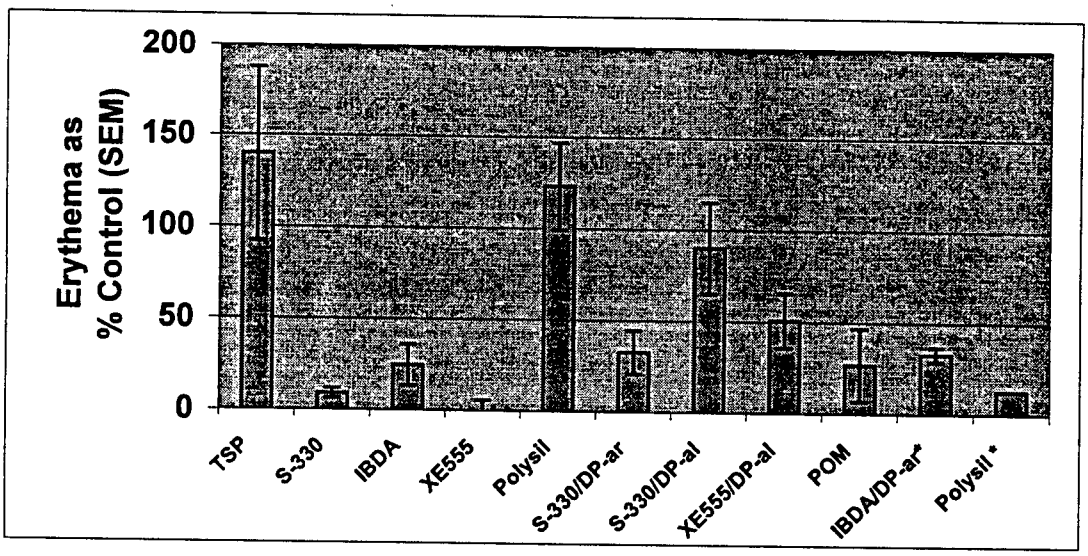


Figure 3. Protection of aTSP vs. HD vapor in weanling pig model (Control = no TSP, * thickness is 0.2mm instead of 0.1mm)

These results indicate that an active TSP designed to protect against blister and nerve agents is within reach. Our goal is to transfer a significantly improved active TSP formulation to advanced development by 2002.

PROTECTION AGAINST CHEMICAL AGENT-INDUCED, SEIZURE-RELATED NEURONAL CELL DEATH

Gerald P. H. Ballough
La Salle University
Philadelphia, PA 19141-1199

Margaret G. Filbert*
US Army Medical Research Institute of Chemical Defense
Aberdeen Proving Ground, MD 21010-5400

Current medical countermeasures for exposure to organophosphorus nerve agents protect against lethality. However, soldiers surviving the initial life threatening effects are likely to develop seizure activity. Protection against seizure-induced neuropathology is of significant military concern. While anticonvulsants such as diazepam are effective against nerve agent-induced seizures when given shortly after the onset of seizures, to control seizure activity the anticonvulsant must be administered within a finite time window. The longer the seizure duration the more difficult it will be to stop them. Diazepam does not afford absolute protection against seizure-related neuronal cell death. There is a clear need for a neuroprotective adjunct that can be administered one or more hours after seizure onset that is capable of preventing nerve agent-induced seizure-related brain damage.

We have demonstrated that a synthetic nonpsychotropic derivative of tetrahydrocannabinol (THC), dexanabinol (HU-211, 7-hydroxy-Δ^6 – tetrahydrocannabinol-1, 1-dimethylheptyl) provides considerable protection against brain damage resulting from soman-induced seizures without stopping seizure activity. HU-211 has been reported to act as a neuroprotectant in animal models of head injury, optic nerve crush and ischemia. Following these insults, a single injection of HU-211 conferred a significant increase in neuronal survival.

To evaluate HU-211 as a potential neuroprotectant agent against soman-induced seizure-related brain damage (SRBD), rats were surgically implanted with screw electrodes for electrocorticographic (ECoG) recordings and connected to a recording system. Following baseline ECoG recordings, the rats were given a subcutaneous injection of 1.6 LD_{50} soman. A control group of animals received an injection of saline. Another group of animals received an intraperitoneal injection of HU-211 (Pharmos Ltd, Rehovot, Israel) at either 5 min or 40 min after onset of soman-induced seizures.

All rats given soman showed ECoG evidence of sustained seizures and status epilepticus (SE) lasting 4-6 h. HU-211 had no effect on either the strength or duration of seizure activity as defined by the continued presence of high amplitude (i.e., greater than four times baseline) rhythmic spike or sharp wave activity.

Twenty-seven h after soman administrations, the rats were euthanitized and their brains were immediately excised and postfixed by immersion in 4% paraformaldehyde in 0.1 M phosphate buffer for 72 h and coronally sectioned at 40 μm. Serial sections were collected onto poly-L-lysine coated slides for immunocytochemical staining for microtubule-associated protein 2 (MAP2). Morphometric assessments were performed of the cross-sectional areas of MAP2-negative staining, i.e., of necrosis in the piriform cortex.

As assessed by MAP2-negative staining, administration of HU-211 at 5 min post seizure onset reduced median lesion volume 86% and when administered 40 min post onset, the reduction in lesion volume was 81.5%. In a separate set of experiments, HU-211 was administered at 5 min post onset and then every six h for the next 24 h. Lesion volumes in these animals were reduced 99%. No evidence of brain damage was discerned from microscopic examination of MAP2 immunostained sections in either saline injected or HU-211 injected controls. Power spectral analysis of ECoG frequency bands revealed a high correlation of lesion volume with Beta-2 (21-31.5 Hz) activity at one hr after seizure onset ($R^2 = 0.91$, $p < .001$).

In a separate set of experiments the effects of HU-211 in combination with diazepam were studied. When 20-mg/kg diazepam was administered to soman-poisoned animals at 40 min after seizure onset, the diazepam failed to stop seizures. However, when the diazepam was given in combination with HU- 211 seizures abated, suggesting a synergistic effect of HU-211 on diazepam.

The results reported here are important in that in the absence of any antidotal therapy, HU-211 reduced neuronal damage without stopping established seizures and when given in combination with diazepam potentiated the anticonvulsant efficacy of diazepam. These findings suggest that this compound may have potential as a multiaction neuroprotectant against brain damage resulting from nerve agent-induced seizures and status epilepticus.

THIS PAGE INTENTIONALLY LEFT BLANK

MAXIMIZING THE PERFORMANCE OF U.S. ARMY AVIATORS IN SUSTAINED OPERATIONS: DEXEDRINE IS AN EFFECTIVE FATIGUE COUNTERMEASURE

J. A. Caldwell*
U.S. Army Aeromedical Research Laboratory
Fort Rucker, AL 36362-0577

ABSTRACT

Dexedrine® appears to be an effective fatigue countermeasure for use in military aviators deprived of sleep due to operational constraints. The present analysis of studies from the U.S. Army Aeromedical Research Laboratory (USAARL) show that Dexedrine maintains flight skills, mood, and activation in sleep-deprived pilots while producing only minor decrements in recovery sleep. It is thus concluded that well-controlled administration of Dexedrine is a viable short-term remedy for severe fatigue in aviation sustained operations.

1. INTRODUCTION

Sustained operations place a strain on personnel by restricting the sleep that is essential for effective functioning (Horne, 1978), and this ultimately produces cognitive impairments that can compromise the mission (Krueger, 1989). The importance of well-planned work/rest schedules has been emphasized (Deparment of the Army, 1997); however, this often is not feasible given the demands of combat. Other countermeasures, such as the administration of dextroamphetamine appear promising based on laboratory (Weiss and Laties, 1967) and field reports (Emonson and Vanderbeek, 1993). However, further study is needed before drawing definitive conclusions.

USAARL has performed several investigations on helicopter pilots (Caldwell et al., 1995; Caldwell et al., 1997; Caldwell and Caldwell, 1997; Caldwell et al., 2000) and these have substantiated the effectiveness of Dexedrine for sustaining flight performance, mood, and alertness despite sleep loss. However, each study was conducted on a small sample (raising concerns about generalizability and statistical power), which made it necessary to determine that the results were reliable across different groups of volunteers. This report combined the four data sets from previous studies into a single larger-scale analysis.

2. METHODS

2.1 Subjects

Twenty-eight UH-60 pilots were tested. The mean age was 29.6 years. Seven were female and 21 were male.

2.2 Apparatus

Flights. Simulator flights (performed in three of the studies) were performed in a UH-60 simulator with computer-generated visuals, a six-degree-of-freedom motion base, and a multi-channel data acquisition system. Aircraft flights (performed in one of the studies) occurred in a UH-60 helicopter equipped with a system that recorded the same aspects of performance collected in the simulator.

Waking electroencephalographic (EEG) evaluations. EEGs were recorded via Grass E5SH electrodes from C_Z. Data were amplified and stored on a Cadwell Spectrum 32. The low and high filters were set at 0.53 and 20 Hz, respectively, and the 60 Hz notch filter was used.

Profile of Mood States (POMS). Mood was assessed with the POMS, a 65-item test which measures tension, depression, anger, vigor, fatigue, and confusion.

Polysomnographic evaluations. Sleep architecture was examined using a Nihon Kohden electroencephalograph. Data were recorded via Grass E5SH electrodes from C_3, C_4, O_1, and O_2 . Electromyographic (EMG) and electrooculographic (EOG) data were recorded via SensorMedics electrodes placed under the chin and at the outer canthus of left and right eyes. Time constants and high filter settings were: 0.3 sec. and 35 Hz for EEG, 5.0 sec. and 10 Hz for EOG, and 0.003 and 120 Hz for EMG.

2.3 Procedure

Test sessions occurred at 0900, 1300, and 1700 on Monday (training day), Tuesday (control), and Thursday (control). On Wednesday (the deprivation day in the first cycle) and on Friday (the deprivation day in the second cycle), testing occurred at 0100, 0500, 0900, 1300, and 1700. On these days, drug (10 mg Dexedrine) or placebo doses were administered at 0000, 0400, and 0800. The study was double blind and counterbalanced.

Flights consisted of standard maneuvers (straight-and-levels, left and right turns, climbs, descents, and a left-descending turn). Performance was computer scored based upon the accuracy of flight control. Scores ranged from 0 (poor) to 100 (excellent). ***EEG evaluations*** occurred 20 minutes after the flights and consisted of a resting eyes-open segment followed by an eyes-closed segment (1.5 minutes of each). Absolute power values were calculated via fast Fourier Transforms based upon 2.5-second epochs from each segment. Only theta activity is presented here. ***POMS*** questionnaires were administered 1 hour after the EEG tests. Volunteers indicated how well each of 65 mood adjectives

described his/her present feelings. A mood disturbance score was calculated based on the average results of all six mood scales (weighting the Vigor scale negatively). ***Polysomnographic*** evaluations were derived from sleep periods on the baseline (predeprivation) and two recovery nights (one after deprivation with dextroamphetamine and the other after deprivation with placebo). The data were scored based on Rechtschaffen and Kales' (1968) criteria.

3. RESULTS

3.1 Flight performance

An interaction between drug (dextroamphetamine vs. placebo) and session (0900, 1300, and 1700 on baseline; and 0100, 0500, 0900, 1300, and 1700 during deprivation) ($p<.0001$) resulted from the lack of baseline differences followed by better performance under Dexedrine than placebo at each of the deprivation sessions from 0500 to 1700. There was a main effect ($p=.0001$) due to better performance under Dexedrine than placebo.

3.2 EEG data

An interaction between drug (dextroamphetamine vs. placebo) and session (1020, 1420, and 1820 on baseline; and 0220, 0620, 1020, 1420, and 1820 on the deprivation day) ($p<.0001$) occurred because there was more theta in the first Dexedrine baseline session (predrug) than on the first placebo baseline session, but the opposite occurred at every later sleep-deprivation time from 0620 to 1820 ($p<.05$).

3.3 POMS data

POMS scores under placebo and Dexedrine at baseline (1120, 1520, 1920, and 2340) and during deprivation (0320, 0720, 1120, 1520, 1920, and 2340) indicated a drug-by-session interaction ($p<.0001$) and a drug main effect ($p<.0001$). There were no baseline differences, but mood scores were lower under Dexedrine than placebo at every deprivation time from 0335 to 2225 ($p<.05$).

3.4 Polysomnographic data

There were main effects on every stage of sleep ($p\leq.0001$). Differences between baseline and post-dextroamphetamine nights were found on every stage except stage 2; differences between baseline and post-placebo nights occurred on every stage without exception; and differences between the two post-drug nights occurred on stages 1, 2, and REM ($p<.05$). Sleep was better after baseline due to higher sleep pressure, and slightly better after the placebo period than after the Dexedrine period.

4. DISCUSSION

The findings from USAARL's studies showed that Dexedrine attenuated decrements in flight performance. The medication also attenuated the adverse impact of sleep loss on EEG and mood. Dexedrine previously was proven effective for maintaining the performance of fatigued non-aviators (Weiss & Laties, 1967), but the present data show that well-controlled administration of dextroamphetamine is an appropriate fatigue countermeasure for aviators in sustained combat operations. However, no stimulant can replace effective crew-rest scheduling or provide a substitute for restful, restorative sleep.

ACKOWLEDGMENTS

The opinions, interpretations, conclusions, and recommendations are those of the authors and are not necessarily endorsed by the U.S. Army and/or DOD.

REFERENCES

Caldwell, J. A., Caldwell, J. L., Crowley, J. S., & Jones, H. D., "Sustaining helicopter pilot performance with Dexedrine during periods of sleep deprivation", *Avn., Sp. Env. Med., 66*(10):30-937, 1995.

Caldwell, J. A. & Caldwell, J. L., "An in-flight investigation of the efficacy of dextroamphetamine for sustaining helicopter pilot performance," Avn, Sp. Env. Med., 68(12):1073-1080, 1997.

Caldwell, J. A., Caldwell, J. L., & Crowley, J. S., "Sustaining female helicopter pilot performance with Dexedrine during sustained operations", *Int. J. Avn. Psy.*_7(1):15-36, 1997.

Caldwell, J. A., Smythe, N. K., LeDuc, P. A., & Caldwell, J. L., " Efficacy of dextroamphetamine for the maintenance of aviator performance during 64 hours of sustained wakefulness," *Avn. Sp. Env. Med.*, 71(1): 7-18, 2000.

Department of the Army. *Aviation: General Provisions, Training, Standardization, and Resource Management*, Chapter 3, Section III, Crew endurance scheduling. AR 95-3. Washington DC: Dept. of the Army, 1997.

Emonson, D. L. & Vanderbeek, R. D., "The use of dextroamphetamine in support of tactical air operations during Operation Desert Shield/Storm," *Avn. Sp. Env. Med.*, 64(5):421, 1993.

Horne, J. A., "A review of the biological effects of total sleep deprivation in man," *Bio. Psy.*,7:55-102, 1978.

Krueger, G. P., "Sustaining military performance in continuous operations: Combatant fatigue, rest and sleep needs." Handbook of military psychology, pp 255-277. New York: John Wiley and Sons, 1989.

Rechtschaffen, A., & Kales, A., *A manual of standardized terminology, techniques, and scoring system for sleep stages of human subjects.* Washington, DC: U.S. Government Printing Office, 1968.

Weiss, B., & Laties, V.G., "Enhancement of human performance by caffeine and the amphetamines," *Pharm. Rev.*, 14:1-36, 1967.

USAISR: EXPLORING MILITARY MEDICAL APPLICATIONS OF LASER TECHNOLOGY

Ronald S. Walton, Kathy L. Ryan, David G. Baer, and Albert T. McManus
US Army Institute of Surgical Research, Ft. Sam Houston, TX 78234

The mission of the US Army Institute of Surgical Research (USAISR) is "to provide combat casualty care medical solutions and products for injured soldiers by integrating laboratory and clinical research." Our responsibility therefore is to design and test innovative medical procedures and devices that can be transitioned to medical applications of interest in the military setting. Laser technology currently is being used extensively in the civilian arena for a number of purposes; for example, the use of lasers has become routine in dermatology and ophthalmology. We are suggesting that small medical lasers might be used under far forward conditions for early decontamination of wounds and for the rapid determination of the amount of tissue damage. In addition, development of laser-assisted tissue bonding and welding techniques may allow rapid repair and maintenance of damaged tissues and limbs that are not possible with current field methods.

The USAISR has recently formed a team to investigate and test medical applications of lasers. This team is unique in that trauma surgeon researchers work in close collaboration with basic science researchers such as physiologists, cell biologists and microbiologists to determine the feasibility and uses for the newest technologies, thereby providing an integrated approach to the eventual implementation of these technologies in the clinical setting. Through collaborative agreements with the Wellman Laboratories of Photomedicine at Harvard University and the Beckman Laser Institute at the University of California at Irvine, we collaborate with internationally known experts to investigate leading-edge laser technologies. USAISR currently has 3 active areas of research into the military applications of medical lasers:

(1) Photodynamic Therapy (PDT) for the Treatment and Prevention of Wound Infection

Microbial contamination occurs at or soon after wounding. Wound infection in the field currently is very common because of the presence of damaged tissue, lost circulation, limited sanitation and unavoidable delays in evacuation. To address the problem of wound infection in military casualties, we are conducting an investigation into the use of PDT as a novel wound sanitation technique. PDT refers to the use of a photosensitizer that is absorbed by bacteria but not by human cells and, upon activation with light of an appropriate wavelength, selectively destroys the microbes. In this study, we are utilizing the photosensitizer poly-l-lysine chlorin e_6, a compound that shows antimicrobial effects when illuminated with 665 nm light and is selectively absorbed by bacteria. We are conducting an evaluation of poly-l-lysine chlorin e_6 in a therapeutically relevant model of wound infection.

We are using the Mason-Walker rat model with 40 cm^2 scald wounds inoculated with clinically encountered species of bacteria. We have genetically modified human wound pathogens to carry luciferase/luciferin genes that cause the living bacteria to glow (luminesce). Not only can we visualize the bacterial growth and infection on the surface of a wound, but our detection system is also sufficiently sensitive to detect deep tissue and organ infections. This capability allows accurate, sensitive and noninvasive monitoring of the progress of infection and of the efficacy of experimental antimicrobial treatments, and allows for the survey of the entire body for infection rather than relying on serial sampling with invasive techniques (biopsy) or sequentially sacrificing animals.

To determine the potential for PDT for use in the prevention and treatment of wound infection, the photosensitizer is applied to the wound and the number of bacteria is determined by measuring luminescence. The wound is then exposed to activating light in several doses and the resultant reduction of luminescence is used to generate a dose-response curve. Animals are then observed for 21 days to determine therapeutic outcome. Future research will include (1) testing the chosen photosensitizer for efficacy against a range of clinically relevant gram negative and gram positive bacteria; and (2) optimization of delivery of the photosensitizer.

(2) Photochemical Tissue Bonding (PTB)

Lasers have also been used to weld together a number of tissues, including skin, blood vessels and nerve. The mechanism by which welding occurs is thermal denaturation and subsequent coagulation of fibrous tissue such as collagen, which can cause additional thermal damage to surrounding tissue. An alternative laser technology that does not require denaturation of proteins is PTB. PTB involves the application of a photosensitizing dye that adheres to the tissue at the wound site and can be activated by light irradiation to close the wound. Wound closure results from the formation of protein crosslinks between the two surfaces to be joined. The process is fundamentally different from the more commonly used welding techniques that rely on thermal denaturation; PTB is a "cold" process that avoids problems of peripheral thermal damage and tissue shrinkage and can retain the structural integrity of the tissue. PTB recently has been used to nonthermally repair cornea, dura mater, cartilage and skin *ex vivo* and cartilage *in vivo*.

In vitro experiments are currently underway to determine the optimal dye and its concentration, as well as the parameters of light irradiation, for skin repair. Once optimized, *in vivo* experiments will be performed that utilize these PTB parameters to attach skin grafts to excised burn wounds in rodents. Similarly, *in vitro* experiments are being performed to optimize PTB parameters for blood vessel anastomosis. Following optimization, PTB will be used to accomplish vascular anastomosis and arteriotomy repair in rats and rabbits, respectively. Likewise, the utility of PTB to accomplish repair of orthopedic injuries is also being assessed. In all of these experiments, the tensile strength of the repair accomplished using PTB will be tested in the biomechanics laboratory against current standard-of-care techniques (e.g., sutures for vascular anastomosis).

(3) Noninvasive Imaging of Damaged Tissue

Thermal injuries result in more than 500,000 hospital emergency room visits each year in the United States alone. Over 20,000 of these patients require hospitalization and extensive medical and surgical treatment. A key problem in these patients is accurate delineation of a partial thickness from a full thickness injury, a distinction often not immediately evident on visual inspection. Accurate assessment of thermal wound depth is a critical factor to determine appropriate therapeutic intervention. A physician currently may wait 2-3 weeks before the distinction between deep second degree and third degree burn becomes apparent. Over the last 50 years, a large number of non-invasive modalities have been evaluated to assess wound depth in thermal injury patients. These include the use of vital dyes, indocyanine green dye fluorescence, fluorescein fluorometry, laser doppler flowmetry, thermography, ultrasound, nuclear magnetic resonance imaging, and spectral analysis of light reflectance. For a variety of reasons, none of these technologies has significantly improved the clinician's ability to assess thermal injuries beyond simple observation.

The Beckman Laser Institute, Irvine CA, has recently developed a new Optical Coherence and Doppler Tomography device that would non-invasively assess thermal injury at the bedside in a "real-time" mode. Pilot research with this prototype device has produced excellent correlation in a rodent thermal injury model. Optical coherence tomography (OCT) and optical Doppler tomography (ODT) has the ability to non-invasively image *in vivo* blood flow with high spatial resolution. The high degree of spatial resolution is possible because light backscattered from the sample is recombined with the reference beam and forms interference fringes only when the optical path length difference is within the coherence length of the source light. ODT essentially combines laser Doppler flowmetry with OCT to produce high-resolution tomographic images of static and moving constituents in biologic tissues. This localized flow velocity detection and imaging is possible by using a technique of coherence gating. Using a Michelson interferometer with a low coherence light source, ODT can measure the amplitude and frequency of the interference fringe intensity generated between reference and target arm and forms a structural and velocity image.

Our established rodent second and third degree-thermal injury model will be used to compare the images generated with the new OCT/ODT and Polarization Sensitive OCT imaging modalities to the gold standard of histopathology. This study will follow subjects for a full 21 days, during which the wound will be non-invasively scanned and biopsied. The image generated by the non-invasive optical biopsy will be compared to a standard histopathology section by our staff veterinary pathologist. Our goal is to have an accurate, reliable technology to guide surgeons in early assessment of wound depth in order that he/she might make key therapeutic decisions earlier than is now possible. This technological application, if successful, will realize a surgery research goal that has been elusive for the last 50 years.

INTERNET-BASED TRAINING: LEARNER PERFORMANCE AND INSTRUCTIONAL FEEDBACK

Robert A. Wisher
U.S. Army Research Institute for the Behavioral and Social Sciences
Alexandria, VA 22333

Michael W. Freeman
U.S. Army Forces Command
Fort McPherson, GA 30330

Kenneth L. Morris
Battle Command Battle Laboratory
Fort Leavenworth, KS 66048

SUMMARY

ABSTRACT

An experiment that examined the use of the Internet for training digital skills is analyzed in this article. A distributed digital skills laboratory was created using low bandwidth media for the delivery of instruction related to military messaging systems. A sample of n=147 military personnel and civilians were trained in a one-day course which included a brief lecture and a lengthy hands-on laboratory. The sample included those trained in a traditional classroom and those trained through distance learning delivered over the Internet using instant messaging as a feedback mechanism. The results demonstrated equal performance between groups.

DISTRIBUTED LEARNING

In the 21st century, soldiers will attend streamlined resident courses, preparing themselves through synchronous and asynchronous learning modules delivered at unit learning centers, at the job site, or in their residence. Much of this training will be delivered over the Internet or through military intranets, transcending time and space barriers. The advantages of training from a distance include a reduction in travel costs to a central facility and greater flexibility in scheduling. An underlying assumption is that the quality of training is maintained whenever and wherever it is delivered to the soldier. Learning outcomes from a distance learning (DL) program must be on par with those from classroom instruction, if not better. A challenge of training from a distance, then, is providing informative feedback, a critical condition for learning, to soldiers about their performance.

The soldier of the future will be surrounded by digital systems. The successful operation of these systems will require proficiency in digital skills. Digital skills are defined as those learned behaviors that allow a trainee to interact with a computer in order to accomplish a task. Because training is most effective when it is one-on-one, the training of many digital skills can benefit from real time, one-on-one interaction and feedback using both instructor and student computer screens along with audio and video. However, current military distributed learning programs provide limited opportunities for guided practice and individual coaching in a learning laboratory environment.

The future delivery of distance learning is clearly in networks and connectivity. However, the current Internet bandwidth and access speeds are inadequate for the delivery of true multimedia instruction combining sound, video, graphics and data. Hybrid approaches to DL use a combination of technologies to increase capacity and choice in designing and delivering instruction.

DISTRIBUTED DIGITAL SKILLS LABORATORY

The distributed digital skills laboratories (D2SL) concept provides the capability to interact in a form that enables synchronous, instructor led and coached training of digital skills. The training originates at a distance in a distributed classroom laboratory environment. Interactions are accomplished simultaneously using a hybrid approach of stable technologies and multiple low bandwidth media (such as plain analog telephone lines and narrow band Internet connections), thus increasing access while controlling costs. The D2SL creates virtual learning environments for each student within the conversational framework of a larger, shared computer laboratory. The following provisions for interaction are provided simultaneously in the D2SL concept (see Figure 1). Informative feedback is provided through instant messaging (IM) technology.

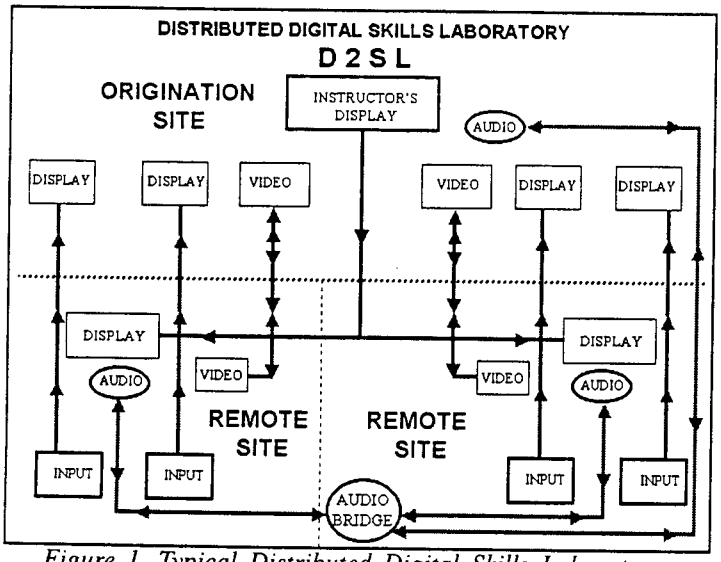


Figure 1. Typical Distributed Digital Skills Laboratory Connectivity

THE EXPERIMENT

The effectiveness of the D2SL for training the digital skills related to the U.S. Message Text Format (USMTF) system was measured in an experiment conducted by the U.S. Army Research Institute and the Office of the Chief, Army Reserve, in conjunction with the Army Reserve Readiness Training Center. The experimental treatment group used the D2SL and the comparison group was trained in the traditional face-to-face classroom. A mixture of military personnel from the Army and Marine Corps were participants, along with a smaller number of military civilians. A total sample of n =147 was tested.

The course consisted of a one-hour lecture on the purpose of the USMTF followed by a hands-on laboratory that required up to five hours. The objective of the course was to enable users to produce and deliver a valid USMTF message. The D2SL version of the course originated from the ARRTC, with three remote sites on line. The classroom comparison group was from USMTF training at major Army and Marine Corps headquarters commands.

A sample of n=38 participated in the DL version, and a sample of n=109 participated in the traditional classroom version of the course. A Chi-Square test showed no significant difference between the groups on standard demographic factors. For each group, the performance on the hands-on laboratory was 100 percent - all students were able to compose the required sample messages. Since hands-on performance was comparable, secondary measures of learning outcomes were analyzed to test for any potential differences. Specifically, students were asked to rate how much more they learned, compared to what they previously knew, on five topic areas, using a five-point scale, from one indicating "nothing more" to five indicating "a lot more":

Topic area	DL	Traditional
Message structure	4.0	4.1
Message composition	4.1	4.1
Message delivery	3.5	3.7
Different msg formats	4.2	4.3
Fix message errors	3.6	3.9

Of these six topics, only the "fix message errors topic" showed a significant mean difference between groups ($t = 2.1$, $p < .05$).

Instant Messaging Results

IM is a relatively new Internet application that enables users to create their own private chat room. IM is the preferred medium of immediate communication between users. In the present experiment, IM was enabled between instructors and students such that the instructor assigned to monitor a particular remote site was able to "converse" with a student through a textbox.

An analysis of the 650 messages during the hands-on training indicated an average message length (in words) of 7 for the 244 messages sent by students and 14 for the 406 messages sent by instructors. An examination of the instructor messages revealed that most were answers to a brief question by the student. The instructors issued about 1.7 messages for each student message. Overall, the fact that instructors sent many more messages reflects the prompting and coaching that occurred during the laboratory exercises.

This experiment illustrates the value of the D2SL for training digital skills at a distance. Every student was able to succeed at the hands-on exercises without the physical presence of the instructor. Importantly, the IM technology was an effective feedback alternative to the personalized verbal feedback a student receives in the classroom. This technology allows questions to be posed by either the student or the instructor; feedback is immediate. The value of being able to ask questions and receive feedback should not be underestimated in a DL environment.

Distributed learning has the potential to enhance individual competency and unit readiness by delivering learning where and when needed. But distributed learning systems must provide the interactions and informative feedback required to satisfy all learning objectives. The D2SL is a viable method for training and coaching digital skills hands-on at a distance while maintaining training effectiveness.

Session E
Environmental and Geosciences

Chair
Dr. Ellis Krinitzsky
U.S. Army Engineer Waterways Experiment Station

Co-Chair
Dr. Richard Lewis
Defense Threat Reduction Agency

Keynote Address
Dr. Jean Bernard Minster
University of California, San Diego

THIS PAGE INTENTIONALLY LEFT BLANK

BIODEGRADATION OF DECONTAMINATING SOLUTION 2 (DS2)

Dr. Michael H. Kim
Geo-Centers, Inc.
PO Box 68, APG, MD 21010

Dr. Joseph J. DeFrank*
U.S. Army Edgewood Chemical Biological Center
APG, MD 21010-5424

SUMMARY

Decontaminating Solution 2 (DS2) is used as a decontaminant for chemical warfare agents such as the blistering agent sulfur mustard (HD) and nerve agents such as GB, GD, and VX. DS2 consists of 70% diethylenetriamine (DETA), 28% ethylene glycol monomethyl ether (EGME), and 2% NaOH. The unique chemistry of the DS2 solution allows DETA to sequester a sodium ion to produce a super base "OH" which in turn abstracts a proton from EGME to yield a strong nucleophile, ethylene glycol monomethyl ethoxide. DS2 is extremely effective in attacking nucleophilic centers in a variety of chemical agents, thereby inactivating the highly toxic properties of the chemical agents. However, DS2 itself is corrosive, toxic, hazardous, and has been recommended for removal from the list of the US Army decontaminants.

There are several ongoing programs aimed at developing non-toxic, non-corrosive and environmentally safe replacements for DS2. When such replacements are fielded, there will be the need to dispose of nearly 2 million gallons of stored DS2. Some of the intact DS2 will be provided to commercial firms for recycling of its components. However, significant quantities of the stockpile may have deteriorated to the point where recycling is not feasible. An alternative approach will be required for dealing with this hazardous material.

In this study, a continuous fed-batch system was developed for DS2 biodegradation. In addition, the high nitrogen content in DS2 (approximately 28.5% by weight) necessitated a nitrification/denitrification process scheme for its removal. Nitrification, conversion of mineralized ammonia from the DS2/DETA degradation to nitrate, is accomplished simultaneously with the DS2 degradation under aerobic conditions. Denitrification, conversion of accumulated nitrate to nitrogen gas, is achieved under anoxic conditions by turning off the air supply. A one-day cycle with 16 hours of air-on and 8 hours of air-off was used.

Several salient process requirements were demonstrated. First, the continuous fed-batch mode of operation for DS2 degradation is necessary to maintain the concentration of DS2 relatively low in the bioreactor. If the chemical oxygen demand (COD) exceeds 500 mg/L, an inhibition on nitrification was evident, resulting in the accumulation of ammonia. The high ammonia in turn also can inhibit its own conversion process. Eventually, the DS2 degradation can also be adversely affected, leading to a process upset. Secondly, the DS2 could not be used as a carbon source during denitrification. In this study 2.8 mg methanol/mg nitrate-N was used to effect denitrification. Lastly, it was likely that the overall capacity for DS2 degradation in the continuous fed-batch process is dictated by the amount of nitrate that could be denitrified under anoxic conditions. A 4 liter continuous fed-batch process system has been successfully used to achieve a greater than 97% removal of COD and 99% N using 1% DS2 (equivalent to 17500 mg/L COD and 2850 mg/L N) at a hydraulic retention time of 16 days.

Use of biodegradation to convert deteriorated DS2 to carbon dioxide, nitrogen gas, biomass and some inorganic salts appears to be a disposal technology that can deal with this hazardous material in a safe and environmentally benign manner.

THIS PAGE INTENTIONALLY LEFT BLANK

SCIENCE AND MODERNIZATION IN HYDROENVIRONMENTAL MODELING SYSTEMS

J.P. Holland*, J.F. Peters, and S. E. Howington
U.S. Army Engineer Research and Development Center
Vicksburg, MS 39180

R.S. Maier
Army High Performance Computing Research Center
Minneapolis, MN 55415

1. INTRODUCTION

The U.S. Army Engineer Research and Development Center (ERDC) is continuing its development of a series of groundwater, surface water, and watershed modeling systems in support of environmental quality and battlespace environment issues for the Army and the Tri-services. Applications of these systems are conducted by multiple organizations (e.g., U.S. Army Corps of Engineers field offices, U.S. Army, Navy, and Air Force installations, Department of Energy, Environmental Protection Agency (EPA), academia, etc.). These applications involve risk and tradeoff analyses for impact assessment, compliance and regulatory issues, site cleanup, risk reduction, and natural/cultural resource management in training/testing environments. These modeling systems are also used to assess littoral and coastal battlespace environmental conditions in support of logistics-over-the-shore, special operations, and mobility. Note that each of these tools is actually a computational system within itself, providing access to multiple models, analysis tools, visualization, animation, parameterization, etc. ERDC has developed three specific production modeling systems: the Surface Water Modeling System; DoD Groundwater Modeling System; and Watershed Modeling System. Current capabilities of these systems are provided at http://chl.wes.army.mil/software/. The models and analysis tools within these systems undergo almost continual computational and scientific modernization.

2. COMPUTATIONAL MODERNIZATION

Many of the hydroenvironmental challenges facing the Army and DoD require computational sophistication orders of magnitude beyond the current state of practice. As such, these problems tax the full capabilities of high performance computing (HPC) resources. Modernization of the computational kernels of ERDC's modeling systems is key to the efficient use of these systems. Flexibility and portability are key aspects of ERDC's computational algorithm modernization on scalable HPC platforms. This is due, in large part, to the diversity of the HPC resources available with DoD. ERDC has targeted the following HPC architectures for implementation of its modeling systems: Cray T3E, IBM SP and SMP, SGI Power Challenge Array, and the SGI Origin 2000. Given this breadth of architectures, and the desire to maintain an optimum amount of model code for both scalable and single-processor machines, ERDC has adopted a scalable algorithm development paradigm centered on the use of:

- FORTRAN 77, 90, and C languages
- Message passing via MPI with single program, multiple data constructs
- Grid partitioning with each processing element owning a portion of the numerical domain
- Use of ghost nodes and elements, where the nodes of a given element are owned by different processors
- Load balancing, using software tools such as METIS from the Army High Performance Computing Research Center
- Use of pre- and post-processing to augment smooth model execution on the scalable HPC machines

Several of the models within ERDC-developed modeling systems have been modernized based on the paradigm listed above. Scalable efficiencies between 50 and 90% have been observed following modernization of these codes.

3. SCIENTIFIC MODERNIZATION

The use of HPC is facilitating improvements in the scientific understanding underpinning ERDC's hydro-environmental modeling capabilities. As an example, several flow and transport processes are fundamental to all hydroenvironmental models, and understanding how to account for scale in conceptualization of these processes is essential to prediction robustness. In the case of reactive transport in the subsurface, a primary process governing such transport, dispersion, occurs at scales generally too small to fully realize with even the best laboratory apparatus. However, the combination of multi-scale, controlled physical experimentation with multi-scale, highly-resolved numerical modeling provides a level of scientific insight heretofore unachieved.

ERDC is employing a "virtual" computational laboratory that provides the detailed observations needed

to quantify the statistical picture of subsurface transport processes (such as dispersion as discussed below) while the physical laboratory serves as a link to reality. Ultimately, the new process discoveries made through the use of the virtual laboratory are codified and implemented within engineering-scale models for field applications.

The traditional approach for simulating transport is built around the advection-dispersion equation (ADE). The ADE simply is a mass conservation statement for the constituent stating that the change in mass within a control volume equals the net flux through its boundaries by advection and dispersion, or

$$\frac{\partial c}{\partial t} = -\nabla \cdot (\mathbf{vc}) + \nabla (\mathbf{D} \cdot \nabla \mathbf{c}) \qquad (1)$$

where **c** is concentration, **t** is time, **v** is transport velocity, and **D** is the dispersion coefficient. This equation lumps the net translation of a constituent (e.g., contaminant) into an advection term and the net spreading into the dispersion term. To apply the ADE, one must *choose* appropriate coefficients for the advective and dispersive terms of the equation. Selection of the dispersivity coefficient is complicated in the subsurface because natural porous media are made up of a series of discrete scales that affect local dispersion as a function of both space and time. Unfortunately, selection of the dispersion coefficient is also key to the numerical solution of Equation (1).

Three types of numerical models (lattice-Boltzman, highly-resolved Darcy-scale, and network) are being used to investigate scale-independent methods to predict the dispersivity coefficient. Calculations of over 1 billion nodes, requiring the use of 216 processors on DoD scalable HPC architectures, were conducted. These calculations required up to several weeks to fully complete execution. These virtual laboratory calculations compared favorably with controlled physical experimental results.

4. RESULTS FROM APPLICATION OF THE VIRTUAL LABORATORY TO DISPERSION

The correlation statistics of subsurface velocity over space and time (referred to as velocity persistence hereafter) are key to producing a physically-correct model of dispersion. Through the use of the virtual laboratory, coupled with physical experimentation at amenable scales as an anchor to reality, we are able to quantify velocity correlation.

Using statistics on velocity persistence derived from the virtual laboratory, dispersion is mathematically conceptualized as the transition of particles from one velocity group to another over an interval of time. Time can be represented as a sequence of finite steps during which the particles change randomly from one group to another. The probabilities of transition are represented by a Markov matrix such that the fraction of particles within a group that are transitioned into another group are given as

$$\{\mathbf{f}\}_{i+1} = [\mathbf{M}]\{\mathbf{f}\}_i \qquad (2)$$

where $\{\mathbf{f}\}_{i+1}$ is the vector of particle fraction in each velocity class at t_{i+1} , $\{\mathbf{f}\}_i$ is the fraction at t_i, and [**M**] is the transition matrix. For each state k, the transition cumulative probability distribution is computed from the kth column in [**M**].

The transition model produces realistic plumes, is easy to incorporate into existing particle tracking transport models and is easy to calibrate. Non-symmetric entries in the transition matrix reflect different rates for sorption and desorption or irreversible reaction paths. Thus, complicated geochemical pathways can be modeled by a simple robust scheme that does not depend on sophisticated solutions to the advective transport equations. Conceivably, all processes could be dealt with as part of a first-order Markov transition process, giving rise to a single efficient algorithm that covers all transport and fate processes. Such a model would make particularly efficient use of HPC resources.

The representation of differential advection as a collection of velocity groups is effectively *a multiple porosity* model. The continuum is envisioned as multiple parallel continua, each having assigned one of the group velocities. The continua interact through exchange of mass. The coefficients defining the rate of exchange among the continua are derived from the transition matrix. The multiple porosity concept is amenable to traditional numerical implementations of the ADE by recognizing that the particle tracking process for a given velocity group is a approximation of the advection-diffusion with source-sink terms. In effect, the mass within a velocity is transported as though it is a distinct species. Thus, the concentration $\sum_\tau c_\tau(t)$ is the sum of concentrations

$$\frac{\partial c_\tau}{\partial t} = -\nabla \cdot v_\tau c_\tau + \nabla \cdot D_\tau \cdot \nabla c_\tau + \sum_i A_{\tau i} c_i \qquad (3)$$

The transfer coefficients A define the rate at which mass from each group is transferred to other groups. These coefficients are related to the matrix [**M**] by

$$[\mathbf{A}] = \frac{1}{\tau} \log [\mathbf{M}] \qquad (4)$$

where [**M**] is defined for a time interval .

We are presently implementing these continuum formulation concepts for dispersion into our engineering-scale subsurface models in order to assure that the best scientific understanding is being used in support of installation cleanup.

ISOLATION OF AN RDX-DEGRADING ACETOGENIC BACTERIUM FROM A MIXED CULTURE THAT DEGRADES TNT, RDX, AND HMX UNDER ANAEROBIC CONDITIONS

Neal R. Adrian* and Clint M. Arnett
Army Corps of Engineers, Engineer Research and Development Center
Construction Engineering Research Laboratory, P.O. Box 9005
Champaign, IL 61826-9005

Hexahydro-1,3,5-trinitro-1,3,5-triazine (RDX), octahydro-1,3,5,7-tetranitro-1,3,5,7-tetrazocine (HMX), and 2,4,6-trinitrotoluene (TNT) are three explosives widely used by the military. Explosives manufacturing and munitions assembly and demilitarization operations generate large amounts of wastewater contaminated with TNT, RDX, and HMX. Improper disposal of this wastewater in the past has resulted in extensive contamination of soils throughout the United States and Europe. Leaching of the explosives through these contaminated soils has resulted in groundwater contamination. Due to the toxicity of TNT and to a lesser extent RDX and HMX, these compounds typically must be removed from the water.

Activated carbon is most frequently used to remove explosives from aqueous streams. Controlling treatment costs, however, by using more cost-effective alternatives to activated carbon is a high priority for the Army. Anaerobic biotreatment is a promising alternative. The objective of this research was to study the microbiological factors controlling the biodegradation of explosives by a mixed culture incubated under anaerobic conditions.

The anaerobic biodegradation of TNT, RDX, and HMX by a mixed culture was studied under methanogenic conditions. Microcosms (160 ml serum bottles) containing a basal medium and the culture (20%, v/v) contained either 10 mM ethanol, propylene glycol, butyrate, or a headspace of 80% H_2:20% CO_2 (1.7 ATM) as the sole electron donor. High pressure liquid chromatography (HPLC) was used to determine TNT, RDX, HMX, butyrate, propionate, and acetate concentrations, while gas chromatography (GC) was used for determining ethanol, propylene glycol, and methane concentrations.

More than 25 μM RDX was degraded within 14 days when ethanol, propylene glycol, and H_2 were added as electron donors, with degradation rates of 3.1, 2.3 and 2.0 μM day^{-1}, respectively. As RDX was degraded, the transient formation of RDX reduction products was observed. The RDX degradation rate in bottles amended with butyrate was similar to that observed for the electron donor unamended control (0.3 μM day^{-1}). Ethanol and propylene glycol were depleted within 6 days, while there was no loss of butyrate. In RDX unamended control bottles, the addition of ethanol, propylene glycol, and H_2 resulted in the formation of CH_4, but in bottles containing RDX no CH_4 was observed, despite the depletion of the electron donor. After RDX was completely degraded, CH_4 production was observed in bottles amended with ethanol and H_2.

Results from the assays indicated the methanogens were reversibly inhibited by the presence of the explosives. Further evidence of this was indicated by the dissolved H_2 concentrations. In the presence of RDX, the dissolved H_2 concentration is at least tenfold more (710 nm) compared to the RDX unamended control bottles. In these bottles the dissolved H_2 concentration averaged 60 nM. The inhibition of the methanogens may influence the ability of the explosive degrading bacteria to compete for the available H_2. Some evidence suggests the explosives may also inhibit butyrate degradation and to a lesser extent ethanol and propylene glycol degradation, although it is not clear whether this is direct inhibition of the butyrate degrading syntrophs or a consequence of unfavorable thermodynamics caused by an accumulation of H_2.

All three explosives (TNT, RDX, and HMX) were degraded when added as a mixture with the rate of degradation being TNT > RDX > HMX (Table 1). Ethanol provided the most rapid transformation of the explosives, followed by H_2 and propylene glycol. Butyrate did not support the transformation of the explosives.

We hypothesized that the H_2 produced during the metabolism of the reduced electron donors supplied the immediate electron donor for the biodegradation of the explosives. This was supported by our studies demonstrating that the addition of H_2 as the sole electron donor supported TNT, RDX, and HMX degradation, and by the studies indicating that in the presence of RDX, the dissolved H_2 concentration was at least tenfold

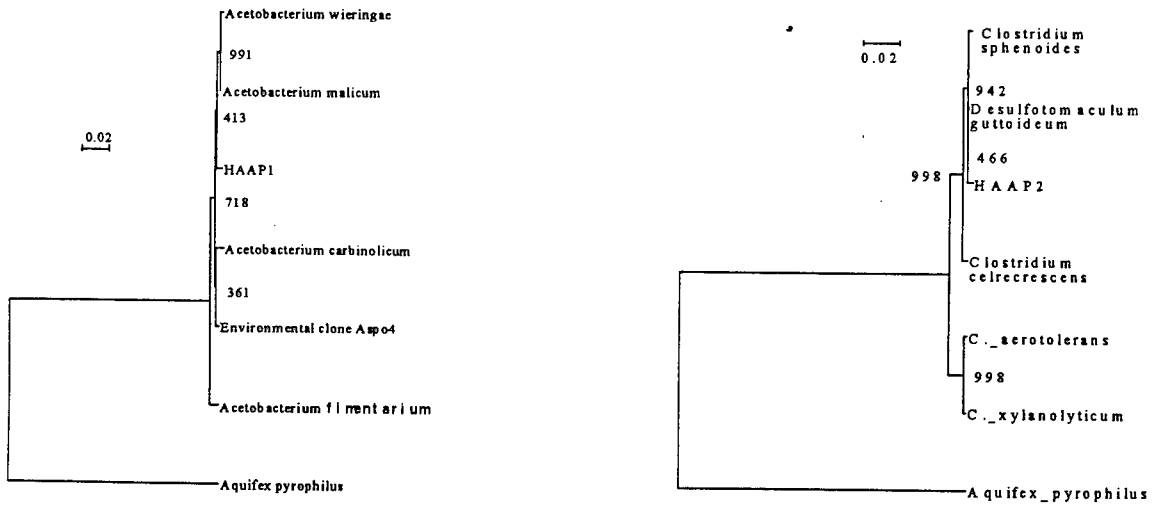


Figure 1. Phylogenetic tree of strains HAAP-1 (left side) and HAAP-2 (right side). Distance reference bar refers to 0.02 base differences per base in the sequence. The numbers refer to the number of times out of 1000 the identified organisms on a particular branch ended up in that location (boot-strap analysis). *Aquifex pyrophilus* is included as an out-group.

more compared to RDX unamended controls. We attempted to enrich for the explosive-degrading bacteria by serially transferring the culture in tubes containing only H_2 and RDX. After several transfers, a culture was obtained that contained predominantly gram-positive, rod-shaped, nonfluorescent cells. Analysis of the culture by denaturing gradient gel electrophoresis of the 16S rDNA revealed one dominant band belonging to the genus *Acetobacterium*. The culture degraded RDX at a rate of 1.6 μM/day and formed acetate at a rate of 2.4 mM/day for 14 days. In the absence of H_2, RDX was degraded at 0.4 μM/day for 14 days. Acetate production was minimal with approximately 1.0 mM being produced in 14 days. RDX degradation did not occur in sterile controls or cultures containing O_2.

Table 1. Explosive degradation rates in serum bottles amended with various electron donors. Degradation rates reported as μM day^{-1}.

Electron Donor	Degradation Rate		
	TNT	RDX	HMX
Ethanol	>50	5.7	0.2
Hydrogen	>50	2.7	0.1
Propylene Glycol	>50	1.6	0.1
Butyrate	>50	0	0

The culture was plated onto solid medium containing 0.1% yeast extract (Y.E.) in a glove box and incubated in an anaerobe jar containing a 80% H_2:20% CO_2 atmosphere. After 5 days incubation two colony types, HAAP-1 and HAAP-2, were observed growing on the surface of the agar. These were transferred to a Balch tube containing a mineral medium with 0.1% Y.E. and a H_2 headspace (80% H_2:20% CO_2, 1.7 ATM). Sequencing of the 16S rDNA of isolate HAAP-1 indicated it was closely related to *Acetobacterium malicum*, while isolate HAAP-2 was closely related to *Desulfotomaculum guttoideum* (Figure 1).

Our studies illustrate the importance of H_2 in facilitating the biodegradation of TNT, RDX, and HMX. The addition of reduced electron donors that result in the release of H_2 during their metabolism provide the immediate electron donor for the explosive-degrading bacteria. The presence of a dominant acetogenic bacterial population in the mixed culture and the isolation of strain HAAP-1, an acetogenic bacterium that degrades RDX, supports our contention. Our findings provide a better understanding of the factors controlling the biodegradation of explosives and indicate several potential strategies for implementing a biotreatment approach for explosive-contaminated environments.

BACTERIAL PATHOGENS OF ANIMALS AND PLANTS: HOMOLOGOUS GENETIC TARGETS WITHIN THE TYPE III SECRETION SYSTEMS

Sheila J Wood*
SBCCOM, ECBC, AMSSB-RRT-BE, APG ,MD 21010-5424
Sheila.wood@sbccom.apgea.army.mil
410 436 8403

The objective of this study is to enable the simultaneous detection of both plant and human bacterial pathogens by targeting the carriage of the functioning virulence capability for Type III secretions.

Biological warfare can be thought of as the terrorists' ability to cripple a campaign or segment of society. This can be accomplished via the delivery of a human pathogen, and/or contamination of our animal and plant food stores. Recently, it has been shown that some human bacterial pathogens and plant bacterial pathogens harbor homologous sets of genes for the production of virulence. These genes are responsible for the production of Type III secretion systems. This study will design tools that recognize these genes to enable predictions about the probable cause of simultaneous human and plant diseases.

Within the last five years, studies have shown that certain bacteria pathogenic for humans and bacteria pathogenic for plants share distinct homologies within gene clusters that encode the Type III secretion apparatus. Type III secretion systems translocate proteins into the cytosol of eukarytic cells, where the translocated proteins facilitate bacterial pathogenesis by specifically interfering with host cell signal transduction and other cellular processes. The genes encoding Type III secretion systems are clustered and evidence suggests that horizontal genetic transfer acquired these systems during evolution. Some Type III secretion systems are activated by bacterial contact with host cell surfaces. Gene expression is coordinately regulated in response to host cell environmental stimuli.

This study will, by comparison of the structure, function, regulation and impact on host cells of the Type III secretion systems, target both homologous and unique genes from *Yersinia spp., Pseudomonas aeruginosa, Shigella flexneri, Salmonella typhimurium,* enteropathogenic *Escherichia coli,* and the plant pathogens *Pseudomonas syringae, Erwinia spp., Ralstonia solanacearum, Xanthomonas campestris,* and *Rhizobium spp.*

Since the genes encoding Type III secretion systems are clustered, homologous areas within these clusters will be targeted. In some organisms, the gene clusters are located on plasmids, which are unique to the pathogen and are not found in pathogenic relatives. In other pathogens, Type III secretion gene clusters are located on the chromosome and often appear to have been acquired during evolution, since related nonpathogenic bacteria lack these pathogenesis islands but share corresponding adjacent sequences.

Results confirm that the targets can be found in each organism using gene amplification with DNA primer/probe sets specific for selected genes.

THIS PAGE INTENTIONALLY LEFT BLANK

SUPPORT FOR RAPID ENVIRONMENTAL ASSESSMENT USING AIRBORNE LIDAR TECHNOLOGY

J. L. Irish*, W. J. Lillycrop
US Army Engineer Research and Development Center
Coastal and Hydraulics Laboratory
Joint Airborne Lidar Bathymetry Technical Center of Expertise
109 St. Joseph Street
Mobile, AL 36602-3630

R. W. Pope
US Naval Meteorology and Oceanography Command
US Naval Oceanographic Office
Joint Airborne Lidar Bathymetry Technical Center of Expertise
1002 Balch Boulevard
Stennis Space Center, MS 39522-5001

SUMMARY

Most military deployments of today are initiated at short notice and involve maneuvering of maritime forces in highly variable littoral waters that are not well known and where opponents pose a significant threat (NATO, 2000). In addition, force projection has changed drastically over the past decade (and continues to evolve) requiring faster, more flexible capabilities in order to effectively, and with minimal risk, deploy rapidly worldwide. Further challenges are created by the requirements to perform missions spanning the continuum of military operations and now including crisis response, peace support and humanitarian operations. Our military must continually train and bring new techniques and technologies into operation to be ready to respond to the most challenging problems.

In April 2000, the North Atlantic Treaty Organization (NATO) conducted the LINKED SEAS 2000 (LS00) peace support training exercise in Portugal. The LS00 objective was to resolve a border conflict between two fictional non-NATO countries. The LS00 focused on NATO's evolving military vision for crisis response, peace support and humanitarian operations, possibly conducted beyond its normal area of responsibility. A primary goal of LS00 was to include a Rapid Environmental Assessment (REA) operation to support 80 Warships, 2 Marine Battalions, 11 Special Forces Teams, and 125 aircraft. REA objectives included characterization of physical, meteorological and hydrodynamic properties of a proposed amphibious landing site. An important component for REA is accurate and detailed terrain mapping.

A primary objective of the LS00 REA Team was to test operational assets for rapidly carrying out a coordinated environmental reconnaissance operation employing air, sea, and space sensors combined with archived data searches and computer modeling. The purpose was to fuse data and information in order to characterize unfamiliar littoral operating areas. One such system used by the LS00 REA Team was the SHOALS (Scanning Hydrographic Operational Airborne Lidar Survey) system for mapping and charting (Fig. 1; Irish *et al.*, 2000). Using state-of-the-art lidar technology from a Twin Otter aircraft, SHOALS collects 400 soundings and elevations per second with an accuracy of 15 cm in the vertical and 3 m in the horizontal. SHOALS is operated through the Joint Airborne Lidar Bathymetry Technical Center of Expertise (JALBTCX), a partnership between the US Army Corps of Engineers (USACE) and the US Naval Meteorology and Oceanography Command. The JALBTCX's main goal for participating in the REA and LS00 was to demonstrate, using a state-of-the-art system, the potential value of airborne lidar mapping and charting to support the warfighter.



Fig. 1: The SHOALS system.

SHOALS bathymetry, topography, and supporting ancillary data were collected at two sites and SHOALS final product for the REA included color contoured depths, beach elevations, and beach survey cross-

sections plotted along several transects through the amphibious landing zone (Fig. 2). This presentation of the data provided the warfighter with instant knowledge of depths, obstacles, and hazards so that a safe approach could be made. The beach surveys accurately measured the beach slope and width so that decisions on appropriate vehicles could be made a priori to the landing. To augment the survey information, digital pictures collected during each flight were included on the final plots, thus giving the warfighter and planner visual detail of vegetation and other potential hazards.

SHOALS participation in NATO's LS00 REA demonstrated its capability for rapidly and accurately collecting environmental data for use in planning amphibious landings. In addition, SHOALS was the only system (of those participating in LS00) capable of collecting data during moderate wind and rough surf conditions. SHOALS' ability to collect bathymetry, topography, and supporting ancillary data, at aircraft speeds, led one LS00 participant to comment "SHOALS put the Rapid in REA."

This paper describes airborne lidar hydrography (ALH) and SHOALS technology and highlights the LS00 mission. Results from this operation clearly demonstrated SHOALS abilities and the potential for airborne lidar technology to support the warfighter.

ACKNOWLEDGMENTS

The projects, analysis, and resulting data described herein, unless otherwise noted, were obtained from work funded by or performed by the US Naval Oceanographic Office/US Army Corps of Engineers Joint Airborne Lidar Bathymetry Technical Center of Expertise. The use of trade names does not constitute an endorsement in the use of these products by the US Government. Permission was granted by the Chief of Engineers to publish this work.

REFERENCES

Irish, J. L., J. K. McClung, and W. J. Lillycrop, 2000: Airborne lidar bathymetry: the SHOALS system. *PIANC Bulletin*, **2000(103)**, 43-53.

NATO, cited 2000: NATO Update: 26 April – 2 May 2000. [Available online from http://www.nato.int/docu/update/2000/0426/e.htm.].

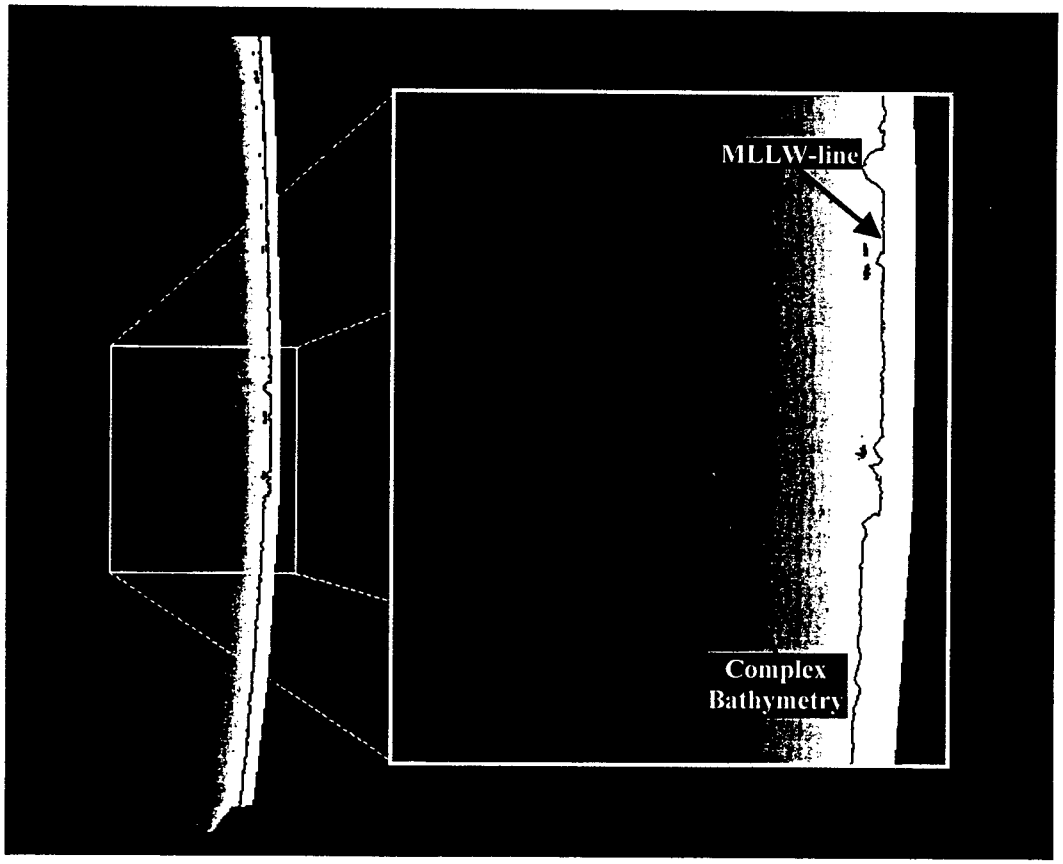


Fig. 2: SHOALS bathymetry and topography at Pinheiro da Cruz, Portugal (April 2000). Deeper depths are darker. North is to top.

NON-THERMAL PLASMAS: A NEW REMEDIATION TECHNOLOGY FOR CLEANUP AND DECONTAMINATION

Michael J. Nusca*, Andrzej W. Miziolek, and Robert G. Daniel
Weapons and Materials Research Directorate
Army Research Laboratory, Aberdeen Proving Ground, MD 21005

Louis A. Rosocha
Los Alamos National Laboratory, Los Alamos, NM 87545

John T. Herron and Robert E. Huie
National Institute of Standards and Technology, Gaithersburg, MD 20899

K. Urashima and J.S. Chang
McMaster University, Ontario, Canada, L8S4M1

SUMMARY

Because of a greater emphasis on environmental issues, increasing regulations, and increased scrutiny by regulators, there is a growing need to control the emission of oxides of nitrogen (NO_x) and hazardous air pollutants (HAPs) - including volatile organic compounds (VOCs) - at DoD installations. These emissions are frequently episodic (e.g., JETCs - jet engine test cells; painting, stripping and cleaning operations) are variable, with toxic gas loadings spanning a large concentration range from parts-per-million (ppm) to parts-per-thousand (ppt). Incentives for implementing new pollution-control technologies are both regulatory and economic. Given considerable regulatory pressure, e.g., the promulgation of a NESHAPS (National Emissions Standard for Hazardous Air Pollutants) for NO_x emissions in CY 2000, new de-NO_x technologies are necessarily being explored. Last year the Army published the "FY99 Army Environmental Requirements and Technology Assessments (AERTA)" report by the US Army Environmental Center. This report provides a prioritized list of technology requirements for all four environmental pillars: Restoration, Compliance, Pollution Prevention, and Conservation. Accordingly, Army efforts aimed at chemical remediation of toxic gases have been progressing. However, existing technologies for high destruction-efficiency NO_x and HAP/VOC control suffer from significant drawbacks. Our overall project objective is to evaluate and develop an emerging technology, namely the non-thermal plasma (NTP) reactor for DoD air emissions and other control applications. In this paper we document the wide applicability of NTPs to the most Army environmental problems, and show that successful deployment of this advanced technology will be of great benefit to the Army through a wide range of restoration and compliance applications.

Non-thermal plasmas (NTPs) represent a promising technology for the destruction of various toxic gases released during military and civilian operations. The history of treating hazardous and toxic chemicals with NTPs goes back over twenty years demonstrating military use for destroying toxic chemical warfare agents with electric discharge reactors and civilian applications for treating flue gases (SO_X and NO_X) from electric power plants and other installations (e.g., steel mills) with electron beams; indeed the electric-discharge-driven NTP-initiation of chemical reactions has a history of nearly one and one-half centuries. NTPs also show promise in the control of toxic gas released from military industrial facilities that treat energetics (i.e., propellants and pyrotechnics) and produce nitro-aromatics and nitramine or nitrite esters, and that process volatile organic compound (VOC) waste from painting/removal and solvent cleaning. The treatment of these wastes produce NO_X. Recently, NTPs have been applied to the reduction of hazardous gases in jet engine and cruise missile test cells (JETC and CMTC) where large amounts of nitric-oxides (NO_Xs) are emitted along with various hydrocarbon (HC) gases on an episodic basis. In April of this year a small, pilot-scale field demonstration using a trailer-mounted reactor and funded by SERDP was carried out at Tinker Air Force Base near Oklahoma City. The field work involved the treatment of a portion of an exhaust stream from a small jet engine test facility and concentrated on the removal of nitric oxide (NO) from the exhaust stream. Preliminary data analysis shows promising performance (in some cases > 80% NO removal). Further analysis of the test data and the writing of a final report on the demonstration is in progress.

The silent discharge or dielectric barrier reactor is used to create transient electrical-discharge streamers in a gas stream that flows parallel to the barriers or plates. The streamer is a source of energetic electrons and other reactive species dissociated from the gas. A relatively high electric field, as determined by the reactor geometry (e.g., gap spacing), gas composition, gas pressure, and gas temperature, is required to cause electrical breakdown in the gas. A circuit connected to the reactor walls supplies

the required breakdown voltage. Charge buildup on the capacitive barriers stabilizes the discharges. Streamers created in all types of atmospheric-pressure discharges can be thought of as cylindrical current filaments with typical radius of about 100 μm lasting only for a few nanoseconds in oxygen or air. These streamers have an average electron energy of about 3-5 eV and an average density of about 10^{14} /cm^3. The electric field strength (E) in the discharge, normalized by the gas number density (N) is about E/N = 100-200 Td (Td = 10^{-17} Volts-cm^2). Electrons in these streamers are hot (1-10s of eV) while the ions and neutral species are near ambient temperature. Electrons do not react directly with NO_X molecules but collide with O_2, N_2 and H_2O molecules producing radical species that are highly reactive and readily decompose entrained pollutants in atmospheric-pressure gas streams; radical-attack reaction rate constants are very large for many chemical species. Non-thermal plasmas generate both oxidative and reductive radicals and therefore can be used to treat a wide variety of pollutants. Using these reactive species, the NTP reactor directs electrical energy into favorable gas chemistry through energetic electrons, rather than using the energy to heat the gas. Radical reactions with NO_X , HCs and VOCs naturally leads to chemical conversion.

In the course of this project our goal has been a closely coupled experimental/computational program aimed at understanding the important physics of the NTP reactor. We have constructed a small-scale channel-flow reactor that includes two ports for inflow and numerous wall-mounted plasma discharge sites distributed along the horizontal channel walls. The power supply provides high-voltage pulses up to 50 kV in amplitude and about 25 ns in duration. A laser-induced florescence (LIF) system, fitted to the reactor for use in the detection of OH, consists of a XeCl excimer laser and a dye laser. The system is tuned to 283 nm and focused into the plasma reactor through windows in the reactor's vertical walls. The red-shifted fluorescence is entered near 315 nm and is collected with a two-lens condenser system. The fluorescence is directed through a broadband interference filter centered at 310 nm (50 nm bandwidth). The laser intensity is measured with a calorimeter. Dispersed fluorescence spectra, collected by an intensified photodiode array, are measured by a monochromator. This system has been made fully operational and test data shows great promise. One of our goals is to compare this data with a computational fluid dynamics (CFD) model of the NTP reactor hat has been developed at the ARL. The CFD code solves the unsteady Navier-Stokes equations including species diffusion, thermal conduction, viscosity, and nonequilibrium chemical kinetics. A reaction mechanism for plasma with dry and wet air along with NO_X and alkenes, including 33 species and 89 reactions, is linked to the code. The computed results shown below demonstrate the ability of the NTP reactor to dissociate NO as gas flows through the NTP reactor. Additional results and comparisons with experimental data are presented and discussed in the paper..

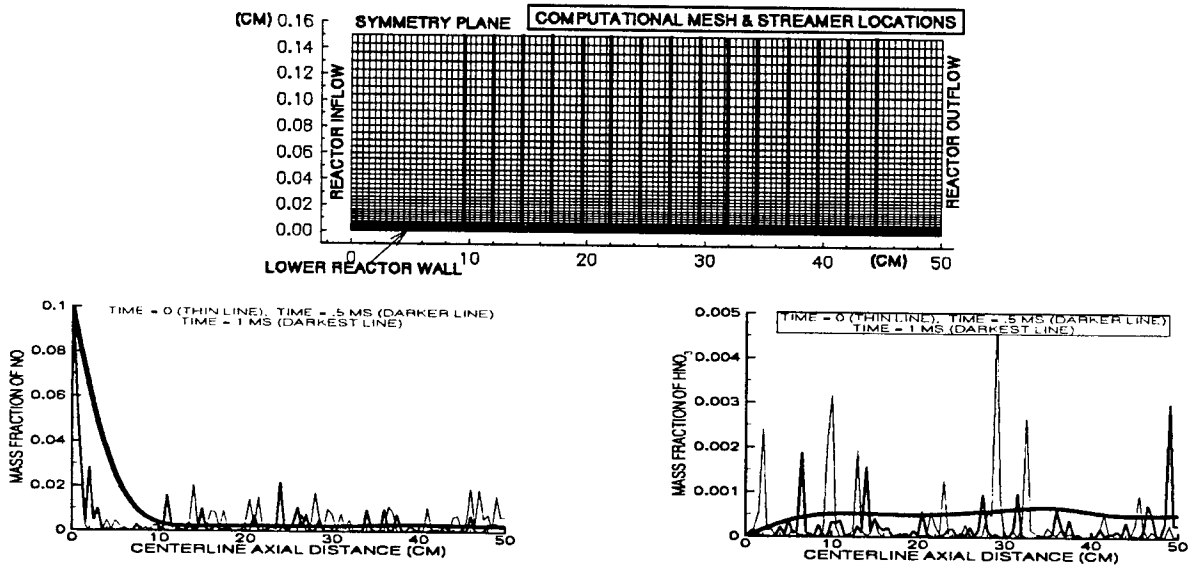


Figure 1. Computational grid for the NTP reactor, showing locations of streamers (top); computed results for channel-flow NTP reactor: left) NO mass fractions, right) HNO3 mass fractions.

ENHANCED COASTAL TRAFFICABILITY USING SAND-FIBER STABILIZATION

R.L. Santoni*, J.L. Tingle, and S.L. Webster
Engineer Research and Development Center
Geotechnical and Structures Laboratory, GSL
Vicksburg, MS 38180

ABSTRACT

Airfield and road construction using synthetic fibers involves mixing small amounts of 2-in-long polypropylene fibers into moist sand using a self-propelled rotary mixer. The sand-fiber layer is compacted, and its surface protected with a resin-modified emulsion. The sand-fiber construction technique reduces construction time, manpower, and construction time by 50, 25, and 25 percent, respectively. Experiments indicate that fiber-reinforced sand roads will carry over 10,000 and 1,000 passes of heavy truck and C-130 aircraft. This technique is applicable for a wide variety of sands and silty sands found around the world.

1. INTRODUCTION

New materials and construction techniques are required to provide civil engineers with alternatives to traditional airfield and road construction during military operations. Quality construction materials are not readily available in many locations and are costly to transport over long distances. Traditional stabilization techniques require specialized skills and equipment to ensure adequate performance. Aircraft operations in a sand environment produce deep ruts up to 14-in, sometimes resulting in aircraft being immobilized. In addition, the new stabilization technique has application for military supply roads and storage areas at remote sites. Therefore, laboratory and field experiments were conducted to evaluate the performance and effectiveness of the sand-fiber stabilization.

2. LABORATORY EXPERIMENT

The laboratory experiment was designed to isolate the effects of sand type, fiber type, fiber length, fiber denier, and fiber dosage rate on the performance of fiber-stabilized sands. The experiment consisted of preparing numerous specimens in which a single test variable was altered to quantify its effect on the specimen's performance. Each specimen was evaluated by conducting unconfined compression tests.

The laboratory experiment involved six different sands ranging from fine sand to coarse sand. The experiment also evaluated the performance of four different types of fibers. The fibers used in the experiment were stabilized for protection against ultraviolet (UV) radiation.

3. ANALYSIS OF LABORATORY RESULTS

The results of the unconfined compression tests were used as an index of specimen performance. The control specimen was a sand specimen prepared at the target moisture content without any fiber reinforcement. The results indicated that all fiber types significantly improved the unconfined compressive strength of all sand types evaluated. The 2-in length fibers significantly increased the performance of the fiber-stabilized specimens at the three deniers evaluated. The results indicated that the optimum dosage rate for stabilizing sands with synthetic fibers lies between 0.6 and 1.0 percent by dry weight of material. The unconfined compressive strength of the test specimens increased slightly with decreasing fiber denier. The specimen performance was enhanced by the inclusion of synthetic fibers at all specimen moisture contents evaluated.

4. FIELD EXPERIMENT

Two full-scale experiment sections were constructed under shelter in Hangar 4 on the Waterways Experiment Station (WES) reservation. In each section, a 12-ft-wide straight traffic lane was designed for channelized traffic over a sand subgrade. For the field experiment, each item was stabilized to a depth of 8 in. The fiber contents and fiber lengths used in the field experiment were selected based upon the results of the laboratory investigation. The field investigation was designed to verify the laboratory results while providing information concerning construction techniques and maintenance procedures. Three resin modified emulsion products were tested: Road Oyl, Pennzsuppress D, and Cousins Pine Sap Emulsion (CPSE). These products were used to protect the fiber on the surface. Plastic hexagonal mats were also evaluated as surfacing material.

Road construction using sand-fiber stabilization technology involves mixing hair-like 2-in long polypropylene fibers into moist sand using a self-propelled rotary mixer. The sand-fiber layer is compacted with a smooth drum vibratory roller. A wearing surface is added by spraying a resin-modified emulsion or emulsified asphalt onto the road surface. Military supply roads over-the-beach or across desert sands can be quickly constructed at remote sites using reduced equipment, manpower, and materials. Experiments conducted at WES indicate that roads constructed using this new technology will carry over 10,000 passes of

heavy military supply traffic with very little or no maintenance required. Sand-fiber stabilization uses existing military construction equipment and requires no special construction skills. Sand-fiber stabilization is applicable for a wide variety of sands and silty sands found around the world (sands classified as SW, SP, SM, and some SM-SC types).

For construction, shape road surface to desired elevation and level sand surface by back-blading with a dozer. If sand is dry add water to bring the moisture content up to a minimum of 2 percent and maximum of optimum moisture content. A moisture content of about 8 percent would be ideal for most sand types. Fiber application rate is 0.8 percent by weight. For roads stabilized to depth of 8-in., the application rate would be 5.1 lb/yd^2 of road surface. Fibers are delivered in 400-lb boxes each containing 20 bags of fibers20-lb/bag. Place one 20-lb bag of fibers on each 3.9 yd^2 of road surface. Open bags of fibers and kick or hand-spread the fibers roughly over the road surface.

Using a self-propelled rotary mixer, mix the fibers into the sand to a depth of 9 in. Usually 4 passes with the rotary mixer will produce a uniform sand-fiber mix. Compact the sand-fiber layer using five passes with a smooth drum vibratory roller. Pre-wet the road surface using a water truck to apply water uniformly at a rate of 1 gal/yd^2. Using a standard bituminous distributor, spray a resin modified emulsion on the road surface at a rate of 1 gal/yd^2. The emulsion should be cold-applied without diluting with water. The modified emulsion will penetrate approximately 0.5 - 1.0 in. into the sand-fiber layer and form a wearing surface. The road can be opened to truck traffic immediately.

6. CONCLUSIONS

6.1 Laboratory

The inclusion of all of the fiber types evaluated in the six sand materials improved the load-bearing capacity of the individual specimens. The optimum fiber length for fiber reinforcement of sand materials is 2 in. The optimum fiber content lies between 0.6 and 1.0 percent by dry weight of material. The fiber denier does not significantly affect the specimen performance. However, the data indicated that smaller-denier fibers appear to slightly outperform larger-denier fibers. An investigation of the effects of moisture on the fiber reinforcement of sands indicated increased performance with increasing moisture content until saturation is attained. Thus, specimen performance was enhanced in both "wet and dry of optimum" conditions. Specimen density decreased with increasing fiber content. The density of the fine sand materials was less affected than the coarse sands.

6.2 Field experiment

The construction and trafficking of the field experiment sections resulted in several conclusions concerning the validation of the laboratory results, the practicality of the construction procedures, and the effectiveness of the maintenance procedures of the stabilized material.

The fiber reinforcement of sand materials was an effective means of stabilization for military truck traffic. The 0.8-percent experiment items provided adequate load support under the applied traffic. The fiber denier did not significantly affect the performance of the experiment items as indicated by the laboratory results. No significant benefit was obtained by using 3-in. fibers instead of the 2-in. fibers. Although only one experiment item contained Yuma sand rather than concrete sand, the results indicated that fiber reinforcement is effective in both sand types. The construction procedures used were extremely practical and effective. The spray-on surfacings were as effective as a mat surfacing. The plastic hexagonal mat can be used as a surfacing but will not provide any added structural support to fiber-stabilized materials. The maintenance procedures used to repair experiment section two were effective in maintaining the performance of the test items. The effective CBR for design purposes, as determined from DCP measurements, is approximately 35 percent. The composite modulus of elasticity of the fiber-stabilized material is approximately 50,000 psi. A Poisson's ratio of 0.35 is a reasonable estimate for design purposes.

ACKNOWLEDGMENTS

Headquarters, U.S. Air Force Civil Engineering Support Agency, Tyndall Air Force Base, and U.S. Army Corps of Engineers sponsored the research reported herein.

REFERENCES

Tingle, J.S. and Webster, S. L. "Contingency Airfield and Road Construction Using Geosynthetic Fiber Stabilization of Sands," Technical Report GL-97-4, U.S. Army Engineer Research and Development Center, Vicksburg, MS. April 1997.

Tingle, J.S., Webster, S. L., and Santoni, R. L. "Discrete fiber reinforcement of sands for expedient road construction," Technical Report GL-93-3, U.S. Army Engineer Research and Development Center, Vicksburg, MS. March 1993.

Webster, S. L. and Santoni, R. L. "Contingency airfield and road construction using geosynthetic fiber stabilization of sands," Technical Report GL-97-4, U.S. Army Engineer Research and Development Center, Vicksburg, MS. April 1997.

BROAD BANDWIDTH LIDAR FOR STANDOFF BIOAERSOL SIZE DISTRIBUTION DETERMINATION

James B. Gillespie, David L. Ligon , Paul M. Pellegrino, and Nicholas F. Fell, Jr. , U.S. Army Research Laboratory, 2800 Powder Mill Road, Adelphi, MD 20783-1197

Current lidar systems used for bioaerosol detection utilize either elastic backscatter to detect the presence of any aerosol cloud or use UV induced fluorescence to detect a potential bioaerosol. Both of these existing technologies have serious drawbacks. A system based on elastic scattering yields no specificity about the optical properties of the particles. In a scanning mode of operation an elastic scattering system can map out a "picture" of the aerosol plume if the plume is detected as it is being dispersed. In many operational situations there will be aerosol plumes everywhere on the battlefield; so this type of information will not be of sufficient use. The fluorescence lidar systems will not work satisfactorily during daytime operation, have short range, and are not eye-safe. They also lack specificity for identification of the aerosol. That type of system should, however, be able to determine the presence of biological aerosol, but there is often a large amount of natural biological material in the atmosphere. We are examining a third possibility—that of using a broad bandwidth (hyperspectral) lidar system to estimate size distributions of aerosol clouds that may possess respirable biological particles. This type of system should have greater range than a UV fluorescence system, would have both daytime and nighttime operation, and provide some optical property information about the aerosol plume. The concept is to illuminate aerosols with a pulse of intense light from a hybrid laser system that puts out a broad bandwidth of light, collect the backscattered light as a function of wavelength, rapidly analyze it with novel inversion algorithms and estimate the size distribution of the aerosol. Our type of system would have a spectral output of 1.4 to 1.8 micrometers. This is in the eye-safe region and is actually optimized for the detection of particles in the one to ten micrometer size range. This is the respirable particle range. Most natural atmospheric aerosols are submicrometer in size except for pollens which are generally larger than fifteen micrometers, fogs and mists which are often much larger than 10 micrometers and which are meteorologically predictable, and blown soil particles which are generally much larger than ten micrometers. There is also a bacteria component that is normally a few
hundred to several thousand particles per cubic meter of air; however measurements can be made beforehand to determine background concentrations prior to operations. For a hyperspectral lidar to be realizable, we must have: (a) a source and (b) a method to analyze the data. We have developed both of these capabilities. We describe and characterize the laser source that we have developed and we describe the inverse Monte Carlo algorithm that we have developed to apply to this problem. We have performed a comprehensive simulation of our inversion method and include noise in this simulation.

The source for this system is a Nd:YAG pumped optical parametric oscillator (OPO) that has been specially designed to operate near the degenerate angle and produce a broad bandwidth idler in the 1.5 spectral region. This OPO, made of BBO, was designed and fabricated for us by researchers at DERA in the UK. Extensive modeling was done to determine a low-angle solution and cavity design that would meet our needs. Figure 1 depicts the modeling solution for the OPO for the idler operation.

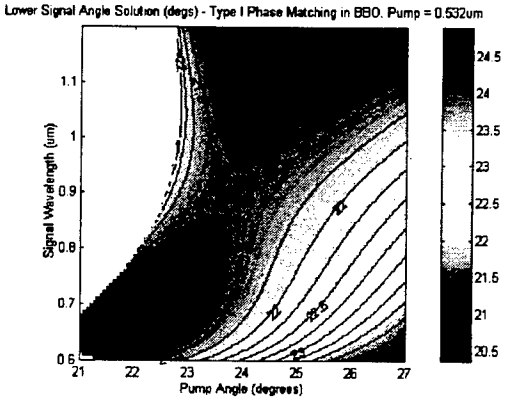


Figure 1. Modeling to determine the low angle solution for broad bandwidth operation.

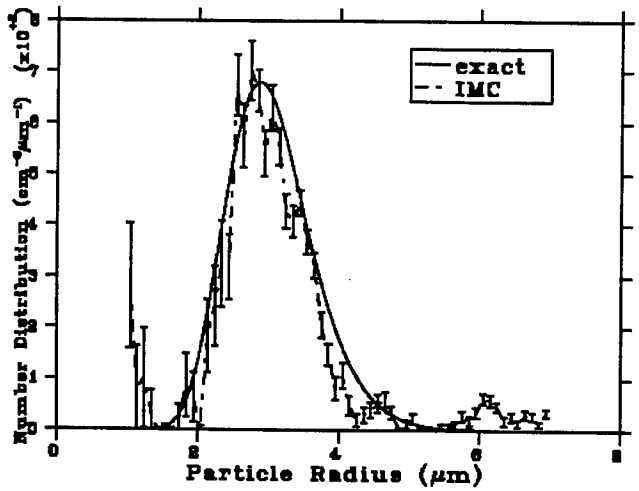


Figure 2 shows the results of a simulation to determine a size aerosol for that has a modal radius of 3 micrometers and has particles that are about 1 to 5 micrometers in radius (typical of bacterial spores).

The Inverse Monte Carlo data analysis method was developed at ARL and used to perform simulations to determine the applicability of the concept. Results show that aerosol size distributions in the 1 to 10 micrometer size range can be successfully inferred by this technique.

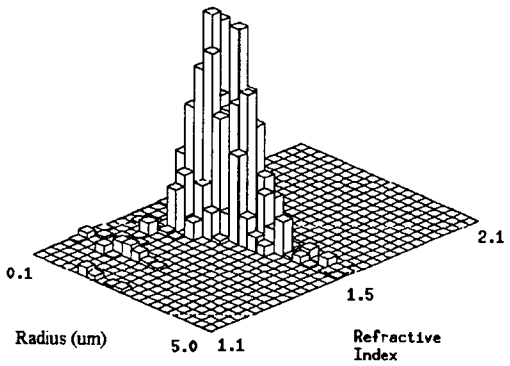


Figure 3 shows the methodology used to construct the size distributions by Monte Carlo techniques. Walkers are distributed on a grid and iteratively moved around to produce a size distribution that will reproduce the original backscattering data within a few percent.

The process solves a Fredholm integral of the first kind (such as for Mie scattering) and takes from a few seconds of computer time to as many as 20 minutes. Typical run times are less than 2 minutes on a desktop workstation. If sufficient data are available, this technique will also accurately estimate the refractive index of the particles.

This type of lidar system is intended to be a first alert, that is, it will detect an aerosol plume that is predominately composed of respirable particles and which could be a bioaerosol threat that would require more specific interrogation.

References:

D.A. Ligon, T.W. Chen, and J.B. Gillespie, "Determination of Aerosol parameters from light scattering data using an inverse Monte Carlo technique" Applied Optics 35, 21, PP4297-4303, July 20, 1996

D. A. Ligon, J.B. Gillespie, P.M. Pellegrino, *"Aerosol properties from spectral extinction and backscatter using an inverse Monte-Carlo method"*, Applied Optics, Aug 20, 2000,

James B. Gillespie and David Ligon, " A Lidar Inversion Algorithm To Remotely Determine Aerosol Size Distributions Utilizing A Broad Bandwidth Laser Technique," *Joint Workshop for Standoff Detection of Chemical and Biological Agents*", Williamsburg, VA, 28 Oct 1998

PASSIVE ACOUSTIC LOCALIZATION IN ATMOSPHERIC TURBULENCE: EXPERIMENT AND THEORY

D. Keith Wilson* and Sandra L. Collier
Army Research Laboratory, AMSRL-CI-EP
Adelphi, MD 20783-1197

ABSTRACT

Turbulence and other random atmospheric phenomena cause the apparent position of an acoustic source to fluctuate, interfering with the ability of a sensor array to track the source. For examination of these fluctuations, a vertical planar array of 32 microphones was constructed and used to monitor the apparent bearing angles of a distant, stationary source. Substantial fluctuations in the angles were observed during both daytime and nighttime conditions. A theory based on calculation of the Fisher information was formulated to predict lower bounds on the variances of the bearing angles. Comparisons between the theory and experimental data suggest that a parametric algorithm that accounts for the turbulence effect is needed to obtain optimal target tracking.

1. INTRODUCTION

Acoustical detection and tracking systems will likely play a prominent role on the future battlefield, where situational awareness will be a key factor affecting the survivability of light forces. The advantages of acoustical sensors include low cost, small size, passive operation, and operational capabilities in non-line-of-sight conditions. But their performance does depend strongly on environmental conditions. In this paper we address the interaction of sound waves with turbulence and other random atmospheric motions, a process that randomly distorts the propagating wavefronts. As the wavefronts propagate from the source (target) to the receiving array, they can accumulate substantial random variations in their orientation and intensity, which are perceived as fluctuations in the apparent bearing angles and strength of the source.

We begin the paper with experimental observations of fluctuations in the apparent elevation and azimuth of a source resulting from propagation over a distance typical of Army tactical scenarios. We then discuss our efforts to develop a theoretical model for these fluctuations based on a calculation of the stochastic Fisher information available to the sensor array.

2. EXPERIMENT

For the purpose of studying fluctuations in virtual source bearing angles and received intensity resulting from propagation through the atmosphere, researchers from the Army Research Laboratory and Penn State's Applied Research Laboratory collaborated in the design and construction of an "imaging" microphone array. Completed in June 1998, the array was a vertical planar configuration with 32 microphones. The microphones were arranged in eight horizontal rows and four vertical columns. The rows were spaced 0.75 m apart and the columns 0.98 m. The large size of the array created a relatively narrow beam pattern, analogous to the manner by which an lens focuses light.

The acoustic source in the experiment was located 1.2 m above the ground at a distance of 770 m from the array. Five harmonic tones between 50 and 250 Hz were broadcast. Three 20-min trials were selected for detailed analysis in this paper: the first took place on a moderately windy evening; the second on a clear, still night with a strong temperature inversion (positive temperature gradient); and the third on a cloudy morning with light winds, shortly after a rain shower.

Figures 1 and 2 show the apparent azimuth and elevation monitored at the imaging array for all three trials. We determined these angles by tracking the maximum of a two-dimensional spatial fast Fourier transform (FFT) beamformer at 250 Hz. The average azimuthal angle is nearly the same for each trial (about 2°). The average elevation angle, however, varies from trial to trial due to refraction by atmospheric wind and temperature gradients. The variance in the arrival angles also exhibits a distinct dependence on atmospheric conditions, being highest for the moderately windy afternoon (1738 on 18 June). For this trial, the observed standard deviations of the elevation and azimuth correspond to displacements of 17 m and 18 m in the apparent vertical and horizontal positions of the source, respectively. At night, strong variations in the bearings are also observed to occur, although more slowly than during the day.

3. THEORY

An attractive method for determining uncertainties in statistical estimates is to calculate the Fisher information available from the observing system (Kay, 1993). This method is usually much simpler than calculating uncertainties for the system and an actual processing algorithm. The matrix inverse of the Fisher information, called the Cramer-Rao lower bound (CRLB), is the theoretical lower limit on the variance of the estimate about its actual value. A well

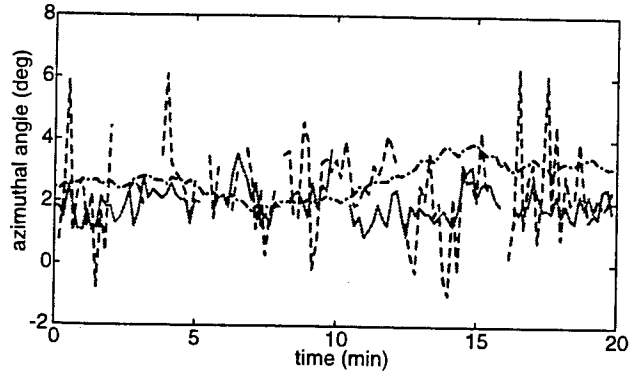


Fig. 1: Apparent source azimuth at 250 Hz. Three 20-min trials are shown, starting at 1738 on 18 June 1998 (dashed line), 2220 on 18 June (dash-dotted line), and 1033 on 19 June (solid line).

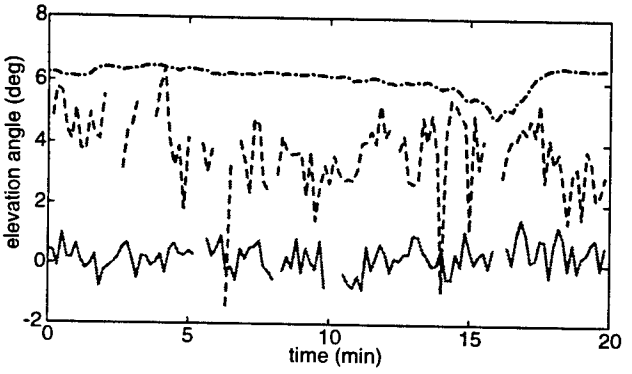


Fig. 2: Apparent source elevation at 250 Hz. Legend same as Fig. 1.

conceived processing algorithm should attain performance close to, but not better than, the CRLB.

In applying the CRLB methodology to target bearing estimates from arrays, we assume that the signal of interest and the interfering noise both have Gaussian statistics. An equation for the Fisher information valid for this situation was derived by Kay (1993). We apply Kay's equation with the unknowns being the azimuth and elevation of the source. The Fisher-information formulation requires the first and the second moments of the propagating sound-pressure field. We calculate these quantities based on results from the theory of wave propagation in random media (Ishimaru, 1978), which predicts the rates of decay of the moments as functions of the turbulence statistics. Our model for the atmospheric turbulence is based on von Kármán's spectrum (Ostashev and Wilson, 2000). The model includes contributions to the sound speed from wind and temperature fluctuations, produced by both shear and buoyancy instabilities in the near-ground atmosphere.

Table 1 compares the CRLB predictions to the standard deviations from our experiment. Generally speaking,

Table 1: Standard deviations of the azimuth and elevation for three different frequencies. Experimentally observed values are followed by the theoretical predictions in parentheses. (No predictions are shown for the nighttime case, as the turbulence model is not valid then.)

	18 June, 1738	18 June, 2220	19 June, 1033
150 Hz, az.	2.76° (0.80°)	0.53°	1.06° (0.76°)
150 Hz, el.	1.20° (0.54°)	0.62°	0.58° (0.49°)
200 Hz, az.	1.76° (0.53°)	0.44°	0.83° (0.46°)
200 Hz, el.	1.34° (0.38°)	0.21°	0.50° (0.30°)
250 Hz, az.	1.40° (0.30°)	0.57°	0.54° (0.17°)
250 Hz, el.	1.24° (0.26°)	0.35°	0.48° (0.12°)

the trends in the data are well predicted: the standard deviation for the azimuthal angle is larger than for elevation, and it decreases with increasing frequency. However, the observed standard deviations tend to be several times larger than the CRLB.

Because the CRLB represents the theoretical lower bound on estimators, the experimental results do not actually contradict the theoretical model. They could simply imply that our FFT-beamforming algorithm is not very close to optimal and we should try using a parametric beamforming method instead, such as maximum-likelihood estimation. In their simulations of acoustic arrays in the ocean, Song and Ritcey (1996) found that a beamforming algorithm similar to ours yielded accuracy equal to about twice the CRLB. The discrepancy between the CRLB and our experimental results could also be due to physical factors that are unaccounted for in our formulation for the Fisher information, such as interaction of the sound with the ground, refraction, and gusting of the wind.

ACKNOWLEDGMENTS

S. Collier is supported by a post-doctoral research fellowship administered through the American Society for Engineering Education.

REFERENCES

Ishimaru, A., 1978: *Wave Propagation and Scattering in Random Media.* Academic Press, New York.

Kay, S. M., 1993: *Fundamentals of Statistical Signal Processing: Estimation Theory.* PTR Prentice Hall, Englewood Cliffs.

Ostashev, V. E., and D. K. Wilson, 2000: Relative contributions from temperature and wind velocity fluctuations to the statistical moments of a sound field in a turbulent atmosphere. *Acustica*, **86**, 260–268.

Song, B.-G., and J. A. Ritcey, 1996: Angle of arrival estimation of plane waves propagating in random media. *J. Acoust. Soc. Am.*, **99**, 1370–1379.

REMOTE SENSING OF ATMOSPHERIC PLUMES WITH A MILLIMETER-WAVE RADIOMETER

Robert W. McMillan* and Osborne Milton, Jr.
U.S. Army Space and Missile Defense Command
Huntsville, Alabama, 35805, USA

ABSTRACT

Strong absorptions due to atmospheric oxygen near 60 GHz provide the means for remote sensing of atmospheric temperature fluctuations that may indicate the presence of disturbances such as high-altitude clear-air turbulence, aircraft wake turbulence, and severe weather. In this paper we evaluate the performance of a radiometer operating at 60 GHz that is designed to detect these plumes of temperature different from ambient. Such an instrument could also be used for remote detection of underground structures and for passive remote wind sensing. A variant of this device can make crude passive range measurements.

1. INTRODUCTION

The group of molecular oxygen absorptions lying near 60 GHz in the millimeter wave portion of the electromagnetic spectrum provides the basis for vertical temperature sounding of the atmosphere from satellites or aircraft based on weighting functions for different frequency channels. This paper describes a radiometer operating near 60 GHz that will be able to sense temperatures on a horizontal path using a similar approach [1,2]. The atmosphere is assumed to be divided into vertically stratified regions of different temperature, thickness, and absorption coefficient. These differences provide the basis for sensing plumes of different temperature.

2. THEORY

The vertically stratified geometry assumed characteristic of a plume of different temperature is shown in Figure 1. Region 1, characterized by temperature T_1, absorption coefficient α_1, and thickness h_1 is the region in which the radiometer is placed, denoted by the horn antenna in Figure 1. Regions 2 and 3 have temperatures T_2 and T_3 and absorption coefficients α_2 and α_3, respectively. To understand how Region 2, which contains the plume, can be sensed remotely, we must integrate the radiometer equation

$$T_{ANT} = \int_0^\infty \alpha(z)T(z)\exp\left[-\int_0^z \alpha(z')dz'\right]dz, \qquad (1)$$

for this simple case. Integration of this equation gives

$$T_{ANT} = T_1 + (T_2 - T_1)\exp(-\alpha_1 h_1) + (T_3 - T_2) \bullet \exp\left[-\alpha_1 h_1 - \alpha_2 (h_2 - h_1)\right], \qquad (2)$$

where T_{ANT} is the antenna temperature measured by the radiometer.

We can simplify Equation (2) even more by assuming that the plume is an anomaly in an otherwise homogeneous atmosphere, so that Regions 1 and 3 are identical and $T_1 = T_3$ and $\alpha_1 = \alpha_3$. Further simplification is possible if we make use of the fact that α changes slowly with temperature and that the temperature differences between the three regions are small in any case, resulting in the approximation $\alpha_1 \approx \alpha_2 \approx \alpha_3$, so that the absorption coefficient is essentially constant over the three regions. Under these conditions, Equation (2) becomes

$$T_{ANT} = T_1 + (T_2 - T_1)\left[\exp(-\alpha h_1) - \exp(-\alpha h_2)\right], \qquad (3)$$

in which the unknowns are T_2, h_1, and h_2. We can measure T_1, T_{ANT} and α at the radiometer site. The parameter T_2, or more precisely its difference from the ambient temperature T_1, is a measure of the severity of the atmospheric disturbance. The distance h_1 is the range to the plume and the difference $h_2 - h_1$ is its thickness. If we can determine these three parameters, we will have a good characterization of this atmospheric disturbance.

It is possible to determine these three unknowns by building a three-channel radiometer with its local oscillator centered on the oxygen absorption at 60 GHz and its channels arranged to give various degrees of absorption. Under this condition, the three antenna temperature equations become

$$T_A = T_1 + (T_2 - T_1)\left[\exp(-\alpha_A h_1) - \exp(-\alpha_A h_2)\right], \qquad (4)$$

$$T_B = T_1 + (T_2 - T_1)\left[\exp(-\alpha_B h_1) - \exp(-\alpha_B h_2)\right], \qquad (5)$$

$$T_C = T_1 + (T_2 - T_1)\left[\exp(-\alpha_C h_1) - \exp(-\alpha_C h_2)\right], \qquad (6)$$

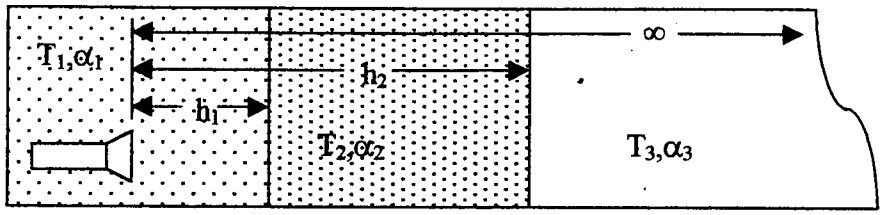


Figure 1. Geometry for plume detection. The center region contains the plume

where A,B, and C refer to the three radiometer channels. Despite their simple appearance, these equations cannot be solved in closed form except for some special cases.

3. RESULTS

We have not built and tested the 60 GHz plume-sensing radiometer, but have solved the above system of equations for some special cases. Figure 2 shows several solutions for different special cases as noted below and in the figure caption. For each of these curves $\alpha_A = 1$ km^{-1}, $\alpha_B = 2$ km^{-1}, and $\alpha_C = 4$ km^{-1}. The value of h_1 is not shown on these curves, but this range parameter varies from 1 to 2 km as the temperature difference increases. These curves show that plumes with temperatures differing from ambient by as little as 2 degrees can be detected at ranges of 1 or 2 km if their thicknesses are on the order of a few hundred meters.

The ability of a radiometer to sense small temperature fluctuations will be limited by its noise performance. Most of these fluctuations will have strong contributions in the low-frequency range, so that long integration times can be used to improve noise performance. This parameter, along with the location of the radiometer sidebands, must be determined by further study if a remote sensing radiometer is to be built.

We have shown that a radiometer operating on the oxygen absorption at 60 GHz can be used for sensing plumes of different temperature in the atmosphere. Such an instrument could be used to detect underground structures based on plumes from their exhaust systems and could make passive remote measurements of wind velocity using correlation of atmospheric turbulence fluctuations.

REFERENCES

[1] G. G. Haroules and W. E. Brown, "A 60 GHz Multi-Frequency Radiometric Sensor for Detecting Clear Air Turbulence in the Troposphere", *IEEE Trans. AESS*, Vol. AES-5, No. 5, Sept. 1969, pp. 712-723.

[2] R. W. McMillan, "A Horizontal Atmospheric Temperature Sounder: Applications to Remote Sensing of Atmospheric Hazards", *International Journal of Infrared and Millimeter Waves*, Vol. 14, No. 5, 1993, pp. 931-948.

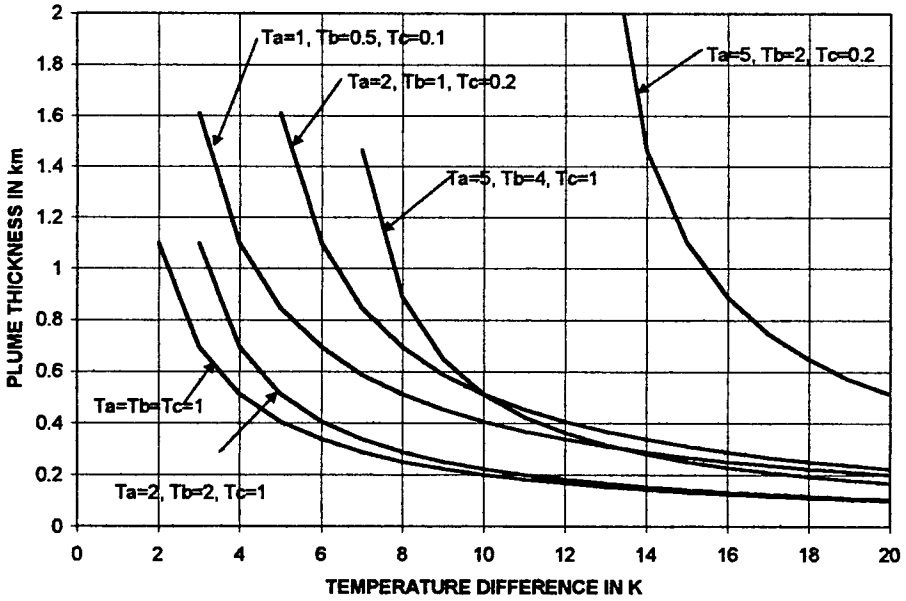


Figure 2. Detectable plume thickness as a function of temperature difference between plume and ambient. The temperatures measured by the three radiometer channels are shown for each of the curves.

EVALUATION OF A HIGH RESOLUTION WIND MODEL OVER A COMPLEX TERRAIN SURFACE

S..S. Chang, R.M. Cionco, J.J. Mercurio*, D.M. Garvey, C.C Williamson, and G. Huynh
US Army Research Laboratory, 2800 Powder Mill Road, Adelphi, Maryland, 20783-1197

ABSTRACT

A description of a high resolution wind (HRW) model is presented. The HRW model has been in development at the U.S. Army Research Laboratory, formerly the U.S. Army Atmospheric Sciences Laboratory, since 1978. This model is a two-dimensional, diagnostic atmospheric surface layer model with a horizontal grid spacing of the order of 100 m over a domain about 5 by 5 km. It uses Gauss' principle of least constraint and a direct variational relaxation method to adjust an initially uniform wind field to conform to constraints imposed by topography, mass conservation, and buoyancy forces. One of the distinctive features of the model is the use of a warped non-orthogonal, terrain-following coordinate system. Recent development of the model has focused on the incorporation of vegetative and urban land features (morphology) both in providing further constraints and in modifying the vertical profiles of the wind field. A valuable observational data set of surface wind has been provided from the field study of Meteorology and Diffusion over Non-uniform Areas (MADONA) at Porton Down, Salisbury, England during September and October 1992. Using the MADONA data, a critical evaluation of the HRW model for 39 cases has been carried out. The results of this study are presented, indicating both the range of validity and the limitations of the HRW model.

Previous general evaluations have shown very good agreement with the observed wind speed and direction data base. The same paired data set was conditionally sampled with respect to wind direction, wind speed, atmospheric stability, and station location. In general, the detailed comparisons fully substantiate the overall correlation results previously obtained even though there is one low correlation very specifically for the stronger wind speed range ($s > 6$ m/s). This low correlation is thought to be related to the gustiness generally existent at higher wind conditions and how such conditions violate the steady state assumptions of HRW. The statistics show that simulated wind directions always correlated very well with the observed directions which ranged from 70 to 360°. Simulated wind speeds also correlated relatively well with observed speeds (0. 5 to 10.5 m/s) despite the inclusion of the one low correlation at a higher observed speed.

THIS PAGE INTENTIONALLY LEFT BLANK

METEOROLOGICAL MODEL IMPROVEMENTS ON SIMULATED ARTILLERY ROUND TARGETING ACCURACY

Terry C. Jameson* and David Knapp
Battlefield Environment Division
Computational & Information Sciences Directorate
Army Research Laboratory
White Sands Missile Range, NM, 88002-5501

ABSTRACT

A meteorological (Met) analysis was performed on data collected during Sense And Destroy ARMor (SADARM) artillery live firings that occurred at Yuma Proving Ground, AZ (YPG). Actual submunition impact data were compared against predicted impacts derived from a trajectory simulation program. Two types of Met data were input to the trajectory simulator (one type from standard battlefield weather balloons and the other from computer model-generated forecasts), in order to test which type most accurately represented the "real" atmosphere. For the most part, the model-generated data were more representative.

1. INTRODUCTION

The purpose of this study was to evaluate the suitability of mesoscale[1] computer model output for artillery aiming applications. Current battlefield doctrine involves the use of rawinsonde weather balloon observations (RAOBs), released near the guns, to obtain the necessary Met information for generating artillery Computer Met Messages (CMMs). CMMs generated in this manner have limitations in their effectiveness, particularly for longer-range artillery and for warheads that interact with the low altitude weather in the target area. The Army Research Laboratory Battlefield Environment Division's Battlescale Forecast Model (BFM) was used to generate *forecast* CMMs[2] for comparison against those data obtained from RAOBs.

[1] The term "mesoscale" refers to an area on the order of 200 km square; that would encompass the dimensions of a typical battlefield.

[2] The BFM produces Met data at grid points spaced 5 km apart and at multiple levels from near the surface to 10 km above ground level. The data are then interpolated to several points along the trajectory, creating the CMM.

2. WEATHER EFFECTS ON ARTILLERY FIRE

All effective artillery firings must include aiming adjustments that are based upon Met information, to compensate for the variations of atmospheric wind, temperature, and density along the shell's trajectory. A recent study of the component errors for the Extended-Range 155 mm artillery round concluded that for a trajectory length of 28 km, 42% of the range error and 56% of the deflection error was attributable to inaccuracies in the Met data (Reichelderfer and Barker, 1993). (Most of the remaining firing errors are due to muzzle velocity and occasion-to-occasion inaccuracies). Thus, reducing the Met errors in the data used for the firing calculations can significantly improve the aiming accuracy of the artillery rounds. Mesoscale models such as the BFM hold the promise of providing that accuracy improvement.

3. COMPARISONS OF METEOROLOGICAL DATA

It is certainly a valid concept to directly compare BFM output to RAOB data. Although an appropriate evaluation approach, a direct comparison assumes that the RAOB data are the standard against which the BFM data should be measured. However, the balloon-borne RAOB has both spatial and temporal limitations that can adversely affect artillery and other military applications. The spatial limitations occur since the balloon can easily drift many kilometers from its launch point (and thus, far from the battlefield area of interest) and because the weather at the launch point may be greatly different from the weather at the target. Temporal limitations exist since a RAOB often takes one or more hours to reach the peak of its flight, with additional time required to process and disseminate the information. Also, it is not always possible to launch a RAOB near the time of firing. For these reasons, a RAOB is not necessarily a standard against which the computer-modeled data should be compared.

Although the BFM forecasts the data rather than measuring it, the model predicts Met conditions at a desired point in space and time (in this case, at the apogee and/or along the trajectory of an artillery round, and at the firing time). Hence, an assessment of the accuracy of artillery fire using RAOB-based CMMs (RCMMs) and BFM-based CMMs (BCMMs) is of greater interest than a simple direct comparison.

5. ANALYSIS APPROACH

A series of SADARM artillery firings were simulated using the ARDEC Firing Tables Branch's General Trajectory Model-Version 3 (GTRAJ3). GTRAJ3 simulations were run using a RCMM, and again using a BCMM. The specific input conditions for a particular firing (SADARM ballistic and aerodynamic parameters, gun azimuth/elevation angle, measured muzzle velocity, etc.) were held identical. The simulated impact points from each GTRAJ3 run were compared to actual submunition impact coordinates obtained at the SADARM Reliability Determination and Assurance Program (RDAP) and the Limited User Test (LUT) conducted at YPG during January and April-May, 2000.

The SADARM rounds experienced and responded to the "true" atmospheric conditions. *Consequently, the GTRAJ3 simulation that resulted in the closest impact to the actual impact location(s) was determined to be the one using Met data most representative of the "true" atmosphere."*

The RCMMs were approximately three hours old during the RDAP (i.e. the RAOB used for the Met message to aim the gun was taken about three hours before the firing). The BCMMs were three-hour forecasts, valid at the time of the firing. During the LUT, the RCMMs were only about 1.5 hours old. For reasons that are explained in the full manuscript, the BCMMs were *five-hour forecasts* during the LUT.

6. RADIAL MISS DISTANCES

Each SADARM round contains two submunition canisters[3]. Thus, the 12 rounds fired during the RDAP (eight on 25 Jan 00 and four more on 27 Jan) resulted in twenty-four ground impacts. On each of four mission-days during the LUT, twenty-four rounds were fired, resulting in a total of 192 impacts. The straight-line distance (called the Radial Miss Distance or RMD) from every submunition impact coordinate to the RCMM-GTRAJ3 and BCMM-GTRAJ3 simulated impact points was determined. Mean RMD (MRMD) values were then calculated for the two RDAP mission-days, and the four LUT mission-days.

[3] The Explosively Formed Penetrators (EFP) can fire from the canisters in any direction downward against their sensed target. Certain aspects of EFP performance are classified and so EFP results will not be discussed herein.

7. RESULTS

Table 1 summarizes the MRMD results (values are in meters):

Table 1. MRMD Values For YPG SADARM Tests

	RCMM	BCMM
RDAP-1	256	222
RDAP-2	123	48
LUT-1	235	188
LUT-2	261	306
LUT-3	178	178
LUT-4	223	141

As the table indicates, the BCMM-based MRMD values were smaller for 4 of the 6 mission-days. This indicates that the BCMMs more accurately represented the atmosphere than did the RCMMs for a majority of the missions. The results were almost identical for LUT-3 (when rounded to the nearest meter). During LUT-2 (18 Apr 00), a powerful disturbance in the upper-atmosphere caused very strong winds (exceeding 50 ms^{-1} near the apogee of the SADARM rounds) that changed direction significantly shortly before the firing. In this case, the RCMM (1.5 hours old) was a more accurate representation of the firing conditions than the five-hour forecast BCMM. Recent upgrades to the BFM might improve the performance of the computer model in a high-wind situation such as during LUT-2. Additional analyses are anticipated using the upgraded BFM.

8. SUMMARY AND CONCLUSIONS

Simulated SADARM artillery firings were compared against live-fire impacts. Both RAOB-based and BFM-based CMMs were used as Met input to GTRAJ3. For a majority of the cases, the BCMMs proved to be a more accurate representation of the "true" atmosphere.

REFERENCES

Reichelderfer, M. and C. Barker, "155-mm Howitzer Accuracy and Effectiveness Analyses," AMSAA Ground Warfare Division, *Division Note No. DN-G-32*, U.S. Army Materiel Systems Analyses Activity, Aberdeen Proving Ground, MD, December 1993.

Session F
Engineering Sciences

Chair
Dr. Billy J. Walker
U.S. Army Aviation and Missile Command

Co-Chair
Dr. Brian Strickland
U.S. Army Space and Missile Defense Command

Keynote Address
Prof. Garry Brown
Princeton University

THIS PAGE INTENTIONALLY LEFT BLANK

Degradation Of Components Of Mustard Agent Filled Assembled Chemical Weapons In Laboratory And Pilot Scale Immobilized Cell Bioreactors

M.A.Guelta*, N.A.Chester, J.J.DeFrank,
U.S. Army Edgewood Chemical and Biological Center
Aberdeen Proving Ground, MD. 21010

S.Lupton, M.Koch,
Honeywell International
Des Plaines, IL. 60017

ABSTRACT

In 1996, public laws 104-208, 105-261, and 106-79 established and expanded the Assembled Chemical Weapons Assessment (ACWA) Program. To address public concerns over the safe destruction of the U.S. chemical weapon stockpile; the ACWA program was tasked to identify two or more viable alternative technologies to the "baseline" destruction method of incineration. Neutralization followed by biodegradation was one technology identified as having potential.

This paper describes the laboratory research and pilot scale studies conducted by the authors, U.S. Army researchers, in cooperation with Scientists from Honeywell Intl., at the Edgewood Chemical and Biological Center (ECBC), APG, MD. Laboratory studies were conducted using 1liter Immobilized Cell Bioreactors (ICB). These studies demonstrated the effectiveness of the ICB system to degrade hydrolyzed HD agent feed. In a follow on study ICB system was scaled-up to a 1000-gallon reactor housed in two 40-ft transportation containers. During the 6-week validation period the ICB degraded the schedule-two agent breakdown products to below detectable levels. The overall destruction removal efficiency (DRE) of the HD agent and hydrolyzed tetrytol by neutralization/biodegradation was greater than 99.999%. During the validation period the ICB system processed 26.6 gallons/day of 3.8% HD hydrolysate and 1 gallon/day hydrolyzed tetrytol.

1. INTRODUCTION

Water Hydrolysis of Energetic and Agent Technology (WHEAT) is one alternative process to incineration proposed for complete destruction of warfare munitions containing energetics, propellants and mustard or nerve agents. The WHEAT technologies will be used to demonstrate destruction of materials representative of M60 105 mm projectile (HD/Tetrytol). The WHEAT technologies include water jet for cutting and boring operations to remove components from metal projectiles, a hydrolyzation step to detoxify and make biologically available projectile chemical components, and a high temperature steam process for 5X treatment of metal parts and other solid wastes. The use of Sequencing Batch Reactors (SBR) has demonstrated the ability to successfully degrade hydrolyzed mustard agent (HD)(Harvey et. al. 1997, Guelta and DeFrank, 1998). SBR technology has been selected as the process of choice for destruction of HD presently stored in ton containers at the ECBC. In an ICB reactor the biomass is grown on an immobile substrate of expanded foam and plastic spacers.

2. METHODS AND MATERIALS

HD Hydrolysate is produced by adding HD to heated water and agitating for a period of time. This process is described by Harvey et al., 1997. The primary product of the hydrolysis of HD is thiodiglycol (TDG). Thiodiglycol is readily degraded by microrganisms who use it as their primary food (carbon) source. The reaction (without intermediates or by-products) can be summarized as shown below.

$$\underset{\text{HD}}{Cl\text{-}CH_2CH_2\text{-}S\text{-}CH_2CH_2\text{-}Cl} + 2H_2O + 2NaOH \longrightarrow$$

$$\longrightarrow \underset{\text{TDG}}{HO\text{-}CH_2CH_2\text{-}S\text{-}CH_2CH_2\text{-}OH} + 2NaCl + 2H_2O$$

The HD hydrolysate used in these studies was prepared at an initial HD concentration of 3.8%. The laboratory reactor was initially used to test the efficacy of employing an ICB reactor to degrade hydrolyzed mustard. The lab scale reactors were successfully operated for 90 days in batch and continuous feed modes to assess potential under these operating conditions for potential scale-up. In 1999 ACWA funded demonstration testing of the ICB system. As part of the larger ACWA program demonstration/validation study the ICB system was operated by U.S. Army researchers for a 6-week validation period.

3. RESULTS

3.1 Laboratory Scale

Efficiency of the laboratory ICB is based on the bioreactors ability to completely degrade the thiodiglycol (TDG) in the feed stock at each feed rate. Process monitoring included Chemical Oxygen Demand (COD), phosphate, pH, mixed liquor suspended solids (MLSS) and nitrogen ammonia. COD was measured daily and is used as a near real-time monitor of ICB performance. TDG and COD results are reported in Table1.

Table 1.Summary of TDG and COD data for IBC-HD

Feed Rate (ml/day)	HRT (days)	Days in Cycle	Analyte (mg/L)	
			TDG	COD)
100	7.5	17	<1.0	1960
200	3.75	17	1.02	2540
300	2.5	9	2678	7350
240 c	1.46	18	1447	6200
120 c	2.92	17	<11.33	2530

c - denotes continuous feed operation.

3.2 Pilot-Scale

HD breakdown products were measured in the feed (S1), chamber 1 (S3) and the ICB out-fall (S5). That data are summarized in table 2. No HD was ever detected in the hydrolysate, feed or any effluents of the ICB.

Table 2. Schedule 2 and Breakdown Products by Week and Sample Location

Sample Date	Analyte	S1 (mg/L)	S3 (mg/L)	S5 (mg/L)
March 24	DITH	15.6	0.7	0.4
	Thiodiglycol	3840	825	ND
	THIOX	24.4	4.9	3.2
March 30	DITH	17.98	5.22	0.52
	Thiodiglycol	3510	55.4	ND
	THIOX	13.0	4.31	3.28
April 7	DITH	14.05	2.88	ND
	Thiodiglycol	3310	ND	ND
	THIOX	28.5	6.52	1.15
April 14	DITH	11.1	1.85	ND
	Thiodiglycol	3257	ND	ND
	THIOX	1	1	ND
April 21	DITH	8.9	9.43	9.45
	Thiodiglycol	3241	186.3	ND
	THIOX	173.7	6.21	6.27
April 28	DITH	10.06	9.83	5.05
	Thiodiglycol	3836	12.4	ND
	THIOX	<1	6.96	6.11

During validation testing air exhausted from the ICB was treated with a CATOX system. Exhaust gases were sampled on the same dates as liquid effluents. No HD, Tetrytol or Schedule 2 compounds were detected during the test period.

The ACWA program designated 8 specific goals and objectives for the WHEAT and biotreatment systems. From the ACWA Program Study Plan, these objectives are listed in the methods, Section 1. Here are the results:

1. The hydrolysis process eliminated HD and Tetrytol in the ICB feed stream to below detectable limits.
2. Data show no HD/Tetrytol was ever detected in the ICB feed, intermediate process or effluent streams.
3. Data show that the WHEAT system and ICB were able to achieve a DRE of 99.999% for HD.
4. Data show that the WHEAT system and ICB were able to achieve a DRE of 99.999% for Tetrytol.
5. Mass loading data was developed for scale-up. However additional data is required and will be developed in a follow-on engineering design study (EDS).
6. Data show that the catalytic treater allowed no release of agent or Schedule 2 compounds.
7. Data show no plugging or fouling of the catalytic treater from the ICB operation.
8. Although not completely reported here, all effluents and waste streams were characterized. No hazardous or toxic agents or Schedule 2 compounds were detected.

REFERENCES

Guelta, M.A., and DeFrank, J.J., Performance of Immobilized Cell Bioreactors For Treatment Of HD And VX Hydrolysates, ERDEC-TR-497, U.S. Army Edgewood Research Development and Engineering Center, Aberdeen Proving Ground, MD, May 1998, UNCLASSIFIED Report

Harvey, S. P., Szafraniec, L.L., Beaudry, W.T., Early, J. T., and Irvine, R.L., Neutralization and Biodegradation of Sulfur Mustard, ERDEC-TR-388, U.S. Army Edgewood Research, Development and Engineering Center, Aberdeen Proving Ground, MD, February 1997, UNCLASSIFIED Report (AD A322 638)

Honeywell International, Advanced Technologies Environmental Systems and Services. 50 East Algonquin RD Box 5016, Des Plaines Il. 60017-5016

Parsons Infrastructure, Assembled Chemical Weapons Assessment Program, Demonstration Study Plan, Parsons Infrastructure & Technology Group, Inc., 1998

A PHYSICALLY BASED CONE PENETRATION INTERPRETATION THEORY TO ACCURATELY CHARACTERIZE SOILS AND EMPLACED GRANULAR MATERIALS

J. B. Johnson
US Army Engineering Research Development Center – Cold Regions Research and Engineering Laboratory
Ft. Wainwright AK 99703

ABSTRACT

A physically based micromechanical interpretation theory for cone penetrometers is developed to account for the effects of material microscale heterogeneity, compaction, and micromechanical strength variations in soils and emplaced granular materials. Microscale processes strongly affect penetration resistance measurements causing their magnitude to vary as a function of cone angle, base area, as and changes in material properties. The theory provides a means to classify soils and coarse granular materials by their microstructural and micromechanical properties, and to extrapolate soil material property data derived from cone penetration measurement to continuum scale "effective" values needed to solve engineering problems. Theoretically predicted penetration resistance for several different soils are in close agreement with measured data.

1. INTRODUCTION

Cone penetrometers are widely used to determine the geotechnical properties of soils, and emplaced granular materials to evaluate the stability of foundations, embankments, and dams to static and dynamic loads. Information about soil shear and compaction strength, elastic modulus, and the potential for liquefaction are of critical importance to an engineer's efforts to improve off-road vehicle mobility and to safely design roads, runways, and foundations for bridges and buildings. Interpretation of penetrometer tests to obtain soil geotechnical properties is, at present, primarily accomplished by empirically correlating penetration resistance (the ratio of penetration force to the penetrometer base area) with the desired soil property because of a lack of physically based theories that accurately describe the penetration process. As a result, developing accurate and repeatable measures of in-situ geotechnical properties from penetrometer measurements has proven difficult. To improve our ability to accurately interpret penetrometer measurements it is necessary to develop a physically based theory of cone penetration in soils and emplaced granular materials. Using a physically based theory to interpret penetration resistance measurements provides a means to determine what factors are acting and to calculate their value, rather than trying to empirically compare penetration data with laboratory data that may or may not be representative of in-situ conditions. In addition, a penetrometer interpretation theory enables us to develop scaling laws that relate the geotechnical properties determined from small-scale penetration tests to large-scale engineering problems; a necessary condition for characterizing heterogeneous materials like soils.

Most theories developed to interpret cone penetrometer resistance are based on the continuum mechanics assumption that a soil completely fills the space that it occupies leaving no pores or empty spaces and that its properties can be described by continuous functions. This approach makes it impossible to describe the important microstructural and micromechanical influences that may include material compaction, variation in microstructural element dimensions, mixed sized granular materials, or variation in microstructural elastic modulus and strength properties. It is usually assumed that penetration through a Mohr-Coulomb elastic-plastic granular material produces a monotonic pressure loading resulting in cavity expansion around the penetrometer. These continuum theories predict that penetration resistance is the result of the cavity expansion pressure and soil/penetrometer friction. Consequently, predicted penetration resistance is independent of the cone diameter, but decreases with increasing cone angle as the effects of friction decrease. These classical theoretical results are contradicted by penetrometer resistance measurements of real soils that exhibit measurement variations as a function of cone base area, and cone angle. In this work, we develop a physically based cone penetrometer interpretation theory and apply it to explain why penetration resistance varies as a function of cone base area and cone angle for a soil with constant geotechnical properties.

2. PENETROMETER THEORY

Experimental observation of the penetration process provides the basis for the assumptions used to develop a statistical micromechanical penetrometer interpretation theory. Experiments indicate that soils support the forces exerted by a penetrometer through microstructural elements that may consist of individual particles connected to each other by cohesive bonds, friction contacts, or through a complex arrangement of

connected fibers or particles. When a penetrometer is pushed into a cellular or granular material the resulting forces arise from a series of loading and failure events. During loading, a brittle-elastic or elastic-plastic microstructural element in contact with the penetrometer will deform elastically in a direction normal to the penetrometer face to a critical state of deflection. Deflection beyond the critical state results in microstructural element failure and a drop in applied force. The failure mechanism, which depends on the properties of the microstructural elements and the contacts between them, may result from brittle failure of cohesive bonds, plastic or viscoplastic yield at bonds or a Mohr-Coulomb bond failure. These mechanisms can readily be incorporated into a micromechanical theory and are important for interpreting penetrometer measurements and accounting for the significance of material overburden. The general physical scheme used to develop the model is shown in Fig. 1.

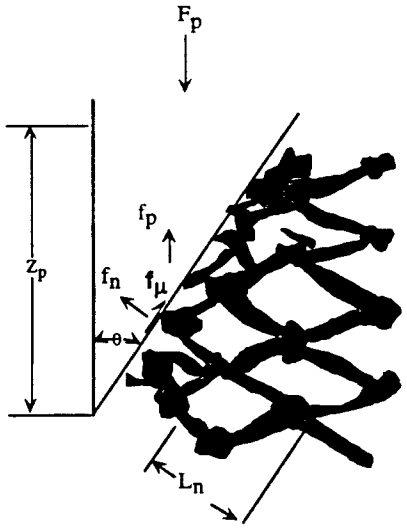


Fig. 1. Cone penetrometer interaction with the microstructural elements of a granular material.

The total force of penetration is the sum of the forces exerted by each microstructural element in contact with the penetrometer surface and, for randomly distributed microstructural elements, is given by

$$F_{p,\max} = N_s P_c \bar{f}_p (1 + 3\sigma) \qquad (1)$$

where the average penetration force is $\bar{F}_p = N_s P_c \bar{f}_p$. The number of microstructural elements adjacent to the penetrometer is given by N_s. P_c is the probability of contact between a microstructural element adjacent to the penetrometer and the penetrometer surface, and $\bar{f}_p$ is the average axial force exerted on the penetrometer face as a result of frictional and deflection forces for each contacting microstructural element. The standard deviation about the average penetration force is σ and the multiplier, 3, is determined from experimental and statistical considerations. The average axial force is given by

$$\begin{aligned} \bar{f}_p &= \left(\bar{f}_n \sin\theta + \bar{f}_\mu \cos\theta \right) \\ &= \bar{f}_n (1 + \mu \cot\theta) \sin\theta \end{aligned} \qquad (2)$$

3. RESULTS AND CONCLUSIONS

The penetrometer interpretation theory described in Eq. 1 has been used to interpret penetration data for penetrometers with different cone angles and base areas to determine material parameters for zirconia foam, seven different soil types, and four different types of snow. Derived material properties include material compaction, microstructural element elastic modulus and strength, microstructural element size, and an estimated grain size. Indentation and penetration forces calculated from the theory, using the derived material properties, are in close agreement with experimental measurements. The theory was also used to develop a scaling law to extrapolate the small-scale material property data to large-scale "continuum" sample size needed to solve engineering problems. The theory has been applied to interpret penetration data for penetrometers with base diameters as small as 5 mm using high-resolution force and displacement sensors. In this application, the rupture of individual microstructural elements can be observed and information about the distribution of microstructural element material properties can be determined. Identifying soil material properties at the microstructural scale may provide a means for quantitatively classifying soils by their microstructural and micromechanical properties. Scaling laws derived from the theory provide a method for rationally comparing penetration data obtained from penetrometers of different size or geometry and to extrapolate small-scale data to large-scale sample sizes that can be modeled using continuum methods.

ACKNOWLEDGEMENTS

This work was funded by USA ERDC-CRREL AT24-EE-003 "Characterization of snow and other granular materials using a small dimension penetrometer".

EXACT NETWORKS FOR RESONANT PIEZOMAGNETIC STRUCTURES

Arthur Ballato
US Army Communications-Electronics Command
Fort Monmouth, NJ 07703

SUMMARY

Much has been written about generic micro- and nano-systems, (e.g., Drexler, 1992), as well as particular embodiments relating to military applications (*Proc. Nanotechnology for the Soldier System Conf.,* 1998). One sees a drive to increasingly smaller scale lengths, with the concurrent imposition of greater functional demands.

At the opposite range of size-scales, a similar transformation in philosophy appears to be taking place: large, monolithic platforms, like the Abrams, are conceived to be evolving toward smaller, (perhaps considerably smaller), but far more numerous, and highly networked entities with a multiplication of robotic features. These trends are complementary. New capabilities are needed at the microscale level to enable features required for embedding in Future Combat Systems.

While microelectronics has recently been broadened in scope by incorporating the coupling of electric fields to mechanical motions (MEMS devices), devices that couple elastic and magnetic fields have received scant attention. Such MMMS devices provide capabilities not available otherwise. Operation in conductive media, such as in subcutaneous pumps and biosensors are examples. Other applications include wideband-tunable microwave filters for military search receivers, and actuators for structural vibration mitigation.

Piezomagnetism

Piezomagnetism is a linear effect coupling magnetic and mechanical variables. It is represented by an axial, third-rank, time-antisymmetric tensor, existing in 66 of the 90 magnetic point groups. Magnetostriction, (mechanical strain quadratic in the magnetic flux density), exists in all magnetic materials (Birss, 1963). Biased magnetostriction is equivalent to piezomagnetism phenomenologically. This effect has a long history (Pierce, 1929). Recently, extremely stable biasing permanent magnets of NdFeB alloys and rare-earth magnet compounds have become available (Leupold, 1996). Formulations exist that have minimal degradations above 350 °C (Liu, et al., 2000). These developments make piezomagnetic devices practical for applications such as engine sensors.

Gyroscopic effects, stemming from the axial nature of magnetism, are manifested in nonreciprocal circuit behavior (Poincaré, 1907; Bloch, 1944). The canonical circuit component embodying nonreciprocal behavior is the gyrator (Tellegen, 1948; Gazin, 1972). This element appears in the representation of our exact MMMS networks.

Types of Piezomagnetic Excitation

To show coupling of magnetic and elastic fields simply, the example of a flat plate actuator supporting acoustic waves driven via the piezomagnetic effect is used. Exact networks have been derived; these are important for time-domain applications requiring broadband networks. The system is considered an electromechanical three-port, with a mechanical port at each surface, and a magnetic port comprised of attachments to the electrode system.

Piezomagnetic plates have two canonical excitation types, depending on whether the exciting field is in the thickness or lateral direction; these are denoted TE and LE. The necessary electrodings for the two cases are shown schematically in Fig. 1. The equations for each kind differ, but all piezomagnetic excitations can be decomposed into these two canonical types. For reasons of space in this summary, no derivations are given, and only the TE networks are shown.

For piezomagnetic excitation in general, div B = 0; thus $\partial_2 B_2 = 0$, and magnetic induction B_2 is a spatial constant. Its value depends on whether the excitation is TE or LE. Electric effects are assumed negligible, so $\partial_t D = 0$, and any electric motive currents are confined to the plate boundaries; therefore curl H = 0 within the volume, so the lateral magnetic fields are constant throughout the plate. Their values again depend on the excitation type. Normal magnetic field $H_2 = H_2(y)$ and lateral magnetic induction $B_1 = B_1(y)$ are permitted.

In the TE case, the forcing function consists of a circumfluent belt of electric current, coextensive with the plate thickness, applied along the distant periphery of the plate. See the top portion of Fig. 1. All current flows normal to x_2, producing a spatially constant B_2. Induced voltage is computed as a line integral with path normal to the x_2 axis, so only the component B_2 is relevant. Major plate surfaces are devoid of currents. Magnetic equipotentials are parallel to the major surfaces, requiring that $H_1 = H_3 = 0$ throughout the plate.

For LE, a spatially constant forcing function H_1 is applied by current sheets of density $\pm K_3$ flowing in electrodes on the plate major surfaces in accordance with curl H = J. The major plate surfaces are covered with electrodes, so transverse voltage gradients vanish, and $B_2 =$

0. Induced voltage is computed as a line integral with path normal to the x_1 axis, so only the component $B_1(y)$ is relevant. See the bottom part of Fig. 1.

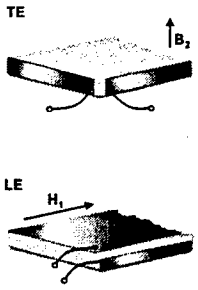


Fig. 1. Electrodings for thickness- and lateral-excitation.

Piezomagnetic Networks

Figure 2 shows the network realization for TE. It consists of an acoustic transmission line supporting the wave motion, and two mechanical ports at top and bottom for application of boundary loads. In series with these ports are magnetic gyrators supplying mechanical tractions to the plate surfaces from the magnetic port, by which the motion is driven. The symbol + L_0 represents normalized inductance of the exciting magnetic field; – L_0 arises from the "wavy" portion of H interacting with the applied field.

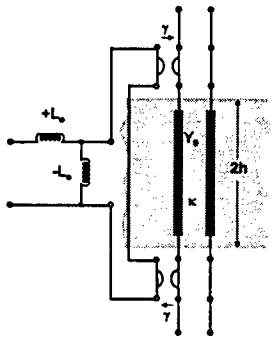


Fig. 2. Exact network for a single mode (TE).

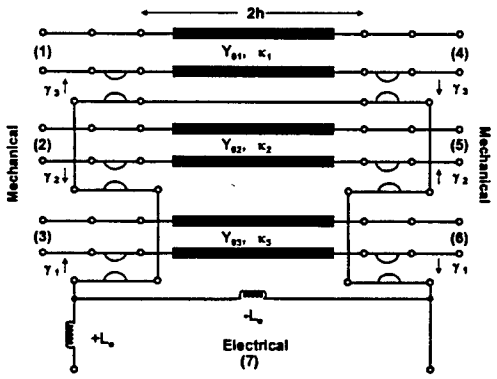


Fig. 3. Exact multi-mode network (TE).

Multi-mode Networks

The network of Fig. 3 is the multi-mode network for the TE case. The acoustic transmission lines represent the orthonormal magneto-acoustic eigenmodes.

Figure 4 shows the multi-mode MMMS resonator. Simplified from Fig. 3 by network bisection, it portrays a plate with mechanical ports devoid of surface loadings.

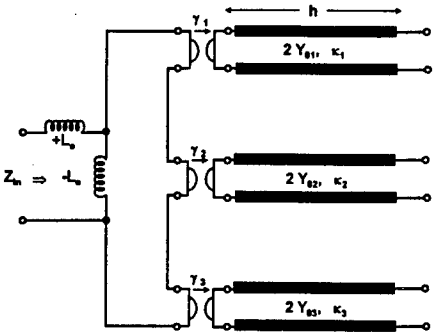


Fig. 4. Multi-mode resonator network (TE).

REFERENCES

Birss, R. R., "Macroscopic symmetry in space-time," *Repts. Prog. Phys.*, vol. 26, pp. 307-360, 1963.

Bloch, A., "A new approach to the dynamics of systems with gyroscopic coupling terms," *Phil. Mag.*, series 7, vol. 35, pp. 315-334, 1944.

Drexler, K. Eric, *Nanosystems: Molecular Machinery, Manufacturing, and Computation*, Wiley-Interscience, New York, 1992.

Gazin, J. -F., "Le gyrateur: Étude, réalisation, applications," *Toute L'Electronique*, no. 368, pp. 23-27, July 1972.

Leupold, H. A., "Static applications," In *Rare-Earth Iron Permanent Magnets*, J. M. D. Coey, Ed., chap. 8, pp. 381-429, Clarendon Press, Oxford, 1996.

Liu, S., Kuhl, E., Chen, C., Walmer, Ma., Walmer, Mi., and Gong, W., "High temperature $Sm_2(Co,Fe,Cu,Zr)_{17}$ magnets and their dynamic thermal stability," *Proc. 16th Intl. Workshop on Rare Earth Magnets and Their Appls.*, Sendai, Japan, September, 2000, in press. US Air Force Contract F33615-97-C-5017 and DARPA/ONR Contract N00014-98-1-0636.

Pierce, G. W., "Magnetostriction oscillators," *Proc. IRE*, vol. 17, pp. 42-88, 1929.

Poincaré, H., "Etude du récepteur téléphonique," *L'Eclairage Electrique*, vol. 50, pp. 221-372, 1907.

Proc. Nanotechnology for the Soldier System Conference, Boston/ Cambridge Hyatt Regency Hotel, July 1998, US Army Soldier Systems Command, Natick, MA.

Tellegen, B. D. H., "The gyrator, a new electric network element," *Philips Res. Repts.*, vol. 3, pp. 81-101, April 1948.

DEVELOPMENT OF A RAPIDLY INSTALLED BREAKWATER FOR ARMY FORCE PROJECTION

D. T. Resio*, J. E. Fowler, and J. A. Melby
U. S. Army Engineer Research & Development Center
Vicksburg, Mississippi 39180

ABSTRACT

A theoretical foundation for a floating breakwater is given along with results from both lab and field tests which provide validation for this theory. An extension of these equations to the case of a structure made from pressurized, water-filled tubes shows that this type of structure should be extremely effective in enabling ship discharge in JLOTS operations to continue through Sea State 3.

1. INTRODUCTION

During the last two decades, U.S. Force Projection has shifted from being primarily OCONUS-based to almost totally CONUS-based. Accompanying this shift has been a dramatic increase in the need for improved transportation assets within the U.S. Army. Presently, a critical element of U.S. Force Projection is a class of operations termed Joint Logistics Over the Shore, or JLOTS. However, a key component of JLOTS is the transfer of cargo in offshore areas from relatively large military Sealift ships to smaller vessels termed lighters. However, this operation is completely curtailed by waves higher than 3 feet. Since waves in the 3- to 5-foot range (Sea State 3) occur a high percentage of the time in almost all coastal areas around the world, this limitation significantly reduces the effectiveness of JLOTS.

In an attempt to extend the Army's capability to conduct JLOTS operations through Sea State 3, the Coastal and Hydraulics Laboratory began a systematic development of a Rapidly Installed Breakwater (RIB) that could reduce wave heights in its lee by 50% to 70%. This capability would increase the potential offloading rate from ships by a factor of 50% to 300% in militarily important areas of interest around the world.

The initial concept for the RIB, a floating V-shaped breakwater (Figure 1) was developed in 1995 and a patent for its unique design was granted in 1997. A systematic series of tests began in 1996 and the development effort became part of an Army Science and Technology Objective (STO) in 1998. In 1999, the effort was selected as one of the Army's Advanced Technology Demonstration (ATD).

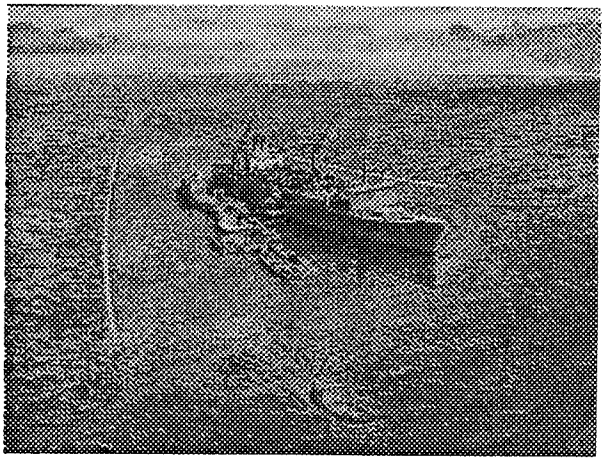


Figure 1. Artist's rendition of RIB system.

2. THEORETICAL FOUNDATION

Over the last 5 years a strong theoretical foundation for the RIB's performance has been developed. Essentially, reflection/diffraction pattern created by the RIB creates a sheltered area with reduced wave heights. The performance of the RIB is typically computed in terms of one minus the ratio of the incident wave height to the wave height in the shadow area, i.e.

$$R = 1 - \left(\frac{H_{sh}}{H_{in}} \right) = 1 - K_T \qquad (1)$$

where R is the fraction of wave height reduction in the RIB interior, H_{sh}, is the wave height in the interior, H_{in} is the incident wave height, and $K_T = H_{sh}/H_{in}$ is the transmission coefficient. A value of R equal to one would indicate that all the wave energy was propagating through the RIB into the shadow; whereas, a value of zero would indicate that no energy was able to propagate into the shadow zone (100% blocking).

Using the equations for random-phase wave spectra, an equation for R for arbitrary incident wave conditions was developed. The form of this equation showed that R is dependent upon wave energy arriving in the shadow zone by three primary mechanisms:

1) energy passing through the RIB via RIB structure bending;

2) energy passing under the RIB between the RIB and the sea bed;

3) energy diffracted around the tips of the RIB.

Each of these terms is dependent upon different RIB characteristics. The first term was found to be dominant in many situations and can be derived as a function of the ratio of bending moment (created by waves reflecting from the RIB) to the moment of inertia of the RIB "legs". An interesting aspect of the equation for this ratio was that it was found to be dependent on the fifth power of the wave length, consistent with the generalized Froude scaling used in laboratory-scale modeling of water wave phenomena. The second term could be derived as an integral function of the vertical distribution of energy in the wave field. The third term could be written directly from the Huygens-Kirchoff diffraction integral, and was found to typically be much smaller than the first two terms.

3. LABORATORY AND FIELD TESTING

The equations for predicting RIB performance have now been validated through a careful series of experiments ranging from laboratory-scale, mid-scale, and full-scale field studies. Figure 2 shows an example of spectral transmission characteristics from the most recent 1 : 4 geometric scale field test conducted in Florida's Pensacola Bay in June 2000. Integrating over the entire spectrum shows that the overall performance for this case shows that the overall performance is 0.7, or that the wave height is reduced by 70% in this case.

4. EXTENSION OF EQUATIONS TO THE CASE OF PRESSURIZED HYDRO-BEAMS

During initial development of the RIB it was believed that the full-scale RIB would be constructed from fabricated steel. However, during several field experiments it became obvious that steel structures were subject to catastrophic failures via two primary modes, exceedance of design stress limits and fatigue. Therefore, over the last year, in order to avoid anticipated problems with steel structures and to enhance the deployability of the RIB, a decision was made to investigate the ability of pressurized, high-strength fabric tubes to form the strength elements of the RIB. After considerable effort, it has been shown that existing high molecular weight materials of the Kevlar class can be used in this context. Typical internal pressures required to resist fabric wrinkling (which would result in no local bending resistance) are well within the range of practical fabrics available commercially today. Results shown in Figure 2 represent field test results (at quarter-scale) of such a fabric structure. A slightly modified full-scale version of this same structure will undergo testing in the Atlantic Ocean off the coast of Florida in FY 2001.

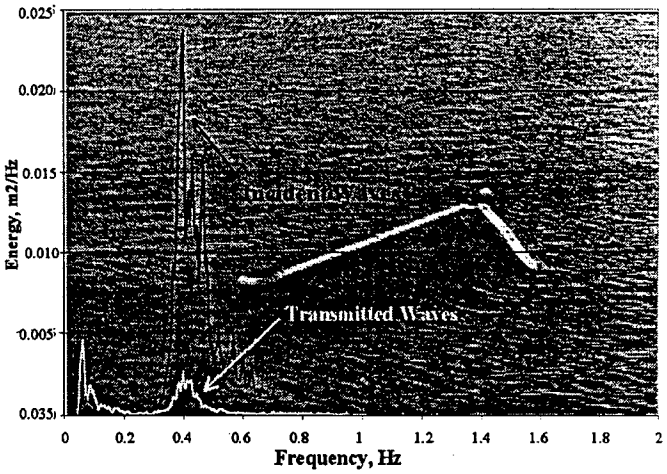


Figure 2. Incident and transmitted wave energy plots superimposed on photo of RIB used in FY 2000 study.

5. SUMMARY AND CONCLUSIONS

Following the development of a strong theoretical foundation for a new class of floating breakwater, a series of laboratory and field tests have been used to aid development of Rapidly Installed Breakwater (RIB) for military applications. Field tests conducted this past summer have shown that this new class of structure is capable of meeting all key metrics for such a system: performance, deployability, employability, survivability, utility, affordability, and size. Based on results such as those shown in Figure 8, the RIB system developed at WES appears to hold great promise for alleviating force projection concerns related to offloading problems associated with higher sea states during JLOTS operations.

ACKNOWLEDGEMENTS

Permission of Headquarters, US Army Corps of Engineers (USACE), for permission to publish this paper is acknowledged with appreciation. This research is being conducted as part of the USACE Military Engineering RDT&E Program of the US Army Engineer Research and Development Center's Coastal and Hydraulics Laboratory. Kepner Plastics Fabricators, Inc., Quantum Engineering Design Inc., Vertigo Inc., Strait Moorings International Inc., and PCCI, Inc. assisted in the design of the assisted in various aspects of the design of the model and field studies.

ROAD CHARACTERIZATION FOR VEHICLE CONTRACT SPECIFICATION

David J. Gorsich, Milton Chaika
U.S. Army Tank-automotive and Armaments Command
Warren, MI 48397-5000

Tzechien Sun
Wayne State University
Detroit, MI

Marc Genton
North Carolina State University
Raleigh, NC

Properly characterizing road roughness is a critical problem for the United States Army. Because the Army has not improved its method of characterization roads, it has lost several lawsuits costing hundreds of millions of dollars. When the Army procures new vehicles, it specifies in the contract the amount of roughness the vehicle must be able to tolerate while driving over terrain. This specification comes in the form of a root mean square elevation (RMSE) number or a power spectral density. The Army uses RMSE to characterize the roughness of the road, and this has been appealing because it is a simple single measure. As an example, cross-country terrain driving is classified as having anywhere from a 0.8 to 1.8 inch RMSE.

New procurement policies as well as the advent of simulation methods has increased the urgency for a new way of characterizing roads and the ability of vehicles to handle their roughness. To reduce the number of field tests and increase the use of simulations, the measure of roughness must be a parameter to be inserted into larger computer models. Because of this, contracts are written without specifying the tests that will be performed after the vehicles are built; for example, in the past the Army might have specified the Heavy Equipment Transporter (HET) must be able to handle driving over the Belgium Block and Perryman courses during 12,000 mile durability evaluations. Now the Army specifies an RMSE and then tests on Belgium Block. This procedure is flawed.

The serious problem is that the assumptions being made, primarily that RMSE represents the courses that actual vehicles are being tested on, are wrong. The simulations that use RMSE are not validated, and also incorrect. When the vehicles fail, and it results in a lawsuit, the Army loses because it is easy to prove that the Army has over-tested the vehicles. Using RMSE requires that some strong statistical assumptions hold for the test course. The course is assumed to be stationary, Gaussian, and to be a one-dimensional time series. Clearly the test course elevation is a function with a two-dimensional domain. Moreover, the test courses are not Gaussian or stationary. All three key assumptions are invalid for the test courses. Is there a better way to characterize the test courses?

This paper describes the proper way to statistically characterize the Perryman and Belgium Block test courses, and describes the way to fit a mathematical model to the courses. This model then can be used as not only a way to describe the requirements for the Program Managers (PMs) and contracts, but also as an input to the simulation models (SIMTLC). The statistical model presented does not assume stationary or one-dimensionality. Moreover the model addresses the non-Gaussian feature of the courses.

At the heart of the new statistical model is the theory of intrinsic random functions. The idea is to be able to take a finite set of measurements and accurately represent a spatial stochastic field given only those measurements. If the spatial field were stationary and Gaussian, then it could be represented by a multi-dimensional covariance function. If differences of the field were stationary, then the stochastic field could be represented by the variogram, a function of variance that need not be bounded. If this assumption fails and if the random field can be detrended, spatial dependence can be defined by a generalized covariance. This paper describes the intrinsic random field model of the test courses, how the courses can be detrended, and the resulting generalized covariance.

Detrending is a statistical method to take out larger overall variations in the spatial field. The functions used to detrend the low frequency variations form the generalized increments for the generalized covariance

functions. The detrending functions annihilate the trend functions. If the trend is polynomial, then the generalized increments must annihilate those polynomials. The trend functions form the null space of the resulting Hilbert space and the generalized covariance is the reproducing kernel of the Hilbert space. Generalized covariances need not be positive definite, only conditionally positive definite. Moreover, there is a formal connection between the intrinsic random field and splines.

In this paper, the authors review the theory of intrinsic random functions and generalized covariances, and apply this theory to the Army problem of characterizing test courses. The current technique of RMSE is reviewed in detail. Elevation data from several test courses is studied. The assumptions of stationary and Guassinity are refuted. Then the intrinsic random function model is fitted to the data. The use of this statistical model for SIMTLC, the CAVE, and general terrain simulations is discussed in depth. Simulations of stochastic fields using the model are studied, and a new contract specification technique for the U.S. Army and the PMs is recommended.

Biography: David J. Gorsich received his Ph.D. from Massachusetts Institute of Technology (MIT) in Applied Mathematics in 2000. His dissertation was on nonparametric estimation of dependences for spatial interpolation. His areas on interest are in approximation, spatial statistics, artificial intelligence and robotics. Prior to attending MIT, Dr. Gorsich received a M.S. in Applied Mathematics from George Washington University (1994), and a B.S. in Electrical Engineering from Lawrence Technological University (1990). He currently is a research scientist for the National Automotive Center in Warren, Michigan, where he is responsible for the 21st Century Truck Program, Vehicle Intelligence, and statistical learning theory projects related to the Army's robotics programs. He has been a key member of the TARDEC ILIR program since 1994.

COMPUTATIONAL FLUID DYNAMIC MODELING OF FLOW OVER FABRIC COVERED CYLINDERS: APPLICATION TO PROTECTIVE CLOTHING

Phillip Gibson
Materials Science Team
U.S. Army Soldier Systems Center
Natick, MA 01760-5020
Phil.Gibson@natick.army.mil

Fabric-covered cylinders provide a convenient geometry to study some of the system-level effects important for clothing systems. The effects of variable air spacing between fabric layers, or between the fabric and the human skin surface, can be important in determining how much heat and mass is transferred into or out of the clothing. In many cases, approximating the human body as an assemblage of fabric-covered cylinders provides sufficiently accurate results. In general, an external air flow due to wind or body motion impinges on the clothed human, and some air flows around the body, while some air penetrates through the clothing system and into the gap between the clothing and body. This is illustrated in Fig. 1, which is a typical CFD simulation of flow over a cylinder covered by a permeable fabric. For a given external air velocity, the amount of air which flows around the body, and the amount which penetrates through the clothing layer is determined by the air flow resistance (air permeability) of the clothing layer. Materials with a low air flow resistance allow a relatively high flow rate through the fabric, with a correspondingly low pressure drop. Materials with a high air flow resistance allow less flow through the fabric, and have a higher pressure drop across the fabric layer (up to the limit of the stagnation pressure for the particular environmental flow conditions).

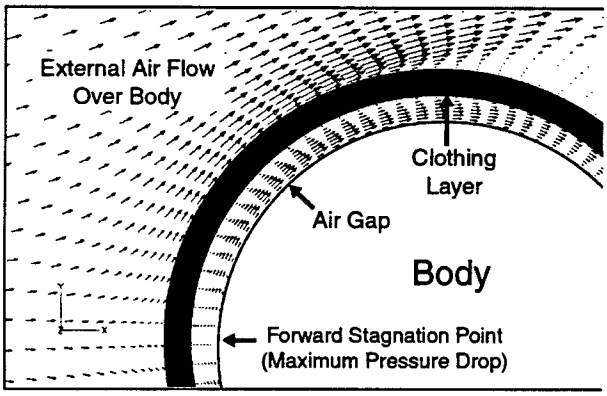


Figure 1. Flow conditions for a fabric-covered body.

The simple flow geometry shown in Fig. 1 is useful for answering some very basic questions about the interaction of the different transport properties characterized individually by laboratory test methods, but which all operate simultaneously in a clothing system. A CFD simulation of the performance of the materials in the fabric-covered cylinder geometry can help to determine how the overall system heat and mass transfer coefficients are influenced by a particular combination of fabric properties.

An illustration of typical CFD modeling of fabric-covered cylinders is shown in Figure 2. A body-fitted mesh is created for a cylindrical geometry. A thermal insulation layer, and an air space, is placed around the cylinder. The air flow resistance property of the insulation layer is varied (while keeping thermal insulation constant). The cylinder diameter was 0.187 m (corresponding the diameter of human thigh), and the air space between the fabric and the cylinder surface was 0.01 m. The cylinder surface temperature was 35 °C (nominal human skin temperature) and the air temperature was 5 °C. Simulations were carried out over a range of air flow velocities from 1 to 40 m/s, although only the results up to 10 m/s are shown in Figure 6. The curve for the bare cylinder case in Figure 6 agrees with heat transfer correlations for gas flow over heated cylinders. These types of simulations, if accurate, would be very useful in efforts to design the proper mix of fabric transport properties to maximize comfort while still providing adequate protection from the environment, and from chemical/biological warfare agents.

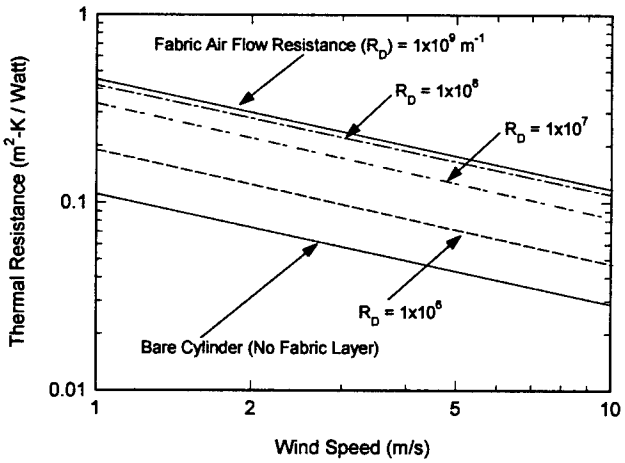


Figure 2. Overall Heat Transfer Resistance of Fabric-Covered Cylinders in Cross-Flow Conditions at Various Wind Speeds.

The simple model of a cylinder, fabric layer, and air space, is also useful for studying questions relating to mass transfer in protective clothing systems. The transport of sweat in vapor and liquid form through a clothing system is an important determinant of thermal comfort properties of clothing. The simulation of vapor diffusion combined with convective transport for a fabric-covered cylinder is straightforward, and is nearly identical to the case of combined convection and diffusion of heat through a clothing system discussed previously.

Of equal importance for military protective clothing systems is the transport of chemical and biological warfare agents into a clothing system. The cylinder model is useful as a starting point for looking at the importance of a property such as fabric air flow resistance on the performance of a particular protective clothing system design.

A battlefield hazard for the soldier is the presence of droplets of liquid chemical agents which have contaminated the outer surfaces of protective clothing. These droplets evaporate and the vapor can diffuse into the clothing system. The droplets can also be carried into the clothing system by convective air flow due to body motion or an external wind.

Figure 3 is an example of a CFD simulation of a liquid droplet placed onto the outer surface of the fabric-covered cylinder model. As for the previous examples, all fabric properties are constant with the exception of the fabric air flow resistance. What is interesting about this particular example is that the fabric with the highest air flow resistance does not produce the lowest total exposure to the chemical vapor. The fabric with low air flow resistance provides a standoff of the droplet from the cylinder surface, while the ventilating air flow carries vapor quickly through the system and away from the cylinder. For the case of the fabric with a high air flow resistance, the total vapor exposure is higher. This is due to the fact that although there is little convective flow into the air space under the fabric layer, the vapor is able to diffuse through the clothing and build up to higher concentrations. In this case there is no ventilating air flow to sweep the vapor out of the system, and the total exposure to the vapor is much higher than for the well-ventilated system.

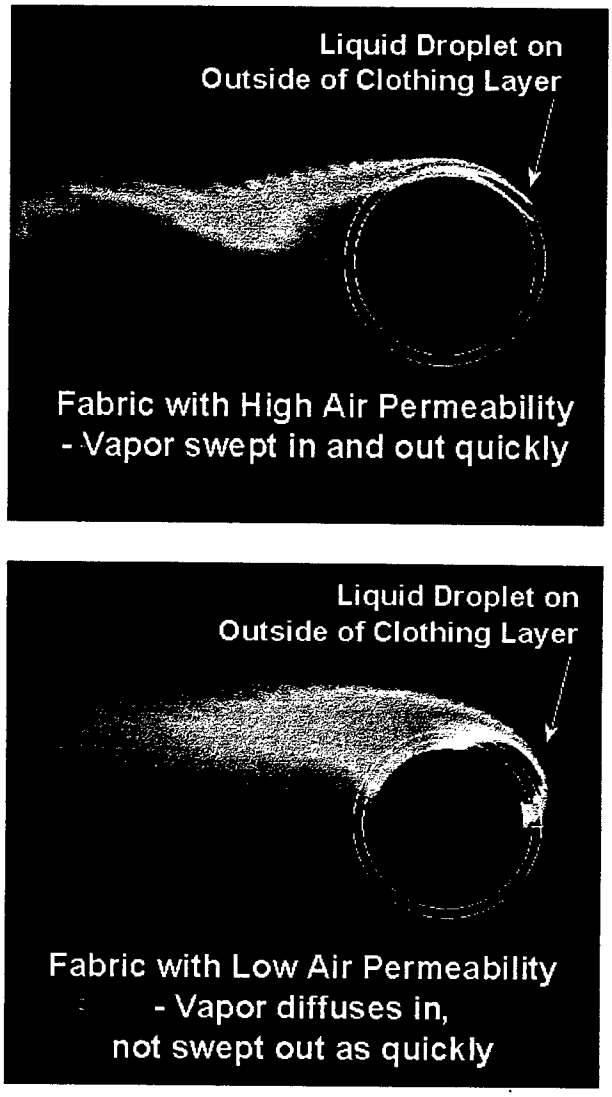


Figure 3. CFD simulation of liquid droplet evaporating on outside surface of an air-permeable fabric layer covering a cylinder (grayscale contours refer to vapor concentration, scale not shown).

Modeling fabric properties in this simple cylindrical geometry provides much of the information required for system-level decisions about various transport property trade-offs between different material candidates for protective clothing materials. However, there are some situations, particularly those having to do with body movement and motion, as well as interfaces and closures between different clothing system components, where more detailed models are desirable.

Nondestructive 2-D and 3-D Visualization of Interface Defeat Based Ballistic Impact Damage in TiC Ceramic Target Disk

J. M. Wells1, W. H. Green2 and N.L.Rupert3

1. U. S. Army Research Laboratory, AMSRL-WM-MC, Aberdeen P. G., MD, USA 21005-5066
2. U. S. Army Research Laboratory, AMSRL-WM-MD, Aberdeen P. G., MD, USA 21005-5066
3. U. S. Army Research Laboratory, AMSRL-WM-TD, Aberdeen P. G., MD, USA 21005-5066

Summary

Future armor systems may achieve improved survivability by the exploitation of the dwell and interface defeat mechanisms at a considerably reduced systems weight. Dwell involves the delay, and interface defeat the prevention, of penetration by a long rod penetrator into a ceramic while the penetrator material contacting the ceramic front face flows laterally. These mechanisms occur at or near the impacted front surface of a highly confined armor ceramic material.. Such confinement of a candidate armor ceramic target material also provides for retention of damage fragments for post-impact evaluation by either destructive or non-destructive methods.

This study was initiated to demonstrate the feasibility of applying the state-of-the-art nondestructive testing methodology known as x-ray computed tomography, CT to ballistic damage assessment. Specifically desired was the capture, digitization and display, in both two dimensional (2-D) and three dimensional (3-D) formats, of the actual mesocracking damage created in a TiC ceramic target from an interface defeat or dwell experiment. A 72 mm diameter by 25mm thick TiC ceramic disk was recovered and mechanically sectioned in half. One semi-circular section was examined in this study (see Figures.1. and 2).

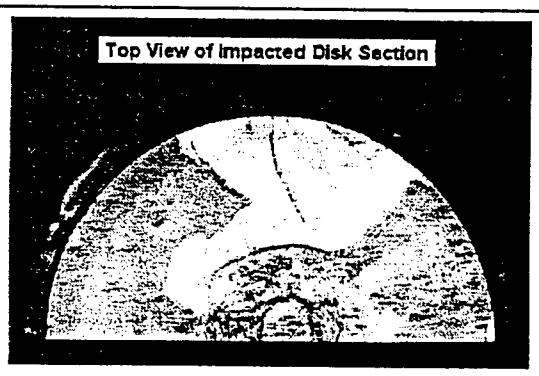


Figure 1a TiC ceramic half disk showing front impact surface

Figure 3 schematically shows the rotate-only (RO) x-ray CT technique.The dimensional accuracy and the digital nature of CT images obtained allow the accurate volume reconstruction of multiple adjacent slices. The slices provide 2-D information through out the entire object or a section of the object (See Fig.4).

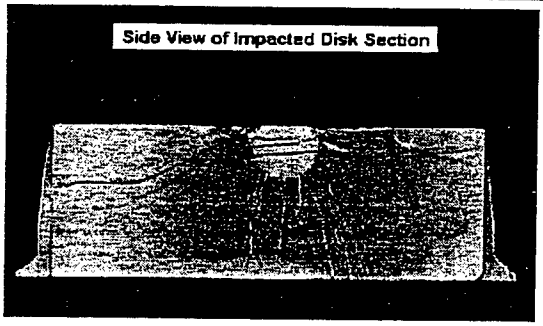


Figure 2. TiC ceramic sample through thickness cross section showing mesocracks

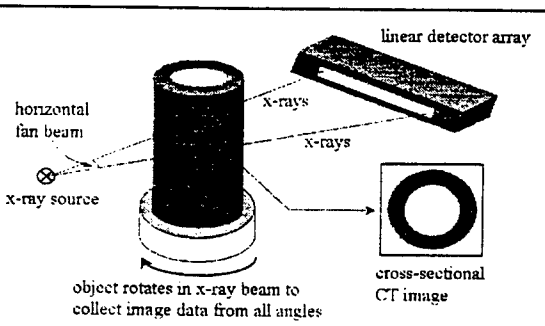


Figure 3. Schematic of rotate-only CT scan technique

Various ways of visualizing volumetric data include multiplanar reconstruction (MPR) Pseudo 3-D and 3-D solid reconstruction. Multiplanar reconstruction (visualization) displays top, front, side, and oblique view slices throughout the object. The orientation of the top slice is parallel to the cross-sectional image plane. The front slice is orthogonal to the top slice. The side slice is orthogonal to both the top and front slices. The oblique slice can be placed on any one of the other three slices.

However, each view (i.e., top, front, side, and oblique) is a slice with finite thickness through the object, not a true 2-D projection. The top, front, and side slices can be moved anywhere in the reconstructed volume (See Fig.5). Dimensional analysis, image processing, and automated flaw detection and measurement can be performed with MPR images. The volumetric data can be displayed as a 3-D solid object in 3-D reconstruction (see Figure 6), and the orientation of the solid in space can be changed to facilitate different views. The solid can also be "virtually" sectioned by only displaying part of the reconstructed volume, which creates a "virtual" cutting plane on the solid showing the x-ray density values on that plane.

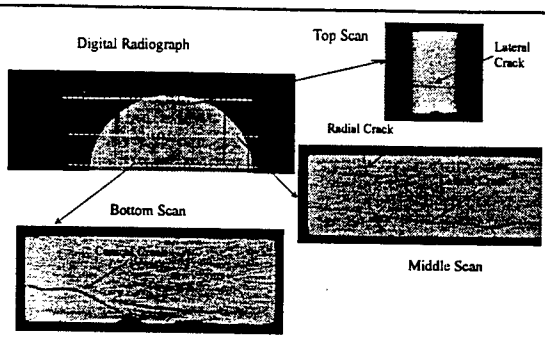


Figure 4. Digital Radiograph and 2-D CT slices

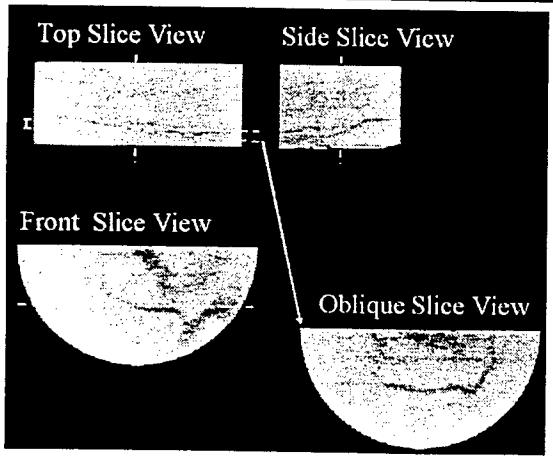


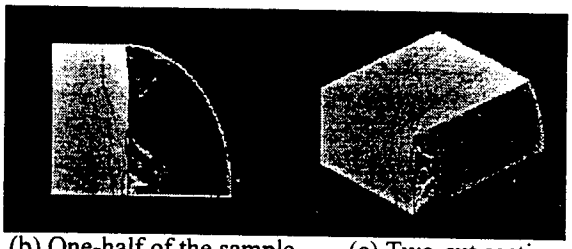
Figure 5. Multiplanar Visualization of Impacted TiC sample

Conclusions & Recommendations

X-ray computed tomography has proven itself as an suitable nondestructive technique for the purpose described herein. Material damage in the form of conical, radial and laminar mesocracks in the impacted TiC specimen were observed. The geometry and depth profile



(a) Original sample



(b) One-half of the sample (c) Two-cut section

Figure 6. 3-D solid visualizations of TiC sample.

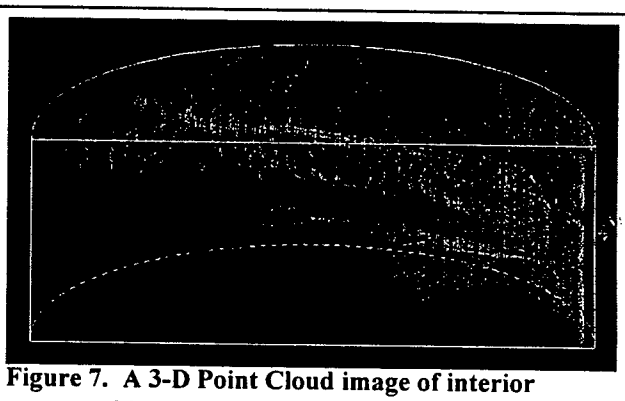


Figure 7. A 3-D Point Cloud image of interior mesocracking network

of the mesocracking are visualized and recorded in multiple adjacent CT slices. Mesocracking damage was significant and nonuniformy distributed throughout the impacted specimen. Multi-planar and 3-D solid visualization shows how the crack damage changed perpendicular to and in the through thickness direction. We have also "skeletonized" the crack damage via advanced image processing techniques to represent the entire mesocrack damage by a 3-D point cloud or wireform, This approach removes the bulk material from the image and completely maps only the mesocracking damage for 3-D visualization as shown in Figure 7. It remains to deconvolute the point cloud into the constituent mesocracking types for both geometrical and semi-quantitative analysis.

THE WEB MAPPING TECHNOLOGY INITIATIVE: A PUBLIC-PRIVATE PARTNERSHIP

Dan Specht, Bill Ryder, and Randy Swanson, Co-authors
U.S. Army Corps of Engineers - Engineer Research and Development Center
Topographic Engineering Center
Alexandria, Virginia 22315-3864

ABSTRACT

The Web Mapping Technology (WMT) Initiative is a collaborative effort between government agencies, international standards organizations, academic institutions, and the commercial geoprocessing sector to develop interoperable web mapping technology. This initiative enables web-based mapping to support applications requiring access to multiple geospatial information sources across the World Wide Web and secure networks. Applications include environmental analysis and management, disaster relief, emergency response and management, and military operations.

I. BACKGROUND: WEB MAPPING IN 1998

Many commercial web-mapping systems were available in 1998. The Web was ***the*** new market for geospatial technology vendors. Developers and clients recognized the power of the Web in delivering geospatial content to distributed users. Several problems however, were inherent in the technology. Each web-based system was an isolated data source with little interoperability between other sources. Each time a data provider attempted to deploy a web-based mapping system, an inordinate amount of data needed to be uploaded. The U.S. national security establishment recognized that we live in a 21st century security environment where the Army faces:

- An increased variety of threats.
- Increased crisis frequency.
- Wider range of interoperability requirements with partners (multinational, interagency, non-state).
- Requirements to integrate resources and capabilities found outside DOD.
- Less planning and execution time.

(*From JV 2010 and 2020*)

New challenges such as Homeland Security, Coalition Warfare, and Disaster Response requiring Army coordination with different information communities were added to a long list of existing responsibilities. Each new challenge has brought new geospatial requirements. Meeting these new challenges means that applications need to integrate geospatial information from multiple and diverse sources, both on the World Wide Web and secure intranets.

II. A NEW APPROACH NEEDED

Analysts believe that commercial web-based mapping technology can provide an intuitive on-line interface to geospatial information and tools to turn this information into usable data. To meet this new set of challenges the technology needed to be augmented with new capabilities. Processes needed to be developed to discover geospatial information from multiple on-line sources, integrate that information into one view, and deliver the data to users in digital map displays. An industry-wide survey indicated that many vendors, when asked for solutions incorporating new capabilities, provided proprietary solutions. Other technology vendors responded with innovative ideas.

To implement this new approach, the Army is required to "engineer" the development process in a method by which the capabilities it desires are built into commercial and open source web mapping components as they are developed. Embedded capability means that map servers can "speak" the language of interoperability in addition to their proprietary language. The capability to access and exploit multiple data sources grows exponentially as old systems are replaced by newer web-enabled ones. Systems that provide new capabilities are better able to respond to Army needs at reduced development and procurement costs.

III. BRINGING THE VISION TO REALITY

Bringing interoperable web-based mapping to reality requires more resources than available to a single agency. The OpenGIS Consortium (OGC) was thus consulted. The OGC is a consortium of government, academic, and industry partners dedicated to establishing standards for open geoprocessing. Various proposals were incorporated into a

framework; the Web Mapping Technology (WMT) Initiative. Participants worked together with the Army and other sponsors to establish operating capabilities and specifications. Multiple agencies sought similar capabilities to support applications such as disaster relief and environmental management. Vendors also responded by providing a three-to-one commercial to government investment in hopes of creating new business opportunities.

IV. SPECIFICATIONS AND INTEROPERABLE COMPONENTS

The WMT Initiative develops components that enable common interfaces necessary for multi-source discovery, display and interaction. These components support diverse applications across web environments, ranging from enterprise intranets to home users. The technology development process acknowledges that there are at least two different client-server distribution cases. The cases distinguish how much actual geospatial information (feature data) or symbolized map displays (i.e. gif or jpeg images or scalable vector graphics) travel across the web and the scope of client-server services necessary to support that transfer. A major focus of the initiative is to assess the content and format of the network messages. Standard methods to discover, portray, and link geospatial information are also developed. Conducting scenarios and pilot projects tests the effectiveness of the components.

V. INITIAL INTEROPERABLE TECHNOLOGY DEVELOPED

The main technology elements developed by the WMT Initiative to date include The Web Map Server (WMS) Interface Specification and Geography Markup Language (GML). WMS is an effective way to format spatial context, query, and server capability messages. GML is an industry-standard, web-optimized data transport format. Companies are now selling interoperable solutions as well as shareware components. Federal agencies have extended databases to serve on-line geospatial information using this technology. Army-funded efforts are building the first Interoperable Delivery Environment for Geospatial Information and Services (IDEGIS) with many dual-use technology aspects. IDEGIS developed and tested a number of technologies to enable interoperability in the including software wrappers and adapters.

CONCLUSION

Interoperable* technologies such as the WMS Interface Specification enable Army users to access geospatial information from civil and military sources. The cost is significantly less than stove-pipe systems as the information and services are reusable. The initiative also develops geospatial infrastructure for the Defense Information Infrastructure (DII) Common Operating Environment (COE), promoting interoperability in a secure and globally networked environment. This technology may also provide improved methods to communicate the Common Operational Picture (COP) in network-centric environments. Finally, the hands-on nature of the WMT Initiative ensures that this technology will prosper in the challenging environment of the 21st century.

METAL-LIKE MECHANICAL PROPERTIES OF CONFINED ENERGETIC MATERIALS

Donald A. Wiegand
Building 3022, Picatinny Arsenal, NJ 07806-5000

For many years the mechanical properties of energetic materials have been studied at atmospheric pressure primarily in uniaxial compression and the results of these studies have been used as guides to material properties such as strength and stiffness. However, energetic materials are most often used in munitions under conditions of higher pressures resulting from mechanical confinement. Explosives are confined by metal casing in most munitions and propellants are confined by the breech and hot gases during burning. In addition, the confining pressure on explosives increases during launch due to set back forces. Therefore, the mechanical properties of these materials at the higher pressures produced by confining conditions are of considerable importance and are now being studied. The results of these studies indicate that many energetic materials are much stronger and stiffer than heretofore thought. While energetic materials have ceramic-like properties under uniaxial loading at atmospheric pressure, i.e. they fail by cracking and fracture, when loaded at higher pressures under confined conditions they have metal-like properties, i.e., they fail by plastic flow and work hardening.

Three methods of confinement have been used in these studies. These are: hydrostatic confinement by oil immersion at constant pressure; radial confinement by a tight fitting thick walled steel cylinder (negligible radial strain); and frictional confinement on the end surfaces of thin wafers. Axial compression is used in all cases. While similar results are obtained by the use of all three methods, the most useful quantitative information is obtained by the use of hydrostatic confinement at constant pressure. The confining pressure is not constant for the other two techniques. For organic crystalline explosives such as TNT {trinitrotoluene} and Composition B {a composite of TNT and RDX (cyclotrimethylene trinotramine)} a constant pressure is not important because properties such as the yield strength and Young's modulus were found to be independent of pressure. However, for the newer plastic bonded explosives and most propellants these same properties are strong functions of confining pressure. This dependence on confining pressure is typical of polymers and indicates the strong influence of the small polymer content on the mechanical properties of plastic bonded explosive and propellants. These results confirm earlier studies of the temperature and strain rate dependence which also indicate the dependence of the mechanical properties of these materials on the polymer properties.

Under uniaxial compression of all the energetic materials investigated at atmospheric pressure the stress initially increases linearly with strain, then curves over and passes through a maximum, and then decreases for further increases in strain, i.e., strain or work softening occurs. After this deformation the sample is cracked and often fractured. In contrast, for confined compression at higher pressures a linear region is followed by yield, plastic flow and work or strain hardening. After this treatment there is no evidence of cracking, but only a change of dimensions due to plastic flow. Thus, the strain softening due to cracking is eliminated by confinement and is replaced by plastic flow and work hardening. These results then indicate that crack growth processes are completely inhibited by confinement and that at higher stresses plastic flow occurs. Plastic flow is not observed without this confinement because the stresses required for crack growth are less than the stress for plastic flow. Thus, there is a change in failure mechanism from crack growth and fracture without confinement to plastic flow and work hardening under confinement. Many metals exhibit somewhat similar behavior, i.e., a decrease in brittleness and increased ductility under confinement.

The yield strength, flow stress, Young's modulus and the work hardening coefficient of plastic bonded explosives all increase very significantly with confining pressure. The yield strength and the flow stress, taken as the stress required for significant plastic flow, increase linearly with confining pressure, Young's modulus increases exponentially and the work hardening coefficient increases approximately linearly with this pressure. Thus, for one material at 138 MPa (20,000 psi) we have the very striking and unexpected result that the yield strength and Young's modulus are about 60% of the values of aluminum and 20% of the values of steel, the latter at atmospheric pressure. In contrast, when this same material is at atmospheric pressure these properties are approximately 3% of the values of aluminum and 1% of the values of steel, the latter also at atmospheric pressure. An noted the yield strength and Young's modulus of crystalline explosives such as TNT are independent of confining pressure.

The pressure dependence of the yield strength can be understood in terms of a frictional stress on the slip plane which resists yield. This frictional stress then increases linearly with the normal stress on the slip plane and so the applied hydrostatic pressure. Alternately the pressure dependence of the yield strength can be attributed to a thermally activated processes for yield with an activation energy which increases linearly with the hydrostatic pressure and decreases linearly with the axial stress. Both of these yield models, which are thought to occur in polymers, also predict other obserables that can be used to determine which is appropriate for the various energetic materials of interest.

The very strong dependence of Young's modulus on confining pressure may also be due to one of two effects. As the intermolecular distance is decreased with increasing pressure, the intermolecular repulsive forces are increased, thus giving increased stiffness and so an increased Young's modulus. In addition, decreased porosity with increasing pressure is known to increase the modulus. The importance of these two mechanisms must be accessed by additional studies. The pressure dependence of the work hardening coefficient may also be related to the increase of the intermolecular repulsive forces with increasing pressure.

In summary, all energetic materials studied exhibit a change in failure mechanisms from crack growth and fracture at atmospheric pressure to plastic flow and work hardening when confined at elevated pressures. Thus, energetic materials have brittle ceramic-like properties at atmospheric pressure but metal-like ductile properties when confined. It is the properties under confinement which have not been available but which are required for predicting the response of energetic materials during most munitions use. In addition, mechanical properties such as the yield strength and Young's modulus of polymer containing energetic materials such as plastic bonded explosives increase very significantly with pressure and have values approaching those of metals at pressures encountered in munitions use. These values are much larger than heretofore thought and have very exciting consequences for munitions design. For example, plastic bonded explosives should be able to withstand much higher accelerations during launch or decelertions during impact without danger of unwanted ignitions. In addition, the higher explosive strength and stiffness can allow for the design of lighter weight munitions.

FLEXURAL BEHAVIOR OF REINFORCED CONCRETE MEMBERS STRENGTHENED USING MECHANICALLY FASTENED FIBER REINFORCED POLYMER PLATES

James C. Ray* and David W. Scott, U.S. Army Engineer Research and Development Center;
Anthony J. Lamanna and Lawrence C. Bank, University of Wisconsin-Madison

Scenario: A U.S. Army task force deploys to an undeveloped nation to complete a time-sensitive mission critical to U.S. security interests. Reconnaissance of the route from the port of debarkation to the mission area reveals the presence of a reinforced concrete bridge without a feasible bypass. The bridge does not have sufficient strength to safely support task force traffic. To support the mission, the task force engineer and his or her assigned soldiers must expediently strengthen the bridge.

In recent years, fiber reinforced polymeric materials (FRP) have emerged as a viable retrofit scheme for strengthening reinforced concrete bridges. All commercially available FRP strengthening systems consist of fiber mats or pre-cured strips which are adhesively bonded to the structural member. While these types of systems have been demonstrated as effective in a wide range of civilian applications, there are hindrances to the adoption of this technology for military use. Any adhesively bonded system will require time for the bondline to cure to ensure effective transfer of load from the existing member into the retrofit. In addition, proper surface preparation of the substrate must be completed for the bond to be effective. This often requires special tools and time-consuming labor. Environmental control during application is critical. Obviously, in many situations Army personnel will not have the time or equipment to effect a proper application of adhesively bonded FRP materials. Furthermore, Army operations are conducted under the broadest range of climatic conditions. For these reasons, an effort is currently underway to develop alternative application methodologies for FRP materials to strengthen reinforced concrete bridge elements.

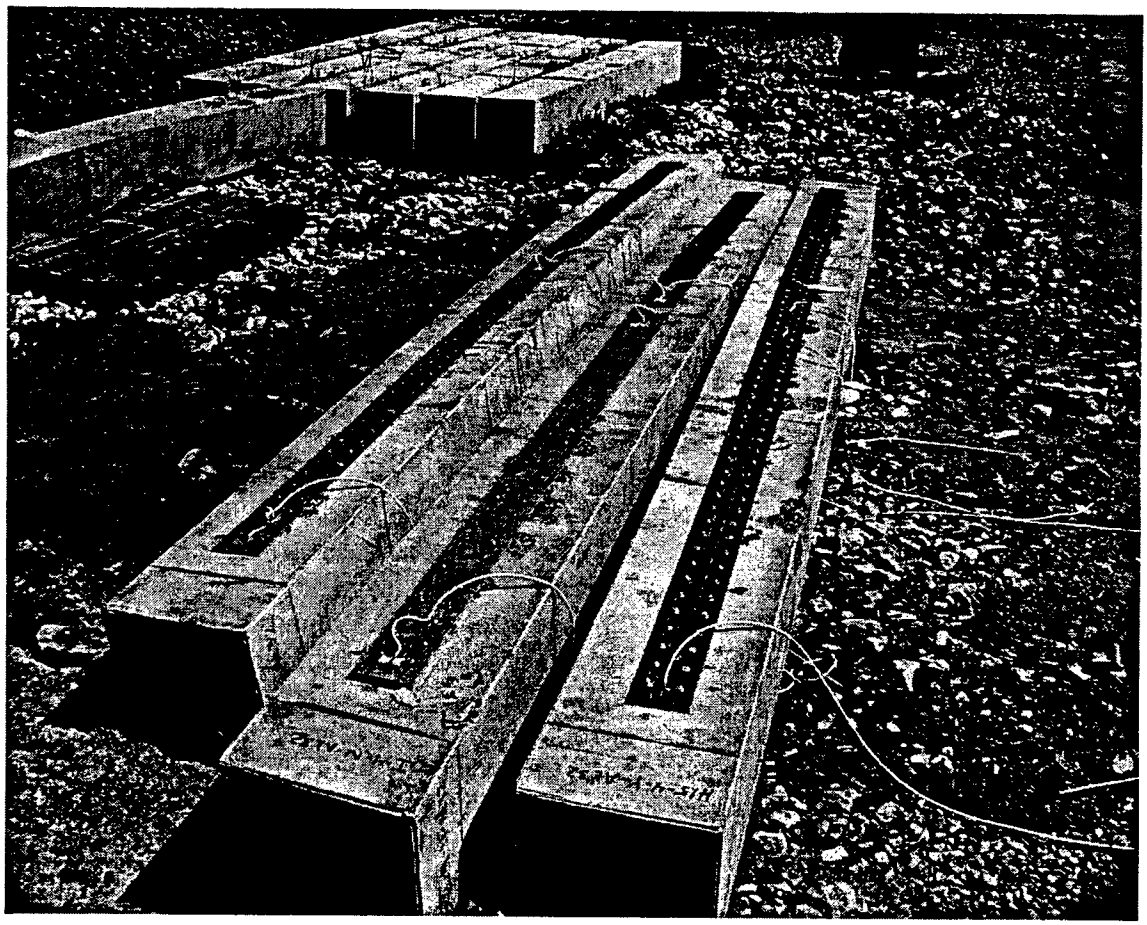
To be effective in a rapid retrofit scenario, FRP must effectively increase the strength of concrete bridge components typically found in the field in a short period of time. Total application time should be measured in hours rather than days. Additionally, the application procedure for the FRP system should not be too complex. U.S. Army engineer squads and platoons may have limited construction experience and may lack some of the tools and equipment used by commercial contractors in FRP applications. Finally, FRP must be viable under a wide range of climatic and environmental conditions that an Army task force can encounter in the field.

One potential application technology for a rapid retrofit scheme involves the use of powder actuated mechanical fasteners to secure FRP plates to reinforced concrete elements. This technology addresses the aforementioned concerns with adhesive bonded systems. Obviously, no curing is necessary using these types of fasteners. Additionally, no special substrate preparation is necessary prior to application. The devices used to drive powder actuated fasteners are easily procured in all parts of the world, and are commonly supplied to Army personnel for other uses. Finally, this application technique is environmentally insensitive under all but the most extreme conditions.

Many issues must be addressed regarding the use of this technology. Primary among these issues is the effectiveness of load transfer when using discrete mechanical fasteners rather a continuous adhesive bond. Feasibility tests on small-scale strengthened members resulted in

increases of 60-70 percent over the capacity of similar un-strengthened elements. Another issue is the governing limit state behavior of the member and how the limit state changes once the section is strengthened. Experiments using the mechanically fastened FRP strips demonstrated that the retrofit could be applied without altering the governing mode of failure – concrete compression. This is favorable in comparison with many adhesively bonded systems, where peeling stresses at the FRP/substrate interface can cause sudden brittle failure in the member.

Once the feasibility of this application technique was demonstrated, a series of near full-scale experiments was accomplished on beams as shown below. These experiments were designed to investigate the effectiveness of load transfer under application conditions approaching actual. A total of 16 reinforced concrete members were fabricated and strengthened using a carbon/glass hybrid FRP composite plate. The experimental results were compared with an analytical model that accounts for the FRP properties, connection capacity, and structural properties of the reinforced concrete members. These experimental and analytical results are being used to develop design and application criteria for concrete structural elements strengthened using mechanically fastened FRP plates.



THE CORDLESS KITCHEN: LOGISTICAL REDUCTIONS WHILE SUSTAINING THE OBJECTIVE FORCE

D.W. Pickard*
U.S. Army Soldier and Biological Chemical Command, Natick Soldier Systems Center
Natick, MA 01760-5018

D.L. Brownell, E.C. Guyer, and K.G. Coumou
Yankee Scientific, Incorporated
Medfield, MA 02052

Reducing logistics is critical to the success of the Objective Force. Many field logistics systems including kitchens, showers and laundries are dependent on the availability of electric power and require generator sets ranging in size from 2kW to 150kW. Reducing this requirement for generator sets will reduce logistics including, weight, cube, and operating costs. Homeowners too, would like to reduce electric power bills and realize their dependence on electricity every time their power fails. The recent deregulation of the electric power industry has provided incentives for the development of innovative technologies that will enable homeowners to generate their own electricity to help cut energy costs and provide a measure of independence from the public utilities (Small-Scale Cogeneration, 2000). In response to this opportunity, innovative technologists are exploring many alternatives including a new process called Liquid Injected Cogeneration (LIC) that has similar commercial and military application.

LIC is a process where water is pumped to high pressure, heated, and then injected into a scroll expander that turns a conventional generator to produce electric power. The expanded water, or steam, is then condensed in a heat exchanger for space and water heating. As a generator of electric power this approach may only be 10% efficient. However, virtually all of the energy provided in the steam can be extracted for heating, providing a cogenerator of heat and electric power that is over 85% efficient. This simple concept would only add a few additional components to a residential heating system and would address the shortcomings of conventional generators by being affordable, quiet, efficient, and maintenance free. These same advantages could be realized in those military field services that are predominantly heat-driven such as kitchens, laundries, and showers. An efficient integral cogenerator would provide logistical reductions, eliminate the need for a separate generator set and provide a "Cordless Kitchen" for the Objective Force.

RANKINE-CYCLE POWER PRODUCTION

In applications where there is no use for the waste heat from a power plant the intrinsic generation efficiency becomes very important. Utilities achieve moderately high efficiencies by using variations on the Rankine steam power cycle and large steam turbines to extract mechanical power from high-pressure steam. Because steam impinges on the turbine blades at high velocity, these systems require that no water droplets, which could erode the turbine blades, be carried along with the steam.

To produce dry steam requires that a large steam disengagement surface be present in the steam generator, and for high-pressure boilers this pressure vessel greatly adds to the expense. There is no cost effective high-pressure boiler technology that can deliver dry steam for power production. In addition to the difficulty in producing dry steam, the use of turbines to produce significant power is difficult to implement economically at the sizes appropriate to residential or field kitchen applications.

LIQUID INJECTED COGENERATION

Cogeneration is the combined production of electric power and heat. Liquid Injected Cogeneration is based on a process similar to the Rankine cycle, but without the expensive boiler and turbine associated with the traditional Rankine cycle. Instead of turbines or reciprocating expanders, a scroll expander is used to efficiently handle steam-water mixtures ranging from pure saturated water to superheated steam.

The thermodynamic cycle for the basic Liquid Injected Cogeneration process is shown on the Temperature-Enthalpy (T-h) chart in Figure 1. The cycle begins with a low temperature water sump at 250°F (Point 1 on Figure 1). The pressure in this tank is controlled to 30 psia. Water from the tank is subcooled to 220 F (2) and then pumped to a pressure of 450 psia (shown coincident with 2). The pressurized water is heated first to the saturation temperature (3) and then is partially vaporized (4). The objective is to produce steam with a quality of between zero and 70% during the heating process.

For a field kitchen, when high temperature loads are to be serviced, the high temperature water-steam mixture releases heat to the griddle and ovens at 400-450°F, thereby reducing the steam enthalpy and quality (5). The

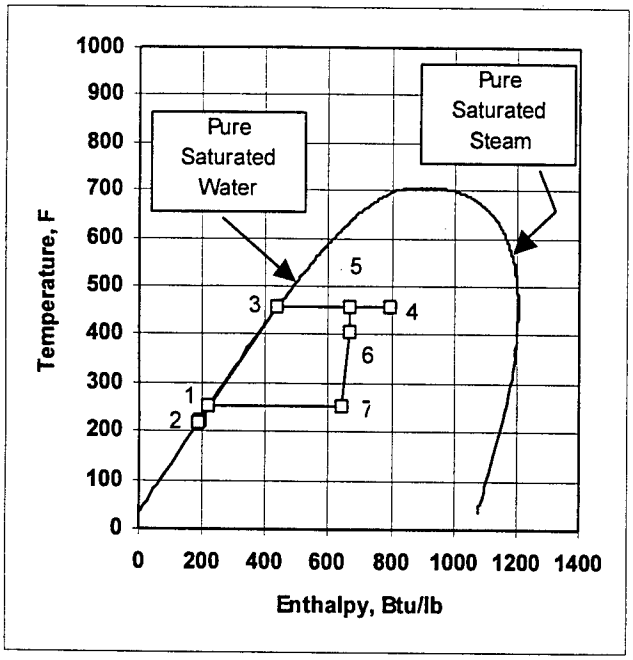


Figure 1 - T-h Diagram for LIC Cycle

steam at (5) is still at a pressure of 450 psia, and is dropped down to 265 psia in a throttling nozzle (6). The 250 psia steam is expanded down to 30 psia (7) in the scroll expander. The low temperature loads are serviced by condensing the steam from (7) to (1).

Although this cycle is a simple modification of the traditional Rankine cycle, the fact that dry steam is not needed from the water heater has a profound effect on the system economics and intrinsic safety. First, the water heating can be accomplished within a small-bore finned tube coil, eliminating the traditional pressure vessel. A 3/8 inch ID tube has a burst pressure rating that is fifty times the maximum system pressure. Also, the total inventory of hot pressurized water in the system is less than one pint. This represents a minimal total contained energy of the system. Finally, if a leak occurs in the hot side of the high-pressure loop the large water fraction present will flash and almost instantly cool the escaping water-steam mixture.

THE CORDLESS KITCHEN

Figure 2 shows a split isometric view of the general layout for the Cordless Kitchen. Two oil burners, of roughly equal size, supply heat to the system. One is fired continuously whenever there are high temperature loads or the batteries require recharging. A second burner is fired intermittently whenever the low temperature loads exceed the cogenerating capacity of the system. The Cordless Kitchen will be able to generate all the heat and power required for the built-in griddle, dual convection ovens, a 40 cubic foot reefer, two 20 gallon steam kettles and a high capacity water heater. The batteries and inverter will service electric loads during start-up and during non-cooking periods. The entire kitchen will be built into a towable 8 foot by 10 foot military ISO container.

The Dual Use Science and Technology (DUST) program has been leveraged by the DoD Combat Feeding Program to cofund a cost sharing Other Transaction with Yankee Scientific, Medfield, MA. ECR, International and the New York State Energy Research and Development Authority have provided additional leverage.

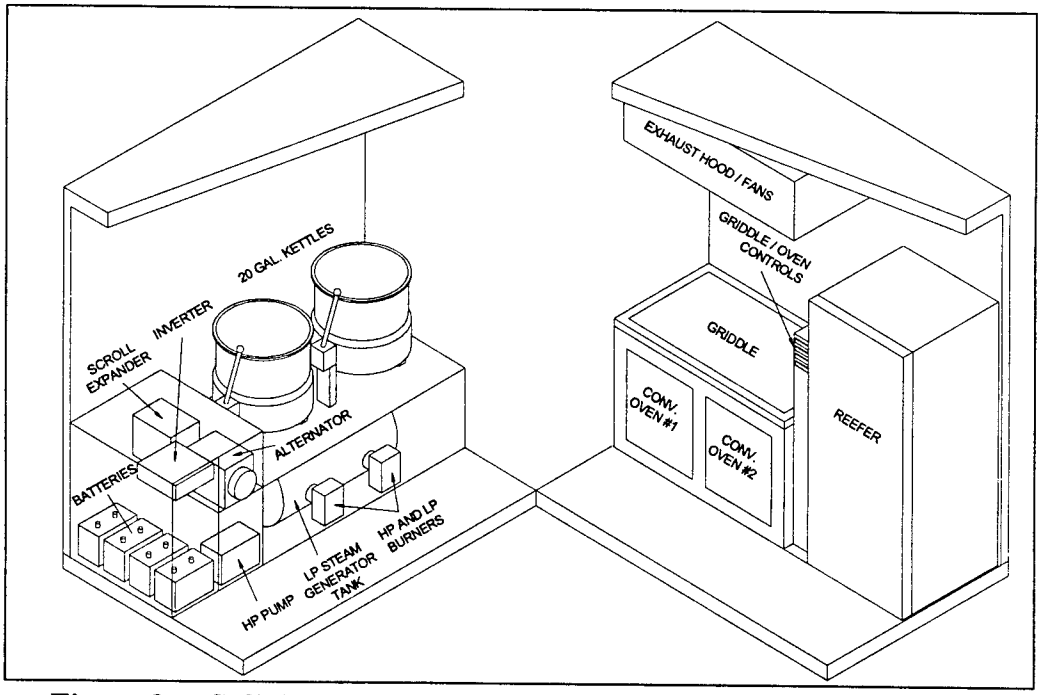


Figure 2 - Split Isometric View of Cordless Kitchen Components

ALTERNATIVE ENERGY CONVERSION TECHNOLOGIES

H. S. Coombe, S. N. Matthews, and P. D. Shively
U.S. Army Communications-Electronics Command (CECOM)
Research, Development & Engineering Center (RDEC)
Fort Belvoir, VA 22060-5817

ABSTRACT

The Army Vision calls for a force strategically responsive and dominant at every point on the spectrum of operations. Tactical power is the linchpin to the operational success of all 21st Century DoD platforms within the Future Combat System. However, the power requirements for the Objective Force in the 21st Century battlefield are unique and can not be satisfied by industry. To meet the power requirements, the DoD has tasked the CECOM RDEC to establish, coordinate, and execute various power programs for the development / advancement of Alternative Energy Conversion Technologies – specifically *Energy Harvesting* and *Thermophotovoltaics*. These two energy conversion technologies show significant promise for affordable, reliable, efficient, and compact power. Each technology offers a unique solution to satisfy the Army's need for power. Each has potential to overcome the limitations of size, weight, and power found in existing commercial power sources in the 8 – 500 Watt range.

SUMMARY

Thermophotovoltaics is an Alternative Energy Conversion Technology in which the system converts electromagnetic radiation from a thermal (non-solar) source directly into electricity. Energy Harvesting should be viewed as a process of capturing, converting, and supplying energy to target loads. Through the use of advanced materials such as piezoelectrics, for example, mechanical energy can be converted directly to electric energy.

The Army Power Division at CECOM is working to satisfy the Army goal to sustain, project, and protect an Objective Force made up of affordable components that are deployable, ensure lethality, and increase survivability. Specifically, the RDEC efforts are aimed at developing tactical power sources for the Objective Force that are lighter, smaller, and signature suppressed. Successful designs will provide the potential to satisfy the critical power needs of the Soldier System. Thus, the Power Division has been working closely with the user community and the Battle Labs to identify and define the operational and performance parameters, which will be compatible with tactical field applications. Programs have been developed which provide the guidelines by which the Army advances & adapts tech base and commercial power systems and integrates both into power systems that are compatible with the Army Vision and support the Objective Force.

CECOM has formulated strategies to transition technological breakthroughs from Technology Concepts / Applied Research to aggressive Tech Base programs. Among the TPV breakthroughs are increased efficiency, logistic fuel compatibility, and the use of novel materials to achieve spectral control. Energy harvesting breakthroughs include increased efficiency through use of novel materials, and increased power density through the use of sophisticated control of resonant piezoelectric structures. Specifically, CECOM has active programs as part of its Science and Technology Objective (STO) Integrated Power Management & Generation) in both Thermophotovoltaics (TPV) (150 - 500 W) and Energy Harvesting (8 – 50 W). This STO is devised to address the R&D challenges associated with the development and demonstration of these advanced power sources. Each effort will ensure that the resulting power source design /prototype has been formatted for a wide range of user needs.

TPV has promise across the power spectrum from very small, soldier loads on the order of a few watts to tactically mobile systems for multipurpose power. Because of the wide power range of applicability, TPV can be of great benefit to the Soldier and to PM-Mobile Electric Power, whose mission is to standardize tactical power systems across DoD. Energy Harvesting, in contrast, is better described as a process comprising many technologies. Energy Harvesting work can be categorized into two areas - energy harvesting from the environment and from humans. Energy Harvesting has the potential to provide power for dismounted soldier missions, and a broad range of other Army missions.

The results of the DARPA sponsored TPV technology advancement program for tactical battlefield applications provide the baseline for the Army's R&D efforts described in this paper. Current Army efforts call for technology development in the application of the physical sciences of direct energy conversion, power electronics, signature suppression (noise and IR), thermal management as they apply to TPV power sources. We

will address CECOM's research issues dealing with logistic fuel operation and development of militarized TPV components: emitters, filters, optical reflectors, and photovoltaic cells.

Energy Harvesting progress has been made recently by DARPA, CECOM, and others. Progress in piezoelectric materials development and modeling of piezoelectric power generation systems has been accomplished. We will illustrate how we are applying this research through the use of piezoelectrics for heel-strike power generation applications. Although heel-strike research is important, it is but one method of harvesting energy from the soldier. We will discuss how we intend to expand energy harvesting research in the future for the benefit of the Army soldier, Army equipment, and Army systems. Future research efforts will capitalize on energy available from the soldier (thermal, kinetic, etc.) and from the environment (thermal, kinetic, chemical, etc.)

CECOM's Alternative Energy Conversion Power Program is structured to meet the most demanding power and energy requirements of the Objective Force, while balancing the need for high technical performance and operational readiness with the constraints we must live under today - dwindling resources and skilled manpower. The R&D efforts within the Power Program are devised to ensure that the system is logistically supportable, R&D costs and development time are reduced, and lower unit production costs are obtained.

This paper focuses on CECOM's approach to advance the state of the art in power technology, to investigate and define tactical power requirements, and to devise/execute the R&D programs established to develop the aforementioned technology areas. Successful results will be incorporated into DoD platforms used in the tactical battlefields of today and the 21st Century - battlefields that have become and continue to become highly automated and technically sophisticated.

In close coordination with DARPA, we are pursuing research in both areas for future Objective Force applications. In this paper, we describe the technologies and technical hurdles, outline our leveraging of existing basic research, and describe our progress in applied research in both areas. We also outline the unique benefits of each technology, what we hope to accomplish, and our future execution paths.

HALON REPLACEMENTS: LABORATORY STUDIES AND FIELD TESTING OF ADVANCED FIRE SUPPRESSION AGENTS

K. L. McNesby, R. T. Wainner, R. G. Daniel, A. W. Miziolek, R. R. Skaggs[a], P. J. Peregino[a], A. E. Finnerty[a]
US Army Research Laboratory
AMSRL-WM-BD
[a]AMSRL-WM-TB
Aberdeen Proving Ground, MD 21005-5069

W. R. Bolt, B. A. Sokolis
U.S. Army Aberdeen Test Center
CSTE-DTC-AT-SL-F
Aberdeen Proving Ground, MD 21005-5059

S. J. McCormick
US Army Tank-automotive and Armaments Command
AMSTA-TR-R/263
Warren, MI 48397-5000

SUMMARY

In response to The Montreal Protocol on Substances that Deplete the Ozone Layer, and the Clean Air Act Amendments of 1990, the Army Research Laboratory (ARL), Aberdeen Test Center (ATC), and U.S. Army Tank automotive and Armaments Command (TACOM) have executed a 7 year R&D effort to identify replacement agents and technologies consistent with mission requirements for current halon uses in combat vehicle crew and engine compartments. Testing of replacements for the engine compartment applications has been completed while testing for fixed automatic and handheld crew compartment replacements is continuing. Two agents (HFC-227ea (heptafluoropropane) and sodium bicarbonate dry powder) were recommended for engine compartment applications. This recommendation was based upon data collected during engine compartment fixture and vehicle fire tests conducted at ATC. PM-Bradley selected HFC-227ea to replace halon 1301 for its engine compartment fire suppression system. PM-Abrams selected sodium bicarbonate dry powder as its engine compartment fire extinguishing system replacement agent. Vehicle retrofit execution is ongoing.

Crew compartment fire suppression tests have been conducted in a combat vehicle hull representative of an actual crew space. An in-house developed fireball simulator, designed to represent an armor penetrating threat which punctures the fuel cell creating a fireball in the crew space, was used as a screening tool for each agent/technology tested. Once acceptable performance was achieved against the simulator tests (after design and distribution optimization), the agent/system was tested against live threat munitions penetrating through the fixture hull and fuel cell filled with heated JP-8. As with halon, the decomposition products of the fluorinated compounds (i.e., HFC-227ea) consist of substantial concentrations of acid gases (hydrofluoric acid and carbonyl fluoride) that can adversely affect the health and incapacitate exposed crewmembers. Therefore, crew compartment system tests have concentrated on agents and technologies that will reduce the concentrations of acid gases produced during the extinction of a fire. Accurate acid gas measurements are difficult in a controlled laboratory environment, and almost impossible under field test conditions due to the characteristics of these compounds. ARL, in collaboration with ATC, developed laser based in-situ instrumentation to measure the quantities of acid gases produced during the extinction of fires under extreme (actual fire) test conditions [1,2]. This effort was specific to meet the Army's requirements to evaluate these agents by providing accurate real-time crew exposure data for the development of the Health Hazard Assessment profile for each candidate agent. Combinations of water (with and without additives) or HFC-227ea with solid propellant gas generators (SPGG) are promising technologies for crew compartment applications but are still being tested for comparable performance to halon 1301 systems. Also, early test results for

hand held replacements have eliminated "drop in" use of current replacement candidate agents due to poor performance with existing extinguisher hardware. Carbon dioxide (CO_2) was selected as the handheld replacement agent in all vehicles except the Abrams M1, due to potential hazardous CO_2 levels that could accumulate in crew occupied spaces. Dry powder, "gelled" powder, and potassium acetate/water mixture agents are currently being evaluated for use as a replacement for the M1 handhelds.

The significant problem of acid gas production with the use of halogenated compounds has led us to engage in laboratory studies of flame suppression by other classes of compounds [3-5]. Data in the literature show a large number of phosphorus-containing compounds (PCCs) to be very effective fire suppressants. A number of these investigations were performed in the 1960s on liquid PCCs in premixed and diffusion flames. Recently, a number of compounds have seen use as fire retardants in materials and in dry chemical fire extinguishers (e.g., ammonium phosphate). Some of the effectiveness of these compounds may be due to their physical properties. The references to phosphorus-containing liquids or gases as flame suppressants are few. These examples show liquid PCCs to be equally effective at flame inhibition. However, some uncertainty exists as to what extent this capability is due to gas-phase reactions involving phosphorus or to particulate formation. On a molar basis, PCCs have been shown to be more than 40 times more effective than N_2 and 2-4 times more effective than CF_3Br [4]. Typically, extinction concentrations are in the range of 0.5-5.0% by volume.

It has been postulated that phosphorus-containing radical species catalyze the recombination of H and OH in the combustion zone and some evidence exists of H and OH being affected by PCC addition. It has also been suggested that the presence and availability of the P atom itself is the sole determiner of the concentration of species such as HPO_2, $HOPO_2$, and HOPO, and is thus the dominant requirement for flame inhibition. However, recent experiments indicate that aromatic phosphorus ring compounds may not be as effective for flame inhibition [4]. Particular attention is thus called to the different behavior of P-N ring compounds and P-O compounds. In our work, radical concentrations are monitored *in situ* in a counterflow diffusion flame for various PCC inhibitant concentrations of both ring and non-ring structures. These measurements employ planar laser-induced fluorescence (PLIF) for imaging the concentration of the OH [5] and PO radicals throughout the flame. Inhibitor concentrations at extinction are also recorded. While the determination of the inhibiting effectiveness of various PCCs and the effect of molecular structure is one goal of this research, another goal is the development and validation of an accurate chemical mechanism for the prediction of phosphorus chemistry in a combustion environment. The end objective of this research is to look at a number of PCCs experimentally and computationally, including DMMP, $P_3N_3F_6$, and $P_3N_3(CH_3O)_6$, in comparison to N_2, HFC-227ea, and CF_3Br, as well as in comparison to model results with the currently developed phosphorus chemistry mechanism.

References

1. K.L. McNesby, R.R. Skaggs, A.W. Miziolek, M.Clay, S.H. Hoke, and C.S. Miser, "Diode Laser-Based Measurements of Hydrogen Fluoride Gas During Chemical Suppression of Fires", Appl. Phys. B, Vol. 67, pp. 443-447, 1998 .

2. R.R. Skaggs, R.G. Daniel, A.W. Miziolek, K.L. McNesby, C. Herud, W. Bolt, and D. Horton, "Diode Laser Measurements of HF Concentrations Produced from Heptane/Air Pan Fires Extinguished by FE-36, FM-200, FE-36 Plus APP, and FM-200 Plus APP", Appl. Spectr., Vol. 53, pp. 1143-1148, 1999.

3. R.R. Skaggs, K.L. McNesby, R.G. Daniel, B. Homan, and A.W. Miziolek, "Measurement of Hydroxyl Radical During Suppression of Low Pressure Opposed Flow Methane/Air Diffusion Flames Suppressed by $Fe(CO)_5$, CF_3Br, and N_2", Comb. Sci. and Tech. (in press).

4. R.R. Skaggs, R.G. Daniel, A.W. Miziolek, and K.L. McNesby, "Spectroscopic Studies of Inhibited Opposed-Flow Propane-Air Flames," *Proc. of the 9th Halon Options Technical Working Conf.*, Albuquerque, p.117-131, 1999.

5. R.T. Wainner, K.L. McNesby, R.G. Daniel, A.W. Miziolek, and V.I. Babushok, "Experimental and Mechanistic Investigation of Opposed-Flow Propane/Air Flames by Phosphorus-Containing Compounds", *Proc. of the 10th Halon Options Technical Working Conf.*, Albuquerque, in press, 2000.

MOORING ANALYSES OF RAPIDLY INSTALLED BREAKWATER (RIB) SYSTEM FOR JLOTS

Z. Demirbilek and C.E. Pollock
USA Engineer Research and Development Center
Coastal and Hydraulics Laboratory
Vicksburg, MS 39180-6199

X. Chen and J. Zhang
Texas A&M University
College Station, TX 77843-3136

ABSTRACT

Field tests and numerical modeling performed to optimize the mooring design of the Rapidly Installed Breakwater system (RIB) are described in this paper. Mid-scale field deployments of the RIB were conducted in 1999 and 2000 at Cape Canaveral and Pensacola, Florida. Emphasis of this paper is the design and modeling of RIB mooring systems and the comparison of the measured and predicted mooring line loads.

1. INTRODUCTION

The US Army Engineer Research and Development Center (ERDC), Coastal and Hydraulics Laboratory (CHL), has deployed scaled versions of the RIB system off the coast of Florida in 1997, 1999 (XM99) and 2000 (XM00), and at Duck, NC in 1996. The XM00 deployment was an ocean-scale model while all others tested mid-scale RIBS. These field studies demonstrated RIBS capability to reduce wave energy by as much as 50 percent in the sheltered area.

The RIB is a floating breakwater with two legs positioned in a "V" shape in plan view. The interior of the "V" provides a sheltered region from waves and currents. The objective of the RIB system is to support Joint Logistics Over The Shore (JLOTS) operations by creating an offshore harbor area that will allow vessel on- and off-loading to continue throughout Sea State 3 (SS3) wave conditions. Laboratory studies and scaled field experiments have proved the effectiveness of the RIB concept. For additional information on the hydrodynamic performance characteristics of RIB, see Briggs, Demirbilek and Matheu (1998).

2. MOORING OBJECTIVES AND BACKGROUND

The primary operational objective for the RIB mooring system is to hold the RIB in position with its bow pointed in the predominant wave direction and to maintain a separation of its legs at approximately 60 degrees. The sheltered area inside RIB legs is used for purposes of on/offloading the military cargo and personnel. It is important that movement of the structure in the horizontal plane be held to a minimum to avoid interaction of the RIB with vessels moored and/or operating in its lee. Also, the mooring lines need to be positioned to avoid navigational difficulties for the vessels. Additionally, dynamic snatch loads due to the mooring lines cycling taught and loose from the wave and current activity must be damped to prevent damage to the structure and to reduce anchor size requirements.

These objectives are achieved using multi-mooring line configurations that resist environmental loading from all directions. Numerical models were used to determine the optimum mooring configuration and develop individual line spec Horizontal movement of the RIB can be minimized by properly selecting a mooring system configuration and pre-tensioning of each mooring lines that could limit RIB's horizontal excursions due to current and wave effects. It is noted that a vertical component of the line tension is also transmitted to the RIB structure by each mooring line. The reserve buoyancy of RIB hull and the weight of mooring lines balance this vertical load. Dynamic snatch loads may be reduced by extensible or stretching components attached to the RIB structure or directly integrating them with the mooring lines (i.e. Seaflex lines). Overall, RIB mooring systems tested to date all have preformed remarkably well, keeping the structure open and in position, and allowing for the RIB streaming in case of a survival event (extreme conditions). The longer lengths of the interior mooring lines with a slope of 1:7 can inhibit the on/offloading of vessel activities inside the V region of the RIB, and must be carefully designed not to introduce any hazard to the vessels operation. Interior mooring lines with shorter scope would be preferred.

3. NUMERICAL MODELING OF RIBS

Extensive parametric numerical experiments were performed to investigate the combined effects of various basic mooring design parameters on the performance of

idealized RIB systems. Design parameters investigated included the number of mooring lines, attachment point, line length (scope) and composition, and also the number, type and size of the surface support buoys required for a given RIB system. We have investigated the influence of current-induced and steady wave drift forces on the overall functional requirements of RIBS and their mooring systems. The effect of various key geometric parameters on the mooring system such as draft, interior angle and shape of the RIB structures have been studied. These studies provided invaluable insight into RIB's performance requirements and also helped to identify the strengths and weaknesses of numerical predictive tools we are using for RIB design and operational issues. The Seaflex lines used for XM00 are similar to a bungee-chord with multiple strands on each line that pick up line loads if it should become necessary. The number of strands controls the extensibility of lines and dampening of dynamic snatch loads transmitted by mooring lines to the hull of RIBS.

Details of a numerical model have been presented in the unpublished XM99 Summary Report byDemirbilek and Zhang. The model provides the equilibrium force and moment data for the entire RIB system. It also provides the most loaded line data, the system failure information (total lift-off of lines from seabed or excessive elongation in the lines and /or exceeding strength limits, checks on design limits for line-anchor interface and seabed). Additionally, force and displacement responses of each mooring line along its length, the predicted tensions at the top and bottom end connection points of each line, line profiles (suspended and unsuspended length) versus spatial tension variation with the water depth, and the estimated elongation of each line are provided. In order to determine the operability limits for RIB at given water depth, it will be necessary to generate force-displacement curves for a wide range values of the expected environmental loads, and perform these analysis with and without pretensions and prescribed movements (offsets) of the RIB.

In addition to the external forcing, each mooring line must be fully described for numerical modeling. Mooring lines may be input to numerical models by defining the fairlead locations (points where lines connect to the RIB hull), anchor attachment points, number of line segments and properties (line length, diameter or other characteristic dimensions, line type, mass of the line material segments in air and water, stiffness and stress limits of line segments, etc.), intermediate attachments mechanisms to lines, if any (i.e. buoys, clump weights, by-pass lines, diverters etc.), seabed data if segments of lines were to contact the sea bottom (type, density, compactness, and resistance properties of the bottom surface), and anchor data (weight, dimensions and type of anchor, and other structural characteristics including load-carrying capacity, drag and uplift features and angle limits, etc As part of evaluating various RIB systems and concepts we have tested to date and validating and verifying numerical models, we have collected extensive field data during the past RIB deployments. After a through verification and validation, mooring analysis models will be judged for their applicability for future full-scale RIB design. In the next section, we briefly discuss the estimation of wave and current forces that play a key role on the design of RIB moorings.

An integrated approach involving physical model experiments, analytical and numerical models, and field measurements is being used to develop an optimum design for the RIB. The RIB will enable JLOTS operations to continue through SS3 conditions. Field measurements will be compared to mooring predictions from analytical and numerical models to determine confidence for using numerical models to predict the mooring requirements of the prototype RIB. As development on the RIB continues, this integrated approach will provide information concerning relevant design, deployment, and functionality of the RIB.

ACKNOWLEDGEMENTS

The authors would like to acknowledge the Headquarters, U.S. Army Corps of Engineers, for authorizing publication of this paper. This contribution was prepared as part of the Military RDT&E Program of the U.S. Army Engineer Waterways Experiment Station's Coastal and Hydraulic Laboratory. We would like to acknowledge contributions of the entire RIB team members, and in particular continual encouragement and support of RIB Program Manager, Dr. Donald Resio and ATD Manager, Dr. Jimmy Fowler.

REFERENCES

Briggs, M. Demirbilek, Z., and Matheu, E., "An Integrated Study of Wave Phenomena Affecting Floating Breakwater Design for JLOTS," Proceedings of the Army Science Conference, pp. 575-580, 1998.

Session G
Force Protection

Chair
Dr. Joseph J. DeFrank
U.S. Army Soldier and Biological Chemical Command

Co-Chair
Dr. David Stepp
U.S. Army Research Laboratory

Keynote Address
Prof. Alan J. Russell
University of Pittsburgh

THIS PAGE INTENTIONALLY LEFT BLANK

LONG-RANGE PROPAGATION OF INTENSE ULTRA-SHORT LASER PULSES IN AIR

C.M. Bowden* and N. Aközbek
U.S. Army Aviation and Missile Command
Weapons Sciences Directorate, Aviation and Missile Research, Development and Engineering Center
ATTN: AMSAM-RD-WS-ST
Redstone Arsenal, Alabama 35898-5000

ABSTRACT

We present numerical simulations on the propagation of high-power ultra-short pulses propagating in ionizing air. It is shown that these pulses propagate significantly after self-focusing. Upon propagation the near IR laser pulse becomes chirped through self-phase modulation turning into a broadband pulse spectrally ranging from the UV to IR. This may have an important application of the remote sensing of Biological and Chemical agents in the atmosphere.

1. INTRODUCTION

The formation of long filaments in air by the use of high-power femtosecond laser pulses has been the subject of interest both experimentally and theoretically for the past several years [1-8]. The long-range propagation of these pulses depends on the shortness of the pulse duration in which there is not enough time for optical breakdown to occur. In other words the pulses must be shorter than the characteristic time for collision in air (~one picosecond) to avoid cascade ionization of air. For example, if one would use a laser pulse with the same input power but longer pulse length, then before the self-focusing threshold is reached the leading edge of the pulse produces strong plasma and the rest of the pulse becomes strongly absorbed and scattered. Thus these pulses would only create a small plasma volume. In this case, no propagation takes place and the long-range propagation and supercontinuum generation does not occur. When the pulse duration is short enough to avoid the breakdown of the medium, the pulse only creates small density plasma, which stops the self-focusing process and provides the further balancing between self-focusing and defocusing of the laser beam, which creates a self-induced light filament in air. In this light channel the laser pulse can maintain its power density and temporal integrity over long distances, in which a white-light continuum is generated. The possibility to create a coherent white-light source at a remote distance, gives the possibility to detect and identify simultaneously different atmospheric components including biological and chemical agents. This technology would be very important since these laser systems do not require high-energy pulses and thus can be made mobile. How far these pulses can propagate in the atmosphere is still an open research topic and depends strongly on the initial laser parameters. However, an experiment performed at the University of Jena in Germany claims that a 120 fs and 2.2 TW peak power laser pulse propagated at least 12 km in atmosphere [4] through the detection of the backscattered white-light. The detailed characteristic of the filament is not known in their experiment but they do observe the generation of the white-light continuum along the filament. In addition to the white-light generation recent experiments reveal that a fast electromagnetic pulse (EMP) is generated along the self-induced light channel. This may have important consequences for jamming the sensor. Furthermore due to the high intensity of the pulse it is possible to induce nonlinear interactions at a target with cloud cause direct or indirect damages to the sensor device. Further studies are underway to explore the feasibility of EMP generation.

We study the propagation phenomenon of such pulses propagating in ionizing air. We show that the long-range propagation is due to a dynamic competing effect between self-focusing and plasma defocusing which alternates along the propagation. The overall dynamics of these pulses is complicated due to the strong reshaping of the pulse both spatially and temporally. Theoretical studies so far have been concentrated to the so called slowly varying envelope approximation (SVEA). In our model we go beyond this approximation and show that the SVEA breaks down and does not correctly describe the white-light continuum generation observed in air. We also discuss transverse ring formation of a focused near IR femtosecond laser pulse propagating in air. All of our results are in qualitative agreement with the experiment.

2. COHERENT WHITE-LIGHT GENERATION IN THE ATMOSPHERE

We show that a near IR laser pulse upon propagation in air transforms into a white-light laser pulse due to the combined effects of self-focusing, plasma defocusing, and the shock formation at the back of the pulse. Figure 1 shows the pulse spectrum at z=1.0 (solid line) and z=1.2 (dotted line) (the propagation distance z is normalized to the diffraction length of the collimated input beam). This spectrum is in qualitative agreement with the white-light continuum observed in the propagation of high-power ultra-short laser pulses in the atmosphere [4].

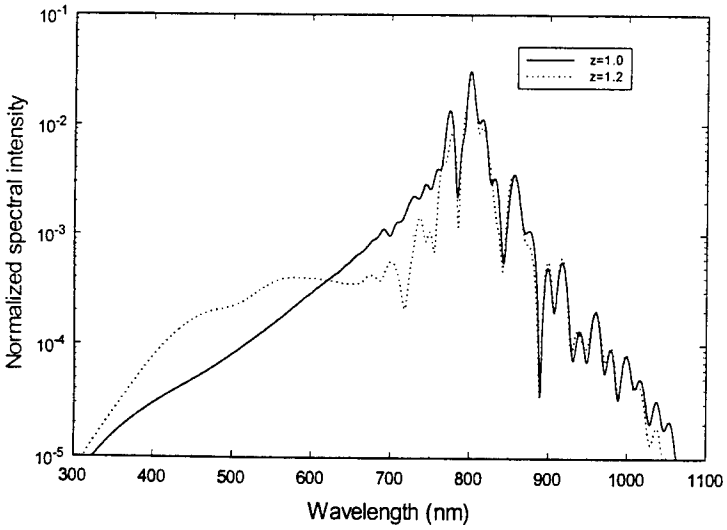


Figure 1 The power spectrum at a propagation distance (normalized to the diffraction length of the collimated laser beam) for z=1.0 (solid line) and z=1.2 (dotted-line).

The generation of white-light continuum at a remote distance in the atmosphere may have important application in the remote detection of biological and chemical agents.

ACKNOWLEDGEMENTS

N.A is a National Research Council (NRC) associate working at AMCOM and would like to thank the NRC for the financial support for this research project. This work is part of an international agreement between the defense departments of the US and Canada. The experiments are performed at Laval University in Quebec City, Canada.

REFERENCES

1. Braun, G. Korn, X. Liu, D. Du, J. Squier, and G. Mourou, *Self-channeling of high-peak-power femtosecond laser pulses in air,* Optics Lett. **20**, 73 (1995).
2. H. R. Lange, G. Grillon, J. F. Ripoche, M. A. Franco, B. Lamouroux, B. S. Prade, and A. Mysyrowicz, *Anomalous long-range propagation of femtosecond laser pulses through air: moving focus or pulse self-guiding?,* Optics Lett. **23**, 120 (1998).
3. A. Brodeur, C. Y. Chien, F. A. Ilkov, S. L. Chin, O. G. Koserava, and V. P. Kandidov, *Moving focus in the propagation of ultrashort laser pulses in air,* Optics **22**, 304 (1997).
4. L. Wöste, C. Wedekind, H. Wille, P. Rairoux, B. Stein, S. Nikolov, C. Werner, S. Niedermeier, F. Ronneberger, H. Schillinger, and R. Sauerbrey, *Femtosecond Atmospheric Lamp,* Laser und Optoelektronik **29**, 51 (1997).
5. M. Mlejnek, E. M. Wright, and J. V. Moloney, *Dynamic spatial replenishment of femtosecond pulses propagating in air,* Optics Lett. **23**, 382 (1998).
6. A. Talebpour, S. Petit, and S. L. Chin, *Re-focusing during the propagation of a focused femtosecond Ti:Sapphire laser pulse in air,* Opt. Comm. **171**, 285 (1999).
7. N. Aközbek, C. M. Bowden, A. Talebpour, and S. L. Chin, *Femtosecond pulse propagation in air: Variational analysis,* Phys. Rev. E **61**, 4540 (2000).
8. J. Kasparian, R. Saauerbrey, D. Mondelain, S. Niedermeier, J. Yu, J.-P. Wolf, Y.-B. Andre, M. Franco, B. Prade, S. Tzorzakis, A. Mysyrowicz, M. Rodriguez, H. Wille, and L. Woste, *Infrared extension of the supercontinuum generated by femtosecond terawatt laser pulses propagating in the atmosphere,* Optics Letters **25**, 1397 (2000).

DEVELOPMENT AND EVALUATION OF SELECTIVELY PERMEABLE MEMBRANES FOR LIGHTWEIGHT CHEMICAL BIOLOGICAL PROTECTIVE CLOTHING

Eugene Wilusz and Quoc T. Truong
U.S. Army Soldier and Biological Chemical Command
Natick Soldier Center
Natick, MA 01760

Abstract

Selectively permeable membranes are widely used throughout the chemical industry for carrying out chemical separations. Work is underway to develop membranes for novel use in lightweight, chemical biological (CB) protective clothing. Membranes, which function without the use of a carbon adsorbent medium, have been developed and evaluated. Mechanical properties, barrier properties, and moisture vapor transmission (MVT) rates have been determined. Prototype garments have been fabricated, and limited field evaluations have been accomplished. Subjective comfort and durability have been determined.

1. Introduction

CB protective clothing has been developed and improved over the years for industrial, medical, and military uses. The threat of exposure to hazardous chemicals and biological agents remains very real, and the need for proper protection is as important today as it ever has been. The materials that have been used to provide protection range across a spectrum from air-impermeable materials to air-permeable materials combined with activated charcoal. Elastomers, plastic films, and multilayer film/fabric composites such as butyl rubber coated fabrics are used in gloves, boots, respirators, and OSHA Level A, fully encapsulating suits, and provide excellent protection, but the clothing utilizing these air-impermeable materials is heavy, uncomfortable, restrictive, and can result in the rapid onset of heat stress.[1] Air-permeable materials combined with activated charcoal such as the US Army Battle-Dress Overgarment (BDO) [MIL-S-43926], the US Marine Corps Saratoga Overgarment (Saratoga®) [MIL-S-29461], are more comfortable than their air-impermeable counterparts, but have the same limitations to a lesser degree. This work was undertaken to develop a new generation of materials for lightweight, CB clothing based on the use of selectively permeable membranes (Figure 1). Membranes have been used worldwide by the chemical industry for carrying out gas separations, in the purification of water by reverse osmosis, and in medical applications.[2,3] . Microporous membranes are used today in rainwear and in cold-weather clothing because they serve as barriers to liquid water while still allowing moisture vapor transport through the clothing, providing relief from heat stress through evaporative cooling. In this work membranes have been developed which serve as barriers to hazardous chemicals and agents of biological origin (toxins, bacteria, and viruses) while still allowing a significant rate of moisture vapor transport.

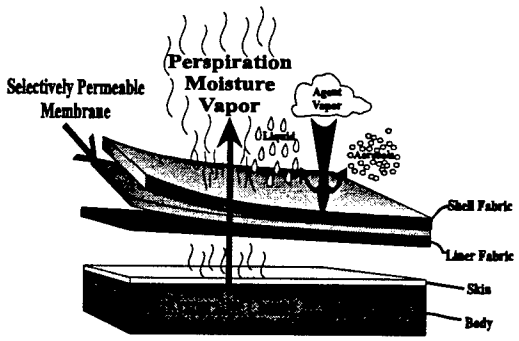


Figure 1. Material Concept

2. Experimental

Numerous candidate membranes were obtained from industry or developed with industrial partners. Membranes were characterized for their physical properties using standard methods. Chemical barrier properties and moisture vapor transmission properties were determined using in-house methods. Two membrane systems of particular interest are a polyallylamine-based membrane developed by W.L. Gore and Associates, Inc. and a cellulose-based membrane developed with Acordis Research.

3. Results and Discussion

The membrane/fabric systems from Gore and Acordis were found to have acceptable physical properties and weigh about half that of the BDO and the Saratoga® fabric systems. Permeation of water and selected organic vapors through Gore and Akzo fabric systems showed that they are highly permeable to water vapor but not to common organic vapor molecules

(Figure 2). The membranes are considered to be waterproof because of their excellent hydrostatic resistance. In order to determine evaporative cooling potential, candidate membrane/fabric swatches were tested on a standard sweating guarded hot plate, and they were found to have lower intrinsic thermal resistance and a lower intrinsic water vapor resistance than any of the fabric systems currently in use in military CB clothing systems (Figure 3).

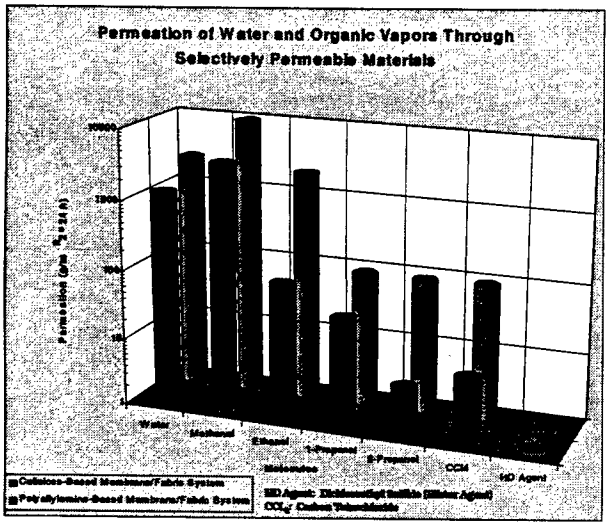
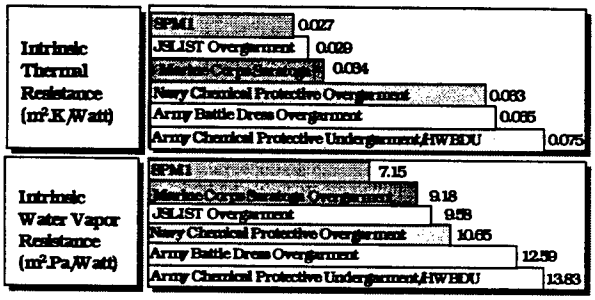


Figure 2. Permselectivity



SPM1: Polyallylamine-Based Membrane Laminated to Nylon Shell Fabric
HWBDU: Hot Weather Battle Dress Uniform
JSLIST: Joint Service Lightweight Integrated Suit Technology

Figure 3. Evaporative Cooling Potentials (Guarded Hot Plate, ISO 11092)

Moisture vapor transmission was determined using a novel dynamic moisture permeation cell developed in-house.[4] Candidate membranes showed very good MVT properties across a wide range of relative humidity as compared to an impermeable film. MVT was also measured using the standard method (ASTM E96-95, Method B), and these tests indicated that the Gore membrane has slightly higher MVT than a semipermeable fabric, but lower than that of a "breathable" carbon-based fabric system and much better than an impermeable fabric system.

Barrier properties against a variety of liquid and vapor chemical challenges were determined using in-house permeation test methods.[5,6] In general, membranes having good MVT properties were not good barriers to chemicals. The Gore and Acordis membranes were found to be exceptions in that they exhibited very good barrier properties to a battery of chemicals while still having high MVT properties. Live agent testing using standard protocols indicated excellent barrier properties to chemical agents.

The membrane/fabric systems were fabricated into prototype jackets and trousers and subjected to wear tests with favorable results. It is expected that rigorous field evaluation of these garments will be accomplished in the near future. Test subjects preferred these garments to BDO and Saratoga®, which were used as standards in the field tests. The users perceived the membrane garments as being lighter weight and more comfortable.

4. Conclusions

Permselective membranes have been developed which serve as excellent barriers to hazardous chemicals and biologicals while allowing moisture vapor transport to occur. It is expected that this novel approach to CB clothing will lead to a dramatic increase in comfort and reduced heat stress in military overgarments as well as the emergence of a CB duty uniform. It is also anticipated that these novel garments will prove useful to individuals involved in emergency response to chemical and biological incidents such as police, firefighters, and emergency medical personnel.

1. Wilusz, E., Polymeric Materials Encyclopedia, J.C. Salamone, Ed., 899, CRC, Boca Raton (1996).
2. Koros, W.J. and Fleming, G.K., Journal of Membrane Science, 83 (1993).
3. Winston Ho, W.S. and Sircar, K.K., Eds., Membrane Handbook, chapter 1, Van Nostrand Reinhold, New York (1992).
4. Gibson, P., Kendrick, C., Rivin, D., Sicuranza, L., and Charmchi, M., J. Coated Fabrics, 24, pp. 322-345 (1995).
5. Truong, Q. and Rivin, D., Natick/TR-96/023L, US Army Natick RD&E Center (1996).
6. Rivin, D. and C. Kendrick, Carbon, 35, 1295-1305 (1997).

RECOMBINANT ANTIBODIES FOR THE DETECTION OF BACTERIOPHAGE MS2 AND OVALBUMIN

Kevin P. O'Connell*, Peter A. Emanuel, Akbar S. Khan, and James J. Valdes
Edgewood Chemical Biological Center, U. S. Army Soldier Biological Chemical Command
Aberdeen Proving Ground, MD 21010

Timothy J. Stinchcombe and Robert Shopes
Tera Biotechnology Corp.
La Jolla, CA 92121

Maha Khalil and Mohyee E. Eldefrawi
Department of Pharmacology and Experimental Therapeutics, University of Maryland School of Medicine
Baltimore, MD 21201

ABSTRACT

Antibodies are currently field-deployed as the biological component of sensors that detect biological threat agents. Previously, we developed an anti-botulinum toxin antibody using a powerful genetic technology known as phage display. We describe here the isolation of additional recombinant antibodies that bind two simulants of biothreat agents: bacteriophage MS2, and the protein ovalbumin. The phage display method allows the rapid selection of genes encoding specific antibodies out of an enormous population of candidates, and the subsequent production of large amounts of the recombinant antibody in bacterial fermentations. A single anti-MS2 antibody was isolated. The screen for anti-ovalbumin antibodies yielded two independent clones with unique nucleotide and amino acid sequences. All antibodies isolated demonstrated specificity for the molecule against which their selections were targeted. A key feature of the method was the use of a recombinant antigen, cloned MS2 coat protein, for the affinity enrichment of clones in place of the intact bacteriophage target.

INTRODUCTION

Antibodies are the essential component in immunological sensors that detect BW (biological warfare) agents, giving them both sensitivity and selectivity for BW agents. The Army and the Joint Program Office for Bio-Defense (JPO-BD) purchase and field biosensor platforms (JBIDS, JPBDS, JBREWS, and PORTAL SHIELD systems) that incorporate antibodies produced in whole animals (polyclonal) and mammalian cell cultures (monoclonal) for biowarfare agent detection.

There is considerable lot-to-lot variability in the current production of antibodies. This is especially true for polyclonal antibodies, which require the injection of a disarmed BW agent into animals. The process of developing antibodies in animals or in mammalian cell culture is also time-consuming, which limits the capacity for "just-in-time" or surge production in time of conflict.

A recent advance in antibody production technology is the cloning of antibody genes and their expression in bacterial fermentations. This technology has been proven capable of producing antibodies for BW agent detection that are of higher quality and greater uniformity from lot to lot; therefore, their inclusion in fielded bioassays would result in greater reliability. Recombinant antibodies are also faster and potentially less expensive to produce and acquire in quantity; therefore, establishing a process for their production would improve the maintainability and supportability of fielded biodetection systems. We previously described the successful cloning and properties of a recombinant antibody that binds botulinum toxin (Emanuel *et al.*, 1996).

We describe here the cloning and initial characterization of three new recombinant reagents, antibodies that bind the biothreat simulants bacteriophage MS2 (a non-pathogenic virus of the bacterium *Escherichia coli*, which is used to simulate viruses) and ovalbumin (a benign protein which is used to simulate protein toxins, such as ricin). To meet the need for high-quality, inexpensive antibody reagents that bind these BW simulants, we have used a powerful technique called phage display to isolate antibody genes from immunized mice. The resulting antibody molecules are called Fabs, indicating that they are comprised of heavy and light chain antibody sequences which form the antigen-binding variable region, but do not contain the IgG constant region.

METHODS AND RESULTS

Immunization, antibody gene amplification and cloning. Antibody genes for immunoglobulin library construction were obtained from B cells in the spleens of BALB/c mice immunized with MS2 and ovalbumin. Antibody heavy and light chain genes were processed and amplified by PCR amplification (Chomczynski and Sacchi, 1987; Hogrefe and Shopes, 1994) and assembled by ligation (MS2) or by PCR assembly (ovalbumin), digested with *Not*I and *Spe*I and cloned into phage

display vectors. The resulting primary antibody library was then expressed on filamentous phage particles by infection of the *E. coli* host cells with the helper phage VCSM13 (Stratagene, La Jolla, CA). The filamentous phages that were produced by the *E. coli* culture displayed recombinant antibodies on their surfaces, as determined by the detection of mouse kappa light chains in dot blots of the expressed phage.

Affinity enrichment ("biopanning") of antibody clones. Phage particles displaying anti-MS2 or anti-ovalbumin antibodies (and containing the corresponding cloned antibody genes) were obtained by a form of affinity enrichment called "biopanning" (Parmley and Smith, 1988). Small amounts of each antigen were immobilized on a solid surface (a well of a microtiter plate), and a population of phages displaying antibodies cloned from the corresponding immunized mice were washed across the surface. Those phage particles displaying antibodies that bind the antigen were retained on the surface, while non-specific phages were washed away. Each phage bound to antigen contains the genes that encode the antibody on the surface of that phage. Three to four rounds of biopanning were typically performed.

Subcloning and expression of the antibody genes. Following the last round of biopanning, individual phage clones containing the desired antibodies were identified by culturing individual clones and screening for binding of the appropriate antigen by ELISA. Verified positive clones were sequenced fully and from the sequence, the IgG subclass of each clone was determined. Genes for each Fab antibody were then removed from the phage display vectors and cloned into expression vectors which incorporate a 6x histidine tag on each heavy chain for subsequent expression and purification in fermentations of *E. coli*.

Detection of MS2 and ovalbumin with recombinant antibodies. Recombinant anti-MS2 and anti-ovalbumin antibodies were used in enzyme-linked immunosorbent assays (ELISAs) to detect their corresponding antigens. Both antigens were detectable at microgram quantities or lower. The recombinant coat protein used for biopanning and screening anti-MS2 antibodies was also detected at submicrogram quantities.

DISCUSSION

The DNA and amino acid sequences of the three antibodies described here have been determined, and each antibody displays canonical sequences flanking each of the six CDRs (complementarity determining regions) per clone. The CDRs are the portions of the antibody chains in which the greatest sequence variability is present. CDRs also form the antigen-binding pockets that determine the affinity and specificity of each antibody for its antigen.

A recombinant products approach to biodefense reagent development has several technical, logistical, and animal use advantages over traditional methods of isolating and producing antibodies. The technical advantages include the potential to produce antibody diversity greater than that obtainable by the immune systems of mammals. In addition, monoclonal antibodies are generally produced by a laborious manual sorting and screening of hybridoma cells, a process that cannot handle more than several hundred clones at a time. The biopanning procedure by its nature allows the library to self-select by allowing particles displaying a desirable antibody to bind to an immobilized target for subsequent retrieval. Logistically, bacteria are much easier to grow, store, and manipulate genetically than mammalian cells. Microbial contamination is much less of a problem and much more easily dealt with when encountered. In general, bacterial fermentations can be scaled up more easily than mammalian cell cultures and their much more rapid growth and harvest provides the capacity for surge production.

Lastly, recombinant antibody production in bacteria is in step with a growing consensus that current methods of producing monoclonal antibodies in quantity are inhumane. The production of monoclonal antibodies in quantity has traditionally been achieved by growing hybridoma cells in animal hosts collecting abdominal fluids (ascites) that contain the essentially pure antibody. This method produces great discomfort in animals and is likely to be banned for large scale production in the future. The cloning of antibody genes in bacteria minimizes animal use by using only those animals initially immunized in the process. All subsequent manipulation and manufacture takes place in bacterial cells, reducing the numbers of animals used from hundreds to fewer than ten per antibody cloned.

ACKNOWLDEGEMENTS

We would like to thank Sarah Cork and Dr. Jun Park of Geo-Centers, Inc. for their expert assistance in expressing and purifying the anti-ovalbumin antibodies. David Lesh of EAI. Corp. purified the anti-MS2 antibody.

REFERENCES

Chomczynski, P. and Sacchi, N. 1987. Anal. Biochem. 162:156-159.

Emanuel, P., O'Brien, T., Burans, J., DasGupta, B., Valdes, J. J., and Eldefrawi, M. 1996. J. Immunol. Meth. 193:189-197.

Hogrefe, H. and Shopes, B. 1994. PCR Methods Appl. S109-S122.

Parmley, S. F. and Smith, G. P. 1988. Gene 73:305-318.

PUTATIVE ROLE OF PROTEASES AND OTHER INFLAMMATORY-NEURONAL MOLECULES IN THE TOXICITY OF NERVE AND BLISTER CHEMICAL WARFARE AGENTS: Implications for Universal Medical Countermeasures

F. M. Cowan*, C.A. Broomfield, D.E. Lenz and W.J. Smith

U.S. Army Medical Research Institute of Chemical Defense
Aberdeen Proving Ground, MD 21010-5400, USA

SUMMARY

The involvement of proteolytic processes in the initiation, modification or regulation of inflammatory, neurologic and tissue pathology pathways suggests a possible role for proteolysis in nerve and blister agent toxicity. Rats poisoned by the organophosphorus (OP) nerve agent soman (GD) display a cholinergic crisis, a systemic mast cell degranulation characteristic of anaphylactic reactions and an excitotoxin-like sequential seizure and neuronal degeneration. Pathological proteolysis and inflammatory mediators have been demonstrated in both anaphylaxis and excitotoxicity and are hypothesized to contribute to nerve agent toxicity [Reviewed, F.M. Cowan et al., J. App. Tox. (1995)16, 25]. The dermal-epidermal separation caused by proteases and bullous diseases compared with that observed following exposure to the blister agent sulfur mustard (HD) has fostered the hypothesis that HD vesication involves proteolysis and inflammation [Reviewed, Cowan & Broomfield, Cell Biol. and Toxicol. (1993) 9, 201]. Proteases play an important role in homeostasis and pathology and can specifically regulate cells by cleaving proteins, peptides or protease-activated receptors (PAR) and are cofactors in activation of transcription factors. Proteolysis can thus mediate the synthesis, expression, release, activation and degradation of a myriad of molecules. Conversely, natural or synthesized protease inhibitors can influence the numerous protease-dependent processes. Protease inhibitors can suppress proteolysis and inflammatory response and reduce the pathogenesis of anaphylaxis, excitotoxins and bullous disease blistering. In rodents serine protease inhibitors can prolong survival of GD-intoxicated animals, and like several classes of anti-inflammatory drugs, protease inhibitors have shown efficacy for HD vesication.

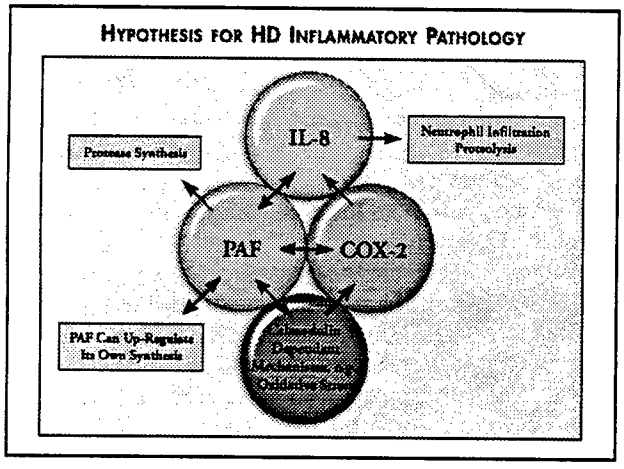


Figure 1.

CANDIDATE ANTIVESICANT DRUG SCREENING

	ICD #	edema	histo
Anti-inflammatory drugs			
fluphenazine dihydrochloride	2040		50
indomethacin	2086	63	96
olvanil	2723	53	91
hydrocortisone	2842	65	71
olvanil (saturated)	2974		53
retro olvanil	2976	62	84
olvanil (urea analog)	2977		81
octyl homovanillamide	2980	65	100
dexamethasone	2845		72
Scavenger drugs			
2-Mercaptopyridine-1-oxide	1304		65
6-Methyl-2-Mercaptopyridine-1-oxide	1307		56
4-Methyl-2-Mercaptopyridine-1-oxide	1308	57	94
dimercaprol	2525	43	92
Protease Inhibitor			
1-(4Oaminophenyl)-3-(4-chlorophenyl)urea HCl	1883		54
N-(O_P)-L-Ala-L-Ala-L-Ala-benzy ester hydrate	2780		63
1(G-T)-4-(4-methyl phenyl)semithiocarbazide	2812		50
PADPRP Inhibitor			
3-(4'-Bromophenyl)ureidobenzamide	1548		74
Benzoylene Urea	1796		54
Other			
Hydrogen Peroxide gel, 3%	2828		58

Statistically positive reduction of at least 50% in edema or histopathology in the mouse ear or hairless mouse

Table 1. Data generated USAMRICD/ Battelle drug screening program

Our Institute has screened nearly 400 compounds in the mouse ear model for HD cutaneous injury, and 19 compounds reduced HD histopathology greater than 50% [Table 1]. The 19 compounds include 4 serine protease inhibitors and 10 anti-inflammatory drugs, consisting of two corticoid steroids, five capsaicin analogues, two cyclooxygenase (COX) inhibitors and a calmodulin antagonist. One possible combination of inflammatory pathways of keratinocytes that could influence HD toxicity and account for the efficacy of many of the anti-vesicant compounds involves PAF, COX-2 and IL-8 [and Figure 1]. In addition to protease inhibitors many drugs that protect against nerve agent toxicity also have anti-

inflammatory activity. Accordingly, we hypothesize that drugs with anti-inflammatory actions against either nerve or blister agent might also display universal efficacy for the inflammatory pathogenesis of both classes of chemical warfare agent. Thus, the realization of universal drugs for multiple chemical warfare agents may not require a random or massive drug discovery effort but only a closer examination of the known anti-inflammatory pharmacological actions of drugs currently being tested against either nerve or blister agent.

The field of neuroimmunology has challenged the perception of dichotomy between nervous and immune systems. The cast of usual suspects implicated in ischemic, excitotoxin and GD-induced neuropathology, anaphylaxis and GD anaphylactoid reactions and HD vesication includes molecules with inflammatory-neuronal activity such as proteases, platelet activating factor (PAF), tumor necrosis factor (TNF), IL-8, cyclooxygenase-2 (COX-2), substance P and endothelin. Because of the plethora of neuronal-inflammatory mediators and receptors, proteolysis, PAF and N-methyl-D-aspartate (NMDA) receptor and to a lesser degree COX-2 and Il-8 mediated response will be discussed as illustrative but not limiting examples of possible mechanisms of HD and GD toxicity. NMDA receptors can mediate glutamate excitotoxicity and are expressed on neurons, microglia, mast cells and possibly keratinocytes. Excitation of NMDA receptors can further precipitate or amplify inflammatory response that contributes to considerable collateral tissue damage in excitotoxin, ischemia and perhaps blister and nerve agent lesions. The NMDA receptor antagonists MK-801 and cannabinoids, the GABA agonist benzodiazepines and adenosine agonists can moderate NMDA receptor excitoxicity. These three classes of compounds have demonstrated neuro-protective efficacy against ischemic, excitotoxin and nerve agent neuronal degeneration. In keeping with our hypothesis for universal antidotes, each of these categories of compounds is currently being developed as an anti-inflammatory agent and can achieve anti-inflammatory pharmacological actions similar to drugs with efficacy for HD toxicity. Both benzodiazepines and cannabinoids, in addition to their respective GABA agonist and NMDA antagonist actions, are specific PAF antagonists and adenosine agonists, and every class of anti-inflammatory with efficacy for HD vesication can suppress PAF activity. Despite the contrasts in chemistry and toxicity, there may exist for blister and nerve chemical warfare agents some analogous mediators, pathological pathways and pharmacological targets for universal medical countermeasures.

McDonough and Shih have proposed a sequence of events for OP nerve agent-induced seizure and neuropathology: Inhibition of AChE → rise in ACh → activation muscarinic receptors → cholinergic crisis → activation NMDA glutamate receptors → intracellular calcium accumulation → seizure and neuronal damage. Tsirka and coworkers have demonstrated a role for proteolysis in excitotoxicity. t-PA knockout mice were demonstrated to be resistant to seizure and neuronal pathology caused by kainic acid and other excitotoxins that target NMDA glutamate receptors. The synthetic protease inhibitor tPA-STOP™ (American Diagnostica, Greenwich, CT) suppressed kainic acid-induced seizure and neuronal degeneration. Based on these and related experiments the authors propose the following sequence for excitotoxicity subsequent to glutamate receptor excitation: *Glutamate receptor → macrophage-like microglia express tPA → activation of the zymogen plasminogen → to active protease plasmin → degrades the neuronal laminin matrix → seizure and neuronal death.*

PAF is a dual pro-inflammatory and neuromessenger phospholipid molecule that serves many physiological functions. PAF also participates in pathological phenomena that include lethal anaphylaxis, protease synthesis, and vesication. PAF is further involved in the glutamate receptor excitotoxicity, GABA receptor synaptic dysfunction and NMDA-induced neuronal apoptosis that can collectively contribute to seizure and neuronal degeneration. Numerous synthesized, e.g., benzodiazepines, and natural, e.g., complement-reactive protein (CRP), PAF antagonists and the enzyme PAF-acetylhydrolase have been used to reduce PAF pathology, and PAF antagonists can inhibit NMDA-stimulated neuronal cell death. NMDA glutamate receptor excitation induces production of PAF that could bind to PAF receptors on microglia, resulting in expression of tPA and ensuing proteolytic neuronal degeneration. PAF can also bind to PAF receptors on neurons precipitating apoptosis. Furthermore GD-induced glutamate excitation of the NMDA receptor complex on brain and peripheral mast cell might further precipitate mast cell degranulation. The resulting anaphylactoid reaction with release of proteases and autacoids might contribute to the lethal broncospasm, seizure and neuronal degeneration associated with GD intoxication.

The science literature is replete with examples of common anti-inflammatory actions of HD and GD medical countermeasures. The interconnecting nature of potential neuronal-inflammatory pathways such as GABA, PAF, NMDA and adenosine receptors and multiple pharmacological drug actions renders predicting definitive mechanisms for agent or antidotes complex. Futhermore, cross reactivity of drugs may reflect deeper biological consequences, wherein different ligand-receptor systems cross-commmunicate to yield coordination of multiple receptor system response. In concert with the demonstrably critical role of cholinergic crisis, proteolysis and inflammation, possibly initiated by either GD-induced anaphylactoid reaction and/or excitotoxicity may complicate GD toxicity. Proteolysis and inflammation pathways are also implicated in sulfur mustard toxicity. Protease inhibitors can reduce the toxicity of both GD and HD, and anaphylactic reactions and excitotoxicity. Thus a single medical countermeasure can have efficacy for multiple pathologies and categories of chemical warfare agents. Proteases and other pro-inflammatory and neuronal molecules may contribute to both GD and HD toxicity and provide targets for universal medical countermeasures for nerve and blister agents.

DEMONSTRATION OF A CRASHWORTHY COMPOSITE FUSELAGE CONCEPT

Karen E. Jackson*, Edwin L. Fasanella
US Army Research Laboratory, Vehicle Technology Directorate
Hampton, Virginia, 23681-2199

Norman F. Knight, Jr.
Veridian MRJ Technology Solutions
Fairfax, Virginia, 22030-7305

SUMMARY

The present paper describes the development of an innovative and cost-effective composite fuselage concept for light aircraft and rotorcraft that is designed to meet structural and flight loads requirements and to provide improved crash protection. The two primary design goals for crashworthiness are to limit the impact forces transmitted to the occupants, and to maintain the structural integrity of the fuselage to ensure a minimum safe occupant volume. To meet these objectives, an aircraft or rotorcraft fuselage must be designed for high stiffness and strength to prevent structural collapse during a crash. Yet, the fuselage design must not be so stiff that it transmits or amplifies high impact loads to the occupants. Ideally, the design should contain some crushable elements to help limit the loads transmitted to the occupant to survivable or non-injurious levels.

The fuselage concept, shown in Figure 1, consists of four different structural regions, each with its own specific design objectives. The upper section of the fuselage cabin is fabricated of a stiff composite sandwich construction and is designed to provide a protective shell enclosing the occupants in the event of a crash. The frangible outer shell is fabricated from a relatively compliant composite material that is wrapped around the entire fuselage section, enclosing the energy absorbing structure beneath the floor, and forming the lower fuselage. The outer shell is designed to provide damage tolerance and aerodynamic shape. Upon impact, the outer shell is intended to deform plastically and to initiate crushing of the subfloor. The energy absorbing subfloor is designed to dissipate kinetic energy through stable crushing. Finally, a key feature of the fuselage concept is the rigid structural floor. The structural floor is designed to react the loads generated by crushing of the subfloor and to provide a stable platform for seat and restraint attachment.

The anticipated benefits of the energy absorbing fuselage design as compared with conventional and retrofit fuselage designs include a substantially lower floor-level acceleration pulse, thus permitting lower occupant loads while maintaining cabin integrity during a crash. In addition, the energy absorbing fuselage design provides improved seat and restraint attachment due to the presence of the load-bearing floor. Finally, the crash effectiveness of the fuselage design is much less dependent on the mass of an individual occupant, since the combined masses of all occupants, seats, and the upper portion of the aircraft itself are reacted by the energy absorbing subfloor during an impact.

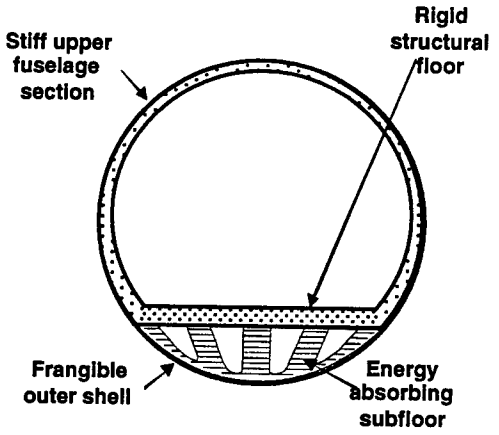


Figure 1. Schematic drawing of the fuselage concept.

In 1997, a three-year research program was initiated to develop the fuselage concept for potential application to light aircraft. The fuselage concept was designed and evaluated during the first two years of the research program through fabrication and testing of a 1/5-scale model fuselage. During the third year of the research program, a full-scale prototype was fabricated by "scaling up" the geometry and constitutive properties of the 1/5-scale model. Both structural and impact design requirements were defined for the fuselage concept. The impact design requirement was to limit occupant loads to survivable levels for a 373-in/s vertical impact onto a rigid surface. The 373-in/s vertical impact velocity is more severe than current regulatory criteria for small aircraft, but it is a realistic, potentially survivable impact velocity observed in actual crashes and in crash tests conducted at NASA Langley Research Center. For the full-scale fuselage section, the primary impact design goal is to achieve an average floor-level acceleration of 25-g for a 373-in/s vertical impact velocity. A secondary impact requirement is to maintain a high level of crash protec-

tion for an off-axis impact condition of 373-in/s vertical velocity with a 15°-roll attitude.

During the third year of the research program, a full-scale composite fuselage section was fabricated and vertical drop tests were conducted at both 0°- and 15°-roll impact attitudes to evaluate the crashworthy features of the fuselage design. A pre-test photograph of the fuselage section is shown in Figure 2. For the 0°-roll test, an average floor-level acceleration of 29.9-g was obtained from an accelerometer placed on a lead plate that was mounted to the floor of the fuselage. Only minor damage was observed in the transition region between the upper section and floor of the fuselage. The maximum displacement of the energy absorbing foam-block subfloor was 7.3 inches, providing a crush stroke of 86%. A second drop test was performed at 373-in/s vertical velocity with a 15°-roll attitude, to determine the crashworthy performance of the fuselage under off-axis impact conditions. The average acceleration ranged from 28.6-g on the right side to 19.4-g on the left side of the floor of the fuselage.

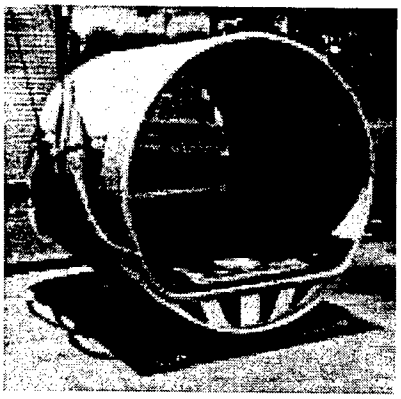


Figure 2. Pre-test photograph of the fuselage section.

Crash simulations were performed for both impact conditions using the nonlinear explicit transient dynamic code, MSC.Dytran. A finite element model of the fuselage section, shown in Figure 3, was developed which contained 26,950 nodes; 32,113 elements; and 60 concentrated masses to represent the inertia of the lead plate on the floor of the fuselage section. Previous simulations indicated a need for an improved material model of the Rohacell foam used in the construction of the subfloor. For this simulation, the Rohacell foam was represented as a crushable foam material with a look-up table of stress-strain response that was determined from experimental crush test data. A typical plot of the crushing response is shown in Figure 4.

A comparison of the predicted and experimental acceleration response for the 0°-roll drop test is shown in Figure 5. The simulation predicts the overall shape and magnitude of the experimental curve well. Also, the accurate representation of the Rohacell crushing response resulted in improved prediction of the magnitude of the peak acceleration that occurs at about 28 ms in the experimental response. The average acceleration of the predicted response is 32.3-g, which is only 8% higher than the experimental value of 29.9-g.

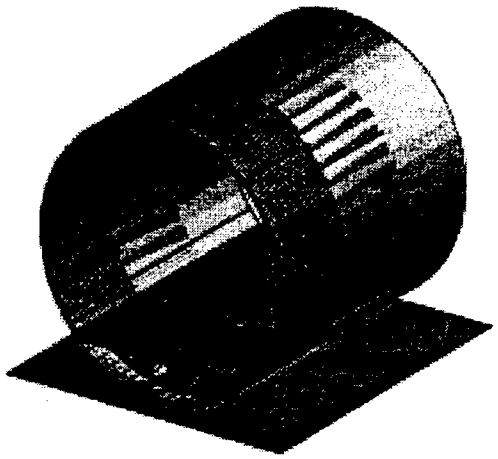


Figure 3. Finite element model of the fuselage section.

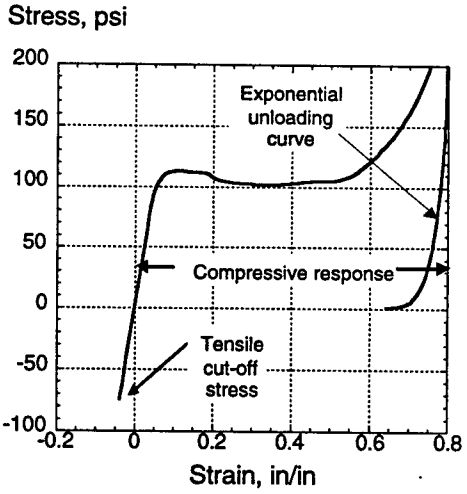


Figure 4. Material response of Rohacell foam.

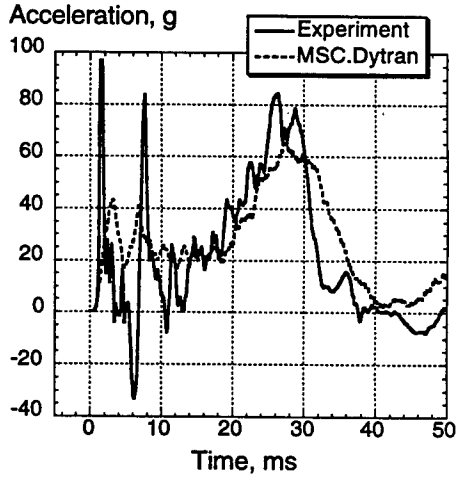


Figure 5. Analytical and experimental correlation for the 0°-roll drop test.

A CONSISTENT APPROACH TO EM PROTECTION OF DIGITAL C4I IN FUTURE JOINT OPERATIONS

Robert Pfeffer
U.S. Army Nuclear and Chemical Agency
Springfield, VA 22150-3198

Summary

Joint operations among equal partners, such as Desert Storm and recent peacekeeping actions in Bosnia-Herzegovina and Kosovo, are expected to be more the rule than the exception in the first few decades of the new millennium. Integral to the success of these joint allied operations will be the use of advanced, digital command, control, communications, computer and intelligence (C^4I) systems to coordinate a wide range of critical military inter-force and intra-force actions. These systems will be few in number, will manipulate enormous quantities of data continuously and in real time, and, because they are digital, could be lightweight, small in size, and have very low operating voltages (1.5 volts or less). If the C^4I system building blocks consist of unprotected commercial-off-the-shelf (COTS) components, these systems could be extremely sensitive to battlefield conditions (nuclear, conventional). Digital C^4I systems will be quickly recognized as mission-critical by enemy/terrorist forces and will become high-priority targets.

One of the projected asymmetric threats against these systems will likely be electromagnetic (EM) in origin. Fieldable EM generators already exist that can upset or destroy first-generation digital electronics. For example, electronic warfare jamming technology is already available to most nations. Radio-frequency (RF) weapons, such as high-power microwave and wide-band weapons, could soon be deployed in the field to jam or damage electronics, and high-altitude EM pulse (HEMP) is already a battlefield-wide threat. This paper addresses a consistent digital C^4I protection methodology against a wide range of wide-band and narrow-band EM environments and effects, including RF and HEMP, which can be adopted by joint forces to protect their critical C^4I systems. It accounts for differences in digital circuit design and can be applied to meet any set of commercial and/or military EM requirements

In this paper, a unified protection methodology was applied to a typical mobile C^4I platform subjected to several human-generated and nature-generated EM environments and effects, including the self-induced electromagnetic interference (EMI), electrostatic discharge (ESD), near-strike lightning, and HEMP characteristics stated in both MIL-STD-464 and several commercial standards. The EM protection requirements were estimated to be 70 dB shield integrity for frequencies between 100 MHz and 5 GHz, and 80 dB penetration protection on the phone line port for frequencies dependent upon the length of the phone line used. This strategy to EM protection is especially useful, and cost effective, since validation testing and maintenance/surveillance testing reduce to simple, low-cost shield and penetration protection tests that can be conducted anywhere, even with the system operating. The application of this protection approach in the original system circuit design reduces the number of breadboard and brassboard tests. Such protection also allows component replacement within the barrier, once the new component immunity level has been measured.

THIS PAGE INTENTIONALLY LEFT BLANK

PHOSPHOTRIESTERASE MUTANTS WITH ENHANCED VX AND G-AGENT ACTIVITY

Steven P. Harvey, Jan E. Kolakowski and Joseph J. DeFrank
U.S. Army Edgewood Chemical and Biological Center

Misty Chen-Goodspeed, Miguel Soborb and Frank M. Raushel
Texas A&M University

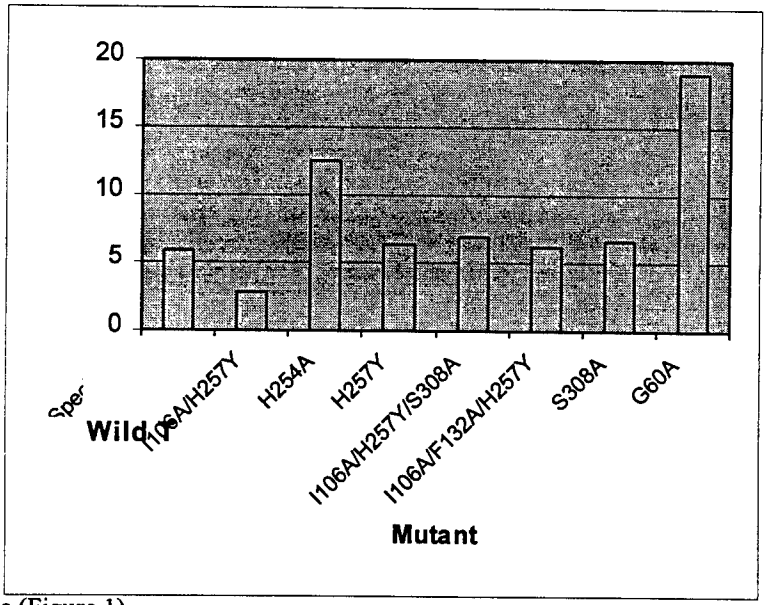
The phosphotriesterase (PTE) enzyme catalyzes the hydrolysis of a number of different pesticides and chemical nerve agents. As a catalytic decontaminant of chemical nerve agents, PTE has several attractive features. The gene for PTE has been cloned into *Escherichia coli* and active enzyme can be produced in quantity[1]. Also, knowledge of the structure of the PTE active site permits rational design of mutants for the purpose of increasing activity or broadening the substrate range[2]. For instance, site-directed mutagenesis studies have previously identified PTE mutants with up 40-fold enhanced soman catalysis[3].

One particularly interesting characteristic of PTE is its catalysis of the P-S bond cleavage of VX [O-ethyl-S-2-(diisopropylaminoethyl) methyl phosphonothioate][4]. PTE has been well characterized and is the only cloned enzyme with this demonstrated property. Since the VX activity of the native enzyme is relatively low, a series of eight site-directed mutants were generated and tested for their catalytic activity on VX. The mutants were constructed using the method of overlap extension[5] and cassette insertion with a synthetic gene[6]. Six of the mutants had no increased VX activity, while the other two possessed significantly enhanced activity. The single mutant H254A had approximately 11 times the VX activity of the wild-type enzyme and the triple mutant I106A/F132A/H257Y had approximately 3 times the activity (Table 1).

Enzyme	AU/min/mg/ml
Wild-type	2.11
H254A	23.72
I106A/F132A/H257Y	5.94

Table 1. VX activity (AU = absorbance units, 400 nm).

The activity of these PTE mutants was also determined with 3 mM soman (GD, *o*-pinacolyl methylphosphonofluoridate) as the substrate. Assays were conducted at at pH 7.2 and 25° C. The wild-type activity of PTE on soman is higher than that on VX, but relatively low as compared to organophosphorus anhydrolase (OPAA) enzyme, for instance. The majority of the mutants tested had activity similar to, or less than wild-type. However, H254A had activity approximately twice that of wild-type, and G60A had activity approximately three



times that of wild-type (Figure 1).

Figure 1. Activity of wild-type and mutant enzymes on soman.

The activity of wild-type PTE on 3 mM sarin (GB, *o*-isopropylmethylphosphonofluoridate) is higher than that of any other enzyme characterized thus far. The same mutants as above were also assayed with sarin and compared to the wild-type enzyme (Figure 2). Assays were conducted at at pH 7.2 and 25° C. Two mutants, I106A/H257Y and I106A/F132A/H257Y, both had more than three times the wild-type activity on sarin. These mutants represented the highest levels of activity yet reported on sarin with any enzyme. Two other mutants, H257Y and I106A/H257Y/S308A each had about twice the activity of the wild-type enzyme.

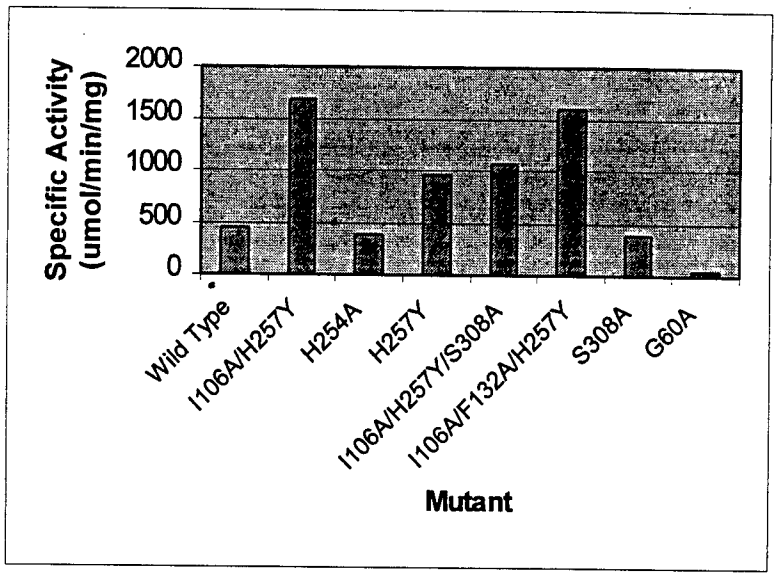


Figure 2. Activity of wild-type and mutant enzymes on sarin.

In conclusion, using rational design based on knowledge of the three-dimensional structure of the active site of PTE, a series of seven site-directed mutants were constructed. These mutants were assayed with VX, soman and sarin. Two of these mutants (H254A and I106A/F132A/H257Y) had increased activity on VX. One of these mutants (H254A) possesses the highest level of VX activity thus far reported for any cloned enzyme. The same H254A mutant also soman activity approximately twice that of the wild-type enzyme and another mutant, G60A, has approximately three times the activity of the wild-type enzyme on soman. Assayed with sarin, four mutants were found with 2-4 fold-increased activity, these representing the most active cloned enzymes reported for sarin hydrolysis.

References

1. Omburo, G.A., Kuo, J.M., Mullins, L.S. and Raushel, F.M. (1992). J. Biol. Chem. 267, 13278-13283.
2. Vanhooke, J.L., Benning, M.M., Raushel, F.M., and Holden, H.M. (1996) Biochemistry 35, 6020-6025.
3. Harvey, S.P. ERDEC-TR-492, April 1998.
4. Kolakowski, J.E., DeFrank, J.J., Harvey, S.P., Szafraniec, L.L., Beaudry, W.T., Lai, K. and Wild, J.R. 1997 Biocatalysis and Biotransformation 15:297-312.
5. Ho, S.N., Hunt, H.D., Horton, R.M., Pullen, J.K. and Pease, L.R. (1989), Gene 77:51-59.
6. Wohlschlegel, J., unpublished experiments.

DETECTION AND IDENTIFICATION OF CHEMICAL AGENTS IN WATER USING SURFACE ENHANCED RAMAN SPECTROSCOPY (SERS) ON GOLD AND SILVER DOPED SOL-GELS

Steven Christesen* and Kate Ong
Research and Technology Directorate, U.S. Army Edgewood Chemical Biological Center
Aberdeen Proving Ground, MD 21010-5424

M. Edward Womble
Raman Systems, Inc.
Boston, MA 02215

Richard Clarke and Ranjith Premasiri
Boston University
Boston, MA 02215

ABSTRACT

The military has identified a need to detect, identify and quantify chemical and biological contaminants in water. The system currently in use (the M272 Chemical Agent Detection Kit) does not meet the current water monitoring standards. The M272 test procedures require 30-40 minutes to complete and are difficult to perform while wearing chemical protective clothing. We have undertaken a program to develop a chemical agent water monitor based on surface Enhanced Raman spectroscopy (SERS). Using SERS, we have demonstrated detection of chemical agent simulants in water at levels as low as 500 ppb.

1. INTRODUCTION

The Operational Requirements Document for a Joint Chemical/Biological Agent Water Monitor (JCBAWM) states that there is an immediate need for a device that will detect, identify, and quantify chemical and biological (CB) agents in water supplies during water point selection, production, storage, and distribution to consumers (including shower points and personnel decontamination stations). The M272 cannot detect chemical contaminants at the required levels to ensure treated water supplies meet the Tri-Service field drinking water standards nor at concentrations necessary to accurately forecast water purification equipment performance. Table 1 lists the detection requirements in μg/L of water for water consumption rates of 5L/day and 15L/day. Also listed are the current capabilities of the M272. Current M272 Chemical Agent Test Kit procedures also require 30-40 minutes to complete a series of analyses for chemical agents. The assorted tests required to analyze for chemical agents are difficult to perform in a mission oriented protective posture (MOPP) level 4 ensemble increasing the potential for errors.

Table 1: DOD Tri-Services Field Water Quality Standards. Values are in μg/L.

	Water Consumption		Sensitivity
CW Agent	5 L/day	15 L/day	M272
Nerve Agents			20
VX	15	5	
GD	12	4	
GB	28	9.3	
GA	140	46	
Hydrogen Cyanide	6,000	2,000	20,000
Sulfur Mustard	140	47	2,000

2. SURFACE ENHANCED RAMAN SPECTROSCOPY

We use Surface Enhanced Raman Spectroscopy (SERS) to identify the contaminating agents in water. Two properties make Raman Spectroscopy particularly well suited to measuring organic contaminants against a water background. First, similar to traditional mid-infrared spectroscopy, Raman Spectroscopy uses the characteristic vibrational features of the contaminants to provide their identity; however, Raman uses inelastic light scattering, instead of transmitting light through the sample. Second, unlike traditional infrared spectroscopy in which the vibrational fingerprint region used for identifying organic contaminants is masked by the strong infrared absorbance of water, Raman scattering is unaffected by the presence of the water background and reports only the contaminant sample.

The downside to Raman Spectroscopy has always been the relatively inefficient scattering and subsequent weakness of the Raman signal. In our program we use a technique known as Surface Enhanced Raman Scattering (SERS) to amplify the Raman signal to a level that allows ppm/ppb detection of the target chemical contaminants.

In this approach a three to six order of magnitude increase in sensitivity, as compared to conventional Raman spectroscopy is obtained by allowing the target molecule to adsorb onto the surface of the metal. The interaction of the conducting electrons of the metal with the electrons of the adsorbed molecule creates a large change in the polarizability for the adduct, resulting in a significant increase in the scattering efficiency by the target molecule.

3. RAMAN INSTRUMENTATION

Raman instruments continue to get smaller and cheaper. A number of companies including Ocean Optics and InPhotonics are building portable Raman systems. Boston University and Bruker Daltronics have built a prototype SERS based water monitor that is hand held and battery operated. This instrument comprises a near infrared diode laser and an Ocean Optics/BAT spectrograph with a linear diode array detector. Testing of this instrument on chemical agents and simulants is ongoing.

4. SERS OF CHEMICAL AGENTS AND SIMULANTS

We have tested a number of different SERS active substrates including gold colloids, gold nanostructures, and sol-gels impregnated with gold and silver particles. Of these substrates, the gold sol-gels have shown the best sensitivity for the agent simulant methyl phosphonic acid (MPA). Figure 1 shows the surface enhanced Raman spectrum of 50 ppb (by mass) MPA in water with the gold sol-gel. Without surface enhancement, MPA is not detected in water at concentrations below 1 part-per-thousand.

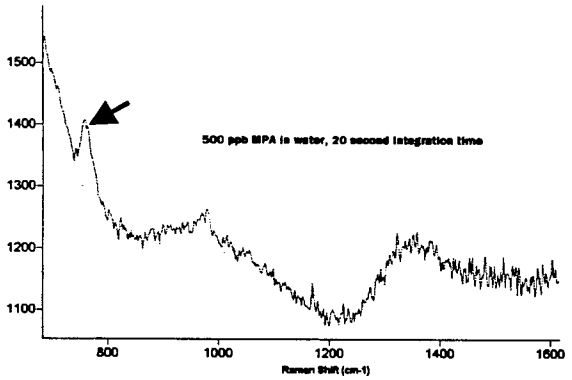


Figure 1: SERS spectrum of 500 ppb MPA in water using the gold-doped sol-gel.

We have also made preliminary SERS measurements of chemical agents in water. Figure 2 shows the SERS spectrum of GA using the gold sol-gel.

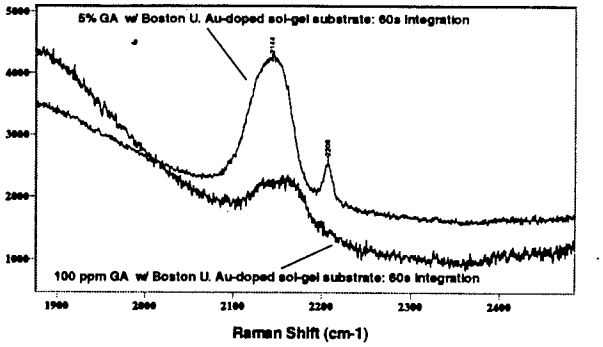


Figure 2: SERS spectrum of the chemical agent GA in water using the gold-doped sol-gel.

5. CONCLUSIONS

In our studies so far we have been able to detect agent simulants down to 500 ppb with Au-doped sol-gels. We have also found that gold provides greater enhancement than Ag for the agents and simulants studied. In preliminary studies, Au-doped sol-gels exhibit only modest enhancement for GA and GB. Lessons learned from these experiments, however, give us confidence that the sensitivity can be improved significantly. More chemical agent testing is to be performed with sol-gels and other SERS substrates.

CHANGES IN GENE EXPRESSION AFTER EXPOSURE TO ORGANOPHOSPHORUS (OP) AGENTS

Jennifer W. Sekowski*, Kevin P. O'Connell, Akbar S. Khan, and James J. Valdes
Molecular Engineering Team, Research and Technology Directorate,
Edgewood Chemical Biological Center,
U. S. Army Soldier Biological Chemical Command,
Aberdeen Proving Grounds, MD 21010

Maryanne Vahey and Martin Nau
Walter Reed Army Institute of Research,
Rockville, MD 20580

Maha Khalil and Mohyee E. Eldefrawi
Department of Pharmacology and Experimental Therapeutics,
University of Maryland School of Medicine
Baltimore, MD 21201

ABSTRACT

The acute effects of chemical weapons have been widely studied since World War I and are fairly well understood. Since the Gulf War, however, there has been increased concern for exposure of personnel to sub-acute and low-levels of chemical warfare agents (Jamal et al., 1998; McDairmid et al, 2000). Additionally, questions have been raised as to the effects of exposure to toxic industrial chemicals (TICs) and materials (TIMs) and other environmental contaminants during deployments to countries where manufacturing and agricultural chemicals (pesticides, herbicides) and methods are outdated and virtually unregulated. Although a sub-acute exposure may not cause immediate or obvious pathology at the time of exposure, it may cause alterations at the molecular level that will be manifest as altered genetic regulation or expression, and this may predispose the exposed person to a disease later in life. In this pilot study we exposed Sprague-Dawley rats to sub-LD50 doses of Sarin (GB, an organophosphorus (OP) compound), Chlorpyrifos (CPF, an OP compound), or a Hepes-buffered saline control. After extracting the RNA from the livers and brains of the animals, the level of gene expression was assessed using DNA microarray analysis. While our studies of GB are ongoing, it appears that exposure to CPF results in several significantly altered patterns of gene expression.

1. INTRODUCTION

Soldiers operating in a CBW environment face the possibility of attack resulting in incapacitation symptoms or death. The mechanisms by which chemical weapons cause acute injury are well understood, thanks to an exhaustive study of these compounds during much of the 20th century. However, personnel involved in decontaminating equipment or destroying chemical weapons, as well as personnel on the periphery of an attack, may also face exposure at low levels that may not induce obvious damage at the time of exposure. In addition, soldiers face a toxicological risk from exposure to Toxic Industrial Compounds (TICs) and Toxic Industrial Materials (TIMs) during deployment in areas of the world where environmental regulations are lacking. Such compounds may also be used as weapons of opportunity against U.S. personnel. Scientists have been assessing the effects of chemical weapons, TICs, and TIMs on living systems for nearly 80 years. For most of that time, toxicology both inside and outside the Army has consisted of chemical exposures to animals followed by observations of a limited number of physiological changes, including death. This work has provided a unique and valuable body of immediate, practical solutions to battlefield toxicological problems: decontamination, personal protection, and antidotes for acute exposures. However, exposure to chemical weapons or TICs and TIMs that does not result in immediate injury may yet predispose soldiers to ailments that arise much later, and whose origins are difficult to determine. Traditional toxicological methods lack the power to determine the mechanisms of action of toxic agents at the most fundamental level: how the very genes that determine how we function respond to toxic insults, and how these changes become manifest as symptoms over time.

The advent of DNA microarrays makes possible the simultaneous survey of the level of expression of hundreds to thousands of genes simultaneously. Microarray analysis therefore reveals which genes have been "turned on" or "turned off" by exposure to a toxicant. In addition, measurement of gene expression may allow us to identify threshold concentrations below which there is little health risk. The number of genes studied in such an experiment and the extent of their expression, which is measured by the intensity of an element's fluorescence on a chip, present a computational challenge to the researcher. A computerized database

keeps track of the identity of each gene represented by each element of the array. A computerized comparison of two arrays to which RNA from treated and untreated tissues have been added reveals the identity of genes whose expression has changed in response to a stimulus (CBW agent, TIC, or TIM). The sequences of the genes affected by exposure to the toxic material suggest their biochemical function in the cell's response to the toxic insult.

We are using this technology to examine the response, manifest as gene expression changes, of mammals after exposure to two OP agents, sarin and chlorpyrifos. Sarin (GB) is a chemical weapon present the arsenals of several nations, while chlorpyrifos (CPF, Lorsban, Dursban) is among the most widely used OP insecticides worldwide in terms of tonnage applied to agricultural fields. Very little is known about the regulation of mammalian genes in response to exposure to these two compounds.

2. DISCUSSION

Since the Gulf War there has been increased interest in the effects of sub-acute and low-level exposure to chemical agents, including organophosphorus compounds. While the acute and overt effects of organophosphorus (OP) agent toxicity are well known, the more subtle and molecular level alterations of these agents are not well understood. Agent–induced damage and alteration occurring at the molecular level has been implicated in the etiology of injury and disease that may present itself weeks, months, and even years after the initial toxicant exposure (NRC, 1997; Jamal et al., 1998; McDairmid et al, 2000). To date, this pilot study demonstrates that exposure to the organophosphate insecticide, chlorpyrifos (CPF), causes significant alterations in the expression of many genes important to key cellular functions and biochemical pathways in the body.

Gene expression analysis using DNA microarray technology has permitted the identification of several patterns of gene expression altered as a result of exposure to the organophosphorus insecticide, chlorpyrifos. After identifying which types of gene expression alteration occur as a result of CPF exposure, we have begun to investigate the connection of several of these genes with critical cellular function and /or key biochemical pathways.

Thus far, the results garnered from this pilot study demonstrate the utility of the DNA microarray technology to identify alterations of gene expression induced by OP agents. The study has also yielded some insight into a few functional classes of altered genes that may play roles in mediating the effects CPF exposure. While we have completed the analysis of CPF in this pilot study of OP agent exposure, the analysis of Sarin (GB) is ongoing. Also, the results from the BuChE activity assay suggest that the response of the rats to CPF exposure was as predicted, however, a study beyond this pilot experiment will require many additional animals to be included at each time point to help decrease the possibility of inter-animal variability in gene response. Furthermore, collection of data at lower doses of OP agents and at time points closer to and further from the initial dose point will be required in order to begin to build a more complete understanding lower–dose exposure to OP agents.

This pilot study represents an important first step toward designing and implementing future genotoxicology studies that will build understanding of the molecular effects of OP agents and other important industrial, agricultural, and warfare chemicals. The future of toxicogenomics promises to yield critical information necessary for preserving the health and improving the performance of military personnel.

REFERENCES

Jamal, G.A. (1998) Gulf War syndrome- a model for the complexity of biological and environmental interaction with human health. Adverse Drug React Toxicol. Rev 17(1), 1-17.

McDiarmid, M.A., Keogh, J.P., Hooper, F.J., McPhaul, K., Squibb, K., Kane, R., DiPino, R., Kabat, M., Kaup, B., Anderson, L., Hoover, D., Brown, L., Hamilton, M., Jacobson-Kram, D., Burrows, B., Walsh, M. (2000) Health effects of depleted uranium on exposed Gulf War veterans. Environ. Res. 82(2), 168-80.

Steiner, S. and Anderson, N.L. (2000) Expression profiling in toxicology-potentials and limitations. Toxicology Letters 112-113, 467-471.

The National Research Council's (NRC) Committee on Toxicology: The First 50 Years 1947-1997. (1997) Natl. Acad. Of Sciences, 1-38.

IMPACT OF WINTER ENVIRONMENT ON RADAR AND INFRARED DETECTION OF BURIED LANDMINES

Gary Koh
US Army Engineer Research and Development Center
Cold Regions Research and Engineering Laboratory
Hanover, NH 03755

ABSTRACT

The US Army has devoted considerable resources to developing and testing mine detection systems. However, comparatively few resources have been directed toward investigating the weather impact on the performance of these systems. The effect of winter environment has been virtually ignored. To address this deficiency, the effect of winter environment on radar and infrared detection of buried landmines was investigated. Standardized test mines with electrical and thermal properties similar to a live mine were buried at an outdoor test site and exposed to varying winter conditions. The effect of snow, frozen ground and sub-freezing temperature on radar and thermal signatures were obtained. These measurements are used to provide practical guidelines for operating radar and infrared mine detection systems in a winter environment.

1. INTRODUCTION

Detecting buried landmines is made difficult by their diverse size, shape, composition and burial depth. The problem is further complicated by the diverse environmental conditions, which these mines are likely to be encountered. At present, no single technology can reliably solve this enormously difficult problem. To achieve an acceptable degree of reliability, a multi-sensor approach incorporating such technologies as nuclear quadrupole resonance, electromagnetic induction, infrared imaging and radar imaging will be required. Although much resources have been devoted to developing these systems, comparatively few resources have been directed toward investigating how environmental conditions impact the performance of these systems. The effect of winter environment has been virtually ignored. To address the deficiency, the effect of winter environment on radar and infrared detection of buried landmines was investigated. Radar and thermal signatures of buried mines were obtained in winter to determine the effect of snow, frozen ground, and sub-freezing temperature on mine detection. These measurements are used to provide practical guidelines for operating radar and infrared mine detection systems in a winter environment.

2. EXPERIMENT

2.1 Test Site

An outdoor test site was constructed to study the effects of meteorological forcing on the ground state, and the subsequent effects on mine detection. The site is located in Hanover, NH, which is a good geographical location for studying winter effects on mine detection. The site can be operated year around and is instrumented with both standard meteorological sensors and buried sensors (thermistor array and soil moisture probes) to monitor the ground state. The site consists of a 10 m x 20 m plot that can be traversed with sensors mounted on a motorized gantry; and is divided into three test beds that consist of gravel, bare soil and vegetation-covered soil.

Simulant mines developed by the US Army Project Manager-Mines, Countermine and Demolitions for testing and evaluating mine detection equipment were buried at the site at various depths. These simulant mines are filled with RTV silicone rubber, which has electrical and thermal properties similar to TNT and Composition B, and therefore interacts with radar and infrared sensors in a way representative of live mines.

2.2 Radar Measurements

Radars are a key component of a multi-sensor package for detecting buried landmines. Radars operate by emitting short electromagnetic pulses or by emitting discrete or modulated frequencies over a finite bandwidth from which a pulse can be mathematically reconstructed. As a radar sweeps across a mine field, it responds to the dielectric discontinuities in the ground. A radar image representing a vertical slice of the ground can then be reconstructed. A frequency modulated continuous wave (FMCW) radar operating at 2-6 GHz bandwidth was used in this investigation. FMCW radar is inexpensive, robust, and easy to operate, and therefore is a good candidate for a low-cost radar mine detection system.

2.3 Infrared Measurements

Infrared sensors measure the thermal contrast between the soil above a buried mine and the surrounding soil. The thermal contrast is solar driven and results from the different rate of heating and cooling of a mine compared to the surrounding soil. The ability to determine the magnitude of the thermal contrast for different mine type, burial depth and environmental conditions is of interest. The diurnal and seasonal variations of the thermal

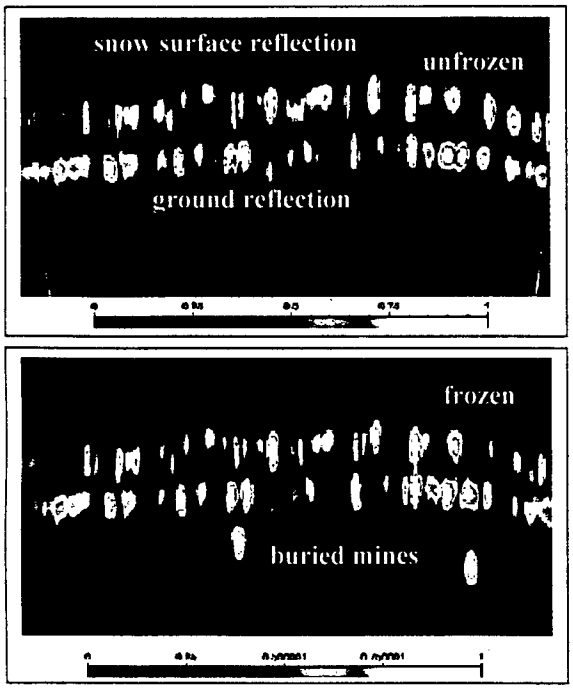


Figure 1. Effect of frozen ground on radar detection of buried landmine.

contrast were investigated using an anti-tank simulant mine (20-cm diameter; 6.6 cm high). The simulant mine and the surrounding soil were instrumented with thermistors. Two parallel arrays of thermistors were placed such that one array passed through the center axis of the mine and the second array passed approximately 12 cm away. The temperature profiles for the two vertical arrays were monitored once every hour for a full season.

3. RESULTS

3.1 Effect of winter on radar sensors

Snow cover over a minefield can degrade the performance of a radar system. This is particularly true for a melting snow cover. The water absorbs radar energy so that very little signal can penetrate into the ground to detect the buried mines. However, under appropriate conditions, the winter environment can enhance the performance of radar system. The ability of radar signals to penetrate frozen ground can dramatically improve the performance of a radar mine detection system in a winter environment.

Figure 1 compares two radar images, obtained approximately one week apart, of two anti-tank mines at a snow covered test site. The enhanced detection capability that is observed in the bottom figure is due to frozen ground. The effect of frozen ground is to enhance radar penetration, which greatly improves the probability of detection.

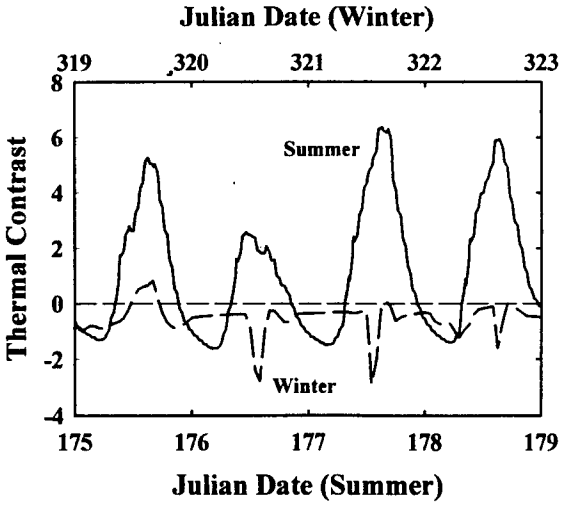


Figure 2. Thermal contrast between soil above a buried mine and the surrounding soil. Results from summer and winter are compared.

3.2 Effect of winter on infrared sensors

The diurnal effects on infrared sensors have been well documented in the past. A key feature of the diurnal effect is the cross over periods, when the thermal contrast between a mine and surrounding soils is negligible and the mine undetectable. The seasonal dependence on thermal contrast is equally important. This is illustrated in Figure 2, which compares the thermal contrast observed in summer and winter obtained in summer with those of winter.

The thermal contrast observed in winter differs dramatically from that observed in summer. Due to the reduced solar loading in winter, the magnitude of the thermal contrast is much lower in winter than in summer. In addition, the cross over periods that are observed in summer do not necessary appear in winter. The temperature above the mine can remain colder than the surrounding for several days. A reversal in temperature contrast is also observed in winter, where a temperature contrast minimum occur late in the afternoon

4. SUMMARY

Winter environment is extremely dynamic and presents a challenge for radar and infrared mine detection systems. The effects of snow, frozen ground and sub-freezing conditions on radar and infrared sensors were investigated. These studies show that infrared sensors will play a limited role in winter mine detection operation. Radars are ideally suited for operation in sub-freezing temperature, since radar signal can easily penetrate frozen ground and dry snow cover.

PEPTIDE EPITOPES AND MIMETICS

Roy G. Thompson*, Akbar S. Khan, Ameneh Aresteh and James J. Valdes
U.S. Army Soldier Biological Chemical Command, Edgewood Chemical and Biological Center
Aberdeen Proving Ground, MD 21010-5424

1. ABSTRACT

The objective of this project is to: 1) identify relatively short peptide sequences that mimic the ability of an antibody to bind to a specific antigen and could thus substitute for the antibody in various assay formats, and 2) identify peptide sequences that mimic antigen epitopes and could be used as positive controls in validating immunoassays. A combinatorial random peptide library displayed in *E. coli* was screened against two biolological toxins, staphylococcal enterotoxin B (SEB) and ricin, and against two monoclonal antibodies generated against SEB and ricin. After five rounds of sequential panning the library against the target ligands, colonies of individual *E. coli* clones were screened by ELISA to identify those clones interacting most strongly with the ligand. The DNA insert encoding for the peptidein each positive clone was then sequences and converted into the corresponding peptide sequence.

2. SUMMARY

Present methods used for the point detection depend heavily on the use of polyclonal or monoclonal antibodies for recognizing and binding to specific biological antigens. As relatively large, complex proteins with secondary and tertiary structural requirements for maintaining optimal activity, the use of whole antibodies imposes a significant logistic tail in meeting requirements for production and maintaining their viability in use outside controlled environments. The traditional hybridoma approach to antibody development is also extremely slow, costly and may only access 10^6 of the 10^9 potential antibody variants thought possible in the immunological genome (Winter and Milstein, 1991). Whole antibodies may also impose a limit on the detection sensitivity in some sensor platforms, where sensitivity is dependent on the concentration of molecules that can be immobilized in a given area.

Advances in genetic technologies have enabled scientists to clone genes encoding for antibody construction into host expression vectors, such as bacteriophage (Smith, 1985) and rapidly screen the resulting library of random gene combinations to identify those antibody fragments that are specific for a given antigen (Krebber et al., 1995; Davies and Riechmann, 1995). Further reductionistic attempts to define the minimal molecular determinants of antibody specificity have been pursued by using combinatorial random peptide displays to map specific amino acid sequences involved in antigen-antibody interactions (Devlin et al., 1990; Schellelcens et al., 1994). Random peptide display libraries can be applied to two significant issues in the development of specific reagents for biodetection: 1) the design of molecular recognition elements that are smaller than whole antibodies and antibody fragments, and 2) the design of peptide sequences that can mimic epitope binding sites on antigens that can be used as positive controls in assay test and validation without requiring biosafety precautions. We are currently employing the FliTrx (Invitrogen) dodecapeptide display library to screen for peptide sequences that bind to the ricin and SEB toxins and to monoclonal antibodies against ricin and SEB.

The FliTrx random peptide library is composed of 1.77×10^8 primary clones of *E. coli* with the peptide fusion inserted into a nonessential domain of the major bacterial flagellin protein and expressed in the bacterial flagella when induced by tryptophan (Lu et al., 1995). The library was panned against each target ligand for five sequential rounds before being plated and individual colonies selected for testing their specificity to bind the target ligand in a competitive ELISA format. Plasmid DNA was isolated from the clones showing positive ELISA tests and the DNA sequenced by the Biopolymer Laboratory at the University of Maryland at Baltimore

The following sequences were derived from the DNA of the cell clones showing positive binding results in the ELISA:

SEB ser-val-gly-ala-gly-ala-*-arg-cys-val-val
ser-arg-leu-val-arg-gly-val-arg-gly-leu-ser-try
ala-cys-tyr-ser-asp-phe-gly-phe-ser-phe-ala-try
thr-val-iso-cys-met-ala-leu-leu-leu-arg-gly-phe

SEB_{AB} iso-ser-pro-ala-gln-tyr-arg-pro-iso-leu-leu

ricin asp-asp-leu-val-val-gln-ser-arg-val-leu-arg
met-thr-*-asp-leu-leu-cys-arl-val-leu-arg
glu-val-ser-ser-gly-gly-ala-thr-gly-ser-gly
arg-val-thr-arg-asp-glu-arg-*-val-phe-val-ser

$ricin_{AB}$ met-asp-arg-val-val-gly-val-ser-arg-leu-val
met-arg-phe-ala-gly-arg-arg-leu-ala-arg-phe
asp-phe-val-iso-asp-arg-met-cys-arg-arg-leu
leu-glu-leu-gly-leu-val-*-iso-glu-gly-val

None of the isolated peptide clones show evidence of a common homology in their amino acid residue sequence, indicating that the peptides are either binding to different structural motifs of the target or that the target binding site exhibits a discontinous epitope that can be recognized by a variety of peptide sequences. The absence of a concensus sequence in the data is not unexpected. One would expect multiple peptide binding sites to be present on large protein targets as well as whole antibody molecules, based on their known structural composition from multi-subunit composition. We have begun screening the library against smaller fragments of the toxins and antibodies to further define the binding target for each peptide sequence. We are also synthesizing the peptide sequences to enable direct peptide-ligand binding studies to measure binding affinity and cross-reactivity with other epitopes.

REFERENCES

Davies, J. and Riechmann, L. " 'Camelising' Human Antibody Fragments: NMR Studies in VH Domains." *FEBS Letters*, Vol 339, pp. 285-290, 1994.

Davies, J. and Riechmann, L. "Antibody VH Domains as Small Recognition Units," *Bio/Technology*, Vol 13, pp. 475-479, 1995.

Devlin, J.J., Pangariban, L.C. and Devlin, P.E. "Random Peptide Libraries: A Source of Specific Binding Molecules," *Science*, Vol 249, pp. 404-406, 1990.

Krebber, C., Spada, S., Desplancq, D. and Pluckthorn, A. "Co-selection of Cognate Antibody-Antigen Pairs by Selectively- Infective Phages," *FEBS Letters*, Vol 377, pp. 227-231, 1995.

Smith, G.P. "Filamentous Fusion Phage: Novel Expression Vectors that Display Cloned Antigens on the Viron Surface, *Science,* Vol 228, pp.1315-1317.

Lu, Z., Murray, K.S., VanCleave, V., LaVallie, E.R., Stahl, M.L. and McCoy, J.M. "Expression of Thioredoxin Random Peptide Libraries on the Escherichia coli Cell Surface as Function Fusions to Flagellin: A System Designed for Exploring Protein-Protein Interactions," *Bio/Technology,* Vol 13, pp.366-372, 1995.

Luzzago, A., Felicir, F., Tramonteno, A, Pessi, A. and Cortese, R. "Mimicking of Discontinuous Epitopes of Phage- Displayed Peptides. I. Epitope Mapping of Human H. Ferritin Using a Phage Library of Constrained Peptides," *Gene,* Vol 128, pp.51-57, 1993.

Winter, G. and Milstein, C. "*Man-Made Antibodies*," Nature, Vol 349, pp. 293-299, 1991.

NON-INTRUSIVE ANALYSIS OF CHEMICAL AGENT IDENTIFICATION SETS (CAIS) USING A PORTABLE FIBER-OPTIC RAMAN SPECTROMETER

Steven Christesen*, Brian MacIver, Larry Procell, and Dave Sorrick
Research and Technology Directorate, U.S. Army Edgewood Chemical Biological Center
Aberdeen Proving Ground, MD 21010-5424

Michael Carrabba † and Job Bello
EIC Laboratories, Inc.
Norwood, MA 02062

ABSTRACT

Portable fiber-optic Raman systems are being used to analyze chemical agents and other toxic chemicals in sealed glass containers. These containers include ampoules and bottles that are contents of chemical agent identification sets (CAIS) developed for use in training military personnel in chemical agent identification, safe handling, and decontamination. Real-time non-intrusive analysis of these sets is required so that the items containing chemical agents can be identified for proper disposal. This paper details the laboratory measurement of Raman spectra of CAIS chemicals and the analysis of CAIS items in the field. We also discuss the evaluation of man-portable Raman instruments for CAIS assessments.

† Present address: Chromex, P.O. Box 3190 Albany, OR 97321-0706.

1. INTRODUCTION

The army used chemical agent identification sets (CAIS) from 1928 to 1969 to train military personnel in the identification, safe handling, and decontamination of chemical warfare agents. These sets, which were produced in large quantities and distributed widely, contain samples of chemical warfare agents as well as other hazardous chemicals. Of the chemicals found in the sets, only mustard (H, HS, or HD), nitrogen mustard (HN-1 or HN-3), and lewisite (L) are still classified as chemical warfare material.

The identification of the CAIS contents is being accomplished with the use of a portable, fiber optic Raman spectrometer system operating in the near IR spectral region. The laser energy and the Raman scattered radiation are readily transmitted through the glass so that the analysis can be accomplished without opening the ampoule or bottle. The fiber optic probe allows for the placement of the Raman instrument up to 25 meters from the CAIS ampoules themselves.

Some of the recovered items were returned to the Edgewood Chemical Biological Center (ECBC) for laboratory analysis using normal gas chromatography (GC) and gas chromatography with mass spectrometry (GC/MS). These intrusive analyses allowed us to assess the accuracy of the non-intrusive Raman analyses.

Although a desired goal, the Raman instrument need not specifically identify the CAIS contents. It is required only to provide sufficient information to determine whether or not the CAIS item contains a chemical agent (mustard, nitrogen mustard, or lewisite).

2. RAMAN IDENTIFICATION

A spectral library was created from the Raman spectra of CAIS standards. Actual CAIS items were then identified by comparing the unknown spectrum to one of the library spectra.

Commercial spectral search software (SpectralID™ from Galactic Industries) is used to provide a preliminary identification of the CAIS contents. The software searches a spectral database comprised of Raman spectra of the CAIS standards. A Raman spectroscopist familiar with the CAIS spectra confirms the identification prior to any disposition of the CAIS item. Raman spectra of most of the possible contents of the chemical agent identification sets were measured in the laboratory (triphosgene was not available).

3. RAMAN ANALYSIS OF RECOVERED CAIS

A portable fiber optic Raman system was taken to Tooele Army Depot (Utah), Ft. Devons (Massachusetts), Ft Polk (Louisiana) and the former Ft. Ord (California) for field analyses of suspect CAIS ampoules. A total of 136 CAIS items have been analyzed by Raman spectroscopy of which 67% were identified. In all of the items that were not positively identified, the Raman spectrum did identify the presence of chloroform. Because no CAIS ampoules were ever filled with neat chloroform, these items were assumed to contain HD, L, chloropicrin (PS), HN-1 or HN-3 in addition to the chloroform. Some of the samples that were identified as "Unknown" (containing chloroform) by the Raman system were subsequently analyzed in the laboratory. Of the 17 samples analyzed, 13 were found to contain HD in chloroform ranging in concentration from 1.3% to 8.7%, and 4 contained L in chloroform at concentrations from 2.6% to 9.4% (an example is shown in Figure 1). Twenty items classified as unknowns were not analyzed further.

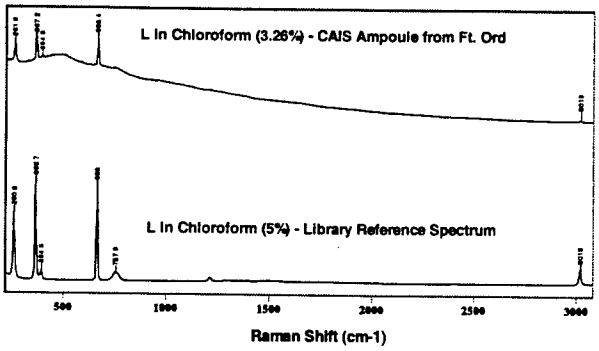


Figure 1: L in chloroform: CAIS item (upper spectrum) and reference sample (lower spectrum). The peak at 394.8 cm^{-1} is due to L, the other peaks are from chloroform.

Some sets contained neat agent adsorbed onto charcoal. These charcoal samples presented the biggest challenge for the Raman system. The large fluorescence background from the charcoal obscured any signal from the liquid, and no Raman analyses of these samples were possible. Luckily, the bottles containing the charcoal samples were clearly etched with the identity of the contents.

4. RAMAN ANALYSIS OF NON-CAIS ITEMS

The Raman system has also been used to identify the contents of ampoules that appear to be items from chemical agent identification sets but are not. These ampoules have been found to contain the fumigant methyl bromide (at the former Black Hills Army Depot and McClellan AFB) and neat chloropicrin used in safe protection devices (at Ft. McCoy and the Oakcreek, WI police station). Raman spectra of these items are shown in Figure 3.

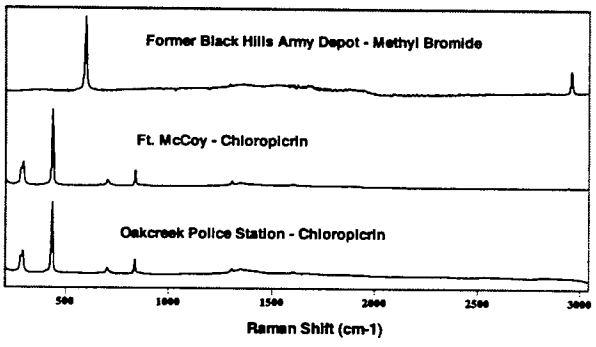


Figure 2: Spectra of non-CAIS items.

5. COMPARISON OF NEW PORTABLE RAMAN INSTRUMENTS FOR CAIS ANALYSIS

The Program Manager for Non-Stockpile Chemical Material (PMNSCM) has developed a mobile Rapid Response System (RRS) for on-site characterization and disposal of recovered CAIS. Housed in a mobile trailer, personnel identify the agent contained in each CAIS ampoule and bottle using a fiber-optic Raman spectrometer, segregate the ampoules and bottles according to their identified chemical contents, and treat the segregated agents on-site.

In addition to the Raman system in the RRS, PMNSCM has a need for a truly man-portable instrument for assessing small numbers of suspect CAIS at military and non-military sites where deployment of the full RRS is not required. This instrument must be able to be shipped by commercial aircraft. To determine the best instrument for this application, we tested 3 commercially available Raman instruments and compared their performance to the Raman system currently in the RRS (EIC Laboratories, Inc. Model RS2000). An instrument that meets these requirements has been selected and the details of the instrument comparison are published elsewhere.

6. CONCLUSIONS

Raman spectroscopy has been used to non-intrusively analyze the contents of glass ampoules and bottles from chemical agent identification sets. A portable, fiber-optic Raman spectrometer was taken to several locations for on-site analysis of recovered CAIS items. After transport, the Raman instrument required no recalibration and was set up and operational within 30 minutes. The portability and ruggedness of the Raman system makes it an ideal instrument for this application where low-level detection is not required.

Not all of the recovered CAIS items could be positively identified, as strong fluorescence backgrounds obscured the HD and L peaks in some of the liquid samples tested. For the recovered CAIS ampoules analyzed, only the HD and L in chloroform items were unidentified. In each of these cases, however, the chloroform was detected. When only chloroform is detected, the CAIS items are treated as if they also contained chemical agents. All CAIS items containing industrial compounds were positively identified.

Originally envisioned only as an assessment tool for the RRS, Raman spectroscopy has proven useful for analyzing of suspect CAIS items in the field. Due to the successful Raman assessment operations at the former Ft. Ord, Ft. Devons, Ft. Polk, Ft. McCoy, and Oakcreek, PMNSCM will field a man-portable Raman system capable of shipment by commercial aircraft.

A NOVEL COMPACT HIGH-POWER-MICROWAVE (HPM) *L*-BAND ANTENNA

Joseph R. Miletta
William O'Keefe Coburn
Steve Kaplan
Louis J. Jasper, ret.
US Army Research Laboratory
2800 Powder Mill Rd.
Adelphi, MD 20783-1197

SUMMARY

As the Army's role evolves into a more highly mobile, agile force with complex missions requiring both lethal and nonlethal weaponry, the technology to accommodate this transformation must be in place to ensure success. Size and weight are key constraints in the design and development of any tactical ground vehicle weapon system. Directed-energy (DE) high-power-microwave (HPM) weaponry will have a major role on the battlefields of the future. weapon design and development. Figure 1 depicts a conceptual tactical DE HPM weapon that could be used in air defense.

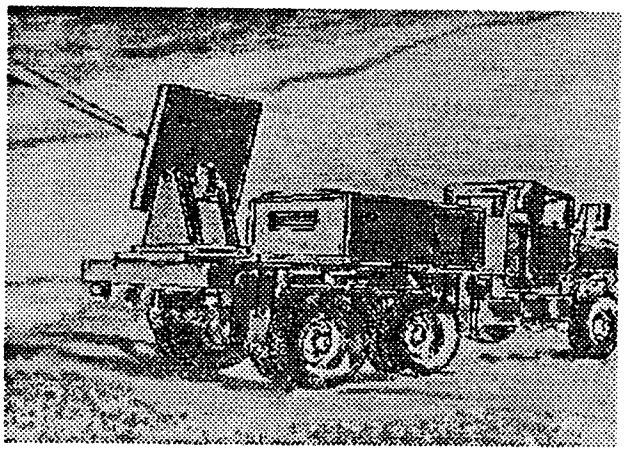


Figure 1 Artist's concept of a tactical DE HPM weapon system.

Presently, DE HPM applications are hampered by the size of antenna systems required to produce the requisite power densities on target with the projected compact HPM sources at the frequencies of interest. This paper addresses ARL research in the reduction of antenna size while meeting the target power density "lethality" requirements. The proposed antenna system would be entirely compatible with and integratable within proposed Future Combat System options.

For HPM applications at *L*-band, where the microwave wavelengths are on the order of 23 cm, antenna volume and weight are technical barriers to producing a highly mobile/lethal HPM weapon. A novel approach to minimizing antenna size and weight while maintaining gain and side-lobe attributes will be presented.

ARL target specifications that we are trying to meet or exceed are:

Weight:	< 250 kg
Cross-sectional Area:	< 7 m^2 deployed
Largest side dimension:	< 1.2 m deployed
Gain:	> 30 dBi
Frequency:	*L*-band (1.3 GHz)
Bandwidth:	>10%
Power:	>100 MW
Pulse Width:	> 5 μs
Pulse rep-rate:	> 100 Hz

Our ultimate goal is to develop an antenna system that can fit within a cube of 4-ft side dimensions. Implicit in our design requirements and goals is that the system be safe to operate, from the standpoint of both weapon operators and collocated equipment and personnel. Thus, antenna sidelobes must be suppressed. Our goal is to reduce sidelobes to 20 dB or better below the main beam.

Antenna gain is directly related to the effective antenna area. For aperture antennas the gain is determined from the expression

$$G = \eta \frac{4\pi A_e}{\lambda_0^2}, \qquad (1)$$

where A_e is the effective area, η is the antenna efficiency (around 0.5 for dish antennas), and λ_0 is the free space wavelength. For a wavelength of 23 cm. and a gain of 30 dB (a factor of 1000) the effective area would be nearly 8.5 m^2 (efficiency of 50%). An antenna with a physical area of those dimensions would pose transportability problems. Compact antenna design is

directed at maintaining the effective area, while constraining the physical area (and volume).

This paper addresses on-going HPM compact antenna efforts at the Army Research Laboratory. We are researching the use of dielectrics in the design of arrays to achieve the above goals. The antenna feed waveguide and the antenna structure incorporate dielectrics. Size benefits are realized in both the antenna and feed structures. We discuss the development of low VSWR (voltage standing wave ratio) transformers (figure 1), which match the source to the antenna via dielectrically load waveguide, and the antenna-to-air radiation interface. Graded and shaped dielectrics that are incorporated into standard waveguide and antenna designs to effect appropriate matching and antenna foreshortening (figure 2) is discussed and the results of measurements presented.

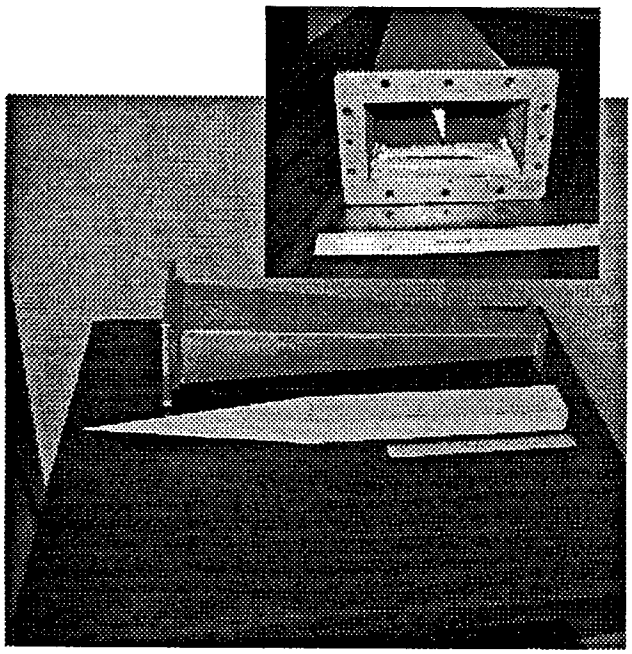


Figure 2 Transformer design.



Figure 3 Dielectrically foreshortened "slow-wave" antenna designed by Astron Antenna Co.

THE POTENTIAL USE OF SUBMILLIMETER-WAVE SPECTROSCOPY AS A TECHNIQUE FOR BIOLOGICAL WARFARE AGENT DETECTION

D. L. Woolard*, T. R. Globus[1], A. C. Samuels[3], B. L. Gelmont[1], M. Bykhovskaia[2], J. L. Hesler[1], T. W. Crowe[1], J. O. Jensen[3], J. L. Jensen[3] and W.R. Loerop[3]

*U.S. Army Research Laboratory
Army Research Office
RTP, NC

University of Virginia
[1]Electrical Engineering Department
[2] Molecular Physiology & Biological Physics
Charlottesville, VA

[3]U.S. Army Soldier Biological and Chemical Command
Edgewood, MD

SUMMARY

This paper discusses the potential use of submillimeter-wave (sub-mmw) spectroscopy as a technique for the future detection and identification of biological warfare agents. New research results are presented that have confirmed a discriminating signature associated with the phonon modes within the DNA of biological material. This paper also addresses the extension of this technique to the environmental monitoring of complete biological microorgamisms. While much work remains to establish sub-mmw spectroscopy as a practical detection and identification tool, this paper will illustrate both the scientific promise and technological problems associated with this novel technique. As will be shown, sub-mmw spectroscopy has the potential for increasing the survivability of the future warfighter and the general public by enabling a novel biological-early-warning capability in the future.

In the past decade, there has been a proliferation of chemical and biological (CB) agents as instruments of warfare and terrorism. Clearly, the most serious threat of CB agents is the potential harm they present to the short and long-term health of the victim(s). However, the actual or perceived threat of CB warfare agents can impact the operational capability of a military force in the field even when conventional counter-measures (i.e., protective equipment and clothing) are successfully employed. For these reasons, the development of reliable approaches for the detection and identification of CB agents in the field of operation is imperative. The CB warfare threat is also of strategic important in relation to the Army's Future Combat Systems (FCS) vision. The FCS concept seeks a radical transformation in land forces where platforms are lighter and more deployable while at the same time increasing lethality and survivability. Furthermore, the issue of establishing an automatic detection, alert, avoidance and protection system for areas contaminated by weapons of mass destruction has always been a component of the FCS concept. Indeed, there are a long list of CB detector and monitor systems supported by DoD programs that exist both in the fielded and development states. While some systems are quite compact, these are usually somewhat limited in either the number of agents that they detect (e.g., limited to certain nerve agents) or in the level of agent specificity (e.g., only assay size and number of particles). The Army's state-of-the-art for CB agent detection actually exists at this time as two large platform systems, namely, one primarily for chemical and one for biological. Unfortunately, both the FOX System (M93A1 Block I), which is primarily a chemical detection system, and the Biological Integrated Detection System (BIDS), which has only a capability of identifying four biological warfare agents, are extremely heavy platforms. Hence, the state-of-the-art systems for both chemical and biological agents are grossly incompatible with the size and weight requirements of the FCS vision. As noted earlier, weapons of mass destruction are broadly

recognized as a very serious threat to the war fighter and the general public. While much work remains to improve the overall capability of chemical sensing in the field (e.g., sensitivity, size, weight, etc.), methods for point-detection are available for all *known* chemical agents. On the other hand, the present capability for point-detection of biological (bio) agents is limited to the identification of only four species. This limitation in point-detection and the absence of any standoff (i.e., remote) capability has recently drawn considerable attention to a number of DoD agencies. When these general problems are combined with the need to realize a compact (i.e., very small size and weight) total CB systems package for the FCS concept, it is obvious that new approaches will be necessary. Recent scientific work in biological spectroscopy at very high frequencies has suggested a novel avenue for a terahertz (THz) electronic approach to warfare agent detection and identification and this is the subject of this paper.

This paper presents results from an ongoing research project that has identified a novel physical mechanism with the potential for achieving both point and standoff detection of bio agents. Preliminary studies earlier suggested that very far-infrared spectra possess features that might be used for the detection and identification of microorganisms and other living matters. Subsequent spectroscopic obtained from DNA and complete cellular biological samples revealed detailed and high-level numerical structures possibly due to vibrational lattice and local phonon modes and other physical mechanisms of interactions between radiation and the biological material. The discovery of this phenomenon was important to bio detection for a number of reasons. *First*, previous theoretical analysis has indicated that the resonant frequencies of such phonons within DNA material are strongly dependent on the weak hydrogen bonds of the double-helix base-pairs. Since all genetic information associated with living cells is encoded in the variety and arrangement of DNA nucleotides, this phenomenon suggested a potentially promising mechanism for biological warfare agent detection because these phonons should be somewhat species specific. Hence, a new fundamental mechanism for bio identification had been suggested. *Second*, this initial work demonstrated that a *large number* of species-specific phonon modes might be detected relatively easily from semi-dry films made from randomly oriented DNA fibers. Hence, sample collection may be the only real field problem if enough spectral bandwidth is employed to distinguish the DNA signature from possible signatures of other cellular agents. Together, these initial results indicated that the unique portion of the phonon signature occurs at long-wavelengths in the frequency band from 0.1 to 1 THz. This is very important because this corresponds to a regime where it is quite feasible to develop miniaturized, low-cost electronic detectors in the future. Furthermore, the atmosphere is quite transparent below about 0.3 THz and this phonon-based approach may offer a means to achieve remote bio detection. Therefore, the preliminary indications of multiple phonon-modes in DNA offered an exciting new approach for both point and standoff detection of bio agents and the potential for a solution for the bio early warning problem.

In order to establish submillimeter-wave (sub-mmw) spectroscopy, as a viable and potentially successful approach for the future realization of a biological detection system, a number of scientific and technological demonstrations must be achieved. First and foremost, the existence of dielectric resonance phenomena that is both a unique characteristic of the biological agents and one that is sufficiently diverse across a class of biological materials must be demonstrated. In fact, the initial focus of this paper is towards a detailed investigation of the phonon-absorption characteristics in DNA materials. Here, the goal is to establish the scientific foundation of spectral signatures associated with the basic building blocks of biological systems. Indeed, this paper will present compelling experimental evidence that confirms the presence of multiple dielectric resonances in the sub-mmw spectra (i.e., ~ 0.01-10 THz) obtained from DNA samples. While these results alone have important implications to biological science and to military defense they only represent the first step towards a future identification and interrogation tool. Indeed, a *practical* sensing capability at THz and sub-THz will be required to detect and identify complete biological organisms. Hence, this paper will also outline preliminary spectroscopic studies of complete cellular biological samples (e.g., Bacillus subtillus and Anthrax) and present new theoretical models for accurately interpreting phonon mode behavior in spectral signatures. This combined work establishes the initial foundation for the future use of sub-mmw spectroscopy in the identification and characterization of biological warfare agents.

Session H
High-Performance Computing and Simulation

Chair
Dr. Chester C. Carroll
U.S. Army Aviation and Missile Command

Co-Chair
Dr. Julian Wu
U.S. Army Research Laboratory

Keynote Address
Dr. Charles M. Bowden
U.S. Army Aviation and Missile Command

THIS PAGE INTENTIONALLY LEFT BLANK

ANALYSIS AND OPTIMIZATION OF EXPLICITLY PARALLEL SCIENTIFIC CODES WITH COMBINED MEMORY CONSISTENCY MODELING

Ms. Dixie M. Hisley*
U.S. Army Research Laboratory
Aberdeen Proving Ground, MD 21005-5067
Dr. Lori Pollock, Associate Professor
Department of Computer and Information Sciences
University of Delaware
Newark, DE 19716

In the past five to ten years, scientists and engineers have typically run large-scale, computationally intensive numerical simulations on high-end multiprocessor supercomputing architectures. Among the architectures gaining widespread availability are shared memory multiprocessors. In order to take advantage of these architectures, sequential scientific codes, such as F3D, Overflow, C3I benchmarks, required modification and tuning into parallel versions using explicitly parallel languages, e.g., Java, OpenMP, and Pthreads [Jav99, Ope97,GBB+98]. Typical modifications by applications programmers involved the insertion of primitives to control concurrent threads of execution in their scientific codes. An important challenge for computational scientists and engineers continues to be how to further modify their codes to obtain high performance from the latest parallel architectures with a reasonable effort. Parallelizing compilers and software development tools can help the computational scientists in extracting parallelism and enhanced performance. However, advances in parallel software development tools are still lagging behind hardware advancements.

Classical compiler analysis and optimizations [ASU86, Muc97] have been developed in the context of sequential programs designed to run on uniprocessors. Therefore, intermediate program representations, such as the control flow graph, and optimization algorithms are heavily influenced by the assumption of sequential control flow. Optimized compiled sequential code can outperform unoptimized compiled code by as much as the performance difference between two successive generations of processor hardware. The future widespread availability of multiprocessors (even at the PC level) indicates a need to extend the analysis and optimization techniques developed for sequential programs to parallel programs without sacrificing any uniprocessor performance.

Midkiff and Padua [MP90] show that straightforward transfers of sequential optimization techniques to parallel compilers fail. Advances in automatically parallelizing compilers and compilers for data-parallel languages (e.g., High Performance Fortran) have arguably made some progress in this area. However, compilation techniques for explicitly parallel programs have not been as aggressively researched [Lee99, NUS98]

An explicitly parallel programming language is one that contains primitives for creation, termination, and synchronization of concurrent threads of execution. The user explicitly uses these primitives to specify the actions to be taken by the compiler and run-time system in order to execute the program in parallel. For example, OpenMP extends Fortran, C and C++ by providing primitives through the following user interfaces; compiler directives, a run-time library, and environment variables. Data races and synchronization issues make it impossible to apply classical methods directly to explicitly parallel programs. Thus, new program representations, analysis, and optimization algorithms are needed for explicitly parallel program compilers, debuggers, and run-time tools. With these new tools, scientific explicitly parallel production codes can be further developed by the applications programmer for improved high performance computing.

Previous research for explicitly parallel codes focused on developing correctness criteria, intermediate program representations,and extending and applying classical sequential analysis/optimization techniques. However, much of the analysis was restricted to a subset of parallel programs and did not deal with all types of explicit synchronization. In addition, there has been a lack of consensus on an acceptable memory consistency model for developing correctness criteria, e.g., sequential consistency versus location consistency [GS94]. Furthermore, very few real implementations of the analysis and optimizations have been performed. Novillo, Unrau, and Schaeffer [NUS98] implement their algorithms in a prototype compiler for the C language using the SUIF compiler system. However, no real benchmarks were tested, nor any performance numbers cited. Krishnamurthy and Yelick [KY96] demonstrated remote access optimization by automatically transforming SPMD source code into Split-C for a suite of five scientific application kernels. Their best performance improvements were approximately a factor of 1.5. Although, full production level codes may be too large for the development process, benchmark codes (e.g, the NAS benchmarks) that are representative of the computational kernels may be used. The usefulness of explicitly parallel software analysis and optimization for the applications programmers

community still needs to be evaluated through experiences with large, application codes, e.g, F3D, Overflow, C3I.

The focus of this paper is to show how classical compiler analysis and optimizations for sequential programs can be effectively extended to be used for compiling scientific codes written in the explicitly parallel shared memory standard OpenMP with the added flexibility of programmercontrolled memory consistency models guaranteed for different parts of the program.

OpenMP is important and interesting to target for this paper because it has become a standard for portable shared memory programming over the past several years. OpenMP augments its parallel constructs with clauses that identify data storage attributes for variables. Clauses such as these are not discussed in previous research. Also, previously researched techniques that are more general than the OpenMP model could be specialized for improved performance in terms of cost, precision and/or scalability.

Furthermore, this paper will propose using a new combined memory consistency approach using both sequential and location consistency for correctness criteria. Previous research advocated the use of one or the other. Parallel programmers should have the option to specify whether they want a particular consistency model for different parts of a program. Allowing this flexibility could significantly improve performance at run time. A software analysis tool will be designed to perform program analysis and optimization for OpenMP programs. This paper will be supported by investigation of the following principal research problems: a) investigate applicability, extension and simplification of existing techniques for intermediate representations, analysis and optimization assuming sequential consistency for the OpenMP environment b) investigate intermediate representations, analysis and optimizations for OpenMP under location consistency memory model c) develop techniques for enabling both location consistency and sequential consistency models within the same application code analysis d) design of experimental prototype and experimental studies for evaluation of research. The implications for weapons system design are explicitly parallel computational simulations that will be more efficient and optimized than current parallel simulations.

BIBLIOGRAPHY

[ASU86] A. Aho, R. Sethi, and J. Ullman. *Compilers: Principles, Techniques, and Tools.* Addison Wesley, NY, 1986.

[Muc97] S. Muchnick. *Advanced Compiler Design and Implementation.* Morgan Kaufmann, CA, 1997.

[Jav99] *Interim Java Grande Forum Report.* http://www.javagrande.org/javagrande1999.html

[MP90] S. Midkiff and D. Padua. Issues in the optimization of parallel programs. In *Proc. Int. Conf. On Parallel Processing*, volume II, pages 105-113, 1990.

[Lee99] J. Lee. *Compilation Techniques for Explicitly Parallel Programs.* PhD thesis, Department of Computer Science , University of Illinois at Urbana-Champaign, 1999.

[NUS98] D. Novillo, R. Unrau, and J. Schaeffer. Concurrent SSA form in the presence of mutual exclusion. In *Proceedings of the 1998 International Conference on Parallel Processing*, August 1998.

[Ope97] OpenMP Standard Board. *OpenMP Fortran Application Program Interface*, October 1997, Version 1.0, http://www.openmp.org.

[GBB+98] H. Gabb, R. Bording, S. Bova, C. Breshear. A Fortran 90 application programming interface to the POSIX threads library. In *Proc. 40th Cray User Group Conference*, 1998.

[GS94] G. Gao and V. Sarkar. Location Consistency: Stepping Beyond the Barriers of Memory Coherence and Serializability, *ACAPS Technical Memo 78*, School of Computer Science, McGill University, Montreal, Quebec, December 1994.

[KY96] A. Krishnamurthy and K. Yelick. Analyses and optimizations for shared address space programs. *Parallel and Distributed Computing*, (38):139-144, 1996.

RIGOROUS ELECTROMAGNETIC MODELING OF TARGETS AND DISCRETE CLUTTER IN A LOSSY HALF-SPACE

Anders Sullivan
U.S. Army Research Laboratory
Adelphi, Maryland, 20783

ABSTRACT

A method of moment (MoM) analysis is developed for electromagnetic scattering from high-fidelity tank targets and several representative tree-trunk models over lossy soil. Results show that at certain angles and frequencies, the tank backscatter is *less* than the tree-trunk backscatter. Also considered is scattering from a perfectly conducting target in the near field of a tree trunk over lossy soil. In the second case, the analysis is simplified by considering the conducting target to be a flat plate, although the algorithm can be applied to any conducting target. For a rigorous account of the interaction between these disparate targets, the conducting target and tree trunk are modeled separately, with interactions handled via an efficient iterative procedure. In addition to yielding accurate results, this procedure has memory and run-time requirements that are significantly less than required of a straightforward brute force MoM approach. Results in this case show that there is significant coupling between the metal target and the tree-trunk model.

1. INTRODUCTION

Recent U.S. Army studies have shown that faster response to a crisis can lead to faster resolution (U.S. Army, 1999). In the context of the Future Combat Systems (FCS) objective force vision (or "Army Vision"), this demands rapid deployment of highly integrated, highly capable systems. In order to deploy these systems effectively and achieve dominance on the battlefield, it is critical that the commander have complete situational awareness and understanding. Situational understanding is the fundamental force enabler across all Army battlefield operating systems and the foundation for risk mitigation. It is built on reconnaissance, surveillance, and target acquisition. For example, an array of unmanned aerial vehicles equipped with radar sensors and processors can provide the detailed information required to achieve situational understanding. The research reported herein seeks to support the Army Vision by providing detailed electromagnetic simulations of recently developed ultra-wideband (UWB), high-resolution synthetic aperture radar (SAR) technology. In this regard, recent work has shown the potential utility of UWB SAR technology for wide-area surveillance (Carin et al., 1999; Jao, 1995).

Future sensors will be compact, low cost, and lightweight, and will have enhanced capabilities for detecting man-made targets (e.g., tanks, trucks, mines, etc.) in the presence of naturally occurring clutter (El-Rouby et al., 2000). Recent developments in low-frequency imaging radar have made UWB SAR a viable technology candidate for the FCS reconnaissance, surveillance, and target acquisition mission. In particular, UWB SAR has shown the ability to detect large tactical vehicles concealed by tree foliage. The development of *reliable* detection algorithms has been hampered, however, by the complexity of the scattering physics, due, in part, to the large number of physical parameters involved and the frequency diversity inherent in UWB. Typical foliage-penetrating (FOPEN) radar requires low-frequency operation to penetrate tree canopy and large relative bandwidth to provide range resolution. Cross-range resolution is provided by the linear motion (synthetic aperture) of the radar. A detailed understanding of UWB scattering from both target and clutter is therefore essential for developing future automatic target recognition (ATR) algorithms.

An important form of clutter encountered in FOPEN SAR is produced by dihedral scattering from large tree trunks. In fact, others have shown (Ulaby et al., 1990) that the backscatter from a typical forest at VHF is dominated by the ground-trunk interaction. While this phenomenon is widely appreciated, there is little detailed information in the literature on the exact nature of this interaction. As a consequence, the effects of tree-trunk scattering and the general clutter environment it creates pose significant challenges for understanding FOPEN SAR imagery.

2. RESULTS AND DISCUSSION

We first consider low-frequency short-pulse scattering from a T-72 tank, situated above a lossy half-space. The incident wave is a 60-MHz Blackman sine wave, vertically polarized, and oriented 35 degrees from grazing. In the azimuth direction, the wave is incident on the front of the tank. The pulse covers the VHF range from 0 to 200 MHz. The response is characterized by two large positive peaks, followed by some late-time ringing. The time-domain response can be transformed into the space domain, via SAR image principles, and mapped on to the surface of the tank. This is shown in Fig. 1. This is

done in order to correlate the peak returns in the time-domain signature to specific physical features on the target, i.e., the cupola and the rear gas tank. These highlighted (white) areas are the local scattering centers on the T-72 for this particular angle of incidence.

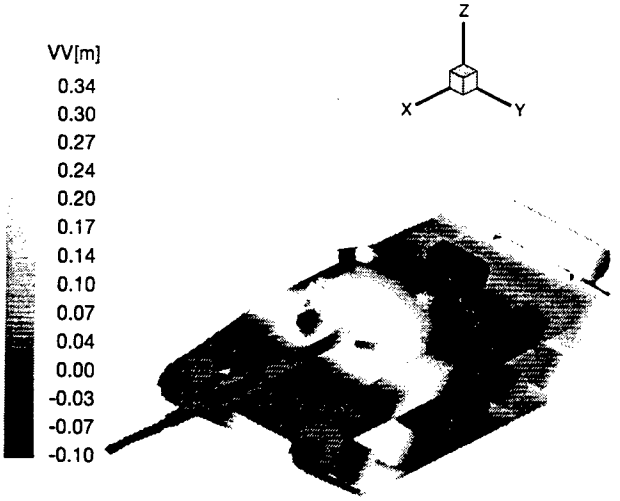


Fig. 1. Time domain response mapped on to the surface of the T-72. Scattering centers are highlighted on the cupola and rear gas tank.

In the next example, scattering from the T-72 is compared to the backscatter of representative tree-trunk models over Aberdeen soil. The frequency is 100 MHz, with vertical and horizontal polarizations considered. The depression angle is 35 degrees, as before. Two cases are presented. The first assumes a "best case" scenario. In this case, the tank is viewed broadside and the tree trunk is 0.30 m in diameter. For HH polarization, the tank backscatter is much larger than the tree-trunk backscatter, particularly for the range of angles that would be of interest for a down-look imaging radar system. This is important for an airborne SAR system, where the goal is to focus target images against a variable clutter background. The second case assumes a "worst case" scenario. In this case, the tree-trunk diameter is 0.60 m, and the tank is now viewed at an off-broadside or oblique angle. The HH response is markedly different, in that the backscatter of the tree trunk is now larger than the tank backscatter. This essentially says that the clutter signature is larger than the target signature. These results suggest that a SAR system would need a wide enough integration angle to be sure it catches a front or side of the target to avoid being overwhelmed by clutter backscatter.

Next we consider the case when the tree-trunk model is near a perfectly conducting flat plate target. The geometry for this problem is specified in Fig. 2. In Fig. 3, we plot the magnitude and flow direction of the electric surface current on the tree trunk for incidence on the rear section of this composite target (φ = 180 degrees),

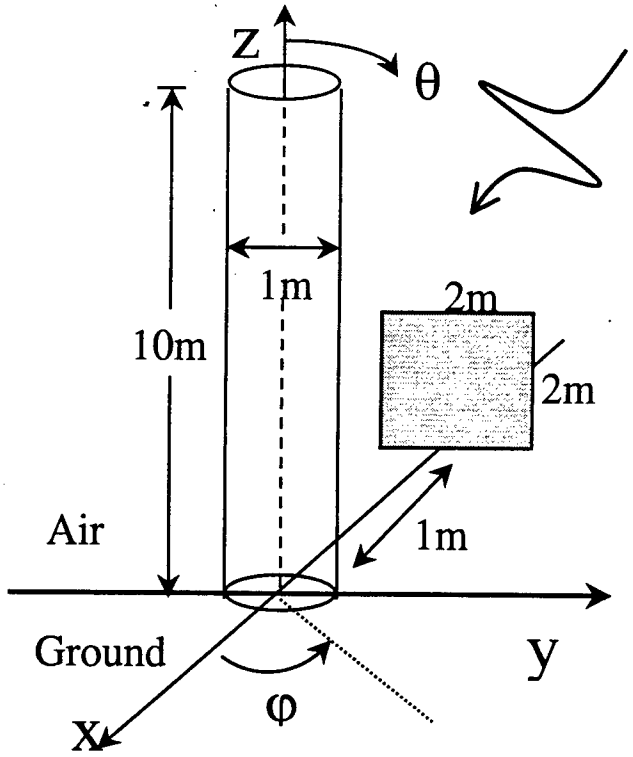


Fig. 2. Dielectric tree trunk and flat plate in a half-space where plate is directly behind tree.

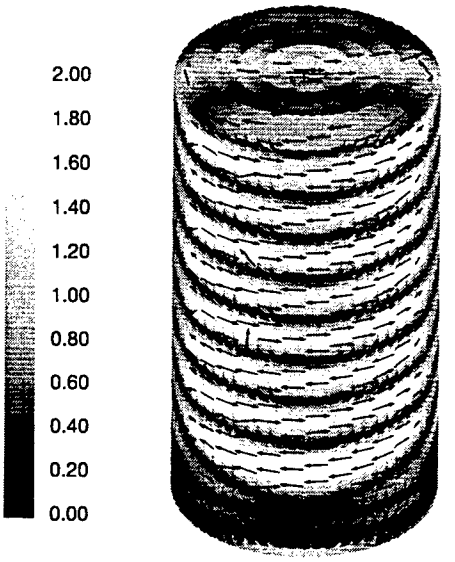


Fig. 3. Normalized surface currents on tree trunk for horizontally polarized plane wave, φ = 180 degrees (incidence form the rear). Plate shadows base of the tree trunk.

assuming a 300-MHz horizontally polarized plane wave at a 30-degree depression angle (θ = 60 degrees). In this figure, the view of the tree trunk is the side facing the plate, which gives the best view of the coupling effect. In this case, the plate shadows the trunk. We can see how this shadowing affects the current distribution at the base of the trunk. We can also see how this is a fairly localized effect, as the remainder of the tree trunk is unchanged.

Navier-Stokes Computations of Finned Missiles at Supersonic Speeds

David J. Haroldsen
U. S. Military Academy
West Point, New York 10996

Walter B. Sturek, Sr.*
Computational and Information Sciences Directorate
U. S. Army Research Laboratory
Aberdeen Proving Ground, Maryland 21005-5067

SUMMARY

Researchers in computational fluid dynamics at the United States Army Research Laboratory are interested in investigating a wide array of complex fluid flow problems. These problems include flow around complex bodies, flow at moderate and high Mach number, and flow at moderate to high angles of attack. A recent study examined the predictive capability of several different Navier-Stokes flow solvers applied to the case of an ogive-cylinder configuration at transonic and supersonic flow velocities at 14° angle of attack (Sturek et al.,1997). This study extends the previous work by examining the predictive capability of the WIND flow solver to predict flow problems for missiles with fins at angle of attack and moderate Mach number.

The WIND package has numerous capabilities that make it potentially attractive for computational researchers. Among these features are the numerous turbulence models, ease of use, portability, parallel processing capability, and the ability to incorporate grids with a generalized topology. This particular feature makes WIND attractive for use with the GridPro grid generation package. GridPro produces structured, multi-block grids with non-overlapping block interfaces.

The focus of this effort is to investigate: 1) the application of WIND for complex flow problems; and 2) the use of multi-block, patched grid topologies. This study considers the application of WIND 1.0 to the study of two different missile configurations at angles of attack of 14 and 40 degrees and at Mach numbers near 2.5. The generation of multi-block, patched grids using the GridPro package is discussed and results for different turbulence models are presented.

Two missile configurations were examined in this study. Both missiles consist of a 3-caliber ogive nose and a 10 caliber cylindrical body. Each missile has four fins, with symmetry about the pitch plane. The specific fin geometry and placement for missile 1 is shown in Fig. 1.

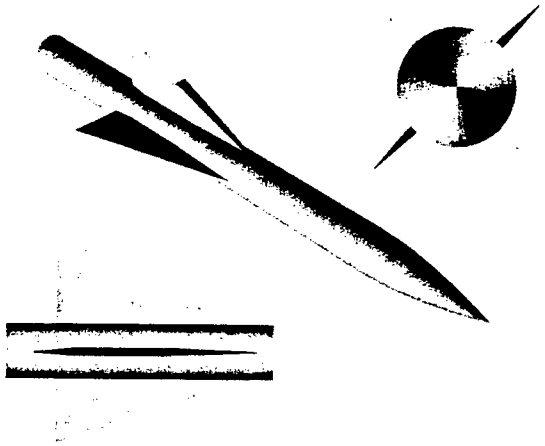


Fig. 1 Missile 1 configuration

Missile 1 (Birch,1996) was studied at roll angles of 0 and 45 degrees, Mach 2.5, and angle of attack 14 degrees with a Reynolds number of 1.12×10^6. Missile 2 (Stallings, et al., 1980) was studied at a roll angle of 45 degrees, Mach 1.6 and 2.7, and angle of attack 40 degrees with Reynolds number of 250,000.

The grid generation for this investigation was done using the GridPro grid generation software. GridPro is a product of Program Development Corporation in White Plains, NY. This package is of interest because it incorporates a topology-based approach to the generation of grids. This approach emphasizes the underlying topology of the geometric shapes and of any flow features rather than focusing on the geometry of the problem. The package consists of a GUI for topology design, the grid generation software, and utilities for manipulating grids. GridPro produces multi-block, structured grids with the capability to output data in a variety of formats. An important consideration when using GridPro is that the adjacent zones abut but do not overlap. The user can also customize GridPro to output initial boundary data relevant to a particular flow solver.

Runs were conducted using the following turbulence models: Baldwin-Lomax (BL), Baldwin-Barth (BB), Spalart-Allmaras (SA), and Shear Stress Transport (SST)

Runs were performed on Silicon Graphics Origin 2000 or Onyx platforms with multiple processors. Runs were typically conducted using 8 processors and converged solutions could be obtained in 8-12 hours.

The parallel performance obtained varied widely depending on the grid used. Speedup factors as high as 7.5 were obtained using 8 processors and as high as 14 were obtained for 16 processors.

Quantities of interest for the study are the pressure coefficient at different stations on the body and fins as well as pitot pressure profiles of the outer flow field.

Fig. 2 shows a comparison of surface pressure predictions on the missile body at various axial stations compared to the experimental data. The variation of results for different tubulence models is shown.

The WIND flow solver has been found to be an efficient tool for increasing and extending the predictive capability of researchers in computational fluid dynamics. WIND has proven to be particularly useful for complex missile configurations with fins in which the multiblock, patched grid generation topology is used.

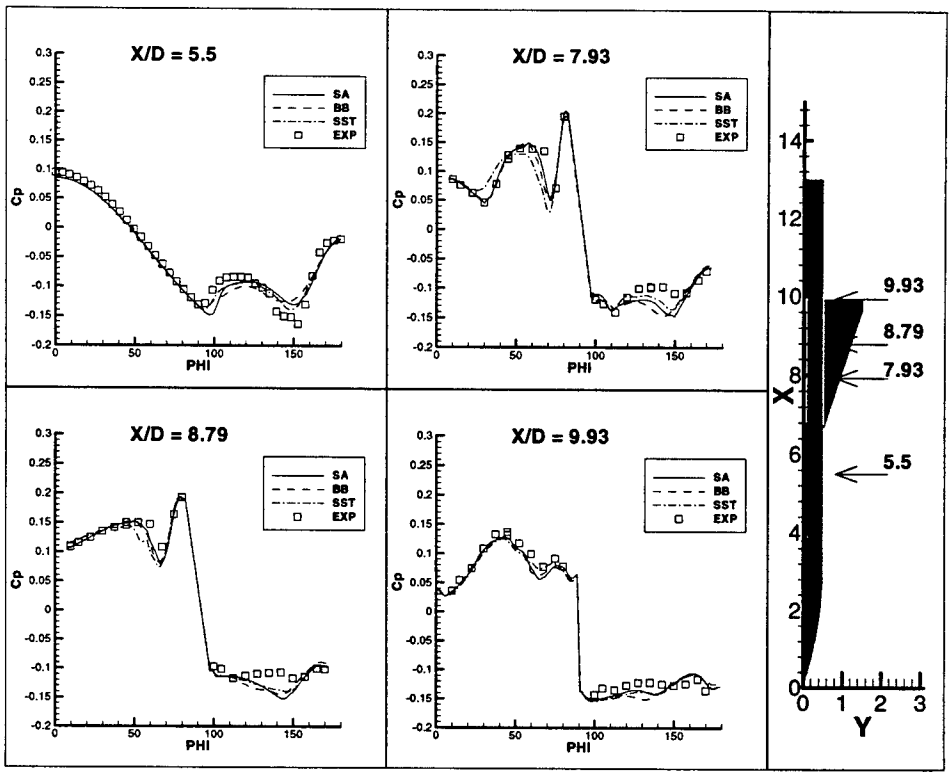


Fig. 2 Comparison of surface pressure predictions on the body of missile 1

COUPLED MACRO-MICRO NONLINEAR TRANSIENT ASYMPTOTIC EXPANSION HOMOGENIZATION METHOD ON SCALABLE COMPUTERS FOR HETEROGENEOUS STRUCTURES

Raju R. Namburu, Peter W. Chung, and Rama R. Valisetty
U.S. Army Research Laboratory
Aberdeen Proving Ground, MD 21050

ABSTRACT

Development and implementation of scalable approaches for nonlinear multiscale problems based on the asymptotic expansion homogenization (AEH) method are presented. Nearly all of the developments in the literature in AEH for practical engineering applications are in the understanding of linear/nonlinear structures subject to quasi-static and static loads. Yet most practical applications, particularly those suited for the Army, require dynamic loads at small time scales such as those found in high velocity impact. Hence, the emphasis of the present investigation is to develop and implement consistent AEH numerical formulations to address the elasto-plastic material response of heterogeneous structures subjected to short duration transient loads. The AEH method provides micro-level information as a direct function of the macro-level variables in a strict, mathematically seamless approach. On the other hand, these nonlinear multiscale simulations increase the computation time substantially. Hence, scalable computational approaches are needed to address this approach. A second-order accurate, velocity-based, explicit time integration method in conjunction with the AEH method on scalable computing architectures is employed to account for short transient loads and large deformation nonlinear material response. The applicability and scalability of the computation approach for linear and nonlinear applications are demonstrated.

SUMMARY

Since the early AEH mathematical foundations established by Sanchez-Palencia (1980), and Bensoussan et al. (1978), a limited number of efforts have attempted to extend the mathematics to more complex engineering situations. Lene (1986) employed the AEH method to evaluate interfacial damage of fibrous composites by exploiting the global-local nature of the approach. Guedes and Kikuchi (1989) applied the approach to quasi-static elasto-plastic problems without updating the micro-level properties between successive numerical iterations. That procedure was later corrected in a paper by Terada and Kikuchi (1995). Ghosh and Moorthy (1995) integrated the AEH method with the Voronoi cell finite element method for the study of actual heterogeneous media. Recently, Galvanetto, et al. (1997) showed a detailed derivation for the elasto-plastic problem in the framework of the AEH method. Despite the existing efforts in this area, those that address elasto-plastic issues simply extend the method as it is applied to elastic problems by replacing Hooke's law with an elasto-plastic rate dependent constitutive relation, Hookean in form. For quasi-static and static problems, such an approach is both permissible and intuitive. However, the typical number of iterations required makes this approach computationally impractical for transient/dynamic situations. Aside from the AEH approach, no other homogenization practices are capable of providing micro-level information as a direct function of the macro-level variables in a strict, mathematically seamless approach.

The algorithm developed in this study exploits the ability of the AEH method to link two structures of different scales to consider micro-structural models locally within each macro element in a parallel computing environment. It begins with the perturbation of the velocities as a function of the ratio of the primary length scales involved. Just as an element's constitutive behavior is sampled at its integration points, the material constitutive behavior now is computed as a micro structural response sampled at the integration points for each time step. The solution is also appropriately termed a corrector step for micro-stresses because it accounts for the heterogeneities at the microscopic level due to the elastic-plastic phenomena. The equations of motion are solved via a self-starting explicit 2^{nd} order accurate velocity-based algorithm (Namburu, 1990). When compared to the traditional central difference method, this algorithm has inherent advantages related to time step size and accuracy for non-linear situations. It is conditionally stable and the time step is still restricted by the Courant stability criteria.

Since an explicit time integration scheme takes a large number of time steps, the present approach for macro- and micro-level computations take much longer times for solution than for traditional single-scale problems. Also, the equations governing the micro-level response of a macro element depend solely on the respective element's macro response variables. As a result, the overall macro or global solution does not require assembly and inversion of a global stiffness matrix. This means that AEH can be implemented on scalable computing environments using domain decomposition approaches. Load balancing strategies to decrease the parallel macro-micro computation times are also examined. The parallelization strategy is based on the observation that the generation of an element's plastic large-deformation controlled stiffness matrix can form a substantial part of it's total computation effort. Thus, using some of the available processors exclusively for the micro-element computations, i.e. in a helper mode, can lead to better scalability.

Coupled macro-micro AEH analysis for the composite armored vehicle hull structure is shown in Fig. 1. Note that the hull structure is a composite construction with different materials. Fully coupled macro-micro structural analysis is performed on this composite construction. The results for the Taylor's impact problem of a composite bar under an impact are obtained (Fig. 2) and the scalability of the computational time (Fig. 3) are examined. The results showed consistent scaling. They indicate that the overall computation time can be reduced if some of the available processors are devoted exclusively for the micro- element computations.

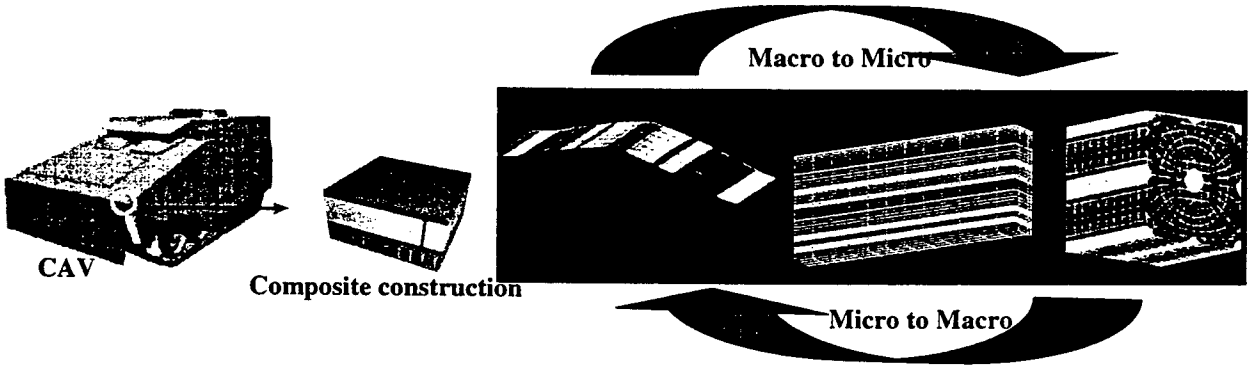


Fig.1: Linear micro-macro structural analysis for Composite Armored Vehicle hull structure

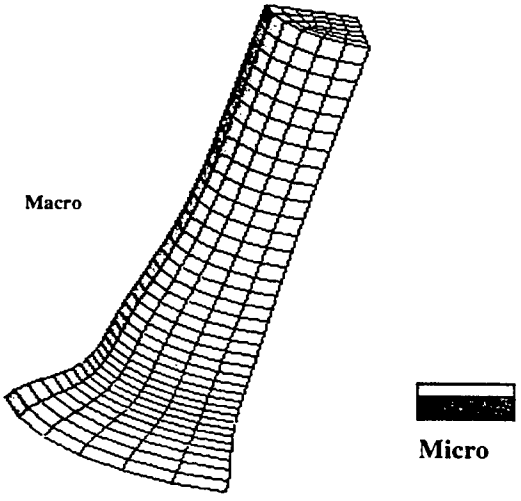


Fig. 2 Composite bar impacting a rigid surface.

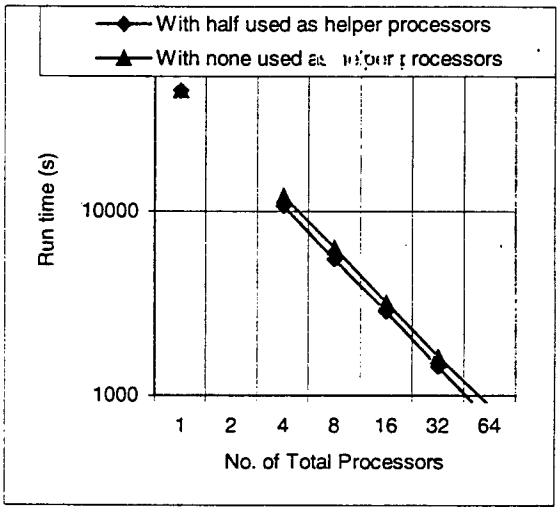


Fig. 3: Scalability studies of the composite bar impact example

VALIDATION OF THE MUVES-S2 COMPUTER MODEL USING BRADLEY FIGHTING VEHICLE LIVE-FIRE TEST DATA

Russell E. Dibelka *
William E. Baker
Richard Saucier
Theodore M. Muehl
Ricky L. Grote

US Army Research Laboratory

For five decades interest in simulation modeling has been expanding, almost keeping pace with the phenomenal rate of growth of computer technology. Lagging somewhat behind have been efforts toward the verification and validation (V&V) of the resulting simulation models; that is, the establishment of some degree of confidence that the model does, in fact, accurately mimic some real-world process. However, over the past several years, the V&V of U.S. Army models has been mandated and appropriate procedures outlined in various regulations.

The Stochastic Quantitative Analysis of System Hierarchies (SQuASH) model was introduced a decade ago for the express purpose of providing a tool for the vulnerability analyst to use in planning, analyzing, and assessing live-fire test shots of armored fighting vehicles. The development of this model has continued over the years. It has evolved from a stand-alone FORTRAN version to its current C version – in which it is embedded in the Modular UNIX-Based Vulnerability Estimation Suite (MUVES) software. The Stochastic Analysis of Fragment Effects (SAFE) was developed in the late 1980's to evaluate the vulnerability of lightly armored vehicles and aircraft to fragmenting munitions and armor-piercing bullets. The two models, SQuASH and SAFE, have been combined to form MUVES-S2. Through a series of exploratory data analyses, we have attempted to show that the MUVES-S2 model produces results consistent with those seen in live-fire testing.

MUVES-S2 is a stochastic, component-level, point-burst simulation that evaluates the effects of kinetic-energy (KE), shaped-charge (SC), and High Explosive (HE) fragmentation threats against ground mobile targets and aircraft. It concentrates on damage resulting from the main penetrator along with damage to interior components resulting from the fragment cloud of behind-armor debris. For each of several different model comparisons we chose 19 direct-fire shots involving six different threats against an armored vehicle and 39 indirect-fire shots. MUVES-S2 was run for 1000 replications and results compared at the component level (kills, crew incapacitation) as well as the overall vehicle level (perforation, mobility loss-of-function, firepower loss-of-function, and catastrophic kill).

For some comparisons we overlaid the distribution of model outcomes onto the live-fire test results to determine if that result fell within the distribution. For other comparisons we merely counted outcomes. In all cases we established whether the live-fire result was a likely/reasonable/unlikely/unrealized event within the distribution of model outcomes. Of 89 direct-fire comparisons overall grades were 65 likely events (73%), 13 reasonable events (15%), 7 unlikely events (8%), and 4 unrealized events (4%). The four unrealized events were due to the difficulties of modeling crew members (which we did not amend in the model) and our misunderstanding of the damage resulting from the main threat penetrating the ready-ammunition compartment (which we did amend in the model). Of 195 indirect-fire comparisons overall grades were 125 likely events (64%), 36 reasonable events (18%), 27 unlikely events (14%), and 7 unrealized events (4%). The seven unrealized events were due to incorrectly recorded burstpoint locations, unmodeled components, and insufficient sampling.

Important conclusions resulted from this effort to validate the MUVES-S2 model:

1. Shotlines with no cross-sectional area make model outcomes highly dependent on geometric detail; that is, small displacements of shot locations can result in major differences for all metrics.

2. Variability, sometimes significant, exists within live-fire testing.

3. Comparisons of crew members are difficult due to differences between the plywood mannequins and modeled crew members, as well as uncertainty in seat position in the live-fire test.

4. A few critical components were not modeled in the target description.

5. Occasionally, the recorded burst locations were inconsistent with the realized damage.

This was a preliminary effort to V&V the MUVES-S2 model; it serves as a template for such efforts in the future. Nevertheless, even this endeavor showed that the model generally does a credible job and is certainly worthy of more intensive efforts. Some shortcomings were exposed; in particular, a tendency to underpredict some component kills. Understanding the reasons for this will probably require an examination of submodels and input to see if we can comprehend and correct such shortcomings.

It is important to keep in mind that MUVES-S2 was evaluated for a single target against a variety of threats. Different types of vehicles or different types of threats would require a re-examination of the model. This does not mean that we must go through the entire process for every new scenario, but we must be cognizant of the simple fact that not all model subroutines were exercised in this recent effort; for example, we looked at only a subset of the possible penetration algorithms. This warning is consistent with published V&V requirements stating that every such effort should provide an understanding of the range of conditions over which it is applicable.

RADAR SIGNATURE PREDICTION FOR ARMY GROUND COMBAT VEHICLES

Ronald J. Chase
U.S. Army Research Laboratory
Adelphi, MD 20783-1197

ABSTRACT

The accuracy and lethality of modern weapons are driving the demand for the implementation of stealth technology into the next generation of Army systems. The development of stealthy, survivable Army platforms that are integral assets to the Army Vision–Future Combat System (FCS) requires advanced predictive design and prototyping that rely heavily on modeling and simulation to assess feasibility, optimize performance, and trade off competing requirements. Radar signature prediction is challenged by the capability of modern radar systems to detect, identify, and target battlefield assets by exploiting the enhanced resolution and imaging available in the millimeter–wave (MMW) region of the electromagnetic (EM) spectrum. At frequencies in the MMW region and beyond, standard EM modeling algorithms quickly overwhelm existing supercomputer resources. A radar cross-section (RCS) computational modeling activity performed as part of an ongoing North Atlantic Treaty Organization (NATO) program has been used to assess the hardware, software, and model requirements needed for radar signature management of the FCS.

1. INTRODUCTION

The Army Research Laboratory (ARL) is participating in an ongoing NATO technology research study group (RSG20 and later SET 030/TG14), with a focus on the military applications of millimeter-wave (MMW) imaging. RSG20 conducted an experiment at Swynnerton, UK, that used airborne synthetic aperture radar (SAR) systems to collect imagery of a military location. The experiment assessed the applicability of MMW imaging for locating and engaging ground vehicles and other fixed targets. One of the ground vehicles used in this test was a ZSU-23-4, a quad 23-mm self-propelled antiaircraft weapon system. ARL conducted a series of measurements at the outdoor signature research facility at the ARL Aberdeen Proving Ground (APG), MD, in August 1996, to characterize the MMW signature of this vehicle for comparison to similar measurements obtained at Swynnerton. In addition to comparing measurements, the participants agreed to perform radar cross-section (RCS) predictive modeling using this target as a baseline. ARL teamed with the Missile and Space Intelligence Center (MSIC) of the Defense Intelligence Agency (DIA) to perform computer modeling of the ZSU vehicle to support the North Atlantic Treaty Organization (NATO) effort. ARL developed the computer geometry model of the ZSU vehicle that was used by all participants. In addition, ARL generated and analyzed the largest and most computationally intensive model configuration in the program.

2. MEASUREMENTS

The fully polarimetric instrumentation radars at the ARL-APG signature research facility were used to collect data on the ZSU vehicle at X-band, K_a-band, and W-band. When measurements are made with this system, the radar is mounted on an elevator on a 125-ft tower. The radar is pointed at an in-ground turntable 153 ft away, and the test vehicle sits on this turntable. Target rotation is always counterclockwise; thus, 90° is always on the left side of the vehicle when one looks at the target head-on. A complete rotation for frequency measurements at 34 GHz takes about 10 min. A fully calibrated RCS plot can be ready in 10 min after the completion of the measurement. A series of inverse synthetic aperture radar (ISAR) images displayed on a CRT as a video is available 25 min after each measurement is completed.

3. MODELING

A computer geometry model of the ZSU-23-4 was obtained in Ballistic Research Laboratory-Computer-Aided Design (BRL-CAD), a combinatorial solid-geometry-based modeling system. The BRL-CAD file served as input to a software package ECLECTIC developed by the Army Tank and Automotive Command (TACOM), which generated a flat, triangular, all-metal facet representation of the ZSU-23-4's exterior structure containing about 78,000 facets. This model is a "coarse" representation of the ZSU vehicle. Later in the program, a high-fidelity representation of the vehicle containing about 852,000 facets was obtained from the Army Targets Management Office. The high-fidelity model is used in our ongoing studies.

The coarse facet model served as input to Xpatch, a high-frequency signature prediction code. Xpatch is an asymptotic analysis code that relies on a ray optic method using shooting and bouncing rays (SBR). With SBR, a dense grid of rays is shot from the radar direction toward the target. The rays are traced via geometrical optics as they bounce around within the target. The effects of radiation polarization, ray group divergence, and material

transmission and reflections are included. When the ray exits the target, a physical optics integration is performed to calculate the far field scattered from the target. Single and multiple bounce contributions are included and first-order edge diffraction can be added as an option. Computations in both the time and frequency domains are available.

4. COMPUTATIONAL RESOURCES

The ZSU vehicle configuration for radar excitation at a 30° elevation angle over a metal ground plane required the most extensive computational resources in the program. A complete set of RCS data involved both polarizations, a full 360° azimuth sweep at steps of 0.015°, with 256 frequencies centered at K_a-band. These configuration parameters were selected to coincide with the radar measurement parameters and allow an exact comparison with measurement data. Xpatch software was installed on each of the SGI-Origin O2000 platforms (four machines) at the Army Major Shared Resource Center (MSRC). The problem was divided into 24,000 jobs (one for each azimuth angle step) that could be run in parallel and unattended on the SGI platforms. A set of UNIX scripts generated and controlled the execution of each job, monitored the number of jobs waiting on the machines, and submitted 40 jobs for execution whenever fewer than 10 jobs were in the queue. This configuration generated over 3 GB of data and took about 4 months to complete.

5. DATA ANALYSIS

The Xpatch data were converted into the data format of the ARL-APG radar measurement system (raw) data. The ARL-APG radar analysis software is used to process the Xpatch data, allowing for a direct comparison between measurement and computed results. The ARL software provides a standard set of statistical tools to characterize the data. It also incorporates a standard format for all RCS polar plots, allowing the ZSU computed data to be directly compared against data from other vehicles measured at the APG facility. The Xpatch data were also plotted directly with the MATLAB™ processing and visualization package as an additional check on the data conversion exercise.

Preliminary data analysis involved visual comparisons of RCS values versus azimuth angle for predictions and measurements. The first point noticed was that the computed data for transmit vertical/receive vertical (VV) and transmit horizontal/receive horizontal (HH) copolarizations were nearly identical for all cases. This was also the case for the computed cross-polarization field components VH and HV. The all-metal representation for the problem is one factor in this data redundancy, since for metal, the reflection coefficient is negative unity for both field polarizations. A comparison of measured data with computed data (using the metal ground-plane configuration) revealed that the ZSU vehicle data were too large in value (in some instances more than 10 dBsm larger than the measured values), and that the RCS plots were visually different. The representation of the ground as a metal conductor was responsible for the discrepancy. However, for the high frequencies involved in this work, the radar measurement data include a unique ground effect (Brewster effect) that occurs for a unique elevation angle and vertically polarized incident radiation. Under these conditions, the reflected wave from the ground onto the target is extremely small (almost vanishing for a unique incidence angle). The implication for the ZSU vehicle analysis is that for a 12° elevation angle with vertically transmitted polarization, the ZSU vehicle data without a ground plane should be used for comparison with the measurement data. This comparison produces a close overlay of the mean values of the RCS data. RCS plots and ISAR videos comparing predicted data with measurement have been generated.

6. CONCLUSIONS

The NATO work has indicated that prediction of RCS of combat ground vehicles at K_a-band is possible with current DoD resources. Xpatch software, designed to work efficiently at X-band, can be extended to K_a-band by limiting ray-tracing accuracy (minimum acceptable) to decrease the required computational time. An accurate earth ground model and high-fidelity vehicle model are also needed. The goal of the modeling work is to compare RCS and ISAR image predictions with ARL radar measurement data at W-band (a factor of three in frequency above K_a-band), a frequency used in munition radar sensors. The nonballistic protection requirements for FCS will include radar signature management involving frequencies in this region of the EM spectrum. Both the ground representation and the high-fidelity vehicle model appear to be adequate for W-band predictions. If the present version of Xpatch is applied at W-band, ARL expects that the predicted data would be in agreement with measurement. However, the computational requirements would be enormous, requiring several million CPU hours to reproduce one case of the radar measurement data on the present generation of HPC machines. A new, faster version of Xpatch, developed under the DoD Common High-Performance Computing Software Support Initiative (CHSSI), will be available this year. In addition, the new generation of HPC machines is continuing to provide greater numbers of processors that are faster than the previous generation. Radar signature prediction for FCS is achievable, but it will consume huge amounts of computational resources.

OBJECTIVE FORCE COMMAND AND CONTROL: COURSE OF ACTION ANALYSIS

Dr. Barry Bodt, Ms. Joan Forester, Mr. Charles Hansen
Mr. Eric Heilman, Mr. Richard Kaste, Ms. Janet O'May
U.S. Army Research Laboratory
Aberdeen Proving Ground, MD 21005

ABSTRACT

Objective Force military organizations will require improved command and control assets able to expediently augment staff planning procedures. The Course of Action (COA) Technology Integration project proposes a three-phase process that will result in improved planning aids. One aspect of the project is analysis of automated COA generation through use of high fidelity combat simulations. Phase I, the subject of this report, began in late 1999 and has progressed through two experiments with more to follow. These experiments are facilitating the development of improved automated COA aids for the Objective Force.

1. INTRODUCTION

Objective Force commanders will be faced with an unprecedented heavy flow of battlefield information. Technologically advanced sensors and communications will provide information concerning threat composition, capability, and disposition. Sophisticated software agents will augment the battle staff, easing the load of identifying significant trends. The nature of a battlefield can change without warning, however, making threat data perishable.

The Battlespace Decision Support Team's goal is to develop technology to assist commanders and their staffs in the expedient production of combat mission plans. Our research is establishing a modular evaluation testbed for Army Course Of Action (COA) Analysis (COAA), aimed at understanding the value of automated COA generation. Emphasis is placed on identifying COA feasibility assessment techniques using a wargaming mechanism. This report covers work done in Phase I of our three-phase project.

2. METHODOLOGY

Our Phase I baseline experimental methodology defines preliminary data collection. Data evaluation capability consists of two software components and three manual processes. Software components include a COA generation program called Fox-Genetic Algorithm (hereafter referred to as Fox) and Modular Semi-Automated Forces (ModSAF), a widely accepted high fidelity combat simulation. Manual processes include Fox COA translation techniques resulting in ModSAF scenarios, data collection, and statistical analysis. Our focus is on understanding the challenges inherent in extending and automating baseline COAA processes.

We use statistical experimental design as a guideline for the collection of data that enable subsequent COA evaluation. Data collection is tailored to support regression and sensitivity analyses to ensure sound conclusions.

2.1 Four-Step Experimental Process

The first step of the Phase I process is the creation of COAs using Fox. Developed by the University of Illinois Urbana-Champaign under the auspices of the U.S. Army Research Laboratory's (ARL) Federated Laboratory, and based on genetic algorithm technology, Fox rapidly generates coarse grained COAs for military planners. A combat simulation within Fox quickly evaluates a large number of COAs and returns those with the highest apparent potential for success. Resulting Fox COAs describe brigade battle postures from the perspective of two sides, friendly and enemy. Data are collected through application of the Fox combat simulation to generated COAs.

The second step is to translate Fox COAs into ModSAF scenarios. Applying military science to analyze the composition of Fox COAs is the key to our ModSAF scenario translation. A detailed force structure is formed from the aggregated military unit representations used within Fox. The resultant ModSAF scenarios accurately capture the COA representation of battlefield shape and interactions.

The third step is scenario execution within ModSAF. Combat in ModSAF is governed by robust behavior mechanisms (involving factors of terrain, maneuver, and engagement) and is represented at

the vehicle and soldier level. Since ModSAF closely approximates actual combat, ModSAF data form a reasonable foundation for detailed COA evaluation. Data collection consists of examining vehicle condition and location relative to stated COA objective areas.

The fourth step, statistical analysis, is the focus of Phase I experimentation. Our data collection regimen is based on two traditional metrics of mission success: ground occupation and force loss. Since both Fox and ModSAF report these metrics, a matrix of military unit position and status forms the basis for data analysis. Preliminary statistical analysis of collected data compares results between Fox and ModSAF.

3. EXPERIMENTATION

A pilot test preceded this study, to demonstrate the mapping of a Fox COA into a ModSAF scenario. This test provided data for a limited comparison of Fox and ModSAF. Our comparison revealed that a predicted victory in Fox was also a decided victory in ModSAF. We could not rule out consistency between Fox and ModSAF, but difficulties with interpretation due to a pseudo- stochastic element and problems with the Fox code precluded us from making strong assertions. Lessons learned were applied to our follow-on study.

The experimentation described in this paper has three goals: (1) explore the utility of selected user-interface controls within Fox, (2) explore the variability inherent in repeated runs of ModSAF, and (3) compare the results from Fox with battle outcomes from ModSAF. We address these goals in turn, describing the experimental strategy and interpretation of results for each.

We used a three-factor crossed design with a fourth factor completely nested to address our first goal, examination of Fox user-interface controls. Three user controls were evaluated: planning time, friendly force strength, and enemy force strength. The fourth factor addressed possible variation among Fox-produced friendly COAs (FCOA) when using the same scenario. We used a bivariate response measure, taking into account ground objectives and friendly force attrition, to evaluate using a multivariate analysis of variance procedure. Multivariate analysis suggests initial strengths have a great effect on FCOA generation and subsequent performance, planning time has no such effect, and similar FCOAs do not perform comparably. This final result draws into question a utility advanced by the developers of Fox, that of providing a varied set of comparable FCOAs for further development.

Our second goal was to better understand the variability inherent in ModSAF. Two distinct cases were repeated 12 times each. No other factors were varied. The two FCOAs came from the FoxGA experiment described above. The variability of ModSAF is best expressed in terms of the kill ratio that the enemy force exhibits. Unlike in FoxGA, where some enemy forces almost always remain, the 5:1 force ratio in ModSAF guaranteed all enemy forces would be killed. Thus, instead of exploring variability in terms of the loss exchange ratio, we examined the question, "What is the variability of the enemy kill ratio?" The raw data for the first scenario showed a kill ratio ranging from a minimum of 0.44:1 to a maximum of 1.27:1. Equivalently, friendly force losses ranged between 10% and 29%, respectively, to defeat the enemy forces. In the second scenario, the kill ratio ranged from 0.25:1 to 0.89:1. Friendly force losses ranged between 6% and 20%, respectively. We understand ModSAF is stochastic and a distribution of outcomes will result from the play of the wargame. However, commanders may gain little COA evaluative value from so great a difference as 10% to 29% losses.

Our third goal was to compare Fox and ModSAF results. Twelve ModSAF runs supported a prediction interval for a next Fox observation. If Fox is providing similar information to ModSAF, the response measure resulting from Fox could reasonably be expected to fall within the ModSAF prediction interval. Our two chosen Fox cases did not agree with ModSAF.

4. CONCLUSION

One of the founding principles for the U. S. Army Objective Force is improved Command, Control, Communications, Computers, Reconnaissance, Surveillance, and Intelligence. Commanders and their staffs will require maneuver support with enhanced automated decision aid tools to achieve dynamic integrated development and resolution of operational COAs. Our efforts reported here begin to address these needs through the rigorous examination of a COA generator and use of a combat simulation evaluation suite. Further experimentation will enhance the speed of COA generation tool development by quickly feeding back to the developer discoveries made during our experimentation. As our research progresses, we will develop new criteria for COAA to fit Objective Force battlefield performance.

METHODOLOGY FOR NONLINEAR ANALYSIS OF THICK-SECTION COMPOSITES

Travis A. Bogetti*, Christopher P.R. Hoppel, and Bryan A. Cheeseman
U.S. Army Research Laboratory
AMSRL-WM-MB, Aberdeen Proving Ground, MD 21005-5066

ABSTRACT

The accurate design and failure analysis of thick-section composite structures is critical to the successful implementation of these materials into advanced Army systems. In structures such as sabots for kinetic energy projectiles and composite armor for vehicle and personnel protection, the U.S. Army is an established world-leader in thick-section composites. To design for these critical needs, the Army has developed a unique analysis methodology for thick-section composite materials. This methodology is being utilized within both the Army and industry for composite design and analysis and was recently recognized in an international composite failure assessment exercise. This paper describes the implementation of this theory and sites examples of its widespread utility in thick-section composite structural applications.

1. INTRODUCTION

The stress analyses of structural components of complex geometry and mechanical loading are generally conducted within the framework of some type of numerical modeling technique, such as the finite element method. The accuracy of these stress and strain predictions are critical since they are often the basis upon which important design decisions are made. However, laminated composite structures are inherently more difficult to analyze than traditional isotropic materials. Since failure predictions of laminated composite structures are based on the state of stress and strain within the constituent lamina or plies, it is necessary to accurately compute the layer to layer stress and strain states throughout the laminated composite structure. To circumvent the difficulties associated with the detailed ply-by-ply analysis, a "smearing-unsmearing" approach is often employed (see Fig. 1).

The practical application of the "smearing-unsmearing" approach to realistic structures of general geometric shape and loading complexity can be very effectively performed in the context of some type of finite element analysis framework. To accomplish this, the analysis methodology outlined in Fig. 1 is systematically applied to each element within the finite element model *at every* load increment throughout the entire incremental loading history. This procedure involves the coupling (or integration) of various analytic laminate models within the finite element analysis algorithm.

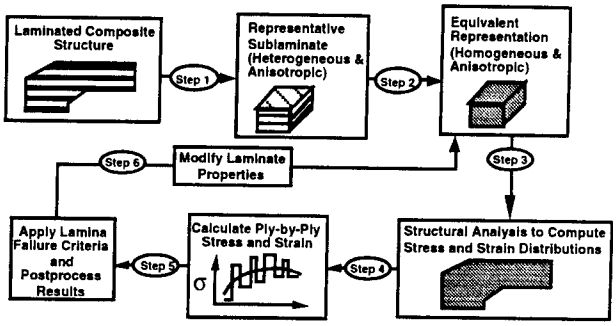


Fig. 1 Analysis methodology

The Army Research Laboratory (ARL) first implemented into a software code the "smearing-unsmearing" methodology in a *patented* design and failure analysis capability for thick-section composite structures nearly ten years ago (Burns and Bogetti, 1995). This first generation code, LAMPAT, was based on linear elastic material behavior and was found to be extremely useful in the establishment of advanced architectural designs for composite sabot applications (Bogetti et al., 1996). The software was also used to assist in the design of thick-section composite panels for mine blast protection (Condon et al., 1995). Over the past ten years, several significant enhancements to the LAMPAT code have been made. Namely, the addition of ply level material nonlinearity and degradation have been included. These enhancements proved to be extremely important in the design and analysis of thick-section composite cylinders for deep submergence vehicles that are of particular importance in naval applications (Olson et al., 1995).

More recently, the LAMPAT code is being adapted for the design and analyses of composite armors for vehicles and personnel protection. Composite integral armor (CIA) for vehicle protection often employs thick-section composite laminates as backing for ceramics and other materials to stop medium to light caliber threats (Fink, 2000). LAMPAT is highly suited for this application and offers a tremendous opportunity for the development of advanced integrated armor configurations through the efficient design of composites. The same opportunity exists for developing advanced integral armor configurations in personnel

protection. To analyze the ballistic response of these structures, LAMPAT has recently been integrated into the commercially available LS-DYNA code (Hallquist, 1999). Having the ability to model thick section composites undergoing a high rate ballistic loading is particularly exciting since composites are considered key materials in the realization of future lightweight armor systems.

In addition to efforts which have focused on integrating the LAMPAT code into various finite element packages, progress related to specific aspects of the laminate models implemented within LAMPAT has also been made. The specific laminated media analysis and composite failure methodology used within LAMPAT has been recognized by the composites community as a unique approach in which to predict the response and failure of composite laminates to mechanical load. Some of the authors were recently invited to formally submitted this approach in the internationally recognized World Wide Failure Olympic exercise, to be published as a special issue of *Composites Science and Technology* (Hinton and Soden, 1998). In this two part exercise, failure predictions of fourteen different composite laminates under various multi-axis loading situations are first compared with other invited participants' predictions and then collectively compared with actual experimental data (Bogetti et al., 1999). Participation in this exercise not only helps to build confidence in our approach, but also provides a direct validation of the methodology against real world experimental data.

2. IMPLEMENTATION INTO FINITE ELEMENT ANALYSES

The laminated media analysis can be used directly to predict the effective response and failure of thick-section composite laminates under idealized three-dimensional loading situations. By coupling sophisticated laminate analysis to traditional finite element analysis techniques, thick-section composite structures for future Army systems can be accurately and efficiently analyzed and designed. In this context, the integration follows directly from the treatment of each element within the finite element model as though it were laminate. The procedure follows that the effective properties or stiffnesses of every element within the finite element model be updated at each load increment during the incremenetal loading history of the structure.

A linear (quasi-static) version of this methodology has been utilized and found extremely successful in numerous case studies as described in the INTRODUCTION section of this summary. Implementation of the linear version of this methodology has been done primarily with the finite element software package ANSYS (1994). To date, the enhanced nonlinear capability has been implemented into the finite element codes ABAQUS (1997), LS-DYNA (Hallquist, 1999), and ANSYS (1998) (in progress).

3. CONCLUSIONS

It is clear that composites offer some of the best opportunities to make our forces lighter and more lethal. Accurate and efficient design capabilities for composites will facilitate this goal. The methodology described in this paper for analyzing thick-section composite structures provides an extremely powerful and unique computational design tool. Various aspects of this methodology have been well demonstrated and the recent enhancements into high strain rate applications offers tremendous opportunities for materials exploitation in the design of state-of-the-art armor and munitions to meet the Army's current and future needs.

In our paper we detail significant aspects of the laminated media analysis used within LAMPAT. We also describe the integration of this theory into the smearing-unsmearing methodology and discuss its implementation in predicting the nonlinear material response and failure of thick-section composite structures.

REFERENCES

ABAQUS User Manual, HKS, Rhode Island, 1997.

ANSYS User Manual, ANSYS Inc., Canonsburg PA, 1994.

ANSYS UIDL Programmer's Guide, ANSYS Inc., Canonsburg PA, 1998.

Bogetti, T.A., et al., "Development of Advanced Lightweight Composite Sabots for Kinetic Energy Projectiles," Army Research Laboratory Technical Report, Aberdeen Proving Ground, MD, ARL-TR-961, February 1996, (report classified SECRET).

Bogetti, T.A., et al., "Predicting the Nonlinear Response and Progressive Failure of Composite Laminates," (submitted to *Compos. Sci. Technol*), August 1999.

Burns, B.P. and Bogetti, T.A., "Method for Assessing the Effects of Loading Forces on a Composite Material Structure," U.S. Patent issued May 1995.

Condon, J.A., Bogetti, T.A. and Hoppel, C.P.R., "Failure Assessment of Thick Composite Sandwich Coupons in 3- and 4- Point Bending," Army Research Laboratory Technical, ARL-TR-797, July 1995.

Fink, B.K., "Performance Metrics for Composite Integral Armor", *Journal of Thermoplastic Composite Materials*, Vol 13, pp. 417-431, September 2000.

Olson, B.D., et al., "Effects and Non-Destructive Evaluation of Defects in Thermoplastic Compression-Loaded Composite Cylinders," *Journal of Thermoplastic Composite Materials*, Vol. 8, No. 1, pp. 109–136, January 1995.

Hallquist, J., LS-DYNA User Manual, LSTC, Livermore CA, 1999.

Hinton, M. J. and P. D. Soden. "Predicting Failure in Composite Laminates: Background to the Exercise." *Compos. Sci. Technol.*, 1998, 58(7), 1001.

VIRTUAL MODELING AND SIMULATION OF MILITARY GROUND VEHICLES

Michael D. Letherwood and David D. Gunter*
US Army Tank-automotive and Armaments Command
Tank Automotive Research, Development & Engineering Center (TARDEC)
Warren, MI 48397-5000

SUMMARY

In support of Department of Defense (DOD) mandated acquisition reform initiatives to reduce vehicle related life cycle costs and timelines, the Tank-automotive and Armaments Research, Development and Engineering Center (TARDEC) is using simulation-based acquisition strategies to investigate the dynamic performance of wheeled and tracked ground vehicles throughout the vehicle development, testing, and fielding life cycle process. The paper will describe how modeling and simulation (M&S) is applied to answer a wide variety of design and performance evaluation questions and will depict a series of simulation-based engineering projects that build on the Army's simulation investments as a tool to investigate and answer real-world vehicle design, acquisition, and engineering support questions.

TARDEC is effectively using M&S to evaluate new designs prior to selection and testing, support operational and developmental testing, evaluate field mishaps and/or accident situations, investigate configuration management changes, product improvement programs, and alternative payloads. The objective of this paper will be to describe the virtual prototyping process and discuss how M&S technologies are being applied to a broad spectrum of prototyping, design, and performance evaluation problems by investigating specific case study examples throughout the life cycle of various types of ground wheeled and tracked vehicle systems. State of the art high performance computing (HPC) facilities are allowing the integration of virtual prototyping and dynamic modeling expertise into a complete wheeled and tracked vehicle system simulation capability. Virtual prototyping technologies are routinely used to provide M&S support to DOD, industry, and academia in order to evaluate the stability, handling, and ride quality performance of virtually all types of wheeled and tracked vehicle systems. Consequently, efforts by Army engineers to develop, validate, and simulate high-resolution, computer-based models of wheeled and tracked military vehicles in order to investigate and quantify a system's dynamic performance will be emphasized. Due to much increased HPC computational speeds, memory, and asset availability, entire spectra of operational mission scenarios are investigated and simulations conducted over a wide range of vehicle speeds and operating conditions. Recent major upgrades in HPC facilities now allow the highly detailed, computationally intensive models to be run in a fraction of the time, and, more importantly, many more 'what if' studies are being performed.

The major performance areas which are impacted most by high resolution vehicle simulations are mobility, stability, reliability and safety. Ground vehicles operate in very harsh environments and are expected to perform their intended missions. Vehicle developers are responsible for setting realistic performance specifications and ensuring that they are met. M&S is making the Army a smarter and more cost-effective buyer and tester of vehicles and equipment, and more importantly, significantly reducing the associated risks to personnel and property that are inherent in a war-fighting environment. In addition, M&S can alleviate and/or avoid the endless build-test-break-fix cycles, common in many vehicle acquisition and testing programs of the past, thereby reducing costs and shortening milestone schedules. Although its difficult to quantify overall life cycle impacts resulting from doing it right the first time, M&S has proven itself to be an excellent tool for decision makers, in response to limited time and budget constraints, as well as, aggressive procurement schedules.

THIS PAGE INTENTIONALLY LEFT BLANK

Simulation with Learning Agents

Michelle Kalphat, Robert Sottilare
U.S. Army Simulation and Training Command
Orlando, FL 32816

Erol Gelenbe, Esin Şeref, and Zhiguang Xu
School of EECS
University of Central Florida
Orlando, FL 32816

Abstract— **We propose that simulation environments be designed to incorporate intelligent agents whose behavior adapts to specific circumstances and events during the simulation run. These learning agents would select tasks to be accomplished among a given set of tasks as the simulation progresses, or they may synthesize tasks for themselves based on their observations of the environment and using information they may receive from other agents. We investigate a goal-oriented approach in which agents are assigned goals when the simulation starts, and then pursue these goals autonomously and adaptively. During the simulation, agents progressively improve their ability to accomplish their goals effectively and safely. Agents learn from their own observations, and from the experience of other agents with whom they exchange information. Each learning agent starts with a given representation of the simulation environment from which it then progressively constructs its own internal representation and uses it to make decisions. This paper shows how learning techniques can support this type of intelligent behavior of learning agents in a simulation environment. An example application is described in which agents represent manned vehicles; they are assigned the goal of traversing a dangerous metropolitan grid safely and rapidly.**

I. Introduction

Typically in a discrete event simulation the time and nature of future events is computed in a pre-determined fashion from the list of past events which have occured. Additional variables driven by random number generators can be used to create an element of apparent unpredictability. The alternative we propose, is that a discrete event simulation should contain a certain number of learning agents. These learning agents store experience during a simulation, and modify their behavior during that same simulation or during distinct simulation runs. Thus the agent's response to identical external conditions (i.e. the event list) will change over time, both within the same simulation run or in distinct runs. This conventional approach to simulation design has the advantage of providing the designer with full control over events. However it also has some major disadvantages. For instance, the behavior of living "agents" or of agents which are controlled by human beings (e.g. manned vehicles) does not just obey physical laws. Human beings will reach a variety of decisions which are not totally dictated by current physical circumstances, and changes in human behavior can occur under the effect of observation, experience and learning, stress, fear and many other factors [4]. Thus it would be very useful to introduce agents in a simulation whose behavior is determined by specific circumstances and through adaptive behavior. There is another advantage to being able to avoid having to completely pre-specify a simulation: this relates to the economy of producing simulation software. For instance if we could introduce exactly the same code in many of the active entities of a simulation (simply by replicating the code), and then provide each distinct entity just with a goal or objective which could be specified in a compact form but which might vary from entity to entity, one would be able to save programming time and also reduce the number of programming errors.

In the approach we propose, each learning agent starts with a representation of the simulation environment. From this information it then progressively constructs its own internal representation or Cognitive Map (CM) and uses it to make decisions. these decisions are implemented as conventional asynchronous or synchronous transitions in the discrete event simulation. Each learning agent progressively refines its own model of the simulation environment as the simulation progresses, and it uses adaptation to make decisions. In the most extreme case, a learning agent might build an internal "private" representation of the state of the complete simulation as it pertains to its own needs. Each agent is assigned a Goal before simulation begins, and the learning agent uses the goal to determine its course of action each time it has to make a decision. Goals can be modified by other agents, or can also be modified by the agent itself, based on its own experience. Learning agents can also be hierarchically structured so that a group of agents share the same goals, use similar sets of rules, and make use of each other's experience. If we are considering a set of LAs simulating entities which have to obey hierarchical orders, some of these LA will simulate the leaders and they will assign or modify the goals of the LAs who paper to them. For instance suppose we consider LAs which simulate a tank which is part of a tank platoon.

A very simple approach to adaptation is to change one's course of action so as to respond to information resulting from the the most recently available observations or data. A slightly more sophisticated approach would be to integrate this past information over a certain time frame. Thus a LA which simulates a vehicle which is on its way from point A to point B, and whose essential goal is not to become a casualty (i.e. not to be destroyed) would simply head back if it encountered danger. If the goal is a weighted combination of the delay (or time to get to the destination) and of the probability of being destroyed, then the decision would be to head back or to persevere toward the objective, depending on a more refined estimate by the agent. Thus, as goals become more complex, simple reactions to external information are not sufficient for decision making, and more sophisticated techniques for integrating external observations and information are needed. An individual LA may find

it necessary to integrate the cumulated experience of hundreds or of thousands of other LAs which may have encountered similar situations. In this section we discuss the learning paradigms that we propose for the LAs. These paradigms allow the LAs to integrate observations and the experience of other agents.

The simplest decision paradigm we will consider is the case where the LA makes the decision which is most advantageous (lowest cost or highest reward) based on the instantaneous expected value of this metric. We will call this approach the *Bang-Bang Algorithm*. This approach has the advantage of being simple and explicit. Its disadvantage is that it does not allow us to easily integrate the values of the cost and of the reward as it is perceived or integrated by other agents over time. In order to take into account a greater wealth of information, we will also investigate two other learning paradigms for the agents:

- *Learning feedforward random neural networks (LF RNN)* [2], [6]. These networks update their internal representation (the weights) using a gradient based algorithm to improve either their predictive capabilities, or to improve their ability to reach decisions which elicit the maximum reward. The LF RNN is used as a learning tool and then as an "oracle". When a decision needs to be taken, the network is presented with the external data and is used to produce a prediction of the cost or reward of different outcomes. The outcome offering the lowest cost or the highest reward is then selected.
- *Random neural networks with reinforcement learning (RNN RL)* [2], [9]. In this case a network is used both for storing the CM and making decisions. The weights of the network are updated so that decisions are reinforced or weakened depending on whether they have been observed to contribute to increasing or decreasing the accomplishment of the declared goal. After an update has been effected, the network explicitly recommends the outcome which appears to it to be the most beneficial.

II. Simulating Traffic in a Dangerous Urban Grid

In order to study the impact of adaptation on the behavior of the agents, we wrote a simulation program in which LAs travel through a dangerous urban grid. The purpose of the simulation experiments was to examine how the adaptive algorithms which we have described will affect the performance of the learning agents. Both a very simple decision algorithm (the Bang-Bang algorithm described below), and the more sophisticated neural network algorithms using learning, were tested. A single simulation program was written, and four simulations were run separately under identical input conditions. One simulation was run with no adaptation at all. Each of the remaining three simulations were run with the learning agents using three different paradigms for adaptation. The system being simulatated is an urban grid: it is composed of streets and intersections. In this particular simulation there are ten streets running vertically from North to South and vice-versa, and ten streets running East to West and vice-versa. This leads to an urban grid with 100 intersections. Each section of street between two intersections is of the same constant length for each street section, and we assume that vehicles proceed at *constant average speed* between any two consecutive intersections. Time is normalized so that *average unit time* is the time it takes a vehicle (agent) to travel between two consecutive intersections (either horizontally or vertically). Streets are "two-way" but there is only one lane in each direction. Thus vehicles can only proceed in a single queue in each direction. We have simplified things so that street sections are long enough to contain all vehicles which have entered them: there is never any blockage back from a street into an intersection.

Agents (vehicles) are allowed to enter and leave the simulation "vertically" either from the top ten intersections or the bottom ten intersections. Thus any vehicle will enter from one of the top or bottom ten intersections, and will leave from an intersection at the bottom or top. Each vehicle entering from an intersection (top or bottom) will be assigned a fixed exit intersection at the opposite end (bottom or top) which it will try to reach. The destination is selected by drawning it at random with equal probability among all possible 10 destinations. At any intersection, a vehicle can either go Forward through the intersection (i.e. continue in the same direction as it came) or go Left or Right. It may also Wait, but it cannot go back the way it arrived. The only exception is at intersections on the East or West edge of the grid: at the East edge, vehicles cannot go East and cannot go back, while at the West edge they cannot go West and cannot go back.

The simulation represents a "dangerous" urban grid by introducing a probability of vehicle destruction. Destruction of a vehicle occurs at random only at intersections (the street's themselves are "safe"). We also make the simplifying assumption that a vehicle which is destroyed does not block other vehicles. At each intersection (i, j), there is a probability $p(i, j)$ that a vehicle crossing that intersection is destroyed. Some intersections will be relatively safe with a small value of this probability, while others may have a high value and be very unsafe. Vehicle destruction was simulated by selecting a small fixed probability of destruction throughout all but a few specific intersections; at those selected few there is a high probability of vehicle (agent) destruction.

References

[1] R.S. Sutton "Learning to predict the methods of temporal difference", *Machine Learning*, Vol. 3, pp. 9-44, 1988.

[2] E. Gelenbe (1993) "Learning in the recurrent random neural network", *Neural Computation*, Vol. 5, No. 1, pp. 154-164, 1993.

[3] P. Mars, J.R. Chen, and R. Nambiar, *Learning Algorithms: Theory and Applications in Signal Processing, Control and Communications* , CRC Press, Boca Raton, 1996.

[4] R.W. Pew and A.S. Mavor (Editors) "Representing Human Behavior in Military Situations: Interim Report", National Academy Press, Washington, D.C., 1997.

[5] Proceedings of the 7th Conference on Computer Generated Forces and Behavioral Representation, 1998.

[6] E. Gelenbe, Zhi-Hong Mao, Y. Da-Li (1999) "Function approximation with spiked random networks" *IEEE Trans. on Neural Networks*, Vol. 10, No. 1, pp. 3–9, 1999.

[7] E. Gelenbe "Modelling CGF with learning stochastic finite-state machines", Paper 096, *Proc. 8th Conference on Computer Generated Forces and Behavioral Representation*, pp. 113-115, Orlando, May 11-13, 1999.

[8] W. Foss, E. Gelenbe, P. Franceschini, M. Petty "Integrating reinforcement learning into Computer Generated Forces", Technical Report, School of Computer Science and Institute for Simulation and Training, University of Central Florida, Orlando, September 1999.

[9] U. Halici, *Reinforcement learning with internal expectation for the random neural network* European Journal of Operations Research (in press).

ZNSFLOW COMPUTATIONAL FLUID DYNAMICS SOFTWARE FOR HIGH PERFORMANCE COMPUTERS

H. L. Edge, J. Sahu, W. Sturek, J. Clarke, D. Pressel,
M. Behr, K. Heavey, P. Weinacht, C. Zoltani, C. Nietubicz

U.S. Army Research Laboratory
Aberdeen Proving Ground, MD 21005-5066

The thrust of the work described here is to further develop an existing computational fluid dynamics (CFD) code and make it more accessible for engineers. The code was developed as part of the Department of Defense (DoD) High Performance Computing Modernization Office sponsored common high performance computing software support initiative (CHSSI). It is now called ZNSFLOW, which stands for zonal Navier-Stokes flow solver. ZNSFLOW is actually a suite of codes that basically includes a zonal Navier-Stokes solver and graphical user interface (GUI) environment for problem setup, interactive visualization, and solver execution. The primary goals of the ZNSFLOW CHSSI project are to 1) develop a scalable version of a zonal Navier-Stokes solver, 2) add features to the ZNSFLOW software which allow general applicability and ease of use, and 3) demonstrate the design utility of the scalable ZNSFLOW software by solving current DoD priority viscous flow problems. In keeping with these goals, a broad overview is given of the ZNSFLOW CHSSI project, the ZNSFLOW solver and its capabilities, as well as the GUI environment. Some results from recent applications will be presented to demonstrate the capabilities of ZNSFLOW.

The ZNSFLOW software has been targeted to operate on both shared memory and distributed memory architectures. To fulfill the CHSSI program requirement that the ZNSFLOW solver be scalable on applicable computers, it was decided to create two versions of the ZNSFLOW solver with one version optimized to operate on shared memory architectures and the other to operate on distributed memory architectures. Both versions of the ZNSFLOW solver apply the same unsteady Reynolds-averaged thin-layer Navier-Stokes equations to compute flow field solutions with no changes in the time-tested solution algorithm. The shared memory version of the solver employs loop-level parallelism that has highly optimized cache management. The distributed memory solver uses the shared memory (SHMEM) library for the Cray T3E and Origin 2000 computers and the message passing interface (MPI) library for other computers where distributed memory programming is desirable, such as the IBM SP. Either current library can be chosen with conditional compiler switches.

As stated earlier, ZNSFLOW is a suite of codes. Part of that suite is the distributed interactive computing environment (DICE). At present, only the shared memory solver has been fully integrated into DICE. DICE provides a GUI that allows a user to create an input file for the ZNSFLOW solver. The DICE GUI is pictured in Figure 1. DICE can also be used to execute the ZNSFLOW solver once the input file has been created. In addition, once the solver is executing, DICE can provide real-time visualization of the flow field as it is being computed. Even if the execution of the solver were initiated from a previous day, DICE would allow the user to connect to the application on a remote computer and visually monitor its progress on a local workstation. DICE provides a number of options for visualizing data. The user can choose surface contours, isosurfaces, x-y plots, or spreadsheets to display the data.

A large portion of the effort spent on the ZNSFLOW CHSSI project went toward increasing ease of use and the general applicability of the ZNSFLOW solver. The DICE GUI allows some of the ZNSFLOW solver's more complex features to be easily employed. For example, the solver allows for one-to-one overlaps between grid zones in any direction. The GUI makes the setup for this generalized data exchange intuitive, and it also provides some simple error-checking capabilities to catch mistakes in creating the input file. Many of the boundary conditions are generalized and can be called for any surface or line. In addition, the solver can perform computations with the chimera composite grid discretization technique. By using the chimera technique, the grid topology and generation for very complex systems can be greatly simplified. One of the disadvantages in using the chimera technique has been the increased complexity and corresponding confusion in applying a turbulence model. A chimera model can be composed of multiple zones, with each zone possibly having a unique grid topology. Most turbulence models have specific directional, orientation, or distance-related

requirements for correct application. For a complex chimera model, applying a turbulence model can be a very complex process. This problem has been addressed in ZNSFLOW by installing a pointwise turbulence model that is not orientation specific. This greatly simplifies the setup of the turbulence model. Wall location information is supplied when the wall boundary conditions are set by the user through the GUI. Currently, there are three available turbulence models: a Baldwin-Lomax model, a one-equation pointwise turbulence model, and two-equation pointwise turbulence model.

Demonstration cases were chosen to show capabilities of the ZNSFLOW software. Both of the demonstration problems require viscous Navier-Stokes CFD modeling for accurate flow field solutions. Two demonstration cases were run on a Silicon Graphics Origin 2000 computer. The first of the two cases to be discussed is the guided multiple launch rocket system (MLRS) missile. The guided MLRS computational model is built to answer questions about the use of canards to perform controlled maneuvers for a missile with wraparound tail fins. The computations will hopefully provide insight into the interaction of the canard wake with the downstream wraparound tail fins. A large computational model, exceeding 20 million grid points, was made for flow field computations of the missile at angle of attack. The computations demonstrated the ability of ZNSFLOW software to handle large data sets. Figure 2 shows a ZNSFLOW computed solution of the guided MLRS missile at a 0° angle of attack.

A second demonstration case shows the capability of ZNSFLOW to model complex multibody systems. Computational models were built for computing the flow field about ten brilliant antitank (BAT) submunitions being ejected from an Army tactical missile (ATACM). The complexity and uniqueness of this type of multibody problem results from the aerodynamic interference of the individual components, which include three-dimensional shock-shock interactions, shock-boundary layer interactions, and highly viscous-dominated separated flow regions. The chimera overset grid technique, which is ideally suited to this problem, involves generating numerical grids about each body component and then oversetting them onto a base grid to form the complete model. The chimera technique allows for different submunition positions to be modeled, with only simple grid modifications necessary. Figure 3 is a flow field computed by ZNSFLOW for ten BATs dispensing from an ATACM.

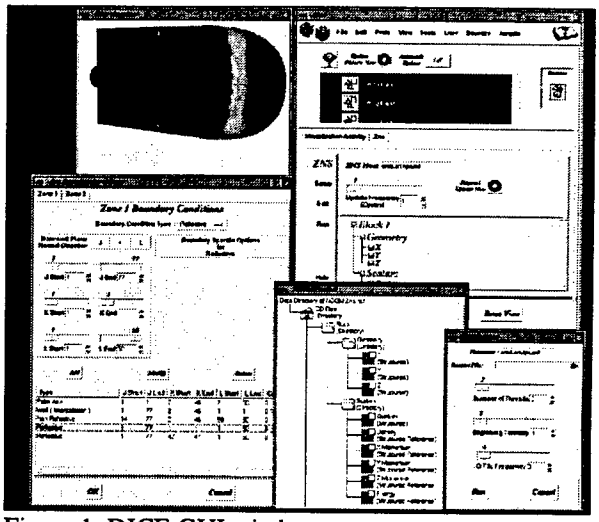


Figure 1. DICE GUI windows.

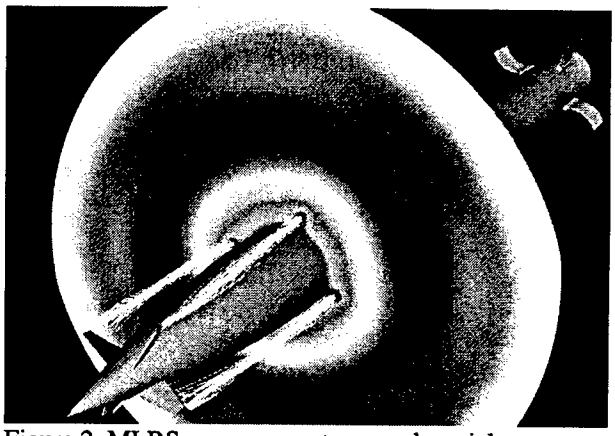


Figure 2. MLRS pressure contours and particle traces.

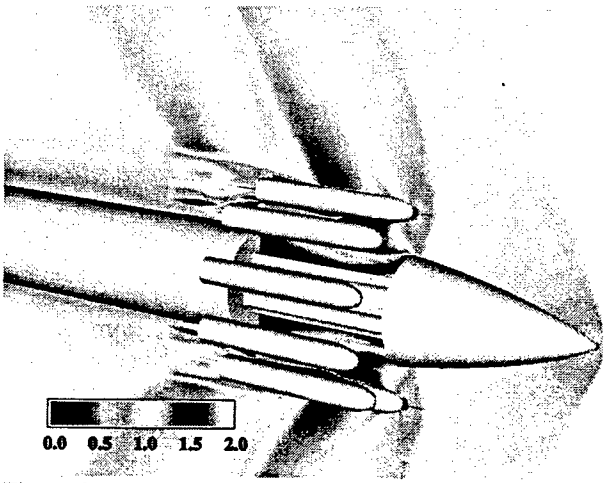


Figure 3. Mach contours of BAT dispensation.

USE OF COMMODITY BASED CLUSTER FOR SOLVING CFD AEROPROPULSION APPLICATIONS

Isaac Lopez*
US ARL, Vehicle Technology Center
Cleveland, OH 44135

Thaddeus J. Kollar
Integral System , Inc.,
Cleveland, OH 44135

Richard A. Mulac
AP Solutions, Inc.
Cleveland, OH 44135

ABSTRACT

U.S. Army Research Laboratory (USARL) and National Aeronautics and Space Administration (NASA) researchers at the Glenn Research Center have acquired a commodity cluster, based on Intel® (CA, USA) processors, to compare its performance with traditional UNIX cluster in the execution of aeropropulsion applications. Since the cost differential of the clusters is significant, a cost/performance ratio is calculated. After executing a propulsion application on both clusters, the researches have demonstrated a 9.4 cost/performance ratio in favor of the Intel® based cluster.

1. INTRODUCTION

The rising cost of developing air-breathing propulsion systems is causing a strong demand for minimizing cost while still meeting the challenging goals for improved product performance, efficiency, emissions and reliability. Computational simulations represent a great opportunity for reducing design and development costs by replacing some of the large scale testing currently required for product development. The army is interest in computational simulations because of the potential for fielding improved land and air propulsion systems with lower development cost, greater fuel efficiency and greater performance and reliability. A greater use of simulations would not only save some of the costs directly associated with testing, but also enable design trade-offs to be studied in detail early in the design process before a commitment to a design is made. A detailed computational simulation of an engine could potentially save up to 50% in development time and cost.

Within NASA's High Performance Computing and Communication (HPCC) program, the NASA Glenn Research Center (GRC) in collaboration with the USARL is developing an environment for the analysis and design of propulsion engines called the Numerical Propulsion System Simulation (NPSS) (Evans, Lytle, Follen and Lopez, 1997). One of the goals for NPSS is to create a "numerical test cell" enabling full engine simulations overnight on cost-effective computing platforms. In order to achieve this goal NASA and ARL personnel at the GRC have been involved since the early 1990s in applying cluster computing technology in solving aeropropulsion applications. In 1993 researchers at the Glenn Research Center successfully demonstrated the use of an IBM 6000 cluster to solve Computational Fluid Dynamic applications. Later on, in a partnership with the US aerospace industry a special project was started to demonstrate that distributed workstation network is a cost-effective, reliable high-performance computing platform. This project demonstrated that cluster computing was indeed a cost effective high-performance computing platform and showed performance and reliability levels equivalent to 1994 Vector Supercomputers at 8% of the capital cost. The next step for ARL/GRC personnel was to apply the experience gained in cluster computing to the emerging commodity hardware for executing aeropropulsion applications.

This paper presents; (1) a detailed description of the commodity based cluster at GRC, (2) a detailed description of a turbomachinery application ported to the cluster, and (3) a cost/performance comparison of the commodity based cluster to a SGI Origin 2000 high performance computer. A brief summary of the three areas follows.

2. COMMODITY BASED CLUSTER – AEROSHARK

USARL/GRC researches utilize the Aeroshark cluster as the primary testbeds for developing NPSS parallel application codes and system software. The Aeroshark cluster provides sixty-four Pentium II 400MHz processors housed in thirty-two nodes. The networking configuration resembles a star, with a gigabit switch connected to eight routers, and each router connecting to four compute nodes, with one full duplex 100BT wire per node. There is one system server providing Network File System

(NFS), Network Information Service, and other management services, and one interactive system through which users gain access to the entire cluster.

Uptime on Aeroshark is in excess of 99%; when the absolute uptimes on all the individual nodes are added together it totals nearly a century. Despite this record, there are a few problems that have been encountered with the configuration. One is that the routers cannot provide the full bandwidth to the compute nodes under a maximal load. This 'star' network configuration was conceived when fast Ethernet switches were still very expensive. Its intention was to allow the incremental addition of ports by inserting another quad port fast Ethernet card into the routers. The cost of this was low compared to a new switch.

The Aeroshark cluster provided standard software parallel tools such MPI, PVM and GNU development packages. In addition, the Portland Group's compilers (F77, F90, HPF, C, C++) were available for better compatibility with other platforms.

3. AEROPROPULSION APPLICATION – APNASA

The Average-Passage flow model (Adamczyk, 1984) describes the three-dimensional, deterministic, time-averaged flow field within a typical blade row passage of a multiple blade row turbomachinery configuration. The equations governing such a flow are referred to as the Average-Passage equation system. For multiple blade row configurations, the model describes the deterministic flow field within a blade passage as governed by the Reynolds-averaged form of the Navier-Stokes equations. Average-Passage NASA (APNASA) code is being developed by a government / industry team for the design and analysis of turbomachinery systems. The code has been used to evaluate new turbomachinery design concepts, from helicopter to large commercial aircraft engines. When integrated into a design system, the code can quickly provide a high fidelity analysis of a turbomachinery component prior to fabrication. This will result in a reduction in the number of test rigs and lower development costs. Either APNASA or the methodology on which it is based has been incorporated into the design systems of six gas turbine manufacturers.

An example application simulated on the cluster Aeroshark using the Average-Passage Code consisted of a single stage fan which was being analyzed to determine noise levels associated with various designs. Compilation of the code itself was very straightforward on the cluster using The Portland Group's Fortran 90 compiler, pgf90.

There is even a compiler option "-byteswapio" which forces the code to perform file reads and writes in the IEEE format compatible with most UNIX platforms. This allowed for easy porting of mesh and restart files between the cluster and various SGI systems.

4. COST/PERFORMANCE COMPARISON

An APNASA simulation consists of running each blade row independently a number of iterations (typically 50) through a Runge-Kutta process until certain convergence criteria are met. This procedure has been termed a "flip". For the single stage fan case (with a mesh size of 407 x 51 x 51 for each blade row), a single "flip" takes approximately 6500 seconds of wall-clock time to run the fan's two blade rows in parallel on a 2 CPU node of the aeroshark cluster. This compares to 2750 seconds of wall-clock time to run the same case on an SGI Origin 2000 system composed of 250 MHz R10000 MIPS processors. This equates to roughly a factor of 2.35 when comparing the processor-to-processor speed of the Intel based aeroshark cluster to the MIPS based Origin system for this application. It takes the same number of iterations for both systems to converge. A cost/performance ratio of 9.5X is obtained when the cost of aeroshark and the SGI Origin is taken into account.

5. CONCLUSION

Clearly the use of commodity based cluster has a tremendous potential of providing a computing platform on which detailed aeropropulsion simulations can be executed in a time compatible with the engine design cycle. In addition the cost/performance ratio shown by the cluster was impressive considering the cost differential between commodity based clusters and traditional UNIX workstation clusters.

REFERENCES

Evans, A. L., Lytle, J. J., Follen, G., and Lopez, I., An Integrated Computing and Interdisciplinary Systems Approach to Aeropropulsion Simulation, ASME IGTI, June 2, 1997, Orlando, FL.

Adamczyk, J.J., "Model Equation for Simulating Flows in Multistage Turbomachinery," NASA TM-86869, ASME Paper No. 85-GT-226, Nov. 1984

MULTIRESOLUTION REPRESENTATION OF URBAN TERRAIN BY L_1 SPLINES, L_2 SPLINES AND PIECEWISE PLANAR SURFACES

John E. Lavery*
Computing and Information Sciences Division
Army Research Office, Army Research Laboratory
P.O. Box 12211, Research Triangle Park, NC 27709-2211

David E. Gilsinn
National Institute of Standards and Technology
100 Bureau Drive, Stop 8910
Gaithersburg, MD 20899-8910

Abstract

Cubic L_1 and L_2 interpolating splines based on C^1 smooth, piecewise cubic Sibson elements on a tensor-product grid are investigated. Computational tests were carried out for an 800 m by 800 m area of Baltimore, Maryland represented by an 801×801 set of 1-meter-spacing (posting) data set. Interpolating splines at coarser resolutions were computed along with ℓ_1, ℓ_2, and ℓ_∞ errors relative to the 800 m by 800 m data set. Piecewise planar interpolations at the coarser resolutions were also computed along with the above errors for comparative purposes.

1. Introduction

Currently, irregular geometric surfaces and, in particular, terrain are often represented by piecewise planar surfaces on triangulated networks (often called "TINs" or "triangulated irregular networks" when the triangles are irregular in shape). However, generating an accurate, error-free surface within a triangulated network framework requires extremely fine triangulations in regions of rapid change and therefore storage and manipulation of huge amounts of data. The conceptual superiority of using smooth surfaces for representation of terrain and of irregular geometric surfaces in general has long been recognized. Recently, a new class of cubic "L_1" splines that perform well in preserving the shape of data sets has been developed (Lavery, 2000a, 2000b, 2001). We will compare L_1 splines with a class of conventional "L_2" splines and with piecewise planar surfaces.

2. Cubic L_1 Splines, Cubic L_2 Splines and Piecewise Planar Surfaces

The cubic splines $z(x,y)$ used in this paper consist of C^1 smooth, piecewise cubic Sibson elements (Han and Schumaker, 1997; Lavery, 2001) on regularly spaced rectangular grids with nodes $(x_i, y_j) = (c_x i, c_y j), i = 0, 1, ..., I, j = 0, 1, ..., J$, where c_x and c_y are known constants. These cubic splines, which exist on the domain $D = (x_0, x_I) \times (y_0, y_J)$, are characterized by their values $z_{ij} = z(x_i, y_j)$ and the values of their derivatives $z^x_{ij} = \frac{\partial z}{\partial x}(x_i, y_j)$ and $z^y_{ij} = \frac{\partial z}{\partial y}(x_i, y_j)$ at the nodes (x_i, y_j). At each node (x_i, y_j), the elevation z_{ij} is given. To calculate a cubic interpolating spline, one must compute the values of the derivatives z^x_{ij} and z^y_{ij}. The z^x_{ij} and z^y_{ij} of a cubic L_1 spline are calculated by minimizing the following weighted sum of the absolute values of the second derivatives of the spline and a regularization term

$$\iint_D \left[\left| \frac{\partial^2 z}{\partial x^2} \right| + 2 \left| \frac{\partial^2 z}{\partial x \partial y} \right| + \left| \frac{\partial^2 z}{\partial y^2} \right| \right] dx\, dy + \varepsilon \sum_{i=0}^{I} \sum_{j=0}^{J} \left[|z^x_{ij}| + |z^y_{ij}| \right] \tag{1}$$

over all Sibson-element surfaces z that interpolate the data z_{ij}. The z^x_{ij} and z^y_{ij} of a conventional cubic L_2 interpolating spline are calculated by minimizing the following weighted sum of the squares of the second derivatives of the spline and a regularization term

$$\iint_D \left[\left(\frac{\partial^2 z}{\partial x^2} \right)^2 + 4 \left(\frac{\partial^2 z}{\partial x \partial y} \right)^2 + \left(\frac{\partial^2 z}{\partial y^2} \right)^2 \right] dx\, dy + \varepsilon^2 \sum_{i=0}^{I} \sum_{j=0}^{J} \left[(z^x_{ij})^2 + (z^y_{ij})^2 \right] \tag{2}$$

over all Sibson-element surfaces z that interpolate the data z_{ij}. The regularization parameter ϵ in (2) is the same as the ϵ in (1). The integral in (2) was discretized in the same manner as the integral in (1). A piecewise planar surface z is calculated by dividing each rectangle $[x_i, x_{i+1}] \times [y_j, y_{j+1}]$ into two triangles by drawing the diagonal from the corner (x_i, y_j) to the corner (x_{i+1}, y_{j+1}) and letting z inside each triangle be the linear interpolant of the data at the three corners of the triangle.

3. Multiresolution Representation of Urban Data

Computational tests were carried out on a set of 801×801 data that consists of an 800 m by 800 m portion of a 1000×1000 set of 1-meter-posting digital elevation data for downtown Baltimore, Maryland surrounding Oriole Park at Camden Yards. The data set was obtained from the Joint Precision Strike Demonstration Project Office (JPSD PO) Rapid Terrain Visualization (RTV) ACTD. In Fig. 1, we present the surface for the 800 m by 800 m, 1-meter-posting subset of the Baltimore data set mentioned above.

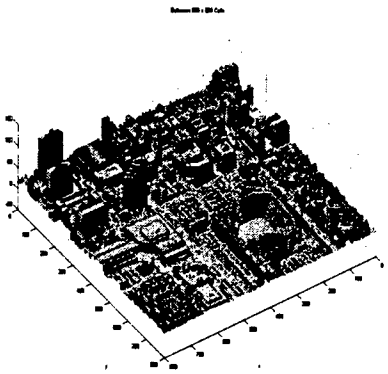


Fig. 1. Surface based on 1-meter-posting for 800 m by 800m area of Baltimore, Maryland.

The first row of the tables below contain the spacings, designated by "s" in meters. In the left hand column of the tables the following notation is used: $\Delta\ell_1 = \|z_{[L_1,s]} - \text{data}\|_{\ell_1}$, $\Delta\ell_2 = \|z_{[L_1,s]} - \text{data}\|_{\ell_2}$, $\Delta\ell_\infty = \|z_{[L_1,s]} - \text{data}\|_{\ell_\infty}$, where data is the original 801×801 data used to plot Fig. 1.

Table 1. Norms of differences between cubic L_1 splines on coarse grids and original data.

s (m)	5	10	20	40
$\Delta\ell_1$	1.314	2.207	3.709	5.987
$\Delta\ell_2$	3.640	5.058	7.582	11.34
$\Delta\ell_\infty$	94.50	108.4	103.1	104.2

Table 2. Norms of differences between cubic L_2 splines on coarse grids and original data.

s (m)	5	10	20	40
$\Delta\ell_1$	1.488	2.450	4.014	6.305
$\Delta\ell_2$	3.726	5.144	7.702	11.69
$\Delta\ell_\infty$	101.2	113.0	98.50	104.1

Table 3. Norms of differences between piecewise planar surfaces on coarse grids and original data.

s (m)	5	10	20	40
$\Delta\ell_1$	1.389	2.346	3.902	6.099
$\Delta\ell_2$	3.690	5.130	7.545	11.15
$\Delta\ell_\infty$	89.82	94.85	95.57	101.1

Overall, this evidence indicates that L_1 splines preserve shape better for this terrain data set than do L_2 splines. With respect to the piecewise planar surface interpolation the criteria for preservation of shape depends strongly on the measure of difference between the interpolation and the original data. Piecewise planar performs better than the L_2 spline for this data set given the three measures of performance used. The comparison with the L_1 spline depends on the error measure.

4. Conclusion

The results in this paper indicate that L_1 splines are excellent candidates for representation of urban terrain. In this article, we have investigated the approximation properties of L_1 interpolating splines on increasingly coarse grids, ignoring intermediate data. In the future, computational experiments with L_1 smoothing splines, which use all of the data, including the data between the coarse-grid nodes, will be carried out. It is expected that the performance of L_1 splines will be further enhanced by doing this.

References

Han, L. and L. L. Schumaker, "itting monotone surfaces to scattered data using C_1 piecewise cubics," *SIAM J. Numer. Anal.*, Vol. 34, pp. 569-585, 1997.

Lavery, J. E., "Univariate cubic L_p splines and shape-preserving, multiscale interpolation by univariate cubic L_1 splines," *Comput. Aided Geom. Design*, Vol. 17, pp. 319-336, 2000a.

Lavery, J. E., "Shape-preserving, multiscale fitting of univariate data by cubic L_1 smoothing splines," *Comput. Aided Geom. Design*, Vol. 17, pp. 715-727, 2000b.

Lavery, J. E., "Shape-preserving, multiscale interpolation by bi- and multivariate cubic L_1 splines," *Comput. Aided Geom. Design*, submitted, 2001.

COMPUTER MODELING TO DEFEAT CHEMICAL EROSION IN GUN TUBES: THEORETICAL CHEMISTRY MODELS OF GUN TUBE EROSION

C. F. Chabalowski*, G. Krasko, M. M. Hurley
U.S. Army Research Laboratory
APG, MD 21005-5066

D. Sorescu
University of Pittsburgh
Pittsburgh, PA 15260

G. H. Lushington
PET-CCM,
Columbus, OH 43212

SUMMARY

State of the art computational molecular modeling methods are used to predict details of the physical and chemical interactions between the interior of the gun tube and the propellant combustion product, carbon monoxide (CO). CO has long been suspected as a main source for the extensive carburization in gun tubes resulting in their accelerated erosion [Conroy et al., 1997]. The physical model chosen to represent the steel interior of the tube is bulk iron. This is assumed to be a good model for steel due to the low concentration of carbon (~0.4%) in gun steel. The modeling methods are based upon quantum mechanics, and are referred to as Pseudo-Potential Plane Wave (PP-PW) Density Functional Theory (DFT) methods. Two versions of this approaches are being used; the CASTEP suite of codes [Payne and Milman, 1992], and the VASP [Moroni et al., 1997] suite of codes.

Table 1. Comparison of Calculated and Experimental Properties of Bulk BCC Iron.

		Theory	
Property	Experiment	PP-PW (CASTEP)	PP-PW (VASP)
Lattice Constant (Å)	2.8664	2.8151(1.8%)	2.8653(0.0%)
Bulk Modulus (GPa)	170	178(4.7%)	161(5.2%)
Effective Magneton Number (n_b)	2.22	2.20(1.0%)	2.86(5.4%)
Saturation Magnetization (M_0)	1750	1809(3.3%)	1876(7.2%)
Carbon Monoxide			
R_e(C-O) Å	1.128	1.144 (1.4%)	1.145 (1.5%)
Vibr. Freq. cm^{-1}	2143 cm^{-1}	2228 (3.5%)	2174 (1.5%)
Bond Energy	259.3 kcal/mol	252.9 (2.5%)	253.6 (2.2%)

The theoretical models used in this study must first be validated, and this is done by comparison of properties determined through reliable experiments with the values for these properties predicted by the theoretical models. A selection of such properties for bulk iron can be seen in Table 1, along with properties for gas phase carbon monoxide. The comparison between the experimental and theoretical values is extremely good, with the largest deviation being 7% for the Saturation Magnetization. The magnetic characteristics of iron are particularly difficult to model, but they are known to play a major role in defining its other properties. Table 1 clearly demonstrates that these modeling methods are capable of predicting, in a quantitative manner, the magnetic properties of iron. In addition, the models accurately predict the molecular properties of CO, such as the R(C-O) bond length, the frequency for the lowest vibrational transition, and the energy to break the C-O bond.

Since we are interested in chemical interactions at the iron surface, we have further validated our methods by predicting the experimentally observed relaxation of the surface layers in iron. For this purpose, we predicted the relaxation in the three top layers of an iron surface created by cleaving bulk iron (Body Centered Cubic lattice) along the (100) Miller plane. The surface and "bulk" iron was built up by adding layers of iron atoms, one layer at a time, in their correct crystallographic position in the bulk. The top two or three layers of atoms were then allowed to relax (energy minimize) their positions, while the underlying layers were held fixed in their crystal positions. It is known from experiment that each layer retains its pattern of repeating squares, but the distance between layers, e.g., d(1-2), in the top three layers, changes. The changes are given as a percent deviation from the bulk structure. Experiment predicts a contraction between the first two layers, d(1-2), of about –5%, and an expansion between the second and third layers of about +5%, with a systematic error of ± 2%. The theory correctly predicts the first two layers to move closer to one another by –4%, and the second and third

layers to move apart by about +3%. Once again, the predictions of the model are in good agreement with experiment.

Having established the reliability of our modeling methods, they can now be used with confidence to explore the interactions of CO, and its atomic components, with the iron (Fe) surfaces. It was deduced from experiment [Moon et al., 1989] that there are at least three unique sites where CO could be binding to the (100) surface. These have been labeled the 1-Fold (1F), 2-Fold (2F), and 4-Fold (4F) sites, depending on the number of iron atoms bonded to the carbon in CO. Temperature Programmed Desorption experiments [Moon et al., 1985] established relative binding energies for CO at each site, such that the binding energy decreases in the order 4F > 2F > 1F, and the absolute binding energies were deduced to be approximately –35 kcal/mol, -25 kcal/mol, -20 kcal/mol, respectively. These binding sites were located by the theory through energy minimizations of CO on the (100) surface for a slab with six layers of iron. The order of the binding strengths predicted by theory (for 25% CO coverage of the surface) is 4F > 2F ≈ 1F, with absolute binding energies of –47 kcal/mol, -35 kcal/mol, and –34 kcal/mol. Within the expected accuracy of our calculations, the 2F and 1F binding energies are essentially equal. But when the surface coverage is increased to 50%, the ordering becomes 4F > 1F > 2F, with the absolute energies being –48, -33, -28 kcal/mol, respectively. These results show that the amount of surface coverage, which is often difficult to establish in an experiment, can drastically change the binding energies at some sites, blurring the interpretation of the experimental results.

Once the CO dissociates on the surface of the gun barrel, carbon and oxygen atoms will bind to the iron, initiating the erosion process. The theory has again located three similar bind sites for these atoms, and these site are again labeled as 4F, 2F, and 1F. Similar to molecular CO, both C and O atoms have relative binding strengths at these sites that decrease in the order 4F > 2F > 1F. However, the absolute binding energies for these atoms is much larger than for CO. For the carbon atom, the binding energies are –186, -154, and –118 kcal/mol, while for oxygen they are –145, -132, -111 kcal/mol. In the case of CO, the largest binding energy was only –48 kcal/mol. Two very important results are obtained from these atomic interactions: (1) The carbon atom binds significantly more strongly to the iron (100) than does oxygen at any one site; and (2) the oxygen atom tends to stay on the surface of the iron, while the carbon penetrates into the iron matrix, with concomitant re-arrangement of the Fe surface atoms. This could explain why carbon can be found at greater depths below the steel surface than can oxygen. Secondly, it implies that oxygen could play a significantly smaller role in gun tube erosion than does carbon. This has been a longstanding controversy.

Preliminary results for CO interacting with a surface constructed from the Fe (111) Miller plane show that CO forms even stronger bonds to this surface than in the (100) case. This is in agreement with experiment, which suggests the possibility of four unique binding sites on the (111) surface, with the largest binding energy predicted to be around –48 kcal/mol [Whitman et al., 1989]. To date, three different binding sites have been predicted via the modeling, which have been labeled 4F, 1Fn, and 1Fd. The relative binding strengths at each site are –55, -41, and –40 kcal/mol. Once again the CO binds most strongly to the 4F site. The Fe (111) surface has much more texture to it than the (100), so it is anticipated that more binding sites will be located, probably exceeding the four sites predicted by experiment.

The results from this study have shown that the computational models used here are robust, and capable of producing quantitative predictions for the chemical interactions and reactions of propellant combustion gases with iron. The early modeling data has already begun to shed light on the relative importance of carbon and oxygen in the gun tube erosion process. As the modeling data increases, we will begin to understand the key components in the chemical processes responsible for the erosion, which should then point us towards propellant or gun tube modifications to drastically reduce the erosion.

REFERENCES

Ashcroft, N. W. and Mermin, N. D., "Solid State Physics," Harcourt Brace College Publishers, New York, p. 655, 1976.

Conroy, P.J.; Weinacht, P.; Nusca, M.J. "120-mm Gun Tube Erosion Including Surface Chemistry Effects", ARL-TR-1526, Oct. 1997.

Kittel, C., "Introduction to Solid State Physics", John Wiley & Sons, New York, pp. 143, 536, 537, 1971.

Moon, D. W., Dwyer, D. J., Bernasek, S. L., "Adsorption of CO on the Clean and Sulfur Modified Fe(100) Surface," Surf. Sci., Vol 163, pp. 215-229, 1985.

Moon, D. W., Bernasek, S. L., Gland, J. L., and Dwyer, D. J., Surf. Sci., J. Am. Chem. Soc., Vol 107, p. 4363, 1989.

Moroni, E.G; Kresse, G; Hafner, J.; Furthmueller, "VASP," J.; *Phys. Rev* B 1997, *56*, 15629.

Payne, M.C.; Milman, V., "CASTEP," Review of Modern Physics Vol 64, p. 1045, 1992.

Whitman, L. J., Richter, L. J., Gurney, B. A., Villarrubia, J. S., and Ho, W., "CO adsorption site occupations on Fe(111) vs coverage and temperature: The kinetics of adsorption and reaction," J. Chem. Phys., Vol. 90, pp. 2050-2062, February 1989.

Session I
Soldier Systems

Chair
Dr. Herbert L. Meiselman
U.S. Army Soldier and Biological Chemical Command

Co-Chair
Dr. Irwin A. Taub
U.S. Army Soldier and Biological Chemical Command

Keynote Address
Dr. Michael Fineberg
Booz-Allen & Hamilton, Inc.

THIS PAGE INTENTIONALLY LEFT BLANK

BACKPACK PACKING OPTIMIZATION FOR REDUCING THE SOLDIER'S ENERGY EXPENDITURE DURING LOAD CARRIAGE

L. Piscitelle*, and S. Yuhaski
Natick Soldier Center (NSC), SBCCOM
Natick, MA 01760

1. INTRODUCTION

SBCCOM Natick Soldier Center (NSC) is currently executing a Science and Technology Objective (STO) titled Optimized Load Carriage for Enhanced Soldier Performance. All of the equipment that a soldier carries will have an effect upon that soldier's mobility and energy expenditure. This STO uses analytical methods and experimental studies to investigate the impact of load carriage on soldier performance. By developing a scientific understanding of the biomechanics of load carriage, NSC will be able to provide tools for the engineer to utilize in designing soldier equipment as well as load carriage guidelines for the soldier. This work directly applies to the future warrior system.

Previous experiments of Col. J. Obusek (USARIEM) found that the expenditure of energy for a soldier carrying a backpack was correlated to the position of the backpack mass center. Experimental measurements of the moment of inertia of a model backpack device (used in Col. J. Obusek's study) were made and used to compute the combined moment of inertia of the torso and backpack device. It was found that the experimental results and the predictions using a pseudo-passive dynamics model agreed qualitatively. This suggested that both position and moment of inertia of the load and human torso were important parameters for a designer to consider in developing equipment for the soldier. Based upon these results, it was apparent that a useful tool for the designer would be one in which he could easily position different backpack items and immediately see the change in both the location of the mass center and the moments of inertia of the backpack and human.

2. PROGRAM DEVELOPMENT

2.1 Graphical Interface

A MATLAB® program and user friendly graphical interface has been developed to allow the designer to experiment with different backpack configurations. In addition, this program has been expanded to include an optimization option, which will allow the program to try different packing schemes and select the one which best meets the designer's needs. The user will be able to describe new backpack items or choose from a list of items within the program. Figure 1. is a representative user screen for the MATLAB® program.

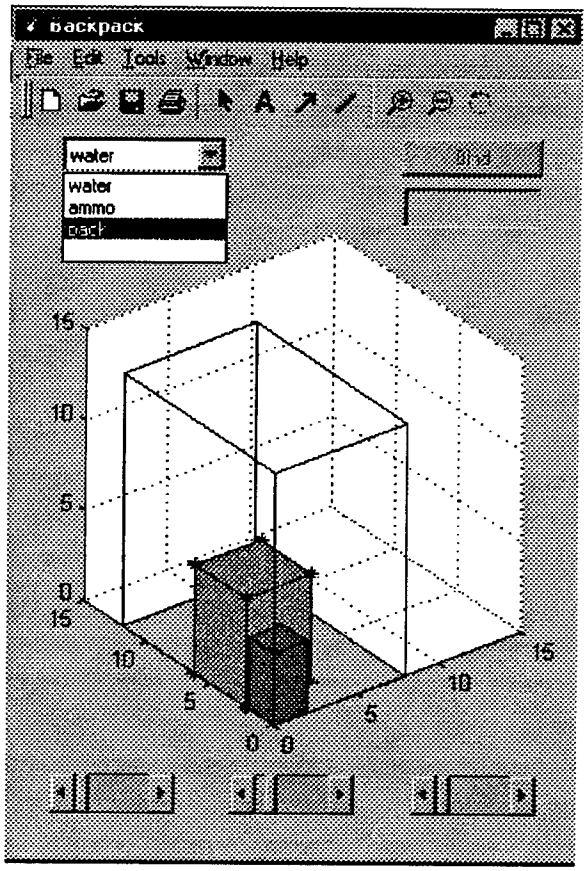


Fig. 1. Typical user screen

When the user creates a new object, it is given a descriptor (name), dimensions and weight. In addition, the user may specify that the object is hollow which will cause the bounding box to be transparent and allow objects to be placed with in its interior. As objects are added and moved, the user is given the mass center location and moments of inertia (updated in real time) for the collection of

objects. Figure 2. shows the user input and output screens.

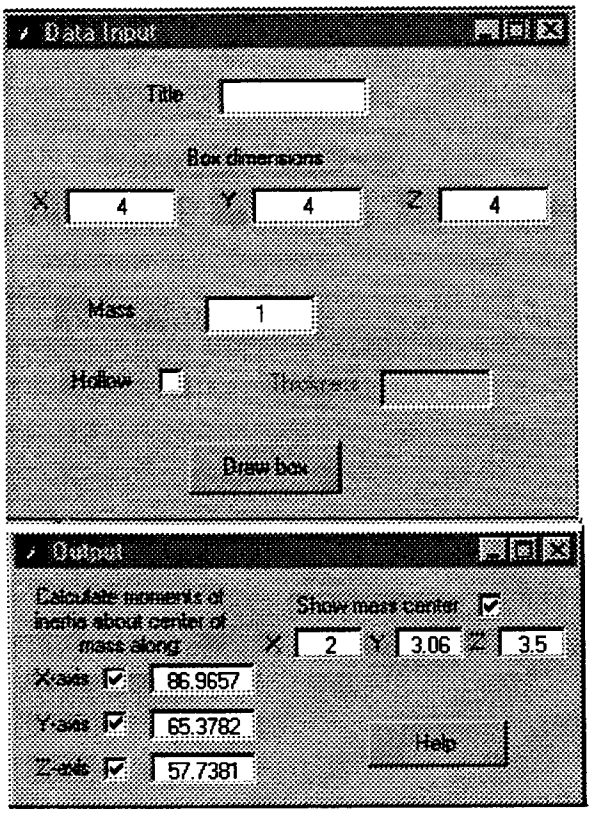


Fig. 2. Typical user input and output screens

2.2 Optimization Scheme

An effective method for optimization, that has recently gained much popularity, is genetic programming. A genetic programming algorithm has been created for a model consisting of a backpack (modeled in two dimensions, with basic structure in place for three dimensions) and approximately a dozen objects, of various solid rectangular dimensions and densities, within the backpack.

The solution domain consists of a two-dimensional grid having increments that are a half-inch in length. The idea is to determine the location and orientation of each of the objects that minimizes the combined moment of inertia of the soldier and his backpack.

In general, the genetic programming methodology consists of iterations having three distinct steps. The first step is the selection of the best solutions to proceed to the next iteration (i.e., generation); the initial population is generated randomly. The next step is the combination of the solutions, with each other (breeding), to build up the population of the new generation, typically to its former level. The last step is the mutation of solutions, in the current population; this is done by the application of perturbations that are randomly generated.

Techniques to increase the effectiveness of the optimization have been implemented in keeping with the underlying nature of the genetic algorithm. For instance, for obvious physical reasons, the objects within the backpack are not permitted to overlap dimensionally (i.e., collide). Constraints to prevent collisions are embedded in the objective function, as penalty functions; to ensure that solutions having collisions are completely eliminated as possible optima during iteration. Also, there are controls within the algorithm that can be manipulated to augment the performance of the algorithm. These include, the size of each generation, the percent of solutions accepted from one generation of solutions to the next, the number of mutations in each generation, and the factors controlling the magnitudes of the mutations. The solutions to which the algorithm converges have been optimal in the verification tests made to date.

FROM THEORETICAL EQUATIONS TO PRACTICAL ARMY APPLICATIONS: THE HIGH PERFORMANCE OF POLYMER ELECTROLYTE MEMBRANE FUEL CELLS FOR INDIVIDUAL SOLDIER AND FUTURE COMBAT SYSTEM APPLICATIONS

Deryn Chu*, Rongzhong Jiang and Charles Walker
Army Research Laboratory
Adelphi, MD 20783-1197

Kris Garnder, Richard Jacobs and James Stephens
Army CECOM, RDEC
Fort Belvoir, VA 22060

SUMMARY

The U. S. Army requires extremely lightweight, quiet, efficient and reliable power-sources for a variety of portable electronics and other applications in the modern battlefield [General Coburn, 2000]. Polymer electrolyte membrane fuel cells (PEMFCs) are most favored as portable power supply devices primarily of their lightweight and high power density. A fuel cell is an electrochemical device that directly converts the chemical energy of the reactants, a fuel and oxidant, into **electrical power**, **water** and **heat** (Fig. 1)

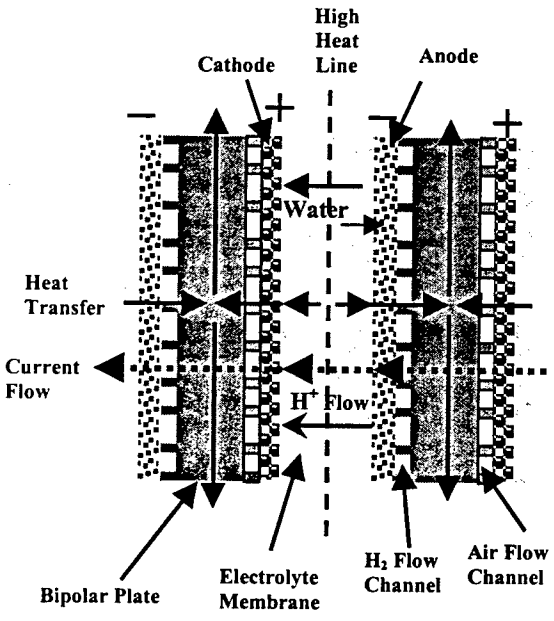


Figure 1. Heat and current flows in a single cell unit in bipolar polymer electrolyte fuel cell stack.

Future man-portable power source systems will need to have a high power density and a long operating life and they must be small and lightweight. Using a lightweight PEMFC system as the portable power source can reduce the physical burden on the carrier. Several key areas need to be addressed for successful production of the desired high-performance, lightweight, ambient-temperature and –pressure fuel cell system: (1) thermal and heat transfer management, (2) water management, (3) environmental factors, and (4) hydrogen storage conditions for high-performance PEMFCs [Chu, D, 1998, 1999 and 2000]. All of these issues may become simple if we can use computer modeling or theoretical equations to express the fuel cell reactions.

This paper will address the progression from mathematical modeling of the performance of a fuel cell system through verification by laboratory esperimental to field exercises. We have used the Nernest , Tafel and Arrhenius principles combined with heat effects to develop an equation. The equation $\{E = E_a - i\,A \exp [1/(T_m - T)] \pm i\,B \exp [N (T - T_o) / (T_b - T_o)]\}$ can be used to describe the electrode processes (activation, ohmic and mass-transfer) of PEMFC stacks over the entire discharge current range.

The ideal thermodynamic potential for a single H_2/air fuel cell is 1.23 V at ambient pressure and temperature. In practice, fuel cells produce useful voltage outputs that are somewhat less than the ideal voltage due to electrocatalyst activation polarization, ohmic polarization and mass transfer limitation (Fig. 2). The Fig. 2 can be expressed as:

$$E = E_o - E_{act} - E_{ohmic} - E_{mass} \qquad (1)$$

Here, E_o is the theoretical thermodynamic open circuit potential of the stack. E_{act} is the electrocatalyst overpotential. E_{ohmic} is the ohmic over potential of the stack, which is equal to the sum of the ohmic over potentials of all single cells linked in series. E_{mass} is the over potential of the stack caused by mass-transfer. The thermal behavior and discharge performances of the

PEMFC system were investigated. The stack temperature-time curves and stack potential-time curves can be described with an equation

$$T = T_o + (T_b - T_o)\, t / (t + S) \quad (S > 0) \qquad (2)$$

Here, T_b (°C) is the stack temperature under steady state conditions, T_o (°C) is the environmental chamber temperature. The t (minute) is discharge time. S (minute) is a time parameter, which affects the rate of stack temperature change. After many factors also consider, the equation (1) can be rewritten as

$$E = E_a - i\,A \exp [1/(T_m - T)] \pm i\,B \exp [N (T - T_o) / (T_b - T_o)] \qquad (3)$$

An advanced portable power source of 50 Watt (PPS-50) PEMFC system was developed under the U. S. Army, DARPA and the Office Special Technology (OST) joint program. The PPS-50 is a 12 V fuel cell supply that is able to provide 60 W continuous and 70 W in bursts for a few minutes. The performance of the PPS-50 fuel cell system was used to verify our theoretical equations. The system was evaluated under different environmental temperatures and humidity conditions. The temperature ranges are from –10 to 50°C and the relative humidity (RH) ranges are from 10% to 90%. The potential-current and power-current curves of a PPS-50 fuel cell system agreed with our theoretical equation under a variety of experimental conditions. The system also operation at –10°C was more than 9 hrs very well. Our experimental results showed that the PPS-50W system performance was excellent at different environmental conditions. The most important issue is that the based on our calculation results the manufacturing company has already increased the maximum system operating temperature from 55 to 65°C without damaging the PPS-50 system.

The PPS 50W system was also used successfully in field exercises by the Marine Corp. at 29 Palms Marine Base in October '99 and the Navy in June 2000 at the Hawaii for the Strong Angle Humanitarian Exercises. The field tests by the Marine Corps. demonstrated that the fuel cells are a reliable, lightweight and cost-effective means of providing power for military applications. The fuel cells performed extremely well during the retransmission site test, operating for over 25 continuous hours. Based on the Marine Corp.'s final report, use of the fuel cell power systems rather than batteries resulted in a saving of $8,000 for one CAX operation alone.

To use fuel cells in place of traditional batteries can reduce the cost of energy up to 80% for the Marine Corp. exercises. Understanding the performance characteristics of stack systems is clearly important for realizing the optimum cost/weight/volume/performance ratios. The results of this study advance the development of the PEMFC stack system for practical individual soldier and future combat system applications.

ACKNOWLEDGEMENTS

We wish to thank the Department of the Army and the Army Materiel Command for their financial support. We also thank to PM Soldier (Natick, SBCOM) for help.

REFERENCES

General Coburn (CG for AMC), speeches at the Fort Lauderale, FL, AUSA Show on February, 2000.

Chu, D., and R. Jiang, 1998: Performance of Polymer Electrolyte Membrane Fuel Cell Stack, *J. Electrochemical Society, Proceedings Volume*, **98-27**, 470-478.

— and — 1999: Comparative Studies of Polymer Electrolyte Membrane Fuel Cell (PEMFC) Stacks and Single Cells, *J. Power Sources*, **80**, 226-234.

— and — 1999: Performance of Polymer Electrolyte Membrane Fuel Cell (PEMFC) Stacks PART I. Evaluation and Simulation of An Air-Breathing PEMFC Stack, *J. Power Sources*, **83**, 128-133.

—, — and C. Walker: 2000: Analysis Of PEM Fuel Cell Stacks Using An Empirical Current-Voltage Equation, *J. Applied Electrochem.*, **30**, 365-370.

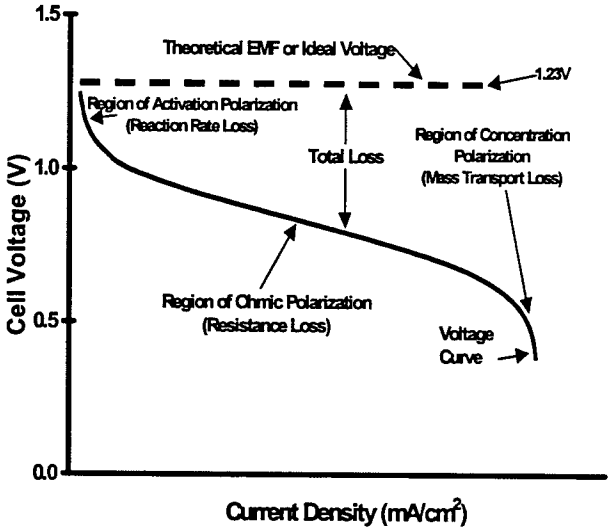


Figure 2. Ideal and Actual Fuel Cell Voltage-Current Characteristic

HUMAN PERFORMANCE ISSUES IN BATTLEFIELD VISUALIZATION

Michael J. Barnes*
U.S. Army Research Laboratory
Ft. Huachuca, AZ 85613

Mary T. Dzindolet
Cameron University
Lawton, OK 73505

Linda G. Pierce
U.S. Army Research Laboratory
Ft. Sill, OK 73503

Jerzy W. Rozenblit
University of Arizona
Tucson, AZ 85721

Christopher D. Wickens
University of Illinois-Urbana
Champaign, IL 61820

SUMMARY

Visualizing future battlefields is an important objective for the 21st century Army. Technological advances promise a knowledge rich battlefield with virtual planning, multi-modal visualizations, disbursed operations, and highly intelligent automated systems. Too often the role of the future soldier and in particular the commander is ignored (Barnes, 1997). Visualization technologies are being developed to aid the commander in understanding future battlespaces including battle trends and possible end states. Obviously, the effects of visualization will cascade over the entire battlefield and influence both the common and specialized views of the battle at all echelons. Yet the demand for improved technology outpaces our understanding of the benefits of the various techniques (Barnes & Wickens, 1998). The objective of this research program is to investigate the effects of important visualization issues on soldier awareness and decision making in areas that we expect to impact future operations. Areas that we have investigated include soldier performance in immersed and three-dimensional (3-D) map related tasks, visualizing uncertainty in highly automated environments, combining machine intelligence with visualization tools, and trust issues for automated environments. The purpose of the visualization research is to develop a cognitive engineering architecture that will help guide the development of visualization systems based on behavioral and operational considerations rather than being based solely on the promise of new technologies. The key to our effort is to develop and use cognitive models of human visualization performance and verify them in the laboratory using important military problem sets and subjects to establish general concepts. These concepts will be used to develop realistic visualization tools that can be evaluated in appropriate field experiments as part of a more general Cognitive Engineering Science and Technology Objective (STO).

Terrain Visualization: As part of the program, researchers from the University of Illinois investigated a variety of military map tasks using United States Military Academy cadre as test subjects. The research purpose was to investigate visualization variables using Silicon Graphics generated synthetic terrain. The initial experiment varied viewing conditions and display dimensionality. The cadre performed better using two-dimensional (2-D) vice 3-D displays for map distance measurement and equally well for mobility assessment. The 3-D displays showed some advantage when the cadres could immerse themselves in the terrain allowing them to make more accurate LOS judgments. Subsequent research indicated serious situation awareness issues with being immersed in the terrain. The cadre became fixated on the immediate environment and would lose track of threats behind them even when the threats were annotated on their display (Wickens, Thomas, & Young, in press). This on-going research points to serious limitations of both 3-D and immersed display formats; cognitive engineering solutions are suggested to utilize the considerable advantages of these formats without being constrained by their limitations.

Visualizing Uncertainty: An ubiquitous battlefield problem is risk management in uncertain environments. The question we addressed is how to best display uncertainty when operators are defending against missile attacks during a national missile defense (NMD) simulation. We compared displaying abstract probabilities of mission success to displaying concrete representations based on expected loss frequencies and found an advantage to the latter for improving display search and visualization memory but we found no effect of format on the trained NMD operators' actual decisions (Barnes, Wickens, & Smith, 2000). In the second experiment, there was evidence of a decision bias related to the sequence of hits and misses of shooting down incoming missiles. The results imply that the operators visualization of trend effects was primarily influenced by their perception of whether the situation was deteriorating as opposed to their understanding of the natural fluctuation of independent probabilities. The results influenced new NMD display concepts and caused us to design a series of experiments to evaluate risk visualization concepts whose purpose is to improve the

operators missile defense decisions using target value and risk as trade-off criteria.

Visualizing Automated Systems: Because of the importance of reacting before the enemy does and also the extreme complexity of combat system of systems, automation is becoming a pervasive component of modern battlefields. However, the human performance issues are not well understood and threaten to interfere with the efficacy of future systems. At least in the near future, human decision-makers will have the final authority for execution and in many cases data interpretation. However, our research into these issues has confirmed that soldiers mistrust the systems when they should not (Dzindolet, Pierce, Beck, & Dawe, in press) and over rely on systems when they should override them. Our on-going research will attempt to develop general principles of displaying information to ensure that the soldiers' battlefield awareness is sufficient to allow understanding of both the state of the system and also the state of battlefield. Improved visualization tools and a more thorough understanding of the cognitive issues involved should allow the human to know when to trust and when to override automated systems.

Models, Architectures, and Field Validations: We will present interim models of battlefield visualization derived from our empirical research and indicate how these models are driving our future research. The inter-relationship of the various efforts is their investigation of transformation of battlefield information into images that decision-makers can use to understand their combat environments. Our research results indicate that more than pretty pictures are involved: cognitive biases are pervasive in all areas investigated. Soldiers can become fixated in immersive terrains; too conservative or not conservative enough in missile defense, over and under reliant using automated systems. Research is continuing into the precise relationship between different data views and the amelioration of these biases. However, our initial results suggest that training as well as the proper type of visualization is crucial to overcoming these biases. This does not limit the utility of visualization concepts but rather broadens the practical applications. Successful visualization techniques will allow the soldier and the commander to understand the implications of various decisions using realistic animated environments that can be used for both embedded training and for battle management. We are in the process of developing a general visualization architecture that is generic enough to investigate these concepts in Support and Stability Operations (SASO) and other non-conventional operations as well as mid intensity combat in order to generalize the results to the expected venues of future conflicts. The general architecture is the initial step into transforming these general models and principles from the scientific to the applications domain.

Results from this research will be used to create specific concepts that are being designed to investigate our results and possible applications as part of realistic field exercises. We discuss the importance of a phased research project that start with well controlled laboratory experiments and simple models and progresses to realistic validations. We point out the advantages and disadvantages of controlled experiments and closed loop simulations and exercises. Our conclusion is the synergy of both results in the understanding of causality and the ability to generalize to complex environments.

REFERENCES

Barnes, M.J. (1997). Process centered displays and cognitive models for command applications. *Proceeding of the IEEE International Conference and Workshop on Engineering of Computer-Based Systems,* 129-135, Monterey, CA.

Barnes, M.J. & Wickens, C.D. (1998). Battlespace visualization: A multi-view approach. *Proceedings of the 4th Annual Federated Laboratory: Advanced and Interactive Displays*, 107-111, College Park, MD.

Barnes, M.J., Wickens, C.D., & Smith, M. (2000). Visualizing uncertainty in an automated National Missile Defense (NMD) environment. *Proceedings of the 4th Annual Federated Laboratory: Advanced and Interactive Displays,* 107-111, College Park, MD.

Dzindolet, M.T., Pierce, L.G., Beck, H.P., & Dawe, L.A. (in press). A framework for automation use. US Army Research Laboratory, Aberdeen Proving Ground, MD.

Rozenblit, J.W., Barnes, M.J., Momen, F., Quijada, J.A., & Fichtl, T. (2000). *Soldier performance course of action aid* (ARL-CR-302). Aberdeen Proving Ground, MD: US Army Research Laboratory.

Smith, M. & Wickens, C.D. (1999). The effect of highlighting and event history on operator decision making in a missile defense system application. *Aviation Research Laboratory Technical Report,* Savoy, IL.

Wickens, C.D., Thomas, L.C., & Young, R. (in press). Frame of reference for display of battlefield information: Judgment –display dependencies. *Human Factors.*

THE INTEGRATION OF AUTOMATIC SPEECH RECOGNITION AND SPATIAL AUDITORY DISPLAYS IN HIGH NOISE, STRESSFUL TANK ENVIRONMENTS

Dr. Ellen Haas
U.S. Army Research Laboratory
Aberdeen Proving Ground, MD

Mr. Robert Shankle
Applied Research Associates
Dallas, TX

Ms. Deborah Travers, Mr. Ted Wheeler
U.S. Army Test Center
Aberdeen Proving Ground, MD

SUMMARY

The introduction and use of complex equipment and systems have made tanks into relatively dynamic, complex cognitive environments where soldiers must simultaneously monitor multiple visual and audio displays, operate multiple controls, and process large amounts of information. The possibility of crew size reduction would make these tasks more demanding. The potential exists for the insertion of advanced technologies such as spatial audio displays and automatic speech recognition (ASR) into future soldier systems to improve soldier efficiency.

The utilization of these advanced technologies raises human factors questions, including the extent to which they can be integrated successfully, separately or together, into demanding crewstation environments. Researchers have not yet determined the extent to which human speech production changes when soldiers are subjected to different levels of noise, workload, and stress, and the degree to which these factors affect soldier performance of ASR control tasks in noisy, stressful conditions. Researchers have not fully explored issues relating to the use of spatial (3-D) audio technology, in which a listener using earphones perceives sounds which appear to originate at different azimuths, elevations, and distances from locations outside the listener's head. Existing tanks contain monaural radios in which the same audio signals are heard in both sides of the user's headset. Previous research showed that the intelligibility of radio messages is enhanced by the use of spatial audio displays because they provide location cues that allow a greater degree of selective attention, especially if multiple messages are present. Few researchers have explored the extent to which spatial audio radio messages enhance the ability of the user in high-noise, stressful tank environments to understand speech communications from multiple channels. No research has been conducted to determine the extent to which spatial audio displays affect the ability of the user to accurately output verbal information into an ASR system.

The goal of this study was to examine the effects of the integration of spatial auditory display and speech recognition technologies into tank environments. The first objective of this study was to determine the extent to which the performance of a noise-robust ASR system is affected by high levels of ambient noise and how well the ASR system recognizes voice commands from speakers who experience some level of workload or stress. A second objective was to ascertain the extent to which user speech is affected when the subject uses an ASR system in a tank environment containing stress, high noise levels, and different levels of workload. A third objective was to determine the effect of spatial audio displays on soldier performance in processing multiple radio communications. A fourth objective was to determine whether the type of incoming auditory information (monaural or spatial), affects user speech output to the ASR system. Research of this nature benefits the Army by defining the human performance limits associated with the use these advanced technologies in future combat systems, and by developing tools and techniques to optimize soldier performance within these limits, thus allowing the soldier to meet the more demanding perceptual requirements of the Army in the future.

This study was conducted during August 1999 at the U.S. Army Research Laboratory Hostile Environment Simulator at Aberdeen Proving Ground, Maryland. Subjects were six (6) male U.S. Army soldiers and six (6) male civilians, between the ages of 23 and 50 who possessed normal hearing. During the experiment, the subject was instructed to give ASR voice commands (change radio channels) in response to simulated

monaural or spatial audio radio communications, while simultaneously performing a simulated tank driving task in the presence of realistic ambient tank noise. Differing levels of workload were manipulated by specifying different speeds of the driving task. Subject stress was introduced by informing the subjects that they would be competing against each other in the driving task. All tasks were performed in the presence of 88 dBA SPL digitized M1A2 interior tank noise, measured immediately outside the subject's headphones. Each subject participated in a total of four experimental sessions on four subsequent days, each 25-minute session containing a different combination of driving speed and auditory display.

A mixed factor, repeated measures design was used for data collection and to structure data analysis. Within-subject variables were auditory display configuration (existing monaural and spatial audio), driving speed (15 or 45 mph), and number of simultaneous talkers in the simulated radio communications. The between-subject variable was subject type (soldier or civilian). All independent variables were fixed effect variables (fixed factors) except for subjects, who were treated as a random effect variable (random factor). In order to eliminate practice or order effects, the levels of each independent variable were counterbalanced so that every combination of every condition was presented in different orders across subjects.

The dependent variables of interest included 1) The number of radio channel change phrases correctly recognized by the ASR device (phrase recognition rate), where a whole phrase was considered incorrect if there were one or more recognition errors; 2) The proportion and types of errors in radio channel change phrases incorrectly uttered by the subjects; 3) The number of times that the subject correctly identified the origin channel of the target message; 4) Subject ratings of stress (including the Specific Rating of Events Scale, SRE); and 5) Subject workload ratings (NASA-TLX). A multivariate analysis of variance (MANOVA) was performed for each dependent variable as an initial overall test of significance to determine whether statistically significant differences existed between main effects or interaction effects in the study. Significant effects were explored on a post hoc basis using a Newman-Keuls Sequential Range Test performed at $p < 0.05$.

The MANOVA for ASR sentence recognition rate indicated that there were no statistically significant effects for the main effects of auditory display type or driving speed, no other significant effects or interactions, and no significant difference between soldiers and civilians. The overall mean for ASR performance (collapsed across subjects and conditions) was 34.37 correctly recognized sentences of 36 total sentences per session (standard deviation 2.26), indicating that 95.5% of all subject sentences were recognized by the Verbex speech recognizer. A total of 4.5% of all user command sentences were not recognized by the ASR. Of these, most (approximately 95%) were attributable to subject speech output errors. An analysis of types of user errors indicated that the largest percentage of errors (46%) were run-in phrases, in which subjects uttered two subsequent phrases but did not insert a long enough pause between phrases to allow the recognizer to recognize both as two distinct phrases. Most often, this resulted in neither phrase being recognized by the ASR.

The results indicated that the type of audio input (monaural or spatial incoming radio messages) had no statistically significant effect on the user speech output and no effect on ASR performance. This demonstrated that there were no discernible integration issues concerning audio display and ASR technologies utilized in the same crew system.

The MANOVAs for the stress (SRE) and workload (NASA-TLX) scales indicated that subjects rated different driving speeds as having significantly different levels of stress and overall workload. Subjects perceived that there was less mental workload and less stress associated with task performance at slower driving speeds.

The MANOVA for listener accuracy data (the number of times that the listener correctly identified the origin channel of the target message) indicated that display type and number of talkers were the only statistically significant effects. The data showed that users were able to process and respond to multiple channel radio communications more accurately with spatial than with monaural displays. As the number of simultaneous talkers increased, the number of accurately identified target messages decreased. These results were also found in previous research involving helicopter pilots.

In general, results indicated that advanced technologies such as ASR and spatial audio displays could be useful in real-life applications in future crew systems in which soldiers must perform complex concurrent tasks in the presence of environmental noise and some levels of stress.

SOLUBILITY AND MOLECULAR TRANSPORT IN A PERMSELECTIVE FABRIC

D. RIVIN, N. S. SCHNEIDER, C. E. KENDRICK, P. GIBSON

USA SBCCOM (NATICK SOLDIER CENTER), NATICK, MA

Current chemical and biological protective clothing employs either an air-permeable fabric containing an activated carbon adsorbent or an impermeable fabric coated with butyl rubber. Both types of barrier materials are relatively heavy and bulky, and are not optimal for projected combat systems. Research on the next generation protective fabric is focused on permselective membranes. These lightweight polymer films are barriers against chemical and biological agents but are permeable to water vapor thus reducing heat stress potential by allowing rapid sweat evaporation. The perfluorosulfonate ionomer, Nafion™ is a representative permselective membrane which is used as a model for determining the relationship of molecular diffusion and solubility to polymer structure and chemistry. Nafion™ is a perfluoroethylene polymer containing 33 wt% of fluoroether side-chains terminated with sulfonic acid groups. Incompatibility between the ionic side groups and the nonpolar hydrophobic backbone is responsible for many of the structural features of ionomeric polymers, and as a result, is a major factor in determining relative permeation of molecules which differ in size and polarity. Since permeation is the product of a diffusion coefficient and solubility, we have supplemented direct measurements of permeation with independent determinations of its component parameters for water and selected organic molecules in both protonated and cation-exchanged Nafion™.

Permeation experiments were performed at high stream velocity over a wide range in vapor activity and film thickness in a specially designed apparatus using either flame ionization or thermal conductivity detection. Solubility was obtained from the absorption isotherm (0.05 to 0.98 activity) determined in a Cahn 2000D digital microbalance controlled by an Hiden Analytical computer interface. Liquid solubility and kinetically derived diffusion coefficients were obtained by gravimetric isothermal solvent immersion.

At high vapor activity, Nafion™ has such a low resistance to diffusion of water and small alcohols that the observed permeation flux is limited mainly by the boundary layer resistance associated with vapor phase mass transfer. Accurate values for membrane permeability require correction for the boundary layer, as well as, for lateral surface concentration profiles and non-isothermal effects. Corrected permeabilities in combination with the corresponding isotherm values yield concentration-dependent diffusion coefficients which exhibit a smooth transition from vapor to liquid phase exposures. This is in contrast to all previous studies of water in Nafion™ which did not take these limiting factors into account, and thus found a large discontinuity between vapor and liquid. The observed concentration dependence is consistent with a mechanism whereby water interacts mainly with the sulfonic acid residues, while the alcohols preferentially solvate fluoroethers and cause structural reorganization of the polymer.

Immersion in water and dry solvents (propanol, butanol, dimethylmethylphosphonate, and triethylphosphate) is used to determine the effect of cation exchange on solvation and molecular diffusion. Steady state measurements of the acid form show solvation enhancement in aqueous alcohols and a significant , but lesser, interaction in mixtures of water and aprotic solvent. The kinetics of solvent uptake is described by Fickian diffusion coupled with a slow relaxation process. Calculated diffusion coefficients are strongly dependent on the cation (K, Cs, Ca, Zn, Al and Fe), decreasing by almost 10^4 for triethylphosphate when the sulfonate proton is replaced by Cs(+1), or Al(+3). In contrast, total solvent uptake is relatively insensitive to proton replacement.

In summary:

1) A method for determining accurate concentration-dependent diffusion coefficients under high flux conditions is demonstrated for water and alcohol permeation through permselective membranes.

2)Conversion of Nafion™ acid form to a sulfonate salt preferentially decreases solubility (especially for monovalent cations) of protic solvents indicating that aprotic molecules are solvating less polar regions of the polymer.

3) Diffusion coefficients and relaxation rates from immersion absorption kinetics are decreased by conversion to the salt, and are very sensitive to the nature of the cation, with lowest permeation and highest selectivity for Ca^{++}, Al^{+++}, and Fe^{+++}.

4) It is suggested that diffusion of moderately polar aprotic molecules in Nafion™ occurs through contiguous laminar microphases primarily composed of perfluoroether side chains.

5) The dimensions and orientation of these microphases are largely dependent on the interaction between solvated sulphonate groups. Since the perfluoroether regions comprise only 30% of Nafion™ the relaxation process involves reorganization of the corresponding microphases which facilitates the diffusion process.

BIOTECHNOLOGY TECHNIQUES TO CHARACTERIZE AND ENHANCE THE ANTIBACTERIAL PROPERTIES OF A NOVEL FOOD PRESERVATIVE

Wayne S. Muller*, Anthony Sikes, Alfred L. Allen and Andy Senecal,
U.S. Army Soldier and Biological Chemical Command,
Natick Soldier Systems Center, Natick, Massachusetts 01760

ABSTRACT

The objective of this study is to characterize the structure and genetics of the bacteriocin produced by *Streptococcus sp.* ATCC 10035. *Streptococcus sp.* ATCC 10035, a reported diplococcin producer, is of particular interest due to its broad spectrum of antibacterial activity. This study consisted of two primary phases of research: (1) To determine the primary and secondary structure of the bacteriocin. (2) To isolate and characterize the gene producing the bacteriocin.

1. INTRODUCTION

Military rations are often subjected to long periods of storage thus requiring rigorous preservation treatments which protects the food however reduces quality and taste. In the military, there is an increasing demand for better tasting foods, food more representative of the commercial sector. Food technologists use hurdle technology, a combination of processing methods which have synergistic effects on prevention of food spoilage and lethality to pathogenic bacteria, to minimize the harsh treatment of foods that affect the quality and taste of food.

In developing a novel, synergistic, hurdle preservation system, a combination of water binding compounds and bacteriocins are used. A bacteriocin used in this investigation exhibited a broader range of activity against food spoilage and pathogenic bacteria than reported in the literature. Due to the broader range of activity of this bacteriocin and the general inherent properties of bacteriocins it is possible, using biotechnology techniques, to enhance the bacteriocin's antibacterial properties.

Bacteriocins are antibacterial peptides that are ribosomally synthesized, unlike antibiotics that are biosynthesized by multistep enzymatic pathways. Bacteriocins produced by Gram-positive bacteria vary greatly in their spectrum of activity. Some inhibit only a single or a few strains of the same species, while others have activities against many strains from different genera of Gram-positive bacteria. The advantage to these gene-encoded peptides is that structural analogs of natural bacteriocins can be constructed by site-directed mutagenesis of the structural gene. By isolating the gene and manipulating by mutation, an altered peptide can be produced having enhanced properties, such as broader inhibition and enhanced bactericidal activity against food pathogens.

2. RESULTS & DISCUSSION

The inhibitory activity of the crude extract from *Streptococcus sp.* ATCC 10035 was assessed against *Lactobacillus plantarum*, *Staphylococcus aureus* and *Bacillus cereus* with varied responses. For *L. plantarum*, a plot of % log survival against increasing levels (50-400 activity units (AU)/ml) of bacteriocin demonstrated a linear reduction of viable cells (Figure 1). The crude

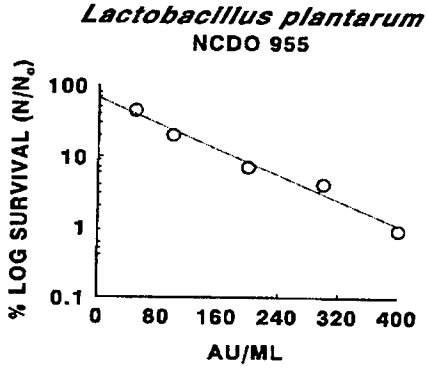


Fig. 1. The effect of varying concentrations of *Streptococcus sp.* ATCC 10035 bacteriocin crude extract on log phase cells of *L. plantarum*.

bacteriocin extract was apparently bactericidal to *L. plantarum*. The bacteriocin extract was inhibitory to *S. aureus* and *B. cereus*, however the effect was transient. When *S. aureus* and *B. cereus* strains were exposed to several concentration of the extract in TSB, growth at 37°C was delayed from 3 to 6 h when compared to the untreated controls. For the treated samples, growth inhibition was apparently transient, since all samples, treated and untreated, attained comparable growth end points.

The *Streptococcus sp.* ATCC 10035 bacteriocin has been isolated and partially characterized. A method developed by Yang et al. 1992 to extract large amounts of bacteriocins from lactic acid bacteria was used to isolate the bacteriocin. Approximately 16 peptides, ranging in size from 5.5kDa–67kDa, were isolated from the bacterial extract. The extract was screened for activity using a bacterial overlay method and indicated that a 5.5kDa peptide exhibited antibacterial activity against *L. plantarum* (Figure 2). Figure 2 shows in lane 1 the protein markers, lane 2 the isolated bacteriocin and lane 3 a clear zone due to the interaction of the isolated bacteriocin and the overlaid *L. plantarum*. Reverse phase HPLC and an electroblot transfer technique to a membrane were used to purify the peptide for amino acid composition and sequence analysis.

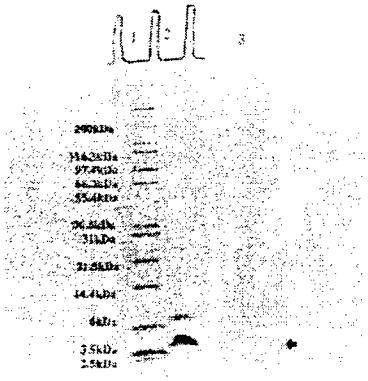


Fig. 2. Lane 3 of a SDS-Page gel, containing the bacteriocin, was overlaid with MRS medium inoculated with *L. plantarum*. In the lower half of gel an oval clearing zone appears indicating growth inhibition of the bacteria (arrow).

The amino acid composition data was very different from what we expected. It has been reported that *Streptococcus sp.* ATCC 10035 is a diplococcin producer; however we found the compositional data to be very different from the reported compositional data of diplococcin (Davey et al., 1981). The presence of lanthionine, a modified amino acid, indicated we had an entirely different class of bacteriocin than the expected diplococcin class of bacteriocin. In addition, the N-terminal sequence data, in which we have a high confidence level of 33 out 45 calls, indicated that we had isolated a unique bacteriocin that had not yet been identified or characterized. In doing a search, no significant homology was identified between our sequence data and the National Center for Biotechnology Information protein sequence databases.

Based on the determined amino acid sequence for the bacteriocin, two DNA probes were constructed and synthesized. The probes constructed were 45 and 54 bases in length and had a high degree of degeneracy. Genomic DNA was isolated from the *Streptococcus sp.* ATCC 10035. In using PCR technology, we found that the two probes did not bind to the genomic DNA. We then did a plasmid preparation to determine if a plasmid was present and contains the gene of interest. The plasmid preparation showed a plasmid present, about 2000bp. Again, using the PCR technology, we did get binding of the primers to the plasmid template indicating the plasmid may contain the gene responsible for the production of the bacteriocin. Further work is being done to verify that the gene is on the plasmid. If this is true it would make the process of identifying the gene as well as the regulatory elements involved in the expression of the bacteriocin, readily accessible.

To summarize, the bacteriocin range of inhibitory activity has been defined. The bacteriocin has been isolated and based on the primary structure data is a member of a different class of bacteriocin than reported in the literature. In addition, the amino acid and sequence data have shown this bacteriocin to be a unique peptide never before identified or characterized. It appears from the PCR data that the gene expressing the bacteriocin is on a plasmid. This gene will be sequenced and characterized along with the plasmid allowing us to clone the gene into an expression vector. Once expressed, the peptide will be examined for inhibitory activity. At this point, directed mutations in the structural DNA can be done to enhance the antibacterial properties of the bacteriocin.

ACKNOWLEDGEMENTS

The authors thank Dr. Charlene Mello, Dr. Michelle Butler, Mr. Steven Arcidiacono, Mr. Robert Stote and Mr. Bill Enslow for their technical assistance.

REFERENCES

Davey, G. P. and Richardson B. C., "Purification and Some Properties of Diplococcin from *Streptococcus cremoris* 346," *Appl. Environ. Microbiol.* Vol 41, pp.84-89, 1981.

Yang, R., Johnson M. C. and Ray B., "Novel Method to Extract Large Amounts of Bacteriocins from Lactic Acid Bacteria," *Appl. Environ. Microbial.* Vol 58, pp.3355-3359, 1992.

APPLICATIONS OF SPATIAL AUDIO DISPLAYS FOR USE WITHIN ATTACK ROTARY WING AIRCRAFT

Russell D. Shilling, Ph.D, LCDR, USN
Naval Postgraduate School
Operations Research/MOVES
Monterey, CA 93943-5118
shilling@cs.nps.navy.mil

Russell L. Storms, Ph.D., MAJ, USA*
U.S. Army Research Laboratory
Georgia Institute of Technology
Atlanta, GA 30332-0862
storms@airmics.gatech.edu

Tomasz Letowski, Ph.D.
U.S. Army Research Laboratory
AMSRL-HR-SD / B-520
APG, MD 21005-5425
trl2@arl.mil

INTRODUCTION

Applications of spatial audio displays (3D Sound) in military environments are rapidly increasing. In the late 1980's, early 3D Sound systems such as the Convolotron and FocalPoint provided researchers with the initial capability of generating real-time spatialized auditory images using headphone technology. Since that time, numerous low-end and high-end systems, capable of generating various spatial auditory images have been offered. The added sense of realism and communication enhancement provided by spatial audio are the main reasons for recent pervasive implementations of these systems. Spatial audio also plays an important role in creating entertainment and training environments immersing participants in both virtual and real world applications.

AVIATION CONTEXT

One emerging virtual and real word application for spatial audio displays is within the context of aviation, specifically within aviation cockpits. The aviation community pioneered the use of simulation and aircraft simulators provide an excellent and cost effective virtual training environment to prepare pilots for the actual (real world) operational environment. The key to a successful aircraft simulator is to facilitate a positive transfer of knowledge from the virtual simulator to the actual aircraft. Conversely, if the simulator trained a pilot to do something different than what is in the actual aircraft (negative transfer of knowledge), the results could prove fatal. The main advantage of aircraft simulators is that pilots gain invaluable education and experience while training in a relatively low-cost technical system (compared to the cost of flying the actual aircraft). In addition, aircraft simulators provide an excellent platform to validate the feasibility of future aircraft systems, tactical doctrines, and user requirements.

EXPERIMENT OVERVIEW

The goal of the presented study was to test the application of spatial audio displays within the cockpit of attack rotary-winged aircraft. An experiment was conducted utilizing the Simulation Training Research Advanced Testbed for Aviation (STRATA), an AH-64A Apache simulator, located at the Army Research Institute (ARI) at Fort Rucker, AL. Five trained AH-64 crews (10 subjects) averaging approximately 2200 hours in the airframe, flew a series of night mission scenarios. Spatial audio displays were used by both the Pilot (P) and the Co-Pilot Gunner (CPG). Both the P and the CPG received the same auditory stimuli, but were independently head-tracked to provide unique spatial cues for each listener. The evaluation incorporated a within-subjects design. Half of the trials used traditional visual displays and the other half used a combination of both visual and spatial audio displays.

PROCEDURE

Spatial auditory threat, navigation, and targeting displays were generated and produced using a Silicon Graphics Indigo 2 and spatialized using a Tucker-Davis Technologies PD1 convolver, CX1 expander, and nonindividualized Head Related Transfer Functions (HRTF). Subjects were free to adjust the loudness of the auditory images to their own comfort levels. All sound

stimuli, including ambient helicopter noise, were presented through the P's and CPG's headsets which were equalized prior to the start of the evaluation. Ambient helicopter noise was presented at 77 dB (A), which is an average noise level experienced by the aircrew while wearing double hearing protection in the actual aircraft. A simple pretest was given to each subject to confirm they could appropriately localize the auditory stimuli. To evaluate the effect of spatial audio displays on aircrew performance, three separate tasks involving threat avoidance, navigation, and targeting were designed and incorporated into the mission scenarios, At the end of the experiment, all Ps and CPGs completed a debriefing questionnaire to evaluate their attitudes towards the individual audio displays and their perception of overall system effectiveness.

RESULTS

Due to the small N (five crews) available for the study, only individual data were analyzed and compared. Four out of five crews found clear performance benefits associated with the use of spatial audio displays in both the threat avoidance and targeting tasks. In debriefing, most subjects (67%) were very enthusiastic about incorporating spatial audio displays in the radar warning systems. Furthermore, the subjects felt that the use of spatial audio in the tactical displays would reduce fratricide and, that the spatialized warnings were both appropriate and useful. Both the Ps and CPGs evaluated the navigation stimulus as moderately effective, but found the stimulus itself to be annoying and distracting from the task. In verbal comments, the subjects reported that the stimulus was distracting and interfered with normal cockpit communication. Given the contradiction between reported effectiveness and annoyance, it can be concluded that the attitudes were not related to the usefulness of an auditory navigation beacon, but rather to an inadequately designed navigation beacon. This would indicate the need to improve methods for developing these types of displays.

CONCLUSIONS

Overall, subjects stated a preference for combined visual and spatial audio displays over visual displays alone. Subjects also suggested incorporating spatial audio into the normal warning displays to give salient cues concerning engine failure. Finally, even though radio communications were not evaluated in the present study, several participants advocated having radio and cockpit communications spatialized.

DYNAMIC NUTRITION MODEL

P.M. Short[1], T.J. Doherty[2], V.E. Middleton[2], I.A. Taub[3], and R.W. Hoyt[4]
[1]Modeling and Analysis Team - Natick Soldier Center, [2]Simulation Technologies, Inc., [3]Natick Soldier Center, and [4]U.S. Army Research Institute of Environmental Medicine, Natick, MA

INTRODUCTION

Performance of the warrior system depends not only on his equipment, clothing, and weapon systems but also on his cognitive and physical capabilities. Nutrition and ration scheduling play a key role in mitigating fatigue and enhancing cognitive and physical performance. This summary describes the creation of the Dynamic Nutrition Model (DYNUMO) to simulate the effects of nutrition and ration scheduling on body metabolic fuel levels, metabolic fatigue, and physical and cognitive performance capabilities. DYNUMO may be used three different ways:

1. as a stand alone tool to analyze nutritional strategies and their effects on metabolic fuel stores;
2. as an algorithm within a food item selection optimization program (e.g., the Ration Optimization Program) to select food items and feeding schedules that optimize physical and cognitive performance capabilities; and
3. as a model object used in scenario-based simulation packages (such as the Integrated Unit Simulation System (IUSS)) to assess the effects of nutrition under different mission scenarios on individual and small unit mission effectiveness.

MODEL REQUIREMENTS

When cells take up and metabolize metabolic fuels, they convert adenosine diphosphate (ADP) to adenosine triphosphate (ATP). ATP provides energy for muscle contraction, membrane transport and other energy requiring processes. Because of the small amount of cellular ATP, ATP production must occur at the same rate as energy expenditure. Metabolic fatigue occurs when performance degrades over time due to inadequate ATP production. ATP production rates depend on the metabolic fuel that is used. Anaerobic glycogen metabolism generates ATP at the fastest rate, while aerobic carbohydrate and fat metabolism generate ATP at slower rates. For "all-out", maximal efforts, only anaerobic muscle glycogen metabolism can produce ATP at the required rates. ATP production slows and eventually stops as muscle glycogen stores are depleted and pH is lowered due to excess hydrogen ion production. For less strenuous activity, aerobic metabolism prevails and a mixture of fuels is used. At these activity levels, the rate of oxygen uptake by the cells is a limiting factor. The amount of stored carbohydrate is also a limiting factor; activity can be maintained at moderate levels only until carbohydrate stores have been depleted and at high levels only until muscle glycogen stores have been depleted. The brain can metabolize only glucose and ketone bodies for fuel and it does not store glycogen. Cognitive performance decrements occur when the blood glucose supply is inadequate. Because liver glycogen is the reservoir used to maintain normal blood glucose levels, the amount of stored liver glycogen is a limiting factor for cognitive performance. To evaluate different nutritional strategies on physical and cognitive performance, DYNUMO must therefore track carbohydrate stores in general, and muscle and liver glycogen stores in particular. DYNUMO must also track the availability of other fuel sources, because these affect the utilization of carbohydrate and muscle and liver glycogen during mixed metabolism.

MODEL DESCRIPTION

DYNUMO is a simplification of the metabolic processes in the human body. Inputs to the model include the amount and complexity of ingested food (carbohydrate, fat and protein), the activity level, and a stress (epinephrine) factor over time. Outputs include the overall caloric balance as well as the status of individual metabolic fuel stores (muscle and liver glycogen, triglycerides, blood glucose and free fatty acids) over time. Ingested food enters the digestive tract and is broken down into its basic components (mono- and disaccharides, amino acids, fatty acids, and glycerol). These components are then absorbed into the blood. From there, nutrients are stored in adipose tissue as triglycerides, stored in the liver or muscle as glycogen, converted to other metabolic fuels in the liver, or utilized for energy. A regulatory system maintains blood glucose at near constant levels and conserves carbohydrate stores. Model algorithms are based on known physiology and biochemistry, with parameter values derived from existing experimental data.

The biochemistry of metabolism is highly complex, incorporating numerous individual metabolic pathways which interact with one another. Each metabolic pathway may include multiple steps, each catalyzed by a specific enzyme. In DYNUMO, all of the steps in a pathway are collapsed into a single net reaction. The reaction rate and regulation scheme are determined by the properties of the enzyme catalyzing the rate-determining step. For example, the glycolytic pathway that converts glucose 6-phosphate to pyruvate is treated as a single reaction whose

reaction rate and regulation are determined by the properties of 6-phosphofructokinase. The model tracks the amounts of substrate and product at the begining and end point of each metabolic pathway over time.

Two types of pathway models are used: pipeline models and quasi-steady state saturation kinetic models.

Pipeline Model:

$$\frac{dS_0}{dt} = -R_{in} - \beta S_0 \cdot$$

$$\frac{dS_i}{dt} = +\beta S_{i-1} - \beta S_i$$

$$\frac{dP}{dt} = +\beta S_n$$

Quasi-steady state saturation kinetic model:

$$\frac{dP}{dt} = v_{\max} \cdot \frac{1}{\frac{k_{M1}}{[S_1]} + \frac{k_{M2}}{[S_2]} + .. + \frac{k_{Mn}}{[S_n]} + 1}$$

where dP/dt is the rate of product generation, R_{in} is the rate substrate flow into the system, S_i represent substrates, β is the rate coefficient for the pipeline model, v_{max} is the maximum value for dP/dt when all substrates are at saturation levels, and $k_{M,i}$ is the concentration of substrate S_i at which $dP/dt=v_{max}/2$ (all other substrates are at saturation levels). Enzyme regulation is handled using the following equations:

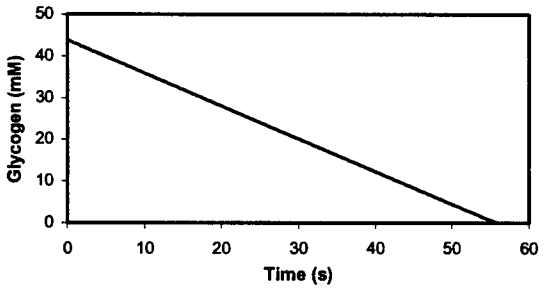
$$v_{\max} = v_{\max,0} \cdot \left(1 + \frac{A}{sf_A} - \frac{I}{sf_I}\right)$$

$$k_M = k_{M,0} \cdot \left(1 - \frac{A}{sf_A} + \frac{I}{sf_I}\right)$$

where A is the activation term, I is the inhibition term I, and sf_A and sf_I are scaling factors. A and I may include substrate concentration(s), product concentration(s), other local factors (e.g. amount of available ATP or Ca^{2+}), or centrally-produced regulatory factors (e.g., Insulin, glucagon, or epinephrine). Insulin and glucagon levels are assumed to be proportional to changes in blood glucose level. Epinephrine level is assumed to increase with increasing activity levels and may also be modified to account for the effects of other stressors.

RESULTS

The graphs below show muscle glycogen depletion resulting from an all-out sprint (2866 kcal/hr).



Simulated muscle glycogen response to an all-out sprint.

This model currently provides realistic predictions of the response to glucose ingestion and high intensity exercise levels. However, the model is relatively weak when it comes to ingestion of other types of nutrients, and lipid metabolism has been given only cursory treatment to date. We expect that parameter value accuracy and robustness will improve as more data are added to the model development database.

SPATIAL-AUDIO (3-D) DISPLAYS IMPROVE SPEECH COMMUNICATION IN THE COMMAND AND CONTROL (C^2V) VEHICLE

COL Nancy Vause, Ph.D., Kim Abouchacra, Ph.D., Tomasz Letowski, Ph.D., Eileen Resta, M.A.

Auditory Research Team, Human Research and Engineering Directorate,
Army Research Laboratory, Aberdeen Proving Ground, MD 21005

Reliable and accurate communication is a critical component of any future combat system. Communication allows enhanced battlefield visualization which improves combat effectiveness throughout the conduct of full spectrum military operations. Previous research confirms field reports that poor communication inhibits combat situational awareness, thereby endangering lives and jeopardizing missions. Peters and Garinther (Army RD&A, Jan-Feb 1990) reported armor mission performance decreased 40% with a 40% decrease in speech communication. On the other hand, if communication is improved by 40%, the probability of mission success will improve 40%!

Several initiatives must work in concert to accomplish this communication "end-state". One initiative investigated by the U.S. Army Research Laboratory (Human Research and Engineering Directorate's Auditory Research Team) is employing state-of-the-art communication audio technology known as spatial audio interface to improve simultaneous multi-channel radio communication as found among vehicles or in command centers. The spatial audio interface is the virtual technology of today in which digital signal processing separates and strategically positions various communication channels into different areas of auditory space, allowing soldiers to perceive headphone-presented sounds in "outside-the-head" locations. Auditory images presented in this manner are commonly referred to as 3-D audio displays (3-DAD), spatial auditory interface displays (SAID), or virtual auditory displays (VAD).

Incorporating this emerging technology enhances communication when soldiers must monitor more than one radio channel with headphones. For example, by the strategic positioning of incoming radio channels in virtual space around a soldier's head, speech messages are more easily heard and soldiers can readily "focus" attention on important messages while perceptually "filtering" other non-critical messages. In addition to radio communication tasks, spatial-audio has the capability of enhancing situational awareness by presenting audio icons or sounds that alert the soldier to look at a gauge that indicates a problem area. There are many potential applications for spatial-audio in the military, and scientists are exploring numerous applications including enhancing situational awareness by presenting sounds that indicate friendly and threat objects in virtual space, thus matching their actual battlefield location; acoustic way-points or "homing" beacons presented via spatial audio in navigational tasks in individual and tele-operated vehicles; enhanced warning signals; aircraft or ship positioning; diver navigation; virtual target acquisition displays; and virtual hearing examinations.

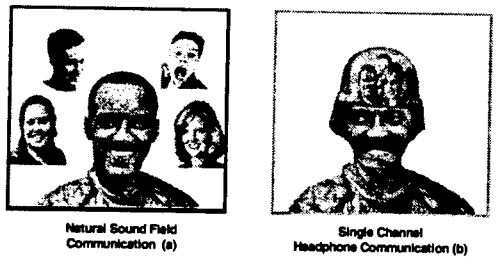


Figure 1. Listening conditions.

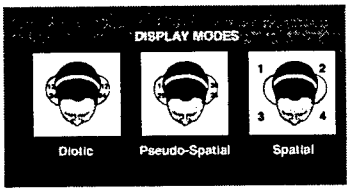
Effective communication or monitoring of auditory signals involves attending to important acoustic signatures while ignoring others, assigning meaning to sounds, and localizing sound sources of interest. In fact, the brain automatically determines the spatial positioning of sounds by analyzing acoustic cues.These time and loudness cues are present because of a sound's arrival time and intensity differences between the two ears. For example, a source is usually located on the same side as the ear that receives the sound *first* and *louder*. Unfortunately, when a soldier dons a headset or a traditional head-mounted communication system, the natural and learned time and intensity mechanisms of localization are lost. Typically, all sounds (warnings, radio traffic, intercom messages) are presented through such systems, with both ears hearing the same signals at the same time at the same loudness levels. If multiple signals are transmitted simultaneously, they are all perceived as located in the center of the listener's head, making communication challenging if not impossible because headphones eliminate the natural localizing cues.



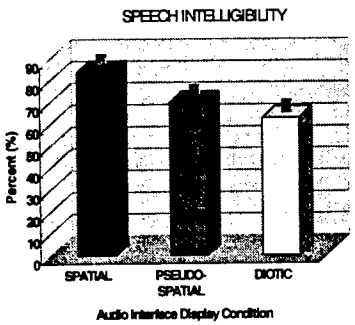
Figure 2. Spatial audio.

Multi-channel communication that presents all signals in the center the head is unnatural listening. As humans, we associate auditory signals and sounds around us, based on direction and distance from us, and we usually draw our visual attention to an acoustically active sound source. The importance of being able to localize sound while wearing headphones or headsets has been demonstrated for many military applications. As a result, equipment designers are working feverishly to restore natural sound localization cues by developing sound systems that synthesize acoustic signals presented over the headphones and give the user the illusion that sounds are emanating from the natural external locations. Spatializing audio signals is the process of perceptually positioning auditory signals in a three-dimensional (3-D) space around a user's head via headphones or a limited number of loudspeakers in order to simulate real-world sounds or voices.This synthesis involves *restoring* the natural effects that our own ears, head, and body have on the sounds and voices we hear, which are removed by listening through a headset by filtering the sound with individual or generic head related transfer functions (HRTFs) .

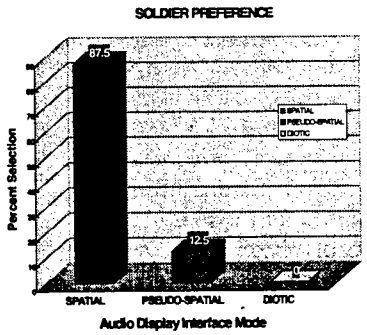
Speech communication improves as voices are separated in space allowing listeners to focus attention on a specific location. In the *true* two-channel headphone transmission, where two independent audio channels (correlation r = 0) deliver signals to the left and right ear of the listener, phantom sound sources are localized at either the left or right ear, respectively (*dichotic listening*). S*tereophonic* two-channel headphone transmission (*pseudo-spatial listening*) provides means to arrange phantom sound sources on the arc connecting both ears of the listener. Stereophonic signal requires some amount of correlation between signals arriving at both ears of the listener. However, in both cases all phantom sound sources are still confined to the space ***inside*** the head. Headset spatialization (*spatial listening*) requires special signal processing to restore the natural effects produced by our own ears, head, and body to produce the illusion that sounds are emanating from natural external locations in three dimensional (3-D) acoustic space .

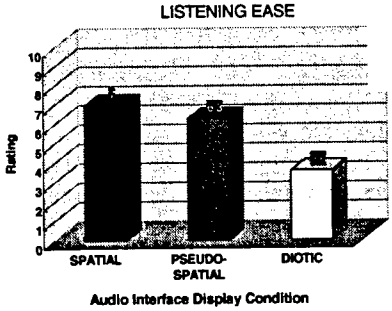


The purpose of this investigation was to examine the effects of audio display (diotic, pseudo-spatial and spatial) on ease of listening and perceived speech intelligibility during battlefield headset radio communications. Additionally, the experiments sought to determine soldier audio display preferences. Our previous studies clearly indicate that angular separation of competing talkers improves speech recognition in quiet and noise. Soldier ratings revealed overwhelming preference for spatial audio display. Results indicated that spatializing simultaneous competing speech messages (1) improves speech intelligibilityand (2) reduces the effort required to understand competing speech signals in multi-channel real-world environments. Furthermore, soldiers overwhelmingly prefer spatial displays and rejected the current diotic communication listening mode.









MICROENCAPSULATED PHASE CHANGE MATERIALS: THERMAL INSULATION APPLICATIONS FOR MILITARY FOOTWEAR

Thomas L. Endrusick*
U.S. Army Research Institute of Environmental Medicine
Natick, MA 01760

James R. Brennick
U.S. Army Soldier Systems Center
Natick, MA 01760

William R. Santee and Richard R. Gonzalez
U.S. Army Research Institute of Environmental Medicine
Natick, MA 01760

ABSTRACT

The U.S. Army constantly evaluates new commercial technologies designed to improve the battlefield survivability of the infantry soldier. This study investigated the performance of a standard military boot and prototypes of the same boot insulated with new phase change insulating materials. The footwear was tested during human trials while volunteers were exposed to moderately cold temperatures. The results showed small improvements in foot thermal comfort when wearing one of the prototype phase change insulated boots compared to the current standard boot.

1. INTRODUCTION

Thermal injury to the feet poses a continuous threat to military personnel deployed to cold and wet operational areas. Significant cases of non-freezing cold injury occurring during military operations have been observed during long-term exposure to both moderately cool/wet and cold/wet environments. Recently, new thermal insulating materials that claim to absorb and release human body heat through a phase change process have appeared on the commercial handwear, footwear, and clothing markets. A phase change material (PCM) can be defined as any material that has the ability to readily absorb and release heat. These new PCMs are proprietary chemical compounds based on paraffin waxes. Current manufacturing processes allow for specific transition temperatures at which point the latent heat of fusion of the PCM is either absorbed or rejected. The wide range of transition temperatures (-40 °C to 132°C) of commercially available PCMs has found numerous applications in the aerospace, automotive, medical, packaging, and protective clothing industries.

For personal thermal insulation applications, PCMs are microencapsulated (15-40 μ in diameter) and then integrated into foams or fibers incorporated into the lining of handwear, footwear, and clothing. Manufacturers claim that encapsulation in a thin (1μ) polymer shell ensures that the phase change process can be continuously repeated without loss of any PCM. The PCMs evaluated in this study were produced with the intent to improve the thermal comfort of the human foot during exposure to moderately cold ambient temperatures. The purpose of this present study was to compare human thermoregulatory responses while wearing a standard U. S. Army boot designed for protection in cold–wet weather and two prototype boots insulated with different PCMs. The study was part of a larger Project Manager-Soldier Pre-planned Product Improvement (P3I) effort to both reduce the weight and expand the operational temperature range of the standard boot.

2. METHODS AND MATERIALS

Eight healthy males with an average age of 24 ±5 years volunteered for the study. The experimental risks were explained to all volunteers before obtaining their written consent. The test protocol was approved by the U.S. Army Medical Research and Materiel Command Human Subjects Scientific Review Board. All volunteers wore a modified version of the U.S. Army Extended Cold Weather Clothing System and a new pair of the test boots each day. The basic experiment consisted of walking on a level treadmill for 15 min at 1.34 $m \cdot s^{-1}$, followed by sitting still on a wooden bench for 70 min at 0°C and at -12.3°C. Temperatures of both small toes (T_{st}), both big toes (T_{bt}), rectal temperature (T_{re}), and a 3-point mean weighted skin temperature (T_{sk},°C) were continuously recorded. Prior to human testing, all three test boots were evaluated for both overall and toe region thermal resistance (R, $m^2 \cdot K \cdot W^{-1}$) using a heated foot model. The three boots tested were the current U.S. Army Intermediate Cold Wet Boot (Control), insulated with 3M Thinsulate™ and two boots

identical to the Control but insulated with different PCMs: Frisby Technologies ComforTemp™ open cell foam (Boot 1); Gateway Technologies Outlast No. 8088™ open cell foam (Boot 2): and Gateway Cortina open cell foam Boot 3). The test temperatures (0 and -12.3°C) represent the upper and lower limits determining the issuance of the Intermediate Cold Wet Boot by the U.S. Army. Table 1 provides a physical description of the test footwear.

3. RESULTS

Overall foot model R values of the dry boots were closely grouped. The highest value measured was with the Control (0.242) and lowest with Boot No. 2 (0.231). Overall wet R values were also closely grouped with both the Control and Boot No. 2 having the highest percentage reduction in overall dry R as a result of a 7 cm water immersion for 18 hr (14 %). Dry toe region R was highest with Boot 1 (0.240) and lowest with Boot 2 (0.225). Exposure to water caused toe region R values to decrease an average of 30% with the highest losses in the Control and Boot No. 1. Absorption of water during the 18 hr immersion caused boot weight to increase an average of 12% with the highest gain in Boot No. 1 (14%). During exercise at 0°C, test volunteer toe temperatures generally rose 3-4°C then gradually declined in all test boots during the 70 min period when the volunteers were sedentary. In general, toe temperatures rose slightly during exercise at –12.3°C then rapidly declined when the volunteers were sedentary. Although mean final T_{st} and T_{bt} values were comparatively high with the Control boot in the 0°C environment, they were the lowest in the -12.3°C environment. Mean final T_{st} and T_{bt} values were higher in both environments when wearing Boot 1. Additionally, the general trend of the Boot 1 temperature curves showed that toe temperatures were cooler during exercise and warmer when volunteers were inactive. These trends also suggest that endurance time would be longer with Boot 1 when compared to the other test boots if the cold exposures had been extended. There were no significant differences in T_{re} or T_{sk} between any of the four test boots during the two different environmental exposures.

4. CONCLUSIONS

Thermal foot model results showed that all test boots were closely grouped in terms of dry and wet thermal insulation with no particular boot indicating that it would provide an increased level of thermal comfort. The U.S. Army Intermediate Cold-Wet Boot, currently issued to personnel operating in cold and wet environments, provided comparatively high toe temperatures at the upper end of the issue temperature range but was less effective at the lower end of the range. Finally, these results show that the phase change material in Boot 1 contributed to maintaining both cooler temperatures during exercise and warmer temperatures while sedentary at the skin surface of both the small and large toes.

Although Project Manager-Soldier has determined that these current phase change materials do not provide for a significant improvement in the environmental protection of the current Intermediate Cold-Wet Boot, it has been recommended that the U.S. Army continue to evaluate developments in improved phase change materials.

Table 1. Identification and Physical Location of Protective Material Layers for all Test Boots.

| | *Foot Skin Surface>>>

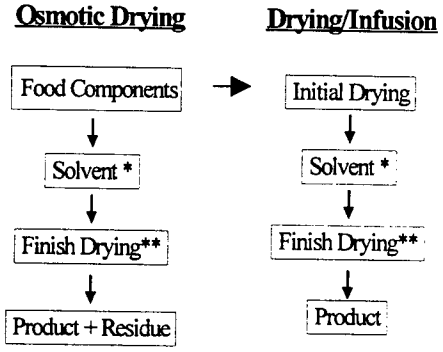
EXPLORING NOVEL DEHYDRATION TECHNOLOGIES FOR MILITARY RATION DEVELOPMENT

T. C. S. Yang*
Advanced Processing and Packaging Team, Combat Feeding Program
Natick Soldier Systems Center, U.S. Army Soldier, Biological and Chemical Command
7 Kansas Street
Natick, MA 01760-5018

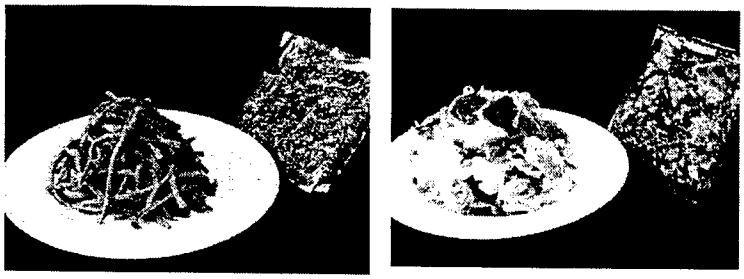
Current wet-packed military rations are bulky and heavy, and dehydrated rations are either of poor quality or expensive. Water is required to provide palatability of wet-packed foods, and in case of dehydrated rations, needs to be removed by expensive low-temperature methods (e.g. freeze drying) to preserve food quality. These problems eventually result in an unnecessary logistic burden or in elimination of the expensive items from the ration system; soldiers often discard the heavy and bulky ration components or are left with few varieties of rations. There is a need to explore novel methods to remove liquids during ration preparation without compromising food quality, and to provide soldiers with rations with reduced weight and volume.

A semi-dry food with infused solute concentration will overcome these problems by using mild drying methods to reduce liquid content that contributes to weight and volume. Using these methods will reduce quality deterioration due to heat damage that occurs during conventional drying methods, and will lower high costs of freeze-drying. Low-heat and vacuum osmosis techniques have been widely applied to foods and non-food commodities (Cohen et al., 1997, 1999; Fito et al., 1994). The methods, with their additional benefits (e.g. nutrition fortification or compressibility), will be transitioned to ration developers as a tool to explore new varieties of rations that were previously impossible due to weight, volume, or cost restrictions. The products can be further stabilized and improved by synergistically combining other microbial growth hurdles such as low pH, antioxidants, and antimicrobial agents, etc. The semi-dry rations will provide reasonable shelf life and be rendered compressible in order to reduce volume.

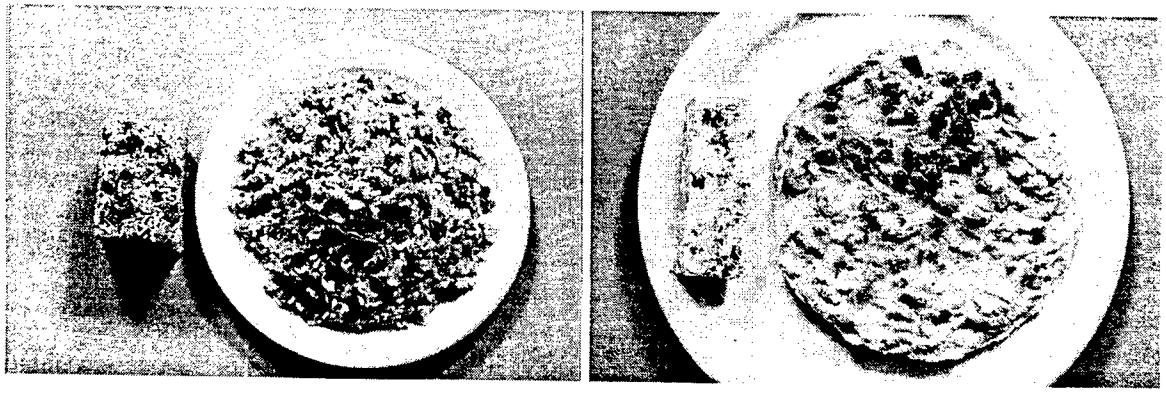
This paper describes exploration and demonstration of novel dehydration technologies, such as a modified osmotic drying and air drying/solvent infusion, in production of shelf-stable, low cube, low weight, instant, high-quality military entrée items and snacks. A 45% solid content was achieved with blueberries and cherries after a 24-hr osmosis at ambient conditions. Raising the temperature to boiling increased the solid content infusion even more. A food/80% infusate solution (e.g. sugar syrup) ratio of 2:1 seemed adequate for rapid osmosis. Most solutes (i.e., sucrose, fructose, dextrose and honey) showed promising effects except for maltodextrin, which was not effective on blueberries. Vacuum osmosis at ambient conditions is a good alternative for boiling when heat damage is a concern. A caffeine uptake of 85-100% and 86-92% was demonstrated in osmotically dried blueberries and carrots, respectively. Air dried/solvent infused vegetables have good compressibility, and a complete meal containing such ingredients will provide a low weight (75% reduction), low volume (66% reduction), high nutrient density, and shelf stable benefits. Osmotic dehydration and air drying/solvent infusion can achieve water removal with relative ease, and also serve as a means for nutrient fortification. This process has both military and civilian applications.



* may contain performance enhancing ingredients
** optional (depending on products)



Compressed carrot and cabbage (Byron Agricultural Co., Australia).



Compressed rice meal and egg omelet products before and after rehydration.

METHODOLOGIES FOR DETERMINING THE IMPACT OF SITUATION AWARENESS ON INDIVIDUAL AND SMALL UNIT EFFECTIVENESS OF DISMOUNTED INFANTRYMEN

Ms. Cynthia L. Blackwell, Human Systems Integration Team Leader
US Army Soldier and Biological Chemical Command
Phone: 508.233.5210; DSN 256-5210; email: cynthia.blackwell@natick.army.mil

Ms. Elizabeth Redden, Chief, Ft. Benning Field Element
US Army Research Laboratory
Human Research and Engineering Directorate
Phone: 706-545-5493, DSN 835-5493; email: reddene@benning.army.mil

1. INTRODUCTION

The United States (US) Department of Defense initiated a program in 1997 called the Military Operations in Urban Terrain Advanced Concept Technology Demonstration (MOUT ACTD). MOUT ACTD is a joint US Army-Marine Corps program led by the US Army Soldier and Biological Chemical Command. The MOUT ACTD's charter is to seek technologies that satisfy 32 jointly derived requirements specific to operations in 'built up' or urban areas. MOUT ACTD evaluates these candidate technologies for military utility and transitions the successful candidates to acquisition programs for further development and fielding.

One of the determinants of military utility that the MOUT ACTD program uses is situation awareness (SA) - specifically, the influence of SA on individual and force effectiveness as a result of the use of MOUT-related capability-enhancing technologies. SA is defined here as the warrior's ability to quickly perceive and then discriminate between facets of the tactical environment, to accurately assess and reassess the where, when and why of that environment, to then know and understand the nature of the tactical situation and to extrapolate near term courses of action based on this understanding. This paper describes the process by which the MOUT ACTD program developed and implemented methods for determining the impact of SA on individual and force effectiveness and reports on emerging results from experimentation.

2. BACKGROUND

With the advent of advanced technologies and battlefield digitization, materiel developers are now required to provide connectivity between the dismounted infantryman (DI) and the digitized battlefield through novel communications, sensing and command and control-enhancing technologies. For example, many U.S. soldiers may soon be provided wearable computers to aid individual and small unit command and control operations. The technologies incorporated in these computers include advanced sensors, communications and navigation. These technologies have the potential to directly impact, both positively and negatively, the ability of the warfighter to perceive his or her environment and to understand his or her place in it. The warfighter must be able to interface with these technologies to best employ the capabilities they provide. Research needs to be done to first understand the impact these capabilities have on the warfighter's cognitive abilities and ultimately to interweave the output of these capability-enhancing technologies into the infantryman's decision-making processes that ultimately impact battlefield outcomes.

This paper will identify groundbreaking work conducted under the MOUT ACTD program in developing and implementing methods to determine the influence SA has on dismounted infantry operations. In this paper we will discuss the development of these methods. We will highlight the Goal Directed Knowledge Elicitation Technique used to generate initial requirements-based SA measures, the use of free-play exercises as an experimentation platform and the evolution from free-play exercises to the development of an Assessment Center for a more controlled experiment. This paper will discuss the use of these tools for obtaining valuable field-relevant data on the influence of SA on individual and unit effectiveness.

3. SITUATION AWARENESS MEASURES OF PERFORMANCE

The MOUT ACTD program has performed 10 Army and Marine Corps experiments. Five of these contained specific limited SA excursions. The MOUT ACTD program have also recently completed a six-week SA/communications experiment with the 3rd Battalion, 75th Ranger Regiment in which we evaluated the impact of SA on units that were provided intrasquad intercoms. Current doctrine does not provide for the use of intercoms by every member of a unit. Traditionally, only unit leaders (squad and up) access this technology. This change in operations is being implemented in the Land Warrior program as well as others. The application of this technology has the potential to effect the unit member's cognitive readiness and so warranted investigation. The purpose of the SA/communications experiment was to: 1) help validate the Freeze Frame methodology as a viable means to quantify, in tactical terms, the enhancements that SA technologies/capabilities provide at the small unit level; 2) quantify SA enhancements provided from a squad intercom, and 3) identify optimal tactics, techniques and procedures (TTPs) for using communications at the intra-squad level. One significant outcome from this work has been the transition of the results of Phase I of our experiment that involved investigation of TTPs for intrasquad intercoms to the Land Warrior program.

4. FUTURE RESEARCH

SA research can provide value both to unit commanders and the materiel development community. In order to fully realize the value SA can provide, more research needs to be done in key areas. These area include the infantryman's internal motivation, risk tolerance, training and innate intelligence as well as the mission environment including mission objective, time of day, weather. Efforts are underway to investigate these areas.

5. SUMMARY

In summary, this paper will discuss the current state of SA measurement for dismounted infantry operations, outline and discuss the development of novel techniques to measure soldier performance as a function of SA, incorporate the results of our latest SA experiment, and suggest future areas of investigation.

Session J
Sensors and Information Processing

Chair
Dr. John M. Pellegrino
U.S. Army Research Laboratory

Co-Chair
Dr. Robert McMillan
U.S. Army Space and Missile Defense Command

Co-Chair
Dr. Nasser Nasrabadi
U.S. Army Research Laboratory

Keynote Address
Dr. Robert Trebits
Georgia Tech Research Institute

THIS PAGE INTENTIONALLY LEFT BLANK

DUAL-BAND FLIR ATR — STATUS AND VALUE TO FCS

Lipchen Alex Chan, Nasser M. Nasrabadi, and Sandor Z. Der
U.S. Army Research Laboratory, Attn: AMSRL-SE-SE
2800 Powder Mill Road, Adelphi, MD 20783, USA

1. INTRODUCTION

The future combat system (FCS) relies on information dominance to compensate for reduced armor on the fighting vehicle. The "See first, shoot first, kill first" paradigm requires that automated algorithms sift through large amounts of data quickly and alert human viewers to potential targets and threats. As illustrated in Figure 1, target acquisition algorithms must also have relatively few false alarms, which can be achieved through increasing the information content of acquisition sensors by the use of multiband or hyperspectral passive sensors.

A number of Army programs are investigating the use of multiple passive bands to improve target acquisition performance. The data sets used for this study, one midwave (MW, 3 to 5 μm wavelengths) and the other longwave (LW, 8 to 12 μm wavelengths), were obtained from the Multi-Domain Smart Sensors (MDSS) program of the Army Research Laboratory. These two bands also have different phenomenology: the LW infrared energy is almost entirely emitted, while during daylight hours the MW contains a combination of emitted and reflected solar radiation. Also, objects often have different emissivities in the two bands, so that even at night objects have different relative grey levels. These differences between the bands have affected the detection results of an automatic target detector. Figure 2 shows the different regions of interest identified by a given target detector on these two bands. Since different conclusions can be made using either MW or LW imagery, we first ask which band alone provides better performance in clutter rejection. The second question is whether combining the bands results in better clutter rejection than using either band alone, and if so, what the best methods are of combining these two bands.

To answer these questions, we use an identical eigen-neural-based clutter rejector in all our experiments. As shown in Figure 3, our clutter rejector consists of an eigenspace transformation and a multilayer perceptron (MLP). The input to the clutter rejector module is the region of interest (target chip) produced by the same target detector, either from an individual band or from both the MW and LW bands simultaneously. An eigen transformation is used for feature extraction and dimensionality reduction. The

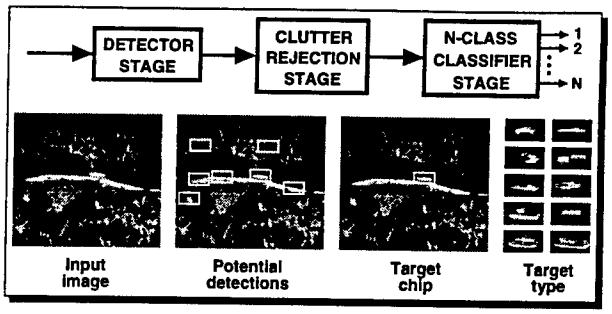


Figure 1. A typical ATR system.



Figure 2. First seven detections at typical mid-wave (MW, left) and long-wave (LW, right) images, with a tank and a jeep near the image center. Note that the tank is detected in the MW band only.

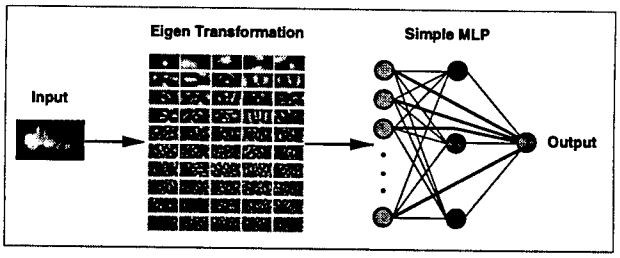


Figure 3. Schematic diagram of clutter rejector.

transformations considered in this paper are principal component analysis (PCA) and the eigenspace separation transform (EST). These transformations differ in their capabilities to enhance the class separability and to extract compact features from a training set. The result of the eigenspace transformation is then fed to an MLP that predicts the identity of the input, which is either a target or clutter.

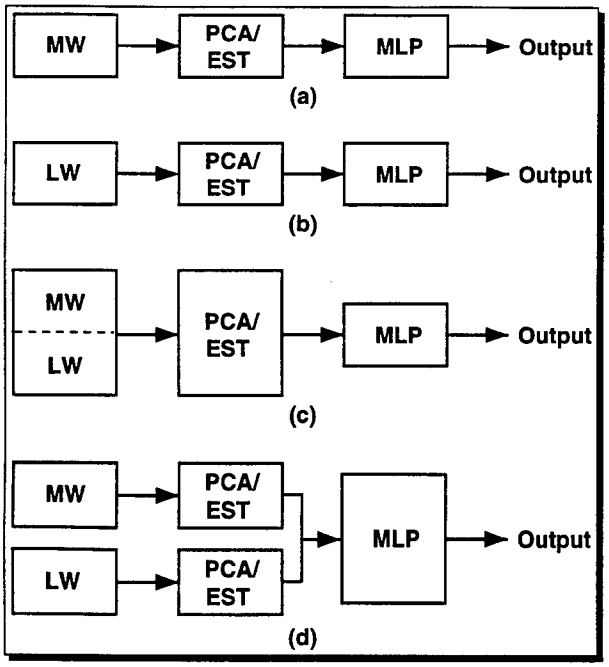


Figure 4. Four different setups for our clutter rejection scheme.

2. EXPERIMENTAL RESULTS

In order to find the answers to the three questions raised above, we designed four different clutter rejection setups. As shown in Figure 4, the first two setups use the individual MW or LW band alone as input. Based on the results from these two setups, we should be able to answer the first question, namely, which band alone may perform better in our clutter rejection task. For setup (c), we stack together the MW and LW chips extracted at the same location before the eigenspace transformations. In this case, the size of each eigenvector is doubled, but not the number of projection values fed to the MLP. If the performance of (c) is better than both (a) and (b), then we may say that there is an advantage of using both bands simultaneously. Finally, setup (d) is almost the same as combining (a) and (b) together, except that the projection values resulting from each eigenspace transformation are now combined before being fed to an MLP with twice as many input nodes. Comparing the performance of (c) and (d), we can find out if it is better to combine the two bands before or after the eigenspace transformation.

The chip extracted from each band has a fixed size of 75 × 40 pixels. The range to the targets varies from 1 to 4 km, so that the size of the targets varies considerably. For the first data set, the chips were extracted from the location suggested by the target detector. Many of these so-called detector-centered chips end up with the target lying off-center within the chip. Furthermore, a clutter chip extracted around a miss point may contain a significant part of a target, which is very similar to an off-center target chip. Therefore, it is almost impossible to find an unequivocal class boundary between the targets and the clutter. We have also created ground-truth-centered chips, which were extracted around the ground truth location of a detected target, as our second data set. However, the size of targets continues to fluctuate considerably at different viewing range. Finally, the third data set consists of chips that were properly centered and zoomed based on ground-truth location and range. The target appears at the center of each chip with a relatively consistent silhouette size.

Table 1. Performance gain (%) by dual-band data.

Data type		Single-band	Dual-band	Gain
Detector-centered	Train	83.43	90.20	6.77
	Test	71.29	78.73	7.44
Ground-truth-centered	Train	91.35	97.02	5.67
	Test	85.88	90.69	4.81
Ground-truth-centered-zoomed	Train	98.93	99.83	0.90
	Test	95.57	97.90	2.33

To reduce the computational complexity while retaining enough information embedded in the chips, we downsampled the input image chip from 75 × 40 pixels to 40 × 20 pixels. For setups (a), (b), and (c), we used the 1, 5, 10, 20, 30, and 40 most dominant eigentargets of each transformation to produce the projection values for the MLP. For setup (d), we used the 1, 5, 10, 15, 20, and 25 projection values of each band to feed the corresponding MLPs with 2, 10, 20, 30, 40, and 50 input nodes, respectively. In each case, five independent training processes were tried with different initial MLP weights, and their best hit rates were recorded at a controlled false-alarm rate of 3 percent. For each data set and setup, the MLP configuration (characterized by the number of its input nodes) with the highest average hit rate was chosen to represent that setting.

In Table 1, we show the average value of the best performance scored by single-band and dual-band setups using the three different data sets. It is obvious that the benefit of dual-band data vanishes gradually, as more and more ground-truth information is added to the process of chip extraction. In other words, if we could find a target detector that was flawless in determining the exact center and range of the targets involved, then the dual-band input would help very little in detection performance for the kind of FLIR imagery that we have. Because such a perfect target detector might not come into existence for a long while, however, we should further explore the benefits of dual-band clutter rejectors under various scenarios. For example, the benefits of using dual-band data could be greatest in high-clutter environments.

USING MAGNETIC SENSORS IN THE BATTLEFIELD AS UNATTENDED GROUND SENSORS

A.S. Edelstein, J. Fine, D. M. Hull, L. D. Flippen, Jr., N. Gokemeijer, and G.A. Fischer
U.S. Army Research Laboratory, Adelphi MD 20783-4605

The objective force will require accurate, reliable information on enemy deployment. The highest quality information on enemy positions will be obtained by fusing the outputs from sensors that respond to different target attributes. By combining inputs from different sensors, the reliability of the information under different conditions can be significantly increased. Magnetic sensors can be part of this suite of sensors because they provide complimentary data and offer some advantages over other sensors. The advantages of magnetic sensors include insensitivity to weather conditions and target motion. Further, it is difficult to make targets nonmagnetic. The reason for this is that most objects contain some ferromagnetic material. Even if the ferromagnetic material in the target is demagnetized to get rid of the residual magnetization, the earth's magnetic field will cause the target to have an induced magnetization. Thus, targets will have a magnetic signature and this signature is present even if the targets are stationary.

The magnetic signature of a target, which is the vector sum of the field due to the residual and induced magnetizations, can be decomposed into its multipole components. For different multipoles at large distances r from the source, the magnetic field is proportional to $r^{-(2l+1)}$ where l=1 for magnetic dipoles, 2 for magnetic quadrupoles, etc. Two major consequences of this r dependence are that (1) the magnetic signature decreases as $1/r^3$ for large r and (2) except very near the source the magnetic signature is that of a magnetic dipole, i.e., the higher order multipoles are difficult to observe. This does not necessarily imply that observed signal will only by that of a moving dipole. If some part of the source moves, e.g., if the gun turret of a tank rotates, then the magnitude and direction of the dipole will change. The rapid decrease of the magnetic signature with distance has the benefit that, if one detects an object, one also knows that it is close to the sensor. An estimate of the magnetic anomaly due to several targets is shown in Fig. 1 as well as experimental confirmation of our estimate of the magnetic anomaly from a tank. The experimental values were taken during tests at Spesutie Island at Aberdeen Proving Grounds using commercial, digital, anisotropic magnetoresistance (AMR) sensors

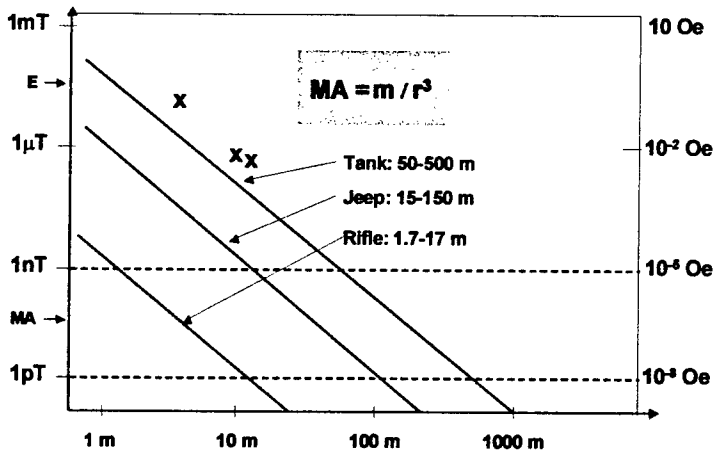


Figure 1 Magnetic anomalies expected from a tank, jeep, and rifle as a function of the distance r away from the object. The symbols E and MA represent the earth's magnetic field and the desired sensitivity of magnetic sensors, respectively. The symbols X are experimental results for the magnetic anomaly from a tank.

from Honeywell. Figure 2 shows some of the original data of the magnetic anomaly observed as a tank moved at constant velocity along a track using of set of 4 AMR sensors arranged in a square 24 ft. on a side with the center of the square 24 ft. from the center of the track. One sees in Fig. 2 that the amplitude of the magnetic anomaly decreases at the position of the more distant sensors, sensors 1 and 2, and that magnetic signature simplifies at the more distant positions to that of a simple dipole.

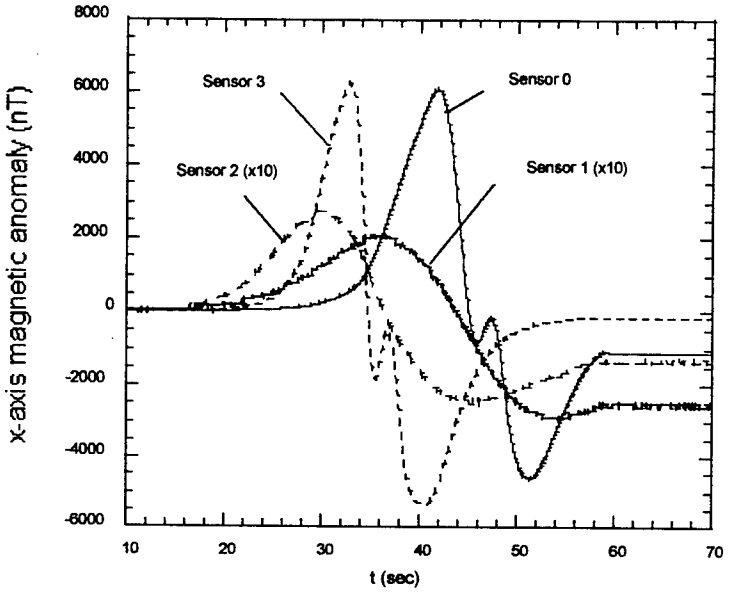


Figure 2 Magnetic fields of a tank measured by 4 AMR sensors positioned as described in the text. Note the fields of sensor 1 and 2 have been multiplied by a factor of 10.

Based upon these measurements, we estimate one could detect the tank at a distance of 30 m. The AMR sensors used in the test can detect a field of 7 nT. The resolution of these sensors is limited by having a 16 bit AD converter. Increasing the sensitivity will increase the detectability range, but because of the 1/r3 decrease of magnetic anomaly signal, one must increase the sensitivity by a factor of 64 to increase the detection range by a factor of 4. Due to the short detection range, a large number of relatively cheap sensors will be required to provide information along a perimeter or to cover a given area. One measure of the quality Q of the magnetic sensors would be the detection length or detection area over the total cost of the system where the total cost must include cost of the sensor, data processor, and communications.

Many magnetic sensors are either too expensive or require too much power to be used in unattended ground sensor system. Fortunately, new types of low-cost magnetic sensors are being developed which have good sensitivities. These sensors are giant magnetoresistance (GMR) sensors[1], spin-dependent tunneling (SDT) sensors[2], and MEMS magnetic sensors[3]. Presently, SDT sensors have the highest sensitivity of this new class of sensors. The change in the resistance of SDT sensors can be as large as 12%/Oe. These new sensors are low-cost because they can be produced by thin film processing techniques. There is considerable current research on these magnetic sensors, because of their potential for delivering even higher sensitivity. The sensitivity of most of these new sensors and many of the older types of magnetic sensors is limited by 1/f noise. Work has begun at ARL on a method of eliminating this 1/f noise.

---

[1] J.M. Daughton, J. Magn. Magn. Mater. **192**, 334 (1999).
[2] J.S. Moodera and G. Mathon, J. Magn. Magn. Mater. **200**, 248 (1999).
[3] R. Osiander, S.A. Ecelberger, R. B. Givens, D.K. Wickenden, J.C. Murphy, and T.J. Kistenmacher, Appl. Phys. Lett. **69**, 2930 (1996).

SUPPORT VECTOR MACHINES AND TARGET CLASSIFICATION

Robert E. Karlsen, David J. Gorsich and Grant R. Gerhart
U.S. Army Tank-automotive and Armaments Command
Warren, MI 48397-5000

ABSTRACT

The ability to segment and recognize objects in imagery continues to be a difficult problem. It is a crucial issue that affects many applications that require automated computer analysis, including target acquisition, machine and robotic vision, and satellite imaging. In this paper, we introduce the Support Vector Machine (SVM) algorithm, which is a wide margin classifier that can provide reasonable results for sparse data sets. We apply SVM to two vehicle classification problems and compare the results to standard neural network architectures. It is found that the SVM algorithm gives equivalent or higher correct classification results compared to the neural networks with some noted advantages.

1. SUMMARY

Currently the Army has many active programs for developing robotic platforms (Gerhart, et al., 1999, 2000). The ability of these platforms to "see" is a crucial element in their eventual use as autonomous vehicles. In order to "see", they must be able to recognize and avoid obstacles in their path. This will naturally entail some sort of "intelligence" in order to make the proper decision in different scenarios. If one is restricted to using only passive sensors, then the application of computer vision techniques is very important for successful implementation.

In this paper we discuss a relatively new algorithm for machine learning that has many nice attributes: the Support Vector Machine (SVM) (Vapnik, 1998; Burges, 1998; Schölkopf et al., 1999). While this algorithm, like other machine learning algorithms, has more general applicability, we are interested in applying it to various problems in image classification. The difficulty with recognizing objects in imagery is the great variability that can occur. Many approaches involve a three-step process, consisting of pre-processing, feature extraction, and a decision algorithm. The pre-processing is generally used to remove redundant information and/or to transform the image to a space where the objects are more easily classified. Examples of this processing include the Fourier, wavelet and Radon transforms, as well as various de-noising techniques. The feature extraction step is often employed to reduce the dimensionality of the problem. Examples of features include peaks in the Fourier spectrum, statistical measures of edge densities, multiresolution energies or a histogram of gray levels. One can also use transforms such as Principal Components Analysis or the Singular Value Decomposition to extract those features that appear to be the most important in the data. In many cases, the type of problem dictates a certain choice for the feature vector. However, in image analysis, the correct features are not always well defined nor easily extracted and much time and effort can be expended searching for an appropriate feature space.

The final step in many systems is a decision module, which takes as input the reduced-dimension feature vector and outputs the classification. Often the decision algorithm contains a learning module, where a sufficiently large number of sample images, with their associated classification, are presented to the algorithm. Internal parameters are iteratively adjusted in order to satisfy a minimum error criterion so as to achieve optimal classification results. Typically, a large number of training samples is required to constrain the error minimization sufficiently and provide good results on other data sets.

In the current application, we avoid feature extraction and work directly with image data. SVM's are wide margin classifiers, which provide reasonable results for sparse data sets, such as images. Being a wide margin classifier means that the SVM not only finds a solution,

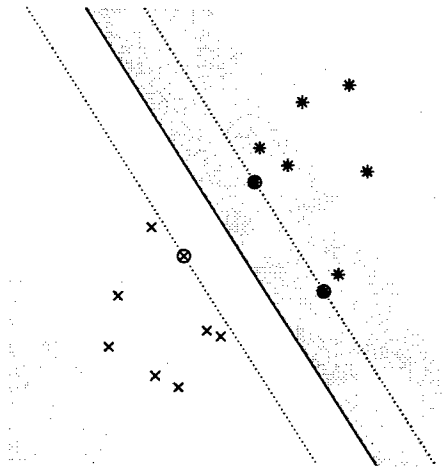


Figure 1: Example of maximum margin classifier.

but it finds a solution that is optimal in the sense that the gap between classes is required to be maximum (see Figure 1). This is conjectured to provide better average performance on testing data. The SVM algorithm has the additional benefits that there are few parameters to adjust and the solutions are unique for a given training set.



Figure 2: Examples of data used to evaluate learning algorithms.

The paper begins by providing a brief tutorial on Support Vector Machines and outlines derivations of some of the important elements. A fast algorithm for SVM training is also discussed. The SVM algorithm is then applied to a variety of data sets, including visual imagery of military vehicles and Synthetic Aperture Radar (SAR) data (see Figures 2). Comparisons are made to Multi-Layer Perceptron (MLP) and Radial Basis Function (RBF) neural networks. For the comparisons, the algorithms will be run within MATLAB® using the MLP and RBF algorithms from the Neural Network toolbox (Demuth and Beale, 1998). We have implemented both the original and fast SVM algorithms in this environment (Karlsen, et al., 2000).

It is shown that the SVM algorithm provides substantially better classification performance than MLP neural networks on both data sets. The MLP algorithm requires numerically finding the global minimum of an error function that has many local minima, which can be difficult to do in many cases. On the other hand, the SVM algorithm involves the determination of the minimum of a quadratic function, which has only a single minimum. We also show that the SVM algorithm with a quadratic kernel achieves classification results similar to the RBF algorithm. However, the RBF algorithm trains orders of magnitude slower than the SVM algorithm, which makes it impractical for large problems. In fact, the SVM is flexible enough to allow RBF-like kernels, as well as kernels that mimic MLP's.

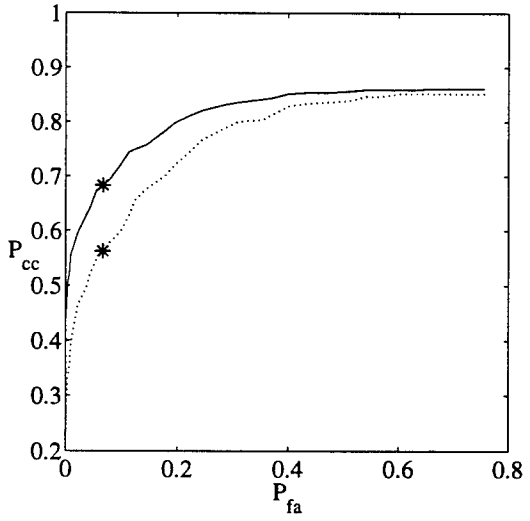


Figure 3: ROC curve for the baseline SAR problem. (BMP – solid, T72 – dotted).

We also show results from a larger SAR classification problem, which required that the fast SVM algorithm be coded as a stand-alone application. We show that the SVM algorithm achieves results much higher correct classification results (see Fig. 3) in comparison to a baseline template matching algorithm (Velten, et al., 1998).

REFERENCES

Burges, C.J.C., "A tutorial on support vector machines for pattern recognition," *Data Mining and Knowledge Discovery* **2**, 1-47 (1998).

Demuth, H. and M. Beale, *Neural Network Toolbox User's Guide*, The Mathworks Inc., Natick MA (1998).

Gerhart, G.R., R.W. Gunderson and C.W. Shoemaker, eds., *Unmanned Ground Vehicle Technology* SPIE Proc. **3693** (1999).

Gerhart, G.R., R.W. Gunderson and C.W. Shoemaker, eds., *Unmanned Ground Vehicle Technology II*, SPIE Proc. **4024** (2000).

Karlsen, R.E., D.J. Gorsich and G.R. Gerhart, "Target classification via support vector machines," *Optical Engineering* **39**, 704-11 (2000).

Schölkopf, B., C.J.C. Burges, and A.J. Smola, eds., *Advances in Kernel Methods, Support Vector Learning*, MIT Press, Cambridge MA (1999).

Vapnik, V., *Statistical Learning Theory*, John Wiley and Sons, New York (1998).

Velten, V., T. Ross, J. Mossing, S. Worrell and M. Bryant, "Standard SAR ATR Evaluation Experiments using the MSTAR Public Release Data Set", *Algorithms for Synthetic Aperture Radar Imagery V*, SPIE Proc. **3370**, (1998). (Available at http://www.mbvlab.wpafb.af.mil/papers/SSAEEutMPRDS/mstar_public_eval.html)

An Electronic Scanning Antenna Concept for Future Combat Systems

Eric Adler, Edward Burke, Robert Dahlstrom, Steve Weiss, Wolfgang Wiebach
Army Research Laboratory

ABSTRACT

There are a number of challenges in developing multi-beam electronic scanning antennas (ESAs) for the Army's vision of Future Combat Systems (FCS). First and foremost is developing a low-cost ESA for long-range sensing. The FCS will require ground-based radar operation out to 10 km and the detection of small targets such as kinetic energy penetrators out to 1 km. On a ground-based system having to contend with very high levels of clutter, radar operation at such ranges requires a narrow-beam antenna. The need for ruggedness and fast scanning might suggest an active phased-array approach. Another focus is on low cost since these ESAs will be proliferated on a large number of FCS platforms. It is possible for an active array with thousands of transmit/receive (T/R) modules to obtain the required small beam width and industry has been focusing on the technical performance and manufacturing issues of T/Rs for years. However, while trends in this field are certainly in the right direction, the necessary amplitude and phase control have prevented the appearance of affordable devices. Further, in an array of T/Rs, the use of simultaneous multiple beams would require a full compliment of T/R's. The requirement for simultaneous multiple beams follows from the realization that the future digitized battlefield requires more and more RF links, while suitable spaces for antennas on a tank or other small ground vehicle are limited.

A beam-former for an ESA that can provide multiple, individually scanned beams for multi-mode, shared-aperture applications is the Rotman lens. Since it does not rely on individual phase-shifting elements for controlling the beam (i.e., it has a lower parts count), the lens can be produced at an attractive cost. It can be implemented at the frequencies suitable for FCS as a shallow cavity or, in an even flatter form, as a pancake-shaped, planar printed circuit. It has the additional advantage that beam formation is accomplished through true time delay. Consequently, the antenna bandwidth can be very wide, so that few, if any, restrictions are imposed on the center frequencies and bandwidths of the individual applications. However, there are a number of significant challenges to expanding a Rotman lens to a functioning multi-beam scanned antenna system. On one side, the lens requires a fast, low-loss switching network to connect the beam ports to the receiver/exciter. Various approaches to low-loss $M\times N$ switching networks, such as micro-electromechanical (MEM) and photonic-actuated switches, are being addressed. On the other side, the lens is coupled and matched to a broadband low-sidelobe aperture array. The challenge will be to maintain low loss and provide a gain-tapered aperture to control sidelobes. The combination of adjacent beams in the switching network can provide some benefits in this regard. Finally, the integration of the power and low-noise amplification will be addressed to maximize the effective radiated power and minimizing the receiver noise figure.

ROTMAN LENS

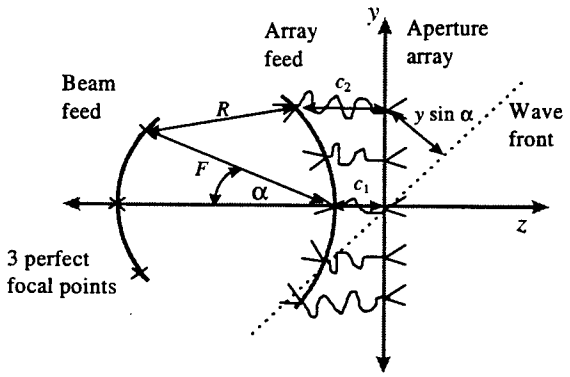
A Rotman lens ESA approach uses true time delay, which allows frequency-independent beam steering. Therefore, it can support multifunction RF sensing requirements. The ESA consists of the beam-former, an aperture, and a beam-switching network. The Rotman lens (Figure 1) is an optical or space-fed device. A source element placed at the beam arc at some off-axis angle creates a wave front with a certain direction; the wave front is produced by means of a particular delay time step between the receptive couplers of the array elements placed along the array contour. The number of elements and element spacing along the array contour ultimately determine beam width, side lobes, etc. The impact on the number of simultaneous beams that can be generated is in the beam-switching network. Other issues are loss and switching speeds for $M\times N$ beam switching requirements.

CURRENT MILLIMETER-WAVE ESA APPROACH

The current millimeter-wave ESA effort integrates the Rotman lens's cavity (Figure 2) to a 34-element horn array and a 2×8 MEMS array. The lens/antenna combination was developed with Georgia Tech and has 19 beam ports. Each beam port has a 3° azimuth beam width and covers a sector of approximately 45°. This lens employs the TE1 waveguide mode, which does render the beam direction slightly dependent on frequency. However, the cavity insertion loss is less than 2.5 dB. The Taylor weighted horn array has sidelobes that are more than 25 dB down. The MEMS array produced by Quinstar uses 8 of 19 array ports for demonstration purposes, has less than 3 dB loss, and switches at microsecond rates. The

insertion of amplifying elements is most easily done on the beam port side of the lens in order not to disturb the equal-time delay requirement between the array ports and array elements. Therefore, we are looking at integrating simple T/R modules between the beam-switching network and the beam ports of the Rotman cavity.

Our current ESA architecture has established a reasonable baseline for FCS requirements. We are continuing to address improvements to each subassembly that makes up the Rotman ESA architecture. With Georgia Tech, we are developing a millimeter-wave Rotman suspended stripline lens. This lens will have 37 beam ports and 57 array ports, offering a tighter beam width and wider scanning capabilities. A photonic actuated 4×18-switching network is being developed with JJW Consultants. This approach may ultimately have lower losses and handle more throughput power than the MEMS approach, at the expense of switching speed. Patch radiators that exhibit broadband performance and polarization diversity are being investigated. We believe this approach will meet both performance and cost projections for the FCS concept.



Path length equality conditions:
electrical lengths $[F + c_1 = R + c_2 + y \sin \alpha]$

Figure 1. Rotman Lens' theory of operation.

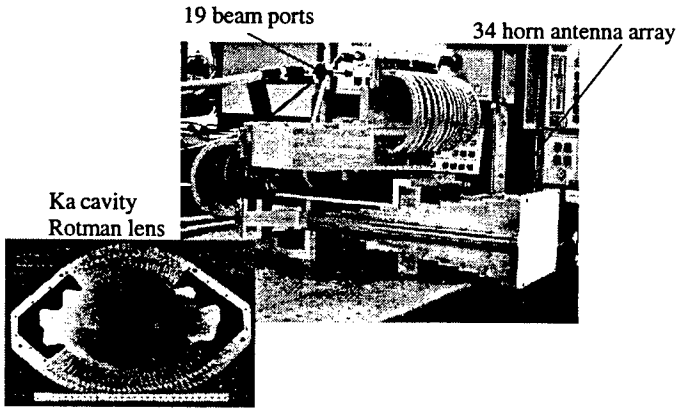


Figure 2. Cavity Rotman lens with horn array.

POLARIZATION IMAGING FOR FUTURE COMBAT SYSTEMS

James D. Howe* [a], Miranda A. Miller [b], Robert V. Blumer [b],
Thomas E. Petty [b], Mark A. Stevens [c], David M. Teale [a], and Matthew H. Smith [d]

[a] U. S. Army CECOM Night Vision and Electronic Sensors Directorate, Ft. Belvoir, VA 22060
[b] TRW Systems & Information Technology, Arlington, VA 22203
[c] Lockheed Martin Missiles & Fire Control – Orlando, FL 32819
[d] Department of Physics, The University of Alabama in Huntsville, Huntsville, AL 35899

ABSTRACT

The survivability of the objective force is critically dependent on target acquisition sensors. Battlefield situation awareness can be improved through the use of advanced sensors that can increase target ID ranges or reduce automated or man-in-the-loop target acquisition times. Passive and active polarization imaging studies have shown improved background suppression that can result in significant improvements to the ability to cue targets and lower false alarm rates. Polarization can also indicate the orientation of a target facet, possibly improving the ability to discriminate the target. This paper describes our efforts to build, calibrate and use passive and active polarization sensors in several wavebands in an effort to better understand polarization phenomenology and to quantify the benefits of polarization imaging for enhanced survivability of the objective force.

1. INTRODUCTION

Previous investigations of the benefits of passive polarization imaging have been very encouraging. Man-made targets tend to have polarized signatures while backgrounds are largely unpolarized resulting in significant background suppression. Recent advances in thermal imaging have led to target acquisition scenarios limited by signal to clutter levels rather than signal to noise. The background suppression afforded by polarization imaging will possibly result in significant improvements to the ability to cue targets and lower false alarm rates, either for a human operator or for an aided/automatic target recognition capability, which will allow our future combat vehicles to maintain a valuable tactical advantage.

Active polarization imaging has also shown great promise as a mechanism for improved target identification. While an active system is more difficult to search with, it has the advantages of stable signatures that are relatively insensitive to diurnal cycling and weather conditions.

Traditional sensing methods for defense reconnaissance and targeting have relied on measurement of the intensity of the radiation, its spectral content or temporal variation. Despite the promise of polarization imaging, research efforts throughout the years have been sporadic, and polarization sensing remains by far the least studied sensing methodology. Significant work remains to be done in the area of clutter characterization and materials and coatings understanding. After we gain a more complete understanding of polarized clutter and target signatures we will be able to determine which missions will benefit from polarization imaging.

In order to investigate polarization phenomenology, NVESD has developed an array of passive and active polarization cameras (Smith et al., 1999a and Howe, 1999). We have developed, calibrated and begun to use complete Stokes imaging polarimeters in the visible, short wave infrared (SWIR), mid wave infrared (MWIR), and long wave infrared (LWIR). These four cameras span the spectral regions from those where signatures are totally reflective (visible), through a band where the signature is a complex mixture of reflective and emitted polarized radiation (MWIR), to a band where the signature is largely due to emission (LWIR). Using the passive polarimeters we have measured tactical target and background signatures and have recorded diurnal signatures of surface mines. The cameras are able to measure all four Stokes components of the radiation, from which one can form images indicating the percent of linear, circular or total polarization, or the direction of the polarization at each pixel.

Because we want to use the measurements from these systems to guide decisions regarding the tactical utility of polarization information, it has been important to carefully calibrate the sensors. While calibration methods are well established for sensors that measure intensity, such as thermal imagers, they do not exist for polarization-based sensors. We have had to establish known polarization sources and develop their use in calibration procedures.

At NVESD complete Stokes active imaging systems are being developed at 830 nm and 1.54 μm. The systems

have the versatility to illuminate a scene with any polarization component and to sense any component of the reflected radiation. The Mueller matrix of each pixel on the target and background can be established. The set of Mueller matrices can then be examined in order to determine which components of polarization will provide optimal discrimination capability. One can also examine which polarization components will enhance target identification. The set of measurements necessary to identify a target can then be reduced to this critical set.

This paper briefly reviews Stokes and Mueller calculus. Polarization camera designs are then presented. Our efforts to calibrate the systems are discussed and compared with typical radiometric calibration techniques. Examples of imagery from the sensors are given. Test results from a representative example field test using the sensors to look at surface landmines are presented. Signal strengths and signal to clutter ratios for polarization and thermal imagery will be compared for diurnal sequences.

2. CONCLUSIONS

The passive polarization signatures of surface mines at steep downlook angles have been measured in the MWIR band. They are presented in this paper as an example of the type of study that has been conducted using the polarization phenomenology sensors developed at NVESD. Diurnal signatures have shown that linear polarization signatures are useful in discrimination of large metal AT mines from clutter objects and backgrounds. Plastic mines and smaller AP mines are difficult to detect through some of the more challenging, colder evening portions of diurnal cycles in MWIR polarization. Because of the improved background suppression from the polarization information, minefield detectability will be improved somewhat when combined with the thermal imagery. For a complete description of passive MWIR landmine signatures, this research should be extended to other system orientation and downlook angles.

We have recently completed the calibration of our LWIR polarimeter that will be used to investigate the passive polarization signatures of landmines as well. It is thought that the LWIR band may be more fruitful since the polarization signatures will be mostly due to target emission. Because of this they may be stronger and less variable than in the MWIR where signatures are complicated by the fact that emitted and reflected components of polarization signatures are often nearly equal and therefore almost completely cancel.

The passive polarimeters in the visible through LWIR bands along with the active polarization imagers will provide the tools needed to establish whether polarization imaging can provide significant improvements in tactical situation awareness for the objective force.

PAPER WITHDRAWN

THIS PAGE INTENTIONALLY LEFT BLANK

MICROWAVE-BASED ARMY AIRDROP GROUND SENSOR

Nicholas P. Rosato, U.S. Army SBCCOM, and
Joseph McGrath*, U.S. ARIEM,
Natick, MA 01760

ABSTRACT

This paper presents the results of work conducted to adapt commercially available Doppler Microwave Radar for use as an airborne ground sensing unit and trigger for a parachute-coupled soft landing mechanism. This work entailed the design and implementation of a micro-controller to interface the commercial sensor with a pneumatic powered landing mechanism. This paper contains the description of the system, along with experimental findings from simulated flight tests.

1.0 INTRODUCTION

The Army Vision 2010 recognized "improved methods of aerial delivery" as a crucial DOD requirement for the rapid deployment of warriors, munitions, equipment and supplies. Worldwide humanitarian relief efforts involving the airdrop of food and medical supplies have become commonplace and are growing in demand. One theoretical method to accomplish the parachute soft-landing of cargo is to decrease the landing velocity of the payload to near zero at ground impact. To implement this method and effect a soft landing, the parachute-coupled payload delivery system must have knowledge representing the position of the payload's bottom surface relative to the ground prior to the landing impact. Non-contacting sensing units would greatly enhance the ability to start the soft landing process. The exploration of the viability of using a commercially developed microwave collision avoidance sensor for soft-landing was undertaken, as a low cost alternative to military range sensors.

1.1 Sensor Theoretical Foundation

The Doppler Effect describes the apparent shift in frequency of a source of oscillation when relative motion exists between observer and source (Skolink, 1980). Continuous wave radar uses this principle to obtain velocity measurement. The shift in carrier frequency of target reflected microwave energy is described by Equation (1).

$$F_d = 2 * f/c * [v * \cos(\theta)] \quad (1)$$

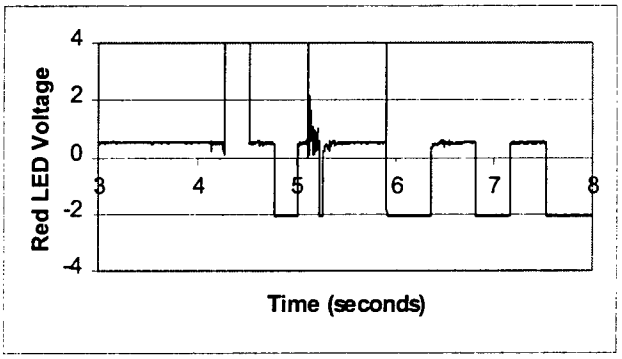
Circuitry that senses changes in carrier frequency can be used to process velocity and produce distance-warning measurements.

1.2 PARACHUTE SOFT LANDING SYSTEM

The supply of medical front line units with plasma and whole blood supplies spawned the invention of a patented soft landing retraction mechanism. The primary function of the mechanism is to draw the payload and the parachute together such that the velocity of the bottom surface of the payload at ground contact is very close to zero.

2.0 EXPERIMENTAL EXAMINATION

Free-fall experiments were performed in order to examine the transient dynamic response of the system. The experiments were used to evaluate the suitability of the collision avoidance radar sensor as a parachute landing ground detector. When the payload is released from rest the radar sensor assumes a linearly increasing velocity as a function of time. In the special case where acceleration is constant (Meriam, 1971) showed that the height of the radar unit as a function of time is given by Equation (1).



$$H = h_0 - 1/2 * g * t^2 \quad (1)$$

Figure 1 Transient Response Behavior

Figures 1 show the typical signal response generated by the free fall flight of the microwave sensing system. The key result determined by this experimental analysis was that a negative edge transition in the red LED signal voltage occurred consistently at 11.3-ft above ground level on average.

3.0 PROTOTYPE CONTROLLER DESIGN

The autonomous soft-landing control strategy consisted of activating the retraction mechanism at some point in time when the payload bottom surface was still in free space. The parachute-coupled soft-landing system descends towards the ground at a quasi-constant velocity level. The red LED voltage signal indicates when the system has flown through the 11.3-ft threshold above the ground in real time. A micro-controller used to monitor the status of this event provides programmable flexibility on when to begin the activation process.

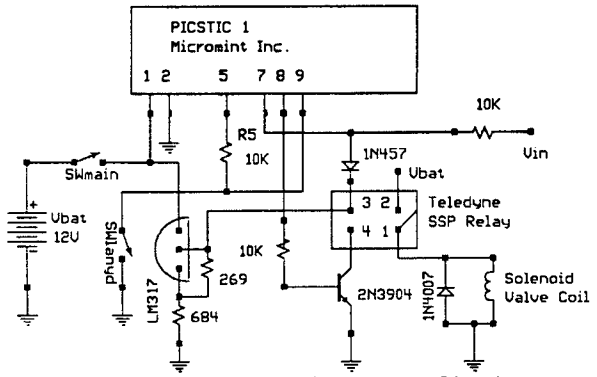


Figure 2 Schematic of Prototype Circuit

Fig 2 contains a schematic of the original prototype circuit used to serve as the interface between the microwave sensor and the retraction mechanism. The circuit is directly connected to the cathode of the indicator unit's red LED. The micro-controller can be programmed to perform a precise count down from the time in which the negative edge transition occurred in the input signal.

4.0 FORT BENNING FLIGHT TESTING

The 250-ft drop towers at Fort Benning were used to deploy the PSLS with the embedded micro-controller. Eleven of the flights were performed using this value of time delay and instrumented with an attached accelerometer that measured the PSLS vertical ground impact shock. Figure 3 is a graph of the superposition of four vertical landing decelerations that the PSLS system experienced during the course of the Ft. Benning flight tests. The data displayed in the graph shows the landing response for the worst and best cases. The 44.4-g peak shock felt at landing represents the most severe landing obtained during the testing. The best landing achieved by the PSLS possessed a 2.7-g impact shock. This represents a 90% improvement in the ability to land the payload. Seven out of the eleven-instrumented flight tests produced a significant improvement to the landing of the PSLS. Two of the eleven flights experienced malfunctions, the device triggered at an altitude far enough above ground to

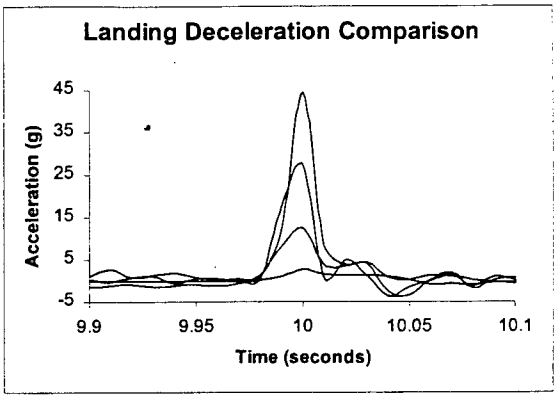


Figure 3 Deceleration Impact of PSLS

not effect a soft-landing. Also, two of the flights exhibited no real improvement to the 27.2-g nominal landing.

CONCLUSIONS

- The commercial sensor with embedded microcontroller demonstrated that autonomous parachute soft-landing is possible.
- For 64% of the instrumented flight tests as configured the sensor with embedded microcontroller produced a measurable improvement in the landing shock experienced by the PSLS.
- Simultaneous time coherent data consisting of the fire control time history, and the landing acceleration needs to be measured to further characterize the performance of the trigger sensor.
- The methodology of using a wait state time delay calculation based upon the crossing of a single distance threshold and average payload descent velocity produced some enhanced control over the landing process.

REFERENCES

John, James E. A., and Haberman, William, "Introduction to Fluid Mechanics", Prentice-Hall, Inc., ISBN 013-483925-0, p. 201, 1971.

Johnson, Guy A., Griffin, Russel E., Laage, Linneas W., "Improved Backup Alarm Technology for Mobile Mining Equipment", United States Bureau of Mines; Circular 9079, p. 18 , 1986.

Howell, C. M. and Hubert, Roger, " Fundamentals of Commercial Doppler Systems and Speed, Motion and Distance Measurements", M/A COM Inc., Technical Paper No. AG320, pp. 1-4, 1987.

Meriam, J., L., "Dynamics", John Wiley and Sons Inc., ISBN 0 471 596019, p. 20, 1971.

Skolink, Merrill I., "Introduction to Radar Systems", McGraw Hill Inc., New York, N.Y., ISBN 0-07-057909-1, p. 68, 1980.

SIMPLE AND ROBUST RADIO MODULATION CLASSIFICATION

Ananthram Swami, Brian M. Sadler
Army Research Laboratory, Adelphi, MD 20783, USA
(aswami,bsadler)@arl.army.mil

ABSTRACT

Automatic recognition of digital modulation formats (i.e., identification of the underlying symbol constellation from observed noisy measurements) is increasingly important as the number and sophistication of wireless digital signaling systems increase. There is an emerging need for intelligent modems capable of quickly discriminating signal types online in real time [Swami and Sadler, 1999]. Modulation classification is a fundamental task in noncooperative (intercept) scenarios. In addition, it may be used to identify interfering signals or to choose the appropriate demodulator during friendly communications. We have developed a low-complexity on-line modulation classification algorithm based on the second- and fourth-order statistics of the data. The algorithm lends itself to a hierarchical structure, and can also be used to mitigate cochannel interference (CCI) Mitigating CCI can affect tactical mobile communications systems in two fundamental ways. First, it enables capacity improvement over current systems due to the ability to reject multi-user interference. This is particularly important in situations where cosite interference is the predominant cause of communications breakdown. The cosite problem has been recognized by CECOM as fundamental and increasingly alarming. Second, mobile communications systems will be much more robust to jamming if they have the ability to reject undesired in-band signals. In order to cope with unknown multipath channel effects, we have extended and optimized a blind alphabet-matched equalizer [Barbarossa and Scaglione, 1997], which outperforms the conventional equalizer based on the constant modulus algorithm (CMA).

Keywords: Signal processing for communications; Modulation classification; Channel equalization.

1. CLASSIFICATION

The problem of modulation classification within a set of known constellations has been fairly well studied in the recent literature. Under the white noise assumption, maximum-likelihood (ML) algorithms have been proposed. However, ML methods suffer from very high computational complexity and are not robust to model mismatches, such as phase and frequency offsets, residual channel effects, timing errors, non-Gaussian noise distributions, and unequal symbol set sizes. These effects arise from the need for blind acquisition, synchronization, and equalization of the signal of interest, and are not modeled in ML-type approaches to the problem. Blind (unaided) equalization of frequency-selective channels is particularly challenging in the case of mobile communications, and can be expected to be imperfect and leave residual distortion effects in the signal that is being fed to the classifier. The problem is further complicated in the mobile case by the bursty nature of the transmissions, which limits data sizes to perhaps a few hundred symbols. Degradations may also be expected due to cochannel and cosite interference.

To cope with this challenging scenario, we have proposed a very-low-complexity online classifier based on the second- and fourth-order statistics of the data [Swami and Sadler, 2000] (the authors received an Army R&D Award for this work in FY99). This approach has a natural robustness to constellation rotation and phase jitter arising from imperfect equalization. The method is particularly effective for discriminating format subclasses, such as phase-shift keying (PSK), pulse amplitude modulation (PAM), and quadrature amplitude modulation (QAM). Thus, the method lends itself to a hierarchical classification structure. This is very desirable, as some classification problems are rather simple, requiring only small data sizes at low to moderate signal-to-noise ratio (SNR), whereas discriminating dense constellations might need significantly more data at higher SNR.

The proposed hierarchical approach, shown in Fig. 1, attempts to first classify the data using "macro" characteristics; it then refines the membership using "micro" characteristics, depending upon the number of samples and/or the SNR. This approach enables us to obtain the best possible solution from the given data.

2. BLIND EQUALIZATION

Our classifier is robust to imperfect equalization; to maintain its performance in the presence of frequency-selective multipath fading, it is desirable to have reliable low-complexity blind equalizers. To this end we have recently combined blind equalization with classification [Swami et al, 2000]. We do this by employing a receiver structure composed of a set of parallel adaptive blind equalizers whose aim is to minimize a cost function matched to a specific alphabet or constellation. The classification procedure compares the different cost functions and selects the constellation that provides the minimum cost. If we specifically impose the finite alphabet constraint (i.e., digital modulation), convergence can be much faster than that obtained with a milder constraint, such as constant modulus. The constant modulus algorithm (CMA) has been shown to be very effective in equalizing nonminimum phase channels blindly. However, CMA suffers from residual inter-symbol interference (ISI) and slow convergence when applied to higher order constellations. We have used a cost function that is specifically tied to the signal constellation. This leads to better equalization and hence less signal distortion, as well as faster convergence. This approach to modulation classification, while of higher complexity than our previous approach, has significant promise in challenging

mobile environments, and is appropriate for short burst transmissions, frequency hopping, and other scenarios.

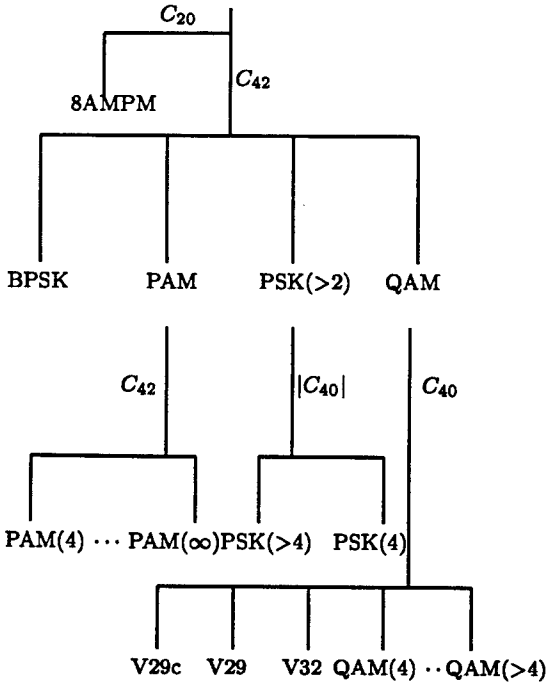


Figure 1. Hierarchical classification scheme.

3. EXAMPLES

We illustrate the performance of the classifier via two examples taken from our previous work [Swami and Sadler, 2000];[Swami et al, 2000]

Example 1: Eight-Class Problem. We illustrate the performance of our classifier on a difficult eight-class problem,

$$\Omega_8 = \{ \text{BPSK, PAM, 4-PSK, 8-PSK, V32, V29, V29c, 16-QAM} \}.$$

Table 1 shows the confusion matrix corresponding to SNR of 10 dB and $N = 1000$ samples. Results are based on a 1000 Monte-Carlo trial. Notice the near-perfect performance of our classifier; most of the errors are due to the misclassification of the V-29 and 16-QAM symbol sets.

Additional examples are provided in [Swami and Sadler, 2000] and [Swami et al, 2000], illustrating the robustness of the classifiers to signal distortions due to imperfect synchronization equalization, phase rotation, phase jitter, frequency offset, non-Gaussian noise, cochannel interference, and self-interference.

Example 2. Fig. 2 shows the performance of our single-channel AMA equalizer for a V29 signal, with channel weights $\mathbf{h} = [1, 0, 0.5]$, $N = 400$ samples, 30 dB SNR, and 20-tap equalizer. Note that the AMA output is clean, whereas the CMA output is unacceptable.

ACKNOWLEDGEMENTS

This work was partly supported by an ARL Director's Research Initiative Grant; parts of the work have been reported in [Swami and Sadler, 2000] and [Swami et al, 2000] in collaboration with Prof. Sergio Barbarossa at the University of Rome "La Sapienza".

Table 1. Confusion matrix for eight-class problem, using the hierarchical classifier. SNR = 10 dB, N=1000 samples, and 1000 trials. C1-C8 correspond to BPSK, 4-PAM, 4-PSK, 8-PSK, V32, V29, 16-QAM, and V29c.

	Classifier output							
	C1	C2	C3	C4	C5	C6	C7	C8
C1	1000	0	0	0	0	0	0	0
C2	0	1000	0	0	0	0	0	0
C3	0	0	1000	0	0	0	0	0
C4	0	0	0	1000	0	0	0	0
C5	0	0	0	0	998	2	0	0
C6	0	0	0	0	5	879	116	0
C7	0	0	0	0	0	71	929	0
C8	0	0	0	0	0	0	0	1000

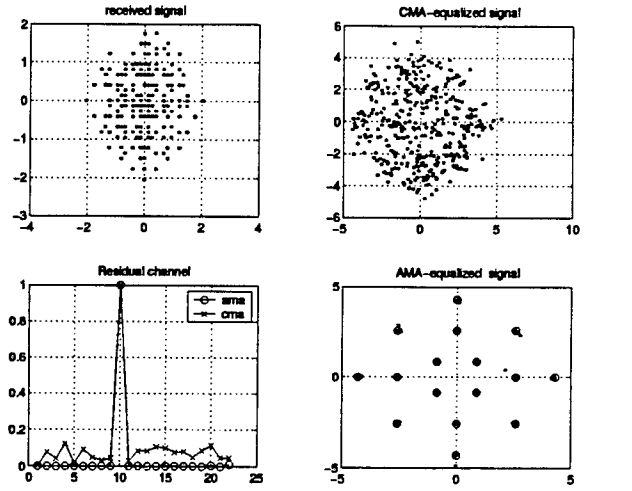


Figure 2. Example 2: V29 signal. Raw unequalized input (top left), CMA equalized data (top right), the AMA equalized data (bottom right) and the CMA and AMA weights (bottom left).

REFERENCES

[Barbarossa and Scaglione, 1997] Barbarossa, S. and Scaglione, A., "Blind Equalization Using Cost Functions Matched to the Signal Constellation," *Proc.* 31st *Asilomar Conf. Sig. Sys. Comp.*, Pacific Grove (CA), vol 1, 550–54, Nov 1997.

[Swami and Sadler, 1999] Swami, A. and Sadler, B., "Issues in military communications," *IEEE Signal Processing Magazine,* 16(3), pp. 31–33, March 1999.

[Swami and Sadler, 2000] Swami, A. and Sadler, B., "Hierarchical digital modulation classification using cumulants," *IEEE Trans. Commun.*, 48(3), pp. 416–429, March 2000.

[Swami et al, 2000] Swami, A., Barbarossa, S., Sadler, B. and Spadafora, G., "Classification of digital constellations under unknown multipath propagation conditions," *Proc. SPIE, Digital Wireless Comm. II,* Orlando, FL, April 2000.

SELECTIVE AND SPECIFIC PERSONAL BIOSENSORS FOR ORGANOPHOSPHATE CHEMICAL TOXINS COMPOSED OF POLYURETHANE IMMOBILIZED ENZYMES

Richard K. Gordon*, Alper T. Gunduz, Shawn R. Feaster, and Bhupendra P. Doctor
Division of Biochemistry, Walter Reed Army Institute of Research,
503 Robert Grant Road, Silver Spring, MD 20910-7500

Organophosphorus (OP) nerve agents are a serious threat to US military personnel. These agents are some of the most potent toxic agents and are specific inhibitors of acetylcholinesterase (AChE). The sequel to AChE poisoning is a cholinergic crisis in man; the clinical effects are directly related to acetylcholine accumulation. Nerve agents can exist as a vapor and be inhaled, can contaminate skin, or can be ingested if food or water is contaminated. Thus, detection of organophosphorus compounds in all of these forms is of paramount importance to prevent casualties due to OP exposure.

Traditional detection and analysis of these nerve agents is performed using gas and liquid chromatography and mass spectrometry. More problematic is the measurement of nerve agents in mixtures, which require extraction procedures and manipulations. These analysis techniques currently have significant drawbacks when considering an individual kit for field deployment, including lack of portability, simplicity, cost, reliability, and rapid results. An alternate technology uses biosensors, which are widely used for detection of diverse biologically, pharmacologically, or clinically important compounds. Enzyme sensors have the advantage of selectivity, sensitivity and, most important, specificity, ease and portability, and markedly simplified instrumentation. Enzyme biosensors can behave as a dosimeter, accumulating only those inhibitors demonstrating exquisite selectivity for the specific enzyme, while ignoring all other environmental interferences. Enzymes act as biological amplifiers, in particular, the cholinesterases are known as a class of enzymes with one of the highest turnover rates. Thus, inhibition of this enzyme can prevent tens of thousands of turnover of molecules (indicators) per minute, providing a marked change between activity (uninhibited enzyme) and no activity (inhibited enzyme). While a variety of biosensors based on cholinesterases (ChEs) immobilized *non-covalently* have been described, they all suffer from leaching from the surface to which the enzyme was non-covalently deposited, sensitivity to denaturing conditions, and short half-life and lack of enzyme stability when in solution. For instance, existing fielded kits for chemical agents (a spot detector kit) uses an eel acetylcholinesterase (AChE) also non-covalently applied and dried onto a fiber sheet to detect organophosphate chemical toxins. These sensing tickets can be exposed to air or vapor only. In another format, the existing kit has been modified for testing liquid samples: a few drops of aqueous material can be placed onto the absorbent fiber/ion exchange paper containing the enzyme. Yet there still remains several significant drawbacks to this kit: we show below that the eel enzyme in these existing kits leaches from the surface to which it was non-covalently deposited and that the enzyme still has an extremely short half-life in solution. This means that the kit can be used to sampling only a few drops of aqueous solution and it lacks the ability to test other potentially OP-contaminated samples such as soil, or long-term testing of bodies of water.

Recently, we combined a porous polyurethane foam formed *in situ* from water-miscible hydrophilic urethane prepolymers and enzymes such as ChEs, producing immobilized enzyme products (figure 1, 2). Some of the advantages of this technique imparted to the immobilized enzymes include resistance to denaturating buffers and the retention of similar kinetic characteristics as the soluble form of the enzyme. Most important, the enzyme will not leach from the polyurethane support so that the biosensor or OP badge now can be used to test a variety of samples from soil, water, or air. Finally, the immobilized enzyme retains most of its original activity after prolonged storage, and it is resistant to the detrimental effects of low and high temperatures. Appropriate enzymes can be chosen to mimic the sensitivity of human enzymes and toxicity to present or future novel OPs. Badges can be

Covalent ChE Incorporation at Aliphatic Amino Group(s)

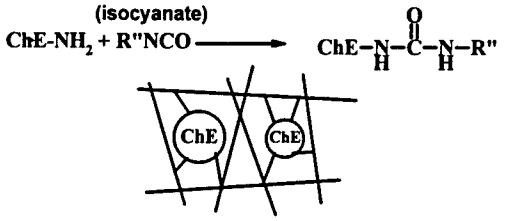


Figure 1. Reaction scheme of ChE and polymer.

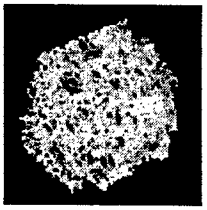


Figure 2. Biosensor, consisting of immobilized AChE and polyurethane polymer. The biosensor depicted here is about the size of a pencil eraser.

designed for multiple purposes in addition to detection of OPs, such as the differential determination of the specific OP present as a chemical toxin. Finally, the badges can yield not only a visual indication of OP contamination like existing kits, but by using a combination of enzymes, they can provide a chemiluminescent, electrochemical, or fluorescent signal that could be processed in a hand-held detector.

A significant difference and advantage the ChE immobilized enzyme biosensor has over the existing OP detector kit is that immobilized enzymes do not dissociate (leach) from the biosensor. We found that the existing tickets, even those specifically designated for testing water, lost more than 80% of their original activity and ability to detect OPs after barely a few minutes of exposure to various aqueous conditions, including pH 8 phosphate buffer or natural water sources such as brackish water from Edgewood, MD and fresh water from the Allegheny River, PA. Therefore, these tickets can reliably detect OPs only in a drop or two of aqueous material placed onto the ticket. In marked contrast to the existing kit, when we exposed immobilized mammalian AChE or BChE badges to the aforementioned water sources at room temperature, the badges retained high activity, even after more than 60 days of continuous immersion. This contrasts to the minutes obtained for the existing OP test ticket. Also, the immobilized enzymes in the badges were resistant to microbial induced degradation since the badges showed identical activity regardless of whether the water samples were autoclaved or left untreated. Thus, the immobilized enzyme biosensor can be used to test water for OPs or even left in the liquid source for extended periods at a remote location, or placed in soil, washed, and then the activity of the badge determined.

We have developed several alternate indicator systems for the ChE badges: OP-exposed badges can be evaluated by visual color changes or by chemiluminescence, and by fluorescence for increased sensitivity in a hand-held detector. The chemiluminescent badges use a coupled reaction of immobilized ChE, choline oxidase, and horseradish peroxidase. Like the immobilized ChEs, we found that soluble and polyurethane immobilized choline oxidase had similar kinetic parameters, and the pH dependent activity of the two forms of choline oxidase was identical. In uninhibited badges, the chemiluminescence indicator persisted for several minutes and was absent in OP-inhibited badges. This type of badge would be suitable for night detection without the requirement for a power source. Another indicator used in the biosensor badge was Amplex Red, a reaction which generates an intense visual red color that is also fluorescent. The fluorescent chromagen yielded about a 4000-fold increase in sensitivity compared to the visual chromagen. This fluorescent indicator would be particularly suitable for use in a hand-held fluorometer, which could provide quantitative values of ChE inhibition and therefore an extrapolated amount of OP present in the sample (air, water, dirt, or swabbed from instruments).

The immobilized biosensors we are developing will have an additional unique attribute not present in the current non-immobilized detector: a field system capable of differential identification of the type of OP contamination that occurred, e.g., sarin or soman. The badge would be subdivided into compartments; each containing immobilized enzymes that behave uniquely to the different OPs. For instance, organophosphorus hydrolase (OPH) hydrolyzes sarin more readily than soman. To this end, we have also immobilized OPH and OPAA (organophosphate acid anhydrase), exploiting the same prepolymer used for the ChEs and choline oxidase. Another enzyme required for the differential detector is immobilized laccase: this enzyme hydrolyzes the OP VX preferentially over the G-agent OPs, and it is readily available from commercial sources. Currently, we are evaluating polyurethane immobilized laccase for long-term stability and kinetic properties of VX hydrolysis.

The immobilized polyurethane enzymes will make versatile biosensors for detecting organophosphates. These badges, by virtue of their high capacity for enzymes, stability, specificity, sensitivity, and resistance to harsh environmental conditions, can be used under diverse conditions encountered by troops in the field. The ability to identify the OP toxin in real-time in the field using the immobilized differential detector would aid in treatment and securing the contaminated area, and in the identification of illegal use of OPs. These badges should be suitable for a variety of sensor schemes for both chemical weapons and pesticides, and they could be incorporated into the telemedicine initiative as fluorescent or electrochemical organophosphate probes. Lastly, the immobilized enzyme badges are lightweight, and require no energy source for qualitative results or will require minimal power (battery) using hand-held optical units.

*Telephone: 301 319 9987; fax: 301 319 9571;
DSN: 285 9987

E-mail: Richard.Gordon2@na.amedd.army.mil

Acknowledgement: This work was supported in part by the Office of Special Technology (Tracy D. Cronin, Program Manager, Chemical Biological Radiological and Nuclear Countermeasures, Technical Support Working Group, Crystal Gate-way North, Suite 116, 1111 Jefferson Davis Highway, Arlington, VA 22202).

LINEAR SHIFT INVARIANCE OF THE ATMOSPHERIC TURBULENCE MODULATION TRANSFER FUNCTION FOR INFRARED TARGET ACQUISITION MODELS

Keith Krapels, Ronald Driggers, and Richard Vollmerhausen
U.S. Army Night Vision and Electronic Sensors Directorate
10221 Burbeck Rd
Fort Belvoir, VA 22060-5806

Norman S. Kopeika
Ben-Gurion University of the Negev
Beer-Sheva, Israel

Carl Halford
University of Memphis
Memphis, TN 38152

SUMMARY

The U.S. Army's next generation of thermal imagers, third generation FLIRs, has a three-pronged approach: inexpensive uncooled low performance imagers, large-format medium performance staring arrays, and ultra-narrow field-of-view (UNFOV) high performance sensors. The later UNFOV sensors are applied to ranges beyond the capabilities of current day sensors. Under these conditions, contributions from atmospheric turbulence blur become significant.

It is desirable to include the effects of atmospheric turbulence blur in the NVESD infrared target acquisition model NVTherm. The Ben-Gurion University (BGU) target acquisition model treats turbulence blur as linear shift invariant (LSI) MTF. The LSI turbulence blur is in addition to the effect of time varying turbulence distortion in an UNFOV scene. This distortion is not LSI and hence cannot be included in the NVTherm model as an MTF. This research investigates whether there is an LSI blur associated with turbulence that can be separated from time-varying distortion.

The effort described here was focussed on the validity and utility of the BGU-type treatment of turbulence blur for inclusion in NVTherm. NVTherm models the imaging system as an LSI system with component MTFs. Inclusion of additional MTFs, to account for the atmosphere, is desired.

In most atmospheric modeling activities that include imaging system performance, two atmospheric properties are considered: atmospheric attenuation and path radiance. These characteristics are predicted either with a gross "broad-band Beer's law" or using more sophisticated models such as LOWTRAN or MODTRAN. For wide FOV systems, these models yield good predictions and the blur associated with atmospheric light propagation is small compared to the point spread function of the sensor. Recent published research suggests that the atmospheric blur is frequently the limiting resolution of the overall system. The turbulence blur is larger in the midwave infrared than in the longwave infrared band. Further, the atmospheric blur associated with narrow and ultra-narrow field of view systems must be considered in overall system performance. Figure 1 shows four bar targets and a tank image that are seen on a long horizontal path in the midwave infrared band. The image shows degradation due to atmospheric turbulence (some of which is manifested as image distortion). The distortion is clearly seen in the edges of the four-bar targets that should have been imaged as straight lines. It is not clear, however, whether the overall system is limited due to the blur, or point spread function, of the turbulence.



Figure 1. Four Bar Targets Through Atmospheric Turbulence.

The transfer function associated with turbulence is split into a long exposure and a short exposure models. The long exposure model transfer function is

$$MTF_{LE} = \exp(-57.4a\xi^{5/3}C_n^{\ 2}\lambda^{-1/3}R) \qquad (1)$$

where a is a wave shape constant, ξ is the spatial frequency in cycles per milliradian, C_n is index of refraction structure parameter, λ is the wavelength and R is the path length. For short exposures the transfer function is

$$MTF_{SE} = \exp(-57.4a\xi^{5/3}C_n^{\ 2}\lambda^{-1/3}R[1-\mu(\xi/D)^{1/3}]) \quad (2)$$

where D is the imaging sensor aperture diameter and μ is 0.5 in the far field and 1 in the near field. There are straight-forward methods for estimating the index structure parameter. These parameters are dependent on the meteorological data along with the path geometry.

The research is a step in the improvement of target acquisition modeling towards UNFOV infrared imagers. Current models used simplistic approaches to atmospheric effects and were limited to transmission and path radiance characteristics. Overall, the blur associated with the atmosphere has not been addressed and, as infrared imager performance extends to longer ranges, must be considered (regardless of whether the effect is LSI). In addition, the LSI characterization of turbulence blur can lead towards improved image restoration techniques. NVESD is working with the Army Research Laboratory in this characterization.

LIBS: AN EMERGING CHEMICAL SENSOR TECHNOLOGY FOR FIELD USE IN WARFARE AND PEACETIME APPLICATIONS

Richard T. Wainner, Kevin L. McNesby, Andrzej W. Miziolek
US Army Research Laboratory
AMSRL-WM-BD
Aberdeen Proving Ground, MD 21005-5069

Russell S. Harmon
U.S. Army Research Office
Research Triangle Park, NC 27709-2211

Patrick D. French
ADA Technologies, Inc.
Littleton, CO 80127-4107

SUMMARY

Laser Induced Breakdown Spectroscopy (LIBS) is a chemical sensor technology that was first demonstrated in the laboratory twenty years ago and is now in the early stages of commercialization. The Army Research Laboratory has been active in LIBS research for over a decade [Morris *et al.*, 1990; Locke *et al.*, 1990; Simeonsson *et al.*, 1993; Simeonsson *et al.*, 1994; Williamson *et al.*, 1998; Lancaster *et al.*, 1999; Wainner, *et al.*, 2000]. The early work was focussed on the use of uv pulsed (excimer) lasers for the production of sparks in gas flows [Morris, 1990] while more recently we have developed LIBS for the detection of halon replacement compounds and refrigerants [Lancaster, 1999] and Pb in environmental samples [Miziolek, 2000]. In the past few years there has been a significant growth in the number of LIBS applications of interest to the military. Application areas include the detection of toxic metals in soils, waters, and airborne particulate matter (e.g. DU particles from kinetic energy weapon testing and use) as well as the detection of hazardous chemicals such as explosives and chem/bio agents. One important application that has been recently identified is the possible use of a hand-held LIBS probe to determine the nature of buried solid objects. Such a sensor would be used in support of mine and UXO detection. Part of our effort in developing LIBS sensor technology involves collaboration with industry towards the commercialization of this technology. This is being done through the Small Business Innovation Research (SBIR) program.

Much of the attraction of LIBS is based on the fact that it is a straightforward technique which requires components whose size and cost is shrinking with advances in technology. This makes it possible for the development of a man-portable reliable field sensor. In LIBS, a solid-state pulsed laser (e.g. Nd:YAG) is focussed on a sample to form a plasma. The plasma, whose initial temperature is 10,000+ °K, produces atomic, ionic, and molecular fragment emissions characteristic of the elemental composition of the irradiated sample. A LIBS sensor can capture the plasma emission spectrum between 200 and 900 nm per each laser spark event. This capability results in tremendous chemical analytical power since most elements emit light throughout the 200-900 nm region. By monitoring the specific wavelength of the detected light and determining its relative intensity, information is generated in real-time concerning the chemical composition and abundance of an unknown or target substance.

During the initial stage of the SBIR program project, a field-portable LIBS instrument was developed by ADA Technologies, Inc. (Fig. 1) and the concept of detecting Pb in paint and soil was validated under laboratory conditions through the analysis of samples with differing Pb contents. During the second stage of the project, the portable LIBS instrument was upgraded and field tested in Panama, Colorado, and California for the detection of Pb in paint flakes and on painted surfaces. The LIBS instrument also was able to detect Pb collected on PM-10 air filters from local air monitoring stations in Panama City, Panama as well as Pb in contaminated soils from sites at Fort Carson, Colorado and Sierra Army Depot in California. This paper discusses the strategy that the US Army has developed to deal with issues related to military site contamination.

In the past few years our group has demonstrated the use of LIBS for the sensitive detection of nanogram amounts of a number of energetic materials including RDX, Comp B, Comp A3, Comp C4, Ammonium Nitrate, Black Powder, PBX 9502, and M43. Initial laboratory results using research grade lasers and

intensified gated array detectors have indicated that each energetic material produces a unique and identifiable spectrum in the 350-600 nm range. As little as a nanogram of sample is consumed per each laser shot and each laser shot produces a usable spectrum. Similarly, we have demonstrated the ability to detect nanograms of a chemical warfare agent (CWA) simulant dimethyl methyl phosphonate (DMMP) using a single laser shot. Currently LIBS is being evaluated as a real-time detector of aerosols containing depleted uranium (DU) for a field test related to the Gulf War Syndrome problem. Yet another application pertains to the ability of LIBS to identify the nature of solid objects during mine detection. In this application a man-portable LIBS sensor would be incorporated into the ground-penetrating probe via optical fibers and would be used to probe the chemical composition of a solid object that is detected by the probe. It has already been demonstrated that LIBS can easily differentiate between glass, rock, aluminum can, steel, and plastic when the full spectrum (200-900 nm) is captured per each laser shot. This technology would be complementary to existing mine detection sensors and would be particularly valuable in eliminating the false alarm rates that are frequently encountered. Ultimately, we envision LIBS sensor technology being incorporated into future FCGV and military robotics platforms providing an unprecedented capability in identifying toxic and hazardous chemicals in real-time in the field.

REFERENCES

Lancaster, E.D., McNesby, K.L., Daniel, R.G., and Miziolek, A.W., "Spectroscopic Analysis of Fire Suppressants and Refrigerants by Laser-Induced Breakdown Spectroscopy," *Appl. Opt.* Vol. 38, pp. 1476-1481, 1999.

Locke, R.J., Morris, J.B., Forch, B.E., and Miziolek, A.W. "A UV Laser Microplasma-Gas Chromatography Detector: Detection of Species-Specific Fragment Emission", *Appl. Opt.*, Vol. 29, p. 4987, 1990.

Morris, J.B., Forch, B.E. and Miziolek, A.W. "A Novel Detector for Gas Chromatography Based on UV Laser-Produced Microplasmas," *Appl. Spectrosc.*, Vol. 44, pp. 1040-1043, 1990.

Simeonsson, J.B., and Miziolek, A.W. "Time-Resolved Emission Studies of ArF Laser Produced Microplasmas", *Appl. Opt.*, Vol. 32, p. 939, 1993.

Simeonsson, J.B., and Miziolek, A.W., "Spectroscopic Studies of Laser-Produced Plasmas Formed in CO and CO_2 Using 193, 266, 355, 532, and 1064 nm Laser Radiation", *Appl. Phys. B*, Vol. 59, p. 1, 1994.

Williamson, C.K., Daniel, R.G., McNesby, K.L. and Miziolek, A.W. "Laser-Induced Breakdown Spectroscopy (LIBS) for Real-Time Detection of Halon Alternative Agents", *Anal. Chem.*, Vol. 70, p. 1186, 1998.

Wainner, R.T., McNesby, K.L., Miziolek, A.W., Harmon, R.S., and French, P.D., "Analysis of Environmental Pb Contamination: Comparison of LIBS Field and Laboratory Instruments," submitted to *Spec. Acta. B*, 2000.

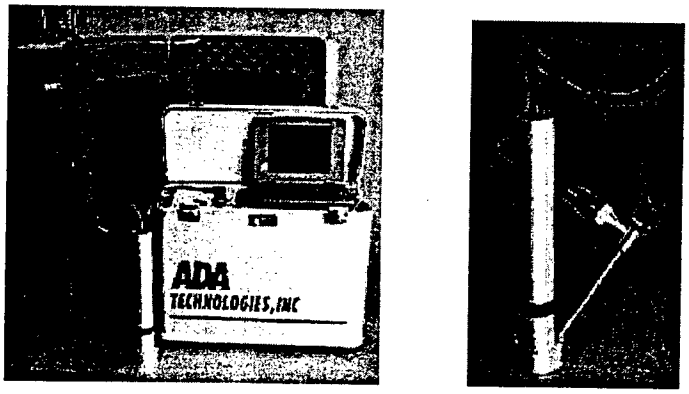


Figure 1. Field-Portable LIBS Sensor (Left- Complete unit weighing 41 lbs., Right- Sampling wand housing the laser head and fiber optic emission pickup to spectrograph(s) in main unit).

SENSING TARGETS IN FOLIAGE USING MULTIPLE LADAR IMAGES TAKEN AT DIFFERENT LOCATIONS

Dr. John F. Dammann Jr.
U.S. Army Research Laboratory
2800 Powder Mill Rd
Adelphi, MD 20783-1197

Locating and identifying targets hidden under foliage is currently a major concern for the U.S. Army. Over the past years, the problem has been extensively researched, with much of the research centered on low-frequency synthetic aperture radar (SAR) sensors. The low frequency of these radars allows them to penetrate the foliage but also imposes a fundamental limitation on their capability to resolve objects. This, in turn, makes target identification very difficult, particularly in areas where civilians are present and identification must be made with a high degree of certainty.

Laser radar (ladar) sensors can generate near-optical quality three-dimensional (3-D) images and, as shown in this paper, can offer a promising way to find targets under foliage. Since the ladar is not good for wide-area searches, the SAR could be used to find areas containing possible targets and the ladar could then be used to provide detailed images of these areas. If the ladar could adequately penetrate the foliage, the extremely rich, high-resolution images it provides would allow the high-certainty target identification that is required.

One technique for achieving foliage penetration for a ladar is to take multiple images of the same area from a variety of aspects. Even though at any particular ladar location the foliage may obscure most of the target, some of the energy from the ladar may pass through small gaps in the foliage and illuminate portions of the target. As the sensor moves, different portions of the target are illuminated and over a reasonable span of different locations, most of the target area will eventually be visible. If these images can be stitched together into a single 3-D image of the scene, then the target can be reconstructed from the fragments visible in each image.

Under Defense Advanced Research Projects Agency (DARPA) sponsorship, the U.S. Army Research Laboratory conducted a proof of principle experiment. ARL mounted the ladar on a boom, moved the boom along a treeline with the ladar cantilevered over the foliage, and took a series of overlapping images. An M35 truck was parked under the trees to determine whether a vehicle could be identified through the foliage.

The ARL ladar possesses at least two attributes that make it advantageous for penetrating foliage. It ranges using FM/cw radar principles with range resolution being 0.25 m by the classical Rayleigh definition; superresolution (i.e. through a mathematical interpolation technique) improves the range accuracy to 1 to 2 cm. The high range resolution that can be achieved with superresolution is crucial in forming a high-quality composite image. A second advantage of the ARL approach is that it is a linear system; that is, any number of target and clutter returns will be separated in the range image if they are physically separated by more than the 0.25-m range resolution of the system. This is a very important feature for foliage penetration where foliage and target returns are quite likely to be in the same pixel.
The ladar is raster scanned with a pair of galvanometer-driven mirrors. The scan parameters were set to collect 46- × 48-pixel images over a 14° × 14° angular region, resulting in a 0.3° difference between pixels. This undersamples the scene, but the compositing makes up for this undersampling.

The boom consists of a vertical section that raises the ladar to approximately 28 m above the ground and a horizontal telescoping section that allows the ladar to be moved perpendicular to the treeline approximately 10 m. ARL drove the boom parallel to the treeline for about 20 m, so that a 10- × 20-m area was covered. The area chosen had deciduous trees and data on a 1 × 1-m grid were taken for a total of 200 images.

At each mirror position in the scan, the ladar measured the amplitude of the scene return as a function of range. I applied a peak detection algorithm to produce one or more target ranges for the position. Knowing the sensor location and mirror pointing direction, I then calculated the 3-D location of each object in the scene.

The overlapping images were 'stitched' together to form a 3-D scene. Scanning an image took approximately 1 minute; during this period the boom moved a significant amount. It has a complex, natural oscillation pattern with both pitch and roll components and a period of about 4 s. This makes it necessary to track the ladar position and attitude during the scan. We use a high-precision kinematic GPS receiver sampled at a 10-Hz rate to measure the location and an inclinometer to measure the ladar pitch and roll at a 5-Hz rate.

The composite 3-D scene shows the truck to be clearly visible and identifiable, even by an unskilled interpreter, when shown in the interactive 3-D stereoscopic display that

I have developed. In this summary, I show 2-D images from this 3-D display. Despite a substantial degradation in the information content of this format, the power of the 3-D imagery is still evident. All the pictures show the same scene with the M35 truck. Figure 1 is from an overhead perspective as the data was originally taken. Since the truck was painted with camouflage paint, there is very little contrast with the surrounding foliage. Figure 2 shows the scene rotated so the viewer is just above ground level. The truck is plainly visible now, as well as the structure of the trees

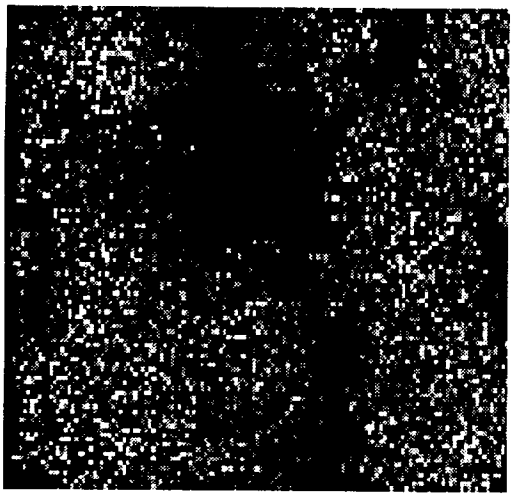


Fig 1. Original perspective

In addition to the scenes themselves, I present a number of image statistics. These include the height distribution of the ladar hits and the percent of the ladar rays that hit the ground. This percentage varies markedly with the ladar position, and I show this spatial variation. Forestry researchers are performing a characterization of the foliage in the experimental areas to compare these areas to other forested areas throughout the world. When these results are paired with our image data, they will provide an estimate of the ability of an airborne ladar sensor to image below a tree canopy in a variety of scenarios.

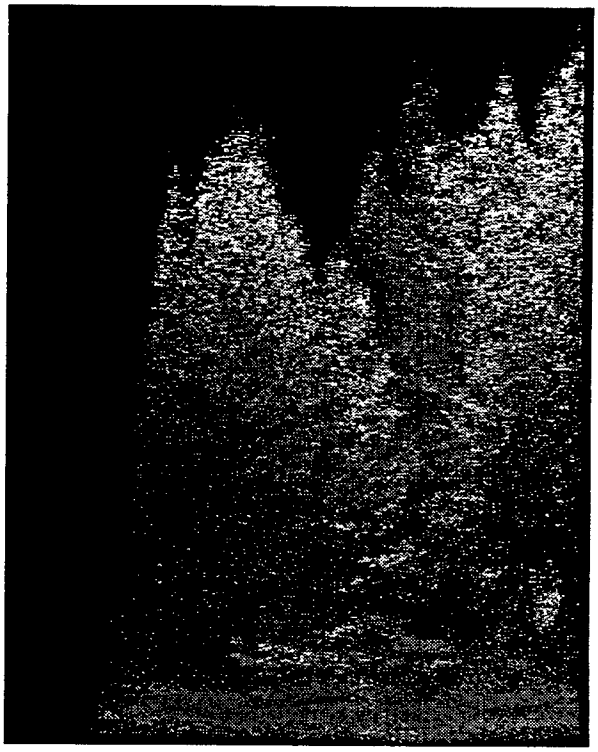


Fig 2. Rotated perspective

LASER-SCANNING ELECTRONIC HOLOGRAPHY

Bradley W. Schilling and Glen C. Templeton

US Army CECOM RDEC
Night Vision and Electronic Sensors Directorate
Ft. Belvoir, VA 22060

SUMMARY

Research in the area of three-dimensional (3D) imaging by electronic holography addresses a critical need of the Army objective force: the need for electronic deception solutions in the optical and electro-optical regimes. Current, state-of-the-art holographic recording and reconstruction techniques cannot meet the 3D-imaging requirements for electronic deception and associated programs. Therefore an effort has been initiated which includes an in-house research effort in electronic holography and 3D-imaging technology. An innovative holographic recording technique has been developed based on scanning an object or scene with a complex optical field, originating from a single laser, and collecting the reflected light using a photodetector. The technique shows promise for future Army applications for many reasons, stemming primarily from the scanning and electronic (verses photographic) aspects of the system. For instance, due to the electronic nature of the technique, the photographic processes associated with traditional holographic recording can be avoided. A hologram is recorded serially, pixel-by-pixel, using a photodetector and is stored as a digital image. This is consistent with the digital battlefield concept, and in addition, real-time holography is possible with this technique. Another advantage, inherent in holography in general, is that in a hologram 3D information is stored in a 2D array, in this case a 2D digital image. The electronic nature of the system offers another advantage over traditional holographic recording systems in the area of spectral flexibility. Theoretically, it is possible to record holograms by this technique in any spectral band where a laser source and detector combination exist. Therefore, the technique is particularly well-suited to multi-color holography and offers the possibility of holographic recording at infrared wavelengths, a previously unexplored area of holography. The scanning aspect of the technique gives it another advantage over traditional holography by relaxing the size constraints of the object or scene to be recorded. In our research, special attention has been placed on demonstrating the ability to record holograms of 3D reflective objects which will lead to holograms of large-scale objects and/or a wide field-of-view scene. For these reasons, laser-scanning electronic holography represents a major advance toward meeting future Army needs in the field of holography.

The technique is based on scanning the object or scene with a complex laser field called a Fresnel zone pattern (FZP) and collecting the reflected light via a photodetector. The FZP is generated by superimposing a plane wave with a spherical wave from the same laser. For heterodyne detection, the FZP is temporally modulated by using two interfering waves at different temporal frequencies adjusted by acousto-optic devices. The 3D location of the scatterer, or object, is encoded in the position and size of the FZP as it scans the object. The experimental setup necessary to create the heterodyned FZP and scan the object is shown in Figure 1. The beam from a laser operating at frequency ω_0 is split into two paths by the first beamsplitter. The first path is simply collimated and then focused by lens L_1, producing a spherical wave at the operating frequency of the laser, ω_0. The second laser path is directed through an acousto-optic modulator (AOM) operating in the Bragg regime, and diffracted into many frequency-shifted beams in accordance with the grating equation. The first order diffracted light is utilized because it is shifted in frequency by Ω, where Ω is the operating frequency of the AOM. This beam, at frequency $\omega_0 + \Omega$, is collimated to produce a plane wave and then combined collinearly with the first beam at the second beamsplitter. The resulting interference pattern is the desired heterodyned FZP laser field. This interference pattern is scanned over the object with intensity reflectance $|\Gamma(x,y,z)|^2$ and the reflected light is collected by a photodetector. The scanning action results in the spatial convolution of the scanning field intensity and the object, thus encoding each individual point in the object by a FZP. The photodetector current, therefore, contains 3D information pertaining to the scanned object. The current is demodulated, amplified, digitized and synchronized with the scanning action of the mirrors. The final image is a

hologram of the scanned object. An example hologram of a simple 3D object, consisting of three points in space, is shown in Figure 2 a).

Optically, the real image reconstruction is achieved by passing a plane wave through the hologram and allowing it to propagate some distance, z, where the diffracted light forms a real image of the recorded object. The optical reconstruction method can be realized using a laser and spatial light modulator containing an image of the hologram. Image reconstruction can also be achieved numerically using Fourier techniques. Figure 2 b) shows such an image reconstruction, in which hologram has been numerically deconvolved with the system's point spread function (PSF). The PSF used for image reconstruction was recorded experimentally at the z distance corresponding to the right-most object point, which was the middle point in the z, or depth, dimension. With these experimental results, we demonstrate laser-scanning electronic holography. Holograms of 3D reflective objects have successfully be recorded and image reconstruction is demonstrated using an experimentally recorded system PSF.

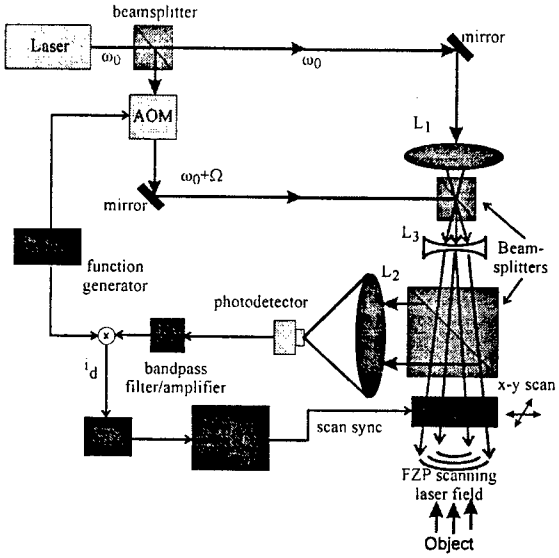


Figure 1 – Experimental setup for laser-scanning electronic holography

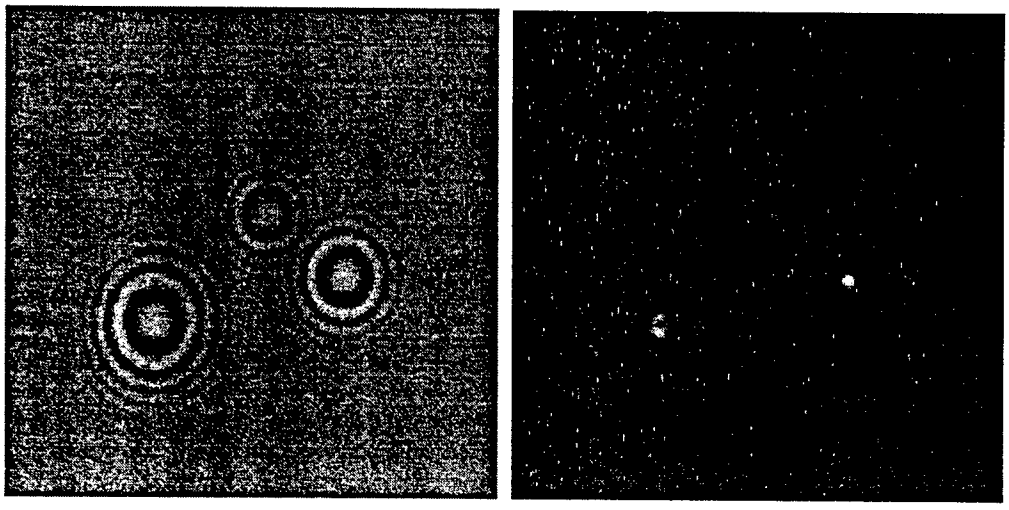


Fig 2 a) Hologram of three point objects at different x,y, and z locations, and b) numerical image reconstruction of one depth plane using an experimentally acquired system PSF for $z=z_2$

DEVELOPMENT OF A CLUTTER COMPLEXITY MEASURE *

K. R. Namuduri L. M. Kaplan
Dept. of Computer Science Dept. of Engineering
Center for Theoretical Studies of Physical Systems
Clark Atlanta University
Atlanta, GA 30314

N. N. Nasrabadi L. A. Chan
U.S. Army Research Laboratory
2800 Powder Mill Road
Adelphi, MD 20783

ABSTRACT

The performance of automatic target recognition (ATR) systems are sensitive to sensor, geometry and scene parameters. One important scene parameter, clutter complexity, measures the extent that the objects in the background of a scene are target-like. In this paper, we describe a technique to derive a clutter complexity measure as a weighted sum of simple image statistics. To this end, we isolate partitions of the U.S. Army COMANCHE database of FLIR imagery so that the other phenomenological parameters are held constant. Then, we use one partition for training where we select the weights so that the resulting measure has maximal correlation with ATR performance bounds over this partition. We then verify the clutter complexity measure by measuring its correlation against ATR performance over other partitions of the database.

1 INTRODUCTION

Future Combat Systems (FCS) will combine computational and cognitive intelligence data for improved battlefield situational awareness. It is important for such a system to understand the level of significance for each piece of information, i.e., processed data, relative to all other information. For instance, it is crucial that the FCS understands the performance envelope of its automatic target recognition (ATR) systems so that it can decide how to act on a target detection and/or identification decision. To this end, the FCS requires a simple quantitative evaluation of its sensor imagery that is known to correlate well with the fundamental ATR bounds.

A large number of parameters affect the performance of automatic target recognition (ATR) systems including sensor, geometry, and scene parameters. Researchers have started to investigate the fundamental performance bounds for ATRs as a function of these parameters. This paper reports on our efforts to evaluate imagery on the basis of the clutter complexity. The term, clutter complexity, refers to the extent that the cultural clutter, i.e. the nontarget objects that comprise the background in the scene, appears target-like. The clutter complexity is also proportional to the number of such target-like objects. Currently, no satisfactory measure exists that quantifies clutter complexity. We are working on ways to devise and justify such a complexity measure.

To be practical, the computation of the measure can not require a large number of operations, and the measure should not require any *a priori* information about the objects in the scene. Note that the measure predicts a bound and not the exact performance of a particular ATR. For example, a low value for the complexity measure for an image would indicate that there exist an ATR that will exhibit a low false alarm count for that image. However, the particular nature of an ATR may generate a large number of false alarms for that scene. On the other hand, a high complexity value for an image must indicate that no ATR can exhibit a low false alarm count for that scene. Currently, no satisfactory measure exists that quantifies clutter complexity. We are working on ways to devise and justify such a complexity measure.

2 The Approach

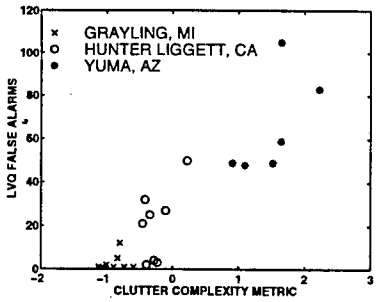
The clutter complexity measure must correlate well with ATR performance bounds, given other factors such as target/sensor geometries are held constant. The initial framework consists of the following steps performed on a database of images: (1) characterization of ATR performance bounds, (2) development of a clutter complexity measure as a sum of weighted image processing features that correlates with the ATR performance bounds over an appropriate subset of im-

*Prepared through collaborative participation in the Advanced Sensors Consortium sponsored by the U.S. Army Research Laboratory under Cooperative Agreement DAAL01-96-2-0001. The U.S. Government is authorized to reproduce and distribute reprints for Government purposes notwithstanding any copyright notation thereon.

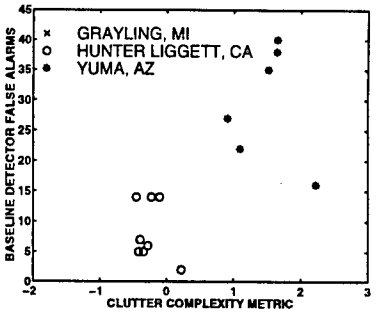
agery, (3) validation of the clutter measure using real ATR performance.

To characterize ATR performance bounds, we use a very finely tuned ATR that takes advantage of a priori information that is unavailable to a realizable ATR. Specifically, the targets that actually exist in the scene are used to develop the exemplar and set the operating points, i.e. thresholds, associated with the ATR approach. In our study, we use an optimized version of the wavelet-based learning vector quantization (LVQ) approach developed at the U.S. Army Research Laboratory (ARL) to develop templates for each target in the scene [1]. Then, we correlate the tuned template with the entire scene and find regions of interests by comparing the correlation values against a threshold. To make the operating point consistent for each scene, we set a threshold that is proportional to the correlation value corresponding to the actual target object in the scene. Finally, we count the number of false alarms after clustering the hits.

The clutter complexity is computed as a weighted sum of eight different image processing features that describe the scene background, e.g. texture features. These features were inspired from [2, 3]. The weights are selected in order to maximize the correlation between the clutter measure and the ATR bound measurements. The final development stage compares the clutter measure against real ATR performance. Currently, we count the number of false alarms in each image when applying the ARL Federated Laboratory baseline FLIR detector [4].



(a)



(b)

Figure 1: Scatter plots collected over a subset of the COMANCHE database: (a) Approximate LVQ ATR bound versus the clutter complexity measure and (b) Baseline FLIR detector performance versus the clutter complexity measure.

3 Experimental Results

We use partitions of the COMANCHE database to illustrate the complexity measure formed from a weighted sum of image processing measures. The COMANCHE database contains images collected by a fielded FLIR system. Each partition includes all images containing a single high contrast vehicle at a range of 2km and an aspect angle between 80° and 100°. These partitions contain images collected at three different sites: (1) Grayling, MI, (2) Hunter Liggett, CA and (3) Yuma, AZ. Over a single partition, every image contains approximately the same number of pixels on target so that clutter is the only variable that affects ATR performance. Figure 1(a) shows a scatter plot of the LVQ ATR false alarm counts versus the clutter measure for a HMMWV partition. The threshold for the LVQ ATR was set low in order to allow for the false alarm count to have enough variability to characterize complexity. The correlation coefficient between the measure and the LVQ ATR is 0.91. Interestingly, the measure is able to separate the three collection sites where Grayling and Yuma contain the easiest and hardest clutter respectively. Figure 1(b) provides the scatter plot of the false alarm count for the baseline detector versus the complexity measure over the HMMWV partition. Unfortunately, detection results over the Grayling scenes were unavailable and left out of the plot. Again, the correlation between the measure and the LVQ ATR results is fairly large. The correlation coefficient is 0.77. Using the weights trained from the HMMWV partition over the M35 partition, the correlation coefficient for the measure against the LVQ ATR and baseline detector is 0.86 and 0.59, respectively.

References

[1] L. A. Chan and N. M. Nasrabadi, "An application of wavelet-based vector quantization in target recognition," *International Journal on Artificial Intelligence Tools*, vol. 6, pp. 165–178, Apr. 1997.

[2] T. J. Meitzler, G. Gerhart, and H. Singh, "A relatic clutter metric," *IEEE Trans. on Aerospace and Electronic Systems*, vol. 34, pp. 968–976, July 1998.

[3] M. J. T. Smith and A. Docef, *A Study Guide for Digital Image Processing*. Riverdale, GA: GA Scientific Publishers, 1997.

[4] J. Cederquist, C. Dwan, J. Wegrzyn, and P. J. Rauss, "Spatial spectral ATR," in *Proceedings of the Third Annual ARL Federated Laboratory Advanced Sensors Symposium*, p. 331, Feb. 1999.

[1]The views and conclusions contained in this document are those of the authors and should not be interpreted as presenting the official policies either expressed or implied of the Army Research Laboratory or the U.S. Government.

PRESENTING AUTHOR INDEX

Adrian, Neal R.	U.S. Army Engineer Research and Development Center	EO3	123
Anderson, Ronald D.	U.S. Army Research Laboratory	CP3	75
Ballato, Arthur	U.S. Army Communications-Electronics Command	FO3	149
Barnes, Michael J.	U.S. Army Research Laboratory	IO3	239
Benson, J. D.	U.S. Army Night Vision Electronic Sensors Directorate	BO2	37
Beyer, R. A.	U.S. Army Research Laboratory	CP4	77
Beyer, Richard A.	U.S. Army Research Laboratory	CO5	69
Blackwell, Cynthia L.	U.S. Army Soldier and Biological Chemical Command	IP7	257
Bloemer, Mark	U.S. Army Aviation and Missile Command	BP7	57
Bodt, Barry	U.S. Army Research Laboratory	HP2	217
Bogetti, Travis A.	U.S. Army Research Laboratory	HP3	219
Bowden, C. M.	U.S. Army Aviation and Missile Research, Development, and Engineering Center	GO1	175
Bradshaw, John L.	U.S. Army Research Laboratory	BO1	35
Braue, Jr., E. H.	U.S. Army Medical Research Institute of Chemical Defense	DP6	107
Bunte, S. W.	U.S. Army Research Laboratory	CP1	71
Caldwell, J. A.	U.S. Army Aeromedical Research Laboratory	DP8	111
Chabalowski, C. F.	U.S. Army Research Laboratory	HP9	231
Chase, Ronald J.	U.S. Army Research Laboratory	HP1	215
Christesen, Steven	U.S. Army Edgewood Chemical Biological Center	GP3 GP7	189 197
Chu, Deryn	U.S. Army Research Laboratory	IO2	237
Coombe, H. S.	U.S. Army Communications-Electronics Command Research, Development and Engineering Center	FP7	167
Cote, P. J.	U.S. Army Tank-automotive and Armaments Command-Armament RD&E Center, Benét Laboratories	AP8	27
Cowan, F. M.	U.S. Army Medical Research Institute of Chemical Defense	GO4	181
Crawford, D. M.	U.S. Army Research Laboratory	AO3	7
Crenshaw, Michael E.	U.S. Army Aviation and Missile Command	BP1	45
Dammann, Jr., John F.	U.S. Army Research Laboratory	JP7	283
DeFrank, Joseph J.	U.S. Army Soldier and Biological Chemical Command	EO1	119
Demirbilek, Z.	U.S. Army Engineer Research and Development Center	FP9	171
Dibelka, Russell E.	U.S. Army Research Laboratory	HO5	213
Dubick, Michael A.	U.S. Army Institute of Surgical Research	DO5	95
Edelstein, A. S.	U.S. Army Research Laboratory	JO2	263
Edge, H. L.	U.S. Army Research Laboratory	HP6	225

Endrusick, Thomas L.	U.S. Army Research Institute of Environmental Medicine	IP5	253
Everitt, Henry O.	U.S. Army Research Laboratory	BO5	43
Fallesen, Jon J.	U.S. Army Research Institute for the Behavioral and Social Sciences	DO1	87
Filbert, Margaret G.	U.S. Army Medical Research Institute of Chemical Defense	DP7	109
Gade, Paul A.	U.S. Army Research Institute	DP4	103
Gibson, Phillip	U.S. Army Soldier Systems Center	FP1	155
Gillespie, James B.	U.S. Army Research Laboratory	EP3	133
Gordon, Richard K.	Walter Reed Army Institute of Research	JP4	277
Gorsich, David J.	U.S. Army Tank-automotive and Armaments Command	FO5	153
Guelta, M. A.	U.S. Army Edgewood Chemical Biological Center	FO1	145
Gunter, David D.	U.S. Army Tank-automotive and Armaments Command-Tank-automotive Research, Development and Engineering Center	HP4	221
Haas, Ellen	U.S. Army Research Laboratory	IO4	241
Harvey, Steven P.	U.S. Army Edgewood Chemical Biological Center	GP2	187
Hathaway, Michael D.	U.S. Army Research Laboratory	CP7	83
Hisley, Dixie M.	U.S. Army Research Laboratory	HO1	205
Holland, J. P.	U.S. Army Engineer Research and Development Center	EO2	121
Hoppel, C. P. R.	U.S. Army Research Laboratory	AO1	3
Howe, James D.	U.S. Army Communications-Electronics Command	JO5	269
Irish, J. L.	U.S. Army Engineer Research and Development Center	EO5	127
Ito, Max A.	U.S. Army Research Institute of Environmental Medicine	DP3	101
Jackson, Karen E.	U.S. Army Research Laboratory	GO5	183
Jameson, Terry C.	U.S. Army Research Laboratory	EP7	141
Johnson, Arthur R.	U.S. Army Research Laboratory	AP6	23
Johnson, J. B.	U.S. Army Engineer Research and Development Center	FO2	147
Johnson, Mark	U.S. Army Tank-automotive and Armaments Command-Armament RD&E Center, Benét Laboratories	BP6	55
Kalphat, Michelle	U.S. Army Simulation and Training Command	HP5	223
Karlsen, Robert E.	U.S. Army Tank-automotive and Armaments Command	JO3	265
Kathe, E.	U.S. Army Tank-automotive and Armaments Command-Armament RD&E Center, Benét Laboratories	CO2	63
Kiserow, Douglas J.	U.S. Army Research Laboratory	AO5	11
Koh, Gary	U.S. Army Engineer Research and Development Center	GP5	193
Krapels, Keith	U.S. Army Night Vision and Electronic Sensors Directorate	JP5	279
Lavery, John E.	U.S. Army Research Laboratory	HP8	229

Lopez, Issac	U.S. Army Research Laboratory	HP7	227
Mackie, David M.	U.S. Army Research Laboratory	BP4	51
McDonough, J. H.	U.S. Army Medical Research Institute of Chemical Defense	DO4	93
McGrath, Joseph	U.S. Army Research Institute of Environmental Medicine	JP2	273
McKnight, S. H.	U.S. Army Research Laboratory	AO2	5
McMillan, Robert W.	U.S. Army Space and Missile Defense Command	EP5	137
McNesby, K. L.	U.S. Army Research Laboratory	FP8	169
McQuaid, Michael J.	U.S. Army Research Laboratory	CP2	73
Mercurio, J. J.	U.S. Army Research Laboratory	EP6	139
Miletta, Joseph R.	U.S. Army Research Laboratory	GP8	199
Miziolek, Andrzej W.	U.S. Army Research Laboratory	JP6	281
Muller, Wayne S.	U.S. Army Soldier and Biological Chemical Command	IP1	245
Namburu, Raju R.	U.S. Army Research Laboratory	HO4	211
Nasrabadi, N. N.	U.S. Army Research Laboratory	JP9	287
Nasrabadi, Nasser M.	U.S. Army Research Laboratory	JO1	261
Nusca, Michael J.	U.S. Army Research Laboratory	CO3 EP1	65 129
O'Connell, Kevin P.	U.S. Army Soldier and Biological Chemical Command	GO3	179
Pfeffer, Robert	U.S. Army Nuclear and Chemical Agency	GP1	185
Pickard, D. W.	U.S. Army Soldier and Biological Chemical Command	FP6	165
Piscitelle, L.	U.S. Army Soldier and Biological Chemical Command	IO1	235
Ray, James C.	U.S. Army Engineer Research and Development Center	FP5	163
Resio, D. T.	U.S. Army Engineer Research and Development Center	FO4	151
Rice, Betsy M.	U.S. Army Research Laboratory	CO4 CP6	67 81
Ringelberg, D. B.	U.S. Army Environmental Research and Development Center	AP3	17
Rivin, D.	U.S. Army Soldier and Biological Chemical Command	IO5	243
Sands, James M.	U.S. Army Research Laboratory	AP4	19
Santoni, R. L.	U.S. Army Engineer Research and Development Center	EP2	131
Schaab, Brooke	U.S. Army Research Institute for the Behavioral and Social Sciences	DO2	89
Schihl, Peter	U.S. Army Tank-automotive and Armaments Command RD&E Center	CO1	61
Schilling, Bradley W.	U.S. Army Communications-Electronics Command Research, Development and Engineering Center	JP8	285
Scozzie, C. J.	U.S. Army Research Laboratory	BP5	53
Segletes, Steven B.	U.S. Army Research Laboratory	AP2	15
Sekowski, Jennifer W.	U.S. Army Soldier and Biological Chemical Command	GP4	191

Senecal, Kris J.	U.S. Army Soldier and Biological Chemical Command	AO4	9
Shen, Paul H.	U.S. Army Research Laboratory	BP3	49
Short, P. M.	U.S. Army Soldier and Biological Chemical Command	IP3	249
Simonis, G. J.	U.S. Army Research Laboratory	BP2	47
Smith, W. J.	U.S. Army Medical Research Institute of Chemical Defense	DO3	91
Smyth, Christopher C.	U.S. Army Research Laboratory	DP1	97
Specht, Dan	U.S. Army Engineer Research and Development Center	FP3	159
Storms, Russell L.	U.S. Army Research Laboratory	IP2	247
Sturek, Sr., Walter B.	U.S. Army Research Laboratory	HO3	209
Sullivan, Anders	U.S. Army Research Laboratory	HO2	207
Swami, Ananthram	U.S. Army Research Laboratory	JP3	275
Synowczynski, Jennifer	U.S. Army Research Laboratory	AP7	25
Taub, I. A.	U.S. Army Soldier and Biological Chemical Command	DP5	105
Thompson, Roy G.	U.S. Army Soldier and Biological Chemical Command	GP6	195
Thurber, Kent	U.S. Army Research Laboratory	BO3	39
Trevino, S. F.	U.S. Army Research Laboratory	AP9	29
Vause, Nancy	U.S. Army Research Laboratory	IP4	251
Walsh, Shawn M.	U.S. Army Research Laboratory	AP10	31
Walton, Ronald S.	U.S. Army Institute of Surgical Research	DP9	113
Weiss, Steve	U.S. Army Research Laboratory	JO4	267
Welch, Gerard E.	U.S. Army Research Laboratory	CP5	79
Wells, J. M.	U.S. Army Research Laboratory	FP2	157
West, Bruce J.	U.S. Army Research Laboratory	AP5	21
Wetzel, E. D.	U.S. Army Research Laboratory	AP1	13
Wiegand, Donald A.	Energetics and Warheads Division, Warheads, Energetics and Combat Support Armaments Center, Armament RD&E Center	FP4	161
Wilson, D. Keith	U.S. Army Research Laboratory	EP4	135
Wilusz, Eugene	U.S. Army Soldier and Biological Chemical Command	GO2	177
Wisher, Robert A.	U.S. Army Research Institute for the Behavioral and Social Sciences	DP10	115
Witmer, Bob G.	U.S. Army Research Institute for the Behavioral and Social Sciences	DP2	99
Wood, Sheila J.	U.S. Army Soldier and Biological Chemical Command	EO4	125
Woolard, D. L.	U.S. Army Research Laboratory	GP9	201
Wraback, M.	U.S. Army Research Laboratory	BO4	41
Yang, T. C. S.	U.S. Army Soldier and Biological Chemical Command	IP6	255